# A novel platform for highly integrated solar heat in carbon capture technology – Final report

**Dia Milani**

**CSIRO Energy**

**10 Murray-Dwyer Circuit, Mayfield West, NSW 2304, Australia**

**Minh Tri Luu, Scott Nelson, Yuqing Li, Si Suo, Ali Abbas**

**School of Chemical and Biomolecular Engineering, The University of Sydney, NSW 2006, Australia**

| | |
|---|---|
| **Project number:** | RDE493-30 |
| **Project start date:** | 16/01/2019 |
| **Project end date:** | 09/06/2021 |
| **Report period:** | 16/01/2019 – 09/06/2021 |
| **Submission date**: | 10/06/2021 |
| **Revision submission date**: | 10/09/2021 |

# Acknowledgment

# Copyright and disclaimer

# Important disclaimer

# Executive summary

## *The problem*

Global warming and climate change are directly linked to ever-increasing anthropogenic fossil-based energy consumption and other industrial activities. Carbon capture and storage (CCS) is widely recognised as one effective option to mitigate the catastrophic impact of the climate change, via decarbonising energy-intensive industrial activities that involve ongoing use of fossil fuels. A well-recognised solution to effectively reduce greenhouse gas (GHG) emissions, particularly from commercial-scale coal-fired power plants, is the prominent technology of amine-based post-combustion carbon capture (PCC). Given the excessive thermal energy demand of PCC and its potential impact on power production, it has previously been proposed that part/all of the energy penalty could be offset by integrating solar power with the PCC solvent regeneration process. To offset part of the substantial energy penalty using solar-thermal technologies, solar-assisted PCC (SA-PCC) has been proposed as an investment strategy option. In this method, a portion of the steam required for solvent regeneration would be directly sustained from a solar collector field (SCF). Through this, the steam bled from the power cycle would be reduced and the power plant capacity would be increased.

In countries such as Australia, with an abundance of land and solar resources, the SA-PCC concept could be an attractive option for either providing thermal energy for PCC, or for power plant repowering when it provides the essential steam for PCC. However, three main techno-economic challenges may hinder the viability of integrating this concept into a PCC plant: (1) solar intermittency, (2) large capital costs for SCF installation, and (3) affordable and reliable thermal energy storage (TES). Moreover, this configuration of solar thermal integration increases the process complexity, escalates and energy/exergy losses, uses more equipment, and increases the cost of the entire PCC plant. To date, the SA-PCC technology option has been far from commercial readiness.

## *The objective*

This project aims at simplifying solar integration by directly utilising solar heat in the solvent regeneration process. In this method, steam is not produced in the SCF, but the rich solvent is pumped into a network of 'solar-strippers' (So-St)s to directly absorb solar heat and promptly release the $CO_2$. As a result, heat transfer is improved, and energy/exergy losses are minimised. As the solvent is directly regenerated in the SCF, the typical desorption unit, including the conventional bulky stripper and reboiler, can be eliminated. This arrangement is anticipated to minimise the interaction between the power plant and the PCC, and promote an independent carbon capture process away from the power plant steam cycle. Achieving this objective can restore the power plant production to full capacity while adhering to low-emission power production goals.

## *The solution*

In this method, the $CO_2$-rich solvent leaving the absorber can be directly pumped into the SCF to run across the receiver tubes of the solar collectors. Instead of generating steam in the SCF, the rich

solvent can directly absorb solar heat and instantaneously release $CO_2$ gas as the solvent flows through the solar receiver tubes. At the end of each tube segment, the gas/vapour can be vented, while the remaining liquid solvent is regenerated in the next segment(s). The key advantage of this novel concept is that it will eliminate the conventional desorption unit while also preventing steam bleeding from the power plant, thus making the capture process completely independent and sustainable. The other advantage of this proposal is that costly TES is no longer needed, and can be replaced by solvent storage. Solvent storage does not require the multi-layer thermal insulation and can be easily managed. Unlike TES, solvent storage can be easily sized to maintain solvent availability in long-lasting stormy or cloudy weather conditions. This configuration would provide convenience for plant operators and assurance that their power cycle will remain intact.

*Key outcomes/findings*

This project is unique in that it transforms the traditional concept of SA-PCC, and introduces a new frontier of 'solar-powered' PCC (SP-PCC). The SP-PCC concept is the first of its kind in the open literature. In this inaugural project, we have developed the first steps of a commercialisation pathway for SP-PCC. Our work has comprised deep theoretical and modelling studies in seven interconnected milestones to evaluate this novel technology, and optimise different processes, designs and sizing variables. The key findings are summarised below.

1. Solvent regeneration can technically be achieved under transient conditions irrespective of thermal media if an adequate source of heat is used. In this project, steam as a source of thermal input has been eliminated.

2. Energy storage is not the only way to address irregularities in renewable energy sources (e.g. solar intermittency) to power a process. Other innovative ways should be explored, such as water storage for a desalination process powered by renewable energyies. In this project, we introduce solvent storage to synchronise the steady-state operation in the absorber with the dynamic operation in the SCF.

3. The So-St network in the SCF can be tailor-designed based on the meteorological data of any location, the target capture rate and techno-economic feasibility parameters. In this work, we developed a design protocol that can rapidly size the project, and compute the levelised cost of captured/avoided $CO_2$ and the impact on the levelised cost of the electricity.

4. Process intensification is a vital part of developing new processes or improving the efficiency of existing processes. In this project, we used a computational fluid dynamic platform to capitalise on revenue for process intensification.

5. Adequate process control is an effective tool to stabilise and optimise operation under transient conditions. In this project, we developed a full process-control expert system to mitigate and digest solar intermittency in a safe and productive manner.

6. The sizing of the SCF is not always driven solely by economic parameters. Sometimes, specific restrictions might be imposed by the site's physical dimensions, adoptable pressure-drop range, temperature cap or the process energy demand. In this project, we developed several criteria to shortlist the most promising designs before conducting rigorous and time-intensive verification for each design.

7. Solvent storage does not need to be bulky to maintain solvent availability at both terminals of the solvent cycle (absorption and desorption). In this project, we developed practical methods to substantially reduce solvent storage capacity using a novel concept of 'mix-match' multi-tank storage.

8. Solvent storage size is inherently related to the size of the So-St network. Unlike thermal energy storage in SA-PCC, increasing the size of the SCF would substantially reduce solvent storage capacity. In this project, we optimised this relationship in our design protocol.

9. The cost estimate of SP-PCC is currently higher than conventional PCC or its optimised SA-PCC counterparts. The levelised cost of electricity for SP-PCC is approximately 58 and 46% higher than the PCC and SA-PCC counterparts, respectively. The high cost of SP-PCC is mainly attributed to its 100% solar energy supply; hence, it would require a large SCF and sufficient solvent storage to fully drive solvent regeneration process in all seasons. It is commonly anticipated that a 100% solar energy supply is usually cost-prohibitive, mostly due to the high upfront investment required. In this project, we deployed several optimisation methods to bring the cost of SP-PCC down to a competitive range, particularly with the SA-PCC counterpart.

10. To fairly compare the economics of SP-PCC with the equivalent SA-PCC, both at 100% solar fraction, the SP-PCC option outperforms the SA-PCC by more than five-fold. In this project, the SCF and solvent storage sizing are conservatively applied for a bare-tube So-St configuration, irrespective of the potential process intensification measures. The reported cost estimates also correspond to this base-case design, but we believe there are many potential avenues for cost reduction.

11. The environmental footprint of SP-PCC is relatively better because of the steam preservation being entirely used for power production. Despite the environmental impact of the bulky solvent and extended SCF, the equivalent global warming potential per energy unit for SP-PCC is relatively lower and the $CO_2$ abatement is relatively higher. The greater sustainability of SP-PCC as a result of preserving the steam only for power production is a major attainment from this project. Therefore, if a process requires 100% solar energy utilisation where steam production is not part of normal routine (e.g. steel and cement industries), SP-PCC would be the best technology option.

12. The techno-economic study in this inaugural is conservatively analysed. Many parameters can be further scrutinised and optimised in follow-up projects. Primarily, two main routes for possible process intensification and improved techno-economics are identified. One route would require systematic solvent screening to identify the optimal solvent or blend of solvents for the SP-PCC process. The second route would pursue improved internal geometries of the So-St tubes for greater heat transfer at the lowest pressure drops.

# Lay summary

Coal is the world's largest single source of electricity. Coal-fired power plants currently fuel 37% of global electricity demand, and will continue to contribute 22% of the world's electricity by 2040. In Australia, fossil fuels contributed up to 79% of the total electricity generation in 2019, including 56% from coal. The greenhouse gas emissions resulting from humanity's reliance on burning coal and other fossil fuels for electricity has contributed to the catastrophic effects of climate change.

To help address climate change through reducing carbon dioxide ($CO_2$) emissions from coal-fired power-plants, cement manufacture and metal refining industries, post-combustion carbon capture (PCC) is regarded as the most feasible, near-term technology. Among several technology options, solvent-based PCC would require the least effort to retrofit to existing coal-fired power plants, and therefore, is the most accessible technology option. However, the very high thermal energy demand of the PCC process and its potential impact on power production has prevented the strategic investment needed for the wide adoption of this technology.

Alternatively, solar-assisted PCC (SA-PCC) has been proposed as an investment strategy option to offset part of the substantial energy penalty of PCC. In an SA-PCC system, a portion of the steam used the drive the power station turbines is either directly generated in the absorber tubes of the solar collectors, or indirectly in the heat exchangers, which are heated by a heat transfer fluid (HTF) mediator. In both routes, a considerable portion of solar energy is subject to heat losses to the surroundings. Additionally, the intermittency of solar resources and interruptions to supply, along with the costly thermal energy storage (TES) requirement, mean that the SA-PCC option is far from commercialization readiness.

In this project, we aim at direct utilisation of solar heat generated by a solar collector field in a solvent-based PCC process to completely stop steam bleeding from the power plant for the purpose of solvent regeneration. This arrangement, called 'solar-powered' PCC (SP-PCC), is anticipated to minimise interaction between the power plant and the PCC plant, and promote carbon capture with an almost zero carbon footprint. Moreover, this novel process can be customised for other emission-intensive industrial processes (e.g. steel, cement and aluminium) that do not have steam production as part of their ordinary routine.

This project comprises a rigorous theoretical study for a 'solar-stripper' (So-St) network design to promote SP-PCC technology over its SA-PCC counterpart. The main objective of the So-St technology is to completely move away from fossil fuel consumption. The multi-scale project started by optimising the physical properties for a single So-St unit, then using the modularity of a So-St unit in the full design of the solar collector field and solvent storage system. The internal design complication of a So-St unit was analysed and optimised using a computational fluid dynamics platform to address the complex thermo-physics, including boiling flow, heat transfer, reaction kinetics and thermodynamics, relevant to the So-St process. The key challenge of this superstructure is in synchronising the operation of the absorber, the So-St network and the solvent storage facilities under the dynamic and transient conditions associated with solar availability. We have addressed

this by developing an advanced process control expert system. With appropriate design and using an effective control strategy, the So-St network can operate transiently while achieving the required $CO_2$ capture target throughout the entire year. The cost of this technology is relatively higher than standard PCC at this inaugural stage, but the process intensification, size reduction and cost optimisation can still be improved. The greater sustainability as a result of preserving the steam only for power production is a major accomplishment from this project.

# Contents

# Figures

# Tables

# Abbreviations

| | |
|---|---|
| AACR | average annual capture rate |
| API | American Petroleum Institute |
| *BEP* | break-even point |
| CAPCOST | Capital Equipment-Costing Program |
| *CAPEX* | capital expenditure |
| CCS | carbon capture and storage |
| CFD | computational fluid dynamics |
| CINSW | Coal Innovations New South Wales |
| CSIRO | Commonwealth Scientific and Industrial Research Organisation |
| *ED* | energy demand |
| *EHT* | enhanced heat transfer |
| FCV | finite control volume |
| *FOM* | fixed operation & maintenance |
| GHG | greenhouse gases |
| HPD | high pressure-drop |
| HTF | heat transfer fluid |
| HX | heat exchanger |
| KPI | key performance indicator |
| LCA | life cycle analysis |
| LCI | life cycle inventory |
| *LCOE* | levelised cost of electricity |
| *LLV* | lean loading value |
| LPD | low pressure-drop |
| MEA | Monoethanolamine |
| MST | multi storage tanks |
| *OPEX* | operational expenditure |
| *PBP* | payback period |
| PCC | post-combustion carbon capture |
| PFD | process flow diagram |
| PTC | parabolic trough collector |
| RANS | Reynolds-Averaged Navier Stokes |
| REC | renewable energy certificate |
| SA-PCC | solar-assisted PCC |
| SCF | solar collector field |
| *SET* | solar energy tolerance |
| *SF* | solar fraction |
| *SHF* | solar heat flux |
| *SL* | solvent level |
| *SM* | solar multiple |
| So-St | solar stripper |

| SP-PCC | solar-powered PCC |
|--------|-------------------|
| *SSC* | solvent storage capacity |
| *SST* | solvent storage tank |
| *SUR* | solvent storage utilisation ratio |
| TES | thermal energy storage |
| *VMF* | vapour molar fraction |
| *VOM* | variable operation & maintenance |

# 1.   Introduction

Coal is the world's largest single source of electricity. Coal-fired power-plants currently fuel 37% of global electricity demand and will continue to contribute 22% of the world's electricity by 2040 [1]. In Australia, fossil fuels contributed up to 79% of the total electricity generation in 2019, including 56% from coal [2]. To address the greenhouse gas (GHG) emissions produced by coal-fired power-plants, carbon capture and sequestration (CCS) is a widely recognised mitigation option. Of the available technology options for CCS, solvent-based post-combustion carbon capture (PCC) would require a marginal retrofit to existing coal-fired power-plants, and therefore is the most accessible option worldwide. The key restraint for the strategic investment and wide adoption of the PCC technology comes from its very high thermal energy demand, which results in a substantial impact on power production. This is often termed the 'energy penalty' [3]. Thermal energy is typically bled from the power-plant steam cycle for the purpose of solvent regeneration in the PCC (Figure 1). The energy penalty can vary from 20% up to 40% of the power-plant capacity [4, 5]. Reducing the cost of this technology to feasible levels would not only require cheaper process designs, but also innovation in the design to minimise the operational energy penalty while responding to relevant market, social, regulatory, political, economic and environmental drivers. Much research has been conducted on heat integration for a power-plant retrofitted with PCC to improve process efficiency and reduce the energy penalty [6-10]. However, the reported improvements on these processes has not extensively improved the popularity or adoption of PCC technology.
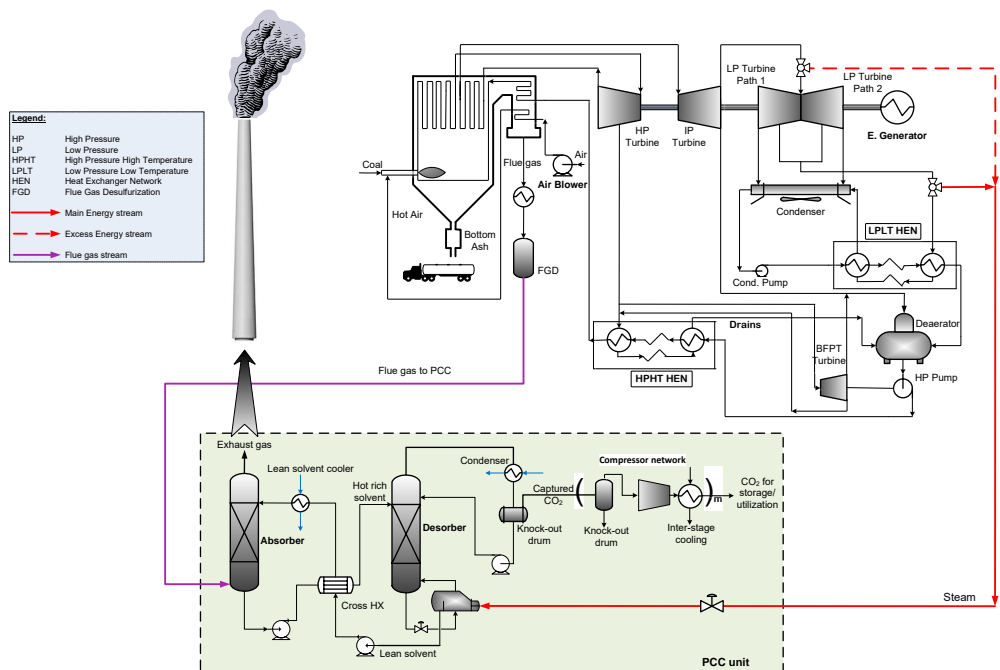


**Figure 1: A schematic of the solvent-based PCC process retrofitted to a power-plant where the reboiler duty is sourced from the power-plant steam cycle.**

Solar-assisted PCC (SA-PCC) has been proposed as an alternative investment strategy option to offset part of the substantial energy penalty via solar-thermal technologies. In countries such as Australia, with its abundance of land and solar energy, this concept could be attractive for either providing thermal energy for the PCC process, or for power-plant repowering. Several solar integration methods with various temperature ranges are discussed in the literature [11]. In the low-temperature integration category required for solvent regeneration, low-pressure steam is often generated in the solar collector field (SCF) using either linear Fresnel or parabolic trough collectors. The generated steam can be sent to the cold reheat line or the low-pressure (LP) admission line (Figure 2) [12].

The three direct steam-generation processes in the solar receivers are: once-through, injection and recirculation. In the once-through process, the feedwater entering the collector rows is gradually converted into superheated steam as it passes through the collector circuit. In the injection process, small quantities of feed water are injected along the collector tubes. In the recirculation process, a water-steam separator is placed at the end of the solar collector system [13]. Solar thermal input into PCC-retrofitted power-plants, also called 'solar repowering', can be implemented by either of two methods [14]. The first is via the installation of an individual boiler to deliver the required steam for the solvent regeneration process and avoid steam extraction from the power-plant steam cycle. The second method is to extract equivalent regeneration energy from the power-plant steam cycle, but use an adequately-sized SCF to compensate for the lost electricity and prevent capacity reduction [14]. Both options would require a large investment in SCF and an exorbitant cost for thermal energy storage (TES) to maintain nonstop operation when solar energy is unavailable.

Generally, solar-thermal energy integration in PCC processes face three main challenges: (1) solar intermittency, (2) large capital cost for SCF installation, and (3) affordable and reliable TES. All the studies noted assumed the use of a working fluid, such as water, which is heated to generate quality steam (or high-temperature water) to be used in the reboiler. An alternative approach is to use other suitable heat transfer fluids (HTFs), such as high-temperature synthetic oils, molten salts or phase-change materials (PCMs) to store thermal energy for later use (when solar is unavailable) to generate steam. Previous studies [15, 16] have shown that a large amount of capital expenditure is required for SCF and TES installation to directly provide a reliable thermal energy requirement for a PCC reboiler. The heat content of the generated steam or hot water would ultimately be used in the desorber to heat the rich solvent and break $CO_2$–solvent reaction bonds [17]. This process is followed by separating the $CO_2$ gas to be compressed and transported to the sequestration site, while the lean solvent is recycled back to the absorbers. This configuration of solar thermal integration not only increases process complexity and energy losses, but also uses more equipment and increases the cost for the entire plant [16]. Furthermore, it is widely accepted that part of the solar energy is subject to exergy degradation via heat conduction through the connecting pipes, heat exchangers (HXs) and TES tanks, which results in over-sizing and over-investment of the SCF [18-20].
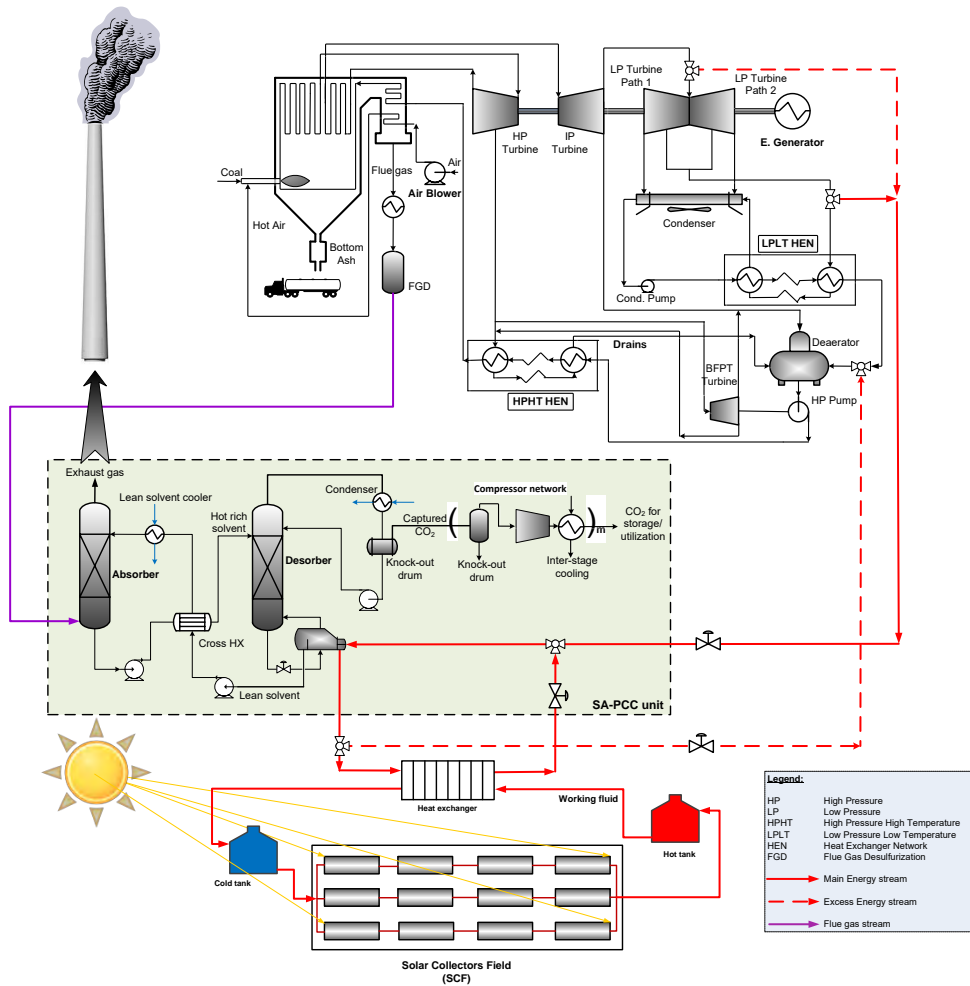
**Figure 2: A schematic of a coal-fired power-plant with PCC sourcing the reboiler duty by integrating the solar thermal energy into the power-plant steam cycle (SA-PCC).**

To reduce exergy degradation in the SA-PCC process, Wibberley from CSIRO has patented a method for solvent regeneration using an SCF along with solvent storage [21]. In Wibberley's method, the rich solvent exiting the absorber can be stored in solvent storage tanks (SSTs) during peak power demand, rather than being immediately delivered to the desorption unit. This option eliminates the steam extraction from the power cycle for the purpose of solvent regeneration in those peak hours, or when solar radiation is unavailable. At off-peak periods or during abundant solar radiation times, the rich solvent regeneration is boosted proportionally to the thermal energy supplied by the sun. The excess regenerated solvent (lean solvent) can then be stored for later use during peak demand hours or at night. The patent also proposed separating the absorption unit from the desorption unit by keeping the absorber close to the power plant, while the desorber and SSTs are kept near the SCF. Placing the desorber near the SCF would allegedly reduce the heat loss from the HTF. However, using a HTF (e.g. synthetic oil or water) to circulate in the SCF and eventually exchange heat with the solvent via a conventional reboiler would still compromise the energy and exergy efficiencies. Furthermore, the desorption unit will need careful sizing to accommodate the surge in solvent/steam flow dynamics during abundant solar radiation times. The operational stability and thermodynamics in the desorber would also be disrupted as a result of frequent start-ups and shut-downs. Hence, it is evident that much more process improvement is required to effectively integrate solar with the PCC technology, entailing continued research and development.

More recently, we proposed a novel proof of concept to improve SA-PCC process integration [22]. In this method, $CO_2$-rich solvent exiting the absorber is directly pumped into the SCF to run across the receiver tubes of the solar collectors. Instead of generating steam in the SCF, the rich solvent can directly absorb solar heat and instantaneously release $CO_2$ gas as the solvent flows through the solar receiver tubes. At the end of each tube segment, the gas can be vented out, and the remaining liquid solvent is regenerated in the next segment(s). In this configuration, we anticipated that the typical desorption unit used in PCC, including the complex stripper and the reboiler, were no longer needed and could be eliminated. The elimination of the stripper and the reboiler could save up to 15–30% of the total PCC cost [23, 24], which can contribute to offset the capital cost of the SCF.

Instead of entering a typical bulky stripper, the rich solvent is directly regenerated in a 'solar-stripper' (So-St) network in the SCF. The key advantage of this novel concept is that it both eliminates the conventional desorption unit and prevents steam bleeding from the power-plant. It thus makes the $CO_2$ capture process completely independent and sustainable. This configuration may provide convenience and assurance for plant operators that their power cycle will remain intact when integrated with solar. As a result, our project elevates the notion of SA-PCC to a new frontier of 'solar-powered' PCC (SP-PCC). Figure 3 presents a diagram of this SP-PCC configuration, where direct steam bleeding from the power-plant is not required for solvent regeneration in PCC.
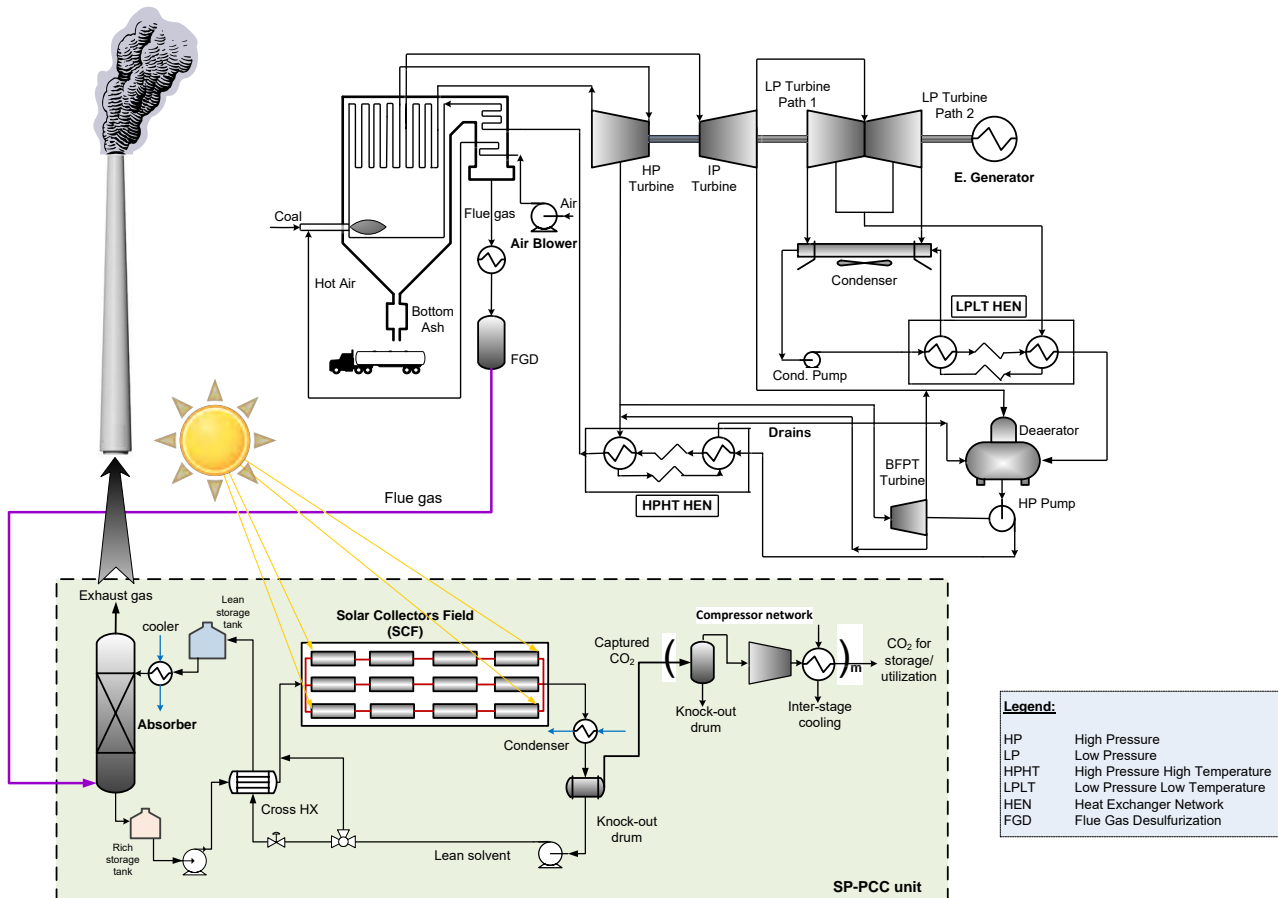


**Figure 3: A schematic of a coal-fired power-plant with PCC where the SCF replaces the desorption unit in the PCC. The SCF provides 100% of thermal energy and no steam is bled from the power-plant (SP-PCC).**

## 1.1    **Aims**

In this project, we aim at direct utilisation of solar heat in a solvent-based carbon capture process that completely stops steam bleeding from the power plant for the purpose of solvent regeneration in the PCC. This arrangement is anticipated to minimise the interaction between the power plant and the PCC plant and promote carbon capture at an almost zero carbon footprint. The objectives of this project are to achieve:

1.  steamless carbon capture

2.  minimal interaction between the power plant and the PCC plant

3.  lower cost for carbon capture at almost zero carbon footprint.

## 1.2    **Scope**

This project comprises a rigorous thermodynamic study for a So-St network design to promote SP-PCC technology over its SA-PCC counterpart. We start by optimising the physical properties for a single So-St unit based on the thermodynamic behaviour of the solvent under a consistent heat source. The internal design physics of a So-St unit is analysed and optimised using a computational fluid dynamics (CFD) platform to address the complex thermophysical parameters, including boiling flow, heat transfer, reaction kinetics and thermodynamics relevant to the So-St process. Once the nominal design parameters are identified, the structure of one So-St module incorporating several segments interconnected in sequence is determined. Then, the modularity of a So-St unit is used to obtain the correct So-St network sizing. As the rich solvent is transiently regenerated within the SCF, the misalignment between the steady-state operation of the absorbers and the dynamic operation in the SCF needs to be regulated/buffered by the SSTs. The key challenge of this superstructure is in synchronising the operation of the absorber, the So-St network and the solvent storage facilities under dynamic and transient conditions, which would require an advanced process control system. This fundamental work will eventually lead to sizing and designing the entire SCF and the solvent storage, tailored for a specific case-study. As the integration of these sub-models into the whole SP-PCC plant superstructure is of particular interest, we continued synergising the sub-models throughout the project. Figure 4 illustrates the multi-level structure of our work and the integration of various sub-models to determine the optimal model for the whole superstructure. In doing this, our rigorous assessment of the SP-PCC involves continual checking against clear and well-defined criteria. We also maintain regular performance checkpoints against the equivalent PCC and SA-PCC counterparts. Accordingly, we define key performance indicators (KPIs) for full techno-economic and life cycle assessments of these three technologies.

For this project, a conceptual commercial-scale, 660-$MW_e$ coal-fired power plant located near Sydney, NSW is selected. This power plant typically emits ~3000 tonnes of flue gas each hour at full capacity. However, because of electricity market demand fluctuations, the power load varies frequently, and the flue gas yield would be proportional to this variation. Assuming a $CO_2$ content of ~20 *wt%* in the flue gas, if a carbon capture rate of a 1.5 million $tonne_{CO2}$ per annum is targeted, then typically we need to process at least ~34% of the flue gas in the retrofitted PCC plant for that

purpose. This arrangement would secure a baseline flue gas flow to the PCC plant. Clearly, if the power-plant works on partial load down to ~34% of the nominal load, for example, the PCC plant can still have the same baseline uptake, which in this case will be equal to the entire flue gas mass flowrate out of the power plant's stack. This configuration also helps to stabilise the operation conditions at the PCC plant and any other plant retrofitted thereafter to capture and sequester 1.5 million tonne$_{CO2}$ per annum.

The reference PCC plant consists of two absorbers and one large stripper. This PCC plant uses the benchmark 30 *wt*% monoethanolamine (MEA) solvent and is able to capture 90% of $CO_2$ emissions (~181 tonne$_{CO2}$/h) at 99% $CO_2$ product purity. Two streams of water and MEA makeups are added to maintain the balance of the solvent and compensate for the lost species in the exit streams. For a steady-state PCC operation running constantly for an entire year, mathematically, this will lead to a capture amount of 1.585 million tonne$_{CO2}$ per annum. However, as the nominal target is set at 1.5 million tonne$_{CO2}$ per year, this arrangement will allow for ~18 days per year stoppage time for the absorber maintenance. This can play a significant role in reducing the size of the SCF and solvent storage capacity (*SSC*) of the SP-PCC. The provision of this stoppage time will be emphasised in the subsequent SCF and *SSC* sizing work.
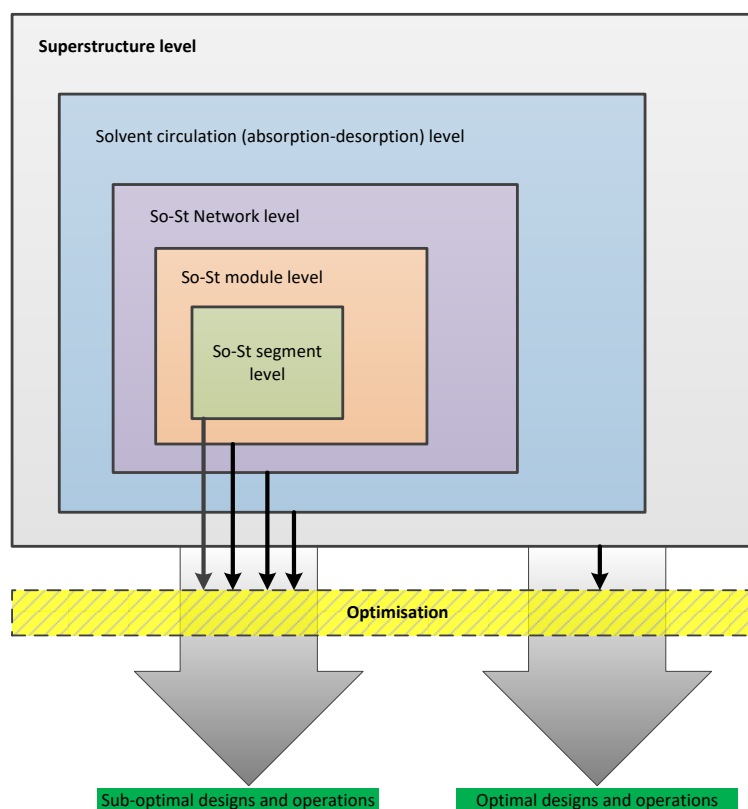


**Figure 4: A representation of the different modelling envelopes. Optimisation can be carried out at individual modelling levels leading to sub-optimal solutions. However, conducting model-based optimisation at higher superstructure levels can lead to optimality in design and operations.**

## 1.3    Report outline

This project facilitated a number of software such as *ASPEN®, COMSOL Multiphysics®, TRNSYS®, MATLAB®* and *SAM®*, in addition to the common *OpenLCA®* platform coupled with the *EcoInvent*

database. During this project, CSIRO worked in close collaboration with the University of Sydney, making use of the university's high-performance computing infrastructure to deliver the project's seven interconnected milestones. Figure 5 illustrates the flowchart of this project, which was frequently revised and updated to reflect the tasks described for each individual milestone. Chapters 2 to 9 of this report highlight these activities in sequence, as illustrated in the flowchart. Table 1 summarises the milestones and their performance measures.
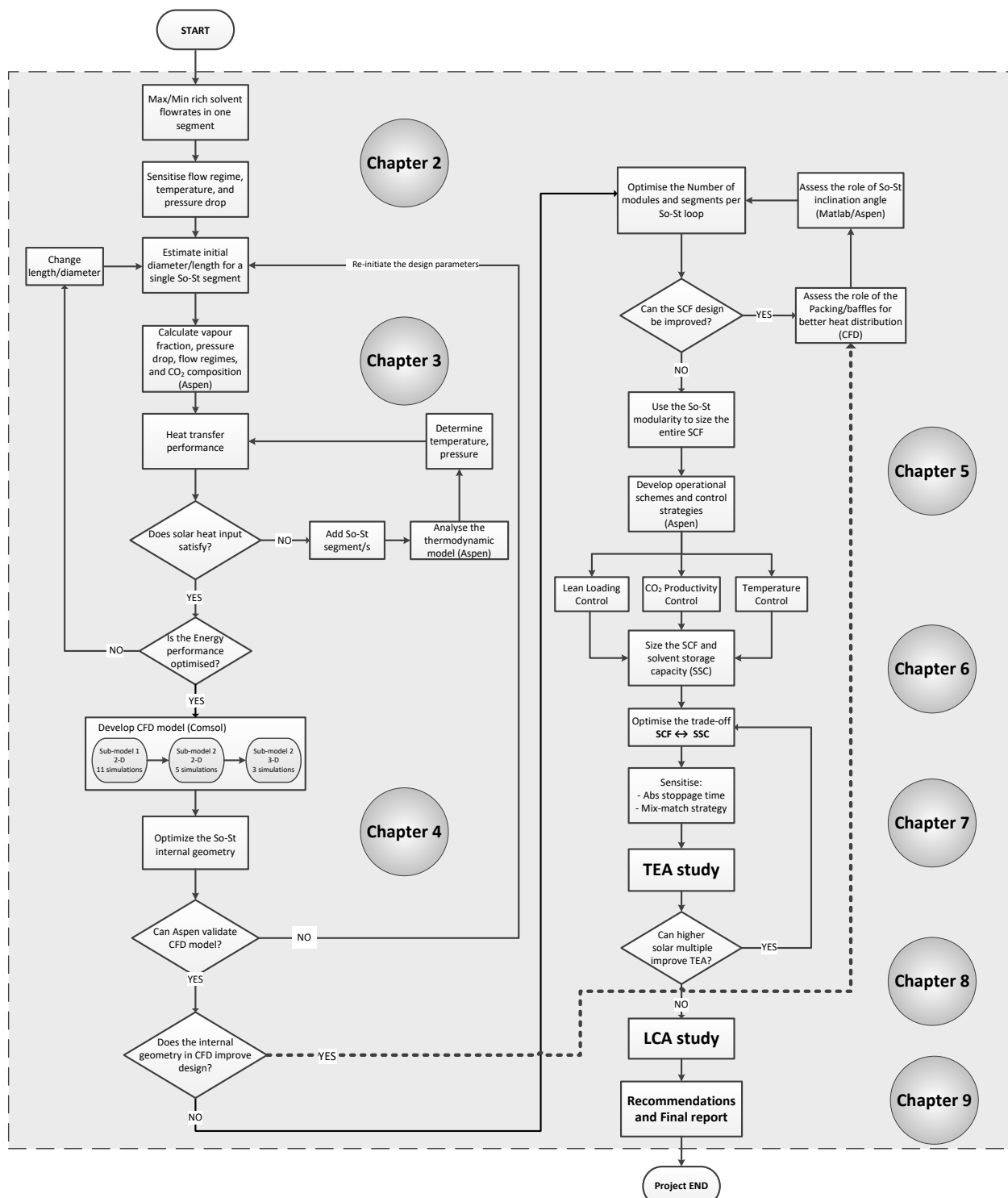
**Figure 5: Flowchart of the structure and the development of this project.**

**Table 1: Project milestones and performance measures.**

| Milestones | Tasks | Performance measures | Status (%) |
|---|---|---|---|
| **M1**<br>Q1 to Q3, 2019 | Identify and optimise the key design parameters for a single So-St. | List the initial process models and baseline conditions and develop the framework. Identify, prioritise, sensitise and optimise the key design parameters for a single So-St segment, by completing the following tasks:<br>• Analyse the flow thermodynamic and reaction kinetics.<br>• Promote hybrid design parameters against the typical co-current and counter-current flows.<br>• Characterise and categorise various flow regimes.<br>• Evaluate the effect of flow pressure and temperature on the phase separation. | 100% |
| **M2**<br>Q2 to Q4, 2019 | Investigate reaction kinetics and physio-chemical under various flowrates and heat profiles. | Reaction kinetics and physio-chemical study under various flowrates and heat profiles. Manipulate the key parameters to promote the target species and limit the reverse reactions. Optimise the $CO_2$ detachment and separation. Identify and optimise the flow control mechanisms by completing the following tasks:<br>• Address the role of water vaporisation.<br>• Characterise the flow regime by the tube layout conditions.<br>• Assess the heat transfer for two-phase flow regime.<br>• Expand the design analysis for a So-St module/loop.<br>• Introduce methods for enhanced heat transfer.<br>• Identify mechanisms for phase separation at the exit of each So-St segment. | 100% |
| **M3**<br>Q1 to Q3, 2020 | Develop CFD model for mass and energy transfer under transient conditions and evaluate possible design improvements. | Develop the CFD model for a single short So-St tube to depict the internal mass and energy transfer. Identify and optimise potential internal inserts to enhance the heat transfer by completing the following tasks:<br>• Set up the design specs in the CFD appropriately.<br>• Validate the CFD model against Aspen® and/or literature.<br>• Evaluate the model performance under uniform and non-uniform heat profiles.<br>• Quantify the effect of the transient conditions and heat distribution on the So-St circumference inducing the multiphase flow and gas separation.<br>• Compare the performance of the tube inserts with the reference bare tube.<br>• Assess the advantages of the tube inserts on the overall SCF size and pumping requirement. | 100% |
| **M4**<br>Q4, 2019 to Q2, 2020 | Develop operational modes and control logics in contingency with solvent inventory. | Scale-up and optimise the SCF and develop operational modes based on valid control logics in contingency with the operation in the absorber and the solvent inventory. Assess various control strategies and create functional control scenarios by completing the following tasks:<br>• Set up a clear structure for control strategies development and testing.<br>• Identify the control variables and constraints.<br>• Assess the influence of solar heat flux on the control actions and logics.<br>• Define the solar energy tolerance range for each control strategy.<br>• Describe the control actions in non-productive solar periods.<br>• Develop the control schemes for day/night and seasonal operation.<br>• Complete the process control system. | 100% |

| | | | |
|---|---|---|---|
| | | • Evaluate the performance of control scenarios over one-year operation.<br>• Examine the control actions for the worst/average/best solar days. | |
| **M5**<br>Q2 to Q4, 2020 | Scale-up and optimise the superstructure SCF and size the solvent inventory to effectively maintain process continuity under solar transient conditions. | Develop a generic design protocol for both SCF and solvent storage that can broadly be used for any case-study. Size the So-St network and the rich/lean solvent inventory under various solar multiple scenarios by completing the following tasks:<br>• Identify the key sizing parameters for the superstructure.<br>• Develop the sophisticated So-St network design protocol.<br>• Generate design database.<br>• Apply the appropriate design filters to refine and short-list promising designs.<br>• Describe the design principles for the solvent storage capacity (*SSC*).<br>• Optimise the absorber stoppage time.<br>• Realise the correlation between the SCF and *SSC* sizing.<br>• Examine the novel idea of mix-match storage strategy.<br>• Calculate the design parameters under various solar multiples and solvent storage methods. | 100% |
| **M6**<br>Q3 to Q4, 2020 | Comparative full-scale techno-economic assessment with the typical PCC and the SA-PCC at both ideal and optimised options. | Setup a fair and transparent appraisal platform to compare the three capture scenarios PCC, SA-PCC and SP-PCC in reference to the power plant only (with no capture) by accomplishing the following tasks:<br>• Define and list the applicable economic parameters and assumptions.<br>• Develop the model structure for *CAPEX*, *OPEX*, and the levelised cost of energy (*LCOE*).<br>• Validate the economic model against the literature.<br>• Sensitise the SCF and solvent storage on economic bases.<br>• Sensitise the key economic parameters.<br>• Compute the steam saving and excess power generation in comparison with the benchmark PCC & SPCC.<br>• Evaluate the influence of government incentive programs on the adoption of various technologies. | 100% |
| **M7**<br>Q4 2020 to Q1 2021 | Comparative life cycle analysis at full-scale in respect to the typical PCC and the SA-PCC at both ideal and optimised options. | Setup a fair and transparent appraisal platform to compare the LCA of the three capture scenarios PCC, SA-PCC and SP-PCC in reference to the power-plant only (with no capture) by accomplishing the following tasks:<br>• Define cycle analysis method and select cradle-to-grave framework.<br>• Describe life cycle inventory for all cycle components.<br>• Explain the cycle impact assessment criteria.<br>• Highlight and discuss the impact analysis results.<br>• Sensitise the impact of flue gas processing rate.<br>• Sensitise the impact of solar multiples.<br>• Summarise the $CO_2$ avoided and abatement costs<br>• Discuss possible improvement concepts for LCA. | 100% |

# 2. Fundamentals of the solar-stripper (So-St)

In this chapter, we analyse the thermodynamic aspects of a single segment of a solar-stripper (So-St) to optimise the $CO_2$ stripping performance. We confirmed that increasing the solvent temperature can help to release the $CO_2$ from the liquid phase. The stripped $CO_2$ should be instantly removed from the vapour phase to maintain low $CO_2$ partial pressure to stimulate further stripping. In this chapter, flow regimes are analysed at different liquid and vapour velocities for a specific So-St diameter. By choosing an appropriate So-St diameter, safe operation flow regime is distinguishable. Hence, we analyse in detail the operation conditions of a So-St segment, aiming to understand the thermodynamic principles of the $CO_2$ desorption process. Those analyses are expected to result in the following outcomes:

- Identify the thermodynamic limitation on the stripping performance.
- Obtain insight on the possible design and $CO_2$ stripping mechanism for efficient operation.
- Attain preliminary conceptualisation of the So-St design and sizing.

## 2.1 Reaction kinetics

For the $CO_2$/MEA aqueous system, the gas phase can be assumed to be ideal because the operating pressure is relatively low (1–2 bar), thus the following equations can be used to calculate the partial pressures of the $CO_2$ ($p_{CO_2}$), $H_2O$ ($p_{H_2O}$), and MEA ($p_{MEA}$) in the gas phase:

$$p_i = y_i P \qquad\qquad Eq.\ 1$$

Where $p_i$ (Pa) is the partial pressure of component $i$ in the gas phase; $y_i$ is the gas mole fraction of component $I$; and $P$ (Pa) is the total pressure of the gas phase. As the ionic concentration becomes significant at high loading, the behaviour of the liquid phase deviates from ideality. As a result, activity coefficients are used to account for non-ideality in the liquid phase:

$$p_i^* = \gamma_i x_i P_i^0 \qquad\qquad Eq.\ 2$$

Where $p_i^*$ (Pa) is the equilibrium partial pressure of the $H_2O$ and MEA, respectively; $\gamma_i$ is the activity coefficient of component $i$ ($H_2O$ and MEA); $x_i$ is the liquid mole fraction of component $i$ ($H_2O$ and MEA) and $P_i^0$ (Pa) is the vapour pressure of the pure $H_2O$ and MEA, respectively. In the case of $CO_2$, because it does not exist in liquid form under the operating conditions of the $CO_2$ absorption system, Henry's law must be used to compute the $CO_2$ equilibrium partial pressure. The expression for $CO_2$ equilibrium partial pressure is as follows:

$$p^*_{CO_2} = \gamma_{CO_2} C^*_{l,CO_2} He_{CO_2} \qquad \text{Eq. 3}$$

Where $p^*_{CO_2}$ (Pa) is the equilibrium partial pressure of $CO_2$; $\gamma_{CO_2}$ is the activity coefficient of $CO_2$ in the liquid phase; $C^*_{l,CO_2}$ (mol/m$^3$) is the concentration of free $CO_2$ in the liquid phase; and $He$ (Pa.m$^3$/mol) is Henry's constant of $CO_2$ in an aqueous MEA solution. Because MEA has a strong affinity for $CO_2$, the physical equilibrium of $CO_2$ in an aqueous MEA solution cannot be measured directly. Hence, Henry's constant of $CO_2$ can be estimated from experimental data reported to the systems that are similar, i.e., non-reacting gases. From the chemical and physical property aspect, $N_2O$ is similar to $CO_2$ and often used as a non-reacting gas to estimate the properties of $CO_2$ [25]. Thus, Henry's constant of $CO_2$ in an aqueous MEA solution can be expressed as follows:

$$\frac{He_{CO_2}}{He_{N_2O}} = \frac{He^{H_2O}_{CO_2}}{He^{H_2O}_{N_2O}} \qquad \text{Eq. 4}$$

Where $He_{N_2O}$ (Pa.m$^3$/mol) and $He_{CO_2}$ (Pa.m$^3$/mol) are the Henry's constants of $N_2O$ and $CO_2$ in an aqueous MEA solution, respectively; $He^{H_2O}_{N_2O}$ (Pa.m$^3$/mol) and $He^{H_2O}_{CO_2}$ (Pa.m$^3$/mol) are Henry's constants of $N_2O$ and $CO_2$ in water, respectively. The activity coefficient for $CO_2$, MEA and $H_2O$ are computed using the Aspen® (AspenTech, USA) properties database. The chemical reactions associated with the $CO_2$ absorption process are assumed to be completed within the gas–liquid interface. As a result, the liquid bulk is in a state of chemical equilibrium. The chemistry of $CO_2$ absorption in an aqueous MEA solution can be described from the following set of reactions:

Overall reaction of MEA and $CO_2$

$$CO_2 + MEA \xrightarrow{K_{eq,1}} MEACOO^- + MEAH^+ \qquad (R.1)$$

Carbamate reversion to bicarbonate

$$MEACOO^- + H_2O \xrightarrow{K_{eq,2}} MEA + HCO_3^- \qquad (R.2)$$

MEA deprotonation

$$MEAH^+ + H_2O \xrightarrow{K_{eq,3}} MEA + H_3O^+ \qquad (R.3)$$

Bicarbonate formation

$$CO_2 + H_2O \xrightarrow{K_{eq,4}} HCO_3^- + H_3O^+ \qquad (R.4)$$

Carbonate formation

$$HCO_3^- + H_2O \xrightarrow{K_{eq,5}} CO_3^{2-} + H_3O^+ \qquad (R.5)$$
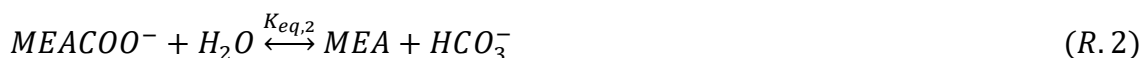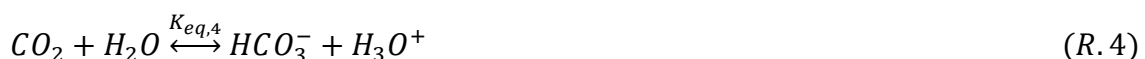
Dissociation of water

$$2H_2O \xrightarrow{K_{eq,6}} OH^- + H_3O^+ \qquad (R.6)$$

For reactions 2 to 6, the apparent (concentration-base) equilibrium constants are given in the following form:

$$K_{eq} = \frac{A^a B^b}{C^c D^d}$$
*Eq. 5*

Where *A* and *B* are the molar concentration of products (mol/m$^3$); *a* and *b* are the reaction's stoichiometry of products; *C* and *D* are the molar concentration of reactants (mol/m$^3$); *c* and *d* are the reaction's stoichiometry of reactants. The equilibrium constant for the overall reaction between MEA and $CO_2$ can be determined as a combination of other equilibrium constants:

$$K_{eq,1} = \frac{K_{eq,4}}{K_{eq,3} K_{eq,2}}$$
*Eq. 6*

Figure 6 shows the calculated $CO_2$ partial pressure at different loadings within the temperature range of interest (80°C to 120°C), showing adequate agreement between the calculated and experiment values [26]. It should be noted that the data fluctuates on both sides of the central line, indicating that the slight disagreements between two sources of data do not necessarily arise from model inconsistency but rather could have been experimental uncertainties.
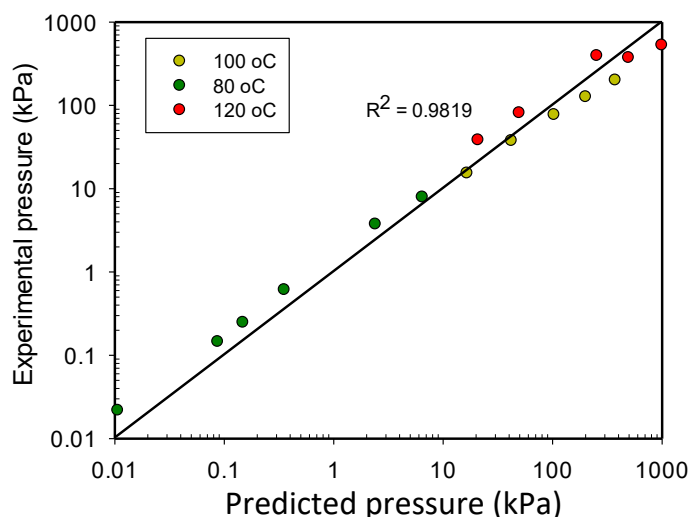


**Figure 6: Comparison of calculated $CO_2$ partial pressure against experimental data from literature.**

Figure 7 (A and B) shows more validation for thermodynamic and chemical equilibrium of various components. The dots represent the experimental values reported in literature, while the solid lines represent our model predictions. The model is able to capture the trend of the experimental data to a large extent. For example, as $CO_2$ loading increases there are dramatic changes in the trend of species mole fractions and these changes are reproduced by the model (Figure 7-B). Although there are some noticeable deviations from experimental data [26], within the range of a typical So-St operation, the model predictions are fairly accurate. Overall, we have successfully implemented and validated the thermodynamic and chemical equilibrium modules using the Aspen® and COMSOL® platforms.
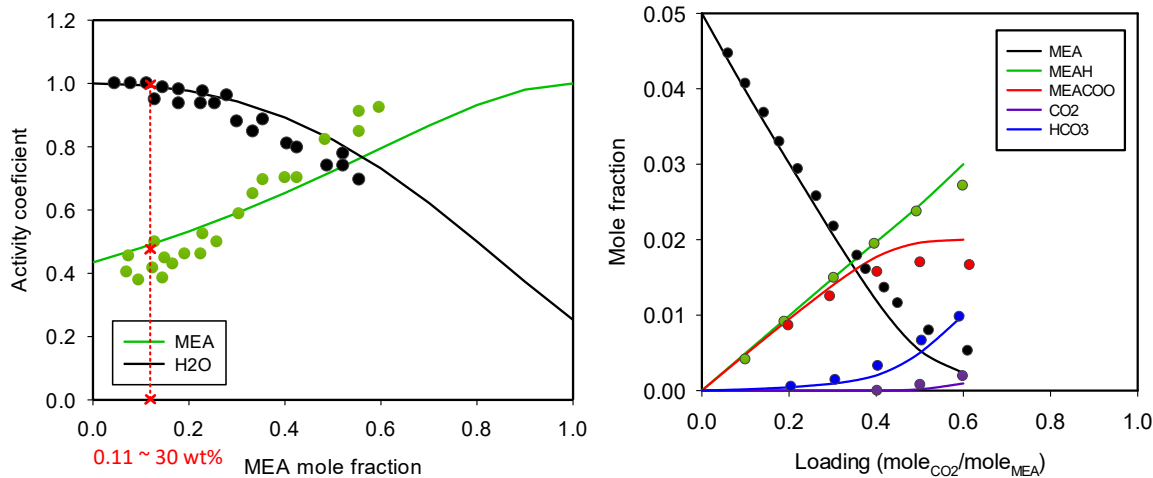
**Figure 7: Comparison of the thermodynamic and chemical equilibrium calculation (solid lines) with experiment data [26, 27] (dots). Subfigure A (left) shows the activity coefficient of $H_2O$ and MEA when the concentration of MEA changes from 0 to 1. For 30 *wt*% MEA, the equivalent MEA mole fraction is about 0.11 (calculated from Aspen®). Subfigure B (right) shows the agreement between the model and the experimental data for different species.**

## 2.2 Thermodynamic analysis

The vapour–liquid equilibrium (VLE) data of the $CO_2$-$H_2O$-MEA system is reviewed here to identify possible $CO_2$ stripping pathways that can be applied for the So-St process. For comparison, we also report and discuss the typical stripping pathway used in a conventional stripper. Figure 8 shows the VLE for 30 *wt*% MEA solvent at different temperatures.
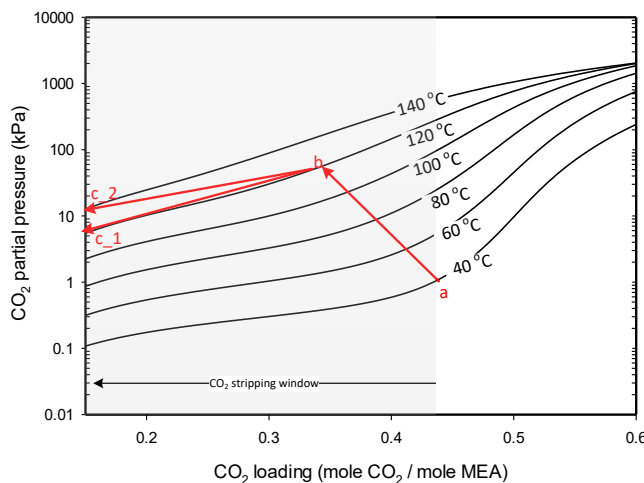


**Figure 8: Vapour–liquid equilibrium for 30 *wt*% MEA system. The red line (a-b) shows the flash process of rich solvent (0.45 loading) from 40°C to 120°C.**

We note here a few fundamental features of the VLE patterns regarding $CO_2$ stripping (i.e. reducing $CO_2$ loading) to facilitate subsequent discussion. In order to facilitate $CO_2$ stripping, one must provide enough driving force, which can be expressed in term of $CO_2$ partial

pressure. Given there is enough thermal energy, the bonds between $CO_2$ and MEA molecules can only be broken when the current $CO_2$ partial pressure is lower than the equilibrium value. Once the process is equilibrated at a specific temperature and the new partial pressure equals the equilibrium pressure, it will not have the tendency to break more bonds and release more $CO_2$. This is illustrated in the transition from (a) to (b) (Figure 8, red line). Point (a) represents the rich solvent at the exit of the absorber and point (b) represents the rich solvent at the outlet of the SCF. The path from (a) to (b) comprises multiple heating steps in the cross heat exchanger (HX) and the SCF, reducing the loading value and increasing the $CO_2$ vapour pressure. The vapour generated during the preheating stage (i.e. in the cross HX) can be separated from the mixture by a knock-out drum before entering the SCF. At point (b), when the rich solvent reaches ~120°C, the solvent becomes ready for the actual stripping; however, the VLE implies more stripping is impossible, because there will be no sufficient driving force. There are only two pathways in which one can influence the process to allow for more stripping to occur, as shown in Figure 8:

1.  Reducing $CO_2$ partial pressure by instantly removing the $CO_2$ in the gas phase (b to c_1).
2.  Increasing the equilibrium $CO_2$ partial pressure by increasing the temperature (b to c_2).

Each of these pathways is verified to confirm its feasibility. An example of the first pathway can be found in the conventional stripper. At every stage in the stripper column, the solvent is not in equilibrium with the vapour, because that was equilibrated in the previous stage. In this way, the vapour–liquid $CO_2$ mass transfer can theoretically be facilitated at every stage. This can be seen in Figure 9, where the solvent moves along the 120°C isotherm line and gradually reduces the loading. This first method is an effective mechanism to drive the stripping process, because it sustains the stripping driving force while not requiring excessive heating of the solvent.
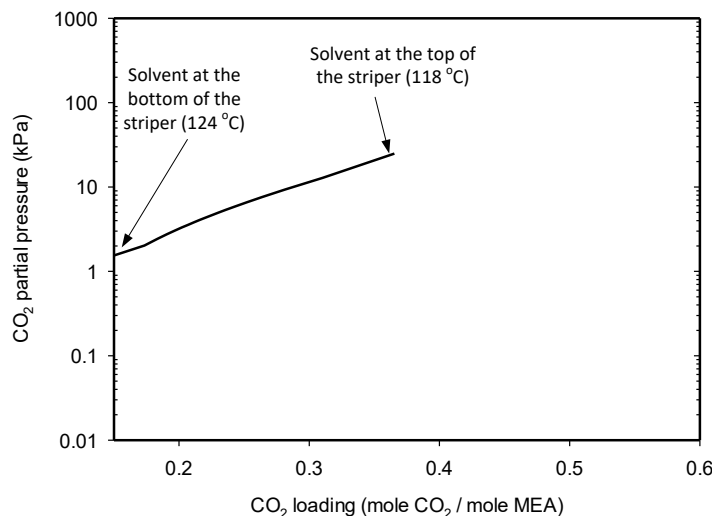


**Figure 9: Mapping the stripping path of the solvent in a conventional stripper.**

The second pathway can be simulated by assuming the solvent enters a solar receiver tube in the SCF where heat is added to the solvent (Figure 10). This heating tube may roughly

represent one of the So-St segments. Compare with a conventional stripper, this process setup is simpler and has fewer heat transfer mediums, and is thus expected to have higher solar exergy efficiency. The geometry of this So-St design represents a design variable. For example, if the tube is tilted, the pressure profile and the flow regime would be affected, causing different operation performance. However, as it does not affect the thermodynamic results, we decided to decouple the tilt angle from the thermodynamic study at this early stage of the analysis.
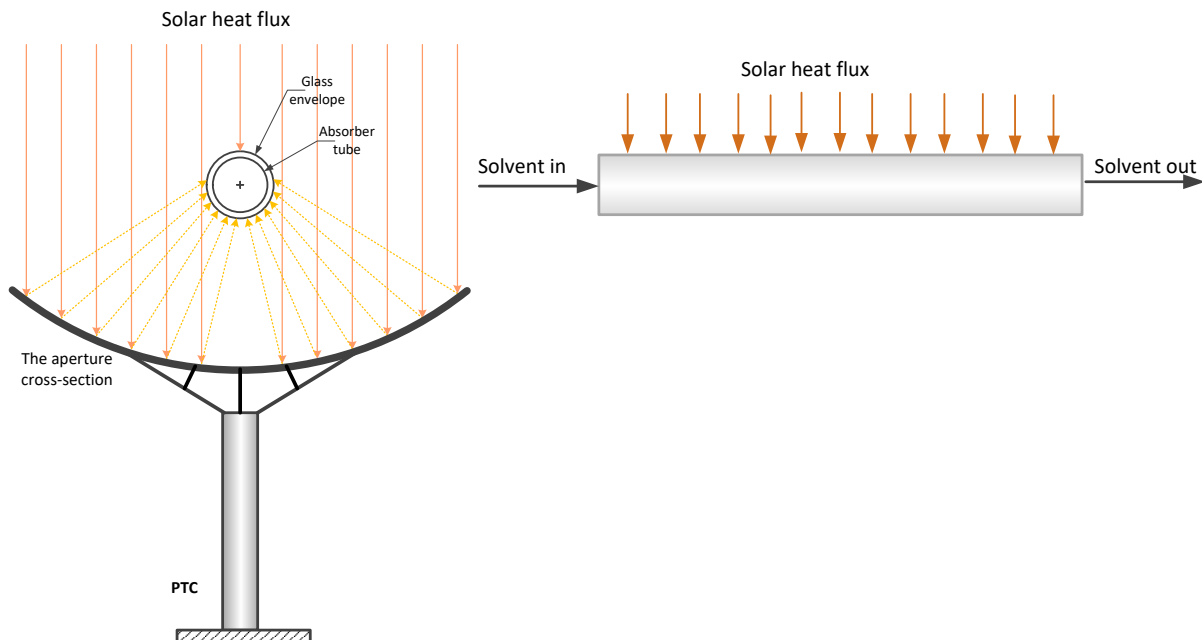
**Figure 10: (Left) a cross-section of the So-St resembling the parabolic trough collector, and (right) a front view of the So-St tube.**

We used the pipe model in Aspen Plus® for simulation purposes. The pipe length and heat flux are sensitised, aiming to reduce $CO_2$ loading in the solvent to the same value as in a conventional stripper. The simulation results are shown in Figure 11-A. It can be seen that with the second method, it is possible to strip the $CO_2$ and reduce the loading to the desired extent. Observing the stripping pathway in Figure 11-A (red line), there are two distinct regions marked from 0.32 to 0.25 and from 0.25 to 0.15, respectively. In the first region, it is possible to reduce the loading value without substantial increasing the temperature value, while in the second region, we must increase the temperature excessively to carry out further $CO_2$ stripping. The latter stripping option tends to be thermodynamically undesirable, diminishing the advantages of the So-St in terms of process simplicity and exergy efficiency. Another important point here is that, this process seems more efficient when it performs stripping for moderately lean solvent, i.e. a lean loading target around 0.25. To achieve a lower loading, the process becomes undesirable, because the solvent temperature needs to be increased above the 125°C cap, resulting in significant solvent degradation. This can be seen in Figure 11-B, which shows the energy demand and the required heating temperature to achieve different lean loading targets. The practical operation region is when the solvent

is below the 125°C cap, while extreme operation is above 125°C. The trend for the energy demand almost linearly increases for lean loadings above 0.2, similar to the reported trend for a conventional stripper [28]. The near-flattening area below 0.18 lean loading might be attributed to excessive water vaporisation, apparently diluting the $CO_2$ vapour pressure and stimulating more $CO_2$ stripping (Figure 11-B). This might be the only advantage of the undesirable water vaporisation phenomenon, as in general it deteriorates the merit of the stripping process. Although it is possible to heat and strip the solvent to a similar extent as in a conventional stripper, two constraints limit the feasibility of this So-St design at excessive temperatures; i) the 30 *wt*% MEA solvent undergoes significant degradation, and ii) it causes significant water vaporisation. For the second constraint, when the solvent reaches 0.15 loading at 140°C, water is expected to vaporise up to 100 kPa (Figure 12-A, red marker). This condition implies the So-St must operate above 100 kPa to make room for both water and $CO_2$ in the vapour phase. This coupled interaction between the temperature and pressure makes the design and operation of the So-St relatively difficult, because a higher temperature is needed for 'deeper' solvent regeneration at the expense of excessive water evaporation.
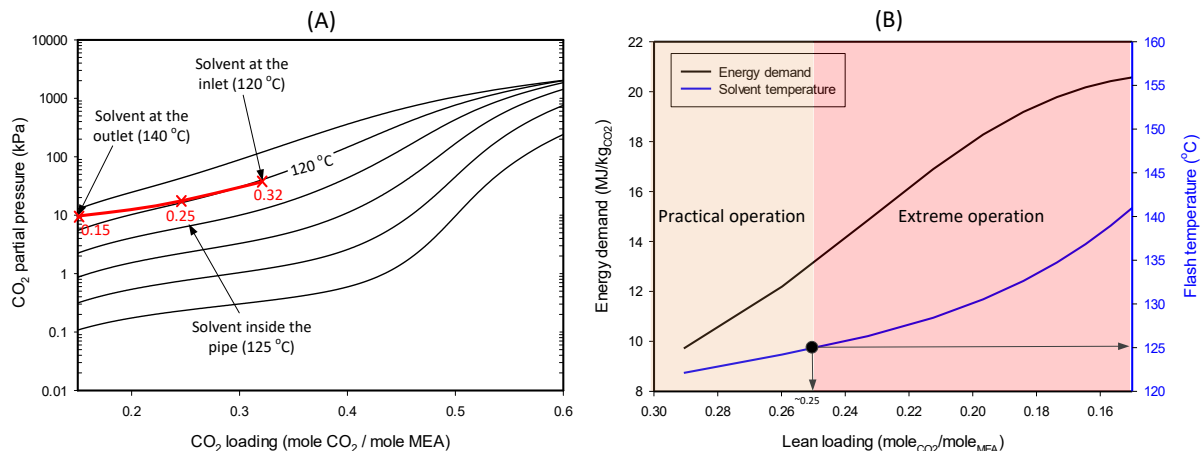


**Figure 11: (A) Mapping the stripping pathway for 30 *wt*% MEA solvent in a model So-St tube. The equilibrium lines are included. (B) Theoretical analysis for different extent of solvent regeneration as a function of the lean loading value; lower loading indicates higher solvent regeneration. Values calculated based on one stage flash at constant 2 bar pressure and different temperatures.**

In summary, we explored two stripping pathways to push the solvent to a low loading region and release $CO_2$ molecules. Once the solvent establishes the first equilibrium point, there is no tendency for more $CO_2$ stripping to occur. The first pathway creates a better partial pressure driving force for greater $CO_2$ release by having a counter-current flow of vapour to sweep away the $CO_2$. This pathway has proven to be feasible and is widely used in conventional $CO_2$ stripper design. The second pathway increases the equilibrium $CO_2$ partial pressure via heating the solvent to a higher temperature. Preliminary assessment of this second pathway reveals few possible undesirable outcomes: i) the solvent temperature may need to be raised excessively to reduce the loading to the target values; ii) high temperatures possibly lead to significant solvent degradation; and iii) a higher solvent temperature also

results in more water vaporisation. Therefore, this solvent regeneration pathway might only be suitable for regenerating lean solvents with moderate loading value(s).
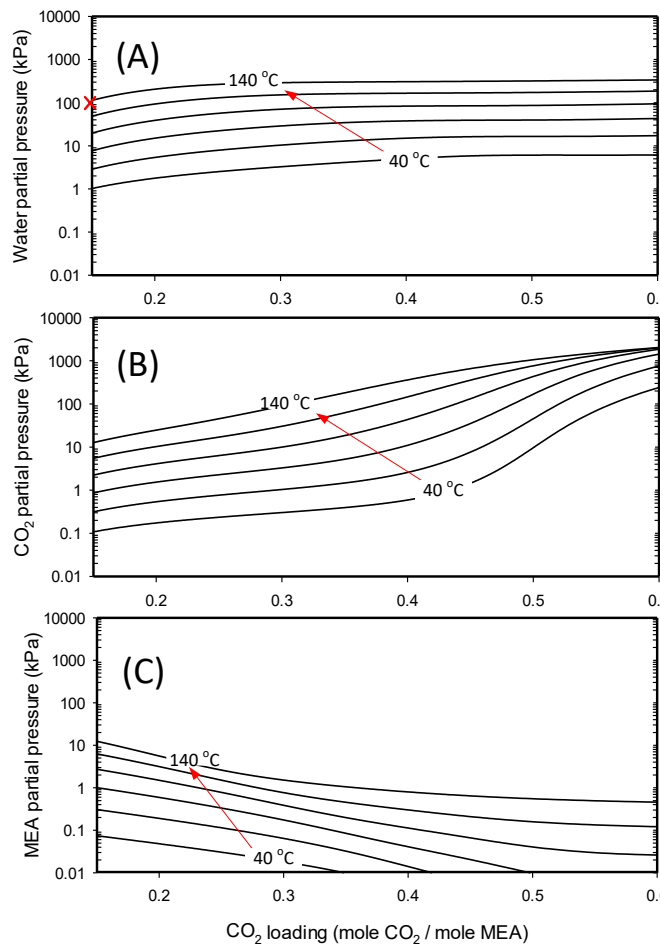


**Figure 12: VLE analysis of water, CO₂ and MEA in CO₂-H₂O-MEA (30 *wt%*) solvent.**

From the above, we have conceptualised three possible preliminary So-St designs and operations as shown in Figure 13. The first design is based on a conventional stripper method, but the solar heat flux (*SHF*) is used in the solvent boiling location. This arrangement might be achievable by connecting a typical stripper column with heating pipes carrying the solar thermal energy via a HTF, but this reduces the exergy efficiency. In contrast, the second design can be thought of as a co-current operation in which vapour carries the stripped $CO_2$ molecules in the same direction as the solvent. This design is simple and easy to integrate with a solar energy harvesting mechanism. However, it does not sustain partial pressure driving force well, thus requiring higher temperatures. Our third, hybrid design is inspired by the former two principles. It combines the geometry of the second design to facilitate solar energy collection with the stripping mechanism of the first design to sustain acceptable $CO_2$ stripping driving force. The main feature of the hybrid design is how to integrate a vapour removal mechanism to reduce/control the $CO_2$ partial pressure. This could primarily be achieved by arranging So-St in series with in-between knock-out drums, or possibly by using existing de-gassing instruments widely used in oil and gas industries. We conclude that the

So-St design should adapt to the hybrid design, because the co-current alone unlikely will result in a techno-economic justifiable operation, while the first counter-current design is physically unfeasible in the SCF setup.
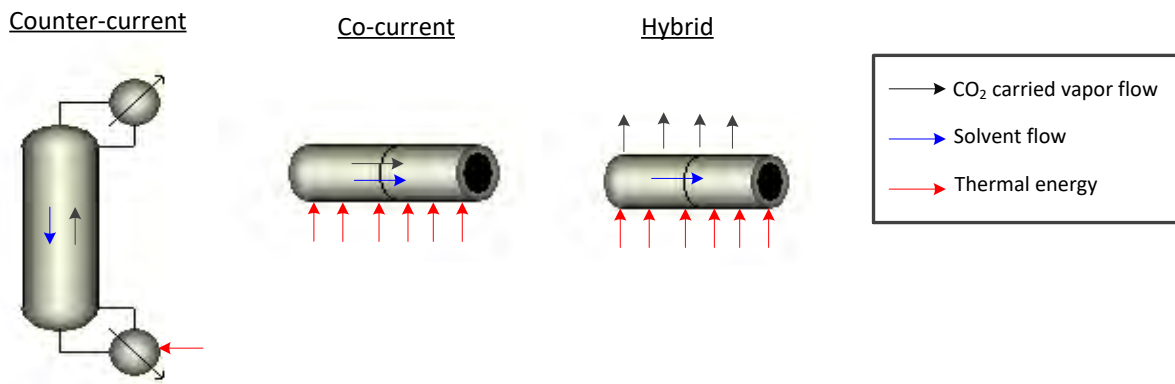


**Figure 13: Conceptualised CO$_2$ stripping pathways for possible So-St design.**

## 2.2.1 Hybrid concept

As outlined in the previous section, our hybrid design has the potential to collect solar thermal energy in the same way as the solar-heated tube. In addition, the vapour could be periodically extracted along the tube to sustain the pressure driving force. The detailed design for achieving this operation will be explored in subsequent chapters. In this chapter, we aim to sensitise the operating conditions and preliminarily determine the length of a So-St segment. Figure 14 shows the theoretical representation of a typical So-St tube design using the Aspen® model. The So-St model uses three ports for vapour to escape, which are expected to proportionally reduce CO$_2$ vapour pressure and allow for further CO$_2$ stripping. Each segment is theoretically represented by a combination of a pipe model to calculate the pressure-drop, a flash drum to separate gas/vapour phase from the liquid, and a pump to restore the pressure to the nominal value before entering next segment. Solar energy collection is primarily modelled as a constant heat flux along the tube. The following assumptions were made for this simulation:

1. Heat is distributed homogenously among the solvent flows in the tube. In real operation, this assumption will not be entirely valid, but it is always possible to improve the heat transfer aspect of the system and bring the thermodynamics closer to that assumption.
2. Two-phase flow behaviour is omitted for the current thermodynamic simulation at this early stage. The detailed phase evolvement will be investigated in subsequent chapters.

**Conceptualized real design**



**Modelling and simulation**
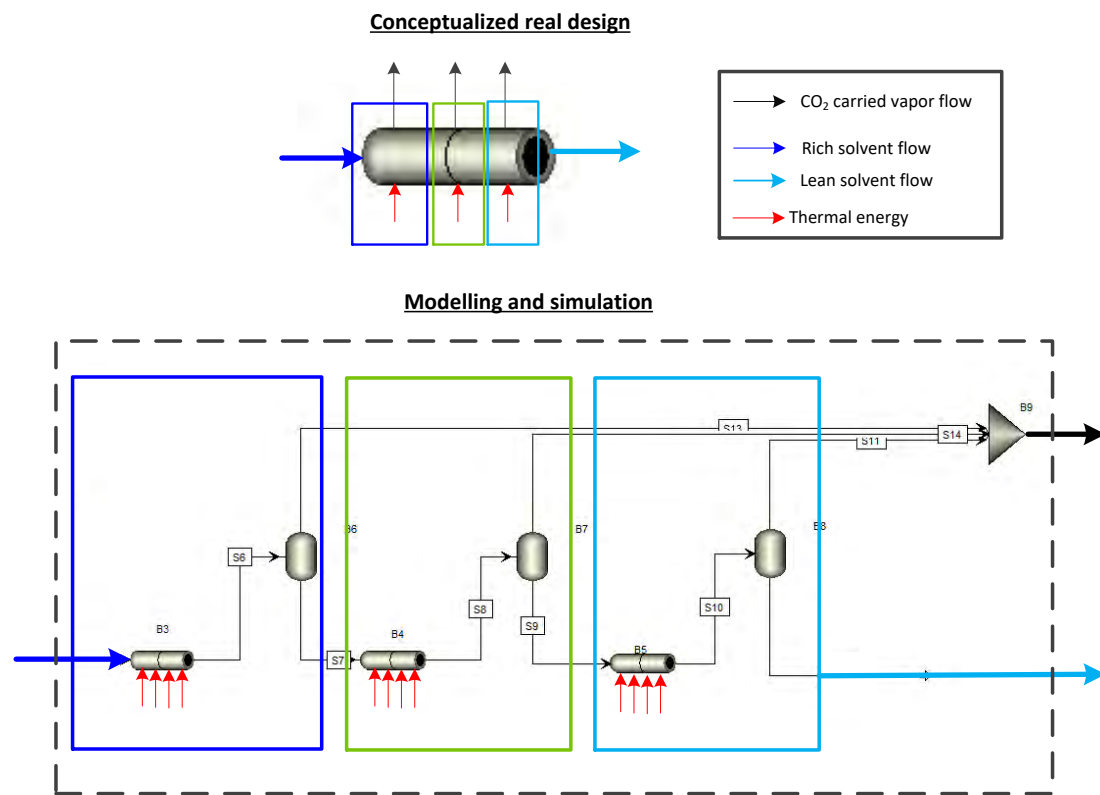


**Figure 14: The modelling approach for hybrid design in Aspen®.**

## 2.2.2 Hybrid vs. co-current design

We compared the hybrid design with the co-current design to ensure the hybrid design performed better. In this simulation, we assume the pressure-drop is neglected. The reason for this assumption is because if pressure-drop occurs, it will cause drops in temperature as per the ideal gas law, assuming that the gases are ideal. This temperature drop would hinder the purpose of verifying the effect of the two designs on the $CO_2$ removal mechanism. The partial pressure plot result shown in Figure 15-A reveals that the hybrid design can lower the $CO_2$ partial pressure in the vapour phase as expected, and bring the trend in partial pressure closer to the conventional stripper counterpart. This would lower both the solvent temperature (Figure 15-B) and the energy demand, as demonstrated in Table 2, because the hybrid design does not entirely depend on temperature to create the driving force for $CO_2$ stripping. This result may help to eliminate the extra portion of solar energy that is required to increase the solvent temperature and vaporise water, as higher temperatures would eventually enable more water vaporisation. Our results confirm that the hybrid design is a promising direction to pursue in addition to the well-established counter-current working mechanism.
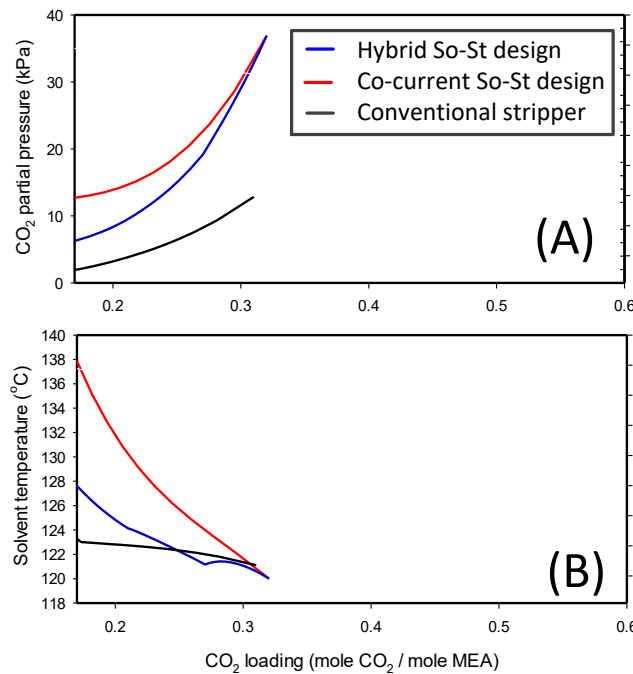
**Figure 15: Plot of CO₂ partial pressure and solvent temperature of the conventional stripper, So-St co-current and hybrid designs.**

**Table 2: Theoretical performance of co-current vs hybrid design, respectively.**

|                                        | Co-current design | Hybrid design |
|----------------------------------------|-------------------|---------------|
| Maximum solvent temperature ($^{o}C$)  | 135               | 131           |
| Energy demand ($MJ/kg_{CO2}$)          | 25                | 11.1          |
| Lean loading target                    | 0.17              | 0.17          |
| Solvent flow (kg/hr)                   | 1081              | 1081          |

## 2.2.3  Thermodynamics sensitivity study

To investigate different aspects of this system, we developed a base case, with the parameters summarised in Table 3. In this test, we focus on the fundamental principles of a So-St segment to improve our understanding. After we determine a feasible and effective working principle for the So-St, we can develop a procedure for calculating detailed design variables. We have assumed the So-St diameter and length to be 0.076 m and 60 m, respectively, which is on a similar scale as a conventional parabolic trough collector (PTC) heating tube. It should be emphasised that the length of the final So-St design is unlikely to be similar to commercially available PTCs, because we have already demonstrated that the co-current design used in PTC will not be technically viable. Our assumption about So-St sizing ensures that we are working with realistically achievable solar heat harvesting performance.

**Table 3: Specification for the test design.**

| Operational parameters | Value | Unit |
|---|---|---|
| Solvent flowrate in one So-St tube [a] | 108,123 | kg/hr |
| So-St length | 60 | m |
| Rich loading before So-St | 0.32 | $mole_{CO2}/mole_{MEA}$ |
| Rich loading temperature before So-St | 120 | ℃ |
| Lean loading target [b] | 0.17 | $mole_{CO2}/mole_{MEA}$ |
| Operating pressure | 2 | bars |
| So-St diameter | 0.076 | m |

[a] *Based on the maximum solvent circulation rate for Sydney case-study of 2,378,710 kg/hr as simulated in Aspen® [29].*

[b] *Based on specified lean loading in absorber.*

We first investigate the pressure-drop aspect of the system. The pressure-drop originates from a few factors, including friction forces and heating of the solvent. Solvent heating could result in possible vaporisation inside the So-St tube, thus resulting in density reduction, which would augment the pressure-drop according to the Bernoulli equation. At a specific So-St diameter, the solvent flowrate will also affect the pressure-drop. Sensitising the solvent flowrate also affects the required solar heat flux (*SHF*) for achieving the target lean loading value (*LLV*). The results of this sensitivity test are shown in Figure 16, where the top x-axis shows solvent inlet flowrate, and the bottom x-axis corresponds to the number of required So-St tubes. It can be seen that as solvent flowrate increases, which translates to fewer So-St tubes required, the pressure-drop increases rapidly and vice versa. This is because given the same So-St diameter (0.076 m), a higher flowrate will increase the solvent velocity. This is based on Bernoulli's equation (*Eq. 7*) as shown below:

$$P + \frac{1}{2}\rho v^2 + \rho gh = Constant \qquad\qquad Eq.\ 7$$

Where $P$ is pressure (Pa); $\rho$ is fluid average density (kg/m³); $v$ is the fluid velocity (m/s); $g$ is the gravitational constant (m/s²); and $h$ is the height (m). The sum of the three individual terms ($P$ is the pressure energy; $\frac{1}{2}\rho v^2$ is the kinetic energy; and $\rho gh$ is the potential energy) must always be conserved, i.e. if the kinetic term is increased (e.g. due to higher velocity), then either or both of the other two terms must be decreased. Inside the So-St, assuming it is horizontal (thus no change in potential energy), the pressure must drop when solvent velocity increases. The *SHF* demand also increases for higher solvent flowrates, because there is more solvent flowing through the So-St tube. This *SHF* demand is on a similar order of magnitude as in the PTC system, which means the So-St has the potential to be technically viable. Based on these preliminary assumptions, we could operate a So-St network at ~3000 kg/hr of solvent flow. Accordingly, the preliminary specifications for the So-St network are reported in Table 4.
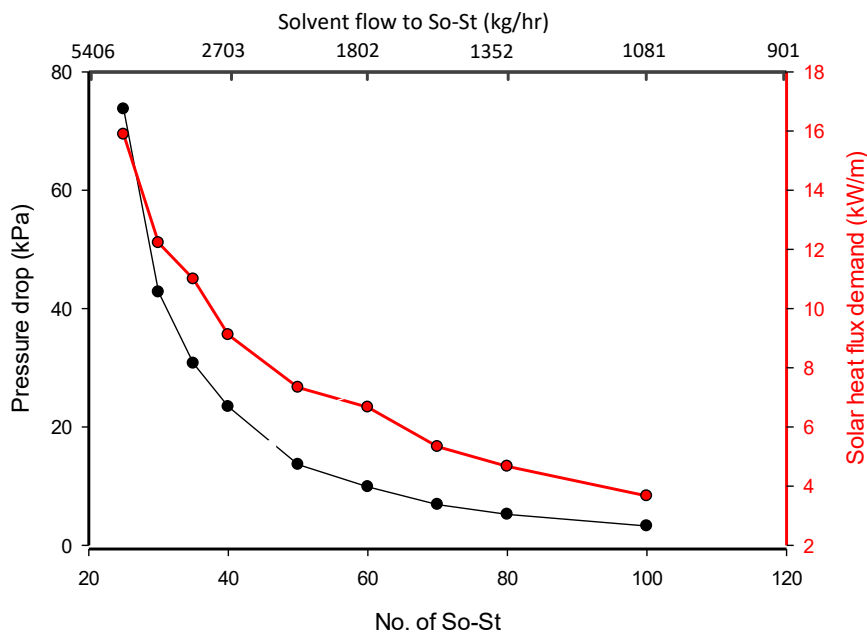
**Figure 16: Sensitising the solvent flowrate into one So-St.**

Based on the specifications in Table 2, we computed the energy demand (*ED*) metric, which shows thermal energy demand (per MJ) to recover 1 kg of 99% pure $CO_2$ as follows:

$$ED = \frac{Total\ solar\ energy\ transfer\ to\ So-St}{Total\ CO_2\ released\ at\ the\ end\ of\ So-St} \qquad\qquad Eq.\ 8$$

The *ED* is ~12 MJ/kg$_{CO2}$ which is significantly larger than the accepted *ED* of a conventional stripper (~4 MJ/kg$_{CO2}$). In terms of energy performance, the two systems might not be comparable (12 MJ/kg$_{CO2}$ *vs.* 4 MJ/kg$_{CO2}$). This is because the conventional optimised stripper only regenerates the solvent up to 0.22 lean loading, while in this assumption of the So-St network, we targeted a lower lean loading at 0.17. To regenerate lean solvent at 0.17 in a conventional stripper, the *ED* is 7.65 MJ/kg$_{CO2,}$ which is closer to the So-St *ED*.

**Table 4: Performance comparison between hybrid design and conventional stripper.**

|  | Hybrid design | Conventional stripper |
|---|---|---|
| Lean loading target | 0.17 | 0.17 |
| Maximum solvent temp (°C) | 127 | 125 |
| Energy demand (MJ/kg$_{CO2}$) | 12 | 7.65 |
| No of So-St in parallel | 35 | Not applicable |

It is important to elaborate further on the *ED* value for the So-St to ensure our So-St simulation represents a realistic $CO_2$ desorption process. This study has led to some very interesting findings, as shown in Figure 17. We found that the heat components constituting the *ED* in the conventional stripper are mostly relevant to the latent heat of vaporisation, while the So-St system has both latent and chemical bond break heat (the sensible heat component is negligible). This is because in a conventional stripper, heat is supplied in the vaporisation zone, not the $CO_2$-MEA bond-breaking zone, and that part of the vaporisation heat is instantaneously utilized for chemical bond breaking. In contrast, the So-St tube receives

incoming *SHF* that is equally distributed to all possible heat sink components, i.e. latent (84%), chemical bond break (16%) and sensible heat (negligible). These terms were back-calculated by using the total mass flow of water vapour and $CO_2$; and the respective heat specifics (2.3 MJ/kg$_{H2O}$ and 2 MJ/kg$_{CO2}$). This back-calculation returns an *ED* of 12.1 MJ/kg$_{CO2}$, in the same order of magnitude as the already determined *ED*.
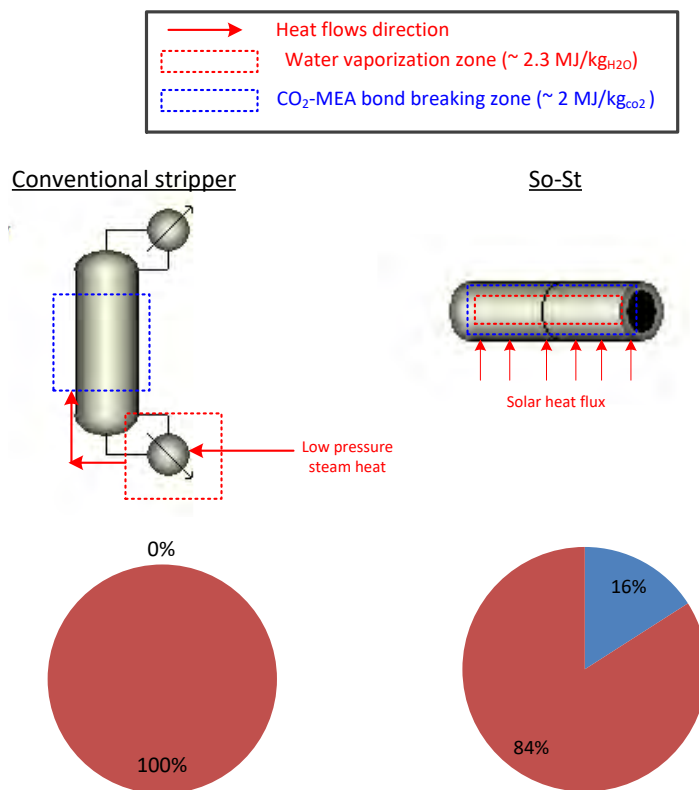


**Figure 17: Elaborating energy flow direction and energy components of conventional stripper and So-St (hybrid design).**

From the above analysis, we found that the So-St system would require an advanced design and control mechanism(s) to direct the solar energy flows to chemical bond breaking, rather than to solvent evaporation. Therefore, we focused on investigating the design parameters and process control in more depth in the upcoming chapters.

The pressure parameter plays a significant role in the design of the So-St. It is desirable to manipulate the pressure in such a way as to suppress the vaporisation phenomenon in the solvent (mostly water), as at higher pressure it is more 'difficult' for water to vaporise. We sensitised different operating pressures and plotted the results in Figure 18. It can be seen that increasing the pressure would reduce the amount of water vapour formation (Figure 18-B), resulting in a lower *ED* (Figure 18-A). This is because at higher total pressure, the equilibrium partial pressure of water increases, thus lagging the vaporisation process. We can achieve a comparable performance to a conventional stripper. However, the solvent temperature increases significantly beyond the recommended operational value for 30 *wt*% MEA solvent system. This is because as we partially suppressed water vaporisation, the solar heat redistributed itself among the sensible heat and chemical bond break categories, thus

leading to increases in solvent temperature. One potential solution could be to apply cooling mechanisms at regular intervals along the So-St tube or in the potential hot spots. This way we could still utilize the benefits of lower *ED* when operating at high pressure, while avoiding the burden of excessive temperatures in the solvent.
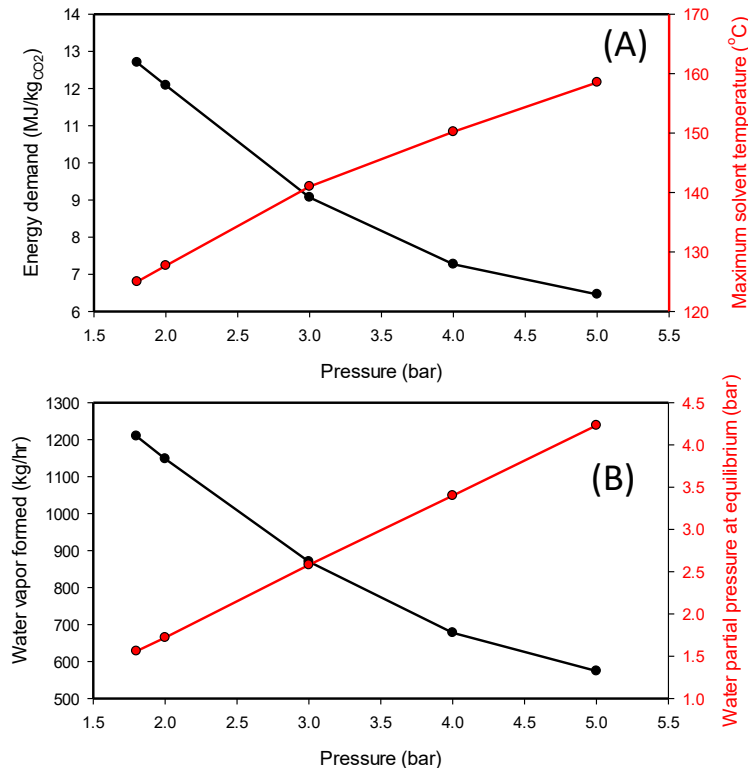


**Figure 18: Sensitising the operating pressure of a So-St; other variables are the same as reported in the base design (Table 3).**

Next, we sensitised the *LLV*. The main reason behind this selection is because the lean loading determines the extent of solvent regeneration. It is important to understand how other variables (e.g. solvent temperature) are affected when the *LLV* is changed. As the lean loading value is not an input into Aspen® simulation, we developed a goal-seek algorithm to calculate the required So-St length for reaching a specific target for lean loading value. There is a close relationship between the So-St length and lean loading value, as the $CO_2$ stripping occurs along the So-St tube length. Thus, a shorter length implies less $CO_2$ stripping and results in higher lean loading value. The results of this sensitivity test are shown in Figure 19. It can be seen that operating at higher *LLVs* leads to some desirable outcomes. At higher lean loading target, both *ED* and solvent temperature can be reduced. This is related to the corresponding reduction in the So-St length, resulting in lowering the heat flux and the maximum solvent temperature. As a result, less water vapour can be formed, which in turn would increase the portion of solar heat contribution for chemical bond breaking; hence *ED* is reduced. One undesirable outcome of increasing the lean loading is that more So-St modules will be required. This is because with higher lean loading operation, the $CO_2$ capture and release capacity per mole of MEA is reduced. To compensate, we must increase the solvent circulation rate; hence extra So-St units are needed for processing the extra solvent flow.
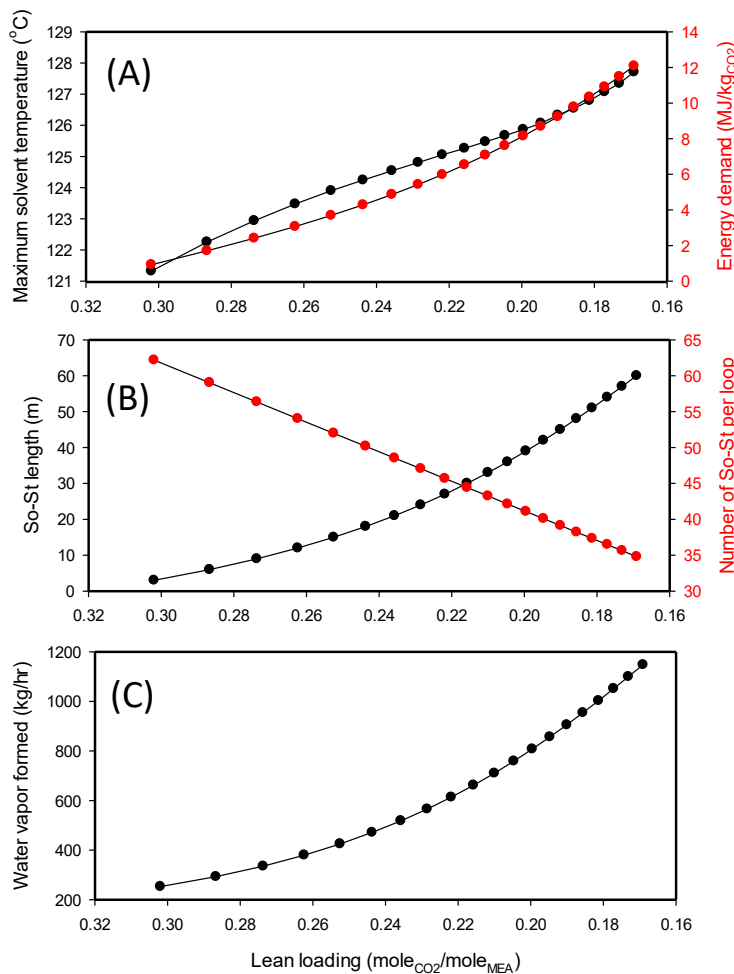
**Figure 19: Sensitising the lean loading target; other variables are as reported in the base-design (Table 3).**

In summary, our analyses report the key findings for the thermodynamics of the So-St by exploring variables that may strongly affect the process performance. We found that both pressure and the lean loading target value are the key potential variables for optimisation. Upcoming work should include both of the manipulated variables in the search for the optimal operation region. To demonstrate the potential for further optimisation, we conducted another sensitivity test for three goal-seek case-studies to search for a better So-St design compared with the base-case as follows (see also Table 5):

➢ Case-study 1: changing the lean loading to achieve lower *ED* with maximum solvent temperature reaching only 125°C.

➢ Case-study 2: changing both lean loading and pressure to achieve lower *ED* than case 1 with maximum solvent temperature reaching only 125°C.

➢ Case-study 3: changing both lean loading and pressure to achieve the lowest *ED* with an assumption that the solvent can reach 140°C.

**Table 5: Case studies formulation.**

| Manipulated variables | Case 1 | Case 2 | Case 3 |
|---|---|---|---|
| Lean loading | ✓ | ✓ | ✓ |
| So-St pressure | ✗ | ✓ | ✓ |
| **Objective** | | | |
| Energy demand | < base case | < case 1 | < case 2 |
| **Constraint** | | | |
| Maximum solvent temperature | 125°C | 125°C | 140°C |

The results of the sensitivity test are reported in Table 6. The objective and constraint of each case-study was achieved. For example, it is possible to achieve an *ED* as low as 2.8 MJ/kg$_{CO2}$, which is well below the conventional stripper, if there is a solvent that can operate up to 140°C. These case-studies confirm the applicability for employing an optimisation approach to determine the optimal design for the So-St network.

**Table 6: Goal-seek results for So-St designs to meet different case studies objectives and constraint.**

| | Base design | Case 1 | Case 2 | Case 3 |
|---|---|---|---|---|
| Lean loading | 0.17 | 0.22 | 0.25 | 0.25 |
| Maximum solvent temperature | 127 | 125 | 125 | 140 |
| One So-St length (m) | 60 | 27.9 | 15.3 | 11.7 |
| One So-St diameter (m) | 0.076 | 0.076 | 0.076 | 0.076 |
| Operating pressure (bar) | 2 | 2 | 2.1 | 3.4 |
| Energy demand (MJ/kg$_{CO2}$) | 12 | 6.1 | 3.7 | 2.8 |
| No. of So-St in parallel | 35 | 45 | 51 | 51 |

## 2.3      Flow regimes

In the previous subsections, we sensitised the key variables that could affect the thermodynamic aspect of the So-St system. In this section, we investigate the physical design variables, including the solvent flow regime in a tube. The outcomes of this study could be combined with a thermodynamic study to develop a complete framework for a comprehensive design and optimisation process for the So-St system. We performed numerous simulations for different combinations of diameters, flowrates and heat inputs, and for each simulation we plotted the solvent flow regime (from Aspen® output) against the superficial gas and liquid velocity parameters. We found four major flow regimes that could govern the solvent flow in the So-St tube at a horizontal layout: stratified, wave, slug and mist flows, as depicted in Figure 20. The characterisation of these flow regimes is based on the superficial liquid velocity, a parameter extensively used in the literature for multi-phase flow regimes [30]. The position of these regimes in Figure 20 agrees with literature data, e.g. the

stratified flow is at the most left side of the plot. It is interesting to observe the partial overlap between the wave and slug regions indicated by the overlapping of the black and green dots, often named a transient zone [31]. This overlap suggests operating near the transient zone between the wave and slug regions might lead to unstable flow, causing difficulties in characterising the heat transfer performance. Hence, the conservative approach is to select an operation area where there is some flexibility to change the liquid–gas velocity without encountering an undesirable or unstable flow regime.
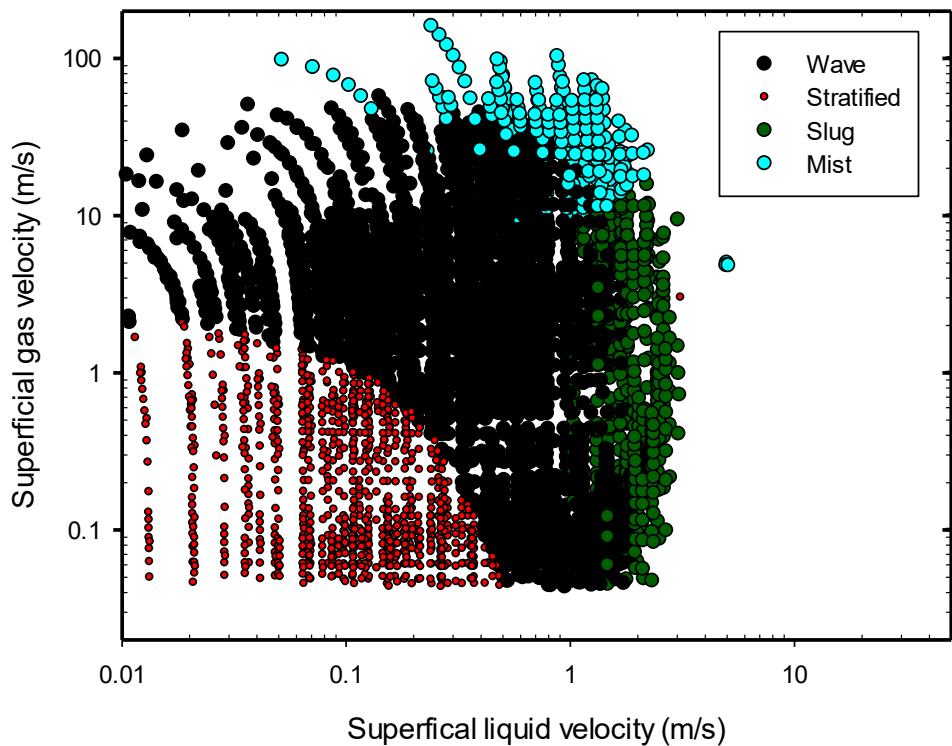


**Figure 20: Correlation of identified major flow regimes for superficial liquid and gas velocities.**

One of the most important variables is the diameter of the So-St tube, because for a fixed solvent flowrate, the diameter would affect the cross-sectional area, and thus the superficial velocities. We developed a plotting method to adapt the log scale of the superficial gas velocity, as shown in Figure 21. The diameter was 0.7 m with a flowrate of 36,041 kg/hr. Figure 21-A shows the profile of the two-phase flow regime, from the starting point of the two-phase flow until the exit of the tube. The tube is discretised into nine sub-sections and plotted as nine points. Figure 21-B shows the same information, but with the log scale on both X and Y axes. A general observation is that the gas velocity changes significantly along the tube. This is due to more $CO_2$ and $H_2O$ being converted to the vapour phase, increasing the vapour volume flow, while the liquid velocity drops slightly.
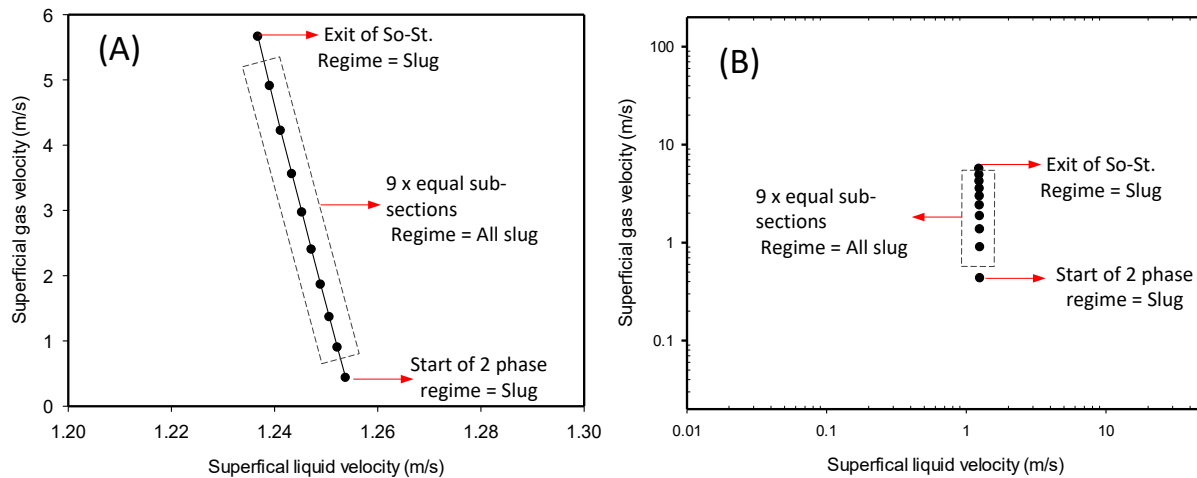
**Figure 21: An example of plotting superficial gas and liquid velocity along the nine equal segments in a So-St tube with linear scale (A) and log scale (B) .**

We sensitised the effect of the tube diameter on the flow regime. The inputs for this test are shown in Table 7. The heat flux was also sensitised, because it will affect the vapour flowrate and hence the superficial gas velocity.

**Table 7: Specification for sensitivity analysis of flow regime at different tube diameters.**

| Variables | Value |
|---|---|
| Solvent flowrate into one tube | 36,041 kg/hr |
| Tube diameter | 0.1 – 0.7 m |
| Flow regime characterisation point along the tube | 1 – 10 m |
| Base heat flux | 42 kW/m$^2$ |
| 5 x base heat flux | 210 kW/m$^2$ |
| 1/5 x base heat flux | 8 kW/m$^2$ |

The results are shown in Figure 22, where subfigure A is for the base flowrate and subfigure B is for a higher flow of 54,061 kg/hr. It can be seen that changing the diameter determines the dominating flow regime in a tube. In subfigure A, the flow regime moves from the wave region to the stratified region as the diameter increases, because higher diameters lead to lower velocities for the same solvent flowrate. It is critical to decide the liquid velocity (i.e. combination of the solvent flowrate and the tube diameter) for the So-St operation, because it does not change significantly along the So-St tube. This can be seen on Figure 22-A; e.g. if we choose the liquid velocity to be at 1 m/s, the dominant flow regime would be the wave flow, and it is difficult to move to the stratified flow regime. The main factor that affects the vapour flow also influences the regime. Changing the heat flux would shift the flow regimes either up (high vapour velocity) or down (lower vapour velocity) as shown in Figure 22-A, because more heat flux would generate more vapour ($CO_2$ and/or water), which would

increase the superficial gas velocity. The effect of increasing the flow is shown in Figure 22-B. At higher flow and a fixed diameter, the liquid velocity will increase, pushing the velocity profile towards the right and vice versa for the case of lower flowrates. This analysis shows the effect of a potential disturbance (changing the flowrate), and suggests the selection of diameter should take into account this type of possible disturbance.
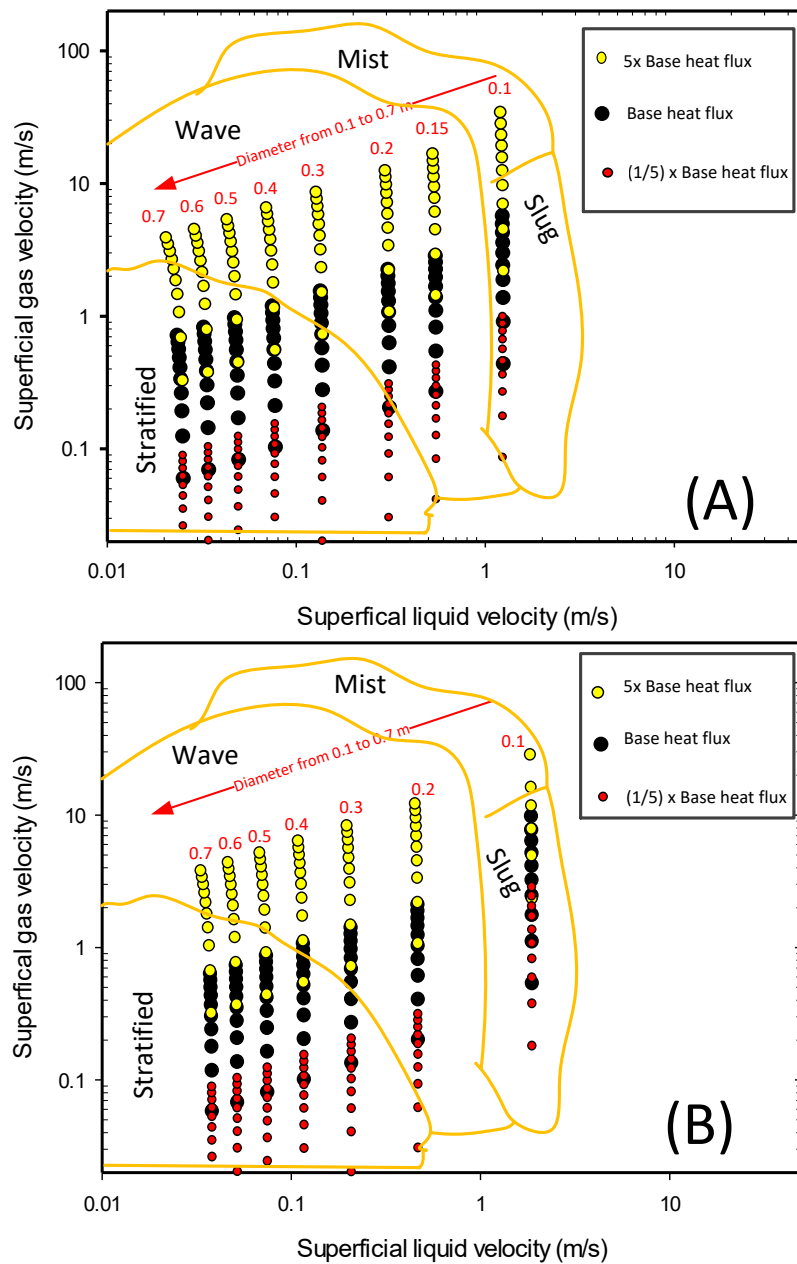


**Figure 22: Plotting superficial gas and liquid velocity at different diameter ; (A) base flowrate 36,041 kg/hr and (B) increased flowrate 54,061 kg/hr.**

Based on the flow regime map, we can first exclude the mist regime, because it means significant solvent evaporation and would bring the system close to detrimental dry-out conditions [32]. The stratified regime can be eliminated as well, because it has the worst heat

transfer performance compared with the wave regime [33]. Hence, the wave and slug flow regimes are the two most promising to investigate. More on flow regime optimisation is described in the CFD study in Chapter 4. In this specific analysis, we would prefer the wave regime at diameter of 0.2 m for two reasons. First, this diameter has been used in the literature to study direct steam generation in a pipe [34]. Second, Figure 22-B shows that with an increased flowrate of up to 50%, the flow regime in the 0.2 m tube diameter still lies within the comfort zone of the wave regime.

In our case, the final value for the So-St diameter will be confirmed when we develop a comprehensive model to analyse the heat transfer performance in the Chapter 3. The performance of solar heated tubes as found in So-St would be strongly related to the tube diameter and the solvent flow regime. While a larger-diameter tube can collect more solar heat due to a higher surface area, heat transfer performance might be poorer because of the larger heat transfer distance from the So-St heating surface to the liquid travelling through in the centre. Some options to improve the heat transfer, e.g. inserts, internal fins or metallic foams (packings) [35, 36], may facilitate better mixing. It is possible to optimise the packing geometry to adapt to the designed operation point. The two most important characteristics of packing for a conventional absorption process are high surface area for gas and liquid contact, and high void space to minimise gas flow resistance [37]. The former characteristic might need to be revised for different So-St geometries, because a high surface area might cause undesirable pressure-drop. The conventional way to design packing is to improve the liquid–gas contact, because the gas (or steam in normal stripper) plays a significant role as a heat carrier; hence it is important to maximise contact between gas and liquid. In contrast, So-St harvests the heat from the solar heating surface. Therefore, it is desirable to design or select packing that can create mixing/heat transfer at the liquid and the heating surface interface. Due to the significant differences in packing design, we look further at packing within the CFD study in Chapter 4.

## 2.4    Thermodynamic pathways

We showed earlier that the thermodynamic path (c_2) used by the hybrid design might need an excessive temperature increase to achieve the lean loading target (Figure 8). Hence, there is merit in investigating whether the equilibrium pressure can be decreased by reducing the temperature, instead of increasing the equilibrium pressure immediately via raising the temperature. This still can create a $CO_2$ stripping driving force, based on *Eq. 9*:

$$CO_2 \ desorption \ driving \ force = P^*_{CO2} - P_{CO2} \qquad\qquad Eq. \ 9$$

In which $P^*_{CO2}$ is the maximum allowable $CO_2$ partial pressure (i.e. equilibrium pressure) in the vapour phase and $P_{CO2}$ is the actual $CO_2$ partial pressure. After cooling, the process reaches equilibrium at low $CO_2$ pressure, and by increasing the temperature, $CO_2$ can be further desorbed. This alternative thermodynamic path is shown in Figure 23, which represents the

principle for hybrid design with intercooling (c_3 pathway) and without intercooling (c_2 pathway).
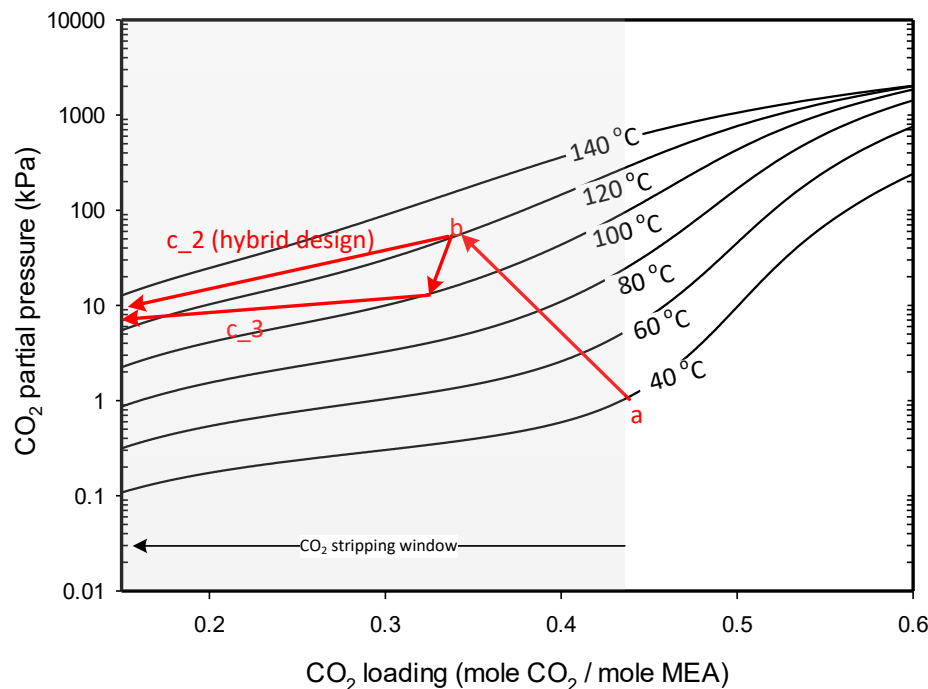


**Figure 23: Alternative thermodynamic path to reduce equilibrium CO₂ partial pressure.**

We demonstrate the uses of intercooling concept for a case-study in which the target lean loading is 0.18. The results are shown in Figure 24: subfigure 24-A without intercooling, and subfigure 24-B with intercooling. In this example, there are three So-St segments in the hybrid design. Each segment carries solvent with a specific lean loading and temperature, which can be plotted to provide a complete $CO_2$ stripping profile. The lean loading profile is similar in both cases with and without intercooling. However, without intercooling the solvent needs to be heated to 128°C, while with intercooling, once the solvent reaches 128°C it undergoes a pressure-drop (to induce cooling) and can desorb more $CO_2$ at a lower starting temperature. The most important consideration in designing intercooling is that the system must be made to equilibrate at the new low temperature, i.e. not subcooling, because only then can the system have a lower $CO_2$ equilibrium pressure, allowing more stripping. One way to induce equilibrium cooling to reduce the pressure using a pressure relief mechanism.
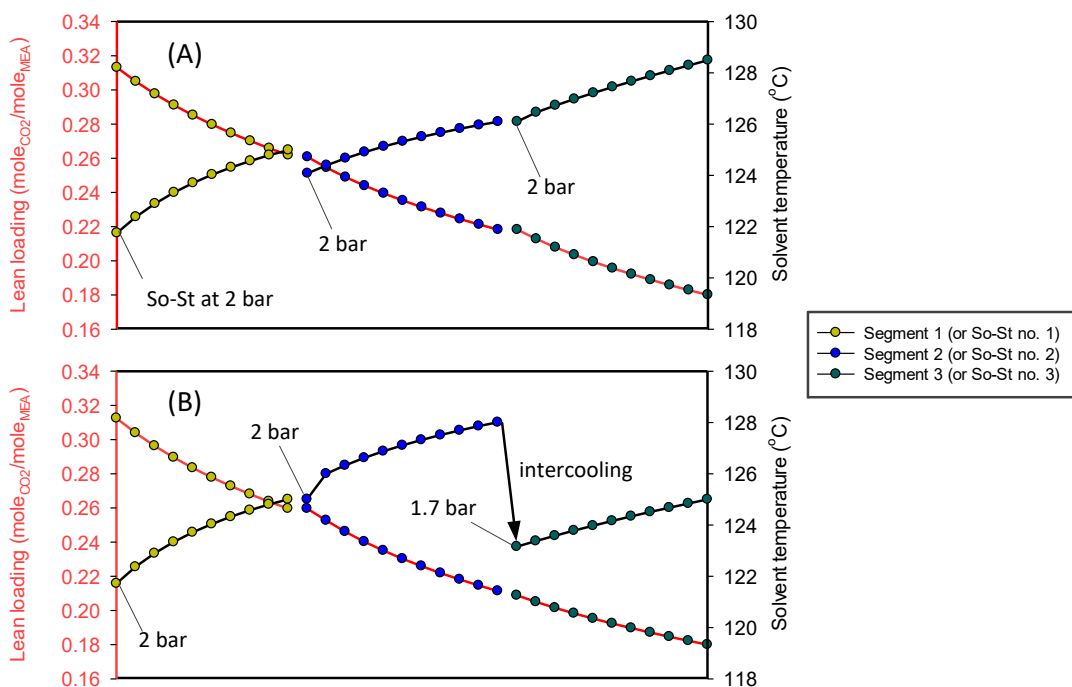
**Figure 24: CO₂ stripping profile in two pathways; without intercooling (A) and with intercooling (B). The *SHF* is assumed constant at 120 kW/m². For demonstration purposes of intercooling, we assume the lean loading target is 0.18.**

Figure 24 also provides an interesting interpretation in view of controllability and optimisation. Each of the So-St segments is responsible for regenerating the solvent to a certain extent. It is possible to interfere with the progress of solvent regeneration (e.g. bleed part of the lean solvent after one segment) to respond to solar variability without significantly interrupting this regeneration process. For example, when *SHF* drops, one might find it is more economical to regenerate 40% of the total solvent up to the target lean loading, while the other 60% is only regenerated up to 30% of the target lean loading. This might be accomplished by bleeding the 60% solvent from the second So-St segment. This type of operation might eliminate the need for auxiliary booster, which may be necessary in the So-St integrated process to ensure process stability. In our opinion, this is a new paradigm in the controllability of solvent regeneration for a solar-integrated process, in which we have the option to decide how much and to what extent to regenerate the solvent to maximise techno-economic performance. However, this option might not be practical in a conventional stripper, or even in a solar-assisted stripper that uses steam generated from solar-heated tubes. This is because in those cases, the entire regeneration process happens in one large column, instead of in small, modular segments as in the case of So-St.

## 2.5     Design integration

In previous sections, we conducted fundamental analysis on the thermodynamics and physical properties of the So-St system. For thermodynamics, we found that pressure is the

key variable affecting process energy demand. For a constant *SHF*, the pressure determines the solvent temperature and the resultant lean loading. Higher pressure is desirable to suppress water vaporisation and enhance heat utilisation in the So-St. One undesirable outcome of the pressure increase is the relatively excessive rise in the solvent temperature, which could possibly be remediated by using the proposed concept of intercooling. As mentioned earlier, the key physical properties of the So-St are the diameter and length. We found that for a fixed solvent flowrate, diameter is the most important variable determining the flow regime in So-St. By selecting the appropriate diameter, the flow regime is unlikely to change along the So-St tube. The So-St tube length has a strong effect on the *LLV*, with longer tube length resulting in more regeneration and lower lean loading.

Incorporating the concept of intercooling with the hybrid design discussed in relation to in Figure 13, the hybrid design can further benefit from temperature/pressure reduction in the intervals between the So-St segments. Figure 25 shows the $CO_2$ stripping pathway of the integrated design of hybrid with intercooling compared with the other stripping systems. It can be seen that the integrated design yields a lower $CO_2$ partial pressure in vapour phase (Figure 25-A), thus allowing for more $CO_2$ to be desorbed while keeping the solvent temperature bellow 125°C (Figure 25-B). Once the solvent is about to exceed 125°C, intercooling takes place to drop the temperature, yet desorption can still proceed to completion at the new lower temperature. From the above, we conclude that the integrated design is effective, confirming the validity of our sensitivity analyses and findings described in the previous sections.
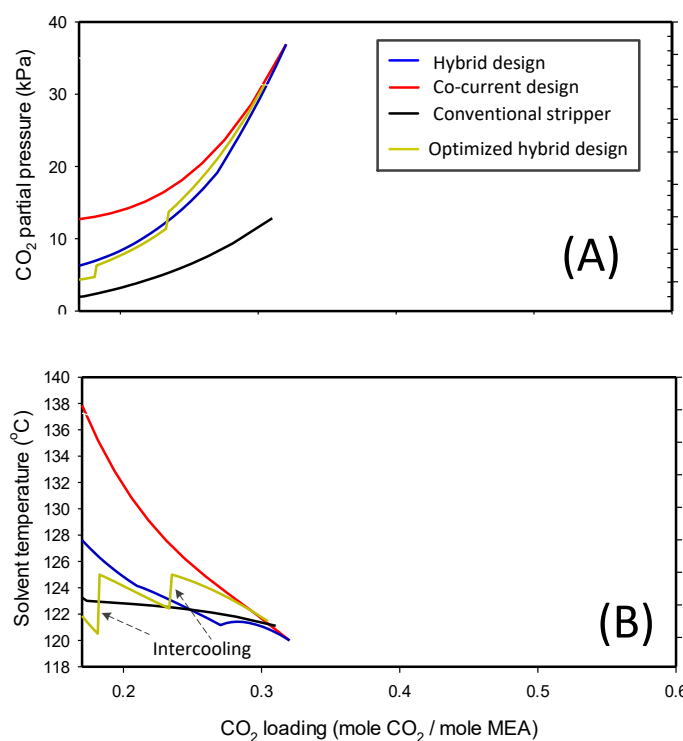


**Figure 25: $CO_2$ stripping path of different systems; (A) $CO_2$ partial pressure and (B) solvent temperature.**

## 2.6       **Concluding remarks**

In this chapter we have presented a detailed thermodynamic analysis of the possible $CO_2$ stripping mechanisms in the So-St setup. $CO_2$ stripping is facilitated by temperature increases, which in turn boost $CO_2$ equilibrium pressure in the vapour phase. As a result, more $CO_2$ can enter the vapour phase. We proposed a hybrid design to lower the energy demand. The hybrid design falls between the counter-current stripping mode (used in conventional strippers) and the long co-current stripping mode (used in typical heated tubes). The principle of the hybrid design is based on connecting short So-St segments in series, with vapour removal ports placed in between segments. This design helps reduce the residence time of the released $CO_2$ molecules, which in turn provides a potential avenue for new $CO_2$ molecules to enter the vapour phase. In other words, the $CO_2$ partial pressure is controlled at relatively low value to maintain a continuous $CO_2$-stripping driving force. Preliminary analyses were also carried out on flow regime, with the results suggesting that it could be controlled by choosing an appropriate tube diameter and superficial liquid/gas velocities in an appropriate range. The concept of intercooling could further improve the performance of the hybrid design, subject to technical or economic feasibility. In the next chapter, we further explore the effect of flow regime on heat transfer, and ultimately the $CO_2$-stripping performance and operational stability of the So-St.

# 3.    Solar-stripper (So-St) design

In Chapter 2, we conducted thermodynamic tests to sensitise the preliminary design for the So-St unit. We found that the proposed technology of using solar heat for $CO_2$ desorption is technically feasible. The rich solvent from the absorber at a loading value of ~0.45 can be regenerated in the solar collector field (SCF) with a flexible lean loading outcome. Different thermodynamic pathways to desorb $CO_2$ were also investigated. During this process, we found that it is critical to have multiple flash points along the So-St tube to enhance the $CO_2$-desorption driving force and reduce the energy demand. Therefore, instead of one long So-St tube, we proposed to divide it into smaller segments and incorporate flashing mechanisms in between for efficient $CO_2$ removal.

The design in the previous chapter was created with an assumption that solar heat is unrestricted; however, in reality, solar radiation varies with location, and in some areas is extremely limited. For example, in a contemporary study, we compared the effect of the location on So-St field design and solvent storage capacity (*SSC*) for three locations in Australia: Townsville, Sydney and Melbourne. Townsville relatively outperformed the other two cities by a large extent due to the better consistency in solar profile in all seasons [29]. In the Sydney case-study, the solar heat intensity averaged ~4.86 kWh/m$^2$/day, which is relatively low and drops significantly in winter. This is an important justification to shift away from stationary solar collectors, such as evacuated tube collectors (ETC), even if they are integrated with a diffuse flat reflector [38]. The temperature range and design parameters of the So-St unit are expected to be closely aligned with the parabolic trough collector (PTC) design. The PTC design is the most mature and affordable solar collector technology that can comfortably deliver temperatures >100°C [14]. They are categorised in the mid-temperature range and have been widely used in a number of applications, such as for power generation [39], solar cooling [40], desalination [41] and industrial process heat [42]. Due to the limited solar heat intensity, designing for larger diameters of the So-St tube might be a naive choice, because it would be difficult to deliver quality heat to the central parts of the tube, even with the ideal packings or inserts. Therefore, as a design strategy, it might be better to reduce the So-St tube diameter (for the purpose of increasing the So-St surface exposure) and increase the number of So-St modules in parallel along with the collector aperture area to increase intercepted solar thermal energy. For the base-case design, we chose a commercial value of 0.076 m inner diameter for all simulations, then we sensitised this value at a later stage. We found with appropriate sizing of the SCF we could comfortably supply up to 60–70% of the heat demand for solvent regeneration, maintaining the balance via other mechanisms such as the cross heat exchanger (HX).

Accordingly, the SCF would consists of a network of So-St loops aligned in parallel, where each So-St loop contains parallel So-St modules consisting of a number of segments in series to

effectively release the $CO_2$ gas on several stages. Figure 26 shows a complete process flow diagram for the proposed design of this novel SP-PCC method. The rich solvent flows directly from the absorber and/or from the rich storage tank and enters the cross HX. By gaining the essential enthalpy from the cross HX, a portion of the solvent might start to vaporise even before entering the SCF. Therefore, a flash drum is installed at the beginning of the desorption process to vent any early gas/vapour formation and ensure the entry to the SCF is all liquid. The SCF consists of two header pipes and a number of loops. The first header pipe, the so-called 'header distributor', provides each loop with an equal flowrate of the rich solvent, while the second header pipe ('header collector') collects the hot lean solvent to return it either directly to the absorber, or to the lean storage tank for use at a later time. At the end of the regeneration process, the lean solvent streams from each module are combined via the header collector and directed to the cross HX to pass the high enthalpy to the rich solvent stream, and be cooled and stored in the lean storage tank. The product gas/vapour mixture vented from the SCF is then cooled to about 23°C in the subsequent condenser to condense the vapours and refine the $CO_2$ product.

Each So-St loop consists of multiple So-St modules in parallel to reduce the solvent velocity when it enters the So-St modules. This is important because the So-St cannot process the entire flow from one solvent loop due to the possible high solvent velocity. The solvent velocity in a So-St loop can reach more than 10 m/s, but a So-St module can only operate at less than 2 m/s. The So-St module consists of successive segments, where each segment represents the lowest operational level in the whole superstructure (Figure 4). Theoretically, each segment consists of three critical components: i) the solar energy absorber tube for harvesting solar heat to regenerate the solvent; ii) a flash unit to separate vapour and liquid (e.g. settling or flash tank); and iii) a pump to recover the pressure back to the nominal pressure value. Multiple segments can be installed to achieve the desired loading value.

In this chapter, we discuss different factors that influence the number of required segments in each So-St module. We conducted a detailed analysis of the thermodynamic and heat transfer aspects of the system. It is sufficient to start from the lowest operation level and simulate the So-St system at segment level, i.e. we only need to simulate one segment. This is because all segments share the same operation principles during the regeneration process. Once we understand the fundamental aspects, the lessons learnt could be used to scale up the number of So-St modules/loops and then size the entire SCF.
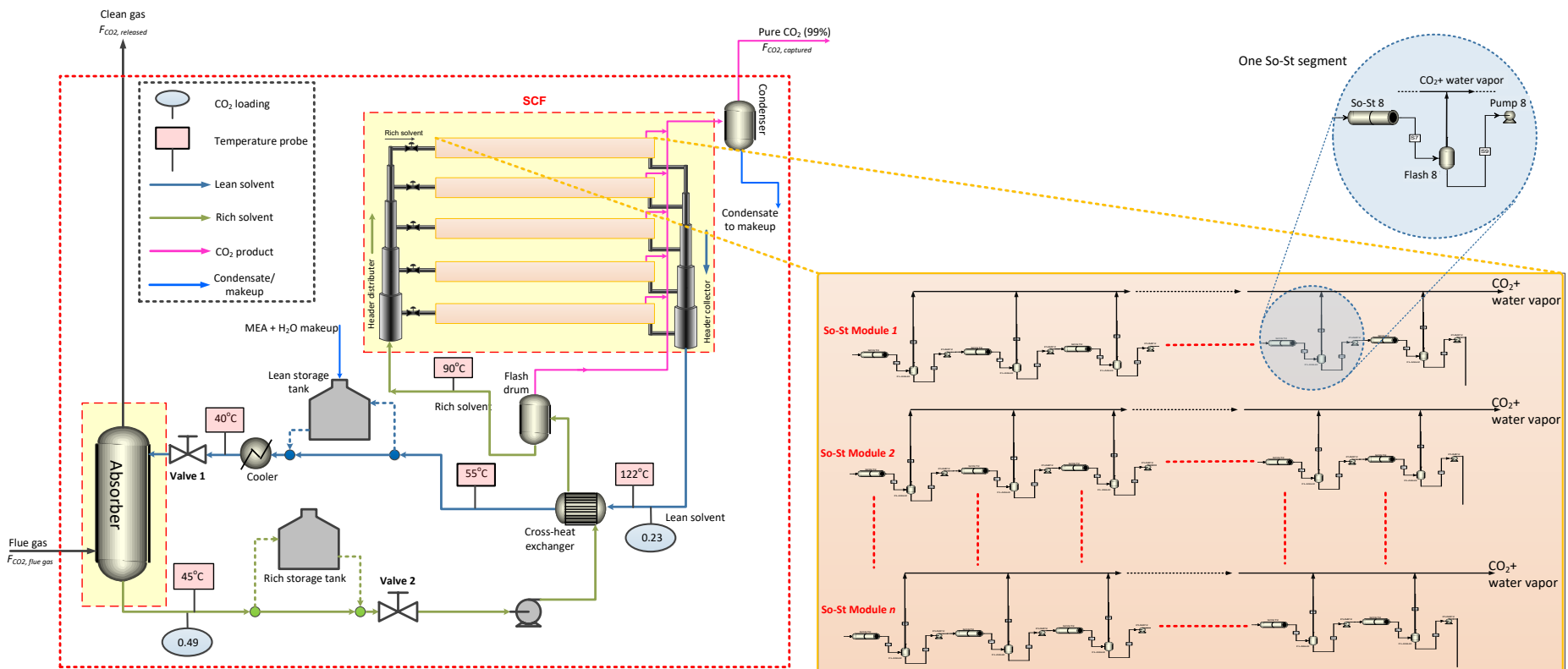
**Figure 26: Full process flow diagram for the whole superstructure (left). The two terminals of the solvent cycle (the absorber vs SCF) are highlighted in yellow. The SCF consists of a number of loops, where each loop contains a number of parallel So-St modules, and each module consists of a number of segments in series (right). Each segment is theoretically represented by a combination of a pipe model (to calculate the pressure-drop), a flash drum (to separate gas/vapour phase from the liquid), and a pump (to restore the pressure to the nominal value before entering the next segment).**

## 3.1    The role of water vaporisation

In Chapter 2, we discussed the vaporisation phenomenon that occurs during $CO_2$ stripping along the So-St tube. This phenomenon is caused by the thermodynamic properties of the $H_2O$-$CO_2$-MEA system. In this chapter, we provide a deeper analysis, aiming to minimise water vaporisation to increase $CO_2$ purity and reduce energy consumption. To reveal the extent and effect of water vaporisation, one So-St segment is simulated with rich solvent entering at 120°C, at 0.32 loading and at 0.5 m/s all-liquid velocity. The result is shown in Figure 27-A. In general, the solvent can be effectively regenerated along the So-St tube, confirming the viability of the proposed So-St technology. However, the normalised energy demand also undesirably increases at similar trend. It is important to shed light on this phenomenon to find an appropriate solution. Further evaluation reveals that the increasing trend of energy demand is due to simultaneous water evaporation. This is because water has a higher equilibrium partial pressure than does $CO_2$ in the relevant $CO_2$ loading range (i.e. < 0.4) (Figure 27-B). This finding suggests that optimising the solvent thermodynamic properties is a highly promising avenue to alleviate undesirable water vaporisation. For example, ionic-based liquids with negligible water partial pressure could be good candidates for So-St application. This is because there will be negligible water vaporisation in the ionic liquid; hence, most of the solar heat will be utilised to desorb the $CO_2$ gas. From the perspective of solvent choice, the So-St can use a larger range than a conventional stripper. This is because So-St operates based on temperature-driven desorption and there is no need for a sweeping steam. Hence, any type of $CO_2$ capture medium (either chemical or physical) could be used in the So-St application, as long as the temperature driving force is required for desorption.
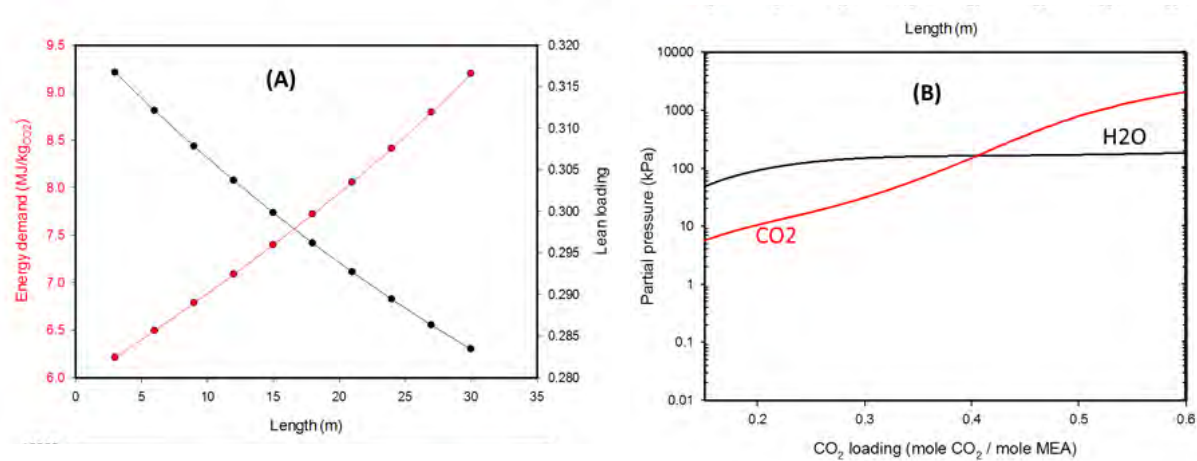


**Figure 27: (A): Simulation results (energy demand and lean loading) along a So-St segment. Solvent enters So-St at 0.31 loading, 120°C and 2 bar; (B) vapour–liquid equilibrium of $H_2O$-$CO_2$-MEA (30 *wt%*) at 120°C isotherm.**

To demonstrate the potential of solvent choice for reducing water vaporisation, we carried out a thermodynamic simulation for another tertiary amine: 30 *wt%* methyl diethanolamine (MDEA). Figure 28 reveals that MDEA has a higher equilibrium partial pressure than does

water, suggesting that MDEA exhibits a lower extent of water vaporisation. MDEA as a solvent has been of significant interest in carbon capture technology; however, it suffers from slower kinetics than the primary amine MEA [43]. We argue that slow kinetics may not cause a significant problem in the proposed So-St design, because the So-St application has larger residence time than a conventional stripper, i.e. it will take longer time for a certain amount of solvent to flow through the SCF than a conventional stripper. At this point, we can confirm that the extent of water vaporisation is solvent dependent; to alleviate this, a new approach from the angle of solvent design/optimisation is more appropriate. We believe through this process that a more compatible $CO_2$ capture media could be discovered. This is because we found MEA results in significant water vaporisation, and the solvent thermal degradation is a large obstacle, because the solvent may need to pass the upper temperature ($> 125^oC$) to reach the lean loading target. This is beyond the scope of the capabilities of this MEA solvent; thus, we would pursue this goal in future project(s).
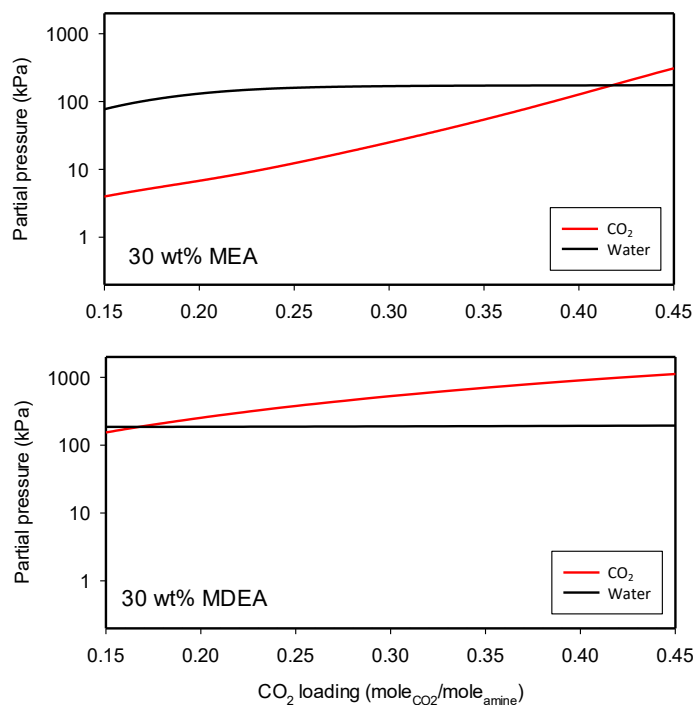


**Figure 28: Equilibrium partial vapour pressure of $CO_2$ and $H_2O$ in 30 *wt*% MEA and MDEA systems, respectively.**

In this chapter, we discuss a strategy to reduce water vaporisation, and ultimately reduce energy demand. In Chapter 2, we found that increasing the pressure can suppress water vaporisation. This strategy is further confirmed here, where we conducted a similar simulation at higher pressure. The result shown in Figure 29 reveals that at higher pressure, a higher portion of energy was consumed to desorb $CO_2$ than at low pressure. This finding suggests manipulating the pressure is a promising method to reduce energy demand. Interestingly, at 4 bar, water vaporisation is significantly reduced, but more energy is consumed by the sensible heat source. This is because at 4 bar, the solvent has a higher saturation temperature, similar to how water boils at a higher temperature if the pressure

increases. In this case, the intercooling strategy discussed in Chapter 2 must be used to prevent solvent degradation. However, this increases process complexity and reduces energy efficiency.
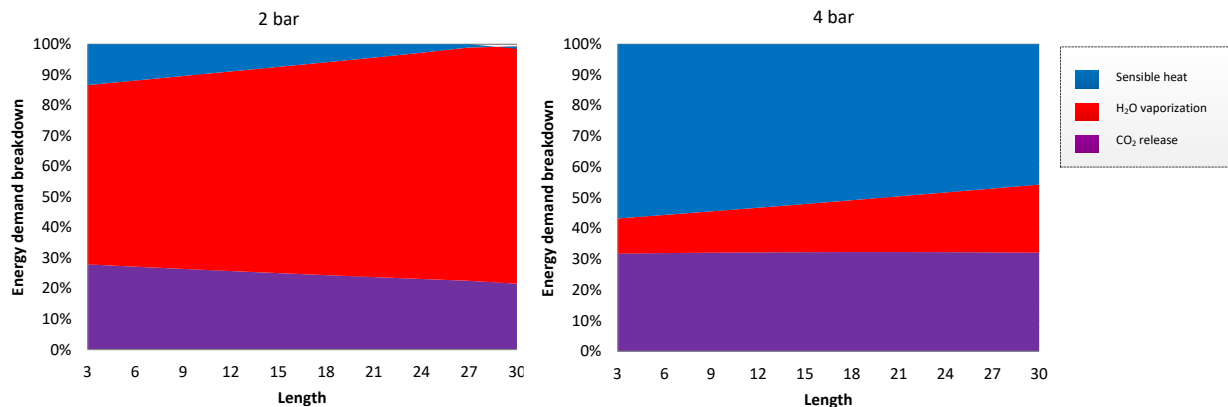


**Figure 29: Breakdown energy demand consumption by sensible heat, water vaporisation and CO₂ stripping for So-St operating at 2 bar and 4 bar.**

In summary, water vaporisation is found to be solvent dependent. Therefore, manipulating operating conditions (e.g. pressure) does not improve the situation. We suggest devoting effort to optimisation and the design of an alternative $CO_2$ capture media, given our discussion above of the flexibility of the proposed So-St design in using different forms of media. This includes the potential capability to adapt a slow kinetic solvent, or a medium with very low water vapour pressure, such as an ionic liquid [44].

## 3.2    Two-phase flow heat transfer

In this section, we look at the heat transfer aspect of the So-St design. In particular, we study the relationship between the vapour fraction/regime on heat transfer and different design variables affecting the heat transfer coefficient. The outcome of this study can be used to develop a design protocol for the So-St system. The built-in Aspen® rigorous HX design was used to determine the heat transfer coefficient of a two-phase flow into a tube at predetermined flowrate. For all simulations, we assumed the heat source is unlimited at this stage. Unless specified otherwise, inputs to Aspen® simulations are shown in Table 8.

**Table 8: Inputs for base-case simulation of one So-St segment with a constant heat flux (no consideration for solar fluctuation at this stage, because this study focuses on heat transfer fundamentals).**

| Process variables | Value |
|---|---|
| So-St diameter (m) | 0.076 |
| So-St length (m) | 15 |
| Rich loading | 0.4 |
| Lean loading | 0.3 |
| Number of So-St segments | 1 |

| Rich solvent flowrate (kg/hr) | 4546 |
|---|---|
| Rich solvent velocity (m/s) | 0.38 |
| Tube surface temperature (°C) $^a$ | 100–111 |

$^a$ *This determines the heat flux on the absorption tube, which is not constant along the So-St tube but depends on the wall temperature; heat flux ranges from 100 to 200 kW/m².*

In a So-St tube, the dominant phenomenon is the vaporisation (i.e. boiling) along the tube. In a boiling flow, heat transfer is governed by two additive mechanisms: nucleate boiling and force convective evaporation. The force convection component has been viewed as similar to the macroscopic convective mechanism for subcooled liquid heat transfer [45]. In contrast, nucleate boiling happens at micro-convective associated with bubble nucleation and growth (i.e. two-phase regime) [45]. The general formulation for heat transfer calculation is as follows:

$$h = S \times h_{nb} + F \times h_{con} \qquad \text{Eq. 10}$$

Where $h_{nb}$ and $h_{con}$ (W/m²/K) are the local nucleate boiling and convective heat transfer coefficient, respectively; $S$ is the suppression factor (0 for no flow and 1 for infinite flow); $F$ is the enhancement factor for the convective heat transfer component to account for the enhancement effect of vapour formation. It is believed that with increasing the vapour fraction to a certain limit, the two-phase mixture increases the turbulence of the flow, thus boosting the convective heat transfer component. *Eq. 10* suggests each heat transfer component could be addressed individually to enhance the overall heat transfer. For example, to boost the convection component (i.e. $F \times h_{con}$), literature studies suggest increasing the flowrate could be effective [45].

To understand heat transfer inside a So-St tube, we conducted a base-case simulation, shown in Figure 30. The profile of the heat transfer coefficient matches the description in [45]. The all-liquid solvent enters the So-St segment at a subcooled temperature (98°C) and 2 bar pressure in two different tube geometry positions: horizontal (Figure 30-A) and vertical (Figure 30-B). The heat transfer coefficient profile is similar to those reported in the literature for a boiling flow [46]. In a horizontal geometry, the gravity force acts asymmetrically on the liquid, resulting in a non-uniform distribution of the liquid layer. In a vertical geometry, the distribution is more uniform, due to the symmetrical force of gravity.
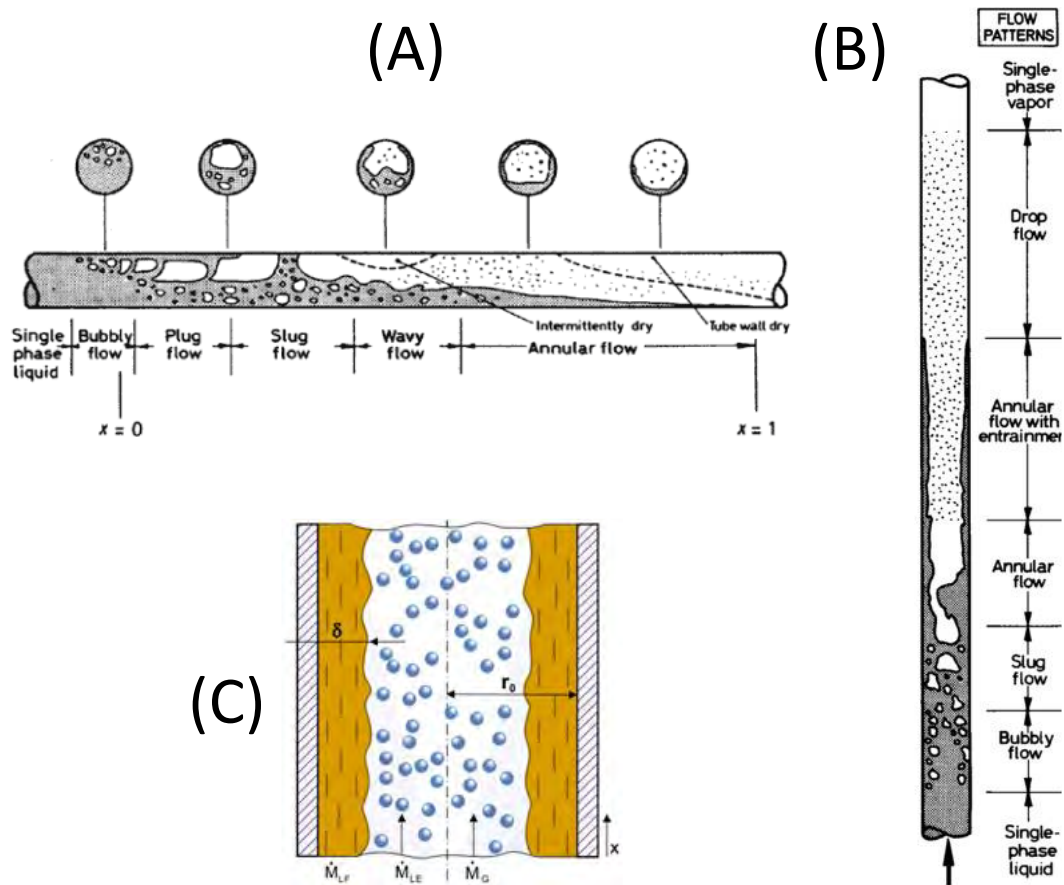
**Figure 30: Schematic showing the possible flow regimes along the So-St in horizontal (A) and vertical (B) geometries. Sub-figure (C) presents an annular flow regime where liquid droplets are entrained due to higher volume molar fraction (*VMF*) and heat transfer coefficient [47, 48].**

The analysis presented in Figure 31 shows that at low vapour molar fraction (*VMF* <0.05), the heat transfer coefficient is relatively small in both configurations (Figure 31-A). This means the nucleate boiling mechanism is predominant, thus contributing most to the heat transfer coefficient value [49]. At higher *VMFs*, the system starts experiencing rapid increases in the heat transfer coefficient (during wavy to annular flow regimes), gradually increasing until the *VMF* reaches about 0.3 (Figure 31-B). During this period, convective heat transfer becomes the dominant component, and the liquid is driven more to the bottom (in the horizontal tube) and to the walls (in the vertical tube) where the vapour flows in the middle ( Figure 31-C). In this regime, the volumetric *VMF* becomes very high (≈70–85%) of the total volume [48]. In the vapour core, there could be entrainments of liquid droplets carried by the higher *VMF*.

In this regime, evaporation often happens at the liquid/vapour core interface; it could also happen in the liquid film in the vicinity of the tube inner wall, when vapour bubbles appear on the heated walls of the tube [48]. The key advantage of the vertical over horizontal configuration is within the low *VMF* range (Figure 31-A). Here, a higher heat transfer coefficient could be attributed to the symmetrical force of gravity helping distribute the liquid forming around the heated walls, and enabling better vapour to escape due to the surrounding thinner liquid layer. In contrast, the horizontal configuration has asymmetric

liquid distribution (Figure 30-A), and the lower part of the So-St cross section will have a thicker liquid layer compared with the vertical geometry (Figure 30-B). At a higher *VMF*, both vertical and horizontal layouts would have almost similar heat transfer coefficient profiles resulting from the very high vapour velocity (Figure 31-B).

From this preliminary analysis, the annular flow regime seems to give the highest heat transfer performance, and the global maximum heat transfer occurs at ≈0.4 *VMF*. For a *VMF* range from 0.4 to 0.6, the heat transfer coefficient starts declining after reaching that optimum at ≈0.4 (Figure 31-B). The underlying driving force for this decline is due to more vapour occupying the tube volume, thus reducing the available volume for liquid flow. As a result, the liquid velocity would be inevitably increased to conserve the mass balance. Eventually, this would also help to increase the convective mechanism of heat transfer. The main risk of operation at a high volumetric *VMF* is that it could bring the system near dry-out conditions. While this behaviour might be interesting to study, we do not devote further analysis to it, because So-St should not operate up to this high level of *VMF*. Hence, it is very unlikely to allow this to happen in the $H_2O$-$CO_2$ flow regime, because at a high *VMF* such as 0.4, there would be a high rate of water vaporisation. This would result in an undesirable $CO_2$-diluted vapour stream ($P_{H2O}/P_{CO2} \gg 1$) as demonstrated in Figure 31-C, making the energy performance for $CO_2$ stripping relatively poor [50].

From the above analysis, we investigated the heat transfer performance for a low *VMF* range, i.e. <0.1. Note that this *VMF* threshold should only be considered for 30 *wt*% MEA solvent, because other solvents may have different thermodynamic properties, resulting in a different *VMF* threshold. In summary, lessons learnt from this exercise are:

1. The local heat transfer coefficient is made up from two contributions: micro nucleate boiling and macro convection.

2. The macro convection effect is enhanced with increasing *VMF* as a result of increasing liquid velocity adjacent to the tube wall.

3. The micro nucleate boiling effect is suppressed by increasing the *VMF* but enhanced by higher heat flux due to the increase in superheat in the liquid film.

4. A higher *VMF* results in significant water vaporisation, thus diluting the $CO_2$ concentration (Figure 31-C) and decreasing the energy performance.

5. So-St segments should not be too long, with the aim of reducing the *VMF* at the exit of each segment.

6. Achieving a higher heat transfer coefficient is more likely at a lower *VMF*, and this can be marginally better achieved using a vertical tube configuration (Figure 31-A).
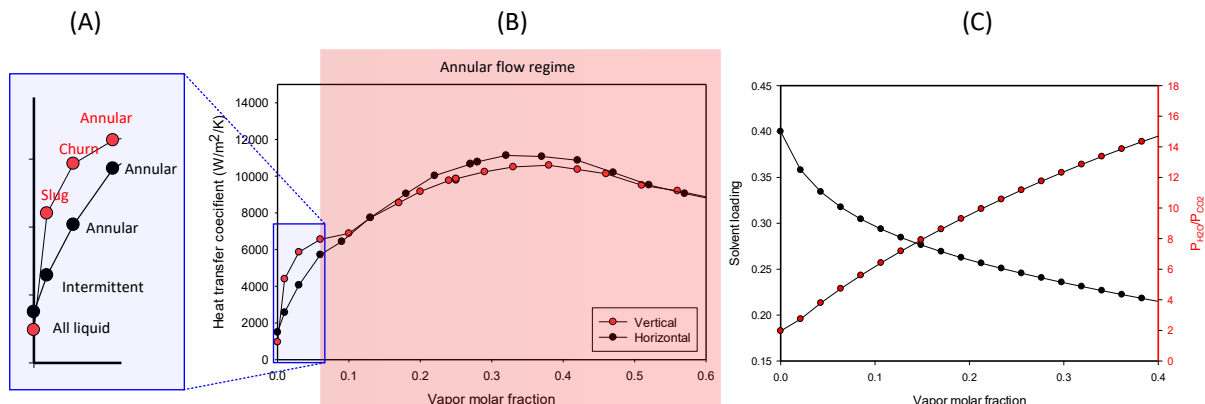
**Figure 31: (A) The magnified heat transfer coefficient pattern for both horizontal and vertical geometries demonstrating the evolving flow regimes at *VMF* ≤5%. (B) The complete profile of the heat transfer coefficient as a function of *VMF* in both horizontal and vertical geometries. (C) Solvent loading profile and the relative partial pressure of H₂O vs CO₂ (P$_{H_2O}$ /P$_{CO2}$ ) as a function of *VMF* [50].**

From the above, we can conclude that a boiling flow could achieve a high heat transfer performance, given a desirable flow regime and vapour fraction can be reached. The heat transfer coefficient peaks around 0.4 *VMF* during the annulus flow regime. For So-St operation, it is very unlikely that optimum conditions will be reached, because this happens at high vapour fraction containing a significant amount of water. This means the energy performance for CO₂ stripping is low. Hence, we will investigate the heat transfer performance at a low vapour fraction, i.e. <0.1 *VMF*.

For practical application, pressure-drop could be used to correlate the *VMF* inside So-St in real-time [51]. Figure 32 demonstrates a relationship between *VMF* and pressure-drop, suggesting pressure-drop might be a good indicator for the *VMF*. In the event of solar energy fluctuation, the solvent flowrate could be manipulated to achieve the pressure-drop set-point, i.e. *VMF*. Next, we investigate different design variables that affect the heat transfer coefficient at a low vapour fraction. Note that the criteria of vapour fraction set out here should only be considered for a 30 *wt*% MEA system, because each solvent (e.g. MDEA or other chemicals) would have different thermodynamic properties, and therefore different vapour fraction thresholds.
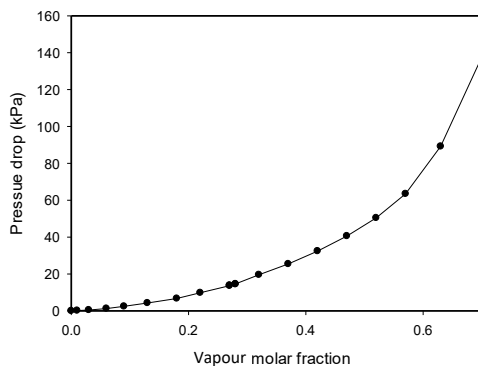


**Figure 32: Correlation between vapour molar fraction and pressure-drop.**

For the sensitivity analysis, the following guidance was taken from the literature [52] to assist our selection of sensitised variables:

- The total local heat transfer coefficient is made up from two contributions: micro nucleate boiling and macro convection.
- The macro convection effect is enhanced with increasing vapour fraction as a result of increasing liquid velocity adjacent to the wall.
- The micro nucleate boiling effect is suppressed by increasing vapour fraction, but enhanced by higher heat flux due to an increase in superheat in the liquid film.

From the above, we think increasing the liquid flowrate and solar heat flux (*SHF*) could increase the heat transfer coefficient. We tested both vertical and horizontal tube layouts. For pressure-drop calculation, the tube inner roughness was set at 0.0015 mm [53]. Figure 33 shows the effect of mass flux on heat transfer and pressure. Note that we use mass flux instead of mass flowrate, because it is more useful for studying heat transfer. The mass flux variable accounts for both mass flowrate and the tube cross section area. The results show that increasing the mass flux leads to a higher heat transfer coefficient, and that the difference is more significant at high vapour fractions. This is because higher mass flux helps promote the macro convection component, which is more significant at high vapour quality. These results agree with literature on the boiling flow, which concludes that convective heat transfer is the dominant component at a higher vapour fraction [49]. In contrast, higher mass flux leads to exponential growth in pressure-drop, most significant after 0.05 vapour fraction. This is because at high vapour fraction, the liquid velocity along the So-St tube is further increased due to less volume being available to flow. Recall that the total pressure-drop in two-phase flow is made up from two components: frictional and acceleration pressure drops [54]. In the case of increasing mass flux, the acceleration component increases significantly.
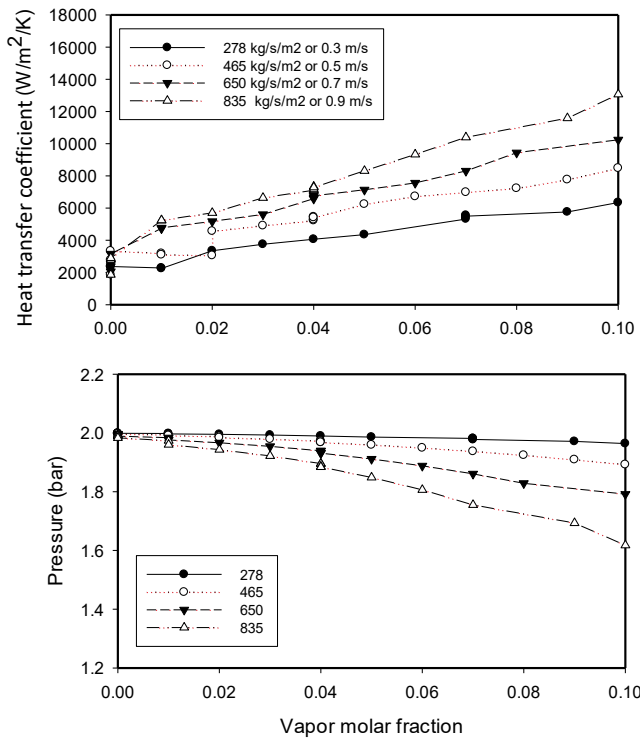
**Figure 33: Heat transfer coefficient and pressure calculation at different mass flux (kg/s/m²). The tube inner diameter is 0.076 m; solvent enters So-St at 100°C.**

To find out how the enhanced heat transfer can benefit So-St design, we determined the total So-St tube length requirement for achieving 0.1 vapour fraction at different mass flux. This total length is calculated by multiplying the number of parallel So-St modules by the length of a So-St tube required to achieve 0.1 vapour fractions. The lengths are then normalised against the longest So-St tube. The result shown in Figure 34 indicates that at higher *SHF*, less mass flux eventually leads to a smaller SCF field. This is plausible, because common sense dictates that higher mass flow will require more heat-exchanging area to account for the extra mass in the system. However, the result suggests the opposite: higher mass flux results in smaller So-St tube length. This means the enhanced heat transfer can successfully provide overall benefit, in this case a smaller So-St network in the SCF. However, the pressure-drop becomes a significant factor, presenting a drawback of high mass flux operation. Too high pressure-drop leads to flow instability, e.g. mechanical vibration, control issues or burn-out on the heat transfer surface [55]. We will conduct more detailed pressure-drop analysis in a later CFD study, because the Aspen® package does not have the capability to explore flow instability that could be caused by several mechanisms (e.g. pressure-drop type or density wave function). In the current simulation, high pressure-drop is considered as problematic when Aspen® returns warnings such as 'choke condition is reached' or 'mechanical vibration issues'.
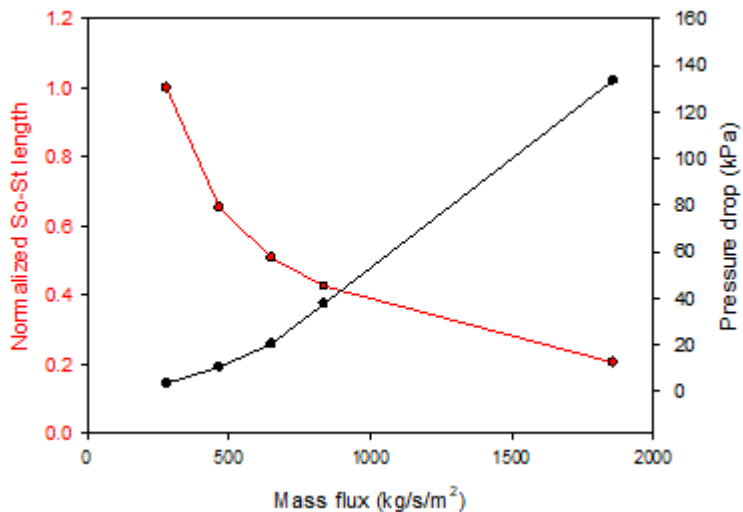
**Figure 34: The effect of mass flux on average heat transfer coefficient (from 0 to 0.1 vapour fraction). The So-St length has been normalised to 1 against the largest value because the actual length would depend on the solar heat flux, i.e. SCF design. The total length is the sum of the number of So-St arrays x (So-St tube length required to achieve 0.1 vapour fraction). The total mass flux from the $CO_2$ absorber is 6,624 kg/s/m$^2$ as calculated by the PCC base-case scenario.**

A similar analysis was conducted for the vertical tube and the results are shown in Figure 35. It can be seen that vertical geometry results in a higher heat transfer coefficient. This is more significant at low mass flux, while at high mass flux, the heat transfer coefficient of both layouts approaches the same value at high vapour fraction. This analysis reveals that a different design layout could be a promising avenue for process optimisation. While vertical So-St tubes are impractical, one might think of inducing the inclination of the SCF to some extent to optimise heat transfer performance [52]. In our So-St design, we will only consider the horizontal tube, because it is practical and easy to implement on the ground.
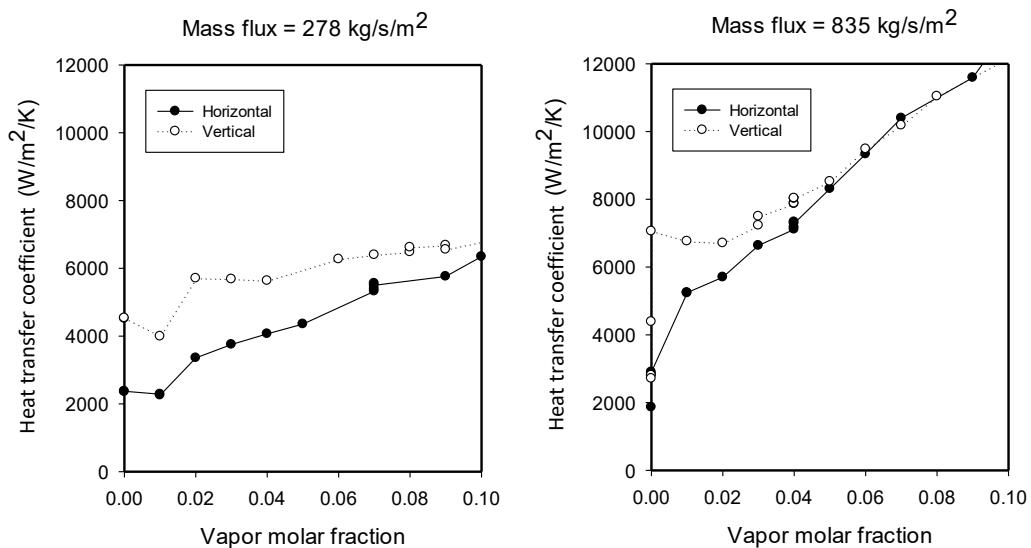


**Figure 35: Heat transfer coefficient for horizontal and vertical tubes at different mass flux. Tube inner diameter is 0.076 cm; solvent enters So-St at 100°C.**

Another method to enhance the heat transfer coefficient is to increase the tube wall surface temperature. This could be achieved by designing the So-St tube for a higher heat flux. This helps increase the heat transfer nucleate boiling component in *Eq. 10*. The tube wall temperature was sensitised from 125 to 152°C and the result is shown in Figure 36. In practical application, a higher tube wall temperature could be achieved by increasing the *SHF* on the tube surface by increasing the amount of solar energy concentration. In this case, a higher wall temperature mostly promotes heat transfer when the vapour fraction is less than 0.02 (Figure 36-A). This is because for flow boiling, the enhancement in heat transfer from the nucleate boiling component only contributes at low vapour fraction, while at higher fractions, its effect is suppressed [49]. The enhancement in heat transfer leads to a smaller So-St tube length (Figure 36-B). Plausibly, the pressure-drop does not increase but rather decreases in line with the So-St tube length reductions. In other words, we can reduce the So-St tube length while also reducing the pressure-drop. This is expected, because shorter So-St tubes mean a smaller friction component in the pressure-drop.

In summary, we have explored two variables: the solvent mass flux (or mass flowrate) and the wall surface temperature (or *SHF*). Both variables could be tuned to achieve a higher heat transfer coefficient, and thus more solar heat could be absorbed for a given heat exchange area. This helps to reduce the So-St tube length requirement. Of the two variables, the heat transfer enhancement associated with mass flux is coupled with pressure-drop; more heat transfer could be gained, but at the cost of higher pressure drop. In contrast, increasing wall surface temperature (i.e. *SHF*) enhances heat transfer and reduces the length requirement, while not causing additional pressure drop. Therefore, we confirm that solvent mass flux could be a promising variable to manipulate for process control purpose while *SHF* is a key design variable to size the So-St field.
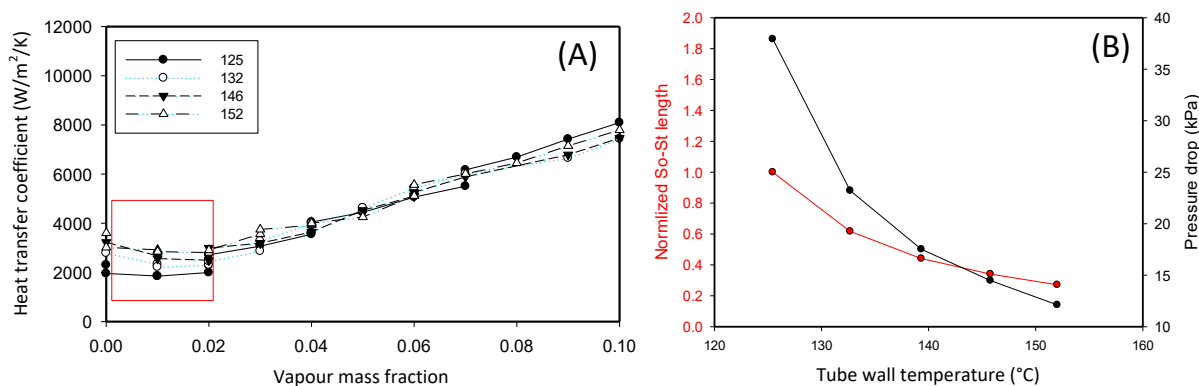


**Figure 36: (A) Heat transfer performance at different tube surface temperatures. (B) Normalised So-St length and pressure-drop. The So-St length is the length required to achieve 0.1 vapour fraction. Tube inner diameter is 0.076 cm; solvent enters So-St at 100°C.**

For the vapour fraction range of interest (0 – 0.1), we can determine the energy performance and the number of So-St segments. In this sensitivity test, we would like to discover the outcomes of sizing the length of each So-St segment to achieve a fixed amount of vapour. We think choosing an appropriate vapour fraction should be the highest priority of the decision-

making process. This is because vapour fraction determines the flow regime, pressure-drop and heat transfer coefficient: all critical parameters in two-phase boiling flow to ensure the system's functionality and operability. The results shown in Figure 37 indicate that increasing the vapour fraction reduces the number of So-St segments required, because fewer flash stages are required. However, this is at the expense of higher energy demand resulting from higher water vaporisation. In contrast, at a lower vapour fraction, the number of So-St segments increases while energy demand decreases.

There is a tangible trade-off between process operation/control effort vs energy efficiency. Interestingly, the number of So-St segments increases exponentially as design vapour fraction reduces, while the energy demand only reduces linearly. In other words, to achieve very low energy demand, the number of segments becomes a significant factor. For example, looking at the energy demand line (Figure 37 – dashed red lines), operating at 0.1 vapour removal requires about 11.9 $MJ/kg_{CO2}$, while operating at 0.02 only requires about 9.7 $MJ/kg_{CO2}$. This equates to about an 18.9% energy saving. Considering the required So-St segment line, at 0.1 vapour, only three segments are required, while at 0.02 up to 13 segments are required. Therefore, we conclude that for lower-energy operation, the number of segments can increase substantially, thus creating extra process complexity. Therefore, operating at very low vapour fraction to achieve a lower energy demand is not practically feasible. From these results, we choose 0.05 as our design point, because it has relatively low energy demand (~10.7 $MJ/kg_{CO2}$) while only requiring six segments.
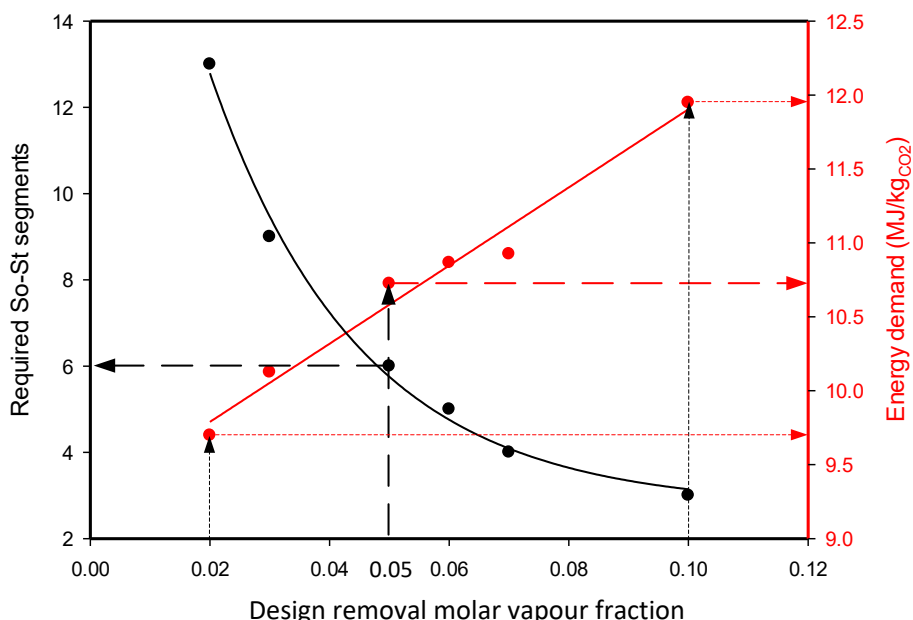


**Figure 37: Sensitising study of different design points for molar vapour fraction. For this result, the solvent enters the first So-St segment at 0.45 and exits the last segment at 0.22–021. So-St diameter is 0.076 cm, solvent velocity at the inlet of the first segment is fixed at 0.5 m/s, and average *SHF* on the surface of So-St is 100 kW/m².**

## 3.3      So-St conceptual design framework

In this section, we develop a conceptual framework to determine a preliminary design for the So-St network. We decouple the PTC design specifications from the So-St design to make it easier to achieve appropriate preliminary sizing, which would facilitate later optimisation. We can design the So-St network for achieving specific goals (e.g. energy efficiency), and then later size the SCF to meet the energy demand based on the optimised So-St network. In this section, we aim to reach the following goals, according to the design specifications and constraints summarised in Table 9:

- Determine the correlation between *SHF* and the So-St module length.
- Determine the length ratio between the segments in one So-St module.

**Table 9: So-St design specifications and constraints.**

| Parameter | Range |
|---|---|
| Loading range | 0.45 – 0.22 (±0.01) |
| First segment all-liquid velocity range (m/s) | 0.9 – 1.7 |
| Maximum solvent temperature | 125°C |
| So-St inner diameter (m) | 0.076 |
| Molar vapour fraction removal | 0.05 |
| Pressure (bar) | 2 |
| Number of segments [a] | 6 |
| Energy demand (MJ/kg) [a] | 10 – 11 |

*[a] Based on* Figure 37*, six segments are required for the design point at 0.05 molar vapour fraction and the energy demand is 10 – 11 MJ/kg$_{CO2}$.*

We briefly discuss each of these design specifications and constraints below.

- Loading range: 0.45 to 0.23. This is a typical range for $CO_2$ absorption-desorption in a conventional PCC working with MEA solvent. The So-St network is expected to only desorb from the loading value of 0.42 because during heat recuperation in the cross HX, some of the $CO_2$ already starts being desorbed and would be flashed out (Figure 26) before entering the So-St network.
- Molar vapour fraction for removal is 0.05 (or 5%). This is referred to as 'vapour quality'. This value is chosen because lower vapour quality leads to an exponential increase in the number of So-St segments. In addition, lower vapour quality results in lower heat transfer coefficient; hence, longer So-St segments would be needed. So-St segments will be sized to achieve 0.05 vapour fraction at the exit of the last segment. For the design, we need to use a constant heat flux. In real operation, we might not maintain exactly 0.05, but it could vary from 0.04 to 0.07 depending on the solar energy availability. Process control

mechanisms can be implemented to correct the vapour fraction. Pressure-drop could be used as an indication of the vapour fraction. Another good indication is the temperature, which is discussed in more detail in the next section about the operational aspect of the So-St.

- The typical velocity in the conventional PTC (liquid phase only) can be more than 2 m/s. However, at this velocity, So-St will experience significant pressure-drop due to the two-phase operation. This pressure-drop results from the increase in velocity, which needs to be compensated by the pressure reduction according to Bernoulli equation (*Eq. 10*). For all-liquid flow, the pressure-drop is due to friction from the tube surface and is almost proportional to the square velocity. However, in a two-phase flow regime, additional factors (e.g. vapour formation and liquid acceleration) would amplify the pressure-drop. This concept can be proved from Figure 38. The correlation plots the velocity (*x* axis) vs the pressure-drop (*y* axis). It can be seen that the *y* value is proportional to more than the square of the *x* value. We have sensitised this trend and found the velocity should be less than 1.7 m/s for the design point of 5% *VMF* (Figure 38). This is because at higher solvent velocities (> 2 m/s), the pressure-drop becomes substantial; and hence the choice of 1.7 m/s is a conservative target for the solvent velocity. In reality, excessive pressure drops in the two-phase regime may cause internal flashing and excessive temperature reduction [56]. Eventually, the temperature drops lower than the threshold to facilitate effective $CO_2$ desorption.



The chart displays: $y = 16.275x^{2.2252}$, $R^2 = 0.9962$. Y-axis: Pressure drop (kPa). X-axis: So-St all-liquid inlet velocity (m/s).
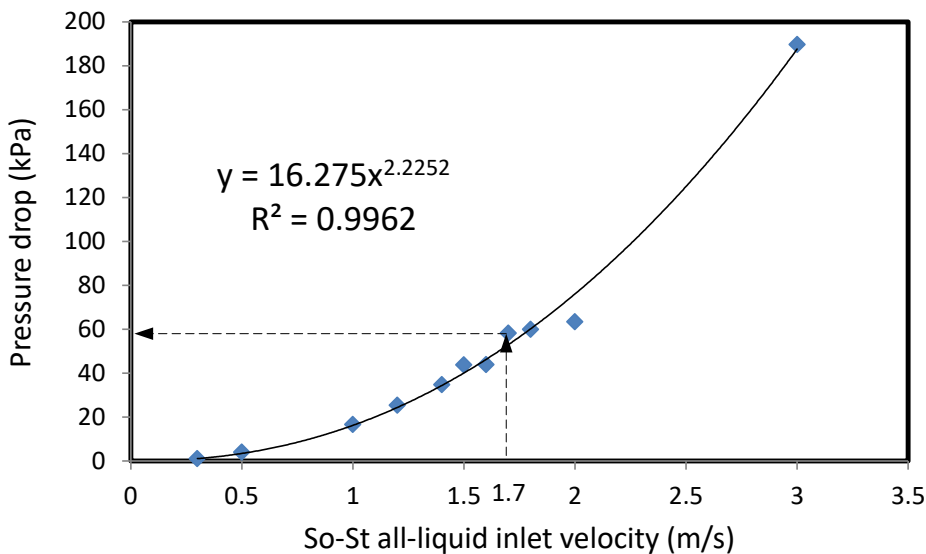
**Figure 38: Pressure-drop at different inlet velocities. One segment was simulated using the inputs from Table 2. The length of the segment influences the pressure-drop; for each velocity we determined the length to achieve the target of 0.05 *VMF* at the exit and calculated the corresponding pressure-drop.**

- The operating pressure is set at 2 bar, because at this pressure the desirable lean liquid boils at approximately 120–125°C and does not experience significant solvent degradation. It has been suggested that for boiling flow, higher pressure (>3 bar) can aid stabilisation of the two-phase flow [56], but higher pressure will also boost the 30 *wt*%

MEA solvent to reach above the 125°C cap. Hence, future work on solvent screening and selection should include operability under high pressure as one of the potential selection criteria for solvents.

- For removal target of 5% vapour quality, we performed a sensitivity test and found that six So-St segments would be required. The loading achieved in each segment would depend on the thermodynamics, hence the vapour quality. The loading in each segment is shown in Figure 39.

- The energy demand was found to be strongly related to the design value for vapour quality removal. A lower design point leads to lower energy demand, but with significant increase in the number of segments. For a design point at 5% vapour quality, energy demand fluctuates between 10 and 11 MJ/kg$_{CO2}$ depending on the pressure-drop value.

Figure 40 shows the process flow diagram of a So-St module consisting of six segments. Recall from Figure 26, there are multiple So-St modules arranged in parallel within one So-St loop. The rich solvent, after recuperating the heat from the cross HX, would reach ~90°C (Figure 26) and then enter the So-St network. The solvent is then distributed equally to the So-St modules via the header distributer, and then flows through a series of segments within the So-St module to absorb the solar energy. Each So-St segment has an absorption tube, a flash drum and a pump, as shown in Figure 40. The total number of So-St modules will be estimated in this section, but will be optimised in the final SCF sizing in Chapter 6.
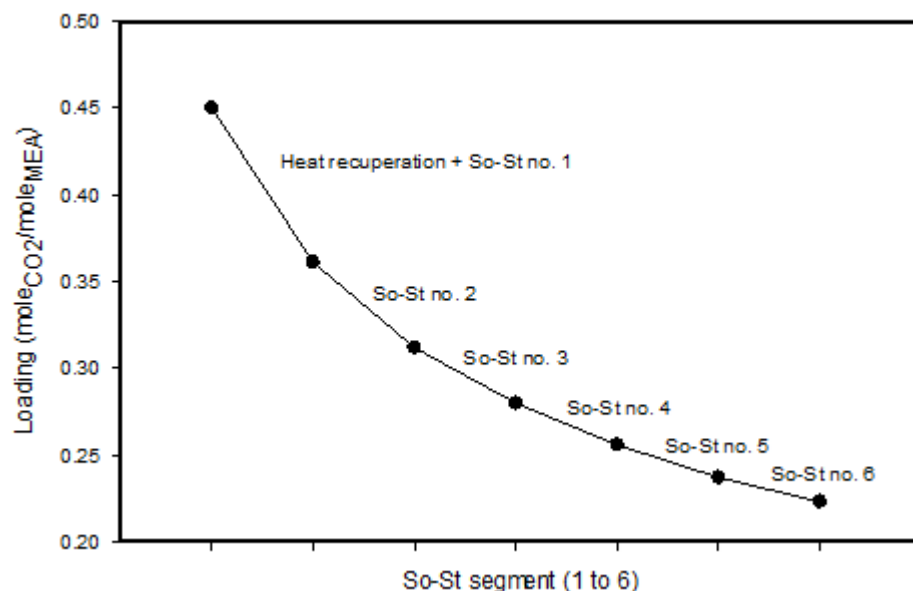


**Figure 39: Loading specification for six So-St segments. The rich solvent at 0.45 loading enters the cross HX to recuperate the heat from the lean solvent. Then it enters the six So-St segments in series.**
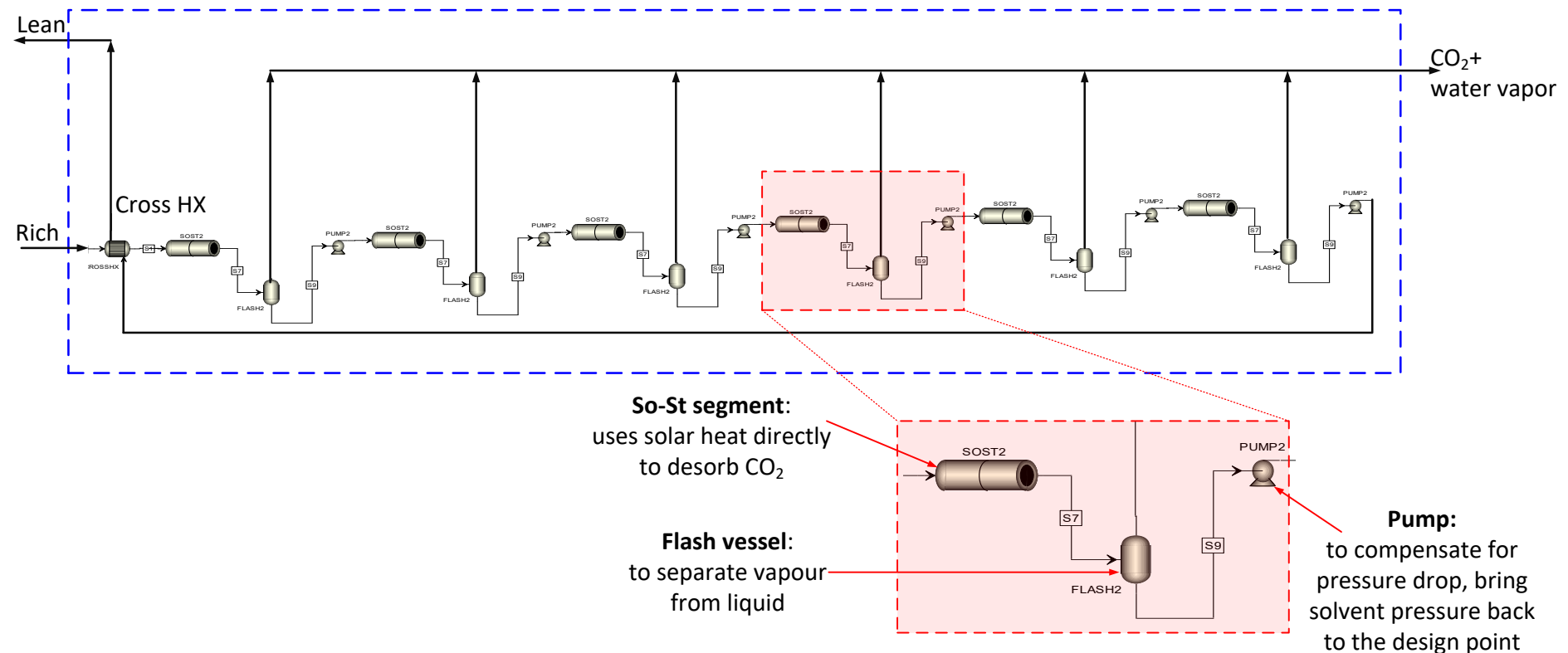
**Figure 40: Process flow diagram for a So-St array comprised of two segments. A segment module comprises an absorption tube, a flash drum and pump. The drum is used for vapour–liquid separation and the pump is used to compensate for pressure drop.**

As stated, the objective of the So-St design is to achieve the design specifications with an appropriate So-St length requirement, while not violating the operational constraints. The rich solvent absorbs solar energy via the surface of the absorption tube. Hence, we can write the heat transfer correlations as follows:

$$Q = U \times A \times \Delta T$$

*Eq. 11*

$$A = \frac{Q}{U \times \Delta T}$$

*Eq. 12*

Fundamentally, for the same amount of energy demand ($Q$) to regenerate a fixed amount of solvent, either the heat transfer coefficient ($U$) or temperature difference between the solvent inlet and outlet ($\Delta T$) should be increased. Accordingly, the required area ($A$) would be decreased and, hence, shorter So-St tubes would be needed. From the above, the heat transfer coefficient ($U$) is an important parameter that can directly affect the total So-St length. To demonstrate its effect, we simulated a So-St network at different 'all-liquid' velocity entering the first segment. The velocity is changed by manipulating the mass flowrate. The length of each segment is calculated for achieving a 5% vapour quality target. It is further assumed that the solar heat demand is readily available, i.e. at any velocity value, we can still achieve 5% vapour quality at the exit of each So-St segment.

From the heat transfer analysis, we learnt that increasing velocity (i.e. mass flux) leads to a higher heat transfer coefficient. This benefit is demonstrated in Figure 41. As solvent velocity increases (i.e. mass flux increases), the total So-St length per module (sum of the length of six segments) would also increase. This is because greater solvent flow into a So-St tube would require more area (i.e. length) to regenerate the extra solvent. In contrast, the number of required modules in parallel reduces significantly. This is because the number of modules required is calculated by taking the total mass flux from one solvent loop (numerator) divided by the mass flux into one So-St module (denominator). Hence, if the denominator (i.e. velocity or mass flux) drops, the number of required modules would exponentially increase. The overall outcome is that the total So-St length (length per one So-St module x number of So-St modules) drops as velocity increases (Figure 41-A). This desirable outcome stems from increases in the heat transfer coefficient. Hence, for a given heat exchange area, more heat can be absorbed at higher velocities as can be seen in Figure 41-B.

From the above results, we chose a solvent velocity of 1.2 m/s as a benchmark for design of the So-St network. This velocity was considered in the literature for a PTC direct steam generation system [56]. Another reason for this choice is to provide more flexibility in process control. For example, when *SHF* becomes excessive, a defocusing mechanism is often used to protect the system from overheating. In this case, solvent velocity might be increased to absorb the excess heat, because at higher velocity, the heat transfer coefficient increased, enhancing the capability of the solvent to absorb more solar energy.
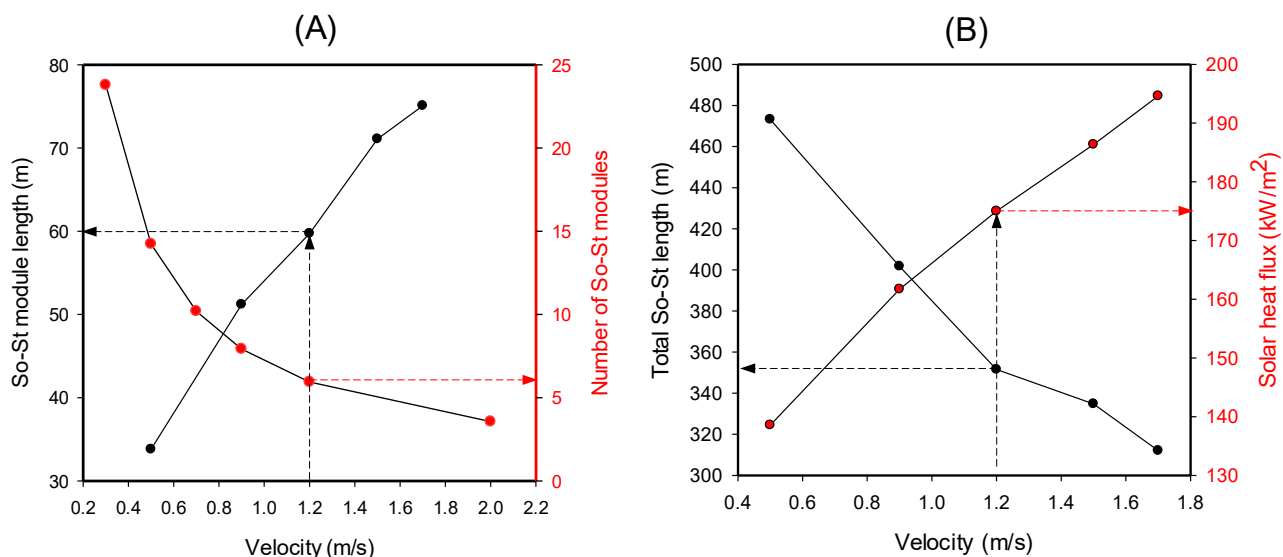
**Figure 41: Sensitising the 'all-liquid' velocity at the first So-St segment for six segments So-St module. (A) The total length of one So-St module (i.e. sum of the length of six segments) and the number of So-St modules in parallel to process the solvent flow from one solvent loop (mass flux = 6,623 kg/s/m$^2$). (B) The total So-St length = length per module x number of modules as a function of the *SHF* absorbed by solvent.**

After selecting the benchmark solvent velocity, we carried out a sensitivity test to correlate the *SHF* with the required So-St lengths. This *SHF* is the amount of thermal power that hits the surface of the So-St tube, termed kW per surface area (kW/m$^2$). The result shown in Figure 42 indicates that for a fixed solvent velocity, the relationship between the *SHF* and the So-St module length is exponential. Note that this length represents the total length of six segments of one So-St module. For example, if the segment length is found to be 100 m, this means the sum of six segments should add up to 100 m and there will be 6 So-St modules in parallel which makes it 6 x 100 m.

At low heat fluxes, the required length becomes significantly high, while at high heat fluxes the length becomes less sensitive to *SHF* changes. This behaviour can be explained by *Eq. 12*. The total energy absorbed (kJ) does not change because we have fixed the solvent velocity at the entrance and the vapour quality at the exit of each So-St segment. Therefore, to increase/decrease the length (i.e. heat exchange area, *A*), the denominator (*U × ΔT*) must decrease/increase. When the *SHF* increases/decreases (the *x* axis in Figure 42), the temperature difference (*ΔT*) increases/decreases, respectively, which in turn affects the heat transfer coefficient (*U*). From the heat transfer analysis, we have learnt that higher temperature difference between the bulk solvent and the inner So-St tube wall (*ΔT*) leads to higher heat transfer coefficient (*U*) in the vapour quality range of interest. This is because a higher temperature difference promotes the nucleating boiling heat transfer component [49]. In real operation, the scenario is more complex, because the *SHF* affects the amount of thermal energy that hits the So-St tube. Because the total area is fixed, the change in *SHF* will affect both *U* and *ΔT*, ultimately affecting the vapour fraction (or loading). Therefore, the ultimate relationship, i.e. solar energy *vs* vapour fraction (or loading), is highly complex and non-linear. From a process control point of view, the So-St solvent flowrate could be used as a manipulated variable to control the vapour fraction (or loading) in events of solar fluctuation. This control problem has not yet been addressed in this chapter, but the findings here about the complex

relationship between solar energy *vs* vapour fraction (or loading) will be used later to develop appropriate control architecture.

In summary, the heat flux affects the temperature difference (*ΔT*), and the temperature difference also affects the heat transfer coefficient (*U*), resulting in a complex relationship between *SHF vs* So-St module length. As a result, at very low *SHF*, the solvent does not absorb the heat as quick as at medium to high heat fluxes. When the heat flux becomes very high, heat transfer performance is not as enhanced; hence, So-St length becomes a less sensitive factor. Figure 42 compares 1.2 m/s and 1/5 m/s solvent velocity. It can be seen that at higher solvent velocity, the required So-St tube length increases. This is because higher velocity means higher flowrate; thus a higher heat exchange area (i.e. length) is required. This is a valuable correlation, because if we design the So-St network at 1.2 m/s, we will have the flexibility to vary the velocity to response to solar availability fluctuation. We will revisit this aspect in detail in the control and sizing chapters.
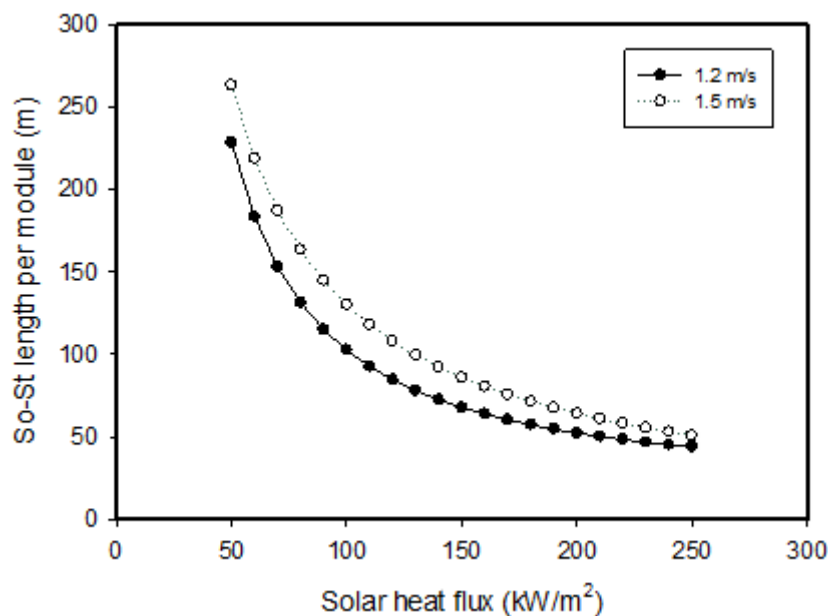


**Figure 42: Required So-St length per module (total length of six segments) at different solar heat flux values.**

In conclusion, we have determined the effect of *SHF* on the required So-St module length, where this information can serve as a useful design benchmark. For example, one can determine the So-St module length for different solar field designs as a function of solar intensity. We convert the curve at 1.2 m/s to a mathematical formulation for practical application as follows:

$$y = (3.691 \times 10^4) \times (x^{-1.322}) + 18.75 \qquad \textit{Eq. 13}$$

Where '*x*' represents the *SHF* and '*y*' is the length per one So-St module. Next, we demonstrate the sizing a So-St network for the SCF with a benchmark heat flux of 100 kW/m$^2$ at the surface of the absorption tube. The key design variables are the same as those reported in Table 9, because they have been selected based on careful engineering adjustments to ensure operability and functionality of the design. To achieve a design with a different specification (e.g. vapour quality), the following information needs to be recalculated: i) the number of So-St segments; ii) the benchmark operating velocity; and iii) the *SHF vs* the So-St module length correlation. We have carried out the sizing in two steps:

**Step 1: Calculate the total length for a So-St module for a benchmark 100 kW/m² solar heat flux**

- Using the correlation in *Eq. 13*, the length is about 110 m at 100 kW/m².

**Step 2: Determine the length of each So-St segment**

- For this step, we have two approaches. One method is using the Aspen® model to sensitise different length segments for achieving the target of 5% vapour quality. Another method is using the correlation we obtained as shown in Figure 43-A.
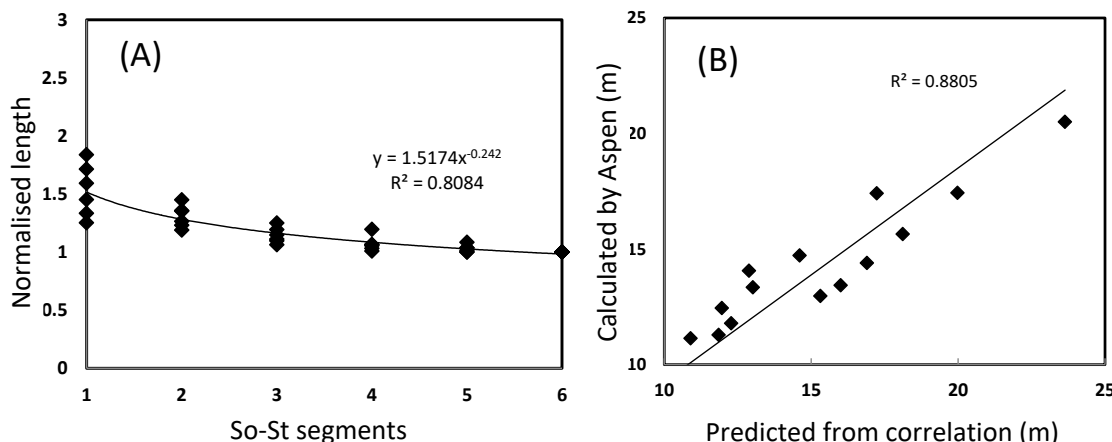


Figure 43: (A) Normalised length between the So-St segments. All segments length were normalised against the length of the last segment. (B) Test of the correlation.

- Using the correlation above, we determined the length of each segment (in metres) as shown in Table 10. There are small differences between the Aspen® model and the correlation. Hence, the correlation could be used to provide a good approximation without the need for time-consuming simulation of the full model.

Table 10: So-St segment sizing for a design point of 100 kW/m² solar flux.

| Length of each segment (m) | Aspen® model | Correlation in Figure 43 |
|---|---|---|
| Segment 1 | 23.6 | 21.5 |
| Segment 2 | 20 | 20.4 |
| Segment 3 | 18.1 | 18.5 |
| Segment 4 | 16.9 | 17.2 |
| Segment 5 | 16.0 | 16.2 |
| Segment 6 | 15.3 | 16.1 |

Another important aspect of the So-St network is the tube diameter. Aside from the benchmark 76 mm inner diameter that we have used in different sensitivity tests, there are more commercial absorber tube diameters we can also sensitise (e.g. 66 mm, 81 mm). In this section, we study the effect of changing the tube diameter on So-St performance. The fundamental phenomenon happening in the So-St tube is heat transfer; thus, we compare the heat transfer coefficient for

different inner tube diameters from 60 to 91 mm. This range sufficiently covers most commercial diameters. The result is shown in Figure 44-A. It can be seen that almost all tube diameters have a similar heat transfer coefficient trend. This could be because in the tested diameter range, the solvent velocity was the same for all tube diameters, where the velocity is the most influential parameter that could affect the heat transfer coefficient. It is plausible to utilize all the findings and correlations developed in previous sections. In particular, the two-step sizing protocol could be applied for any tube diameter within this range to size a reasonable So-St field for any case-study. There are small variations in heat transfer coefficient between various diameters, but no clear distinguishing trend can be identified. Thus, the small variations can be attributed to the numerical result uncertainty in Aspen®.
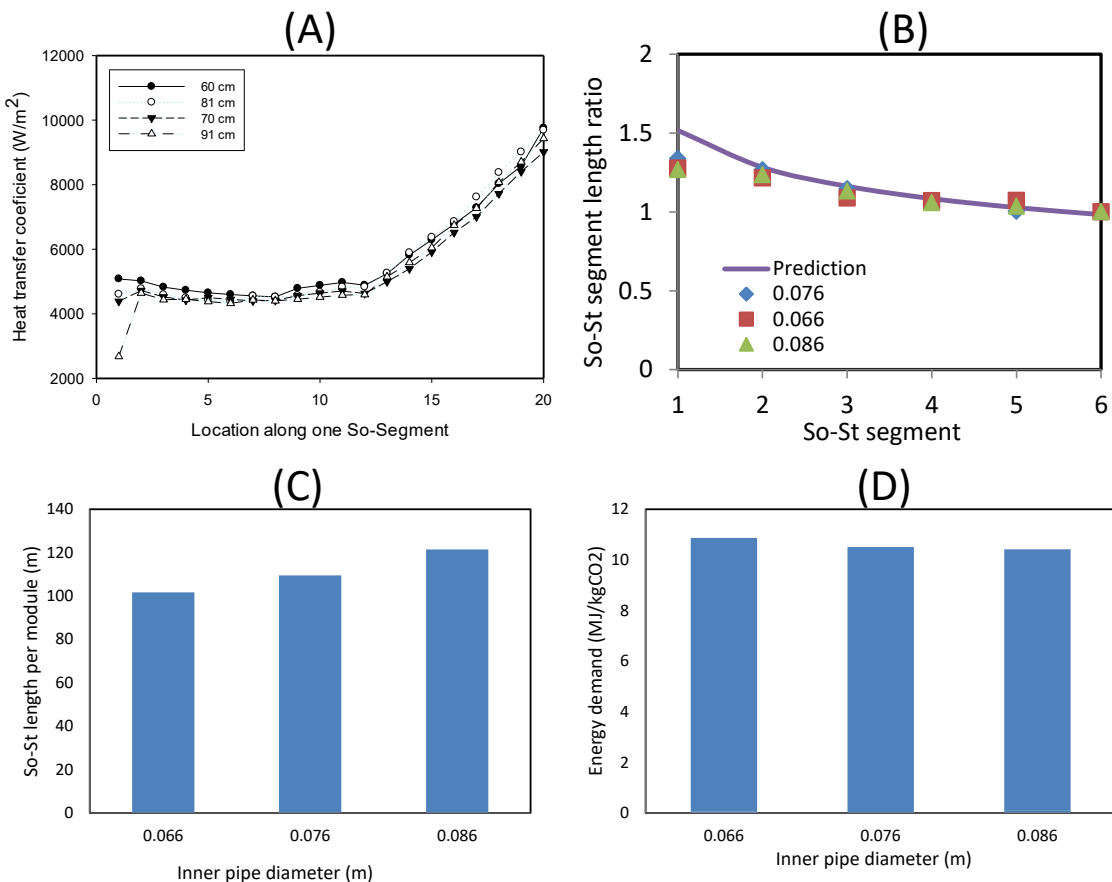


**Figure 44: (A) The effect of the So-St tube inner diameter on heat transfer coefficient. The 'x' axis represents 20 points equally distributed along a So-St segment. (B) The length ratio of each segment, all segment lengths were normalised against the length of the last segment, i.e. the length ratio of segment 6 = 1. (C) The length for one So-St module at different diameters (each So-St module has six segments). (D) the energy demand for different diameter. For each inner diameter in (A), the flowrate was calculated to achieve the same velocity, i.e. 1.2 m/s. The average heat flux was 100 kW/m$^2$ for all simulations; For (C) and (D) simulation, the entire So-St module was simulated with 1.2 m/s in the first segment inlet, 100 kW/m$^2$ average heat flux and specified *VMF* removal of 0.05.**

We used the designed procedure applied for 76 mm tube dimeter (the result for this sensitivity is reported in Table 10) for other two commercial diameters: 66 mm and 86 mm. Recall that in the procedure demonstrated in Figure 44, we determined the approximate length of a So-St module for these tube diameters. The design for other two diameters would still require six segments, because the vapour removal was fixed at 0.05. Then, we determined the length per segment with the

correlation shown in Figure 43-A. The predicted segment lengths were then fine-tuned in Aspen® to meet the design target of 0.05 *VMF* at the end of each segment. This automatically helps achieve the lean loading target of 0.22 in the last segment, further proving that the final lean loading ultimately depends on the number of segments and designed vapour removal. It was found that the predictions were reasonably good, as can be seen from Figure 44-B, which shows the normalised segment lengths for different tube inner diameters against the predictions using the correlation shown in Figure 43-A. These predicted segment lengths were used in the Aspen® model to simulate and refine the length for achieving the desired lean loading and vapour removal target. The results are shown in Figure 44-C, where the So-St module length slightly increases at higher diameter(s). At 66 mm diameter, the total length of six segments is about 100 m, while at 86 mm it is about 120 m; this results in approximately 20% longer So-St tube length if the latter diameter is used. This is an interesting outcome, because we have observed there is no trend in heat transfer coefficient when we sensitised the diameter, as shown in Figure 44-A. Further investigation revealed this outcome is due to the extra mass flowrate when increasing the diameter. We elaborate further as follows. The temperature of the solvent has the following relationship:

$$T \propto \frac{Q}{m} \qquad\qquad\qquad Eq.\ 14$$

where *Q* (kW) is the thermal power absorbed by the solvent and *m* (kg/s) is the solvent mass flowrate. This equation indicates that solvent temperature is proportional to the thermal power divided by the solvent flowrate. Higher power or lower flowrate will increase the solvent temperature, and that helps to reduce the So-St tube length requirement. *Eq. 14* can be further elaborated as follows:

$$T \propto \frac{Q}{m} = \frac{Q_{flux} \times (\pi \times D \times L)}{\left(v \times \rho \times \left(\pi \times \frac{D^2}{4}\right)\right)} \qquad\qquad Eq.\ 15$$

where $Q_{flux}$ (kW/m$^2$) is the *SHF*, fixed at a benchmark of 100 kW/m$^2$ in all simulations; *v* (m/s) is the solvent velocity; *D* (m) and *L* (m) are the So-St diameter and length, respectively; *ρ* (kg/m$^3$) is the solvent density. *Eq. 15* can be simplified further as follows:

$$T \propto \frac{Q}{m} = \frac{D}{D^2} = \frac{1}{D} \qquad\qquad\qquad Eq.\ 16$$

*Eq. 16* suggests that for the same So-St length (*L*), heat flux ($Q_{flux}$), and solvent velocity (*v*), a smaller tube diameter will achieve a higher temperature. In other words, the larger tube diameter will need longer So-St tubes to achieve the same temperature compared with the smaller diameter. This explains why the 66 mm tube diameter requires only 100 m, while the 86 mm tube diameter requires 120 m tube length, i.e. an extra 20 m. We have determined the effect of the tube diameter on a So-St module. Recall that the So-St network consists of multiple modules in parallel. The tube diameter does not have any effect on the number of required modules, because this number is determined by how many solvent loops there are. Next, we determined the effect of changing the tube diameter on the overall size of one loop. The results are shown in Figure 45. It can be seen that reducing the tube diameter leads to more modules being required (Figure 45-A) because a smaller diameter means a smaller flowrate given a constant solvent velocity. Hence, more modules in parallel would be needed to process the total solvent flowrate. Recall from Figure 44-C that a higher

tube diameter would require longer So-St segment lengths in one module; but Figure 45-A suggests that a higher diameter requires fewer So-St modules. As a result, Figure 45-B shows that a longer tube diameter leads to smaller total So-St network length, which is the sum of all So-St modules. These results suggest operating at relatively large diameter results in smaller So-St network.

Another aspect of using a larger tube diameter is the greater solar heat concentration, i.e. more *SHF* on the So-St tube surface is intercepted. We sensitised the diameter and determined the *SHF* while keeping the aperture width of the receiver the same. The results are shown in Figure 45, C and D. It can be seen that smaller diameter has a higher heat flux (Figure 45-C). While this might suggest using smaller diameter is more beneficial, the trade-off is clear, as seen in Figure 45-D, which suggests operating at smaller diameter results in higher heat flux at the expense of more So-St modules required. Considering the trend of the two lines (red and black) in Figure 45-D, one can see that the black marked line is steeper than the red marked line. This means at small diameters, the enhancement in heat flux is not sufficient to justify the extra demand of the So-St modules. From the above, we can summarise that the So-St tube diameter has a stronger influence on the total size of the So-St network (i.e. length per one So-St module and the number of required So-St modules) than the heat flux. Therefore, we are confident in our approach of decoupling the design of the two key attributes: i) the So-St module responsible for the solvent regeneration, and ii) the receiver width of the solar collector responsible for the solar heat harvest and concentration.
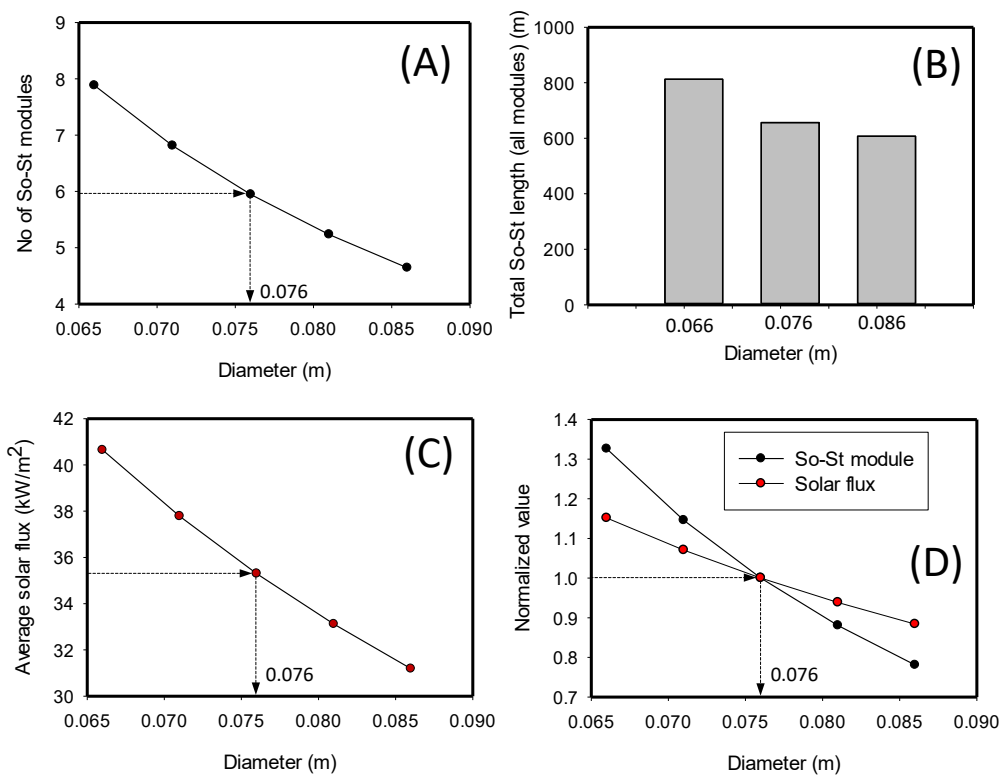
**Figure 45: (A) Sensitising the number of So-St modules required per So-St tube diameter. (B) The total length of So-St modules required for different tube diameters, the *SHF* was kept at 100 kW/m² in all cases. (C) Calculated the average *SHF* (exclude zero-flux period, e.g. night time) for different tube diameters with the same So-St module length (100 m) and parabolic trough width (5 m). (D) Normalised plot of the two variables (So-St module and solar flux) for all diameters against those of 0.076 m, in this subfigure we compare the trend (not absolute value) between the two lines (black and red).**

## 3.4     **Phase separation**

Instantaneously removing $CO_2$ gas from the So-St tube is essential to maintain a continuous $CO_2$ desorption driving force. For efficient $CO_2$ removal, a number of separation methods can be proposed. Some well-known technologies in vapour–liquid separation are summarised in Figure 46. The T-junction design (Figure 46-A) features a compact size for phase separation [57], which can be easily installed at the exit of each segment. The disadvantage of this design is that it has a low volume for liquid hold-up, which means it does not offer extra capacity to provide a clear buffer (e.g. to maintain the feed flowrate into the next segment) for process control purposes. The cyclone design (Figure 46-B) is not suitable for our application, because it is designed for separating high vapour fraction mixture (99% volume is vapour), while the So-St only has up to 80–85% in liquid. The cyclone design is often employed to remove liquid droplets from the gas stream [58]. We think the most suitable technology is the flash drum, often referred to as a vapour–liquid separator, or settling tank (Figure 46-C). It operates based on gravity; the vapour flows to the top and liquid settles at the bottom. The flush drum is more effective in phase separation because of having an inlet diffuser to reduce the velocity and spreads the incoming mixture across the full cross-section of the vessel. Moreover, it has a mesh pad in the upper part of the vessel prevents liquid from being carried over with the vapor. We selected this technology because it is widely used in many industrial applications [59]. In addition, it can be modified to carry extra solvent buffering capacity (i.e. each tank is a small, intermediate solvent storage tank) for process control purposes.
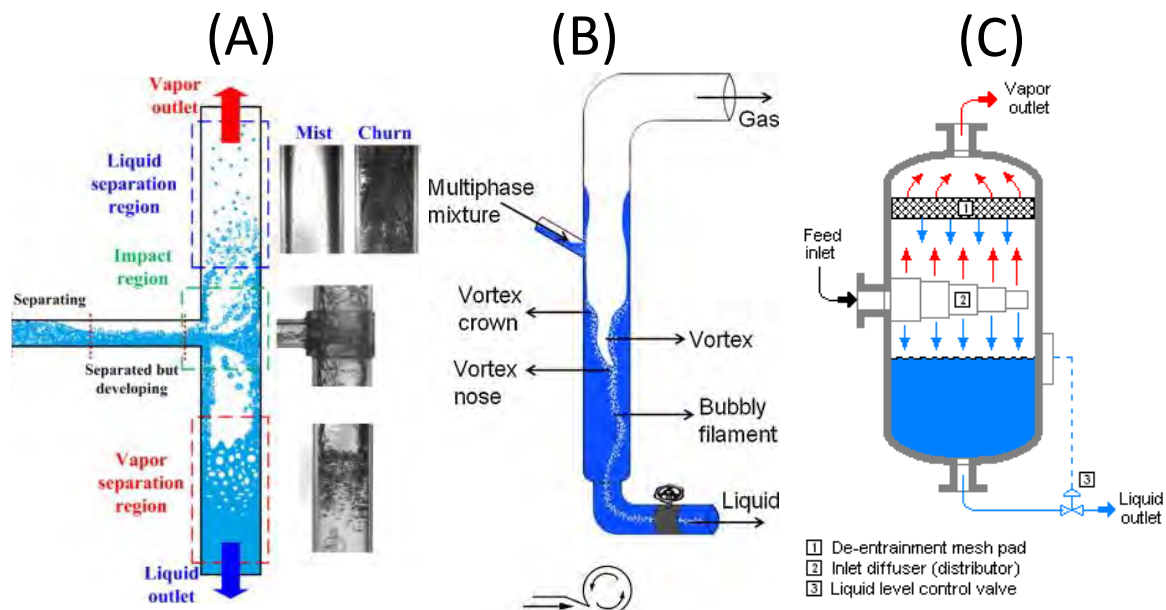


**Figure 46: Techniques for vapour liquid separation at the exit of each So-St segment. (A) T-junction; (B) cyclone design; and (C) knock-out drum (flash drum, settling tank, vapour–liquid separator). The separation mechanism of (A) and (C) is based on gravity, while in (B) the effect of high vortex drives the liquid to the bottom.**

Another important aspect is to remove water from the $CO_2$-$H_2O$ vapour mixture at the end of each So-St module. The conventional approach is to condense water by cooling the vapour mixture to the dew point temperature. This approach is highly effective, and can produce highly pure $CO_2$ (99% by mole). The cooling medium is preferably an air stream, because So-St is designed to be a

standalone operation in locations where water supply may be limited. The concept of air cooling has been demonstrated to be applicable for standalone solar systems [60]. Alternatively, a membrane could be used to separate $H_2O$ and $CO_2$; however, this approach has not been proven in industry [61].

One important aspect of the operation of the So-St network is the process control. In this section, we reveal some important control variables that are critical for efficient $CO_2$ desorption. These include the temperature, $CO_2$ loading, *VMF* (or mass fraction/volume fraction) and the pressure-drop. Typical profiles of those variables along this preliminary six-segment So-St module are plotted in Figure 47. It can be seen that the loading and the temperature share similar profiles; increasing temperature leads to similar decreases in loading. In contrast, the pressure and vapour fraction profile have a similar patterns, reflecting the six So-St segments in series. A typical pattern starts from 0 vapour fraction (all liquid) and 2 bar pressure. As the vapour fraction increases as a result of heating, the pressure starts dropping.

From the process control perspective, two major concerns may affect the plant performance (e.g. how much $CO_2$ is desorbed) and the plant operation stability (e.g. if the two-phase flow causes pressure fluctuation). For the former aspect, temperature could be used to indicate the extent of solvent regeneration (i.e. solvent loading), because we can measure temperature along the So-St segments and determine the $CO_2$ loading (Figure 47-B). Therefore, if we control the temperature (e.g. via manipulating the flowrate or the receiver focus/defocus mechanism), the $CO_2$ loading target can be met, thus ensuring the plant performance is on the track.

Note that we have worked through the analysis on various design aspects using one main variable, i.e. the *VMF*. We have sensitised different *VMFs* to determine how many So-St segments would be needed and the corresponding energy demand (Figure 41). Hence, it is logical to think that the *VMF* determines the $CO_2$ loading. This is correct, because in all simulations we found if we control the *VMF* at each segment exit to be 0.05, the final loading is always in the range of 0.21–0.22. However, for process control purposes, we do not recommend *VMF* to be used as an indication for $CO_2$ loading for two reasons. First, it is not easy to measure the instant *VMF.* We could use pressure to determine the *VMF,* but this would result in time delay and a high risk of inaccurate interpretation due to the pressure being unstable when the plant encounters significant abnormal operating conditions. Second, the profile of *VMF* along the So-St tube is very different from that of $CO_2$ loading (Figure 47, black line in A *vs* black line in B). This will create challenges in tuning the controller.

For the latter, plant operational stability is mostly about keeping the *VMF* and the pressure-drop within a desirable range to ensure process stability [56]. This is because pressure-drop is of the most concern for the boiling flow, as proposed in the So-St tube. The *VMF* and pressure-drop are interrelated, because the process of vapour generation contributes significantly to the pressure drop. We suggest that measuring and controlling either variable could maintain plant stability, but the pressure variable is more convenient. A potential variable that could be manipulated when the plant is on the verge of being unstable is the solvent flowrate. For example, when there is excessive solar heat input, excessive vaporisation could dry out the tube. In this case, the temperature controller (plant performance control) will initiate defocusing, but the pressure controller (plant stability control) can also act to control the flowrate in synchrony with the temperature controller.

From the above, we have identified two main control variables (temperature and pressure) and two manipulated variables (focus/defocus mechanism and the solvent flowrate). However, the focus/defocus mechanism may not be always available, because it depends on solar availability. Hence, there will be some periods where we only have one manipulated variable, but there are always two control variables. Recall that in the two control variables, one is related to the desorption performance and the other one more related to operational stability (i.e. pressure-drop or *VMF*). Hence, effective control architecture needs to be able to decide during those periods, which aspects have higher weighting towards a control decision. We will revisit the process control aspect in detail in Chapter 5.
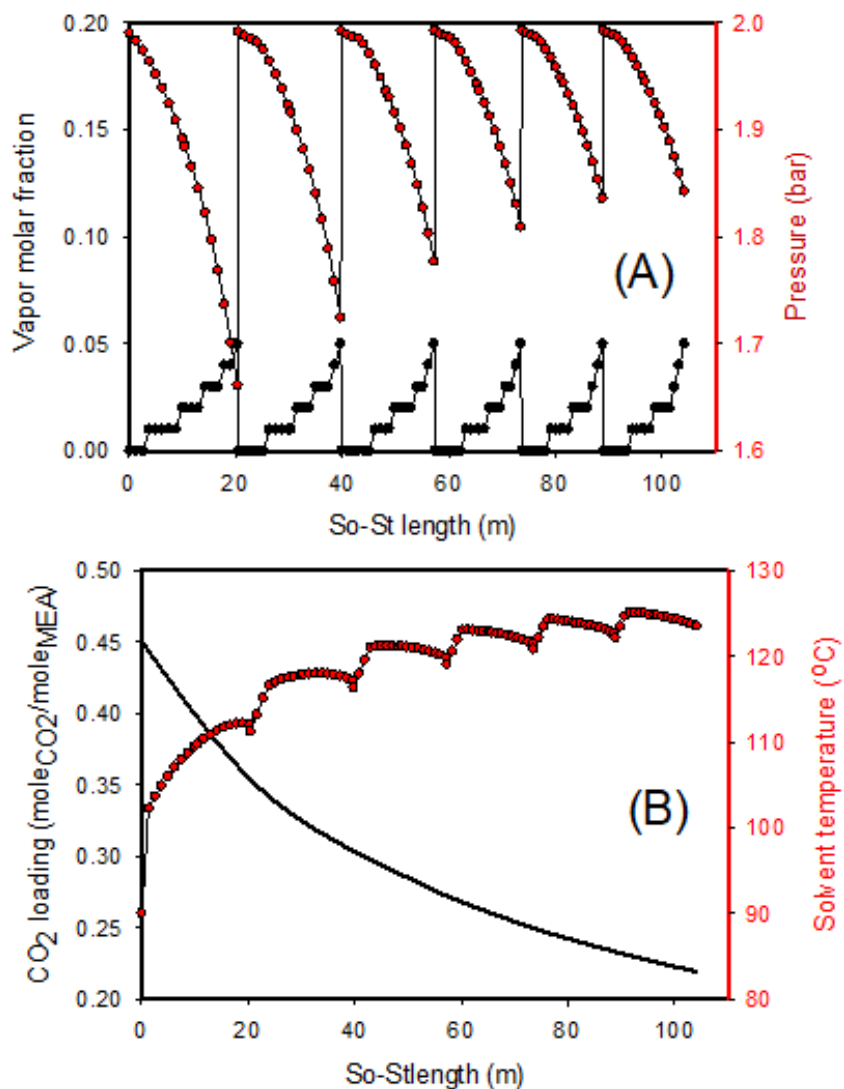


**Figure 47: Variations in key process variables along 6 So-St segments. The total length is 105 m, the average *SHF* was kept at 100 kW/m². (A) Vapour molar fraction and pressure profiles, at the end of each segment the *VMF* is 0.05 and the pressure drops below 2 bar. At the beginning of the next segment, *VMF* drops to 0 as it was removed in the flash drum in-between segments and the pressure is restored back to 2 bar. (B) The $CO_2$ loading and solvent temperature profiles; the temperature generally increases but slightly drops due to the pressure-drop effect.**

The effect of the So-St module tilt angle on the two-phase formation and flow regime was preliminarily investigated. The results are shown in Figure 48. The design point of the So-St operation is marked in the 'tilt angle = 0°' sub-figures. It can be seen that going from 0° to 15° tilt angle, the flow regime map changes slightly. The slug flow regime is expanded, and the mist or

annular flow regimes only exist at very high vapour velocity. For higher angles, the change is more significant and new flow regime (disperse bubble) starts emerging. As we do not have specific topographical parameters for the SCF site, we are unable to investigate this aspect further. However, the site landscape may be modified to improve the gas–liquid phase separation and improve process efficiency. We will discuss the phase separation in more detail in the next chapter.
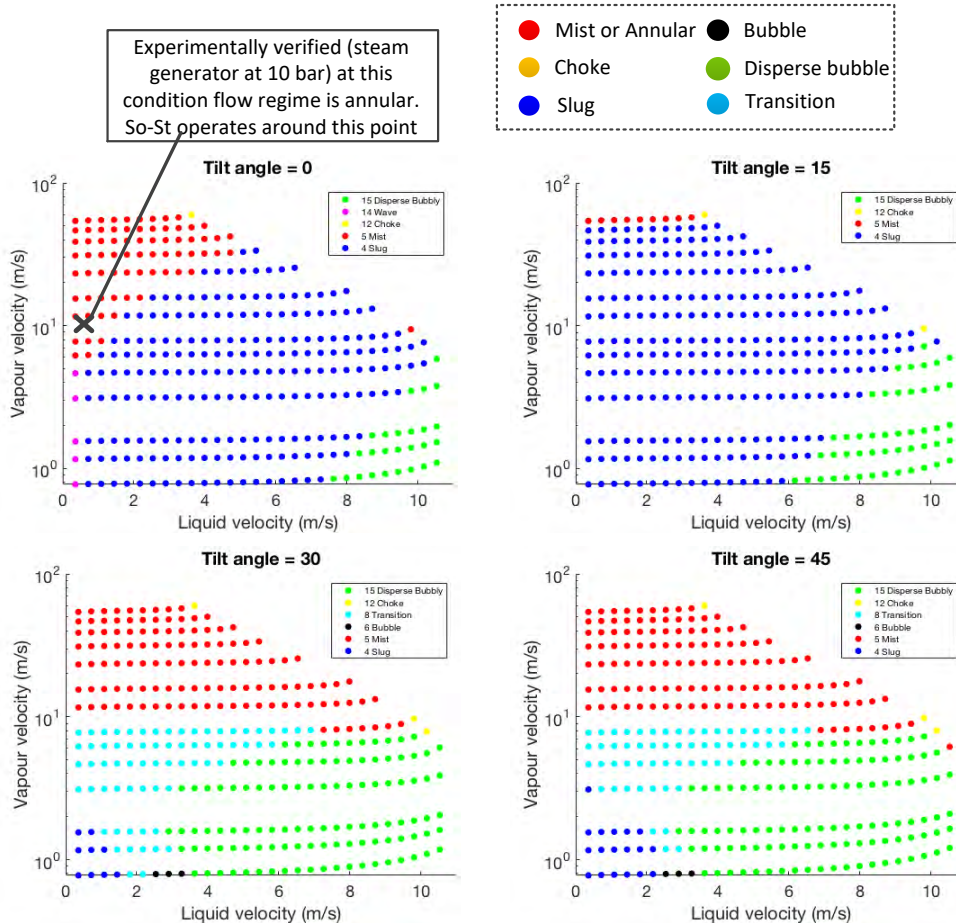


**Figure 48: The effect of the So-St tube tilt angle on flow regime at different superficial gas and liquid velocity. Note that the vapour superficial velocity (i.e. vapour velocity) was plotted in log scale while that of liquid is in linear scale.**

## 3.5    Heat transfer enhancement

We have previously discussed the role of boiling in heat transfer enhancement. This section discusses other factors that would affect heat transfer. A comprehensive literature review on that regard can be found in [62]. Most relevant to the So-St design is the internal geometry of the So-St tube. Different geometries could be implemented to enhance the heat transfer coefficient, e.g. packing or other types of inserts. Figure 49 presents three types of inserts that are often used to better mix the species and/or enhance heat transfer in a tube.

The overall aim of those inserts is to enhance passive vortexes (i.e. mixing) and boost the heat transfer coefficient. It is possible that the impact of these inserts in the So-St tube design is limited, because the heat transfer enhancement comes mostly from the boiling phenomenon at the chosen *VMF* design point (0.05). Alternatively, it is also possible that modification (such as metal foam)

increases liquid velocity (i.e. mass flux), with higher mass flux leading to a higher heat transfer coefficient as demonstrated by Figure 35. However, pressure-drop is an important aspect that must be considered. With inserts, the pressure-drop is significantly higher than without inserts (e.g. up to five times) [62]. We think the pressure-drop would be the main constraint in deciding if packing should be used, due to the nature of So-St operation and concerns with flow stability. We will revisit this aspect in more detail in the CFD study which is more accurate in simulating the hydrodynamic condition in the So-St tube. In this preliminary design, we exclude any tube internal modification. This means once the CFD model is ready to simulate the effect of internal modification, we will have a smaller So-St field, since the inserts would supposedly enhance the heat transfer coefficient of the So-St tube.
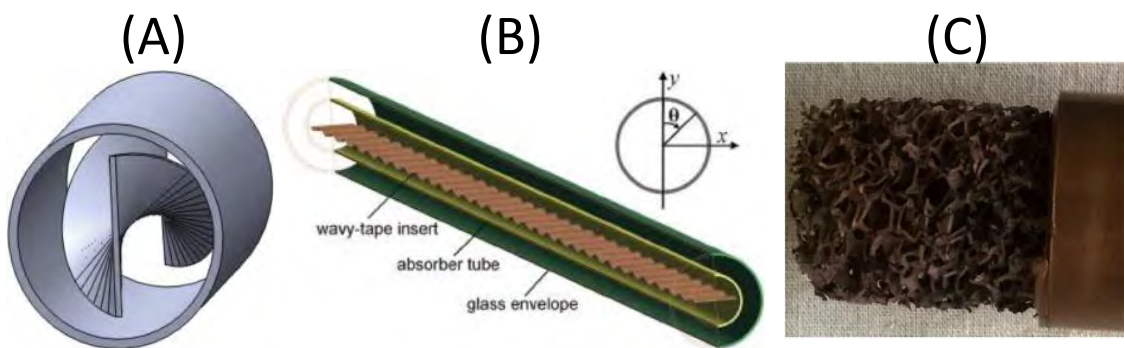


**Figure 49: Different inserts or geometries for heat transfer enhancement [62]; (A) wall-detached twisted tape insert; (B) wavy-tape insert; (C) metal foam packing.**

## 3.6    **Species concentration**

In this section, we analyse the composition of the three major species in vapour phase ($H_2O$, MEA and $CO_2$). The results of this analysis can be used to support the CFD modelling in Chapter 4. This is because at high loading range (>0.4), it is anticipated that more $CO_2$ is in the vapour phase than water, hence the bubbles forming within this range will have a high $CO_2$ concentration. This would ultimately affect the model formulation later in CFD. The simulations conducted in this section are purely thermodynamic, thus only temperature and pressure affects are studied. The simulations were done in Aspen® using a heater model that allows the user to specify the temperature and the pressure. The inlet is either pure water or 30 *wt%* MEA solvent (0.55 loading) and the outlet is a mixture of the vapour and liquid components. We extract the outlet results to calculate the water vapour flow in the vapour stream (Figure 50) and species composition (Figure 51). The flow of boiling water has been investigated intensively, in particular in the nuclear power industry. Hence it is useful to compare water with the solvent here. Water experiences a sharp increase in water vapour composition at 120°C, indicating the saturation temperature for water at 2 bar. However, the solvent system behaves dramatically differently. Water vapour starts forming at about 105°C then increases steadily and approaches the same composition as in the pure water system. This variation is because in the solvent system, $CO_2$ is released, thus continuously diluting the water vapour partial pressure. To keep up with temperature increases, more water vapour has to be generated. Eventually when there is no more $CO_2$ to be released, the water vapour flowrate will approach equilibrium as in the case of pure water.
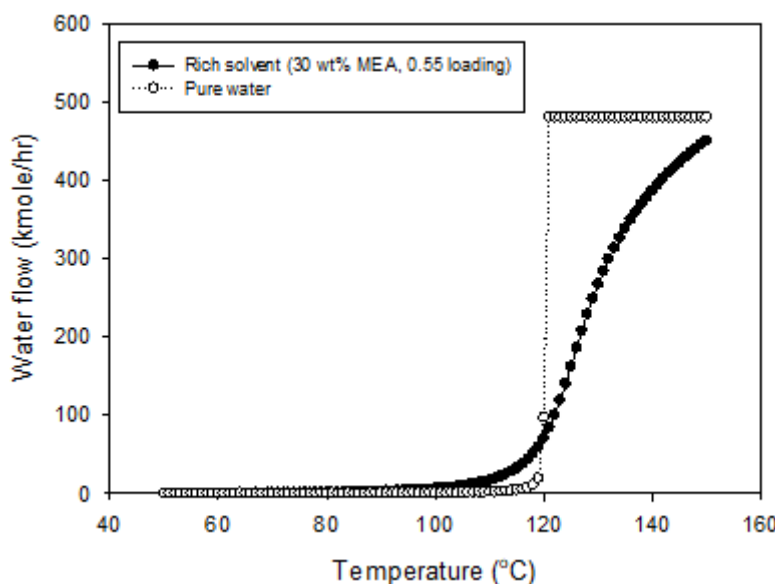
**Figure 50: Water vapour composition at different temperatures; 2 bar pressure system for pure water and rich solvent, respectively. Simulation was conducted using the equilibrium flash model in Aspen®.**

One implication of Figure 50's result is the aspect of flow regime formation. The saturation temperature of the solvent-based system varies from 105 to 150°C, which affects the nucleate boiling heat transfer component in the local heat transfer coefficient. Next, we will explore the vapour composition more in the CFD study to better understand the species composition in the vapour phase. The result is depicted in Figure 51. At high $CO_2$ loading, most of the vapour phase consists of $CO_2$, and as the loading decreases, more water is added. The amount of MEA in the vapour phase is negligible throughout the entire range of loading. However, its trend starts to rise at very low loading (~0.139) due to the high temperature in the system (~150°C) and most of the water being vaporised. The result in Figure 51 suggests the bubble formation will have different compositions of $CO_2$ and water under different loadings. Therefore, the CFD model formulation will capture this effect to adequately simulate the So-St operation.
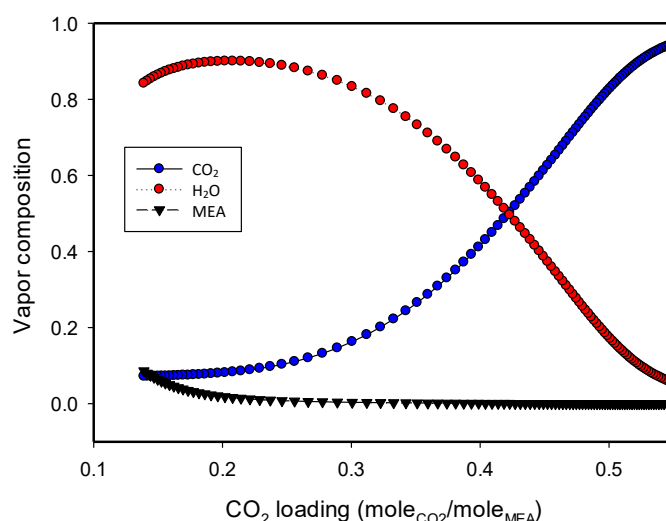


**Figure 51: Species distribution in vapour phase at different $CO_2$ loading values. At 50°C the loading is 0.55, and at 150°C the loading reaches as low as 0.139. Simulation was conducted using the equilibrium flash model in Aspen®.**

## 3.7    Concluding remarks

This chapter presented an advanced thermodynamic analysis for a solar stripper (So-St) design that can replace a conventional stripper in the PCC process. By evaluating the role of water evaporation in a reference amine-based 30 *wt%* MEA solvent, we compared the performance of this solvent with the MDEA as an alternative solvent. We was found that solvent selection is a very important aspect to reduce excessive water vaporisation. A detailed thermophysical study for solvent properties relevant to So-St application, therefore, becomes vital for the process thermodynamic and energy demand. For physical layouts, we have studied the heat transfer phenomenon in a two-phase flow for both vertical and horizontal tube geometries. We found that vapour molar fraction (*VMF*) is the foremost variable that can command the flow regime and heat transfer coefficient. As the *VMF* and the pressure-drop are interrelated, the nominal value for the *VMF* was systematically optimised for the design of a So-St network. Accordingly, the length, diameter and number of So-St segments and the parallel So-St modules can be modelled, allowing the whole So-St network to be sized. Different commercially available tube diameters were considered and compared. We found that a smaller diameter requires a longer So-St tube length. We adopted the tube diameter of 76 cm for the finalised design, because it requires a shorter So-St length and gives higher heat flux. We have developed a symmetrical design protocol to size the whole So-St field given a nominal solar heat flux (*SHF*). Different operational aspects, including process control, vapour–liquid separation and $CO_2$ purification, were discussed. Overall, deriving a robust So-St design protocol presented in this fundamental analysis can help in sizing the appropriate SCF for SP-PCC at any scale and any location. In the next chapters, we further develop our rigorous So-St model and size it for the Sydney case study, by incorporating asymmetric *SHF* to fine-tune the reliability of the simulation results. We also demonstrated potential SCF size reduction when comparing the proposed So-St technology with a conventional PTC.

# 4.    The So-St design from a CFD perspective

So far in this report, the flow behaviour in a So-St segment has only been investigated through the lens of a black-box model, which relates inputs and outputs without considering the internal geometry of the design. Although we have proposed the geometry and sizing for the So-St to meet the SP-PCC design target for our case-study (1.5 million tonne$_{CO2}$/year from a 660 MW$_e$ coal-fired power-plant), the previous modelling approach assumes a complete transfer of heat and that the system operates at the thermodynamic design point. This method has value for computational simplicity; however, it has limitations in accuracy. For example, the solar heat profile for parabolic trough collectors (PTCs) is non-uniformly distributed around the receiver tube [63], which may promote local hotspots and eventually impact the overall flow and heat transfer behaviour.

Figure 52 shows the cross-section of a PTC and the heat concentration ratio around the receiver tube. It can be seen that some spots on the tube circumference could have up to 45 times greater heat input than other spots. Accordingly, such steep temperature gradients may form local hot spots accumulating the heat near the tube surface, and the heat is not necessarily delivered to the centre of the tube. The temperature gradients may impact the boiling flow regime and can be detrimental to the physical properties of the MEA solvent, which is reported to undergo thermal degradation at temperatures >125°C at a conventional desorber pressure of 1.6 atm [64]. Therefore, to evaluate the performance of the So-St tube with greater accuracy, it is essential to develop a model that accurately describes the thermochemical events inside the tube.
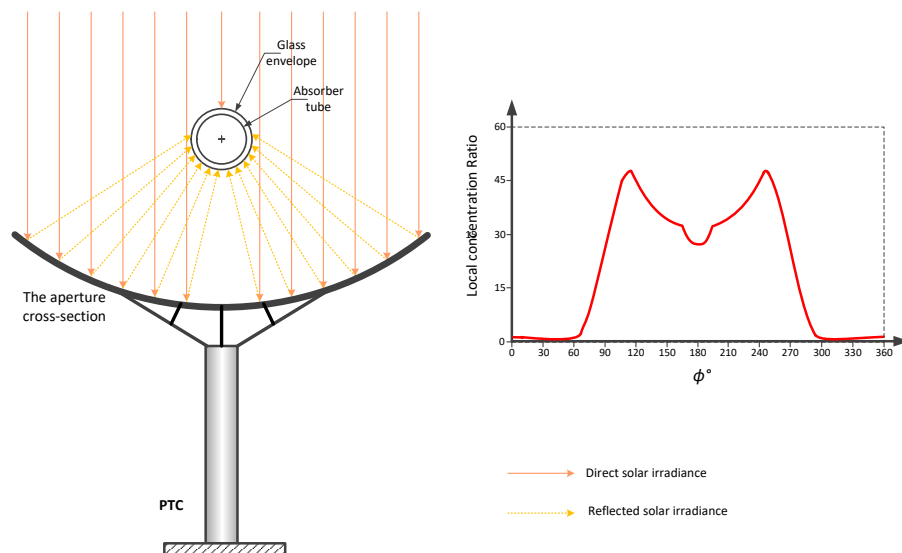


**Figure 52: Non uniform heat distribution around a solar tube (right) using a PTC receiver tube (left).**

Such a model has further implications for determining methods of improving $CO_2$ removal to enhance So-St capability via heat transfer augmentation techniques [65]. Since solar thermal energy is constrained by PTC efficiency and solar availability across day/night and seasonal variations, passive methods of enhanced heat transfer (*EHT*) are ideal for integration with a PTC. As described in section 3.5, these methods aim at modifying the geometry within a So-St tube through inserts or augmentations, which increase the heat transfer coefficient via greater effective heat transfer area and increased turbulence to disrupt boundary layer growth [65]. Their main drawback is the creation of larger pressure-drops, which must be offset by greater pumping power. Therefore, heat transfer must be enhanced while minimising pressure-drop. A model that accurately describes the internal workings of the So-St tube and can compare its performance to passive *EHT* configurations, has great implications for improving $CO_2$ removal. A direct benefit of this will be a possible reduction in SCF size and capital costs.

As the solvent flows inside a solar receiver tube, a portion of the liquid is vaporised, and the $CO_2$ molecules are eventually released. The vapour molar fraction (*VMF*) of the flow gradually increases along the length of the receiver tube, and subsequently, different flow regimes will evolve (Figure 53). Describing this complex physio-chemical process mathematically under transient conditions is a challenging task. The asymmetrical solar heat profile around the tube cross-sectional area adds more complexity to predicting vapour phase evolution and flow regime along the receiver tube, which would require robust and intensive modelling. Adding more complexity is the unknown extent of the desorption chemical reactions on various species compositions under these transient conditions. Computational fluid dynamics (CFD) offers an attractive method of exploring the internal complexities of a So-St segment and fluid behaviour. The So-St has complex physical phenomena, in particular boiling flow, which is a problem commonly solved using CFD [66]. In the literature, multi-phase boiling flow has been modelled within PTC receiver tubes primarily for the purpose of steam generation [67-69]. However, we are interested in a CFD model formulation that is specific to the So-St tube geometry and design specifications. CFD has also been used in PTCs to assess the capabilities of *EHT* methods, which entail the addition of inserts with surface augmentation [70]. For the So-St, CFD may reveal designs that effectively enhance $CO_2$ removal.

This study details the construction of a CFD model, using the COMSOL Multiphysics package, to understand the internal design of a single representative So-St tube. The So-St is evaluated in terms of heat transfer, vapour formation and flow development. Here, the CFD model reveals *EHT* methods to be a necessary component of the So-St design. The *EHT* configurations are compared with the bare So-St tube to reveal increases in heat transfer and vapour formation. CFD modelling shows that the So-St process could become an economical and efficient method for $CO_2$ desorption, which would ultimately eliminate the current reliance on the power-plant steam cycle.
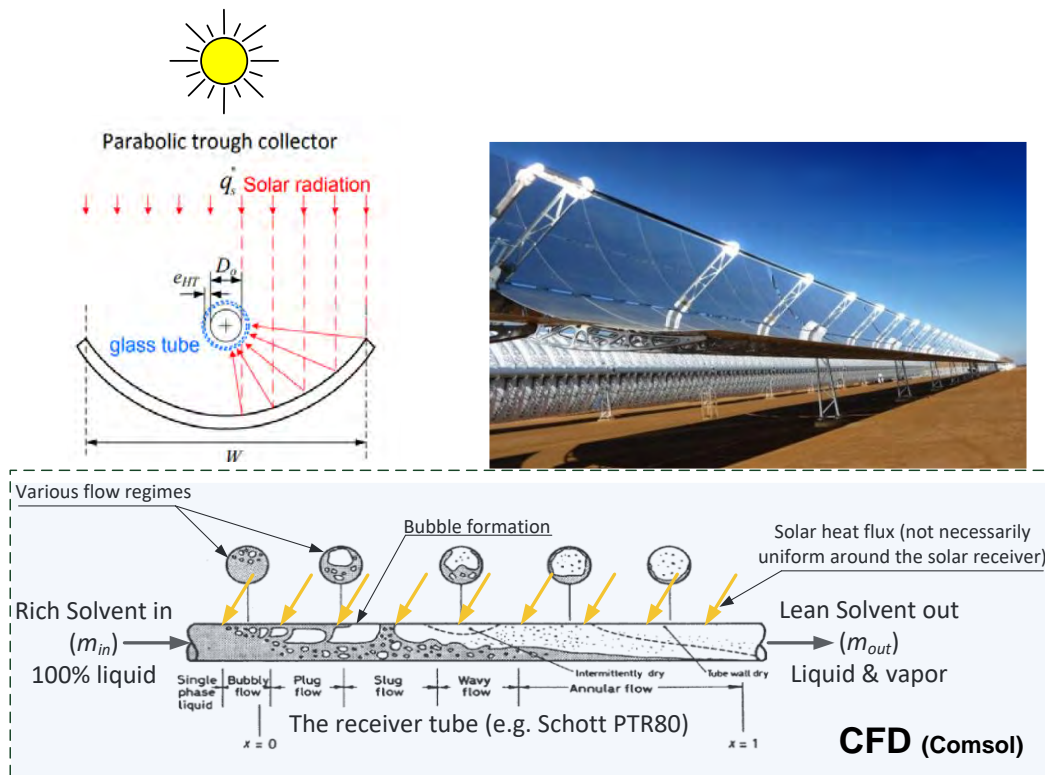
**Figure 53: Schematic of flow regimes formation within the solar receiver tube of the PTC. Computational fluid dynamics (CFD) is used to investigate the flow regime and optimise the heat transfer as a function of solar heat availability.**

## 4.1    CFD modelling framework

CFD modelling was conducted in COMSOL using the finite volume method, which discretises the entire spatial domain into a mesh of small control volumes. The COMSOL Multiphysics package is ideal for describing the So-St design, which incorporates a wide range of important physical phenomena: heat transfer, thermodynamics, multi-component chemical reactions, fluid flow and multiphase evolution. However, it is a challenge in CFD at large to couple all five physical phenomena into a single model. This is due to the difficulty in dynamically tracking the gas–liquid frontier, as it acts as an interface for multi-species diffusion between the two phases. This problem is yet to be resolved by the CFD developers' community. More details about the challenge of multi-physics coupling can be found in Appendix A in this report.

Accordingly, a compromise was made by decoupling the phenomena into two distinct sub-models, as summarised in Figure 54. Sub-Model 1 couples the thermodynamics and the chemical reactions of multi-chemical species, but in a single phase. This sub-model would be simulated in a liquid phase only, excluding the evolution gas, while describing heat transfer, hydrodynamics and chemical reactions in the presence of water, $CO_2$ and MEA components. Sub-Model 2 describes the liquid–gas interface evolution and is therefore in multi-phase; however, it is in a single-component water-only scenario, excluding all other chemical species and reactions. Although the assumption of a single component strays from the real scenario,

the concentrations of MEA and $CO_2$ components are dilute, and thus the formation of the water vapour phase is used as an analogy to $CO_2$ gas evolution. This single-component Sub-Model therefore enables us to evaluate the So-St in its ability to promote vapour phase evolution, and hence $CO_2$ removal.

The heat transfer module is used in both sub-models, being a necessary driving force for the respective chemical reactions and vapour evolution. In reality, the So-St will function dynamically throughout the day and will alternate between single-phase and multi-phase responding to solar availability. Sub-Model 1 therefore gives insight into the flow behaviour in the initial start-up conditions shortly before vapour evolution is achieved, whereas Sub-Model 2 shows the fluid behaviour at ideal process conditions during $CO_2$ removal. The proposed modelling framework allows the So-St to be evaluated for separate physical phenomena, and the conclusions from both sub-models can be integrated to inform improvement of So-St performance. The detailed CFD model structure and validation work can be found in Appendix A.

| Sub-Model 1<br>*Single Phase*<br>*Multi-Chemical Component*<br><br>**Key Physics**<br>Hydrodynamics<br>Heat Transfer<br>Chemical Reaction | Sub-Model 2<br>*Multi-Phase*<br>*Single Chemical Component*<br><br>**Key Physics**<br>Hydrodynamics<br>Heat Transfer<br>Liquid-Gas Interface Evolution |
|---|---|
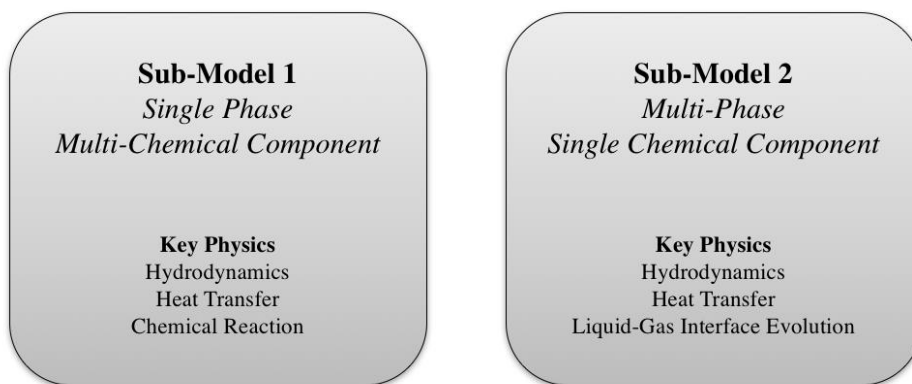
**Figure 54: Summary of CFD sub-models and their contributing physics.**

CFD modelling was used to investigate different insert configurations in terms of their heat transfer enhancement and pressure-drop effects. A wide variety of *EHT* inserts have been studied in PTCs, and it is necessary to choose a suitable option for the So-St. When choosing inserts to study using the CFD model, it is important to account for geometric limitations of the 2-D model. Twisted tape, wavy tape, metal foam and wire coils (Figure 49) are well-known inserts that have been widely studied in the literature [71, 72]. However, they are impossible to model with a 2-D CFD platform, since they rotate the flow in a circular or irregular regime, and thus require the third dimension.

Baffles or discs are *EHT* inserts that can be effectively modelled in a 2-D model. Solid baffles are semi-circular plates that are placed perpendicular to the fluid flow, altering the flow in the vertical axis. They are usually mounted alternately on the top and bottom sides of the tube. A more common modification to solid baffles is porous baffles, which include numerous small holes. The holes lower the frictional losses and reduce the pressure-drop penalty, while also favouring heat dispersion by increasing flow turbulence due to greater surface-area-to-volume ratios. Porous baffles have been studied extensively and are shown to be effective in

heat transfer enhancement [73-76]. In this study, we investigate both solid and porous baffles, a schematic of which is shown in Figure 55. Although porous baffles are more common as an *EHT* method, solid baffles can be used as a control to observe the impact of porosity on baffles. Many design parameters can be investigated for baffles, such as baffle spacing, baffle height and width, porous hole diameters and the baffle axis configuration. Among these, baffle spacing has a significant effect on heat transfer. Thus, the CFD model focuses on this parameter to investigate the compromise between *EHT* and pressure-drop.
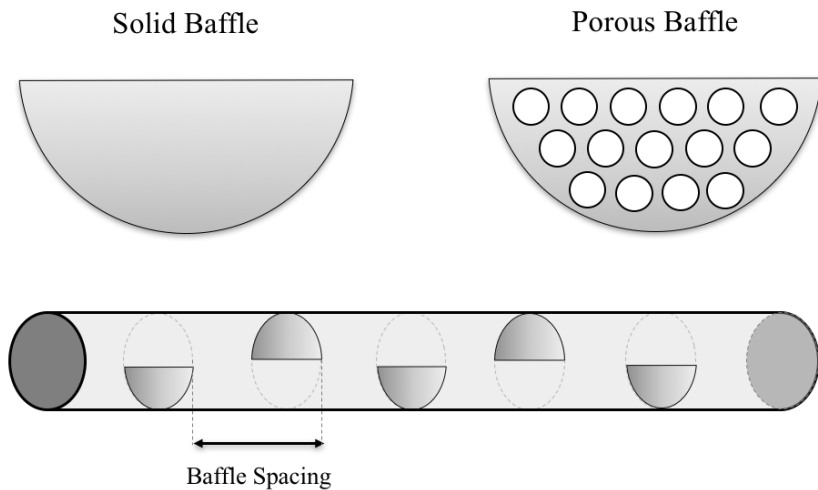


**Figure 55: Schematic of solid and porous baffles. Baffles are placed alternately on the top and bottom of the tube. The baffle spacing is sensitised in this CFD study.**

CFD modelling generally requires substantial computational time and power. It is important to minimise this load without compromising the model's accuracy. For example, can limit the range of simulation time, tube length and mesh size. A further method of optimising the modelling stages is using a hierarchical structure, where preliminary simulations with low computational load and lower accuracy are executed for a larger sample space, before executing more comprehensive and accurate simulations with greater computational loads for a smaller sample space. Sub-Model 1, being in single-phase, has a significantly lower computational load than Sub-Model 2, being in multi-phase. A preliminary simulation can also consider the So-St in a 2-D geometry. This is characterised by a rectangular cross-section along the length of the tube, with the height corresponding to the tube diameter and gravity defined along the vertical axis. Compared to a 3-D tube model, the 2-D tube model is less accurate, since it does not account for flow and heat transfer across the third dimension that occurs along the sides of the tube. However, it is an essential step for producing a wider sample space of simulations to provide insight into the solvent's thermo-physical properties. The 2-D model results and analysis are used to inform the design for the more advanced 3-D model. The 3-D model of the So-St is formulated and investigates a smaller sample space, specific to the successful configurations determined using the 2-D model.

Figure 56 summarises the hierarchical modelling structure used in this study. Sub-Model 1 is conducted in 2-D geometry for a large sample space of 11 simulations (one bare tube, five

porous baffles, five solid baffles). Sub-Model 2 is conducted in 2-D geometry for a smaller sample space of five simulations (one bare tube, two porous baffles, two solid baffles), with the samples chosen based on the results of Sub-Model 1. This culminates in the execution of Sub-Model 2 in 3-D geometry for the smallest sample space (one bare tube, one porous baffle, one solid baffle). The key design parameters for the So-St tube used in these simulations are given in Table 11.

**Table 11: Key design parameters for a So-St tube.**

| Design Parameter | Value | Unit |
|---|---|---|
| So-St tube length | 2 | m |
| So-St tube diameter (inner/outer) | 76 / 81 | mm |
| Operating pressure (inlet) | 2 | bar |
| Inlet temperature | 120 | °C |
| Rich loading | 0.4 | $mol_{CO2}$ / $mol_{MEA}$ |
| Lean loading target | 0.3 | $mol_{CO2}$ / $mol_{MEA}$ |
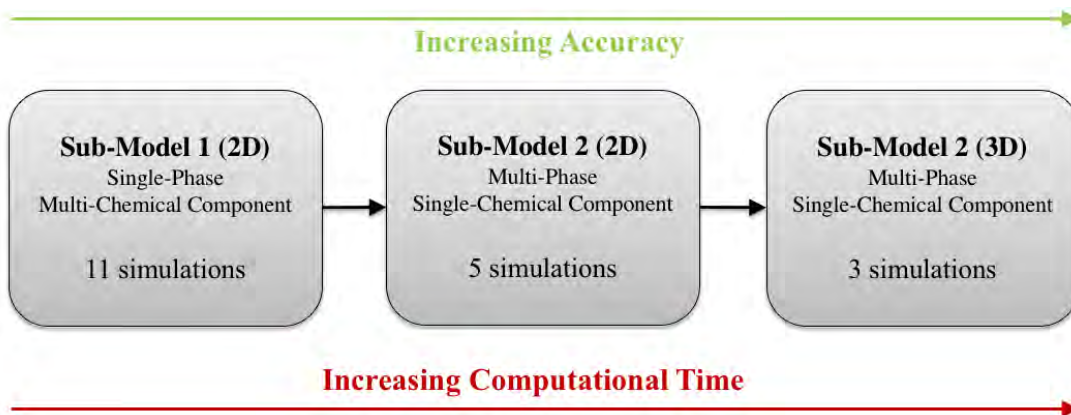


Figure 56: Schematic of modelling method. Sub-Model 1 is single phase with multi-chemical components, and Sub-Model 2 is multi-phase with single chemical component (water). Increasing accuracy of the model takes more computational time; therefore, more simulation runs are completed at lower accuracy (Sub-Model 1) to determine the best design simulations to run at higher accuracy.

## 4.1.1  Sub-Model 1 – Single phase multi components

Sub-Model 1 investigates the So-St tube in purely liquid phase and includes the $CO_2$ and MEA components and their corresponding reactions. This investigation has implications for evaluating gradients in temperature, velocity and pressure, and is highly relevant in determining fluid behaviour before the So-St boiling flow has begun. The So-St model geometry consists of a $2 \times 0.076$ m rectangular cross-section, corresponding to the tube length and diameter, respectively (Table 11). The inlet velocity of the fluid is a boundary condition set at 0.3 m/s, resembling the velocities calculated in previous Aspen® modelling. Sub-Model 1 was run for a simulation time of 10 s, with results reported for intervals of 0.01 s. The fluid flow is assumed to be incompressible and Newtonian, and the Reynolds-averaged Navier Stokes (RANS) equations are used, as seen in *Eqs. 17 & 18* [77]:

$$\rho \frac{\partial U}{\partial t} + \rho U \cdot \nabla U + \nabla \cdot (\overline{\rho u' \otimes u'}) = -\nabla P + \nabla \cdot \mu (\nabla U + (\nabla U)^T) + F \qquad Eq.\ 17$$

$$\rho \nabla \cdot U = 0 \qquad Eq.\ 18$$

Where $\rho$ is the fluid density (kg/m$^3$); $U$ is the averaged velocity field; $u$ is the velocity vector (m/s); $\otimes$ is the outer vector cross product; and $\mu$ is the dynamic viscosity (Pa s). The turbulent flow $k$-$\omega$ model is used to solve the RANS equations. This involves solving the turbulent kinetic energy ($k$) equation (*Eq. 19*) and the specific dissipation rate ($\omega$) equation (*Eq. 20*). COMSOL uses the Wilcox revised $k$-$\omega$ model [78]:

$$\rho \frac{\partial k}{\partial t} + \rho u \cdot \nabla k = P_k - \rho \beta^* k \omega + \nabla \cdot \left((\mu + \sigma^* \mu_T) \nabla k\right) \qquad Eq.\ 19$$

$$\rho \frac{\partial \omega}{\partial t} + \rho u \cdot \nabla \omega = \alpha \frac{\omega}{k} P_k - \rho \beta \omega^2 + \nabla \cdot \left((\mu + \sigma \mu_T) \nabla \omega\right) \qquad Eq.\ 20$$

Where $P_k$ is the production of turbulence kinetic energy; $\mu_T$ is the eddy viscosity; $\alpha$, $\beta$, $\sigma$, are closure coefficients for the specific dissipation rate equation; $\beta^*, \sigma^*$ are closure coefficients for the turbulent kinetic energy equation. The heat transfer interface is used, which solves the heat equation in *Eq. 21*:

$$\rho C_p \frac{\partial T}{\partial t} + \rho C_p u \cdot \nabla T = \nabla \cdot (k \nabla T) + Q \qquad Eq.\ 21$$

where $C_p$ is the specific heat capacity at constant pressure (J/kg/K); $T$ is the absolute temperature (K); $k$ is the thermal conductivity (W/m/K); and $Q$ refers to heat sources other than viscous heating (W/m$^3$). A limitation for modelling PTC tube flow in 2-D is the difficulty to appropriately resolve the PTC heat flux distribution. Heat transfer for the PTC is at a constant heat flux boundary condition, which is non-uniformly distributed around the circumference of the tube. For the 3-D model, it is natural to define this heat distribution profile around the circumference according to the local solar concentration ratios. However, the 2-D cross-section is of an infinitesimal width and the boundary conditions can only include heat transfer from the top and bottom edges of the cross-section. The direct top and bottom of the PTC are not the areas of the highest solar concentration (Figure 52); the maximum occurs at an angle of ~100° [63]. It is important to have an appropriate heat transfer driving force that is not solely defined by the top and bottom surfaces of the tube. To resolve this issue, we instead set the heat transfer boundary condition to be a constant surface temperature, rather than a constant heat flux. Using previous Aspen® modelling results, we found a constant surface temperature of 140°C created an equivalent heat flux to that of the constant heat flux boundary condition. Thus, the boundary condition used in the 2-D geometry is a constant surface temperature of 140°C. The transport of diluted species interface is used in COMSOL. The mass transport of species ($H_2O$, $CO_2$, MEA and their ionic

species) between control volumes is governed by diffusion and convection, which are driven by concentration and pressure gradients, respectively, according to the following mass balance equation:

$$\frac{\partial c}{\partial t} + \boldsymbol{u} \cdot \boldsymbol{\nabla} c = \boldsymbol{\nabla} \cdot (D\boldsymbol{\nabla} c) + R \qquad\qquad Eq.\ 22$$

Where $c$ is species concentration (mol/m³); $D$ is the diffusion coefficient (m²/s); and $R$ is the reaction rate expression for the species (mol/m³/s). The chemistry associated with $CO_2$ absorption/desorption in MEA solution is described earlier in Chapter 2 by reactions $R1$ to $R6$ and the equilibrium constants are defined by $Eqs.\ 5$ & $6$.

### 4.1.2  Sub-Model 2 – Multi phase single component

Sub-Model 2 is used to investigate the vapour formation within the So-St tube. This sub-model includes water as a single component. The neglected $CO_2$ and MEA species would simplify the process, which is a reasonable assumption considering that these chemical components are much diluted compared with the water component. The vapour phase behaviour for the single-component water is therefore used as an analogy for comparison to the actual phenomenon, since $CO_2$ molecules leave the solution concurrently with the water molecules. To model the interface evolution, a separated multiphase model is used, which dynamically tracks the gas–liquid interface and its evolution across the tube using the phase field method. The method is ideal for smaller-scale models and has greater accuracy than dispersed phase models. For gas–liquid flow, the liquid phase is characterised by the incompressible Navier-Stokes and continuity equations, while the gas phase is characterised by the compressible Navier-Stokes and continuity equations.

$$\boldsymbol{\nabla} \cdot \boldsymbol{u} = 0 \qquad\qquad Eq.\ 23$$

$$\frac{\partial(\rho\boldsymbol{u})}{\partial t} + \boldsymbol{\nabla} \cdot (\rho\boldsymbol{u}\boldsymbol{u}) - \boldsymbol{\nabla} \cdot (\mu\boldsymbol{\nabla}\boldsymbol{u}) - \boldsymbol{\nabla}\boldsymbol{u} \cdot \boldsymbol{\nabla}\mu = -\boldsymbol{\nabla}p + \boldsymbol{F}_{st} + \boldsymbol{F}_{ext} \qquad\qquad Eq.\ 24$$

The phase field method is characterised by the Cahn-Hilliard diffusion equation (*Eq. 27*), which introduces the dimensionless phase field variable $\phi$, where the pure liquid phase is $\phi = 0$ and pure vapour phase is $\phi = 1$:

$$\frac{\partial\phi}{\partial t} + \boldsymbol{u} \cdot \boldsymbol{\nabla}\phi = \boldsymbol{\nabla} \cdot \frac{\gamma\lambda}{\epsilon^2}\boldsymbol{\nabla}\psi \qquad\qquad Eq.\ 25$$

$$\psi = -\boldsymbol{\nabla} \cdot \epsilon^2\boldsymbol{\nabla}\phi + (\phi^2 - 1)\phi + \left(\frac{\epsilon^2}{\lambda}\right)\frac{\partial f}{\partial\phi} \qquad\qquad Eq.\ 26$$

$$\lambda = \frac{3\epsilon\sigma}{\sqrt{8}}$$

*Eq. 27*

where $\psi$ is the auxiliary variable; $\epsilon$ is the capillary width; $\lambda$ is the mixing energy density; $\sigma$ is the surface tension; and $\gamma$ is the mobility. The heat transfer interface is similarly governed by the heat equation, seen previously in Sub-Model 1 (*Eq. 21*). The phase field model is constructed using the COMSOL Multiphysics package and is used to model the So-St tube as a 2-D rectangular cross-section, similar to Sub-Model 1. Similar geometry and boundary conditions are used, where the tube cross-section is $2 \times 0.076$ m, the liquid inlet temperature is 120°C, and the surface temperature is constant at 140°C. However, there is one boundary condition defined differently for the phase field model; this is a pressure difference constraint between the inlet and outlet of the tube, instead of defining a constant inlet velocity. This pressure-drop is defined as 1 kPa, which was chosen to reflect the pressure-drop seen in previous Aspen® modelling over 2 m of So-St tube length. This alteration was chosen because a constant inlet velocity for boiling flow has greater potential for creating back-flow and unstable conditions due to the evolution of vapour creating significant increases in volume. Preliminary simulations were conducted with the velocity boundary condition, which caused convergence issues in the model. In Sub-Model 2, the inlet velocity is therefore a function of time. Because the phase field method introduces a considerable computational load, the simulation time was reduced to 2 s, instead of 10 s simulation time used in Sub-Model 1. Results are reported with time intervals of 0.01 s.

## 4.2    2-D Design elements

### *4.2.1  2-D geometry for Sub-Model 1*

Sub-Model 1 was simulated for 11 cases: the bare So-St tube and five baffle spacings for the solid baffles and porous baffles, respectively. The temperature distributions along the length of the tube are seen in Figure 57. Qualitatively, the implementation of *EHT* inserts increases the heat transfer, as indicated by the exit temperatures reaching higher values. This is because the inserts create greater mixing, which disrupts boundary layer growth and favours a greater heat transfer driving force. High-temperature zones also accumulate near the boundaries of the baffles, especially in the wake regions created immediately downstream of the baffles. For both inserts, the shorter baffle spacings result in greater heat transfer compared with the wider baffle spacings, since their disruption to the flow is more frequent and enables greater mixing.
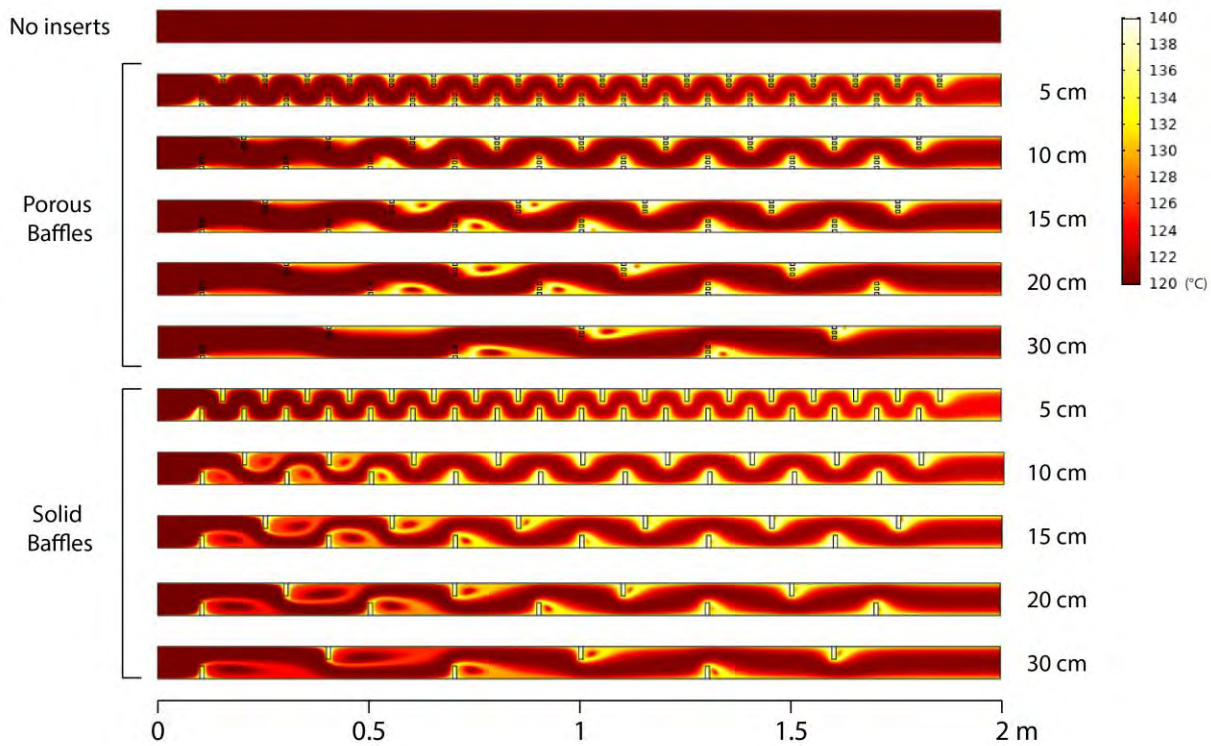
**Figure 57: Temperature distribution of a So-St tube with no inserts, porous baffles and solid baffles at different baffle spacings at the final time step (10s).**

Heat transfer enhancement can be quantitatively assessed by considering the temperature differences between the inlet and the outlet of the tubes for different baffle spacings. A dimensionless temperature difference ratio ($\Delta T/\Delta T_0$) is used to compare the temperature difference ($\Delta T$) for all inserts with the temperature difference without inserts ($\Delta T_0$). This is shown in Figure 58. The solid baffles create consistently greater temperature differences compared with the porous baffles of the same baffle spacing. This is because the solid baffles create more vertical mixing compared with the porous baffles with holes. This creates greater boundary layer disruption and better distributes the heat within the fluid.
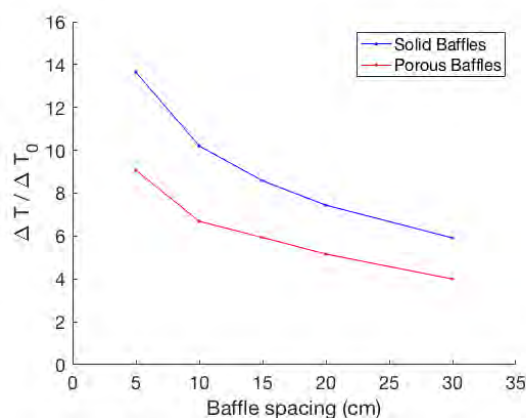


**Figure 58: Dimensionless temperature differences for solid and porous baffles according to different baffle spacings at the final time step (10s).**

Although solid baffles have the greatest heat transfer performance, their suitability for the So-St design must be compared while taking into account the penalty of greater frictional losses, characterised by a larger pressure drop. The pressure-drop ($\Delta P$) for each configuration is displayed in Figure 59. The bare tube has a negligible pressure drop, since the flow is highly uniform, and the tube length is short. A logarithmic scale is used in Figure 59, which displays an extreme magnitude of frictional losses as the baffle spacing is shortened. Evidently, the solid baffles have a larger pressure-drop than the porous baffles. This is because the holes in the porous baffles increase the ease of passage for the flow along the tube. A shorter baffle spacing also creates a larger pressure drop, which is due to the greater density of obstacles that hinder the flow. The baffle spacings of 5 and 10 cm had a pressure-drop >1 bar. Considering that this pressure-drop is along only 2 m of So-St tube and that the So-St tube will be modularised, this pressure-drop is too extreme to be feasible for the overall So-St process. Therefore, although the 5 and 10 cm baffle spacings have the greatest heat transfer performance, they will not be feasible for the So-St design due to the high pumping power requirements.
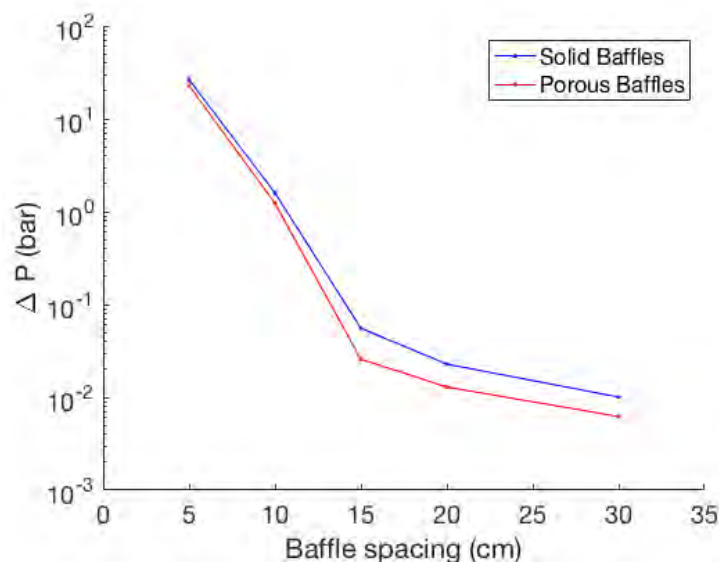


**Figure 59: Pressure-drop along the tube as a function of baffle spacing with a logarithmic scale at the final time step (10s).**

It must be noted that these pressure-drop values are reflective of the flow under single-phase. These values therefore indicate the frictional losses in the So-St tube during pre-saturation conditions when vapour formation has not yet begun. When boiling flow begins, the evolution of gaseous species will increase the volumetric flowrate, creating an additional pressure-drop component. The pressure-drop values from Figure 59 must be integrated with the analysis from Sub-Model 2 to determine the most suitable insert. The enhancement ratio can also be investigated to evaluate the compromise between heat transfer and pressure-drop. This ratio is a dimensionless number that integrates these two phenomena and holistically evaluates the performance of an insert [79]. It describes the efficiency of heat transfer increase relative to the frictional losses. The enhancement ratio is defined as:

$$\boldsymbol{Enhancement\ Ratio} = \frac{Nu/Nu_0}{(f/f_0)^{\frac{1}{3}}} \qquad\qquad Eq.\ 28$$

Where *Nu*, *Nu₀*, *f* and *f₀* are the Nusselt numbers and friction factors for tube configuration with and without inserts, respectively. The Nusselt number and friction factor are defined as:

$$\boldsymbol{Nu} = \frac{hL}{k} \qquad\qquad Eq.\ 29$$

$$\boldsymbol{f} = \frac{\Delta P}{\frac{L}{D}\cdot\frac{\rho V^2}{2}} \qquad\qquad Eq.\ 30$$

where *L* is the characteristic length of the tube; *k* is the solid surface conductivity, and *D* is the tube diameter. The dimensionless ratios can be simplified, considering that only $h$ and $\Delta P$ vary between the two configurations, while all other parameters are constant. The enhancement ratio can be simplified by computing the dimensionless Nusselt number and friction factor ratios as follows:

$$\frac{Nu}{Nu_0} = \frac{h}{h_0} \qquad\qquad Eq.\ 31$$

$$\frac{f}{f_0} \sim \frac{\Delta P}{\Delta P_0} \qquad\qquad Eq.\ 32$$

The energy balance for single-phase internal flow along the length of a tube with constant surface temperature yields the following equation for the mean heat transfer coefficient ($\bar{h}$):

$$\bar{h} = \frac{\rho \dot{V} c_p}{A_s} ln\left(\frac{T_s - T_{m,i}}{T_s - T_{m,f}}\right) \qquad\qquad Eq.\ 33$$

Where $T_s$ is the constant surface temperature; $T_{m,i}$ and $T_{m,f}$ are the mean temperatures at the initial and final temperatures along the *x*-coordinate, respectively; $A_s$ is the internal surface area of the tube; $\rho$ is the fluid density; $\dot{V}$ is the volumetric flowrate; $c_p$ is the fluid specific heat capacity; and $h$ is the mean heat transfer coefficient [80]. A dimensionless ratio ($\bar{h}/\bar{h}_0$) is constructed, with $\bar{h}_0$ being the heat transfer coefficient of the bare tube. The values $A_s$ and $V$ are constants and the narrow temperature range of 120–140°C means the average $\rho$ and $c_p$ can be appropriately assumed constants. Thus, the dimensionless heat transfer coefficient ratio can be written as:

$$\frac{\bar{h}}{\bar{h}_0} = \frac{ln\left(\frac{T_s - T_{m,f}}{T_s - T_{m,i}}\right)}{ln\left(\frac{T_s - T_{m,f,0}}{T_s - T_{m,i}}\right)} \qquad\qquad Eq.\ 34$$

The enhancement ratio is shown in Figure 60 as a function of baffle spacing. Shortening the baffle spacing decreases the enhancement ratio, which makes the heat transfer process inefficient. A sharp decrease in enhancement ratio is also seen from 15 to 10 cm baffle

spacings. The solid baffles have a consistently greater enhancement ratio than porous baffles at the same baffle spacing. This means that solid baffles have greater heat transfer enhancement relative to the increased work requirements for pumping power for the single-phase flow. Naturally, this analysis must be further integrated with Sub-Model 2, where the calculated frictional losses will indicate the So-St behaviour under boiling flow rather than single-phase. Evidently, the enhancement ratio is effective for comparing the efficiency of various configurations; however, it is not necessarily a useful parameter for solving an optimisation problem. Increasing the efficiency of heat transfer does not necessarily mean that the net heat transfer enhancement is sufficient for improving So-St performance. The ideal optimisation problem will therefore look at specifying a maximum critical pressure constraint on each So-St segment, and then choosing the baffle spacing that creates a pressure-drop below this constraint.
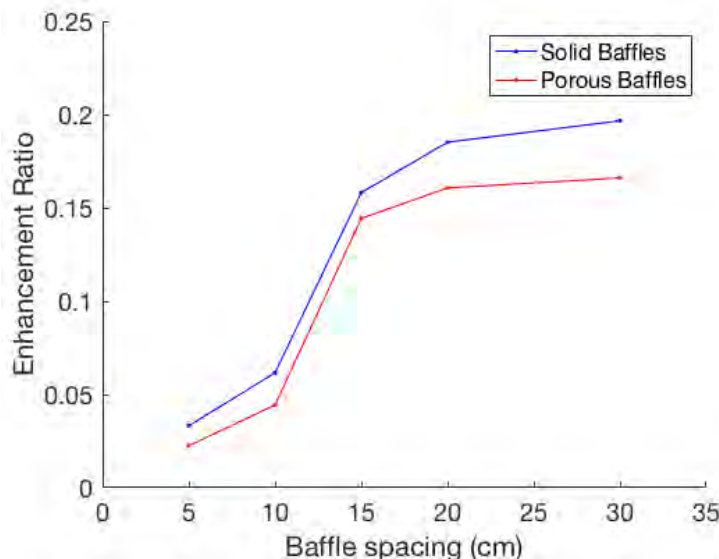


**Figure 60: Heat transfer enhancement ratio as a function of baffle spacing.**

Another factor that can be investigated is fluid mixing, which can be observed in the velocity profiles in Figure 61. For the bare tube (no-inserts) case, there is only a horizontal flow at a constant velocity (0.3 m/s), characterised by the horizontal contour lines. The introduction of baffles creates greater vertical mixing, with regions that reach more than double the average inlet velocity, hence causing the increase in heat transfer as discussed previously. However, with regions of increased local velocity, there must also be regions of decreased local velocity to maintain the volumetric flow balance. These are areas of stagnation in the fluid and can be observed in the wake regions downstream to the baffles. Some of the wake regions consist of recirculation zones. These are local regions created by the obstacles amid the path of the fluid flow, which cause the fluid to separate from the bulk flow and recirculate behind the obstacle. The recirculation zones are caused due to the obstacles creating areas of low pressure downstream that suck the fluid back and create a circular vortex. This phenomenon is characterised by the circular contours seen in wake regions in Figure 61. They are mostly evident in solid baffles at spacings ≥10 cm and in the porous baffles at spacings ≥15cm. The

benefit of the recirculation zones is that they create local temperature hot spots seen in Figure 57. These regions may therefore create greater vapour evolution in Sub-Model 2.
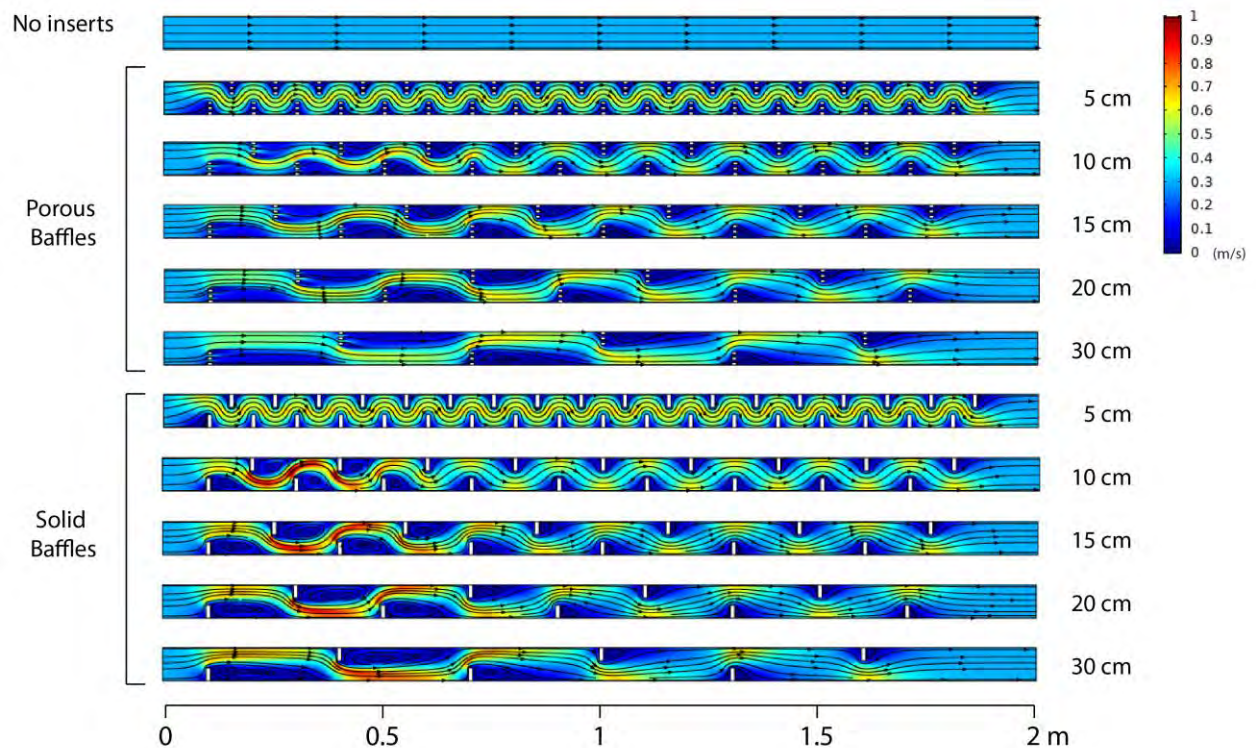


**Figure 61: Velocity profile (m/s) along the So-St tube with no inserts, porous baffles and solid baffles at different baffle spacings at the final time step (10s).**

The concentration of $CO_2$ distribution is shown in Figure 62. The baffles create local concentration maxima in the baffle boundary layers, and higher concentration gradients are seen for shorter baffle spacings. Additionally, these concentration maxima are observed within the recirculation zones created by the baffles. Thus, these stagnant regions, which are removed from the bulk fluid flow, may become areas of significant $CO_2$ accumulation. This is because the removal of $CO_2$ is driven by the saturation pressure, which is a function of $CO_2$ saturation concentration. The concentration maxima indicate local regions where the concentrations are greater than the saturation concentration, indicating that these areas may become the sites for $CO_2$ nucleation into the gaseous phase. Overall, the results for Sub-Model 1 indicate the preferred *EHT* inserts to increase heat transfer and create greater concentration gradients. The heat transfer is enhanced more for solid baffles than for porous baffles, and a baffle spacing ≤10 cm creates too much of a significant frictional loss to be feasible for the So-St design. These results and conclusions must be integrated with that of Sub-Model 2 to determine the most suitable insert configurations for the So-St design.
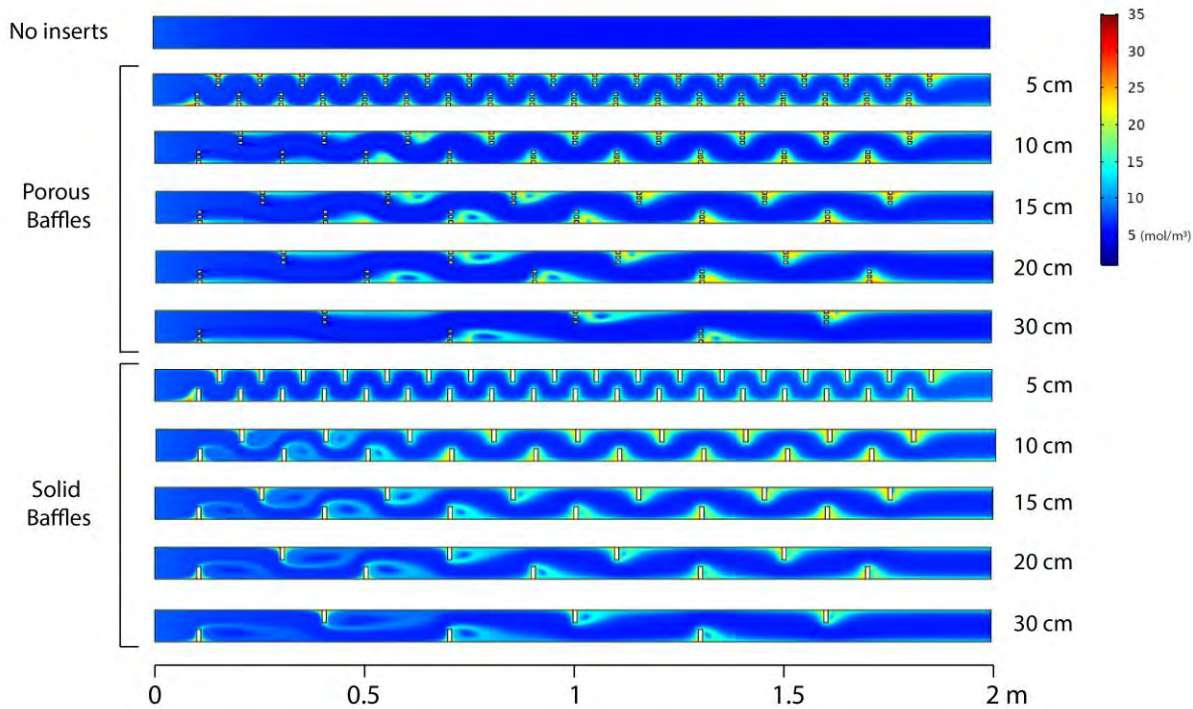
**Figure 62: Concentration of CO₂ (mol/m³) along the So-St tube with no inserts, porous baffles and solid baffles at different baffle spacings at the final time step (10s).**

## 4.2.2  2-D geometry for Sub-Model 2

Sub-Model 2 uses the phase field method to track the vapour fraction along the length of the So-St tube. This enables an investigation into the gas evolution within the tube, which is used as an analogy to describe the $CO_2$ removal. Sub-Model 2 was conducted for the 10 and 20 cm baffle spacing insert. The 20 cm spacing was chosen since it had high heat transfer performance without compromising the pressure-drop ($\Delta P < 0.05$ bar). Although the 10 cm spacing had a significant pressure-drop in Sub-Model 1, we also investigated it in Sub-Model 2 to display the difference in effectiveness when vapour formation is present. The distributions for vapour phase for each insert case study are compared in Figure 63 at the final time step of 2 s. All configurations display the desired bubbling phenomena over the tube length. The bare tube has large bubbles forming near the inlet and the vapour phase develops over the length of the tube. This is characterised by the inlet of the tube being predominantly liquid phase, and a consistent decrease in liquid fraction being observed until the end of the tube, where the vapour phase is more predominant. The porous baffles have a similar gradient compared with the bare tube; however, the solid baffles have a more evenly distributed vapour distribution across the length of the So-St tube. This is because the solid baffles act as trenches that collect and periodically stabilise the liquid flow along the bottom of the tube as well as the gas flow along the top of the tube, whereas the holes in the porous baffles allow fluid to pass through, hence relaxing the effect of the fluid segregation. The baffles act as nucleation sites for vapour evolution. Streams of gas phase can be seen exiting the porous baffle holes and are most obvious closer to the tube inlet.
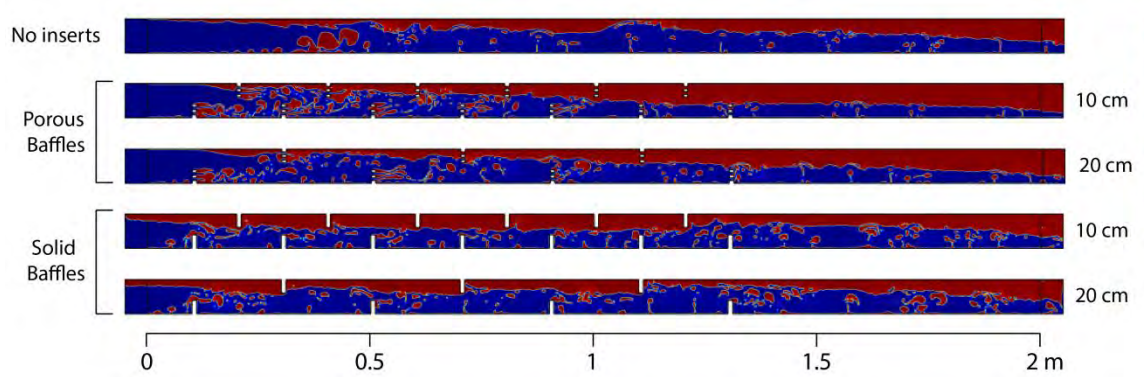
**Figure 63: Vapour fraction profiles along tubes for phase field model after 2 seconds of simulation time. The *EHT* insert cases are: (top) no inserts, (middle) porous baffles, (bottom) solid baffles.**

These streams can also be observed at the top of the solid baffles, particularly at earlier time steps as evident in the timely depicted Figure 64. The vapour gradients have great importance from an operational standpoint for the So-St design. This is because the evolved gas must be periodically vented out from the lean solvent, in order to maintain the driving force for gas removal and ensure that drying-out conditions do not occur. This outcome supports the use of multiple segments in one So-St module, which we initially proposed to enhance $CO_2$ desorption. From our CFD observations, we can conclude the multi-segment approach has dual benefits in achieving effective $CO_2$ desorption and stabilising the boiling operation.
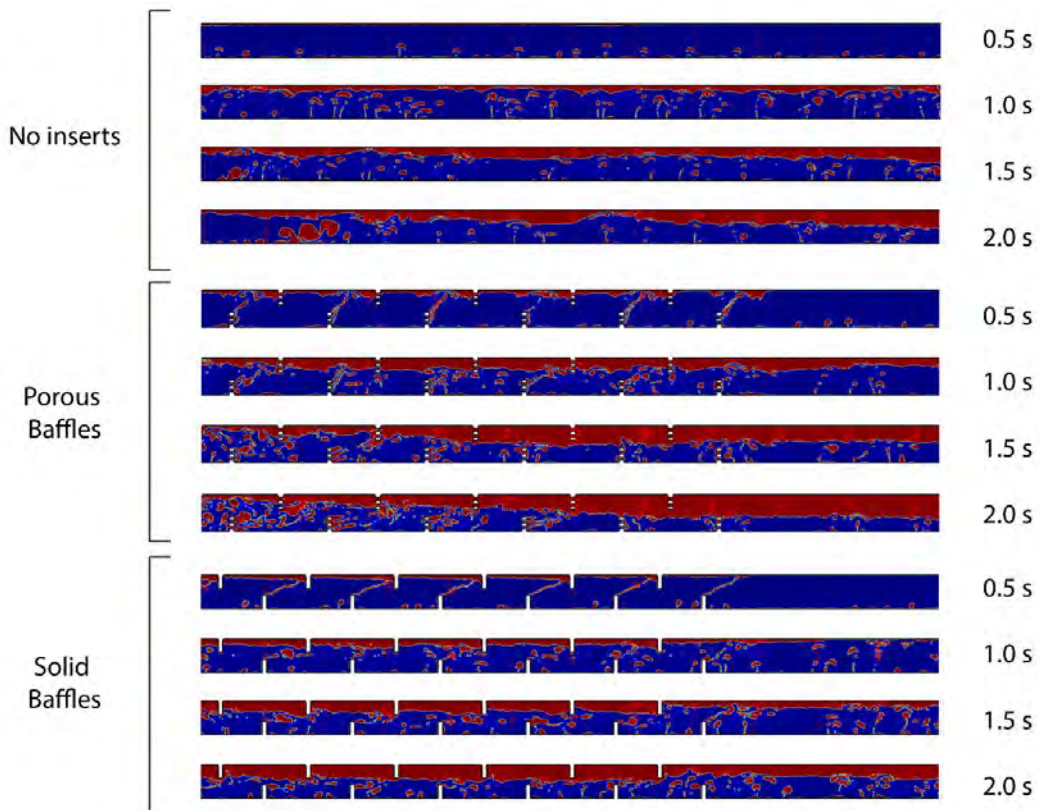


**Figure 64: Vapour evolution over time for no inserts, porous and solid baffles. Porous and solid baffles with baffle spacings of 10 cm and 20 cm.**

Figure 65 shows the average vapour fraction throughout each tube as a function of time, along with a normalised vapour fraction ratio ($\phi/\phi_0$) where $\phi_0$ is the vapour fraction of the bare tube without baffles. This enables a direct comparison of the *EHT* insert's dynamic performance compared with the bare tube. The vapour fractions for all cases increase steadily, which is expected, since the surface temperature boundary condition creates a constant driving force to provide energy for the latent heat of vaporisation.
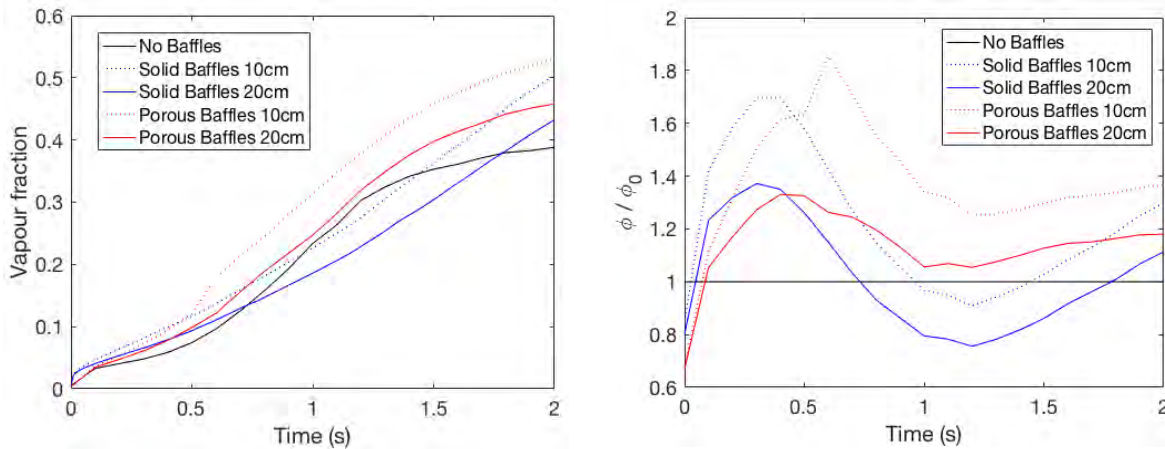


**Figure 65: Average vapour fraction (φ) within tube (left) and dimensionless vapour fraction (φ/φ_0) (right) as a function of time, where φ_0 refers to the bare tube vapour fraction.**

There is a similar trend for $\phi/\phi_0$ across all the inserts. During the first 0.7 s, all the insert configurations reach vapour fraction values higher than that of the bare tube, indicating that the presence of inserts speeds up phase development in the early stages of the process. The 10 cm baffle spacings also display greater peaks in vapour fraction compared with the 20 cm spacings. From 0.7–1.4 s, there is a sharper increase in vapour fraction for the bare tube, which causes a local minimum in $\phi/\phi_0$ at approximately 1.2 s. After this, a slight increase is seen for $\phi/\phi_0$ until the end of the time period. Interestingly, the porous baffles have vapour fractions consistently greater than that of the bare tube. This indicates an enhancement to So-St performance, since the process can create greater amounts of vapour along the same length of tube. However, the solid baffles have lower amounts of vapour fraction compared with the bare tube between 0.7 and 1.4 s. This is likely a result of the solid baffles having less impact on the flow mixing at higher vapour fractions. By localising the vapour phase at the top of the tube, and the liquid phase at the bottom, the amount of vertical mixing is reduced. The porous baffles, having holes, enable a more mixed profile and the holes continue to be sites for vapour nucleation even at high vapour fractions. The above results suggest the *EHT* inserts further complicate vapour evolution during non-steady state operation. One direct implication is that the overall process control should not employ vapour fraction as a controlled variable directly. This is because the complexity in its dynamic responses creates significant challenges for the controller design and tuning.

The temperature distributions for the tube configurations are shown in Figure 66. The trend in temperature parallels that of vapour phase distribution. Since the liquid phase is at

saturation, it remains at a constant temperature of 120°C. Thus, all the temperature gradients reflect the gaseous phase, which reaches heightened temperatures. Of particular interest is the presence of large bubbles in the bare tube, which correspond to the extreme hot spots near the entrance of the bare tube. The hot spots indicate that sensible heat is transferred into the bubbles and wasted, since it is not mixed into the bulk fluid to be used as latent heat. As alluded to previously, the temperature hot spots may have detrimental effects on the thermophysical properties of the MEA solvent. It is therefore very important to reduce the temperature gradients. The large bubbles also affect the flow stability, where local surges in volume and temperature could damage the tube. On the baffled tubes, the bubble hot spots are not present in the baffle configurations, which shows that the baffles prevent the growth of these larger bubbles. Naturally, the models are only run over 2 s of simulation time and have not reached the steady-state condition, so it is difficult to infer the resulting effect of the large bubbles in the bare tube.
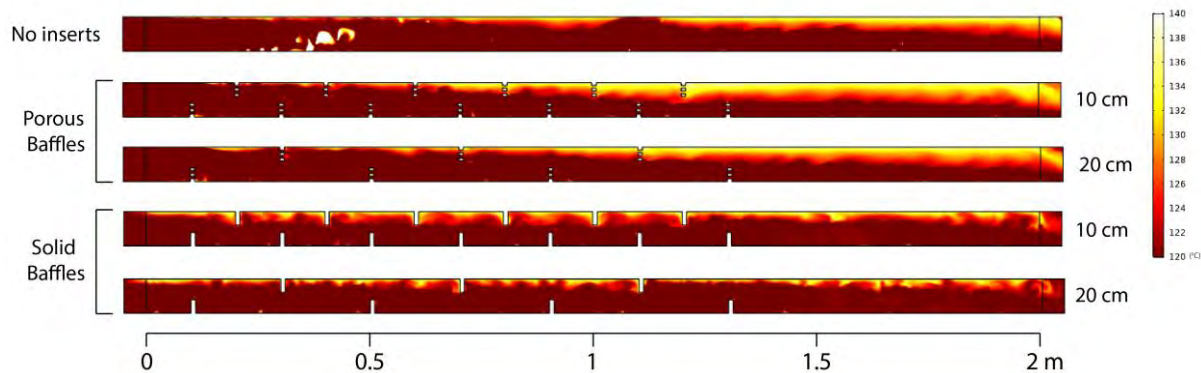


**Figure 66: Temperature profiles along tubes for phase field model after 2 s of system time. Insert cases: (top) no inserts, (middle) porous baffles, (bottom) solid baffles.**

Sub-Model 2 has an alternative boundary condition to Sub-Model 1; namely a constant pressure difference, rather than constant inlet velocity. Thus, the frictional losses must be investigated differently from Sub-Model 1. Here, the inlet velocity is a function of time, meaning that the impact of the baffles on the frictional losses can be compared by observing their impact on the velocity. Furthermore, the constant pressure-drop means that the dimensionless friction factor ratio must be formulated alternatively as follows:

$$\frac{f}{f_0} = \frac{u_0^2}{u^2}$$

*Eq. 35*

Figure 67 displays the average inlet velocity and the dimensionless friction factor as a function of time for each configuration. The velocities for all configurations steadily increase with time, which is due to vapour formation causing an increase in liquid velocity due to the smaller liquid flow area. The tubes with porous baffles have velocities slightly lower than that of the bare tube, which is due to the baffles hindering the flow. This is seen also for the tubes with solid baffles; however, the velocities are significantly lower than the other configurations. This deviation begins at ~0.5 s, where the fluid velocity in the solid baffles'

plateaus. The behaviour can be accounted for by considering that the increases in velocity overall result from the gas phase evolution causing a larger volume flowrate of the fluid. However, for the solid baffle configurations, the vapour phase accumulates at the top of the tube and is stopped by the top side baffles. This means that only the liquid phase can flow under the top-side baffles, and not the vapour phase, which causes the overall velocity to be lower. This phenomenon is further confirmed by observing the behaviour of the solid baffles for 10 cm spacing near the end of the 2 s simulation time. The velocity profile shows a distinct increase, which is characterised as the point where the vapour phase accumulation on the topside has become great enough that it can pass under the top-side baffles. This critical point can be seen in the time evolution distributions between 1.5 and 2.0 s (Figure 64). A greater volumetric rate is therefore allowed to pass through the tube, causing a sharp increase in the inlet velocity. For the 20 cm solid baffles, we can expect that a similar phenomenon will be observed if the simulation time is increased. Visually, the phase distribution shows the vapour phase to not be low enough to pass under the top-side baffles at the final time-step. A longer simulation time will be necessary to determine how close the velocities of the tubes with solid baffles approach that of the porous baffles.
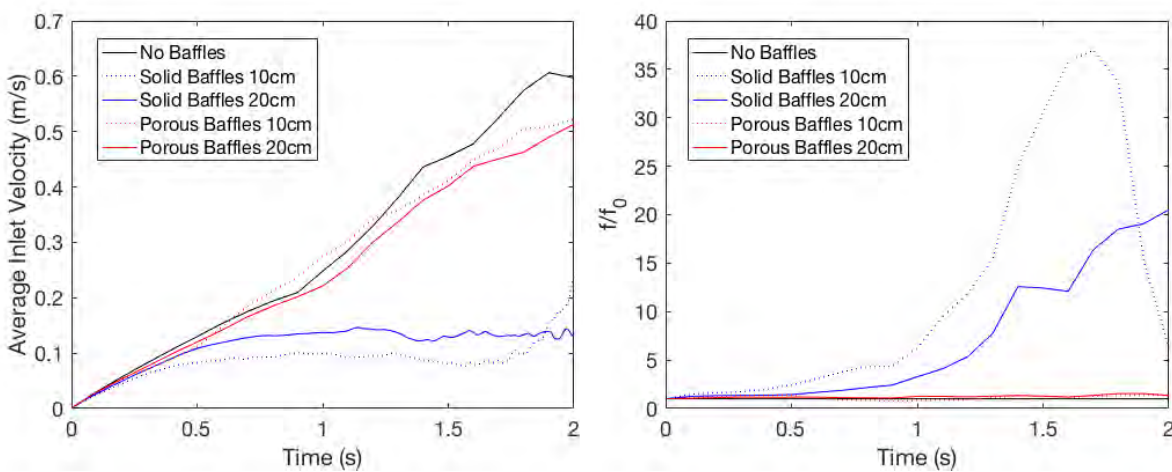


**Figure 67: Average inlet velocity (m/s) (left) and dimensionless friction factor (right) as a function of time, where f_0 refers to the bare tube vapour fraction.**

The dimensionless friction factor shows further insight into the configuration comparisons. This factor is approximately 1 for the porous baffles, showing minimal frictional losses compared with the bare tube. As expected, the solid baffles show a significantly high dimensionless friction factor, due to the baffles preventing vapour flow. However, for the 10 cm spaced solid baffles, the friction factor sharply decreases near the end of the simulation time (Figure 67-right), corresponding with the vapour velocity behaviour previously discussed. A longer simulation time would be necessary to determine its minimum value and to confirm whether the 20 cm spacing solid baffles will reach a similar local maximum.

Under real conditions, the So-St will function dynamically throughout the day and will alternate between single-phase and multi-phase according to the solar availability. Hence, the

suitability of the inserts must be evaluated by integrating the conclusions from both Sub-Models 1 and 2. In terms of heat transfer, the solid baffles had the greatest thermal performance overall. However, the porous baffles were able to create greater vapour fractions, due to an increase in heat transfer from the porous holes, which aid the nucleation of bubbles due to the greater surface area-to-volume ratio. Shorter baffle spacings showed greater heat transfer enhancement and greater vapour evolution. The inserts created greater frictional losses; however, the extent of this was much more significant in the single-phase (Sub-Model 1) than the multi-phase (Sub-Model 2). Hence, the *EHT* inserts have the greatest heat transfer enhancement in the presence of boiling flow. The porous baffles also had lower pressure-drops than the solid baffles.

## 4.3    3-D design elements

Despite the significant computational time, a CFD model for the 3-D geometry has greater accuracy and better informs the conclusions made from the design perspective. Compared with the 2-D model with a So-St length of 2 m, the 3-D model was instead undertaken at a So-St length of 1 m. This was done to reduce the computational load without compromising the validity of the results. The 3-D model is important for ensuring the results of the 2-D models are valid and enabling a deeper investigation into the internal events of the So-St design. Using the 3-D model, we aim to achieve the following goals:

1.  Investigate the So-St tube under different solar profiles, namely a uniform and non-uniform heat distribution.
2.  Investigate the So-St with inserts chosen from the conclusions of the 2-D modelling results.
3.  Reach decisions on the *EHT* inserts in terms of increased vapour generation, flow stability and the potential for reducing the So-St field size.

### 4.3.1  Uniform vs non-uniform solar profiles

A key limitation in the 2-D modelling work was the use of a constant temperature boundary condition, instead of a constant heat flux condition. In the 3-D model, there is no longer a limitation, since the solar heat distribution can be readily defined around the So-St tube circumference. The need for a non-uniform heat flux distribution about the solar collector receiver tube is essential for ensuring that the model accurately describes the dynamic fluid behaviour. We first convey this by simulating the bare So-St segment for two different heat distributions, namely a uniform and non-uniform heat flux distribution, and compare their flow behaviour. The non-uniform heat flux distribution about a PTC receiver tube has been characterised by Cheng et al. [63], and their solar profile is used in this simulation, as seen earlier in Figure 52. To ensure a valid comparison, the uniform heat flux distribution had a

heat flux of 17.8 kW/m$^2$, which is equivalent to the average heat flux of the non-uniform distribution, thus ensuring the overall energy input to the tube circumference is very similar.

The vapour phase distribution is displayed in Figure 68. Visually, both uniform and non-uniform distributions have similar flow regimes, with bubbling in the middle of the tube and a distinct phase separation at the end of the tube. However, a key difference is that the bubbling in the non-uniform distribution is much more vigorous with larger bubbles. This is accounted for by considering that the evolving gas phase collects at the top side of the tubes as a result of buoyancy forces, compared with the liquid phase, which resides on the bottom side. The non-uniform model localises the heat at the bottom of the tube, meaning the heat is absorbed primarily by the liquid, which causes greater bubbling. In the uniform model, the heat is distributed evenly, and a significant portion of heat is focused on the top of the tube where the gas phase has collected, instead of the desired liquid.

The temperature distributions are displayed in Figure 69, which further confirms this phenomenon. Near the end of the tube, the uniform distribution has a sharp gradient in temperature, while the non-uniform distribution has a smoother gradient. This reflects how the uniform distribution has large amounts of heat entering the vapour phase as sensible heat, rather than the liquid phase as latent heat [81]. Therefore, the non-uniform distribution has a greater heat transfer efficiency with less wasted heat, and better favours vapour removal. The above result suggests parabolic trough designs should enhance the solar energy localisation towards the bottom of the tube to facilitate boiling.
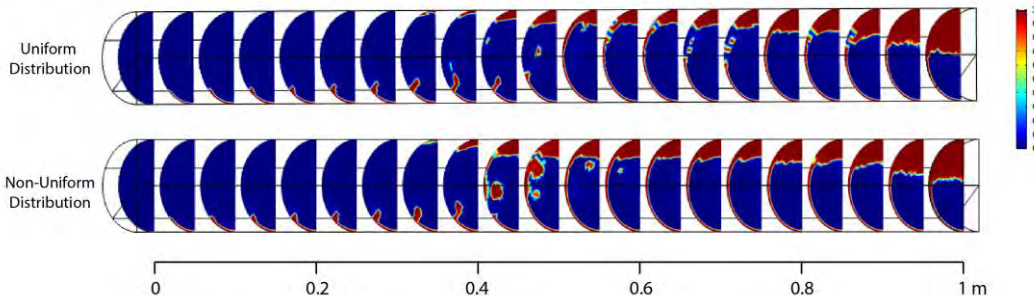


**Figure 68: Vapour phase distributions along 3-D So-St tube model for uniform and non-uniform solar profiles at the final time step.**
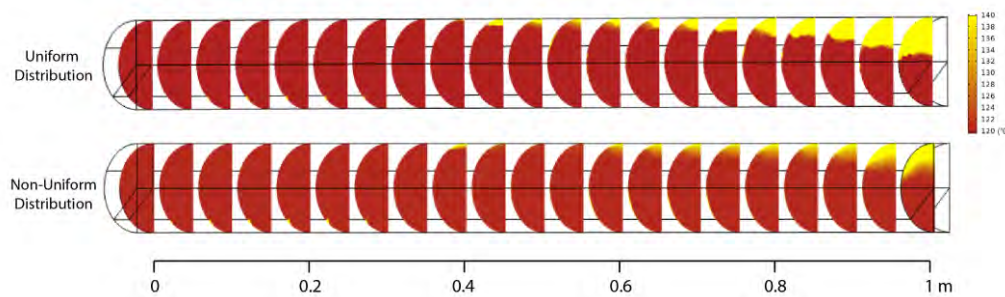


**Figure 69: Temperature distributions along 3-D So-St tube model for uniform and non-uniform solar profiles at the final time step.**

The vapour fraction in the tubes is plotted as a function of time in Figure 70. The vapour fraction for the non-uniform distribution is consistently higher than that of the uniform distribution, which further confirms that more vapour is being generated in the non-uniform distribution.
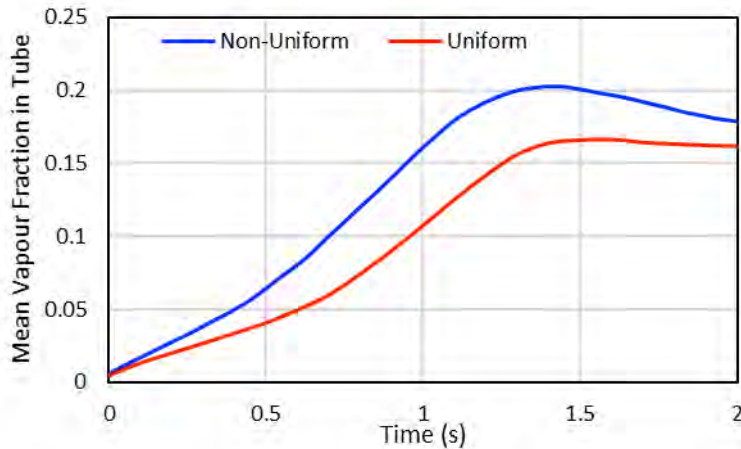


**Figure 70: Vapour fraction distributions along 3-D So-St tube model.**

The heat transfer coefficients can also be analysed. The boiling heat transfer coefficient is defined appropriately as:

$$h = \frac{q''}{T_s - T_{sat}} = \frac{q''}{\Delta T_e}$$                                        *Eq. 36*

Where $T_s$ is the surface temperature; $T_{sat}$ is the saturation temperature and their difference $\Delta T_e$ is termed as the excess temperature. The liquid phase is at saturation $T_{sat}$ is equivalent to the temperature of the liquid fraction $T_l$, which remains constant at 120°C. The boiling heat transfer coefficient was calculated at intervals along the length of the So-St tube. The values for $T_s$ and $T_l$ were assumed to be the average surface temperatures and liquid temperatures at each length interval. The heat transfer coefficient for the non-uniform and uniform heat flux distributions are compared in Figure 71. Over the initial length of the tube, the heat transfer coefficient is significantly high, due to the fluid being predominantly in liquid phase. Both models require a similar length of tube (~0.35–0.40 m) in the entrance region to reach a developed flow region, where vapour phase has evolved. This is indicated by the shaded grey region and characterised by the extreme drop in heat transfer coefficient values at the entrance region (Figure 71). The decrease in heat transfer coefficient is because a solid–gas interface has a significantly lower value compared with that of a solid–liquid interface. After reaching a developed flow, the non-uniform model shows a heat transfer coefficient consistently greater than that of the uniform model. This behaviour is accounted for by investigating the trend in surface temperature, as seen in Figure 72. After boiling begins from 0.4 m onwards, the uniform model displays a consistently higher surface temperature than the non-uniform model. This is accounted for by our earlier discussion of significant heat being localised at the top of the tube for the uniform distribution compared with the non-

uniform distribution. Thus, for the same heat flux input, the non-uniform heat distribution is more efficient at transferring heat into the liquid phase to effectively contribute towards the latent heat of vaporisation.
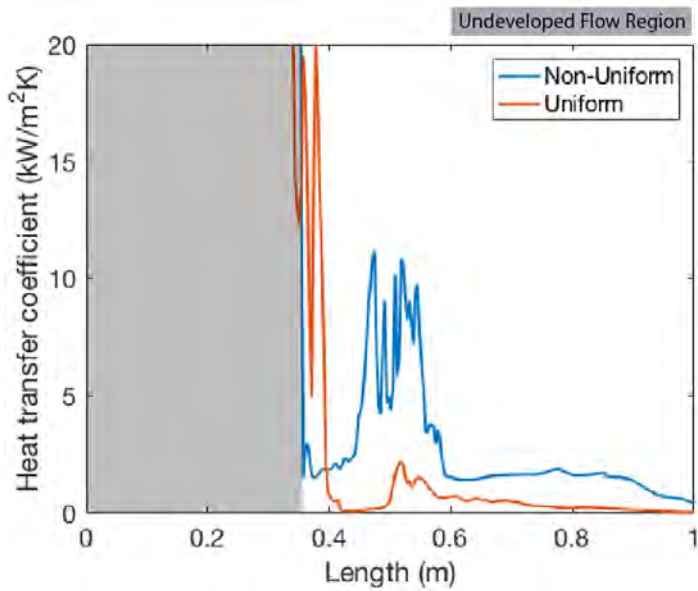


**Figure 71: Heat transfer coefficient along 3-D So-St tube model.**
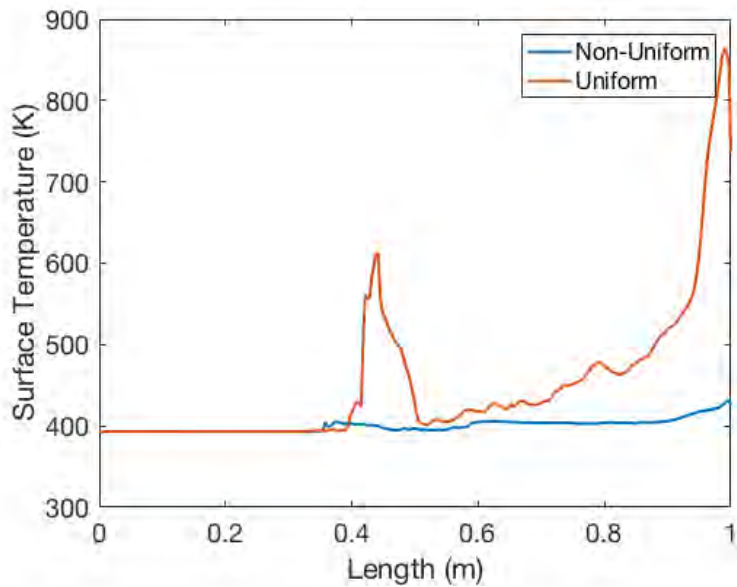


**Figure 72: Average surface temperature along 3-D So-St tube model.**

Overall, a So-St tube would have different flow behaviours depending on the solar profile. Our comparison displays the need for a 3-D model that accounts for all heat input in the radial direction from the entire circumference of the tube. The non-uniform heat distribution, which reflects the real performance of a PTC tube, performed better than the uniform heat distribution. The greater heat flux at the bottom of the tube causes better flow boiling performance by having a larger heat transfer coefficient and favouring a greater vapour fraction along the length of the tube.

## 4.3.2  Enhanced heat transfer by tube inserts

The 3-D CFD model was then used to investigate the implementation of *EHT* inserts into the So-St tube. A configuration with solid baffles and porous baffles was constructed, each having non-uniform heat distribution. In terms of the baffle spacing chosen for the 3-D CFD models, both configurations used 20 cm baffle spacing. This is based on the conclusions of our previous 2-D modelling results, where baffle spacings shorter than 20 cm caused significant pressure-drops in the single phase. The 20 cm baffle spacing also performed satisfactorily in the 2-D geometry of Sub-Model 2. The *EHT* insert configurations are compared with the bare tube results to determine the enhancement in thermal performance of the *EHT* inserts.

The vapour phase distributions are displayed in Figure 73 and Figure 74, showing two forms: periodic semi-circle cross-sections and an overall rectangular cross-section, respectively. The baffles cause significantly more vapour to accumulate in the tubes. This is characterised by the gas–liquid interface being much lower for the solid baffle configuration. Interestingly, the solid baffles immediately evolve gas at the beginning of the tube, which is due to back flow of the gaseous phase because of the solid baffles intermittently hindering the vapour flow. A key difference between the configurations is that the bare tube has significant bubbling, whereas the baffle configurations have minimal bubbling; in the latter, the vapour evolves in the form of film boiling along the tube's internal circumference in an inverted annular flow regime. This indicates that baffles create a more well-mixed fluid with greater flow stability and less sporadic bubbling [81]. The comparison further highlights the limitations of the 2-D modelling, which only accounted for vertical flow in the centre cross-section of the tube. The bubbling in all configurations is also less extreme than that seen in the 2-D geometry results. This is likely due to the constant surface temperature (140°C) boundary condition causing more heat input than desired.
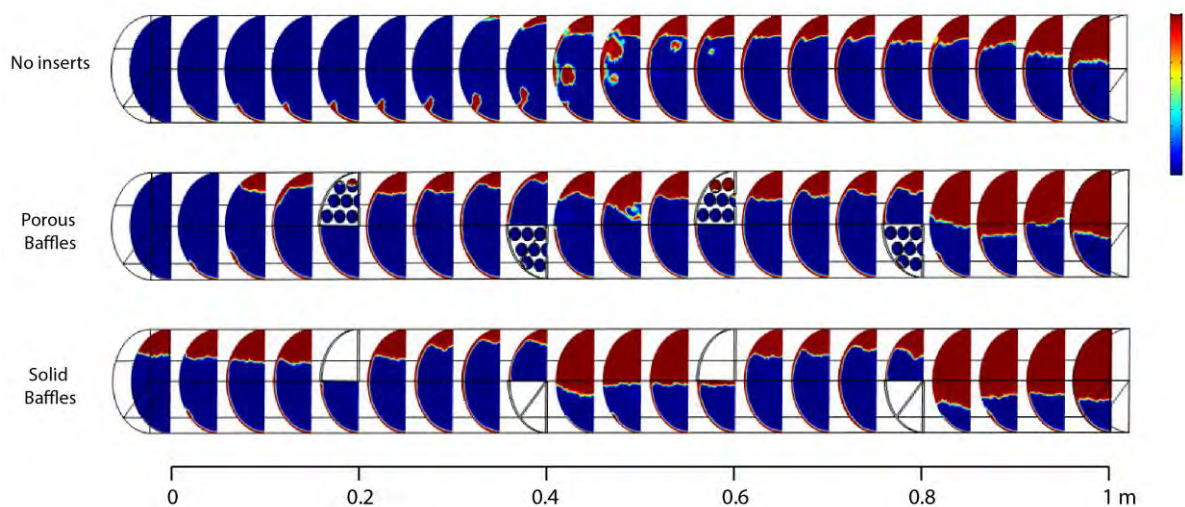


**Figure 73: Vapour phase distributions along 3-D So-St tube model for porous and solid baffle inserts at 20 cm baffle spacing. Semi-circle radial cross sections are normal to the fluid flow and are at intervals of 0.05 m.**
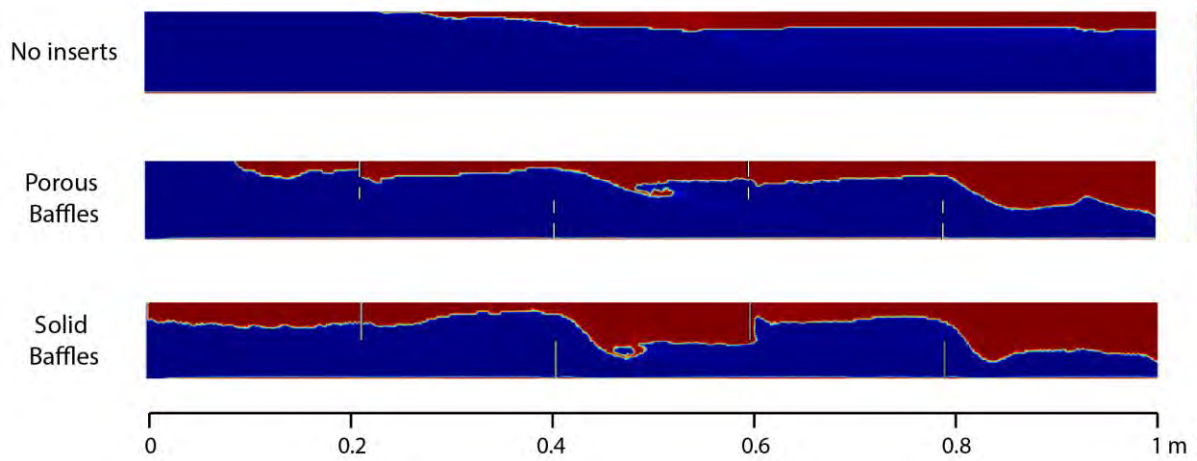
**Figure 74: Vapour phase distributions along 3-D So-St tube model for porous and solid baffle inserts at 20 cm baffle spacing. Rectangular cross sections are along the fluid flow, which can be compared with the 2-D model geometries.**

The temperature distributions are displayed in Figure 75 and Figure 76, which also show the two respective cross-sectional forms. Similar to the 2-D geometry, the high temperatures form near the top side of the tube where the gas accumulates. For the solid baffles, high temperatures are seen in the upstream regions of the top-side baffles, since the gas phase builds up there and cannot flow underneath.
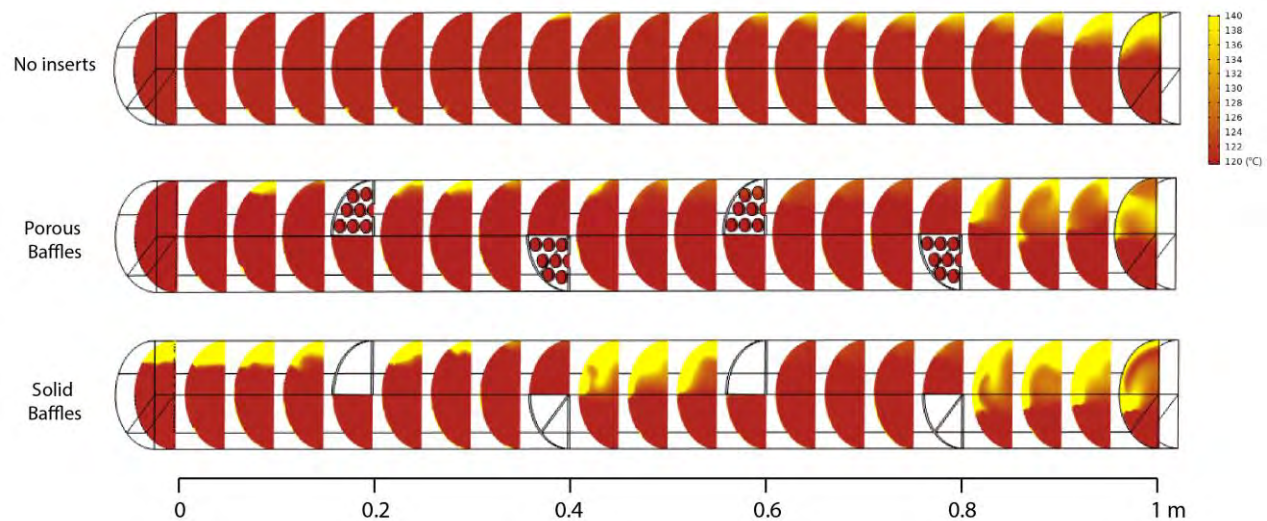


**Figure 75: Temperature distributions along 3-D So-St tube model for porous and solid baffle inserts at 20 cm baffle spacing. Semi-circle cross sections are normal to the fluid flow and are at intervals of 0.05 m.**
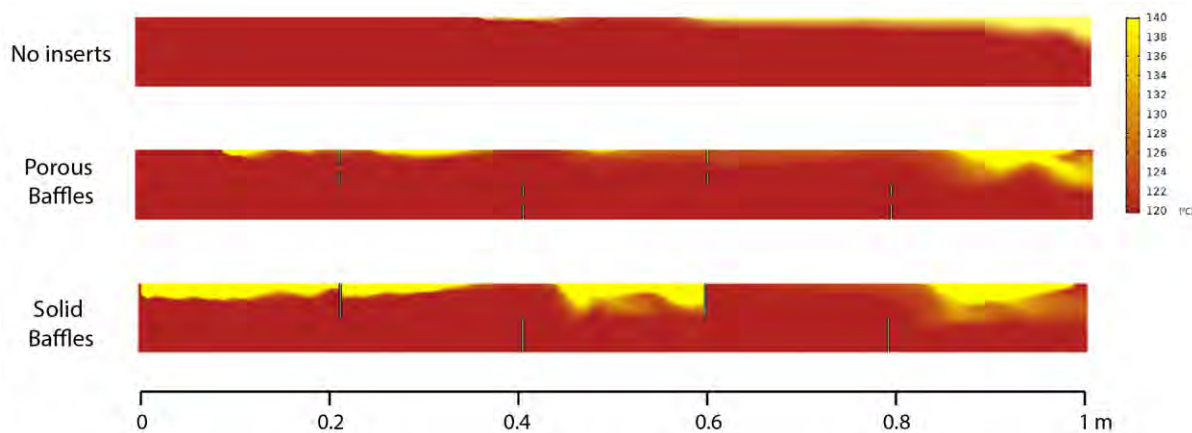
**Figure 76: Temperature distributions along 3-D So-St tube model for porous and solid baffle inserts at 20 cm baffle spacing. Rectangular cross sections are along the fluid flow, which can be compared with the 2-D model geometries.**

The vapour fraction along the length of the So-St tubes is plotted as a function of time in Figure 77. The solid baffles require a longer period of time (~0.75 s) before a sharp increase in the vapour phase; however, this configuration has a greater amount of vapour compared with the others. The porous baffles also perform better than the bare tube. Although it appears that this behaviour is accounted for by the increase in heat transfer efficiency caused by the baffles, this cannot be concluded yet. We must also recognise that the configurations have different flow velocities due to the constant pressure-drop boundary condition, and this may also contribute to the trend.
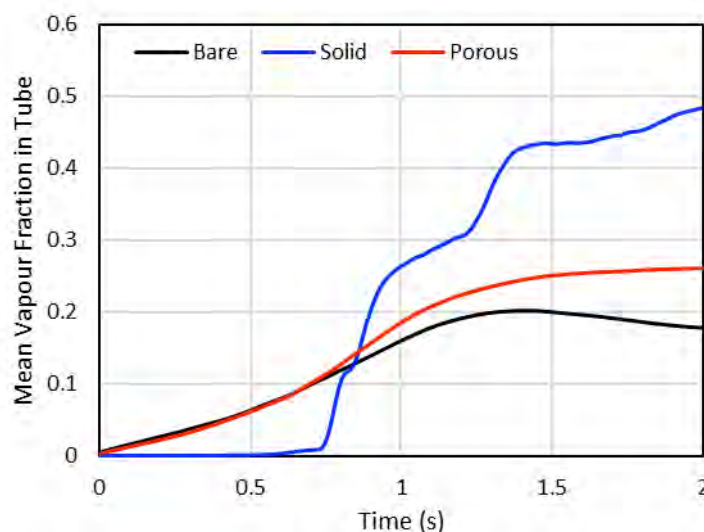


**Figure 77: Vapour fraction within different 3-D So-St tube models as a function of time.**

The mean inlet velocity profiles are plotted in Figure 78 as a function of time. Note that although this velocity is taken at the inlet, it also reflects the mean velocity across the entire tube, since the flow is incompressible. The bare tube has the greatest velocity, while the solid-baffle tube shows the lowest fluid velocity. This partially accounts for the increase in vapour phase along the tube in the solid-baffle tube. The slower velocity creates a longer residence

time for the fluid in the tube, which means that the fluid has more time to evaporate and a higher vapour fraction at the exit of the tube.
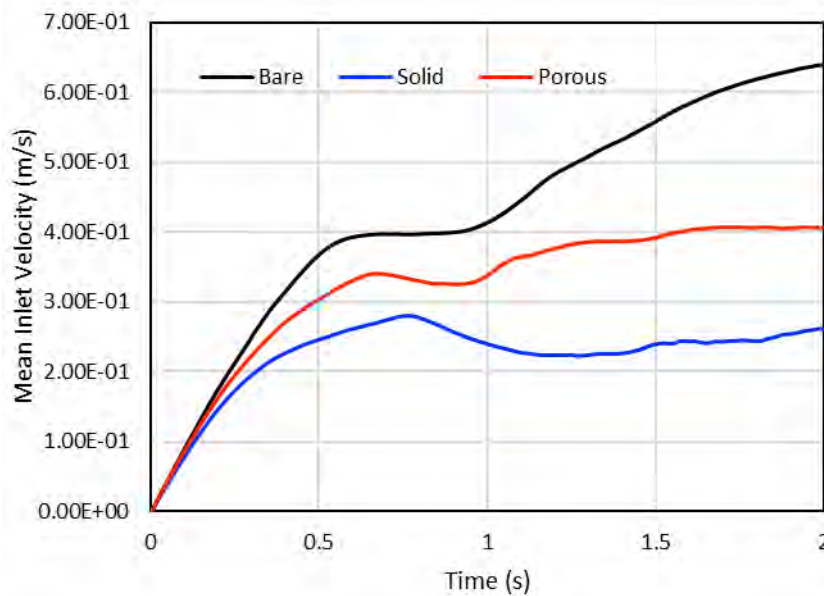


**Figure 78: Average inlet velocity within different 3-D So-St tube models as a function of time.**

To determine the impact of fluid velocity on vapour generation, the vapour flowrate exiting the end of the tube is computed in Figure 79 as the total volume flowrate multiplied by the vapour fraction. The bare tube has a greater vapour flowrate at the outlet, while the solid-baffle tube has the lowest flowrate. Although the solid-baffle configuration has the greatest vapour fraction along the tube, this does not mean it has the largest amount of vapour exiting the tube. From our observations, the bare tube has the greatest vapour generation performance. However, we must recognise that this comparison is at a constant pressure-drop and assumes the same pumping requirement. In Sub-Model 1, the enhancement ratio was computed (Figure 60) and found to be ≤1 for the baffles, showing that the baffles have greater frictional losses compared with the heat transfer enhancement. Thus, it is expected that at a constant pressure-drop, the bare tube will be more efficient. Yet, a valid comparison must attempt to normalise the flowrates to determine the vapour generation for the different configurations, assuming that they have the same velocity profile. From an operational point of view, adding inserts will increase the pumping power requirements as a cost for greater heat transfer enhancement, instead of keeping the pumping power constant. To meet the $CO_2$ capture targets, it is essential that the volumetric flowrates of the baffle configurations increase to a similar target as the bare tube.
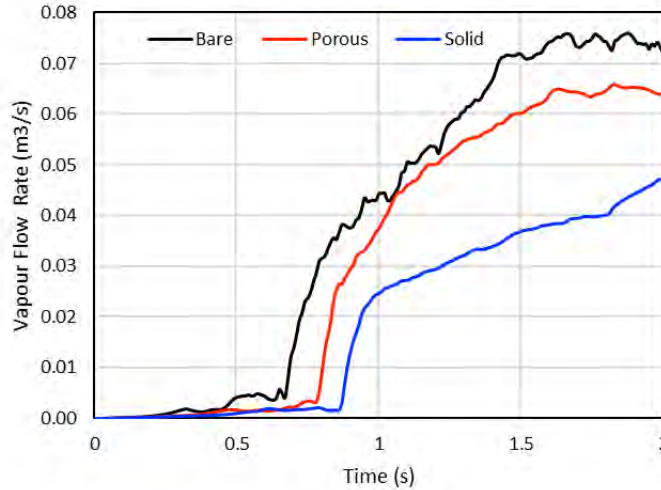
**Figure 79: Volume flowrate of vapour exiting different configurations of So-St tubes as a function of time, at a constant pressure drop.**

A normalised volumetric flowrate of vapour is displayed in Figure 80, according to the following equation:

$$Q_{norm} = Q_{actual} \cdot \frac{u_0}{u}$$

<div align="right">*Eq. 37*</div>

Where $Q_{norm}$ is the normalised vapour volume flowrate; $Q_{actual}$ is the actual vapour volumetric flow shown in Figure 79, $u$ is the velocity of the configuration; and $u_0$ is the velocity of the bare tube. This formula computes the flowrate of vapour assuming that the configurations have the same velocity profile, and a varying pressure-drop. This method also assumes that vapour profiles are not changing at higher velocity levels. The baffle configurations have a larger flowrate of vapour the bare tube. From 1–1.5 s, both baffle configurations have very similar vapour flowrates, but this eventually deviates, with the flowrate in solid baffles tube is being greater than the porous baffles. Thus, if increased pumping power is available to ensure *EHT* inserts have the same velocity profile compared to the bare tube, both baffle configurations will relatively perform better.
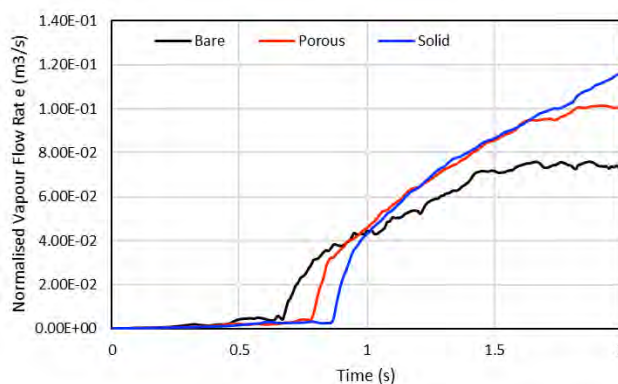


**Figure 80: Normalised volume flowrate of vapour exiting different configurations of So-St tubes as a function of time, assuming constant velocity profiles.**

The potential of So-St field size reduction can now be estimated. We can confidently claim that the baffle configurations have greater normalised vapour flowrates over the 1 m length of the So-St tube. Assuming the So-St field size and the vapour generation are proportional, which is a reasonable assumption due to the constant heat flux input, this enables us to calculate the length of the baffle configuration So-St tubes that will produce the same level of vapour flow as the bare tube. We can calculate a normalised length reduction in the single So-St segment, according to the following equation:

$$\boldsymbol{SoSt\ Size}\ \% = \frac{Q_{norm,bare}}{Q_{norm}}$$    *Eq. 38*

This equation represents the percentage length of a So-St tube necessary for the baffle inserts to have the same vapour generation as that of the bare tube. *Eq. 38* is calculated at the final time-step of the simulations, and the results are displayed in Figure 81. The porous baffles tube shows a size reduction of 28.6%, while that of the solid baffles tube is 37.9%. The exact magnitudes of these numbers must be treated with caution, since Sub-Model 2 treats the So-St tube as having only pure water. However, the trend in values demonstrates the potential for *EHT* inserts to favour vapour formation, which can be interpreted as the $CO_2$ removal percentage at a similar order of magnitude.
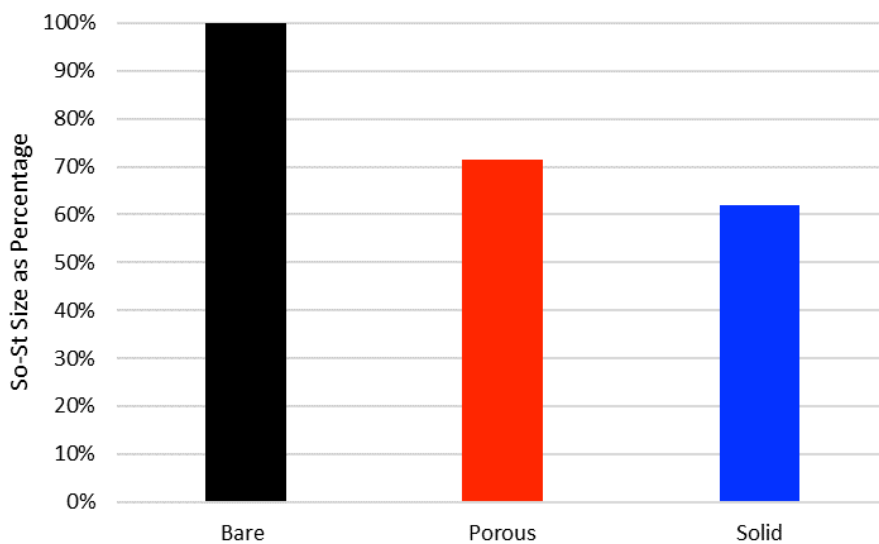


**Figure 81: So-St size with different configurations as a percentage of the bare tube length, computed at the final time-step of the simulation.**

Certainly, tThe increase in thermal performance of the So-St tube with baffles comes at a cost of increased pumping power. The extent of the pumping power increase can be investigated by considering the dimensionless friction factor, seen previously in *Eq. 35*. This is plotted in Figure 82. The solid baffles have a significantly high friction factor ratio, reaching >6, while that of the porous baffles reaches >2. As previously defined, the friction factor ratio is equivalent to the ratio of pressure-drops, which can be used to determine the increase in pumping requirement. Therefore, at the final time-step, the solid-baffle tube requires six

times the pumping power requirement of the bare tube, while the porous-baffle tube requires 2.5 times.
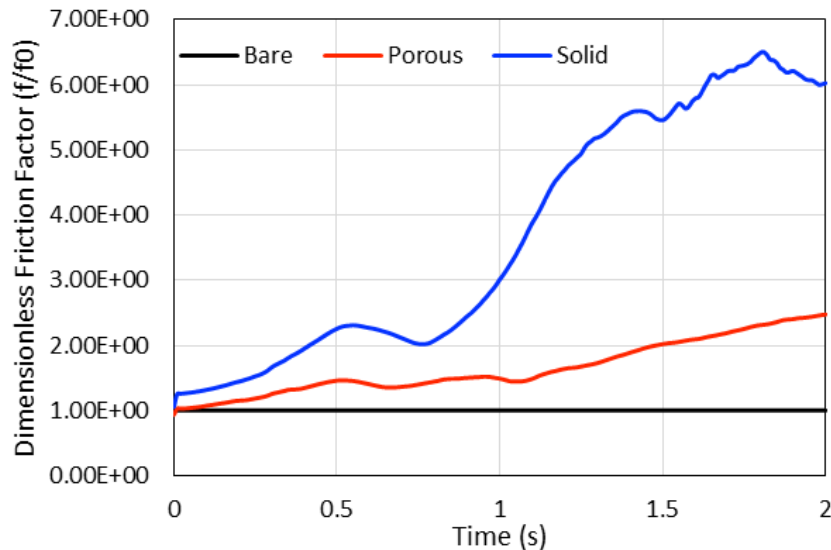


**Figure 82: Dimensionless friction factor within 3-D So-St tube models as a function of time.**

Although the solid baffles have the greatest heat transfer performance, they are extremely expensive to operate. The porous-baffle tube is more feasible, having a balance between pumping power and heat transfer enhancement. These results therefore show the extremes of *EHT* inserts in terms of their advantages and disadvantages, while showing the porous-baffle tube configuration to have a suitable balance between these extremes. These results confirm the ability of *EHT* inserts to enhance So-St performance, and there is a continual need for their further optimisation of the *EHT* inserts to maximise this performance. In particular, other geometric parameters for the porous baffles can be sensitised in a future study. A range of other *EHT* inserts, such as wire coils and twisted tape, can also be tested within the So-St tube.

## 4.4    CFD model limitations

In this section, we address the limitations of the CFD modelling in general and highlight the justification of our approaches.

- Simulation time: the So-St in real-time operation often experiences frequent *SHF* variations. However, it will be prohibitively expensive to simulate the full real-time operation in a CFD model, even at an hourly timescale. In our simulations, the quickest and easiest simulation took about 3 d for only 2 s simulation time on a high-performance computing system. If we want to scale up to 1 h for example, the computing time required will be unaffordable.
- So-St tube length: currently we simulated a 2 m tube length, whereas the actual So-St tube length extends to 78 m per segment and 705 m for one module. Even for a 2 m tube,

a 3-D model would take about 1 month, equating to more than 30 months for one segment and ~300 months for one module of So-St. Hence, it will be impractical to simulate the entire So-St module.

- Water-only boiling: The COMSOL Multiphysics package is ideal for describing the So-St design, which incorporates a wide range of important physical phenomena heat transfer, thermodynamics, multi-component chemical reaction, fluid flow and multiphase evolution. However, it is a challenge in CFD at large to couple all five physical phenomena into a single model. This is due to the difficulty to dynamically track the gas–liquid frontier, because it acts as an interface for multi-species diffusion between the two phases. This problem is yet to be resolved by the CFD developers' community. Thus, a compromise was made by decoupling the phenomena into two distinct sub-models, as summarised in Figure 54.

Accordingly, we justify our approach for each limitation as follows.

- Simulation time and So-St length: since we scaled down the value in those criteria due to the prohibitively long computation time requirement, the CFD results are not sufficient to provide a comprehensive insight into So-St transient performance on an hourly timescale. However, we think such transient behaviour can be accurately obtained by the experimental setup and prototyping of the So-St. However, we found the current results provide valuable insight into the boiling phenomenon. As a result, the current CFD model is a versatile tool for evaluating and screening different So-St designs for *EHT*. Designs with higher heat transfer can be chosen for experiments, and at that stage we can obtain comprehensive dynamic characteristics at the relevant timescale of So-St operation.

- Water-only boiling: since we focused on the heat transfer aspect to evaluate boiling performance of different designs, it is appropriate to use water as fluid, because its key thermal physical properties (density, heat capacity, viscosity, surface tension) are almost similar to 30 *wt%* MEA solvent. By fixing the So-St size (i.e. solar collection area) and the *SHF*, we determined the amount of vapour generated for different So-St designs. In practical application, each So-St module will need to generate a specific amount of vapour to bring the loading down to the target value. Essentially, the solvent absorbs solar heat to release $CO_2$ and $H_2O$ in the form of bubbles, forming vapour above the liquid surface. Hence, the amount of vapour formation can be used as a metric to evaluate the relative segment length per So-St module design.

Hence, we recommend the current CFD model, and conclude that the results are suitable for So-St preliminary assessment of the heat transfer performance evaluation and screening. High heat transfer design(s) can result in more boiling (i.e. solvent regeneration), thus potentially reducing the SCF size. Good designs can be chosen for testing in the next experimental and prototyping project. Due to the limited CFD capabilities, this model is not suitable for studying detailed dynamic characteristics for the entire solvent regeneration

process. However, we believe such a task can be completed using experiments at a smaller cost and with more accurate insights by considering the results and findings of this CFD study.

## 4.5    So-St network sizing based on CFD results

From the above results, we determined two metrics which could be used to scale-up the SCF size under different So-St design scenarios. The first one is the sizing factor obtained from Figure 81. This metric can be used to calculate an equivalent So-St module length to generate the same amount of vapour (i.e. solvent regeneration). The bare tube is used as a benchmark; hence, its weighing value is 1 and the value for other two designs is 0.714 and 0.621 for the porous and solid baffle, respectively. This means for the same amount of vapour generation, one can replace every 1 m of the bare So-St tube with either 0.714 or 0.621 m of porous or solid baffle tubes, respectively. The size factor can be used to calculate the segment length per So-St design based on the bare So-St segment length. The second metric is the pressure-drop factor. This metric originates from Figure 82, which shows for the same flowrate, different So-St designs would have different pressure-drop values. This metric can be used to calculate the number of segments requirement per a So-St design.

If the maximum pressure-drop per module is 0.1 bar for the bare tube and 0.2 bar for the porous tube, respectively, then the segment length of the latter must be halved to bring the pressure-drop down to 0.1 bar (recall the design pressure-drop is set at 0.1 bar). This means one segment of bare tube design (length $x$) needs to be divided into two segments (length $x$/2). As a result, the number of pumps required for the porous-baffle tube design is double that of the bare tube design. One might argue that within one So-St module (either bare or porous baffles designs), different segments would have different pressure-drop values up to 0.1 bar. Hence, it is only necessary to consider the segment that has the highest pressure-drop (i.e. 0.1 bar) and split that particular segment for the porous design. However, the main concern is that during transient operation, the other segments which have lower pressure-drop at the design point, start experiencing increasing pressure-drop. Therefore, it is conservative to split all segments within one So-St module. For the bare tube, the pressure-drop factor is 1, while for the other designs, the factor is 2.5 and 6 for the porous and solid-baffle tubes, respectively. We use those factors to calculate (and round off to the nearest integer) the number of pumps per design.

Based on the above, we estimated the SCF size for a solar multiple (*SM*) of 1 and 2.5 in Table 12. The bare tube results are the benchmark calculation for these two *SMs*. In addition, the number of So-St modules is the same for all designs, because we want to compare them based on the same design flowrate. We then used the size factor and the pressure-drop factor to scale the SCF size for the respective designs. It can be seen that both baffle designs result in smaller SCF, but at the cost of more pumps required (Table 12). Comparing porous *vs* solid-baffle designs, one can see the porous-baffle design results in almost similar saving as the other design, but requires significantly fewer pumps. This means we need to consider the

economic aspects in this comparison to make a sound decision. We anticipate the porous-baffle design might be more favourable because it results in smaller SCF with only a moderate number of extra pumps required.

**Table 12: Estimating SCF size with different So-St designs (the saving is calculated in respect to the base-case bare tube); the pump numbers correspond to the number of segments (each pump restores the nominal pressure after each segment). *SM* = solar multiple.**

| | *SM* = 1 | | | *SM* = 2.5 | | |
|---|---|---|---|---|---|---|
| | Bare tube | Porous baffle | Solid baffle | Bare tube | Porous baffle | Solid baffle |
| Pressure-drop factor | 1 | 2.5 | 6 | 1 | 2.5 | 6 |
| Size factor | 1 | 0.71 | 0.62 | 1 | 0.714 | 1 |
| Total So-St modules | 1,413 | 1,413 | 1,413 | 3,534 | 3,534 | 3,534 |
| Length per module (m) | 705 | 503 | 438 | 705 | 504 | 438 |
| Number of segments | 9 | 23 | 54 | 9 | 23 | 54 |
| Length per segment | 78 | 22 | 8 | 78 | 22 | 8 |
| SCF size (km$^2$) | 15.557 | 11.572 | 10.851 | 38.904 | 28.939 | 27.137 |
| Saving in land (km$^2$) | - | 3.984 (26%) | 4.705 (30%) | - | 9.964 (26%) | 11.766 (30%) |
| Extra pump (unit) | - | 19,782 | 63,585 | - | 49,469 | 159,008 |

## 4.6    Concluding remarks

In this chapter, we have investigated the effect of internal geometries (i.e. inserts) on the heat transfer enhancement and associated pressure-drop using a CFD platform, which is a higher-resolution modelling tool than Aspen®. Two sub-models were formulated: Sub-Model 1, being the single-phase multi-chemical model; and Sub-Model 2, being the multi-phase single-chemical model. A hierarchical modelling structure was applied to capitalise on 2-D geometries of a So-St tube with a low computational load to inform the more accurate 3-D geometries with a high computational load. The *EHT* methods were incorporated, in particular the insertion of porous and solid baffles. The baffles were evaluated in terms of their capacity to improve So-St thermal efficiency, vapour formation and flow stability, as verified by preliminary modelling in a 2-D tube geometry. The modelling culminated in the advanced 3-D geometry in multi-phase, to account for the non-uniform heat distribution about the solar tube. The fluid regimes and exit vapour flowrates for the baffle configurations were compared with the reference bare tube. The porous and solid baffles were estimated to reduce the So-

St field size by 56 and 65%, respectively, but at a cost of 2.5 and 6 times more pumping power required, respectively.

Overall, the CFD model provides valuable insight into the internal fluid behaviour of the So-St, by providing both quantitative and visual verification of the So-St functionality and providing numerical predictions for the So-St design capacity. The screening of various *EHT* inserts displays their potential to enhance So-St performance and intensify the process. Due to the limited capabilities, the CFD model is not yet suitable for studying detailed dynamic characteristics for the whole or part of the So-St network through its daily operation. Such a task can be best completed using prototyping at less cost and with more accurate insights compared with CFD modelling. However, future CFD studies can evaluate alternative and complex *EHT* inserts, e.g. twisted tapes or wire coils, which may also have enhanced design benefits. The CFD results can also be integrated with decisions for process control, aiming to maintain the So-St at a constant solvent regeneration efficiency under varying solar availability. Therefore, process control can address real-life operation by balancing the benefits of vapour formation and preventing detrimental dry-out conditions and flow instabilities. Overall, the CFD model is a useful tool for screening design enhancement and process intensification, and in this study has provided greater details on the dynamic events evolving inside the So-St tube.

# 5.     Process control expert system

In the previous chapters, we outlined different aspects of the SP-PCC concept, including a design protocol for So-St sizing, and analysed the fundamental physical/chemical phenomena that occur during solvent regeneration process. In Chapter 2, we analysed the thermodynamic aspect of the So-St system and identified a favourable path for energy effective operation. In Chapter 3, we started formulating a systematic design protocol to aid in So-St network sizing for a specific loading target and a normalised solar energy. This exercise extended to the overall So-St process design and optimisation aspect. Chapter 4, on the other hand, investigated extensively the physical/chemical phenomena occurring inside a So-St tube using a CFD platform. The results have provided valuable insights, allowing us to identify potential avenues (e.g. using packing/baffles) for internal So-St design optimisation. We recommend further investigation in that direction, aiming to conceptualise an improved design protocol for So-St technology.

In the current chapter, we capitalise on the overall So-St process control to address the challenge of intermittency and irregularity in solar energy resources. We develop a process control expert system that can maintain process continuity at the $CO_2$ capture target of 90% in the absorber. Essentially, we assume continuous capture in the absorber, which equates to approximately 1.6 million tonnes of $CO_2$ captured per year. We analysed different control strategies for the real-time operation of the So-St process. The ultimate control objectives are to achieve 1.5 million tonnes of captured $CO_2$ while ensuring high process performance and operational stability. For a specific application, the number of capture hours could be adjusted to meet the annual capture budget. During solar transient periods, the absorber operation might be affected if the So-St network produces varied lean solvents with different loading values. For example, we discuss different control strategies to mitigate *SHF* disturbances that could result in lean loading variations. Therefore, we have included both terminals of the solvent: the absorption (conventional absorber), and the desorption (So-St network) in the process control formulations. We identify the important operation constraints which could limit the tolerable solar energy range (i.e. the maximum solar energy in kW/m that should be delivered to a So-St segment) and discuss how this solar range can be expanded by process control optimisation.

## 5.1     Process description

Figure 83 illustrated a complete process flow diagram (PFD) for both absorption and desorption terminals. In the initial design, we sized a preheating SCF before the So-St network to bring the solvent temperature to the edge of the regeneration process, particularly for the start-up and ramping stage. However, we found that the preheating SCF can be eliminated by optimising the use of a cross HX. This means we can use part or all of the So-St network for the start-up and ramping stage to bring the temperature to the edge of solvent regeneration

process. Then, we use the cross HX for full heat recuperation. Accordingly, we have revised the overall PFD and abolished the preheating section. In this effective arrangement, the rich solvent flows directly from the absorbers and/or from the rich storage tanks to enter the cross HX and is then equally divided into the parallel loops of the So-St network. Each loop comprises multiple So-St modules arranged in parallel configuration, and each So-St module consists of sequential segments. The outlet of each So-St segment is a mixture of vapour ($CO_2$ and $H_2O$) and liquid (lean solvent). The liquid solvent is then retrieved in the following flash tank and directed to the next segment. The lean solvents at the end of parallel So-St modules are combined in the header collector and directed to the cross HX to pass the high enthalpy to the rich solvent and be cooled down and stored in the lean storage tank(s). The gas/vapour mixture from the So-St modules is then cooled to about 23°C in the subsequent condenser to condense the vapours. The $CO_2$ gas is considered as almost pure product (>99 *wt*%) while the $H_2O$ and other condensed species are recycled back to the makeup stream to maintain the balance in the lean solvent tank.

In this chapter, we develop the appropriate control strategies around both the So-St and the absorption terminals as shown in the simplified block diagram (Figure 83-A). The solvent cycle between absorption and desorption would pass through multiple components (e.g. rich solvent tank, lean solvent tank, cross HX and/or by-pass line). For simplicity, we only represent the tanks and flow manipulating valves as the main components of the process in Figure 83-A. The ultimate control objective is to ensure the 90% hourly capture target is met. This can be achieved by appropriately manipulating valve 1 and 2 around the two solvent storage tanks (SSTs). For simplicity, the by-pass line is also not shown in this simplified block diagram, because the main control action is to manipulate the flow between the two terminals irrespective of the route. Once we obtained the full-year profile of the solvent flow to the SCF, detailed process control (e.g. when to use the by-pass line and to what extent) could be then established around the solvent tanks to implement the comprehensive control action scheme. The control of other parts (e.g. the cooler before the absorber) is not investigated in this work, because they have been well studied in the literature. For example, it is a common practice to control the cooler temperature by choosing the appropriate cooling medium and varying the cooling fluid flowrate. In the following sections, we discuss the process control development steps in the following order:

- the effect of solar intermittency

- control statement and strategies

- testing control strategies.
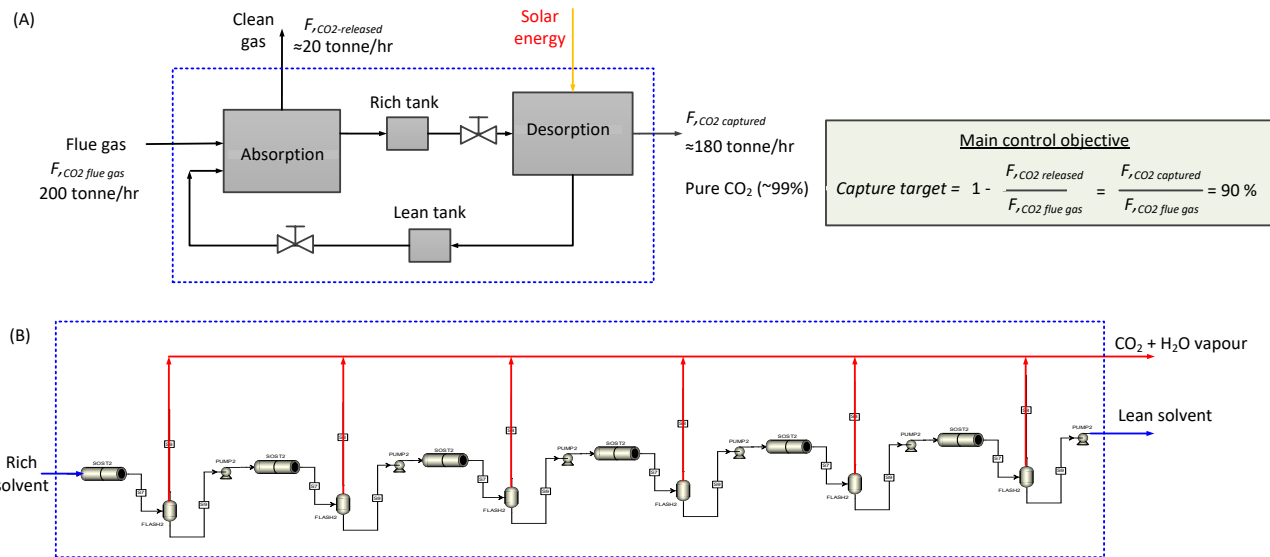
**Figure 83: (A) A block diagram of the superstructure highlighting the main control objective, and (B) A theoretical presentation of a six-segment So-St module process flow diagram.**

## 5.2    The effect of *SHF* fluctuations

The effect of solar irradiation variance is analysed in this section. We have developed the absorber model in Aspen® and performed detailed optimisation to determine the appropriate operating conditions (lean loading, rich loading, and solvent flowrate) to achieve 90% $CO_2$ capture rate. The total solvent flowrate to the absorber is then used to calculate the required number of So-St modules in the SCF. In this work, we have updated the lean loading target to the absorber from 0.17 as previously analysed to a more realistic and achievable value of 0.23 in this chapter. This modification is supported by the detailed analysis presented in Chapter 2, when we found that lower lean loading target would substantially increase the energy demand. Hence, we raised the lean loading target to update the design of the So-St network accordingly. The typical *LLV* for 30 *wt*% MEA solvent in the literature is around 0.23 [82], thus we adapt this value as the design point. A summary of the design parameters/assumptions is listed in Table 13.

**Table 13: Design point for one So-St module comprised of nine segments.**

| Key variables | Value | Notes |
|---|---|---|
| $CO_2$ in flue gas (tonne/hr) | 200 | Design point |
| Absorber capture rate (%) | 90 | Design point |
| Rich loading (from absorber outlet) | 0.49 | From Absorber simulation |
| Lean loading (from So-St outlet) | 0.23 | From literature |
| Solvent flow per module (tonne/hr) | 4.88 | Design point |
| Energy demand (MJ/kg$_{CO_2}$) | 8.7 | Design point |
| Nominal *SHF* (kW/m) | 1 | Average *SHF* $^a$ |
| Total $CO_2$ produced per module (tonne/hr) | 0.293 | Design point |

| Solvent temperature at module inlet ($^o$C) | 90 | Before desorption occurs [b] |

[a] *This value is averaged from one-year SHF data excluding the time steps of zero value. The amount of intercepted solar heat is calculated as kW per a unit length of the So-St tube.*

[b] *For all simulations, this value is kept at 90$^o$C to simplify the comparisons, except for the real-time simulations in Section 5.5, where this value is calculated by an actual Aspen® HX model with 5$^o$C minimum temperature approach.*

We first perform the base-case sensitivity test by varying the solar concentration and observing the effect on the key performance indicators (KPIs). The results are shown in Figure 84. As the solar energy increases, the lean loading drops (Figure 84-A), increasing the $CO_2$ productivity (Figure 84-B) and vice versa. Interestingly, those trends start reversing when the *SHF* exceeds a certain value. After this specific *SHF* value, the lean loading starts increasing and the $CO_2$ productivity relatively drops. This reversed trend is attributed to very high *SHF* (> 2 kW/m), when the solvent temperature would be substantially increased (>130$^o$C). At this high temperature, the MEA molecules increasingly vaporise, reducing the lean loading (recall loading is inversely proportional to the number of MEA molecules in the liquid phase). The presence of MEA molecules in the vapour stream is detrimental, because the vapour will then be condensed to produce a pure $CO_2$ stream. If there is a significant amount of MEA molecules, they will be condensed into the liquid phase and start reacting with $CO_2$, as some $CO_2$ molecules will enter the liquid phase. This mechanism continuously depletes the $CO_2$ in the liquid phase, thus drawing more $CO_2$ from the vapour phase to maintain the vapour–liquid equilibrium (VLE) balance. Usingtilizing all the *SHF* does not necessarily mean effective operation. This is demonstrated in Figure 84-C, where utilising more *SHF* results in increasing energy demand for the desorption process, because more solar energy is consumed for water vaporisation.

It is therefore important to have an appropriate control strategy to deal with solar energy intermittency, ensuring the $CO_2$ capture target is met within a stable and reliable operation throughout the whole year. Alternatively, it was shown in Chapter 3 that the *SHF* variation could cause significant and undesirable changes in *LLV*. If lean loading is not controlled, it would fluctuate significantly and push the absorber outside the comfort zone of operation. The control of hourly $CO_2$ productivity in the SCF is not compulsory as long as the annual carbon capture target is met (i.e. 1.5 tonne$_{CO2}$/y). However, it needs to be controlled in coordination with the *SHF* profile. For example, when solar energy is high, process control needs to increase the productivity to compensate for low or no-solar periods.
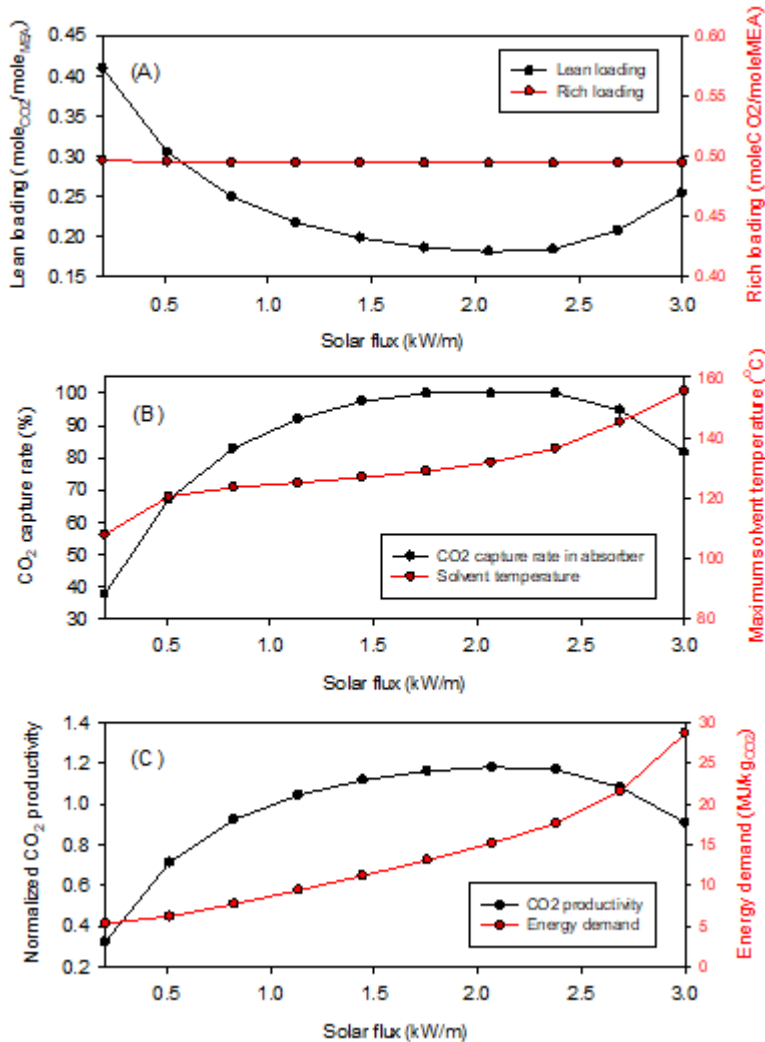
**Figure 84: The effect of variation of solar concentration on the key performance indicators (KPIs) when there is no process control strategy. (A) Lean loading and solvent temperature at the SCF outlet. (B) The CO$_2$ productivity (or flowrate) at the SCF outlet and the energy demand.**

## 5.3    Control problem definition and open loop analysis

In this section we formulate control statements. For a solar-based system, the main control objective is to stabilise the operation and maintain the process at a desirable operation point during *SHF* variations. The overall process has two functions: CO$_2$ capture in the absorber and CO$_2$ production in the SCF. These two terminals need to be controlled effectively so the entire plant can operate stably. Table 14 show the main process variables, sorted into controlled variables, manipulated variables and disturbances. We discuss the logic behind those sections, respectively. The effect of disturbance (*SHF* variations) was sensitised in the previous section. It has detrimental effects on both absorption (i.e. reduces the CO$_2$ capture rate) and desorption (i.e. reduces the extent of solvent regeneration) portals. This variable is re-stated in this section to complete the description of the process control problem.

**Table 14: Main process variables considered in process control study.**

|  | **Absorption** | **Desorption** |
|---|---|---|
| Potential controlled variables | Capture rate<br>Rich loading | Lean loading<br>$CO_2$ productivity<br>Solvent temperature |
| Manipulated variables | Solvent flowrate | Solvent flowrate |
| Disturbance | Solar heat flux | |

In the absorber, two potential controlled variables are the $CO_2$ capture rate and the rich loading. The former is the main controlled variable for $CO_2$ absorption in the absorber, and the typical set-point is 90%. This value has been used in numerous studies, possibly because the absorber operates most effectively at 90% capture rate as shown in *Eq. 39*, where the $F_{CO2,clean\ gas}$ and $F_{CO2,flue\ gas}$ are the $CO_2$ flowrate in the clean gas and the flue gas, respectively.

$$Capture\ rate = 1 - \frac{F_{CO_2,clean\ gas}}{F_{CO_2,flue\ gas}} \qquad\qquad Eq.\ 39$$

The $F_{CO2,flue\ gas}$ is often not considered as control variable. This is because if the capture rate is always controlled at 90%, the operating rich loading range for 30 *wt%* MEA solvent is between 0.4 and 0.5 $mole_{CO2}/mole_{MEA}$. This is governed by the MEA chemistry and the $CO_2$ gas concentration in the flue gas. Overall, absorption only needs one control loop to control the $CO_2$ capture rate at 90% by manipulating the lean solvent flowrate. Figure 85 shows the effect of the solvent flow on the absorber capture rate. It can be seen that increasing the solvent flow boosts the $CO_2$ capture rate and vice versa. There is a plateau for the $CO_2$ capture rate near the design flowrate (~100%). This result confirms that solvent flowrate is an effective manipulated variable for the capture rate. It also shows that the absorber capture rate is optimum at about 90%. Thus, we should not try to select a set-point above 90%. This is because the relationship between solvent flowrate *vs* $CO_2$ capture rate is linear until the capture rate goes above 90%. Above this value, the gain in the $CO_2$ capture rate is not sufficient to justify the increase in the solvent flowrate as evidenced by the non-linear relationship at that region. There are other control loops that play supportive roles; e.g. the solvent cooling loop that controls the lean solvent temperature at 40°C, or the lean solvent tank loop, which controls the flow direction of the lean solvent from the SCF to either the storage tanks or directly to the absorber. These complementary loops are not included in this process control study because we want to first design/analyse the process control for the main operation aspects, i.e. absorption and desorption. The other control loops can be followed up later to adapt the main process control.
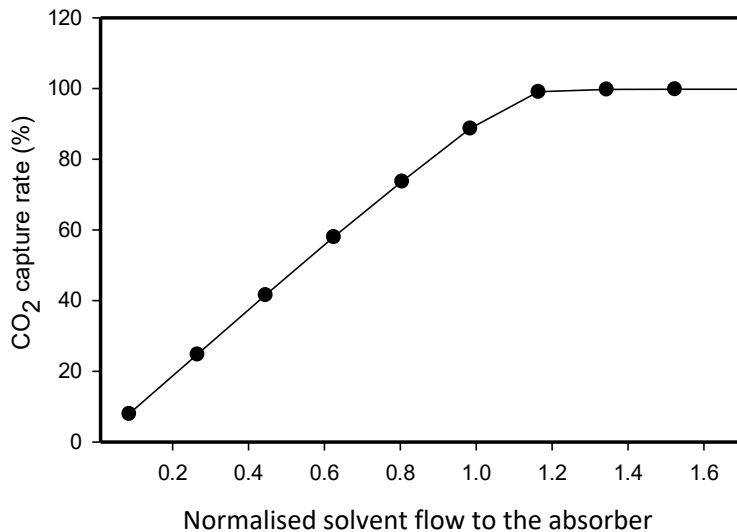
**Figure 85: The effect of absorber solvent flow inlet on the resulted CO$_2$ capture rate. The flowrate has been normalised against the design value.**

In the desorption portal, the main control approach would be to increase its regeneration capacity (i.e. solvent flowrate) when solar energy is abundant and vice versa, as the main function of the So-St network is to regenerate more solvent, thus maintaining the continuity of the absorber operation. An indirect metric for solvent regeneration capacity is the CO$_2$ production rate. If the lean loading is lower or more solvent is pushed through the So-St network, the CO$_2$ production rate would also be increased. Therefore, we need to choose a control variable which can lead the So-St network to increase the solvent flowrate, or to lower the lean loading during high solar periods and vice versa. To achieve this goal, all three variables (lean loading, solvent temperature and CO$_2$ production) are potential control variables. This conclusion is supported by the simulation results shown in Figure 86, which show the effect of changing the solvent flowrate on those variables.

In Figure 86-A, increasing solvent flowrate leads to higher lean loading, i.e. less regeneration. This is expected, because for the same solar heat input, increasing solvent flow would result in a lower maximum solvent temperature, as shown in Figure 86-C. A lower temperature implies less CO$_2$ desorption, hence higher lean loading and lower CO$_2$ productivity, respectively. These effects can be used to control the So-St process. For example, when *SHF* increases, without control actions the lean loading would drop. But when there is a control scheme in place, the control action would increase the solvent flowrate to counteract that lean loading drop effect. In other words, when *SHF* increases, the control action boosts the solvent flow, i.e. increases the regeneration capacity. This satisfies the control requirement specified above for the So-St network. Similar outcomes could be obtained when using the other two variables as a controlled variable. For example, when solvent flow increases, the CO$_2$ production increases. A possible control action is when *SHF* increases; one can increase the CO$_2$ productivity by increasing the solvent flowrate (i.e. increasing regeneration capacity). Overall, all the variables could be used as a control variable. This is because they can be used

to inform the So-St process to increase or decrease the regeneration capacity following the rise and fall in *SHF*, respectively. Although there is only one manipulated variable, there are three controlled variables. We cannot control them all at the same time, but must use them in individual control strategies as outlined in the next section.
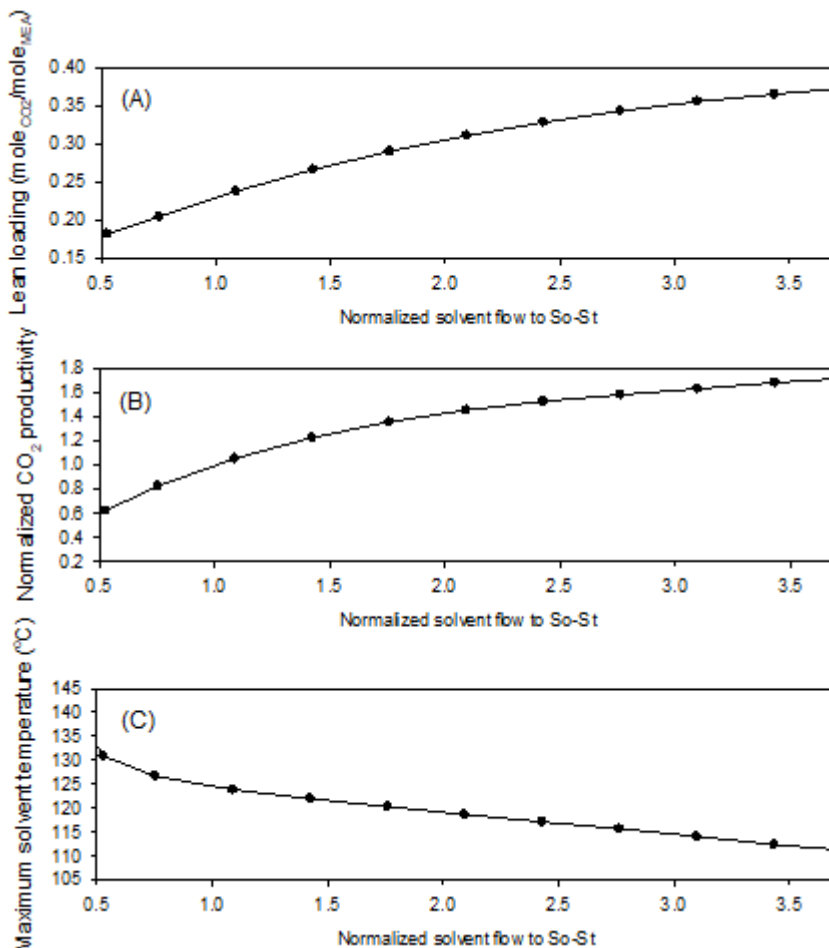


**Figure 86: The effect of the solvent flowrate to the SCF on key process control variables. In this sensitivity study, *SHF* is kept constant at 1 kW/m. The solvent flow to the So-St is normalised against the nominal value.**

## 5.4     Control strategies development and testing

In the previous section, we discussed the process control formulation, shedding light on different process variables involved and their role in the process control problem. In the absorption, we would control the $CO_2$ capture rate at 90% by manipulating the lean solvent flowrate to the absorber. This could be delivered by the lean storage tank and/or directly from the So-St lean solvent returned line. In the So-St part, there are potential three control variables but only one manipulated variable. This yields three control strategies for the So-St field, each controlling a different variable. Combining absorption and desorption control, we developed three control strategies that differ by which control variable is used to govern the So-St network. In practical application, the three control strategies will only have different process control instruments, e.g. the $CO_2$ production control needs a $CO_2$ flow sensor to

measure the CO₂ flow. The control strategies are graphically presented in Figure 87 (A, B and C). All control strategies have the same control loop 1, while they vary in control loop 2; each strategy controls a different process variable. There are two main control loops in absorption and desorption, respectively. In absorption, the main control loop is to control the $CO_2$ capture rate at 90%. This can be achieved by controlling the amount of $CO_2$ in the clean gas ($F_{CO2,clean\ gas}$) according to *Eq. 39*. In desorption, we have confirmed the main control objective is to increase the regeneration capacity (i.e. solvent flowrate) when *SHF* increases and vice versa. This could be achieved with either control loop 2A, 2B or 2C, respectively.
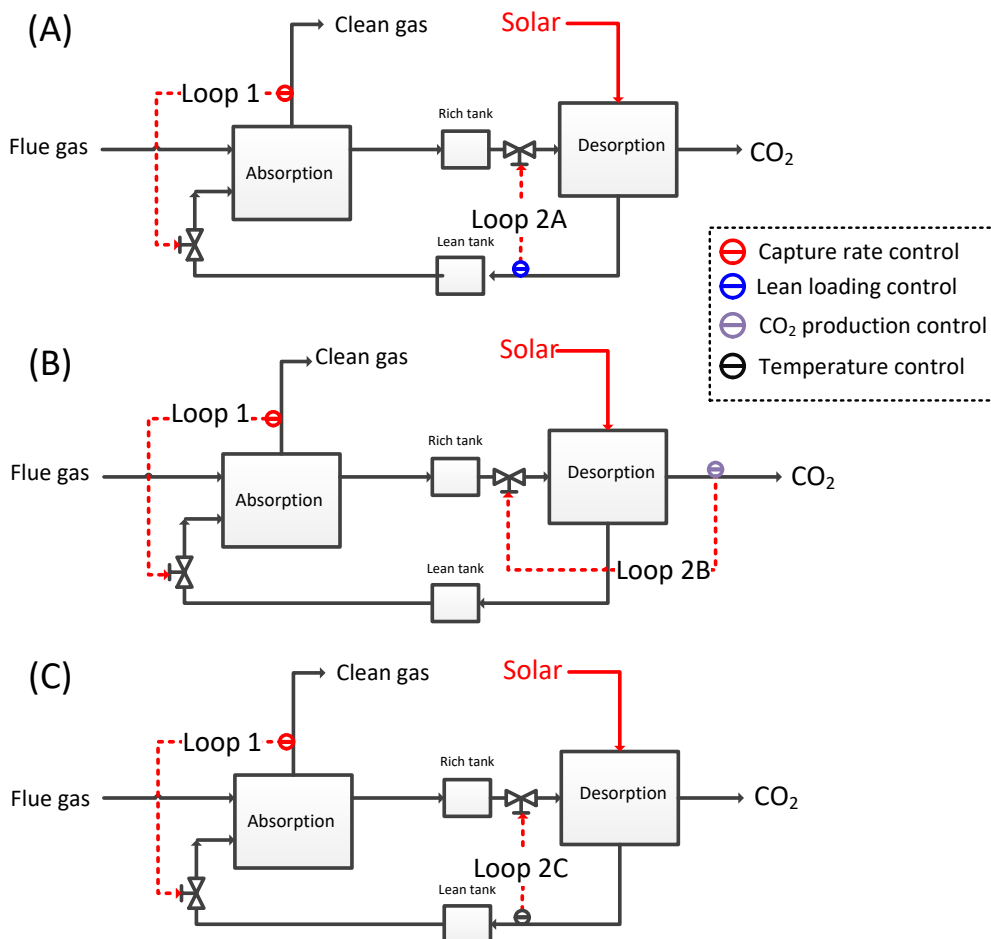


**Figure 87: Proposed control strategies based on different control variables in the desorption part. All strategies have the same control loop 1, but different control loop 2 (2A, 2B and 2C).**

## 5.4.1  Control strategy A

We evaluated the first control strategy based on the released-CO₂ benchmark. Instead of using a real-time data, we sensitised the potential range of *SHF* input for testing purposes. This is because we want to test if the control strategy can actually work across all potential solar energy spectra. An Aspen® goal seek algorithm was set up to search for appropriate rich solvent flowrate to a So-St tube to keep the lean solvent value at 0.23 while *SHF* changes. Since the lean loading is maintained at a constant, the absorber operation would be constant

and control loop 1 does not need to execute control actions. This is because the absorber operation is only affected by the lean loading, assuming the flue gas condition is constant, and the lean solvent temperature is always controlled at 40°C at the entrance of the absorber. Thus, the lean solvent flow to the absorber does not change. The results are shown in Figure 88.
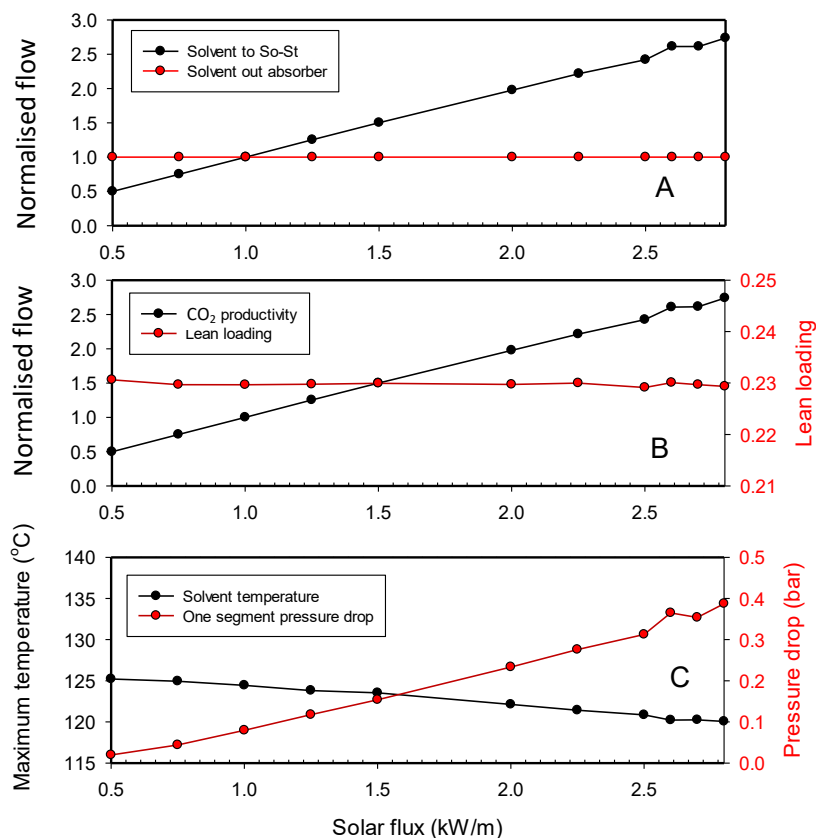


**Figure 88: Control actions when solar energy changes in control strategy A (based on fixing the *LLV*). The rich solvent flow to the So-St is manipulated to control the lean loading target at 0.23. The value on the y-axis (plot A, B and C) has been normalised against the design values reported in Table 13.**

When solar energy changes, the solvent flowrate to the So-St network is manipulated by the control loop 2 (Figure 88-A, black line) to achieve a lean loading set-point at 0.23 (Figure 88-B, red line). This control action allows the absorber to operate at the optimum conditions despite the variation in solar energy, because those variations have been fully absorbed by controlling the solvent flowrate to the So-St network (loop 2). If the lean loading is not controlled at a set point, the lean solvent flow to the absorber will change proportionally (Figure 89) to respond to the lean loading variation while keeping the capture rate at 90% in the absorber. This result confirms the value of keeping the lean loading constant in stabilising the absorber operation. One potential undesirable implication is the variation in the $CO_2$ production from the So-St field as can be seen in Figure 88-B (black line). Increasing *SHF* leads to more $CO_2$ production and vice versa. The change is almost linear, e.g. *SHF* at 2 kW/m would have twice the amount of $CO_2$ production compared with *SHF* at 1 kW/m. This is because the solvent flow is increased by control loop 2; thus more $CO_2$ could be stripped per the same

operation time-step. Figure 88-C shows two important operational constraints: the highest solvent temperature and the highest pressure-drop (among nine segments in one So-St module). The former should be kept below 125°C to prevent solvent degradation, and the latter is chosen to be at 0.5 bar; this is a conservative value based on the current design pressure of 2 bar. This means if the pressure drops by up to 0.5 bar, the system is still operating at 1.5 bar, which is safely above the atmospheric pressure; or we can adapt a different value for the pressure constraint to suit specific applications. At high solar heat flux (*SHF*), the control loop increases the solvent flowrate, thus causing an increase in the pressure-drop. At low *SHF*, the solvent flow is reduced, which translates to less pressure-drop; thus the solvent temperature would relatively increase. From the thermodynamic viewpoint, when there is minimal pressure-drop (at low *SHF*) and the lean loading is controlled at 0.23, the solvent temperature should be maintained around 125°C. Practical operation should avoid approaching this temperature cap, since the solvent is kept on the edge of the thermal degradation point. Therefore, lean loading control should not operate when the *SHF* drops to a specific value, e.g. 0.5 kW/m. From the above, both extremes of the *SHF* range pose a significant risk of violating the constraints.
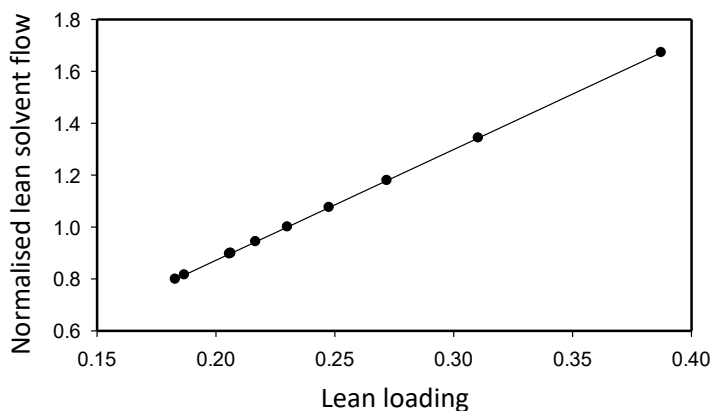


**Figure 89: Required lean solvent flowrate to keep the CO$_2$ capture rate at 90% when the lean loading changes.**

Pressure-drop can be a significant factor, which may pose a problem for two-phase flow stability as discussed in Chapter 4. When solar energy increases, control loop 2 boosts the solvent flow to the So-St network to maintain the lean loading at a set-point. Otherwise, if the solvent flowrate is kept constant, the lean loading will drop, as higher solar input would result in higher solvent temperature for that constant flowrate. On the other hand, the higher solvent flow ultimately causes higher pressure-drop, as shown in Figure 90-A. Figure 90-B also shows that the solvent temperature at the segment's exit drops dramatically due to the pressure-drop, suggesting the vital role of pressure monitoring and control. Considering the solvent operating pressure is 2 bar, we have decided to put a cap on the maximum allowable pressure-drop at 0.5 bar as shown in Figure 90-A. This equates to 50% of the pressure budget above atmospheric pressure, because solvent pressure must be kept between 1 bar and 2 bar (below 1 bar would allow air to leak into the system, and is hence not practical).
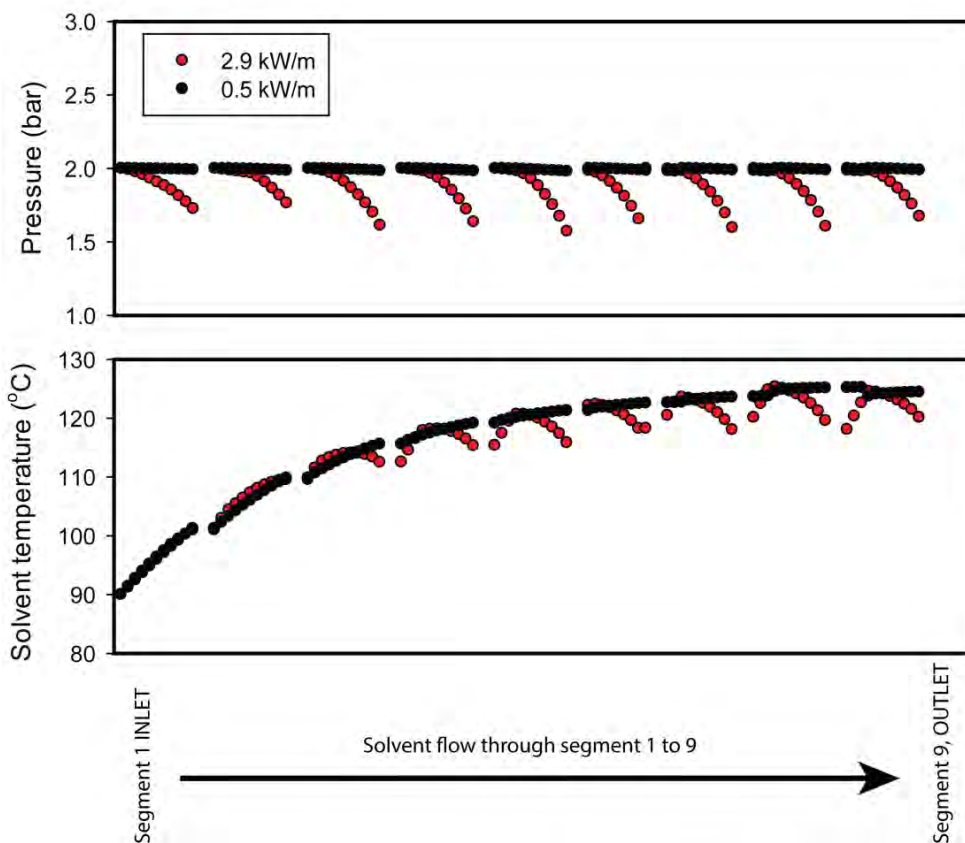
**Figure 90: Plotting key variables in each So-St segment operation under two *SHF* inputs. There are nine gapped lines, representing nine segments. For example, in the pressure plot, the red curve always starts at 2 bar and gradually drops. This is because the solvent enters at 2 bar, then the pressure decreases due to the pressure-drop.**

## 5.4.2 *Control strategy B*

In this control strategy, we control the $CO_2$ production rate from the So-St network, instead of the *LLV* as we did in the control strategy *A*. The results are shown in Figure 91. Interestingly, as solar concentration reduces, the solvent flowrate to the So-St must be increased (Figure 91-A, black line). This is in contradictory to most solar processes, in which the common practice is reducing the solvent flow when the solar drops. In this control strategy, one would need to increase the solvent flowrate instead of reducing the load when the solar energy drops. $CO_2$ productivity is maintained reliably at the set-point despite solar concentration changing dramatically (Figure 91-B, black line). Further analysis reveals that this control strategy influences the lean loading (Figure 91-B, red line). When solar intensity reduces, the control strategy orders an increase in the solvent flow to maintain the $CO_2$ productivity at the set-point. As a result, the final lean loading increases (i.e. less regeneration due to the poor solar intensity). To understand this outcome, we revised the formulation for $CO_2$ productivity as follows:

$$CO_2\ Productivity = Solvent\ flow \times (Rich\ loading - Lean\ loading) \qquad Eq.\ 40$$

As the *LLV* decreases corresponding to the solar intensity increase, the solvent flowrate to the absorber is reduced to maintain a constant $CO_2$ capture rate. This is because lower loading means that for one mole of MEA solvent, more $CO_2$ can be captured. Due to the lean loading variations, control loop 1 manipulates the lean solvent flow to the absorber (Figure 91-A, red line) to control the capture rate at 90%. Increasing *SHF* leads to lower lean loading, thus reducing the lean solvent flowrate to the absorber. This is because leaner solvent has more capability to capture $CO_2$ in the absorber, thus a lower flowrate would be required.

Similar to control strategy *A*, control strategy *B* also affects the solvent's highest temperature and the pressure-drop (Figure 91-C). The pressure-drop increases with increasing flowrate and follows the same profile as the solvent flowrate (Figure 91- A, black line vs C, red line). At low *SHF*, the solvent flow to the So-St network is proportionally increased, thus resulting in increasing the frictional pressure-drop. From Figure 91-C, one can easily observe the solvent temperature poses a more significant risk than the pressure-drop. This is because the former increases significantly; at 2.5 kW/m *SHF* it would even exceed 140°C. In control strategy *A*, at similar flux, the solvent temperature is less than 125°C. Based on the temperature constraint, the operational *SHF* should not exceed 1.1 kW/m, which is only 10% extra than the nominal design value (1 kW/m). For the pressure-drop, the control strategy *B* assures a 'safe' operation as the pressure-drop remains within the tested range.

This $CO_2$ productivity control approach is relatively new in the research area of solar integration, because the load (i.e. solvent flowrate) is increased when the solar energy is reduced. In contrast, the common approach involves reducing the load corresponding to the solar energy reduction. In our opinion, So-St technology is highly suitable for this new control approach. This is because in conventional solar-assisted desorption, steam is often produced from the SCF and supplied to the reboiler of the desorption unit. Hence, the steam temperature must be maintained; otherwise, the reboiler cannot sustain the nominal temperature for sufficient stripping via steam. Therefore, if solar energy drops, the load must be reduced too (in this case the load is the water flowrate). This fluctuation in steam production is often compensated for by bleeding a safety buffer steam from the power-plant steam cycle, which eventually would impact the stability of power production. Therefore, a conventional solar-assisted stripper has less flexibility and fewer process control options than the So-St technology under highly intermittent solar irradiance.
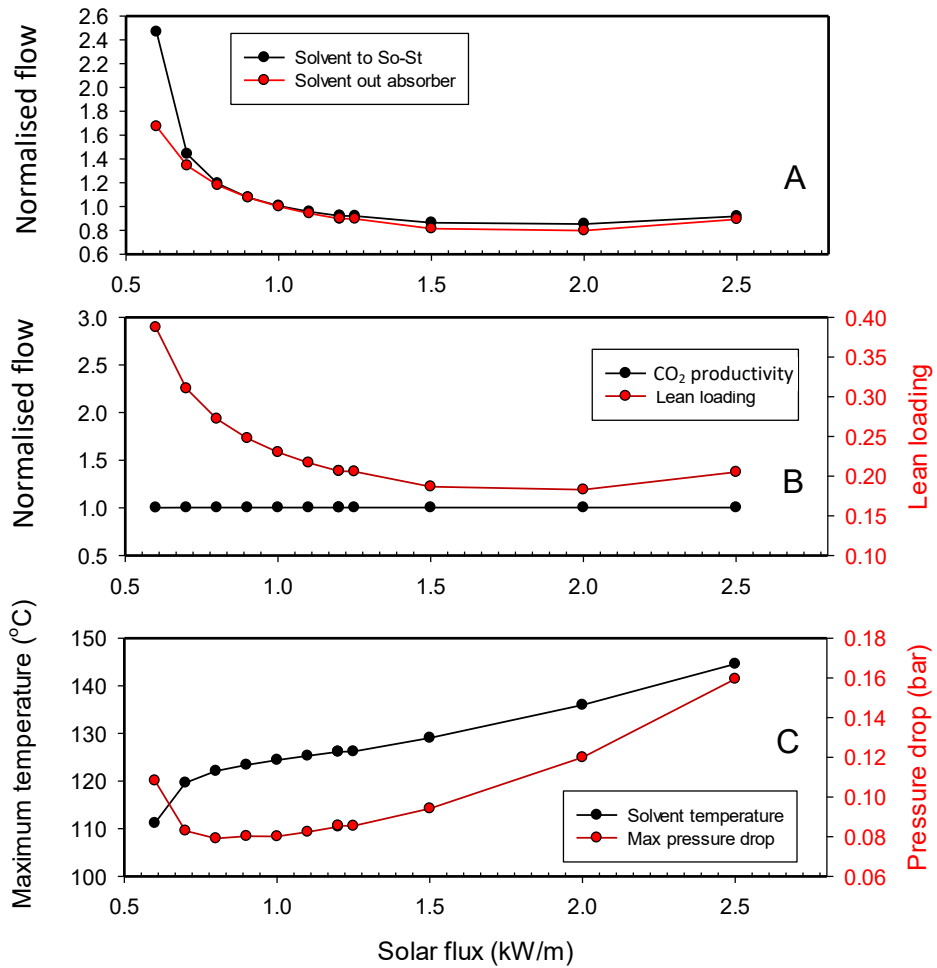
**Figure 91: Control actions for CO₂ productivity control. The rich solvent flow to the So-St is manipulated to control the CO₂ production at a set-point. The value on the y-axis (plot A, B and C) has been normalised against the design values reported in Table 13.**

### 5.4.3 *Control strategy C*

In this control strategy, we control the maximum solvent temperature at 125$^\circ$C cap. This is the temperature of the solvent exiting the last segment of the So-St module. The results are shown in Figure 92. It can be seen that when *SHF* increases/decreases, control loop 2-C also increases/decreases the solvent flow, respectively (Figure 92-A, black line). This is due to the energy formula; i.e., temperature increase is proportional to the solvent flowrate. The lean solvent flow to the absorber is manipulated by control loop 1 to keep the capture rate at 90%, because the *LLV* was changed by the control loop 2-C. This can be seen by the red line in Figure 92-B; as *SHF* increases, the lean loading is relatively reduced.
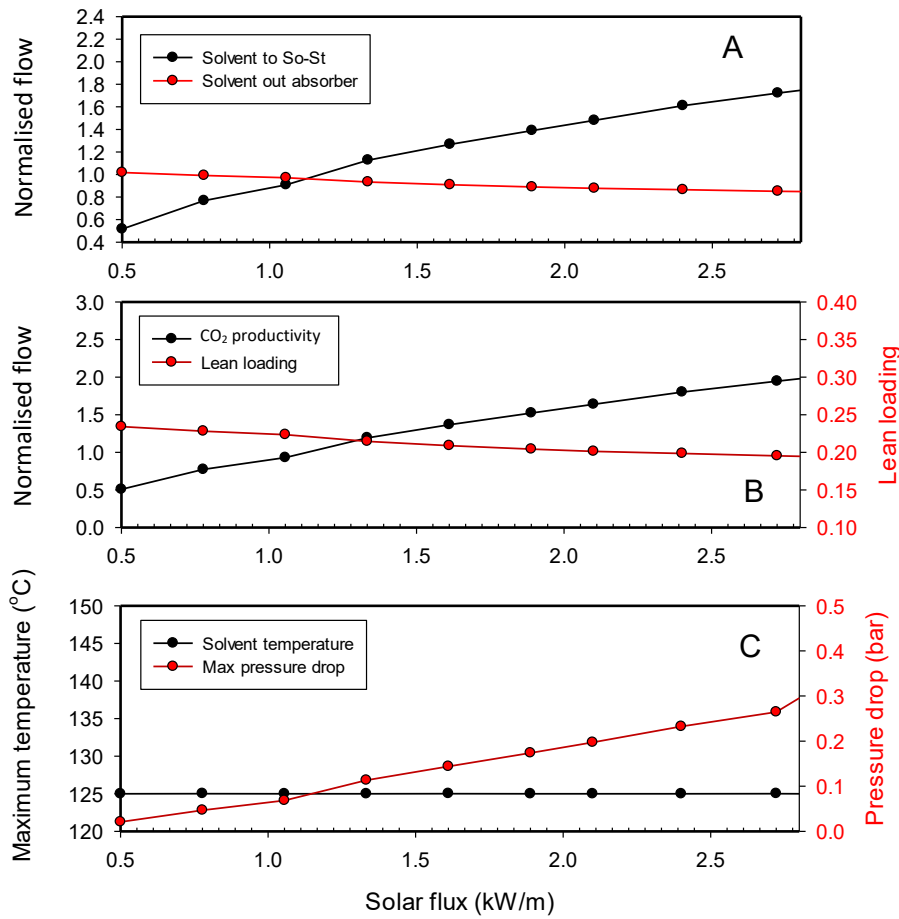
**Figure 92: Control actions for the temperature control. The rich solvent to the So-St is manipulated to control the final solvent temperature at a set-point. The value on the y-axis (plot A, B and C) has been normalised against the design values reported in Table 13.**

Based on the thermodynamic viewpoint, we would expect the lean loading to remain constant, because the solvent temperature does not change (Figure 92-C, black line). However, in real operation there would be increasing pressure-drop at high *SHF* (Figure 92-C, red line); therefore, additional vaporisation is caused by the increasing pressure-drop. This phenomenon results in more $CO_2$ entering the vapour phase, and hence lowering the lean loading in the liquid phase. Like the other two control strategies, control strategy *C* can violate the constraints of maximum solvent temperature and/or pressure-drop. This can be seen in Figure 92-C. We are not concerned about the temperature constraint violation, because it is directly controlled at an appropriate set-point (i.e. 125°C). However, the pressure-drop can exceed the 0.5 bar cap at a high *SHF*. This is the same as in control strategy *A*, in which the control action increased the solvent flowrate, resulting in higher pressure-drop.

In summary, we have explored and demonstrated the workability of three different control strategies to control the $CO_2$ capture rate at 90%. All strategies are able to control the capture target at 90% by manipulating the absorber solvent flowrate. We need to implement an additional control loop to control the solvent regeneration capacity of the So-St network based on the dynamic nature of the solar resource, as we need to regenerate more solvent

when solar energy is abundant to compensate for the no/poor solar periods. This control loop is critical to ensure the operability of the whole plant. In control strategy *A*, this loop controls the *LLV* by manipulating the rich solvent flowrate to the So-St network. When solar energy increases/decreases, the rich solvent flowrate is also increased/decreased to keep the lean loading at a set point. This control action satisfies the aforementioned requirement (i.e. need to increase solvent regeneration capacity when solar energy is abundant). In control strategy *B*, we use the same manipulated variable (rich solvent flowrate) to control the $CO_2$ produced by the So-St network. This results in opposite behaviour to strategy *A*; when solar energy input increases the rich solvent flowrate is decreased, but with a lower lean loading. Thus, this control loop still satisfies the aforementioned requirement to some extent. In the last control strategy, the control action is similar to that of the strategy *A*. That is, when *SHF* increases, the solvent flowrate is increased (hence more solvent can be regenerated) and vice versa. We also highlighted two important constraints (solvent temperature and pressure-drop) that could limit the operation range of these three control strategies. Next, we formulate different operation modes as a function of *SHF*. The temperature and pressure constraints are also considered to ensure stable operation in each mode.

## 5.5    Operation mode development

In this section, we develop different operation modes that could be applied at different times of day. These modes dictate how and when a control strategy would be used. In the previous section, we developed and demonstrated effective control strategies to deal with variations in solar energy input to ensure the capture target of 90% is achieved. It was found that the control strategies could violate the constraints depending on the available *SHF*. For example, it is possible that a control strategy executes control actions to deal with *SHF* variations, but at the same time those actions can cause either significant pressure-drop or excessive solvent temperature levels. For each control strategy, we define a 'safe' solar energy tolerance (SET) range to deal with solar intermittence. When the  is outside the desirable range, the control actions cannot be executed, but would be overridden to perform a different task, e.g. defocusing the receiver instead of increasing solvent flowrate. Based on the control testing results, we have summarised the *SET* range for each control strategy as shown in Table 15. The threshold for each control strategy was determined by examining the *SHF* value at which at least one of the two constraints (temperature <125°C and pressure-drop <0.5 bar) is violated. For control strategy 1, there is a lower *SET* in which the solvent temperature can exceed 125°C due to minimal pressure-drop (i.e. higher pressure-drop provides cooling effect). For the other two control strategies, the Aspen® model results inform no lower SET, because none of the constraints are violated. Practically, there should be a lower SET, because there must be a point for the So-St to start the solvent regeneration process and produce $CO_2$. Conservatively, we apply the lower *SET* of control strategy 1 for the other two control strategies for consistency. We should emphasise that the lower *SET* of 0.5 kW/m is an assumption in this work to facilitate the process control study at an hourly timescale level.

This timescale is reasonably accepted in the literature, although an accurate estimation would require a higher resolution of the simulation (e.g. second timescale), which would require intensive computational work. We found that with about 1/3 of the total solar available hours, the heat flux is less than 0.5 kW/m. Assuming 12 h solar per day (6 am to 6 pm), that means the So-St will be able to operate for about 8 h and the other 4 h would be used for either start-up or shut-down.

**Table 15: Solar energy tolerance (SET) (kW/m) range for different control strategies to ensure the maximum solvent temperature stays below 125°C and the maximum pressure-drop does not exceed 0.5 bar.**

| Control strategy | Lower *SET* cap (kW/m) | Upper *SET* cap (kW/m) |
|---|---|---|
| 1[a] (lean loading control) | 0.5 | 3.6 |
| 2[b] ($CO_2$ production control) | 0.5 | 1.1 |
| 3[c] (temperature control) | 0.5 | 4.2 |

[a] *Data taken from* Figure 88-*C with extended SHF to find the upper SET.*

[b] *Data taken from* Figure 91-*C with extended SHF to find upper SET.*

[c] *Data taken from* Figure 92-*C with extended SHF to find the upper SET.*

Table 15 indicates the application range for each control strategy. It is possible that the second control strategy might not outperform the other strategies due to narrower *SET* range, e.g. all the *SHF* above 1.1 kW/m would need to be defocused. One might argue that the current So-St design is not suitable for the second control strategy. This is a valid argument, because control strategy 2 has different control actions than the first and third control strategies. For example, when *SHF* increases, the second control strategy will reduce the solvent flow, while the first and third will increase the solvent flow. However, we still consider the second control strategy in our assessment as a potential strategy during the operation.

Next, we develop the operating procedure for the So-St plant to deal with different *SHF* conditions. Table 16 shows different operation modes based on the *SHF* value. At low *SHF* (0–0.5), this could be early in the morning (start-up), cloudy hours (stand-by) or late in the afternoon (shut-down). The upper *SHF* limit was determined based on the lower *SET* range of the three control strategies. In other words, if all three control strategies cannot deal with *SHFs* below 0.5 kW/m, the regeneration process cannot continue safely. When heat flux is above 0.5 kW/m, three control strategies could potentially be used.

**Table 16: Operation modes and applicable control strategies.**

| *SHF* range (kW/m) | Operation mode | Applicable control strategy |
|---|---|---|
| 0 − 0.5 | Start-up, shut-down, stand-by | Special instruction |
| 0.5 − 1.1 | Solvent regeneration | 1,2 and 3 |
| 1.1 − 3.6 | Solvent regeneration | 1 and 3 |
| 3.6 − 4.2 | Solvent regeneration | 3 |

**Start-up and stand-by mode**: this mode is dictated by no or very low *SHF*; thus it is important to accumulate the solar heat in the solvent and increase the temperature to be prepared for regeneration when solar heat starts rising. In this mode, we propose that the solvent in the So-St loops is being continuously recycled to accumulate and store the solar heat. The solvent at the last segment inlet will by-pass the cross HX and re-enter the SCF. During solvent recirculation, any vapour generated will be vented into the primary flash drum for $CO_2$ collection. As a result, extra solvent will need to be added to the recirculating loop to prevent possible dry-out.

**Solvent regeneration mode**: during this mode, solvent regeneration and $CO_2$ production can occur. However, appropriate control strategies need to be implemented for stable and effective operation. The applicable control strategies are listed in Table 16 as a function of *SHF* range. For example, control strategy 2 cannot operate above 1.1 kW/m; hence it is only applicable for the range of 0.5–1.1 kW/m. The rich solvent from the absorber outlet (around 44°C) either enters the rich SST or is directly pumped to the So-St field, depending on the flowrate of that solvent. For example, the rich solvent from the absorber is calculated at 3,108 tonne/hr, but if the flowrate demand from the So-St field is 14,000 tonne/hr, the deficit amount needs to be withdrawn from the rich SST to meet the demand. The rich solvent at 44°C then enters the cross HX to recuperate heat and increases its temperature to about 90°C. This increase does not need to be precisely controlled, because the solvent temperature at the beginning of So-St modules does not need to be controlled at a certain value; only the last segment's temperature is critical. For example, the So-St inlet can be at 70°C, but the control strategy will manipulate the flowrate to ensure an effective solvent regeneration process. The return lean solvent is fed back to the absorber and/or the lean SST depending on the lean solvent storage level. Preferably, the lean solvent is returned to the lean SST first, helping to normalise the *LLV* and reduce potential sudden changes in the lean loading sent to the absorber.

**Shut down mode**: In this mode, the solvent flow stops completely if there is no night-time freezing risk. All the vapour in the loop is flushed out by pumping 100% liquid solvent through the SCF. This helps the start-up process the next day to start with only one phase. If there is a freezing risk, solvent recirculation is employed to prevent freezing. If necessary, a portion of the warm rich solvent exiting the absorber can be directly pumped into the recirculating loops.

Figure 93 presents the possible operation modes on a daily basis. The operation modes are dictated by the instantaneous *SHF*. The minimum heat flux is 0.5 kW/m for solvent regeneration to occur; below that it could be either start-up, stand-by or shut-down depending on the time of the day. For example, during intensive cloudy hours, the So-St field is put on stand-by mode, instead of shut-down mode. For the start-up, stand-by and shut-down modes, the operation is based on pre-set procedures as discussed above; whereas for the solvent regeneration mode, there is a need for an effective control strategy. There are

three basic control strategies (1, 2 and 3), which can also be 'mix-matched' to create a more desirable control strategy. For example, strategy 1 only operates up to the 3.6 kW/m cap; any excess amount needs to be defocused. Strategy 3, on the other hand, can operate up to 4.2 kW/m (maximum *SHF* during the year). Hence, it is reasonable to combine strategy 1 and 3 to avoid defocusing. In total, there are five possible control scenarios arising from: strategy 1, strategy 2, strategy 3, strategy 1+3 and strategy 2+3 (Figure 93). Among these control scenarios, we do not vary the operation procedures of the other modes (start-up, stand-by and shut-down) as they do not affect the solvent regeneration. Therefore, we only change a control strategy/scenario in the solvent regeneration mode.
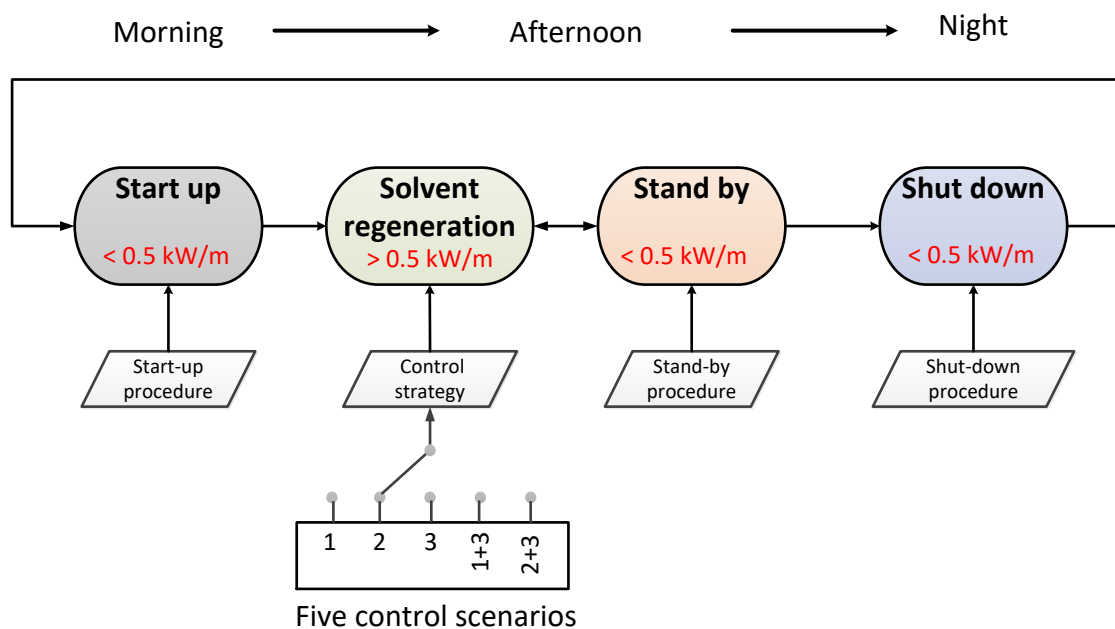


**Figure 93: Summary of the operation modes for a typical day. In the solvent regeneration mode, there are five potential control scenarios; each uses one or combines two control strategies from the three adapted strategies.**

For the main three scenarios, if the *SHF* is above the *SET* range, typically the excess amount would need to be defocused. The annual *SHF* range for this case-study (Sydney, Australia) is converted to kW per metre length (kW/m) of the So-St tube as shown in Figure 94. For example, the *SET* range for control strategy 1 is shown in Figure 94 by the pink and green lines indicating the lower limit of 0.5 kW/m and the upper limit of 3.6 kW kW/m, respectively. It can be seen that for scenario 1 (which only employs control strategy 1), a reasonably large amount of *SHF* at high range, particularly in summer, will need to be dumped. Therefore, it is beneficial to increase the *SHF* upper limit to use more of the available solar energy. This is the motivation behind scenario 4, which integrates control strategy 3 to capture all the *SHF* above 3.6 kW/m. This is because the third control strategy can handle up to 4.2 kW/m without constraint violation.
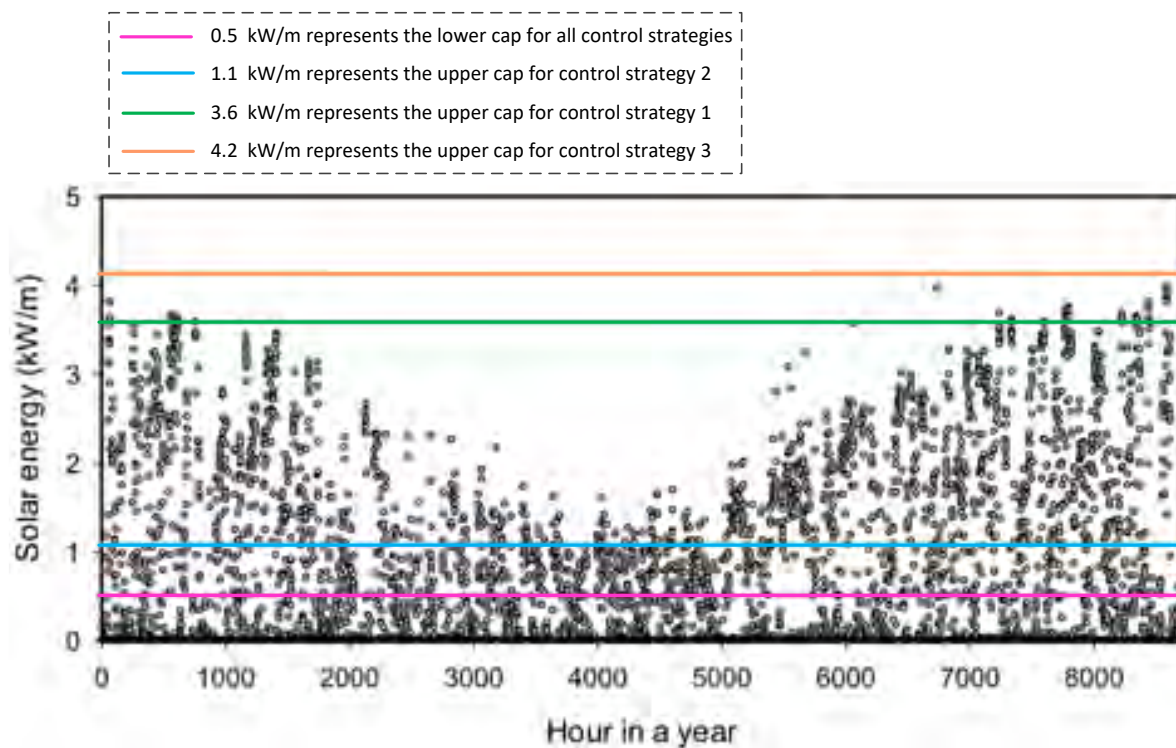
**Figure 94: Annual solar energy profile (SET) is marked between 0.5 kW/m (lower cap) and 1.1 kW/m for scenario 2, or 3.6 kW/m for scenario 1, or 4.2 kW/m for scenario 3. Solar energy above *SET* range is typically defocused while that below the range is not directly usable for solvent regeneration process.**

Consequently, five control scenarios are proposed and presented in a process control expert system as charted in Figure 95. The expert system will command one of the operation modes depending on the *SHF* value at each timestep. When the *SHF* enters the solvent regeneration mode, the five control scenarios are differentiated by their logic and *SET* range. The first three control scenarios are based on the original control strategies 1, 2, or 3 and only differ by the variable being manipulated. For each scenario, if the *SHF* drops below the designated *SET* upper limit, there is no need for defocusing and vice versa. Depending on the *SET* range of each control strategy, the amount of defocus would be different. For example, for a typical *SHF* of 1.5 kW/m, if control scenario 1 in place, there is no need for defocusing, because the strategy 1 has a *SET* upper limit of 3.6 kW/m and can easily digest this *SHF* value. On the other hand, control scenario 2 uses control strategy 2 with upper limit of 1.1 kW/m, and will be able to only digest up to 1.1 kW/m; therefore the excess heat (0.4 kW/m) is defocused. Control scenarios 4 and 5 integrate two control strategies. For scenario 4 and 5, the entire *SHF* range could be used, because control strategy 3 can handle the maximum *SHF* of the year up to 4.2 kW/m. In those control scenarios, if a *SHF* value is below the upper limit of control strategy 1 or 2, those strategies could be directly implemented. Control strategy 3 is only deployed when the *SHF* exceeds the *SET* upper limit of these strategies. The operating algorithm for the solvent regeneration mode continues until the *SHF* drops below the lower *SET* limit of 0.5 kW/m. After that, So-St enters either stand-by or shut-down modes, respectively.
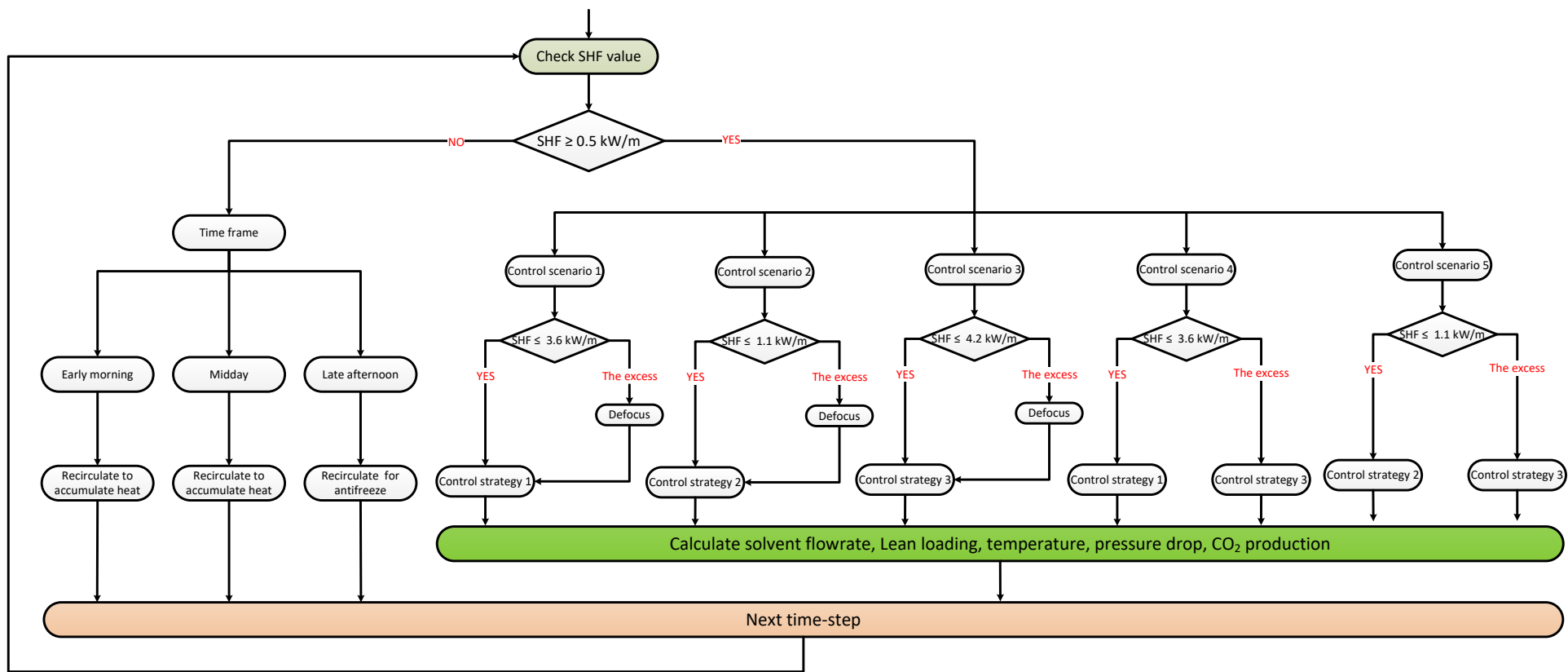
**Figure 95: The process control expert system for operation modes and the different control scenarios for solvent regeneration. The five control scenarios are distinguished by their solar energy profile (SET) range and control logic.**

## 5.6     **Performance evaluations of control scenarios**

The aim of this evaluation is to develop effective control scenarios for our SP-PCC structure. In doing so, the two main control objectives are maintaining the 90% $CO_2$ capture rate in the absorber, and ensuring sufficient solvent regeneration in the SCF to meet the $CO_2$ capture target and the absorber demand. It is possible to extend this work by monitoring all control actions and compare them between potential scenarios; however, this approach could dissipate our focus due to potential complexity from the key control outcomes caused by different hierarchical variables. Therefore, we chose two KPIs by which to compare different scenarios on an annual basis: i) the cumulative $CO_2$ production profile, which is an excellent indication of a control scheme performance, and ii) the *SSC*, which is another indication for compliance with storage sizing and design. More KPIs could be added to this comparison in future work, such as those related to techno-economic analysis. Accordingly, we pursued the following steps in this performance comparison study:

1. Evaluating the performance of individual control scenarios to ensure they comply with the control objectives. If a control scenario cannot achieve the control objective continuously, it should never be considered as a candidate for this performance evaluation. Note that only the control scenarios relevant to the basic 'standalone' control strategies (1, 2, and 3) are considered in this evaluation, while the other two control scenarios are just different combinations of the originals. In this step, an appropriate So-St network is sized to test the operation of individual control strategies in achieving the control objectives, because each individual control strategy would only be able to excel when deployed for the matching So-St design.
2. Comparing the annual performance between different scenarios, excluding the control scenarios that did not pass the previous checkpoint. In this step, the same So-St network design compares the annual performance (e.g. cumulative $CO_2$ production) for the three original control scenarios.
3. Examining the hourly control actions in those high-performance scenarios selected in the second step. In this step, the same So-St network design compares the hourly control actions for all control scenarios.

### 5.6.1  Annual simulation of each control strategy

In the So-St network, the control objective is to guide the solvent regeneration process, following the solar energy availability. Specifically, when solar energy is abundant, the control strategy should boost solvent regeneration and vice versa. To carry out the verification, we check two main variables: i) the lean solvent storage level profile and ii) the cumulative $CO_2$ production. The former variable relates directly to the solvent regeneration capacity in the So-St field. For a properly working control strategy, the cumulative lean solvent should increase during summer when there is more solar energy, and vice versa during winter. This

means the control strategy should inform the So-St process to regenerate more solvent for later use in winter. For efficient process continuity, the final solvent storage level at the end of the year should be at the same level as the starting level. The latter variable represents $CO_2$ production and not lean solvent production; however, these are inter-related, because higher lean solvent production means higher $CO_2$ production and vice versa. We consider both variables because we want to provide a convenient alternative method when checking a control strategy's workability. It will be at the user's discretion to decide which one is more suitable. For example, the former directly reflects the solvent regeneration process; however, it does not inform the total operating hours of the absorber, i.e. the amount of $CO_2$ capture. We elaborate on one example to demonstrate that. Recall the absorber capture rate is always controlled at 90%; hence, one might think the annual capture rate should be 90% as well. This is only true when there is always enough lean solvent available to continuously operate the absorber at 90% capture capacity. If there is insufficient lean solvent at any timestep, the absorber capture rate needs to be reduced during that period, resulting in lower annual $CO_2$ capture. This effect can only be seen using the cumulative $CO_2$ production profile and not the lean solvent storage profile.

For the purpose of checking, we assume the absorber will operate continuously through the year and the capture rate must be controlled at 90%. Based on the mass balance, the amount of $CO_2$ production is expected to be 1,576,800 tonnes (i.e. 90% x 200 tonne/hr x 8760 hrs). It is also possible to back-calculate the total operating hours to achieve a different $CO_2$ production value to achieve a specific design requirement. For all simulations, the absorber is controlled at 90% for the full 8760 operating hours per year, unless stated otherwise. We use the same design point reported in Table 13 for all control strategies and only change the number of total So-St modules. This is because each control strategy results in a different $CO_2$ production rate per a So-St module. Hence, to reach the same $CO_2$ production target, the number of So-St modules needs to be determined. The lean loading used in control strategy 1 is kept at the 0.23 target, while control strategy 2 and 3 are sensitised to make the starting lean loading of the year equivalent to the final lean loading. This is because the latter two control strategies do not control the lean loading at a set-point and could possibly deviate from 0.23. Hence, it is possible that the 0.23 value is not a balanced condition. For example, control strategy 2 can only utilize a *SHF* up to 1.1 kW/m, and at that condition the produced lean solvent loading value is ~0.22. When *SHF* is below 1.1 kW/m, the *LLV* will be higher than 0.22. Therefore, a balanced lean loading would depend on the *SHF* in one year and the value does not necessarily equal 0.23. The design parameters are reported in Table 17, based on the design variables listed in Table 13. We want to emphasise that the purpose of this test is to check if the proposed control strategies could flawlessly fulfil their duties all the time, irrespective of the final tuned So-St design procedure. Therefore, the designs reported in this section are suboptimal and should be used as a reference only.

**Table 17: So-St field design parameters for different control scenarios.**

|  | Scenario 1 | Scenario 2 | Scenario 3 |
|---|---|---|---|
| Annual $CO_2$ capture target (tonne) | 1,576,800 | 1,576,800 | 1,576,800 |
| Total So-St modules | 1425 | 2320 | 1752 |
| Starting lean loading | 0.23 | 0.27 | 0.2 |
| Final lean loading | 0.23 | 0.27 | 0.2 |
| Starting normalised lean storage [a] | 0.67 | 0.78 | 0.67 |
| Final normalised lean storage | 0.67 | 0.78 | 0.67 |

[a] *Normalised against the solvent storage volume of each scenario. We used normalised value and not the actual value since we do not intend to compare between designs.*

The results are shown in Figure 96. It can be seen that all control strategies can achieve the required $CO_2$ production (the actual $CO_2$ production is normalised against the theoretical capture target). Interestingly, control strategy 1 and 3 (i.e. scenario 1 and 3) have very similar $CO_2$ cumulative profiles. The profile gradient is higher in the summer compared with that in the winter due to the normally higher solar availability during summer. The similarity in the cumulative profile is interpreted as both control strategies (1 and 3) having a similar trend of control actions, i.e. when solar energy increases, the control commands an increase in the rich solvent flow to the So-St field and vice versa. On the other hand, control strategy 2 has an opposite profile gradient for summer and winter. In summer, there is less $CO_2$ production than in the other scenarios and vice versa for winter (Figure 96-A). In fact, the profile gradient of scenario 2 almost resembles a linear trend, while other two scenarios do not inherit that similarity. This means regardless of the season, scenario 2 has a more stable $CO_2$ flow outlet than the other two scenarios. This desirable outcome stems from the intrinsic control action, which is designed to keep $CO_2$ production at a steady state. Overall, the normalised cumulative $CO_2$ production reaches the normalised value of 1 (with ± 5% uncertainty due to Aspen® model error tolerance). This result proves the absorber could operate as designed and the total $CO_2$ capture would be 1,576,800 tonnes/year. In other words, all control strategies can keep the absorber at 90% $CO_2$ capture rate and guide the So-St operation to generate sufficient lean solvent for the absorber operation. If the final value is <1, the cumulative $CO_2$ production would be less than 1,576,800 tonnes, indicating the absorber was not able to capture 1,576,800 tonnes/year. Recall from the mass balance that $CO_2$ production from the SCF must be equal to the $CO_2$ capture at the end of the year. This means there was not enough lean solvent to keep the absorber running at the designed capture rate. Therefore, when the normalised cumulative $CO_2$ production reaches 1, the control strategy is said to meet the control objectives.

Figure 96-B shows the lean storage capacity profile, which is a different variable but reveals the same information as in the cumulative $CO_2$ profile discussion. In general, all control strategies have the same starting storage level as the final storage level. This proves the

control strategies provide sufficient solvent regeneration for absorber operation. Observing the profile, one can see the similarity between the scenario 1 and 3, while scenario 2 has a distinct trend particularly during winter. Interestingly, there was more solvent regeneration during winter, which is often associated with lower solar energy. This is a completely opposite behaviour to the other two scenarios. This is because when solar energy is low, scenario 1 and 3 command the system to reduce the solvent flow and vice versa. But in scenario 2, the solvent flow is increased when solar energy is low. However, this does not suggest the superior performance of scenario 2, because while more solvent is regenerated at reduced solar energy, the *LLV* is also increased, i.e. 'shallower' regeneration (Figure 91-B).

The fundamental reason behind the scenario 2 control is that when solar energy reduces, the $CO_2$ production can drop; hence, the control action keeps pushing more flow to So-St field until the $CO_2$ production reaches the set-point, irrespective of the *LLV*. This observation sheds some light on how scenario 2 ($CO_2$ production control) might destabilise the absorber operation due to its lack of consideration for the *LLV*. We will further elaborate this point in the next subsection, where we compare the performance of the control scenarios.

In summary, we can customise a So-St field design for the three basic control strategies. The results show all three can achieve the control objectives, proving their suitability as control strategies for the So-St process. As a result, all five scenarios are considered as valid control scenarios and will be possible candidates for the final performance comparisons.
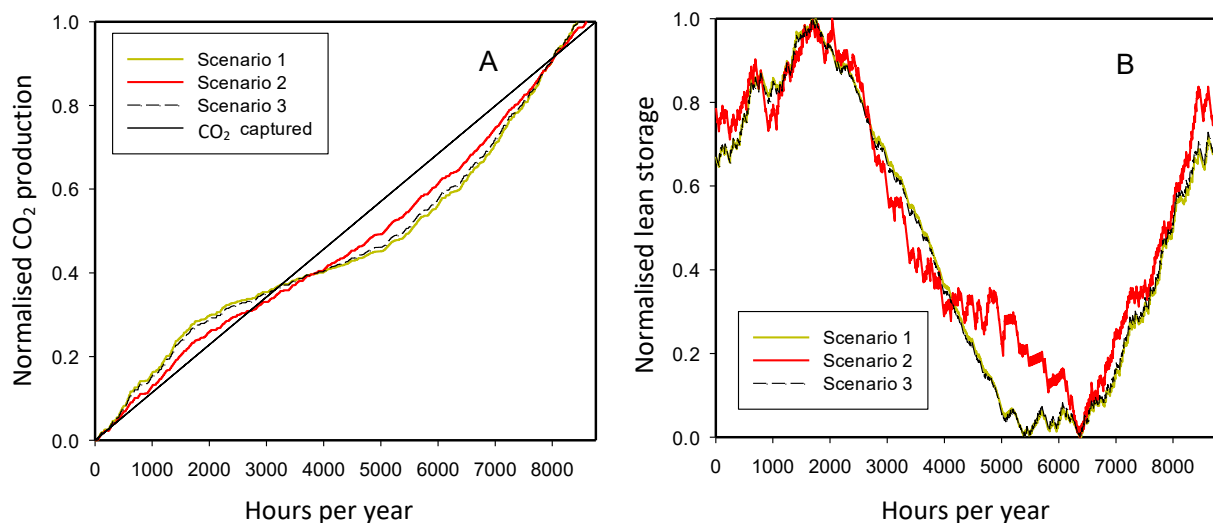


**Figure 96: Cumulative $CO_2$ production and lean storage level for different scenarios. Note that the cumulative value has an error of ± 5% due Aspen® error tolerance in matching the mass balance 100%. The solid black line in (A) represents the $CO_2$ captured in the absorber.**

## 5.6.2  Comparing the performance of control scenarios

In this subsection, we compare the performance of the different control scenarios. We focused on the overall performance in one year and not at hourly control actions. The latter aspect will be investigated once we finalise the optimum control scenario(s). Recall that during control strategy development, we synchronised the operation at the two terminals of the solvent cycle: the absorber and the So-St field. In the former, we control the $CO_2$ capture rate by the solvent at 90%. In the latter, we aim to guide the solvent regeneration rate so that at the end of the year, the entire solvent used by the absorber is regenerated in the SCF to the same *LLV* as the beginning of the year. From the above, we compare the control scenarios based on the so-called average annual capture rate (*AACR*), calculated as follows:

$$AACR = \frac{M_{CO2,produced}}{M_{CO2,flue\ gas}}$$
<div align="right">*Eq. 41*</div>

Where $M_{CO2,produced}$ (tonne/year) is the cumulative $CO_2$ production per year; and the $M_{CO2,flue\ gas}$ is the cumulative $CO_2$ in the flue gas. Assuming the power-plant operates 8,760 hours per year, the $CO_2$ in flue gas would equal 1,752,000 tonnes (i.e. 8,760 x 200 tonnes/h). If the So-St field could regenerate sufficient lean solvent to keep the absorber operating continuously (8,760 hours per year), the *AACR* will be equal to 90%. To achieve a fair comparison, we use a fixed So-St field size (i.e. equal number of So-St modules) and only change the adapted control scenario. This is because in real application, we can switch between control scenarios as illustrated in Figure 93.

From the design aspect, it is possible that a typical design can favour one control scenario over the others. To understand this aspect, we investigate different possible nominal operation conditions for one nine-segment So-St module. The inputs to the So-St module Aspen® model are the solvent flowrate, segment length and the target lean loading. At the nominal point, the lean loading is designed at 0.23; hence, we can only vary the solvent flowrate, and must calculate the segment length required to achieve the target lean loading. This sensitivity test should reveal possible designs for a nine-segment So-St module. The results for different possible designs are shown in Figure 97. Subfigure C shows all the design specifications while the other two subfigures show the performance of the respective designs. We pick two representative designs for the control performance comparisons. The first one is named the low pressure-drop (LPD) design, which has a lower pressure-drop, less $CO_2$ production and shorter segments. The second one is named the high pressure-drop (HPD) design, which induces more $CO_2$ production but uses longer segments. The motivation behind this selection is that the $CO_2$ production control (scenario 2) has a constant $CO_2$ production; thus, it could be valuable to have a design with high levels of $CO_2$ production. Therefore, choosing two dissimilar designs with different $CO_2$ production rates ensures a fair comparison between control scenarios.
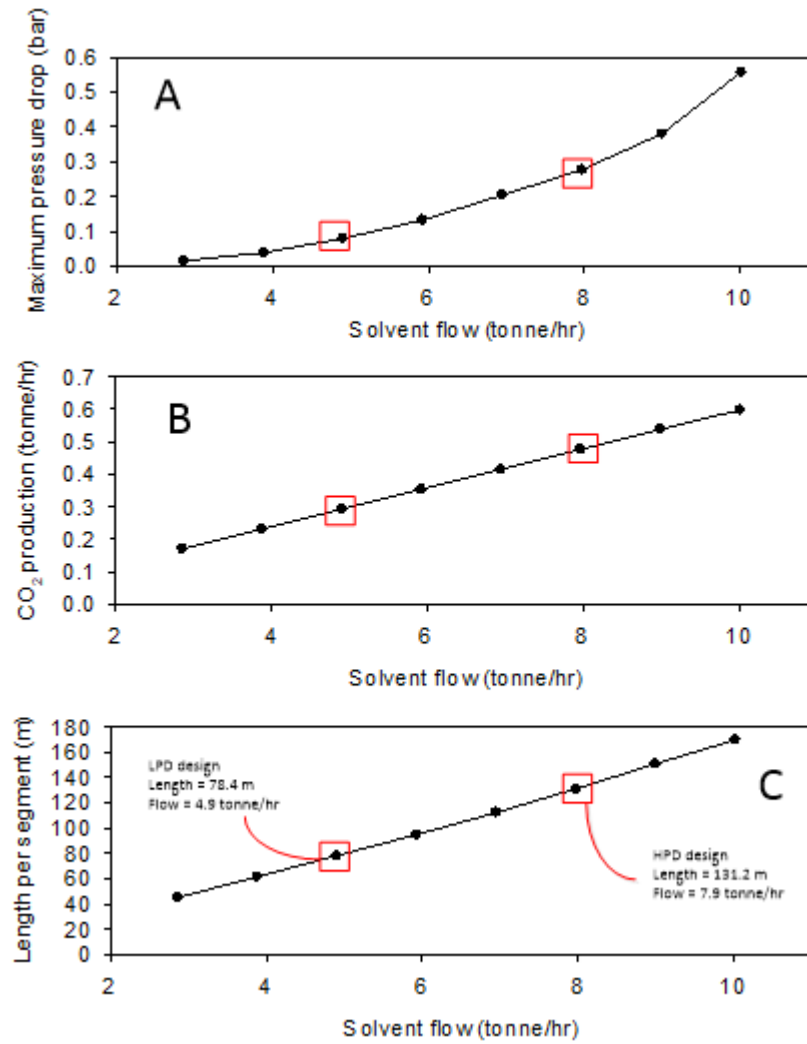
**Figure 97: Results for different designs: (A) the maximum pressure-drop among the nine segments; (B) the CO₂ production per a So-St module; and (C) the required length per one segment to achieve lean loading of 0.23 when *SHF* equals 1 kW/m. LPD = low pressure-drop design and HPD = high pressure-drop design.**

Next, we apply the respective control scenarios for each of the two chosen So-St designs. We perform an hourly timestep integration to compute the control actions and outcomes for calculating the *AACR*. Having five control scenarios and two designs, we obtain a total of 10 *AACR* values. The full design parameters for the LPD and HPD are reported in Table 18. The total number of So-St modules is calculated for each design to ensure the total physical So-St tube length is the same. This means the resulting *AACR* from the same control scenario is still comparable between the two designs. If the total physical tube length is not the same, one design will harvest more solar energy than the other (recall that longer So-St tube, means more *SHF* is collected); hence, the *AACR* of the two designs would not be comparable.

Figure 98 shows the cumulative $CO_2$ production profile for the entire year from each one of these control scenarios. In general, $CO_2$ production increases at faster rate during summer and vice versa in winter. Each control scenario has different rates of increase, suggesting it is possible to obtain different $CO_2$ production rates per control scenario despite having the same

So-St field design. This result highlights the significance of choosing an appropriate control scenario to ensure high-performance operation.

**Table 18: Two designs used to assess the control scenarios performance (LPD = low pressure-drop design; HPD = high pressure-drop design). The two designs have different flows per So-St module, but they have the same total physical tube length of all modules, i.e. same SCF size.**

|  | LPD | HPD |
|---|---|---|
| Number of segments | 9 | 9 |
| Segment length (m) | 78.4 | 131.2 |
| Total So-St modules | 1425 | 852 |
| Total physical tube length (m) | 1,005,095 | 1,005,095 |
| Solvent flow per module (tonne/hr) | 4.9 | 7.9 |
| $CO_2$ production per module (tonne/hr) | 0.294 | 0.477 |
| $CO_2$ in flue gas (tonne/hr) | 200 | 200 |
| Hourly absorber capture rate (%) | 90 | 90 |
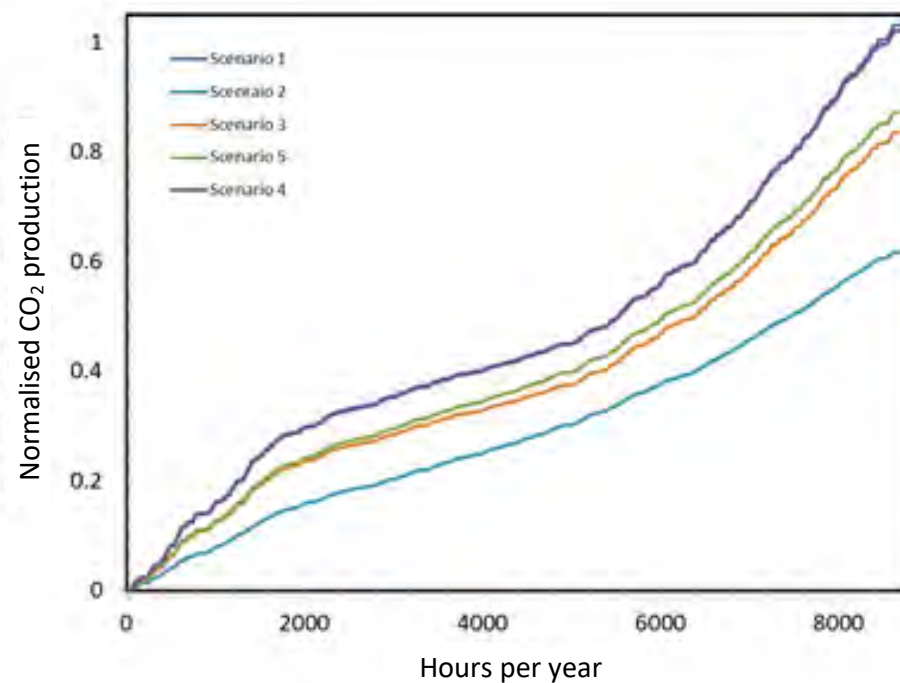


**Figure 98: Normalised $CO_2$ production for different control scenarios using the low pressure-drop design.**

Although the annual cumulative profiles are heading upward in Figure 98, different scenarios have different total $CO_2$ production values. One might perceive this result as contradictory to the previous result shown in Figure 96-A, in which all scenarios have the same $CO_2$ production. We need to emphasise that the former design test was set to check whether the control strategies could achieve the control objectives; hence, the So-St field was sized for the respective control scenario to aid them in reaching the $CO_2$ production target. In the current

design test, we seek to provide a $CO_2$ production rate for the same So-St design to learn which control scenario results in higher $CO_2$ production. From Figure 98, we extract the cumulative $CO_2$ production rate at the end of the year and calculate the *AACR* for each control scenario. We summarise the *AACR* for all control scenarios in Figure 99. Note that there is an associated error bar of ± 4% due to the Aspen® model error tolerance in the mass balance (i.e. $CO_2$ captured in the absorber must equal the $CO_2$ produced in the So-St field). If there is even a very small error in each integrating time-step, the cumulative effect of a large number of these tiny errors over a year of simulation could result in a noticeable error. We think the error bar range is acceptable since we obtained the results only to distinguish between different control scenarios. Figure 99 partially suggests that scenario 1 has the highest performance, but subject to using the LPD design. At this stage, we can preliminarily conclude that the scenario 1 has the best performance.
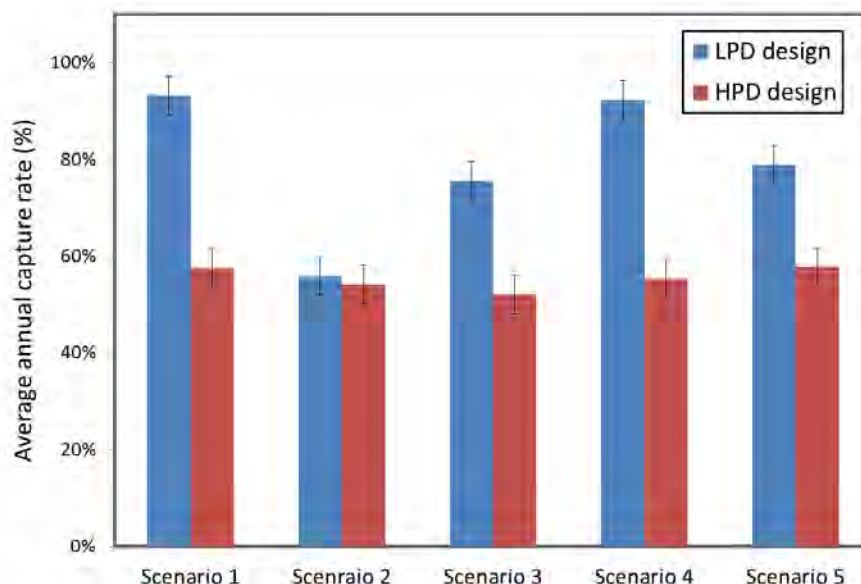


**Figure 99: Average annual capture rate (cumulative CO₂ produced divided by cumulative CO₂ in flue gas) for different scenarios and designs. The error bar is ± 4% of the capture rate, due to Aspen® model error tolerance. LPD = low pressure-drop design; HPD = high pressure-drop design.**

It can be seen from Figure 99 that the overall So-St performance is affected by the control scenarios and the design choice. For example, control scenario 1 has an outstanding *AACR* when using the LPD design, while the same outcome cannot be obtained using the HPD design. This is because the HPD has higher pressure-drop, thus lean loading control can only increase solvent flow to a lesser extent when dealing with increasing *SHF*. The pressure-drop in the HPD design is ~0.45 bar, while that of the LPD is ~0.1 bar and the maximum allowable pressure-drop is 0.5 bar. In other words, if a design has a pressure-drop close to the maximum allowable pressure-drop, it cannot tolerate solvent flow increments to a similar extent as in the LPD design. Less solvent flow means less *SHF* is used to reach the control target (e.g. lean loading or temperature). This means more defocus is required to avoid excessive *SHF*. As a result, the scenario 1 HPD design has a lower solar utilisation percentage than the LPD design

(59% *vs* 95%). Specifically, the HPD design can only tolerate *SHF* up to 1.2 kW/m when the pressure-drop is about to exceed the cap of 0.5 bar. In contrast, in the LPD design the tolerated *SHF* can reach up to 3.6 kW/m.

We found that when the control action is to increase solvent flow when *SHF* increases, the HPD will deteriorate the performance, because fewer solvent increments can be made available before the pressure-drop exceeds the allowable value. This type of control action is found in scenario 1 (lean loading control), scenario 3 (temperature control), scenario 4 (lean loading + temperature control) and scenario 5 (temperature + $CO_2$ control). In all these scenarios, the HPD design deteriorates the high performance of the LPD design, as can be seen in Figure 99. In control scenario 2, the control action is opposite, i.e. solvent flow is reduced when increases. This might be the reason why the HPD design does not deteriorate the performance of control scenario 2, because when *SHF* increases, the resulting pressure-drop is always reduced, and thus would never exceed the 0.5 bar cap. From the above, we can conclude that the design actually dictates to what extent the solvent flow could be increased when *SHF* increases because of the maximum allowable pressure-drop constraint. In other words, the design affects the *SET* range; hence, for the same control strategy, less solar input results in less $CO_2$ capture and vice versa. The above conclusion brings one possible complication for the process control study relating to the So-St. It can be said that there are 'good' (e.g. LPD) and 'bad' (e.g. HPD) designs for process control performance comparison. The 'bad' design would not fully reveal performance differences between control scenarios. For example, if one uses the HPD design, they will conclude that all the control scenarios have similar performance. In fact, control scenario 1 shows superiority. To avoid this false impression, we suggest one should carry out sensitivity tests as we did in Figure 97, to determine suitable So-St design(s) used for process control performance evaluation. We recommend comparing at least two designs per control scenario to ensure a valid and comprehensive comparison.

From the above, we have learnt that the dramatic change in the *AACR* value of scenario 1 is due to the 'bad' design rather than the control performance. Therefore, only the LPD design should be used for process control evaluation. Among the three basic control strategies (lean loading, $CO_2$ production and temperature control), the lean loading resulted in the highest *AACR* value as evidenced by the high performance of scenario 1 (lean loading only) and scenario 4 (lean loading + temperature). To investigate further the attributed factor to the superior performance of the lean loading control over the other two control strategies while in fact all three control strategies could achieve their control objective. Figure 100 shows the absorber operating time for each of those control scenarios, where the absorber operation is limited based on the adapted design and control scenario (absorber is being switched off due to the insufficient lean solvent yield in the SCF).It can be seen that the bar heights of Figure 100 correspond to the *AACR* profile presented in Figure 99, which confirms the fact that the *AACR* value proportionally corresponds to absorber operation at the nominal 90% capture rate. Therefore, to understand why the lean loading control has the highest *AACR*

value, we need to better understand why lean loading control allows for more operating hours in the absorber, i.e. more solvent regeneration. There are two factors that could influence the solvent regeneration: i) *SHF*, which affects the solvent regeneration rate; and ii) lean loading value, which the former affects the solvent regeneration rate and the latter affects the solvent regeneration quality 'depth'. Compared to the lean loading control, the $CO_2$ production control strategy uses a lower maximum *SET* (Table 15); thus, less solar energy could be used for solvent regeneration purpose. Recall the low value of the upper *SET* cap in the $CO_2$ production control is due to the solvent temperature rapidly exceeding 125°C for *SHF* above 1.1 kW/m (Figure 91-C). This is because the $CO_2$ production control action reduces the solvent flowrate when *SHF* is increased, resulting in elevated solvent temperature.
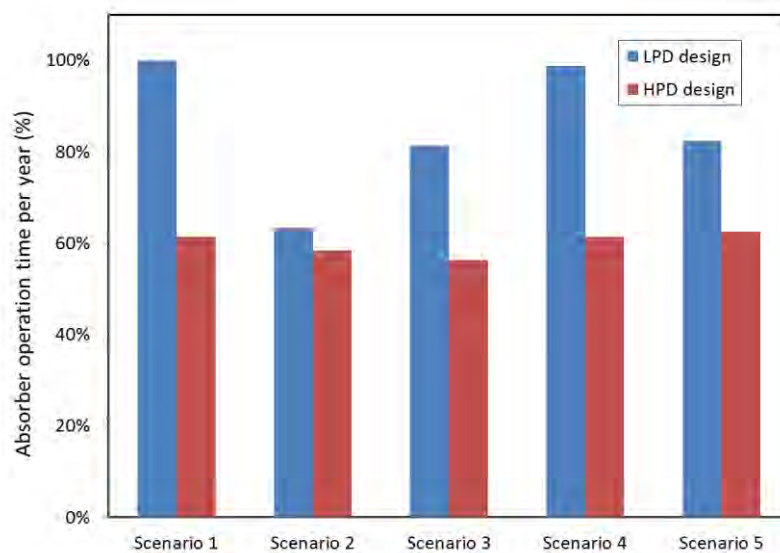


**Figure 100: Total hours (100% means 8,760 hours/year) of the absorber operation with hourly CO₂ captured rate controlled at 90% in the absorber. When the percentage is less than 100%, it means the absorber had to be switched off due to the insufficient lean solvent in the storage tank. LPD = low pressure-drop design; HPD = high pressure-drop design.**

The temperature control strategy has a higher upper *SET* cap than the lean loading control strategy, and thus should have been able to generate more lean solvent compared with the lean loading. However, this is not the case, because the temperature control actually generates lean solvent at lower loading values (i.e. <0.23) as *SHF* increases above 1 kW/m (Figure 92-B). As the lean loading drops, the amount of required solar energy to regenerate lean solvent would increase. Based on the thermodynamics of the 30 *wt*% MEA solvent, lower lean loading means less $CO_2$ 'dissolved' in the solvent and less $CO_2$ in vapour phase. This means there will be more water vaporisation as a way to dilute the $CO_2$ content in the vapour phase. Therefore, more solar energy is actually used to vaporise water rather than for $CO_2$ desorption.

Figure 101 shows the amount of lean solvent demand from the absorber and the supply from the So-St network for different *LLV*s. It can be seen that as the lean loading reduces in value, less lean solvent could be regenerated to the required loading, indicating less solar energy

goes to solvent regeneration and more solar energy was used for water vaporisation. As the lean loading reduces in value, the absorber would correspondingly require less lean solvent flow, because each MEA molecule would have higher capture capacity. Interestingly, there is a mismatch in the gradient of the lean solvent supply and demand trends on both sides of the cycle, revealing the supply will not be able to meet the demand. In other words, there will be not enough lean solvent to operate the absorber all the time.
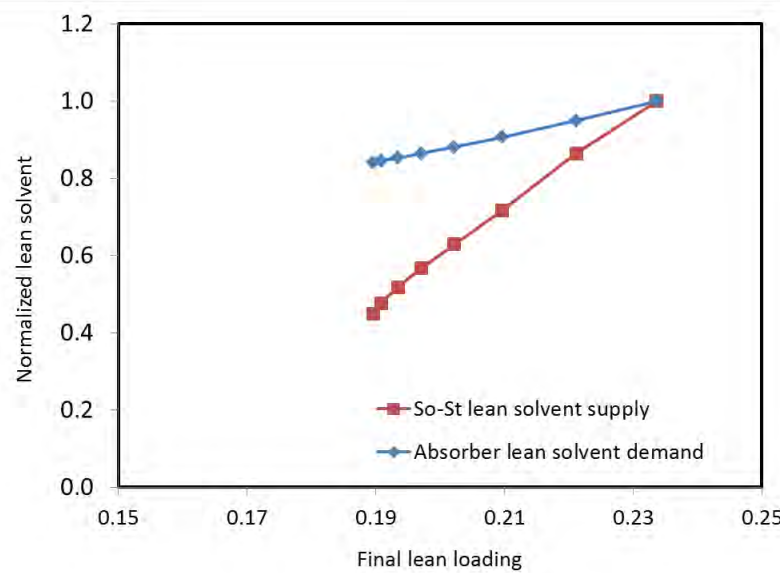


**Figure 101: Normalised lean solvent demand and supply for different *LLV*s.**

From the above, the lean loading control outperforms the temperature control mainly because the temperature control could result in lower *LLV*s. This pushes the solvent regeneration process into the thermodynamic regime, which has significant water vaporisation and a lower lean solvent regeneration rate for meeting the absorber demand. This result also highlights the significance of controlling the lean loading to ensure the solvent regeneration remains in a desirable thermodynamic regime. Therefore, lean loading control (scenario 1) is the most desirable control strategy for the So-St process. It is arguable that a combination of lean loading and temperature control (i.e. scenario 4) could be more desirable. This is because both have very similar control architecture because they actually measure different variables (temperature or loading), but of the same process stream. The advantage of using temperature control is appealing more when considering the solvent management aspect. The lean loading control does not maintain the temperature directly but instead only the lean loading. As the loading and temperature are inherently correlated, one can choose a lean loading set-point which results in an acceptable temperature value. Real outcomes could deviate from the overall thermodynamic behaviour; thus, it is possible to have local hot spots in the solvent with excessive high temperature as highlighted in our CFD study. The effects cannot be predicted by thermodynamic analysis only. By using an effective temperature control, one can always ensure the solvent temperature is well managed within the acceptable range. From the above, a combination of lean loading and temperature (i.e.

scenario 4) is beneficial in which the former control actions ensure hourly high-performance operation, while the latter would ensure appropriate management and long-term solvent stability. Since the temperature control reduces process performance, it should be used to monitor the solvent temperature and provide immediate remedial actions when the solvent temperature reaches 'alarming' values. Up till now, we have discussed the control scenario performance in the context of designing a new So-St plant and seeking an optimum control strategy. It is possible that one might start with an existing design and seek an optimum control strategy. We think that the lean loading control would plainly outperform other control strategies, because other control scenarios will affect the *LLV* at the exit of the SCF and in the lean storage, as shown in Figure 102. This means the control strategy could move the existing plant operation away from its initial design point. For example, scenario 3 (temperature control) results in reducing the *LLV* over a year; this implies there will be less solvent required in the absorber. It is possible that the existing absorber design could not adapt to the new lower flowrate, resulting in undesirable hydrodynamic conditions in the absorber. From the above, it is conservative to select the lean loading control option, which provides the operator with the ability to integrate the process control strategy into the existing plant operation without affecting the operating conditions of other components.
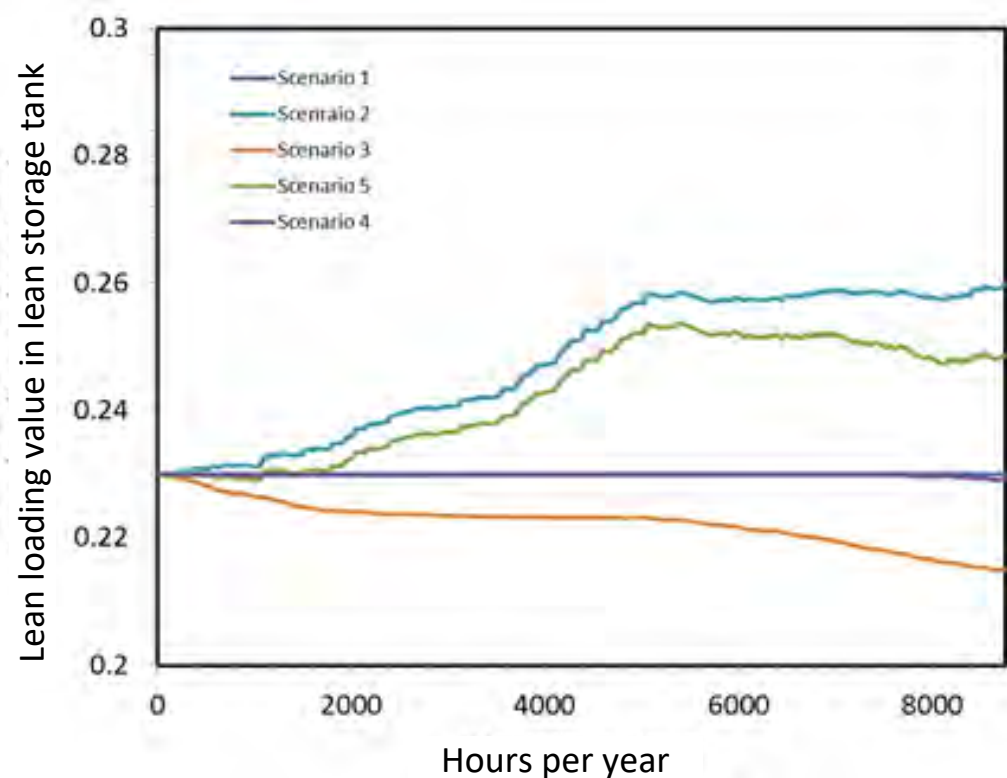


**Figure 102: Lean loading profile for a case study in which control scenarios are tested for a So-St field designed to regenerate the solvent for an existing PCC, where the *LLV* is set at 0.23 at the beginning of the year.**

### 5.6.3  Analysis of the control actions

In the previous section, we found the lean loading scenario (scenario 1) results in the highest *AACR* value among other control scenarios for a given fixed size So-St field. We also discussed how the temperature control (scenario 3) could be integrated with scenario 1 (i.e. as in scenario 4) to provide appropriate long-term solvent stability management. In this section, we examine the control actions of the desirable control scenarios (1 and 4), to ensure they not only resulted in a high *AACR* value, but also provide process stability during transient operation. The results of this analysis are presented in Figure 103, comprising the hourly control actions for scenario 1 (lean loading control) and 4 (lean loading + temperature control). We also include scenario 3 (temperature control) in this comparison because it partially contributes to the control actions of scenario 4.

In any control scenario, the So-St solvent flow (subfigure B) profile closely resembles the *SHF* profile (subfigure D) at hourly and daily levels of *SHF* availability, e.g. the 23 June has the lowest daily *SHF* and the lowest solvent profile compared with the other selected days. This indicates that when solar radiation increases, the control scenarios could guide the process to increase solvent regeneration. This is the most vital role of the process control, because the process needs to regenerate more solvent when solar energy is high to compensate for low solar periods. All the control scenarios also execute control actions for the absorber operation to achieve a 90% capture rate. The transient nature of the control actions of the So-St, however, did not affect the absorber operation. This desirable outcome is achievable with scenario 1 wherein the lean loading is controlled at the set-point. As the *LLV* does not change, the lean solvent flow to the absorber will not change either. For other scenarios, the steady operation of the absorber is attributed to the lean loading buffering capacity of the lean storage tank. In summary, all control scenarios provide appropriate control actions for both the absorber and the So-St network, respectively.

In comparing the control actions of these control scenarios, there are some subtle differences. Recall control scenario 4 is a combination of scenario 1 (lean loading) and 3 (temperature control); when *SHF* exceeds the upper *SET* cap of scenario 1, scenario 3 will be deployed directly. This can be seen clearly in subfigure D of Figure 103, showing scenario 1 *vs* scenario 4. For 3 Jan, there are two distinct red data points (i.e. two hours) in subfigure C, which are the available *SHF*. The utilised *SHF* is less than the available *SHF*, indicating there was defocusing action at those two hours. Comparing those actions with scenario 4, at the same two hours, the utilised *SHF* is the same as the available solar heat flux, indicating the temperature control component in control of the So-St operation instead of the lean loading control. However, in those two hours in scenario 4, the So-St solvent flow is reduced (subfigure B, scenario 4). This is because the temperature control component regenerates less solvent, as we have discussed in the previous section (recall the temperature control produces a varied *LLV* which could push the process into an energy-intensive thermodynamic regime). This is further evidenced from the scenario 3 (subfigure C) in which there was

insufficient lean solvent for the absorber on 23 June. This event of solvent deficit did not appear in scenario 4 (lean loading + temperature control), indicating the temperature control contributes less to controlling the process than does the lean loading control; otherwise, there would have been similar solvent deficit.

In summary, we have discussed in detail the control action for individual control strategies (lean loading or temperature control) or the integrated strategy (lean loading + temperature control). We confirmed that the role of the temperature control is to use the 'very high' *SHF* that exceeds the lean loading control *SET* upper limit. However, the temperature control contribution is not significant (i.e. there are not many hours with very high *SHF*), because we did not observe the solvent deficit event which occurred in the temperature-only control scenario 3, but not in scenario 4 (the lean loading + temperature control scenario). This result confirms that practical application of the integrated control should minimise the use of the temperature control component to solely monitor the solvent temperature.
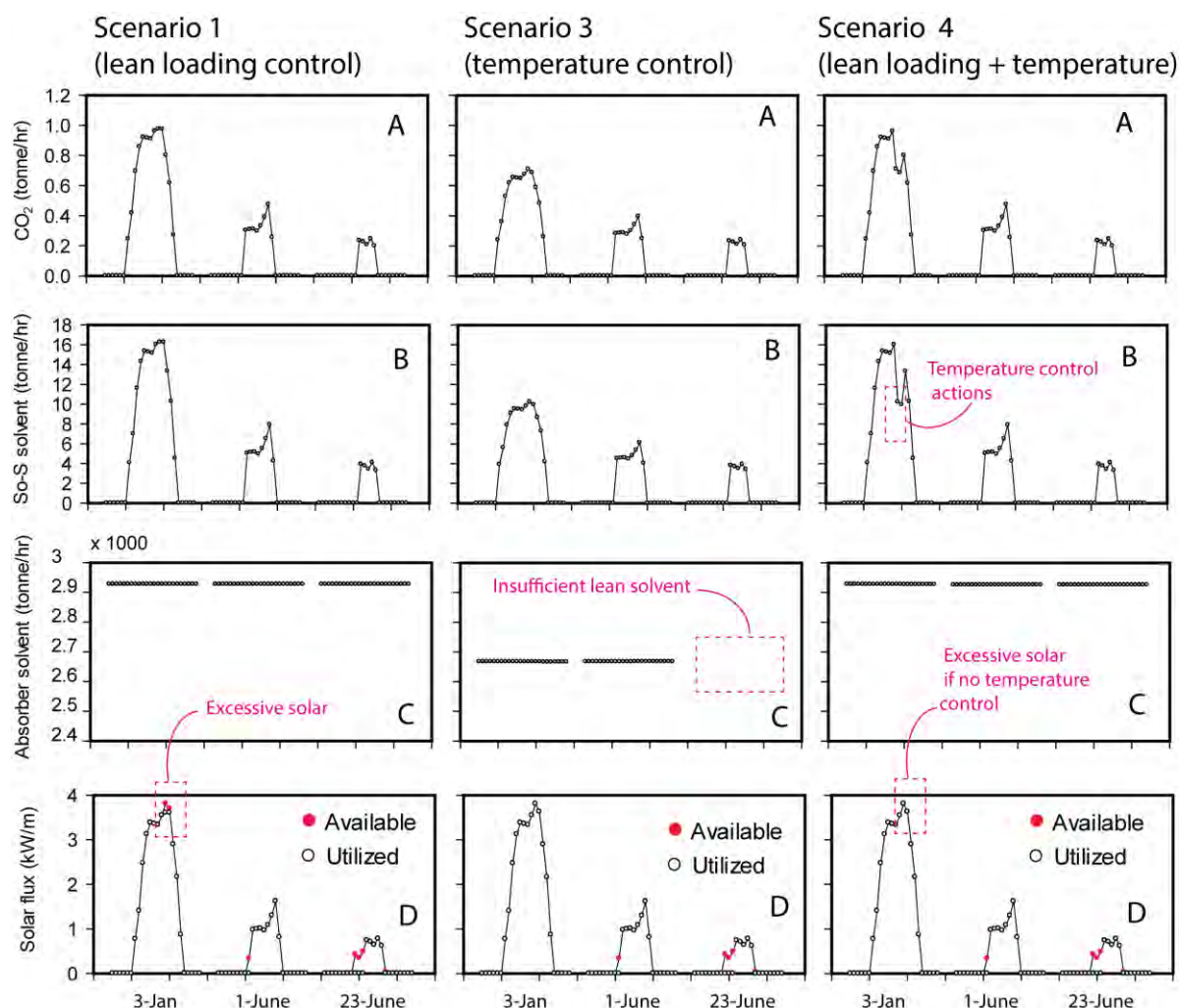


**Figure 103: Hourly control actions and outcomes for three different days (best, average, worst solar flux) from different control scenarios. Different x axis: CO₂ = CO₂ production per module; So-St solvent = rich solvent flow per one module; absorber solvent = lean solvent flow to the absorber; solar flux = hourly *SHF*.**

## 5.7      Concluding remarks

In this chapter, we have developed a process control expert system designed for the So-St process. The aim is to construct effective control strategies that could guide the transient operation of the absorber and the So-St network while maximising the annual $CO_2$ capture rate. Specifically, the absorber is always controlled at 90% capture rate, while the So-St is controlled to generate more lean solvent at higher *SHF* periods. The latter goal could be achieved by controlling different variables (i.e. lean loading, $CO_2$ production, solvent temperature). Three different control strategies were investigated for the same control objectives but with different manipulated variables. An operational procedure has been developed as a higher-level control to determine a suitable control strategy based on dynamic solar irradiation. Based on the defined control strategies, we developed five control scenarios and compared their associated average annual $CO_2$ capture rates. It was found that the control scenario with lean loading component (i.e. control scenarios 1 and 4) can provide the highest capture rate. This is because the lean loading control can deal with a relatively large *SHF* range (up to 3.6 kW/m), and it also helps maintain the solvent regeneration process within the desirable thermodynamic regime. Practical application of lean loading control should also incorporate temperature control to monitor the solvent temperature and provide appropriate remedial control actions in case the lean loading control pushes the solvent into thermally unstable conditions.

# 6.    So-St and solvent storage sizing

In the previous chapters, we have developed a design protocol for a steady and constant solar heat flux (*SHF*), and hence, performed a preliminary sizing for a nominal *SHF* value. This study was useful because it provides a basic understanding about this novel process in the early stage of research. The outcomes from the preliminary sizing facilitated detailed studies in CFD and process control aspects.

Now we have arrived at a good control strategy, it is important to revisit the sizing domains. We think it is more appropriate to tune-up the final So-St sizing in respect to the process control expert system. This is because solvent flow is the main manipulated variable for the process control, which can basically drive $CO_2$ capture in the absorber and production in the SCF. Hence, it is vital to account for solvent manipulation in the sizing protocol. A good example to prove this point is the pressure-drop aspect. During process control, the solvent flowrate might need to be increased, thus resulting in higher pressure-drop. If we design the So-St at the maximum allowable pressure-drop, there will be not enough capacity to accommodate additional pressure-drop caused by possible increase in solvent flowrate.

In this chapter, we combine the results from the steady-state sizing with the process control during solar transient periods, to develop a complete sizing protocol for the entire So-St field by taking into account the solvent regeneration demand and the intermittency of *SHF*. The overall design goal is to size a SCF that can regenerate all the rich solvent generated by the absorber on recurring annual bases. The annual $CO_2$ production from the SCF is fixed at 1.5 million tonnes/year of $CO_2$. The outcome from this SCF sizing exercise will serve as the main inputs for both techno-economic and life-cycle analysis studies.

## 6.1    Process description

Figure 26 illustrated a complete process flow diagram (PFD) for both absorption and desorption terminals of the solvent cycle. As mentioned in Chapter 5, we have revised the overall PFD and decided to remove the preheating section. This is because the preheating section only needs to bring the solvent temperature to the edge of the regeneration process at 90℃, just before desorption (i.e. vaporisation) can occur. Alternatively, the preheating function can be achieved either in the cross HX or early segments of the So-St modules. We found a similar temperature rise could be achieved in the cross HX when the flow develops enough to recuperate the heat directly from the return line of the hot lean solvent exiting the SCF. Since the So-St tube resembles the function of a parabolic trough receiver tube, part of the So-St field could be utilised for preheating function during start-up time. Accumulated vapour needs to be frequently flashed out until the *SHF* reaches the nominal design value. We revised the entire process and summarised different operating conditions during the

start-up when there is no preheating section. The operating procedure for each condition is listed in Table 19.

**Table 19: List of start-up conditions based on the operation procedure discussed in report 4. The numbers (1 to 5) indicate operational decisions and are also explained in the text.**

| | Control scenarios | | | | |
|---|---|---|---|---|---|
| | 1 | 2 | 3 | 4 | 5 |
| Solar heat flux (kW/m) | <0.5 | <0.5 | <0.5 | <0.5 | >0.5 |
| Solvent temperature in last segment outlet ($^{o}$C) | <125 | >125 | <125 | >125 | Any |
| Pressure-drop in any segment (bar) | <0.5 | <0.5 | >0.5 | >0.5 | Any |

The value for each condition was chosen as follows. For the *SHF*, the minimum value for solvent regeneration was chosen to be 0.5 kW/m. There are two reasons why we chose that number. First, there must be a minimum value of *SHF* to begin the process, as before this point there would be insufficient solar heat to drive continuous solvent regeneration process. Second, the numeric value for that minimum *SHF* is assumed to be 0.5 kW/m, because at such low *SHF*, the rich solvent flow into the So-St tube needs to be reduced accordingly to maintain effective solvent regeneration. Our simulation result for operation at 0.5 kW/m *SHF* reveals the pressure-drop in a So-St module is negligible and most of the solar energy is used to heat the solvent. Based on thermodynamics, the solvent temperature would be around 125$^{o}$C to meet the 0.23 *LLV* if there is negligible pressure-drop. This result might pose a solvent thermal degradation risk for the adopted 30 *wt*% MEA solvent. From the above, we conservatively chose 0.5 kW/m as a benchmark *SHF* to start the solvent regeneration process. If one uses a different solvent with different temperature tolerance range, the numeric value of the minimum *SHF* will need to be re-determined. For the solvent temperature, the 125$^{o}$C cap was used to avoid potential solvent degradation. For the pressure-drop, we chose the maximum allowable pressure-drop at any point along the entire So-St module to be 0.5 bar which was chosen based on our proposed design protocol in the next section. We formulated the operating procedure for each set of conditions as follows:

1. Keep recirculation at 2.7 tonnes/h (nominal flowrate when *SHF* equals 0.5 kW/m based on lean loading control in Chapter 5) and by-pass the cross HX. All the vapour forming is vented into a flash drum prior the entry to the SCF to avoid excessive vapour accumulation in the early segments of the So-St module.
2. Stop recirculation, start the cross HX, monitor the So-St inlet temperature. If it drops below 90$^{o}$C, adopt operating procedure 1.
3. Adopt operating procedure 2
4. Stop recirculation, start the cross HX, switch on lean loading process control scheme.

Typical start-up will follow the sequence: 1 – (2, 3 or 4) – 5. This is because during step 1, the solvent in the So-St would have been accumulating more solar heat to raise the temperature and generate vapour. During this stage, excessive temperature increase may cause spikes in pressure-drop, exceeding 0.5 bar at some point along the So-St module. Then the second procedure is used for flushing out the current batch of hot solvent. If at this time the *SHF* is still below the minimum value, the So-St inlet temperature will eventually drop below 90°C, because the hot solvent cannot sustainably heat the cold solvent in the cross HX due to insufficient solar heat input. Then stage 1 is resumed to further accumulate solar heat and keep the So-St ready for normal operation. As soon as *SHF* picks up (>0.5 kW/m), normal operation can be started immediately. After that, the rich solvent flows directly from the absorbers and/or from the rich storage tank to enter the cross HX.

Inside the cross HX, there could be some $CO_2$ desorption, which can occur as soon as the temperature exceeds 90°C. The rich solvent at the cross HX outlet is taken to the primary flash drum for $CO_2$ vapour removal (Figure 26). The 100% liquid solvent would then be equally divided into multiple So-St loops and modules arranged in parallel configuration. The outlet of So-St segments contains a mixture of vapour ($CO_2$ and $H_2O$) and liquid (lean solvent). The vapour and liquid component of the mixture is then separated in a flash. The lean solvents from each module are combined and directed to the cross HX to pass the high enthalpy to the rich solvent, and be cooled and stored in the lean storage tank/s. The gas/vapour mixture is then cooled to about 23°C in the subsequent condenser to condense the vapours. The $CO_2$ gas is considered as almost pure product (>99 *wt*%) while the $H_2O$ and other condensed species are recycled back to the makeup stream to maintain the balance in the lean solvent tank.

## 6.2    So-St design protocol

In this section, we outline our developed design protocol. This design protocol has been optimised to minimise the need for real-time simulation while ensuring adequate agreement with the real-time simulation. We present a step-by-step calculation, and then condense the steps into a graphical presentation. The main objective of the So-St technology is to completely move away from fossil fuel consumption; hence the 100% solvent regeneration energy input would be sourced from the renewable solar source. Therefore, the nominal solvent flow to the So-St field should be larger than the constant rich solvent exiting the absorber at steady-state operation mode. This is because the So-St field needs to regenerate more solvent than that produced by the absorber in abundant solar times, to compensate for the no or poor solar periods. For example, during the night, while the absorber continuously operates and generates rich solvent, the So-St field will not be able to regenerate that solvent instantaneously. Therefore, solvent storage tanks (SSTs) are necessary to buffer the dynamic operation of the So-St field and the steady-state operation of the absorber. Accordingly, the accumulated rich solvent in the storage tank needs to be regenerated in the upcoming periods of abundant solar. This means the nominal rich solvent flowrate to the So-St field will not

necessarily be equal to the rich solvent flowrate from the absorbers. Therefore, the most important step is to determine the nominal amount of rich solvent to send to the So-St field to maintain balance and stability in the operation for the entire year. Table 20 presents the basic design parameters for the desorption process as used in the design protocol. These values were chosen based on the analysis conducted in previous chapters. In this design protocol, we take into account which type of control strategy is used in real-time operation. In our process control work (Chapter 5), we discussed different control strategies including lean loading, $CO_2$ production and temperature controls. It was found that the lean loading strategy resulted in the highest annual $CO_2$ capture rate. Therefore, the lean loading control was chosen as the main control strategy when sizing the entire So-St field because it results in higher $CO_2$ capture, and thus a smaller SCF compared with the other control strategies.

**Table 20: Basic design parameters**

| Design parameter | Value | Reference |
|---|---|---|
| So-St inner diameter (mm) | 76 | Chapter 3 |
| Aperture width (m) | 7 | Chapter 3 |
| So-St pressure (bar) | 2 | Chapter 3 |
| Solvent maximum temperature ($^o$C) | 125 | Chapter 3 |
| Design lean loading ($mole_{CO2}/mole_{MEA}$) | 0.23 | Chapter 3 |
| Design rich loading ($mole_{CO2}/mole_{MEA}$) | 0.49 | Chapter 2 |
| Control strategy [a] | I (Lean loading control) | Chapter 5 |

[a] *Tolerance solar energy (SET) = 0.5 kW/m – 3.6 kW/m. Below 0.5 kW/m, So-St will not produce $CO_2$ and above 3.6 kW/m, excess solar energy will be defocused. The upper limit was determined in our process control work. At such high SHF, the pressure-drop in the So-St module exceeds the assumed maximum tolerance (0.5 bar). This is because the control actions need to increase the solvent flow per SHF increase.*

### 6.2.1  Calculate solvent regeneration requirement

The amount of $CO_2$ in the flue gas that enters the entire solar-powered post-combustion capture (SP-PCC) process is approximately 200/h. Given the absorber optimum $CO_2$ absorption rate is 90%, the amount of $CO_2$ captured in the solvent would be 180 tonnes/h. Accordingly, the total operation hours are calculated as follows:

$$H_{absorber} = \frac{M_{CO2}}{m_{CO2}} * f_m = \frac{1.5x10^6}{200*90\%} * 1 \approx 8333 \frac{hr}{year} \qquad Eq.\ 42$$

Where $H_{absorber}$ (h/year) is the total operating hours of the absorber in a year; $M_{CO2}$ ($tonne_{CO2}$/year) and $m_{CO2}$ ($tonne_{CO2}$/h) are the $CO_2$ captured per year and per hour, respectively; $M$ and $m$ indicate the flowrate per year (tonnes/year) and per hour (tonnes/h), respectively; and $f_m$ is the coefficient to account for maintenance. We assume the absorber

operates almost continuously throughout the year, hence a value of 1 is used in the calculation. After knowing the total operation hours per year, we can calculate the total rich solvent generated in the absorber, i.e. the solvent that needs regeneration. In Chapter 2, the rich flow was simulated at 2,378 tonnes per hour to reach the lean loading equal to 0.17. In Chapter 3, we have determined a more appropriate lean loading target for the absorber operation is 0.23 to minimise solvent regeneration energy demand. The updated rich solvent flowrate would be about 3,024 tonnes per hour. Therefore, the total solvent needing regeneration per year is as follows:

$$M_{rich} = m_{rich} * H_{absorber} = 3024 * 8333 = 25.2x10^6 \frac{tonne}{year} \qquad \textit{Eq. 43}$$

Where the subscript '*rich*' indicates the rich solvent flow. Once we know the solvent regeneration energy demand per year, we need to convert it to an hourly basis. We first must determine the operating hours of the So-St field. This is not the same as the absorber operating hours because the So-St network operates based on solar availability. We demonstrate a useful protocol to work out So-St operating hours. First, we collect the *SHF* distribution for the Sydney location on an hourly basis normalised per metre length of the So-St tube at the specified diameter and the collector aperture width (Table 20). The solar energy fluctuates significantly between a minimum of 0 and a maximum of 4.2 kW/m as shown in Figure 94. Hence, the hourly solvent flowrate to the SCF will vary depending on the *SHF* availability, while the design protocol will need a nominal flowrate. As a result, the nominal *SHF* value input needs to be approximated as a constant value. The motivation behind our assumption of a constant *SHF* is because we want to evaluate the potential design/s in the design optimisation step and using a constant *SHF* is a necessary step to speed up the optimisation process. Once we shortlist the good designs, we then carry out the dynamic hourly *SHF* integration to refine the design specification. We decided to pick the average *SHF* value for the whole year of solar irradiance, which is about ~1 kW/m (ignoring 0 kW/m values where the operation in the So-St field will seize). The cumulative *SHF* obtainable per year for Sydney case-study is found to be 4,181 kWh/m. Accordingly, the total equivalent So-St operating hours at the nominal solvent flowrate could be computed as follows:

$$H_{So-St} = \frac{Q_{solar}}{q_{solar}} = \frac{4181}{1} = 4181 \frac{hr}{year} \qquad \textit{Eq. 44}$$

Where $Q_{solar}$ (kWh/m/year) is the annual cumulative solar energy per one metre of So-St tube length; $q_{solar}$ (kW/m) is the average solar power in a year; $H_{So-St}$ (hour/year) is the total So-St field operating hours at nominal conditions in a year; the subscript 'solar' and 'So-St' relate to the solar energy and So-St field, respectively. The above calculation means that if we use solar power of 1 kW/m for the total 4,181 hrs, the cumulative energy will be 4,181 kWh/m, exactly the same as the value calculated by hourly integration. Knowing the total operating hours, we can calculate the nominal rich solvent flowrate to the So-St field as follows:

$$m_{so-st} = \frac{M_{rich}}{H_{so-st}} = \frac{25.2 x 10^6}{4181} = 6,027 \; tonne/hr \qquad Eq. \; 45$$

The above solvent flowrate would be used to determine how many parallel So-St modules are required. For example, if one So-St module can regenerate 4.9 tonnes/h of rich solvent, the total modules can be determined to be 1,230. This example demonstrates a quick back-of-the-envelope calculation to give a ballpark design specification for a So-St field.

## 6.2.2  Estimating nominal pressure-drop

After knowing the nominal rich solvent flowrate for the entire So-St field, we need to work out the solvent flow per So-St module. In other words, we need to determine the nominal pressure-drop. This is because the nominal pressure-drop would eventually determine the solvent flowrate per So-St module. This is the next critical design decision, because if the nominal pressure-drop is chosen near the maximum allowable pressure-drop, the So-St module will not be able to handle extra flowrate during process control. Therefore, one must select the nominal pressure-drop with a reasonable margin below the maximum allowable pressure-drop. This means that one needs to over-design the So-St module to account for this margin in pressure-drop.

In this work, the solvent enters the So-St field at a pressure value of 2 bar. Theoretically, the maximum allowable pressure-drop can be 1 bar before the ambient air has a chance to leak into the system. Conservatively, we chose the maximum allowable pressure-drop of 0.5 bar. To work out the nominal pressure-drop, we have calculated the velocity ratio between the nominal and maximum value of the *SHF*. This is because the pressure-drop ratio is roughly proportional to the square of the velocity ratio [83]. The solvent velocity ratio can be estimated from the *SHF* ratio as shown in Figure 104-A, which reveals the velocity ratio (i.e. flow ratio) has almost a linear relationship with the *SHF* ratio as a result of the lean loading control action. For example, if the *SHF* ratio increases from 1 to 2 (kW/m), the control action increases the rich solvent flowrate per So-St module from 10 to 20 (tonnes/h). This equivalent to when the *SHF* ratio is 2 (on the x axis), the flow ratio is 2 (on the y axis). The nominal *SHF* is 1 kW/m and the maximum usable *SHF* was chosen to be 2.5 kW/m based on the utilisation curve shown in  Figure 104-B. We chose the maximum flux to be 2.5 kW/m because above this value, the utilisation percentage does not increase significantly, while further over-designing the So-St network would eventually adversely impact the economics of the project. When the actual *SHF* is above that maximum value, the excess amount needs to be defocused. The solar energy utilisation is a function of the maximum usable *SHF*. This utilisation curve is determined by calculating hourly *SHF* and considering the percentage of solar energy needed to be defocused throughout the year per specification. For example, if the maximum solar flux is 2.5 kW/m and the real time *SHF* is 3 kW/m, the excess power (3 – 2.5 = 0.5 kW/m) will be dumped. Accordingly, we calculate the design pressure-drop value as per the following steps:

$$\frac{v_{design}}{v_{max}} = \frac{q_{solar,design}}{q_{solar,max}} = \frac{1}{2.5} \qquad \text{Eq. 46}$$

$$\frac{P_{drop,design}}{P_{drop,max}} = \left(\frac{v_{design}}{v_{max}}\right)^2 = \left(\frac{1}{2.5}\right)^2 \qquad \text{Eq. 47}$$

$$\boldsymbol{P_{drop,design}} = \boldsymbol{P_{drop,max}} * \left(\frac{1}{2.5}\right)^2 = \boldsymbol{0.5} * \left(\frac{1}{2.5}\right)^2 = \boldsymbol{0.08\ bar} \qquad \text{Eq. 48}$$

Where $v$ is the solvent velocity (m/s); $P_{drop}$ is the pressure-drop (bar); and Subscript '*design*' and '*max*' indicates the design and maximum operating condition, respectively. Based on the above, the nominal pressure-drop is 0.08 bar (±0.02), with the tolerance range used to account for Aspen® model solver tolerance.



**(A)**                                                                       **(B)**
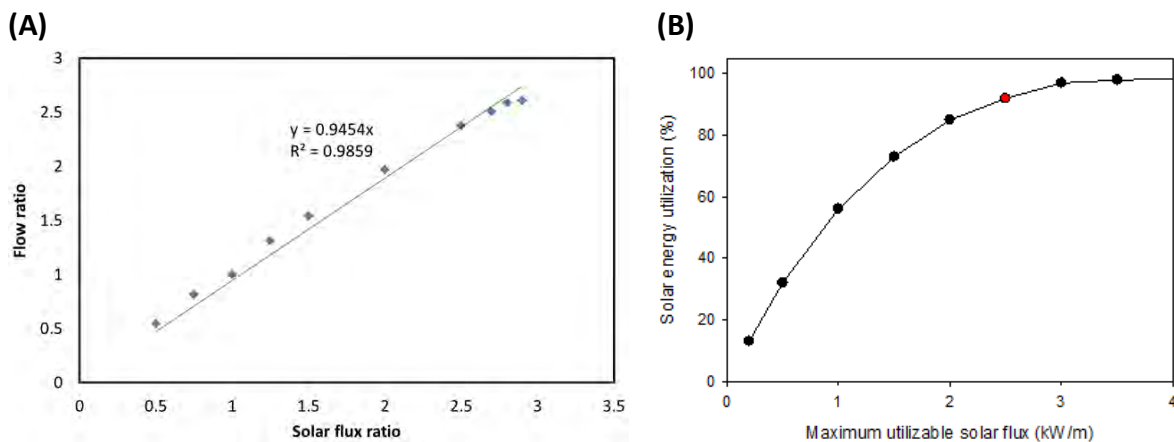
Figure 104: (A) Normalised solvent flow and *SHF* when lean loading is controlled at 0.23 (control strategy I), and (B) solar utilisation curve.

## 6.2.3 Generating a design database

After knowing the nominal rich solvent flowrate, we can use the Aspen® model to calculate the number of parallel So-St modules, the subsequent segments per one So-St module and the length per each segment as shown in Figure 105. As there is an unlimited combination of So-St field designs (*n* x *m* x *L*), we decided to generate a database of equivalent designs. This database could be used together with 'look-up' algorithm to search for a particular design that meets specified criteria (e.g. segment length must be less than 50 m). This could be done with the Aspen® goal-seek algorithm.

We have specified the design must result in a *LLV* of 0.23. The manipulated variables are the total number of So-St modules, number of segments per module (3, 6, 9, 12 and 15) and the length of each segment, respectively. We chose an increment of three modules as an initial educated starting point to probe the trend in the design performance variation. Later results

in this work show this incremental value is sufficient to reveal the performance trend. These segment numbers were found to be sufficient for generating a representative sample in the unlimited design space. If one finds none of the designs match the design requirements (e.g. energy demand metric), the database can be used to find an 'approximate' design and the Aspen® model can further refine the design parameters for better matching. The total So-St modules variable is replaced with solvent velocity in the first segment due to the Aspen® model input requirement. Once we know the solvent velocity, we can work out the flowrate per a So-St module and the total number of parallel modules using the calculated 6,027 tonnes/h nominal flowrate (*Eq. 45*). As a result, if the rich solvent flow changes, one can still reuse the database we reported here, but needs to update the total modules as follows:

$$n = \frac{m_{so-st}}{v_{design} * \rho_{solvent} * A_{so-st}}$$
*Eq. 49*

Where $\rho_{solvent}$ is the rich solvent density (kg/m$^3$); and $A_{so-st}$ is the cross-section area of the So-St tube (m$^2$).
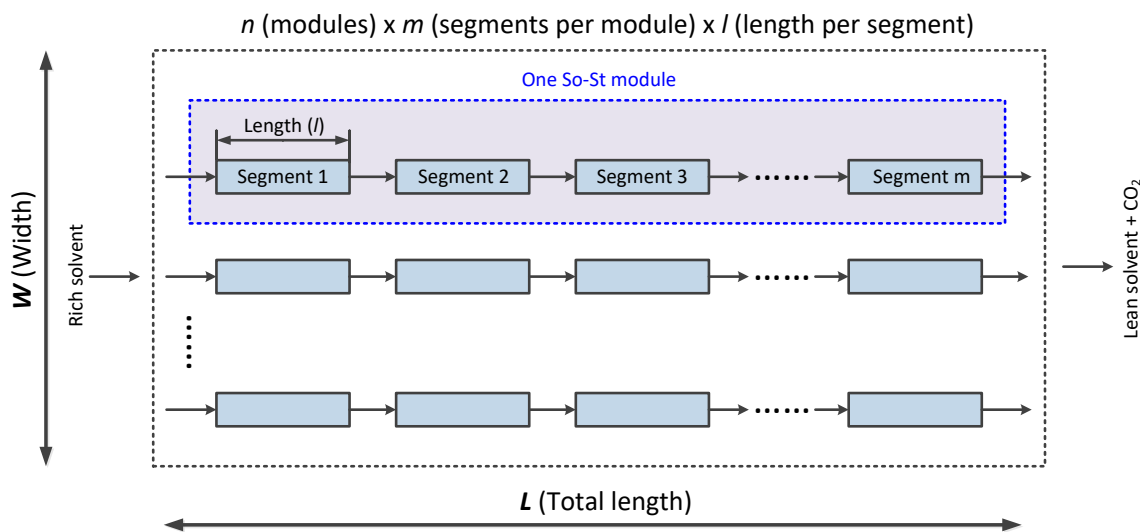


**Figure 105: So-St field design parameters.**

This case-study has resulted in 47 different designs mostly with a tolerable pressure-drop, but differing by physical and/or performance parameters. The full details of these 47 designs are presented in Table 21. Figure 106 categorises these designs based on the solvent velocity variation at the entrance of the SCF and relatively illustrates the physical and performance trends classified by the number of segments (*m*) per So-St module. Notably, the number of segments inherently represents the number of vent-points to release the $CO_2$ and reinitiate the nominal pressure for the next segment to maintain a consistent $CO_2$ desorption driving force. As illustrated in Figure 26, each So-St segment is theoretically modelled in Aspen Plus® by a combination of a pipe to calculate the pressure-drop, a flash drum to separate the gas/vapour phase from the liquid, and a pump to restore the pressure to the nominal value before entering the next segment.
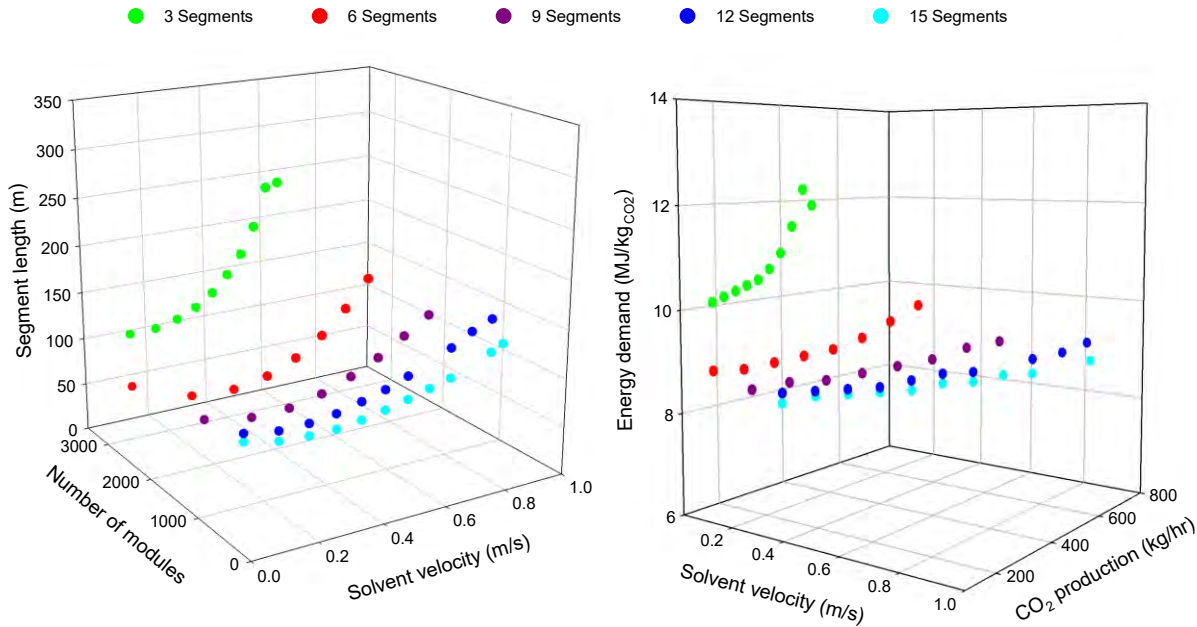
**Figure 106: Physical (left) and performance (right) parameters of different designs based on the solvent velocity at the SCF entry and categorised by the number of segments per So-St module.**

For each number of segments, there will be at least one design that meets the pressure-drop constraint. This can be seen in Figure 107, where if we draw a horizontal line at a constant pressure-drop, that line will intercept the pressure-drop line for each number of segments. In other words, there are different combinations of velocity and number of segments, which all result in the same pressure-drop. Other designs are reported for general use because the pressure-drop constraint is case-by-case design specific. For example, later experimental work might reveal the maximum allowable pressure-drop can be higher than 0.5 bar, which means we can design with higher nominal pressure-drop. Among the seven potential designs coloured in bold red in Table 21, we can compare the energy demand to filter good designs only. The energy demand accounts for the total So-St tube length and the $CO_2$ productivity.
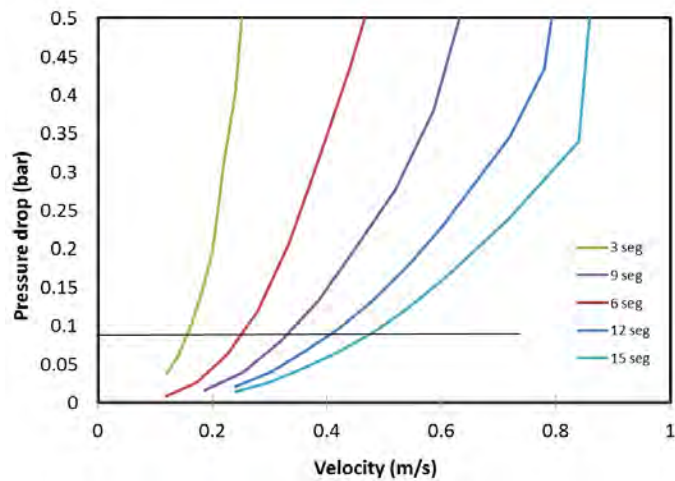


**Figure 107: Pressure-drop as a function of velocity and number of segments.**

Based on energy demand category in Table 21, the optimum designs would be 40 or 41, because they have the lowest energy demand. We should emphasise that we used the energy demand as a 'design filter'. There are other useful filters that may suggest an alternative design other than the energy demand filter. The motivation behind this design filter search is that the energy demand of designs 13, 21, 29, 30, 40 and 41 is very similar. Thus, we want to provide more advanced filters aiming to help designers sort out 'good' and 'bad' designs more effectively. We discuss these filters in the next subsections. It is possible to mix and match different filters for determining the optimum design given a design database input.

**Table 21: Design database (lean solvent loading of 0.23).**

| Design | Velocity (m/s) | Total modules $n$ | Number of segments $m$ | Segment length in metre $l$ | Maximum pressure-drop (bar) | $CO_2$ production (kg/hr) | Energy demand (MJ/kg$_{CO2}$) |
|---|---|---|---|---|---|---|---|
| 1 | 0.120 | 3277 | 3 | 104 | 0.04 | 110 | 10.2 |
| 2 | 0.140 | 2808 | 3 | 123 | 0.06 | 128 | 10.3 |
| **3** | **0.160** | **2457** | **3** | **142** | **0.09** | **147** | **10.4** |
| 4 | 0.180 | 2184 | 3 | 161 | 0.14 | 165 | 10.5 |
| 5 | 0.200 | 1966 | 3 | 181 | 0.20 | 184 | 10.6 |
| 6 | 0.220 | 1787 | 3 | 203 | 0.31 | 202 | 10.8 |
| 7 | 0.240 | 1638 | 3 | 226 | 0.40 | 220 | 11.1 |
| 8 | 0.260 | 1512 | 3 | 255 | 0.57 | 239 | 11.6 |
| 9 | 0.280 | 1404 | 3 | 294 | 0.74 | 257 | 12.3 |
| 10 | 0.300 | 1311 | 3 | 300 | 0.89 | 269 | 12.0 |
| 11 | 0.120 | 3277 | 6 | 46 | 0.01 | 110 | 8.9 |
| 12 | 0.173 | 2268 | 6 | 66 | 0.03 | 159 | 8.9 |
| **13** | **0.227** | **1735** | **6** | **87** | **0.06** | **208** | **9.0** |
| 14 | 0.280 | 1404 | 6 | 108 | 0.12 | 257 | 9.1 |
| 15 | 0.333 | 1180 | 6 | 130 | 0.21 | 306 | 9.2 |
| 16 | 0.387 | 1017 | 6 | 154 | 0.32 | 355 | 9.4 |
| 17 | 0.440 | 894 | 6 | 181 | 0.43 | 404 | 9.7 |
| 18 | 0.493 | 797 | 6 | 210 | 0.57 | 452 | 10.0 |
| 19 | 0.187 | 2106 | 9 | 45 | 0.02 | 171 | 8.5 |
| 20 | 0.253 | 1552 | 9 | 62 | 0.04 | 233 | 8.6 |
| **21** | **0.320** | **1229** | **9** | **78** | **0.08** | **294** | **8.6** |
| 22 | 0.387 | 1017 | 9 | 95 | 0.13 | 355 | 8.7 |
| 23 | 0.453 | 867 | 9 | 113 | 0.20 | 416 | 8.8 |
| 24 | 0.520 | 756 | 9 | 131 | 0.28 | 477 | 8.9 |
| 25 | 0.587 | 670 | 9 | 151 | 0.38 | 539 | 9.1 |
| 26 | 0.653 | 602 | 9 | 170 | 0.56 | 598 | 9.2 |
| 27 | 0.240 | 1638 | 12 | 43 | 0.02 | 221 | 8.4 |
| 28 | 0.300 | 1311 | 12 | 53 | 0.04 | 275 | 8.4 |
| **29** | **0.360** | **1092** | **12** | **64** | **0.07** | **330** | **8.4** |
| **30** | **0.420** | **936** | **12** | **75** | **0.10** | **385** | **8.4** |

| Design | Velocity (m/s) | Total modules *n* | Number of segments *m* | Segment length in metre *l* | Maximum pressure-drop (bar) | $CO_2$ production (kg/hr) | Energy demand (MJ/kg$_{CO2}$) |
|---|---|---|---|---|---|---|---|
| 31 | 0.480 | 819 | 12 | 87 | 0.13 | 440 | 8.5 |
| 32 | 0.540 | 728 | 12 | 98 | 0.18 | 496 | 8.6 |
| 33 | 0.600 | 655 | 12 | 110 | 0.23 | 551 | 8.6 |
| 34 | 0.720 | 546 | 12 | 134 | 0.35 | 660 | 8.8 |
| 35 | 0.780 | 504 | 12 | 148 | 0.43 | 717 | 8.9 |
| 36 | 0.840 | 468 | 12 | 158 | 0.75 | 753 | 9.1 |
| 37 | 0.240 | 1638 | 15 | 34 | 0.01 | 220 | 8.2 |
| 38 | 0.300 | 1311 | 15 | 42 | 0.03 | 276 | 8.3 |
| 39 | 0.360 | 1092 | 15 | 51 | 0.04 | 331 | 8.3 |
| **40** | **0.420** | **936** | **15** | **59** | **0.07** | **385** | **8.3** |
| **41** | **0.480** | **819** | **15** | **68** | **0.09** | **441** | **8.3** |
| 42 | 0.540 | 728 | 15 | 77 | 0.12 | 496 | 8.4 |
| 43 | 0.600 | 655 | 15 | 86 | 0.16 | 551 | 8.4 |
| 44 | 0.660 | 596 | 15 | 95 | 0.20 | 606 | 8.5 |
| 45 | 0.720 | 546 | 15 | 103 | 0.24 | 659 | 8.5 |
| 46 | 0.840 | 468 | 15 | 124 | 0.34 | 770 | 8.7 |
| 47 | 0.876 | 449 | 15 | 131 | 0.65 | 807 | 8.7 |

## Design selection filter 1 – *W: L* ratio

We have used energy demand as a selection criterion to choose the good designs. We discuss here another design selection filter that might be applicable in specific circumstances. For each design listed in Table 21, we could calculate the length (based on the total So-St modules length that consists of a number of subsequent segments) and the width (based on the total parallel modules) and compute a new metric 'width to length' ratio (*W:L* ratio). The definition of this ratio is explained in Figure 108, which calculates the width (*W*) and the length (*L*) based on the number of modules, segments and including spacings. Although there are numerous possible designs, we list only the 47 designs reported Table 21 to approximate the entire design space within the sensitised range of the key variables (e.g. number of segments). These 47 designs provide us with 47 data points for the *W:L* ratio metric. We plot them as a function of solvent velocity as shown in Figure 109. Interestingly, the *W:L* ratio metric varies significantly as a function of solvent velocity, but independently from the number of segments. This might be because the magnitude of changes caused by the number of segments is significantly less than that by the solvent velocity. Hence, there are still small variations between the data points at the same velocity but different number of segments. Figure 109 is a useful plot to immediately inform us about the SCF size ratio, which might be a design constraint. For example, if an existing area of land is used for a SCF, and it has *W:L* ratio of 20, this means the velocity must be 0.36 m/s (calculated from the correlation between all data points shown in Figure 109). Applying this to the previous design selection, an

acceptable design would be 29 (21), instead of 40 or 41, which have the lowest energy demand. If there is no constraint on the *W:L* ratio, we can skip this design filter and move to the next design filter we will discuss.
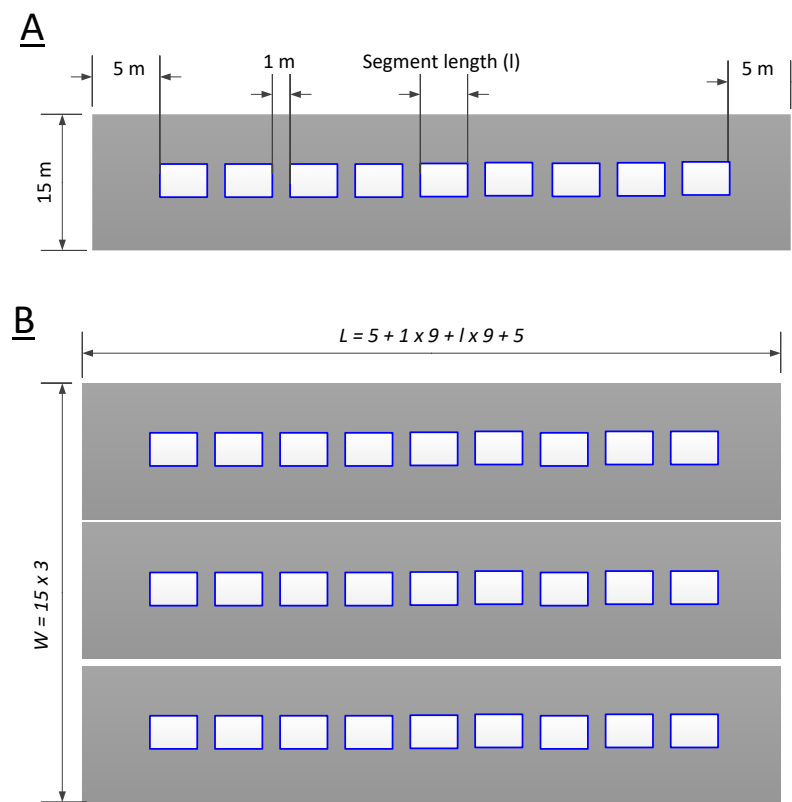


**Figure 108: SCF size calculation for a nine-segment module design. A specific length is considered for segment spacing and overall So-St module margin.**
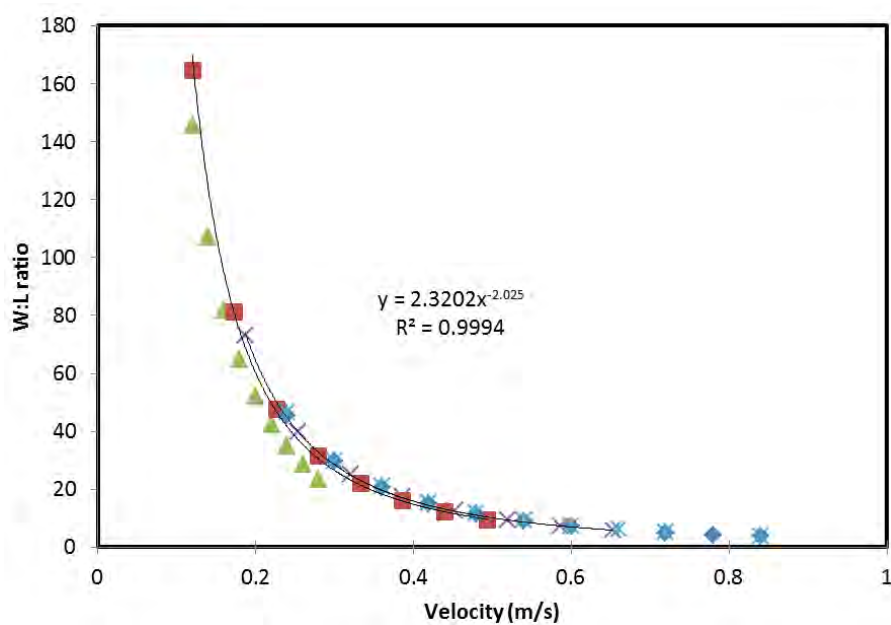


**Figure 109: SCF width-to-length ratio as a function of solvent velocity. Each data point is a design point adopted from Table 21.**

**Design selection filter 2 – Number of pumps**

This design selection filter is an 'upgraded' version of the energy demand metric. In this design filter, we take into account the number of pumps required. The motivation behind this analysis is that the lowest energy demand design might require more pumps as compared with the highest energy demand design. An example of this concept can be seen in Table 21. Design 3 has a higher energy demand than design 41, but requires only 7,371 (2,457 x 3) pumps as compared with 12,285 (819 x 15) pumps for 41. This will ultimately affect the SCF sizing and the pumping requirement when calculating the cost metric. This cost metric reports the normalised cost for a particular design in terms of monetary units per one tonne of the captured $CO_2$. In this subsection, we do not aim to finalise the numeric value of the cost metric, but intend to develop a preliminary formulation and discuss how it would be useful as a design filter. Assuming '$a$' is the cost of SCF per m$^2$, including land, solar collector and So-St tube cost. By using '$a$', we can calculate the total SCF cost for other designs given a specific land area. Recall the land area can be calculated as shown in Figure 108-B using the value of $n$ (the number of So-St modules), $m$ (the number of segments per module) and $l$ (the length per segment) as reported in Table 21. Assuming '$b$' is the cost per pump, we can calculate the total pumping cost by multiplying $b$ by the number of pumps. The absolute value of variables '$a$' and '$b$' would be determined next. In the current subsection, we only perform simulations using the relative value of '$a$' and '$b$'. The data reported from Table 21 could then be used to calculate the cost metric. For example, design 3 has a total area of 16,576,977 m$^2$, and the cost of the SCF would be 16,576,977 multiplied by $a$. The number of pumps is 7,371; the pump cost would be 7371 multiplied by $b$. The total capital cost can then be calculated as follows:

$$Cost = 16,576,977\,a + 7,371\,b \qquad\qquad Eq.\ 50$$

From the cost function, we can see the land component has a very large constant multiplied by '$a$' while the pump component has a very small constant multiplied by '$b$'. We have sensitised relative combinations of '$a$' and '$b$' numeric values. The results are shown in Figure 110. We plotted the normalised cost against pressure-drop for each number of segments. Pressure-drop is chosen for the $x$ axis because not all number of segments have the same solvent velocity range. For example, in Table 21, the 3-segment design (10) has a maximum solvent velocity of 0.3 m/s, whereas design 15 has a maximum solvent velocity of 0.876 m/s (design 47). Hence, using the pressure-drop at the $x$ axis makes the comparisons between the data point more consistent. Figure 110 suggests that only when '$b$' has a value of three orders of magnitude higher than '$a$', the pump cost component would become a major factor. If one selects the design with nominal pressure-drop of 0.1 bar with '$b$' equal to 1,000, the number of segments should be 6 to minimise the cost whereas if '$b$' equals 100, the number of segments can either be 9, 12 or 15 because they would have similar cost.
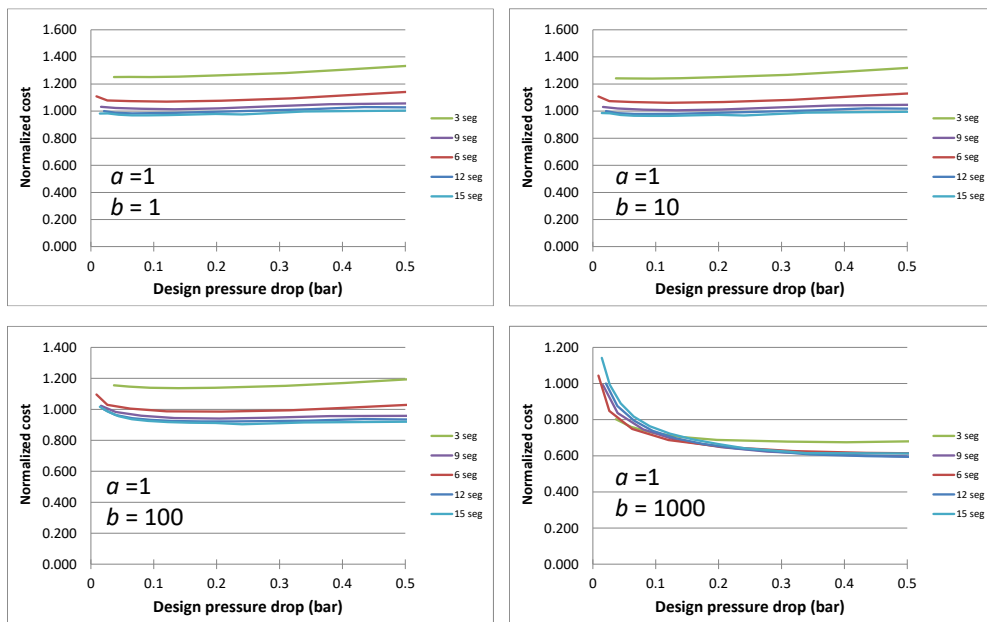
**Figure 110: Normalised cost for different values of '*a*' and '*b*'.**

Consequently, we have narrowed down some good designs (where the pressure-drop value fall within a desired range) in the database and plotted them in Figure 111 as a function of the number of segments. The 'y' axis is the normalised cost when either considering only the land or the pump costs, respectively, to demonstrate the two extremes of the cost calculation. Depending on the magnitude of the costs for the land and pump, the result will differ substantially. For example, if pump cost is the dominant factor, fewer segments are preferred because it results in smaller cost (yellow dots), and vice versa if the land cost is the dominant factor (black dots). Another observation is that the plateau occurs when the number of segments exceeds 10. This means the sensitised range for the number of segments (3 to 15) is representative because it covers up to the plateau region of the Figure 111. In other words, sensitising the number of segments at more than 15 will most likely not result in a significant impact on the normalised cost.
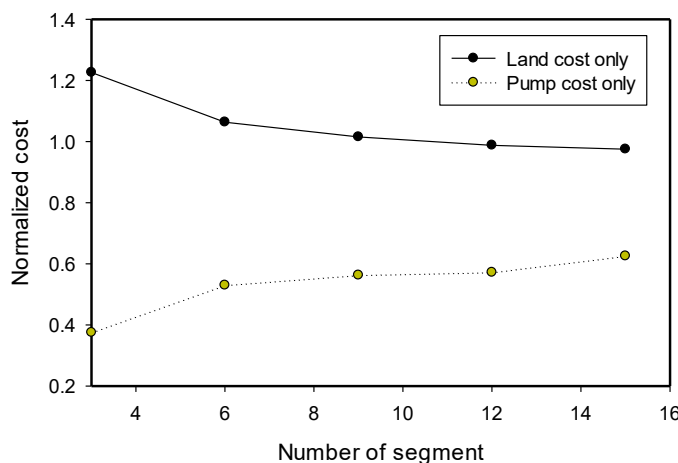


**Figure 111: Hypothetical normalised costs for accepted designs with different number of segments.**

Above, we have presented detailed design calculations and some design selection filters, to aid fellow designers in decision-making process to sort out good and bad designs. We have narrowed the list to seven potential designs listed in Table 22. The optimum design would largely depend on which filter is mostly applicable. We have arrived at an inclusive cost function to aid our design selection and the techno-economic analysis in Chapter 7. Figure 112 summarises the design protocol in a chart form to facilitate its application. There are two major components of the design procedure: design generation and design selection. In the former, one can trail our reported calculations to determine the value for key variables (e.g. rich solvent regeneration requirement per hour, etc.). These values are required for Aspen® model inputs to seek potential designs.
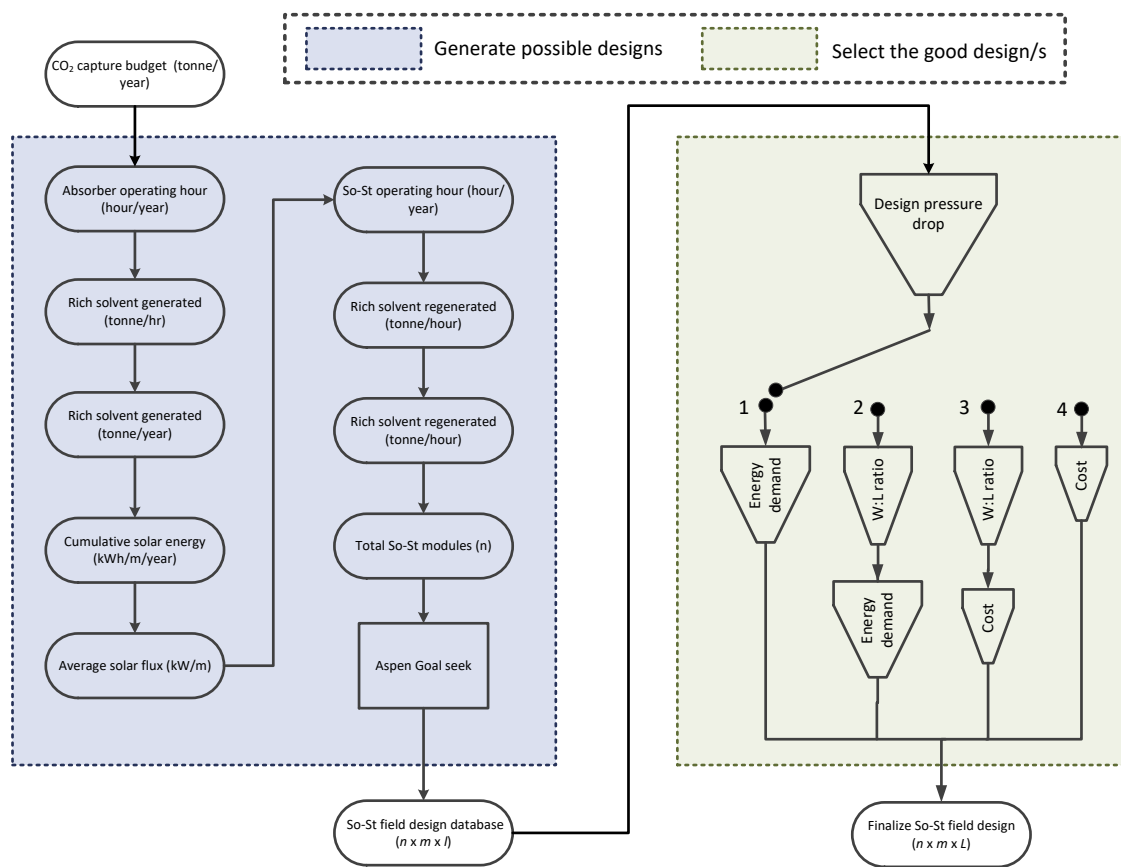


**Figure 112: Summary of preliminary design protocol. The final design would need a rigorous techno-economic analysis as reported in Chapter 7.**

After we generate a design database, we need to refine and select good designs. Based on Figure 112, there are currently four design selection paths. For example, path 1 guides selection based on pressure-drop constraint and comparing energy demand. We think only path 3 and 4 (which involve the cost) would provide a tangible meaning of the overall optimum design since they consider techno-economic aspects. The other two paths, which use the energy demand filter, are more suitable for preliminary and early stage design formulations. This is because the energy demand only considers the solar energy input that is essentially reflected onto the solar collector aperture area, but not other key components (e.g. pump, spacing).

To this point, we have identified a few potential designs, but not an optimum one. This is because we need to incorporate the economic result from the techno-economic analysis. In addition, there is no predetermined requirement on the *W:L* ratio of the SCF. Applying the design pressure-drop filter, some potential designs are summarised in Table 22. As a reference point, we calculated the normalised cost, but have ignored the pump cost at this stage. In Chapter 7, we can update the normalised cost to account for the pump cost and arrive at a realistic optimum design.

**Table 22: Nominated designs (design in bold red is the example used later for real-time simulation to carry out sizing for solar storage tanks).**

| Design number | Velocity (m/s) | Number of modules *n* | Number of segment *m* | Segment length *l* (m) | Pressure-drop (bar) | W:L ratio | Normalised cost [*] |
|---|---|---|---|---|---|---|---|
| 3 | 0.160 | 2457 | 3 | 142 | 0.09 | 82 | 1.3 |
| 13 | 0.227 | 1735 | 6 | 87 | 0.06 | 48 | 1.1 |
| **21** | **0.320** | **1229** | **9** | **78** | **0.08** | **25** | **1** |
| 29 | 0.360 | 1092 | 12 | 64 | 0.07 | 21 | 0.98 |
| 30 | 0.420 | 936 | 12 | 75 | 0.10 | 15 | 0.98 |
| 40 | 0.420 | 936 | 15 | 59 | 0.07 | 15 | 0.97 |
| 41 | 0.480 | 819 | 15 | 68 | 0.09 | 12 | 0.97 |

*[*] Irrespective of the actual pump cost.*

## 6.2.4  Layout optimisation

We have described the design protocol and arrived with several potential good designs as shown in Table 22. We have hypothetically calculated the normalised cost and showed there is an optimum cost of the design; however, the intrinsic *W:L* ratio could be undesirable. For example, design 41 is the hypothetical optimum design, but it has *W:L* ratio of 12, which means the land shape must have the matching size ratio. In some cases, this requirement can be a bottleneck, limiting the design flexibility. In this subsection, we describe an approach to mitigate the *W:L* ratio constraint. The reason for not including this remedy in the design protocol above is because it is not a design-critical parameter, and its effect only emerges when the land size ratio would be a constraint. If one wants to use the calculation method we described in this section, filter path 1 or 4 (Figure 112) would have more significance in the selection criteria of the optimum design. We have demonstrated the concept of this mitigation approach in Figure 113. It can be seen that the current *W:L* ratio is calculated based on a single SCF (A). This could be used as a reference point to optimise the multi solar subfields layout (as shown in B, two sub-fields), which allows one to manipulate the overall width and length of the main SCF. This helps in designing the So-St network to meet the size ratio constraint of the SCF. However, caution must be exercised in subdividing the SCF to multi subfields in terms of the nominal pressure range in the headers of the subfields [29]. The *W:L* ratio with multi subfields designs can be calculated as a function of the subfield (*a*):

$$WL_{ratio,multi} \cong \frac{\frac{W}{a}}{L*a} = \frac{W}{L*a^2} = \frac{WL_{ratio,single}}{a^2} \qquad\qquad Eq.\ 51$$

Where $WL$ is the width to length ratio; the subscript '*multi*' and '*single*' indicates multi solar field and a single solar sub-field layout; $a$ is the number of sub-fields; $W$ (m) and $L$ (m) are the width and length of a single solar sub-field layout as shown in Figure 113-A. For example, if one wants to make the ratio of the nine segments design (shown in Table 22) equal to 1, the number of subfields would need to be five using the above formula given ($a^2 = 5^2 = 25$) and ($WL_{ratio,single} = 25$). Given the total number of So-St modules is 1,229, the number of modules in each sub-field will be $\frac{1129}{5} \cong 249$ modules. Using this formula, one can expand the design protocol to output different *W:L* ratio layouts given the number of possible sub-fields.
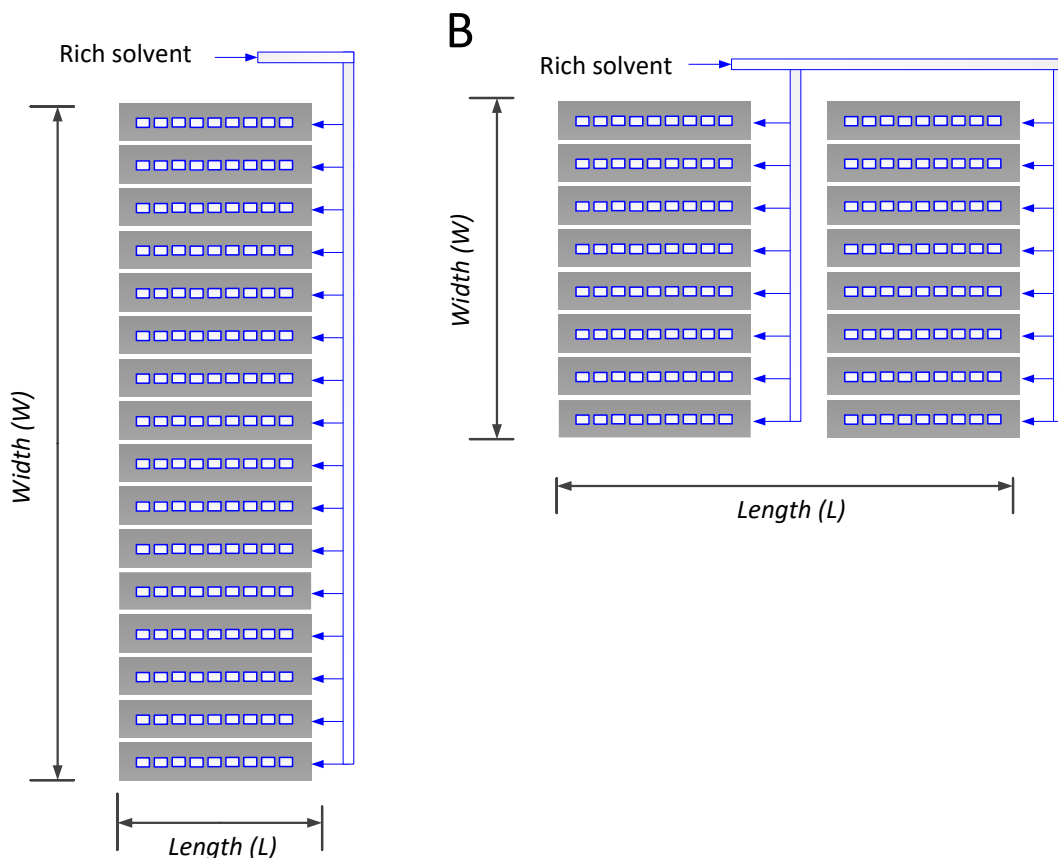


**Figure 113: Two different layouts for arranging the same number of So-St modules, (A) a single SCF, and (B) multiple SCFs.**

## 6.2.5    Reduced model simulation

To simulate the superstructure for the whole year at reasonable real-time intervals, a reduced model was developed to assess the performance of critical variables, while other variables were kept constant with an assumption that there is a control loop to maintain them at a set-point as reported in Table 23.

**Table 23: Variables that are not changed during one-year simulations.**

| Variable description | Value | How to keep at a constant value |
|---|---|---|
| Flue gas flowrate | 1,081 tonnes/hour | Fixed flowrate [a] |
| Flue gas $CO_2$ content | 200 tonnes/hour | Fixed flowrate [b] |
| Lean solvent temperature to the absorber | 40 °C | Temperature control |
| Solvent composition | 30 *wt*% MEA | Via water and MEA balance delivered by make-up system |
| $CO_2$ product purity | 99 *wt*% | Temperature control |
| $CO_2$ capture rate at the absorber | 90% | Set by simulation |
| Rich loading out of the absorber [c] | 0.49 | Set by simulation |

[a] *It is assumed only 34% of the flue gas at the power plant's full capacity is processed in the PCC. When the electricity demand drops to 34%, the reference PCC would still operate at full capacity [84].*
[b] *Assuming the carbon composition in the feed coal is constant, e.g. the coal is extracted from the same coal mine.*
[c] *If the flue gas flow is not changed, the rich loading in the absorber is found to be ~0.49 when the capture rate is controlled at 90%.*

The model was developed in Aspen Plus® and packed into executable correlations in Microsoft Excel (Microsoft Corporation, USA). This model package comprises three sub-models shown in Figure 114. The overall outputs are the cumulative storage volume for lean and rich solvents, which can be used to assess the solvent availability at both terminals of the solvent cycle to ensure operational continuity and sustainability. For example, if the final lean solvent storage level ($SL_L$) at the end of the year is noticeably less than at the beginning of the year, the lean storage level will be depleted in the next year's operation and may drain at winter peak times. In the absorber model, the capture rate is controlled at 90% (Table 23). Hence, by knowing the $LLV$ at the absorber inlet, the required lean solvent flowrate and the resulting rich solvent flowrate can be calculated. Other variables that could affect absorber operation (e.g. flue gas flowrate) are kept constant, and thus excluded from this Aspen® goal-seek problem to reduce computation power demand. The Aspen® goal-seek results are correlated into the following equation using polynomial regression in Excel:

$$LTA = 1407 * exp(2.747 * LLV) + 3.862 * expt(18.63 * LLV) \qquad Eq. 52$$

The rich flowrate can then theoretically be computed as follows:

$$ROA = LTA + Cap_{CO2} \qquad Eq. 53$$

Where the $LTA$ is the lean solvent flowrate to the absorber; the $LLV$ is the lean loading value; $ROA$ is the rich solvent flowrate out of the absorber; and $Cap_{CO2}$ is the $CO_2$ captured in the absorber as calculated by Aspen® model, respectively.
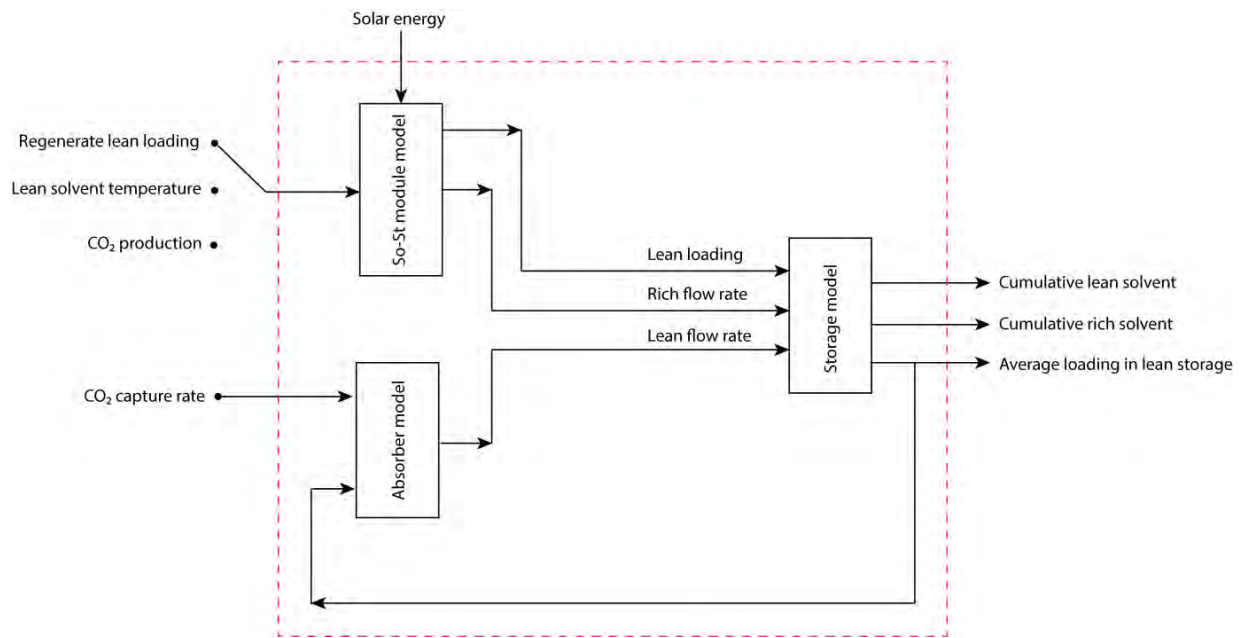
**Figure 114: Model structure for the whole plant. In the current work, the control strategy used in So-St sub-model is the lean loading set-point at a constant value of 0.23.**

In this case-study, the amount of $CO_2$ captured in the absorber is set at 180 tonnes/h; this comprises 90% of the $CO_2$ content of the flue gas stream. In real applications, the rich solvent flowrate would be less as a result of the water loss that often happens during the absorption process. However, it is assumed a water balance system always exists to compensate for the water losses. The rich solvent exits the absorber at a 0.49 loading value and does not change significantly with mild variation in the operation conditions in the absorber. Therefore, the rich solvent supplied to the So-St field has an approximate constant loading value of 0.49. The next sub-model is related to the So-St operation; another goal-seek algorithm is set in Aspen® to determine the required solvent flowrate to achieve a lean loading target of 0.23. To execute this sub-model in Excel, the goal-seek results are converted into polynomial correlations. It should be emphasised that these correlations are design-dependent and would be trend-fitted based on each design, respectively. For example, based on the polynomial regression for the adopted 21st design (Table 22), the following correlations are computed:

$$RTSCF = 5.142 * SHF^{0.8976}$$

*Eq. 54*

$$Prod_{CO2} = 0.0599 * RTSCF^{1.0006}$$

*Eq. 55*

Where the $RTSCF$ represents the rich solvent flowrate to the SCF; and $Prod_{CO2}$ is the amount of produced $CO_2$ out of the SCF. By solving these correlations for the whole year, the sizing of the solvent storage capacity (*SSC*) for both rich and lean solvents becomes a straightforward calculation.

## 6.3    Solvent storage capacity (*SSC*) sizing

To solve the operational inconsistency between the steady-state mode of the absorber and the dynamic mode in the SCF, typically two completely immiscible sets of SSTs must be sized. One is set to store excess rich solvent delivered by the absorbers when the solar radiation is poor/unavailable, and the other is set to store excess lean solvent when the SCF productivity is higher than the absorber demand. In sizing the *SSC*, the main objective is always to ensure adequate solvent availability throughout the year and to maintain the solvent level (*SL*) at 0<*SL*<100% of the *SSC*. Under-sizing the *SSC* would result in solvent overflow at some stage (i.e. in winters when rich solvent accumulates in the storage tanks because of the poor solar resources), while over-sizing the *SSC* would involve excessive capital cost, larger land area, and additional parasitic and maintenance expenses. Solvent storage construction and solvent inventory could be cost prohibitive, particularly for regions with a poor solar exposure rate and/or severe seasonal variation [29]. For lower solar multiples (e.g. *SM* =1), the number of above-the-ground SSTs is substantially high, which also would occupy a massive area of land and require a complex piping network. Accounting for the standardised American petroleum institute (API) tank sizes, the *SSC* can be optimised in-line with the *SM* value at the lowest economic footprint. In this section, the method for *SSC* sizing is conducted using the Aspen® model. For annual simulation, hourly timesteps are chosen to calculate the cumulative *SL* in the storage tanks. The cumulative rich solvent in the rich storage tank can be calculated as follows:

$$CRS_t = RF_{IN,storage} - RF_{OUT,storage} + CRS_{t-1}$$        *Eq. 56*

Where $CRS$ is the cumulative mass rich solvent stored in the storage tanks (tonnes); $RF$ is the flowrate of the rich solvent (tonnes/h); the subscripts '*IN*' and '*OUT*' indicate the inlet and outlet to the rich SST, respectively; the subscript '*t*' is the simulation timestep (hour). At any timestep, when the flowrate of the rich solvent exiting the absorber is larger than the flowrate to the SCF, a portion of that is directly delivered to the SCF and the balance is stored in the rich storage tank. This operation mode is called mode 1–A, and the mathematical presentation of this mode is expressed in *Eqs. 57 & 58*:

$$RF_{IN,storage} = RF_{OUT,absorber} - RF_{IN,SoSt}$$        *Eq. 57*

$$RF_{OUT,storage} = 0$$        *Eq. 58*

In this mode, the rich solvent volume in the rich solvent tank ($SSC_R$) will increase and the rich solvent level ($SL_R$) will rise. In mode 2–A, the rich solvent exiting the absorber is equal to the rich solvent required for the SCF at that timestep. In this mode, the solvent flowrate to or out of the $SSC_R$ will be nil and $SL_R$ will remain unchanged. The mathematical presentation of this mode is expressed in *Eqs. 59 & 60*:

$$RF_{IN,storage} = 0 \qquad\qquad\qquad\qquad\qquad \textit{Eq. 59}$$

$$RF_{OUT,storage} = 0 \qquad\qquad\qquad\qquad\qquad \textit{Eq. 60}$$

In mode 3–A, the rich solvent flowrate out of the absorber is less than the amount required by the SCF. In this case, the whole rich solvent exiting the absorber will be directly delivered to the SCF and the supplementary rich solvent is withdrawn from the $SSC_R$. Therefore, the rich solvent volume in the $SSC_R$ will decrease and $SL_R$ will decline. The mathematical presentation of this mode is expressed in *Eqs. 61 & 62*:

$$RF_{OUT,storage} = FR_{IN,SoSt} - FR_{OUT,absorber} \qquad\qquad \textit{Eq. 61}$$

$$RF_{IN,storage} = 0 \qquad\qquad\qquad\qquad\qquad \textit{Eq. 62}$$

Likewise, the cumulative solvent in the lean storage tanks ($SSC_L$) can be calculated as follows:

$$CLS_t = LF_{IN,storage} - LF_{OUT,storage} + CLS_{t-1} \qquad\qquad \textit{Eq. 63}$$

Where $CLS$ is the cumulative mass of lean solvent in the $SSC_L$ (tonne); and $LF$ is the lean solvent flow (tonne/hr). If the lean solvent flow required by the absorber is less than the lean solvent that is coming out from the SCF, the excess lean solvent will be stored in the $SSC_L$ for later use. This operation mode is called mode 1–B, and the mathematical presentation of this mode is expressed in *Eqs. 64 & 65*:

$$LF_{IN,storage} = LF_{OUT,SoSt} - LF_{IN,absorber} \qquad\qquad \textit{Eq. 64}$$

$$LF_{OUT,storage} = 0 \qquad\qquad\qquad\qquad\qquad \textit{Eq. 65}$$

If the lean solvent flow required by the absorber is equal to the lean solvent flow out from the SCF, then the whole amount of the lean solvent will be directly delivered to the absorber and no change will happen to the lean solvent level ($SL_L$) and the lean solvent volume in the $SSC_L$ will remain intact. This mode is called 2–B and the mathematical presentation of this mode is expressed in *Eqs. 66 & 67*:

$$LF_{OUT,storage} = 0 \qquad\qquad\qquad\qquad\qquad \textit{Eq. 66}$$

$$LF_{IN,storage} = 0 \qquad\qquad\qquad\qquad\qquad \textit{Eq. 67}$$

Similarly, if the lean solvent flow required by the absorber is larger than the lean solvent flow delivered from the SCF field, the balance will be maintained from the $SSC_L$ facility, and the mathematical presentation of this mode (mode 3–B) is expressed in *Eqs. 68 & 69*:

$$LF_{OUT,storage} = LF_{IN,absorber} - LF_{OUT,SoSt} \qquad \text{Eq. 68}$$

$$LF_{IN,storage} = 0 \qquad \text{Eq. 69}$$

At any simulation timestep, the cumulative mass of the lean and rich solvents is calculated. The solvent mass is then converted into volume using the density of the solvent at the storage temperature. From the Aspen® property database, the densities for the MEA solvent are 1,086 and 1,127 kg/m$^3$ for the lean (*LLV*= 0.23) and rich (*RLV*= 0.49) solvents, respectively. To compute the solvent level ($SL_L$ & $SL_R$) at any timestep, the solvent storage volumetric capacity (*SSC*), must be calculated using the density and the maximum value of the cumulative mass in each storage facility. The *SSC* for lean ($SSC_L$) and rich ($SSC_R$) storage will be slightly different in volume because they have dissimilar solvent densities. For practical and convenient design, the *SSC* is conservatively assumed equal to the maximum value between the lean and rich solvent storage. For example, if the lean storage is 12,000 m$^3$ and the rich storage is 12,100 m$^3$, the larger value is chosen for storage design. *Eqs. 70*, *71* and *72* mathematically present the calculation of *SSC* and *SL* for both lean and rich solvents at any timestep:

$$SSC = max \left( \frac{CRS_{max}}{\rho_{sol,L}}, \frac{CLS_{max}}{\rho_{sol,R}} \right) \qquad \text{Eq. 70}$$

$$SL_{L,t} = SL_{L,t-1} + \frac{(\dot{m}_{sol,abs,t} - \dot{m}_{sol,So-St,t})/\rho_{sol,L}}{SSC} * 100 \qquad \text{Eq. 71}$$

$$SL_{R,t} = SL_{R,t-1} + \frac{(\dot{m}_{sol,abs,t} - \dot{m}_{sol,So-St,t})/\rho_{sol,R}}{SSC} * 100 \qquad \text{Eq. 72}$$

Based on the annual $CO_2$ production budget (i.e. 1.5M tonne$_{CO2}$/y), the absorber does not need to operate continuously throughout the year because that will exceed the $CO_2$ production budget. Accordingly, the absorber can offer to stop operation for a period of time (i.e. for maintenance), while the SCF continues to catch-up on the accumulated solvent in the rich storage tank, which may allow a substantial reduction in the volume of the *SSC*. In this case-study, it is found that the absorber can safely stop for ~18 days for maintenance [29], while the So-St field continues to catchup on the process to reduce the cumulative stored solvent, therefore helping to reduce the size of the *SSC*. This stoppage period is likely to happen around winter when the rich solvent storage is reaching the peak level. At the beginning of the year, both storage facilities need to be prefilled to a certain level to ensure there is sufficient supply of the solvent for both terminals of the solvent cycle. The amount of the prefilled solvent needs to be optimised to ensure that the solvent in both storage facilities is not being dried-out or over-spilled in long-term operation. At any timestep, the *SL* is only allowed to fluctuate within 0%<*SL*<100% boundaries within a well-sized *SSC* for both solvents.

In this study, the *SSC* volume is optimised to only tolerate the *SL* fluctuating in between the two extremes of 0% and 100% of the *SSC*. In practical applications, a safety margin can also be added to the calculated *SSC*. Figure 115 shows a flowchart of the *SSC* sizing algorithm. It is an interactive procedure involving two main inputs: the storage tank's prefilled solvent mass and the total number of the So-St modules in the SCF. For hourly timesteps that have a *SHF* >0.5 kW/m (the minimum usable threshold for the lean loading control scenario) [85], the *SHF* value is used for calculating the solvent flowrate for both solvent cycle terminals: the absorber and the So-St field. These flowrates are then used for computing the cumulative solvent mass in both storage facilities and the *SL* in the storage. Then the *SHF* is updated for the next hourly timestep until reaching the end of the year. The hourly cumulative solvent is used to calculate two main metrics. The first metric calculates the solvent storage utilisation ratio (*SUR*) as a function of maximum and minimum *SL* values of the entire year. Basically, a good design aims to size the *SSC* in a way that brings the *SUR* closer to 100%. If the *SUR* is substantially lower than 100%, it means the solvent storage facility is oversized. The second metric addresses the break-even point (*BEP*) by comparing the starting *SL* vs the final *SL* (i.e. for a balanced operation, the final *SL* must be equal to the commencement *SL* to be qualified for continuous operation in next year). A *BEP* <1 means the storage system will overflow, while a *BEP* >1 means the storage system will be drained in the coming year(s) of operation. These two metrics are calculated in *Eqs. 73* & *74*. Ideally, the design is optimum only when the *SUR* value is 100% and the *BEP* value equals 1.

$$SUR = \frac{SL_{max} - SL_{min}}{SL_{max}} \qquad\qquad\qquad Eq.\ 73$$

$$BEP = \frac{SL|_{t=0}}{SL|_{t=T}} \qquad\qquad\qquad Eq.\ 74$$
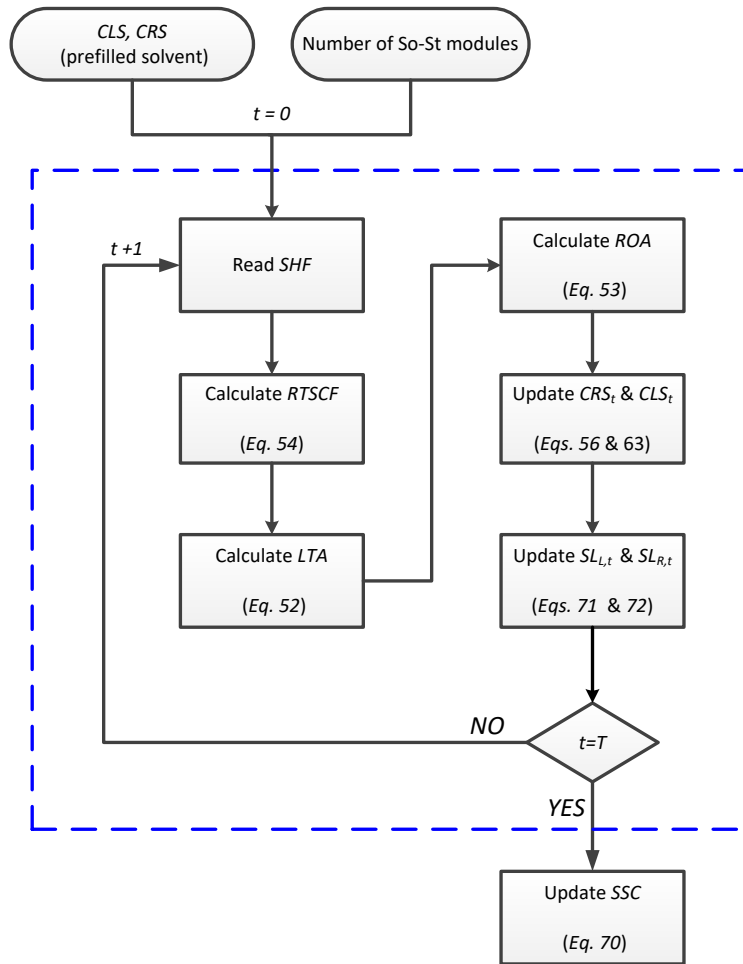
**Figure 115: The design protocol flowchart to determine the cumulative rich and lean solvents level under the CO₂ capture rate in the absorber controlled at 90% and the lean loading controlled at 0.23.**

In an ideal design, the sizing of the *SSC* must be synchronised with the SCF size and adopted *SM* value. Accordingly, the optimum design for the *SSC* is when the *SUR* value reaches 100% and the *BEP* value equals 1. It is found that the *SUR* and *BEP* values are mostly affected by the solvent prefill level and the number of the deployed So-St modules in the SCF (i.e. *SM* value) as demonstrated in Figure 116-A. It can be seen that varying the number of So-St modules deviates the *BEP* away from 1. This means increasing the number of So-St modules causes a mismatch in the *SL* values at the start and the end of the year. This mismatch is demonstrated by comparing the *SL_L* profile for the optimal number of modules (1,413 modules) *vs* a hypothetical test of 1,500 modules (Figure 116-B). The blue trend represents an ideal design, which shows the final *SL* almost equal to the starting *SL*. The black trend is an undesirable design, since the final *SL* is higher than the starting level. Additionally, the *SUR* value for the black trend is <1 because the *SL_min* value is visibly higher than zero. The low *SUR* is attributed to having excess So-St modules in the SCF, which are able to use more solar energy and regenerate more solvent beyond the instant absorber capacity. Hence for a specific *SM*, there is an optimal number of deployable So-St modules that results in a *BEP* equals to 1. If one either goes above or below this optimum, the final *SL* in the lean SST will be either higher or lower than the starting level, respectively.

The *SUR* value is also sensitised against the solvent prefill ratio as shown in Figure 116-C; increasing the prefill solvent mass reduces the use of the storage facility and vice versa. If the prefilled amount is higher, the $SL_{min}$ value will become larger than zero and the *SUR* will be lower as computed by *Eq. 73*. The *SUR* concept is demonstrated in Figure 116-D. The blue line is the ideal design, which reveals the $SL_L$ conveniently swings between 0% and 100% throughout the year, while the black line is the undesirable result because the *SL* never reaches 0% and, therefore, the *SUR* is <1. This means for a specific *SSC*, increasing the prefilled solvent above the optimum point results in less use of solvent storage. In other words, the solvent storage is needlessly over-sized. In summary, these results have shown that one needs to sensitise the solvent prefill percentage and the number of So-St modules to achieve an optimum solvent storage design.
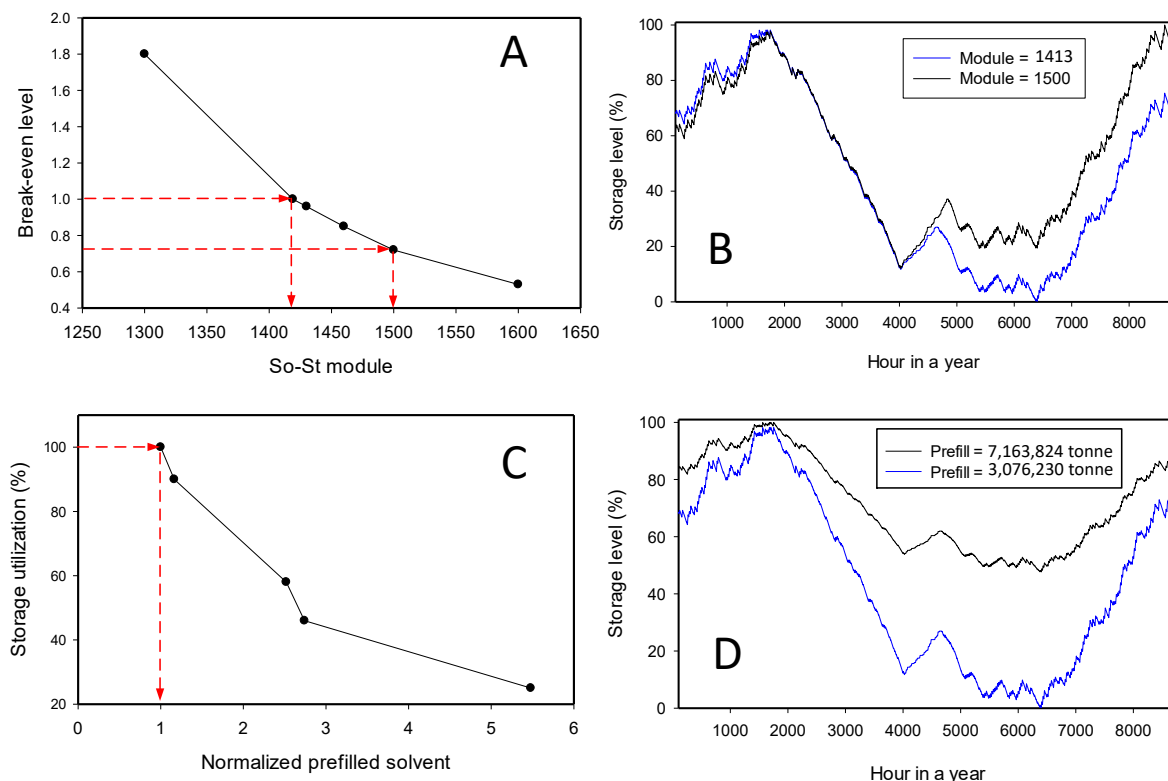


**Figure 116: (A) Sensitising the prefill percentage and the number of So-St modules to calculate the *BEP* when the *SUR* equals a 100%. (B) The SLL profile for a SCF consists of the optimal number of So-St modules (1413 modules) vs a hypothetical larger SCF of 1500 So-St modules. (C) The *SUR* trend when the *BEP* equals to 1. Note that, the prefilled solvent has been normalised against the nominal 3,076,230 tonne. (D) The SLL profile for the same number of So-St modules, but at different prefilled portions, the blue trend is for the nominal prefill, while the black trend represents a hypothetical doubled prefill solvent.**

The proposed design protocol initially estimates the number of required So-St modules, which can be used as an approximation input into the *SSC* sizing algorithm to reduce the computation demand when searching for an accurate SCF design. For example, in the 21st design (9-segment modules) in Table 22, it is found that the design protocol estimation for the number of So-St modules is 1,229, while the optimised number should be 1,413. So, the

design protocol in fact underestimates the So-St field by approximately 13%. This can be attributed to the constant *SHF* assumption that has been made in the design protocol. This estimate is not accurate but may be necessary as a starting point, because it is difficult to practically simulate a full-scale one-year operation for every single design. To limit the estimation uncertainty, one can determine a correction coefficient to the SCF sizing when using the design protocol.

Moreover, the total $CO_2$ production (or captured) per year is also affected by the number of assigned So-St modules in the SCF. For example, doubling the number of So-St modules essentially means doubling the $CO_2$ production. Therefore, it is reasonable to be concerned that changing the number of So-St modules only for the purpose of *SSC* optimisation might ultimately deviate the amount of $CO_2$ production per year away from the capture target (i.e. 1.5 M tonne$_{CO2}$/y). In fact, this will never be the case and the $CO_2$ production will always be 1.5 M tonne per year. This is because the *SSC* sizing is based on the rich solvent flow out from the absorber as indicated by the design protocol flow chart presented in Figure 115. This flowrate is back-calculated based on the 1.5M tonne$_{CO2}$ budget and it should not change during the *SSC* sizing calculation. If one unrealistically deploys a larger number of So-St modules, the availability of rich solvent for regeneration would be in deficit mostly in summer, and a portion of those So-St modules will need to be idle, otherwise the algorithm will return a negative SLR value. We also examined a number of *SSC* size reduction techniques to reduce the overall solvent storage volume and, consequently, the capital cost. Three *SSC* size reduction approaches are considered in the following subsections.

## 6.3.1  Optimising the absorber stoppage time

For a steady-state absorber operation for the entire year at 90% $CO_2$ capture capacity, mathematically, this will lead to capture 1.585 M tonne$_{CO2}$ per annum. However, as the nominal target is 1.5 M tonne$_{CO2}$/y, this arrangement will allow for ~18 d/y stoppage time that can be used for the absorber maintenance. This ~18 d/y stoppage time can play a significant role in reducing the size of *SSC* by optimising the schedule of this stoppage time. A sensitivity test of this 18 d stoppage of the absorber is initiated at the beginning of each calendar month. Once the absorber stops generating more rich solvent for 18 d of that month, the SCF continues to uptake the rich solvent from the rich storage tank(s). Hence, this approach is expected to reduce the demand for solvent storage and provide room for potential *SSC* size reduction. It is anticipated that the optimum stoppage period would be during autumn to winter; this is when the rich storage accumulates a significant amount of rich solvent and the SCF displays deficits in regenerating more solvent due to poor solar irradiance. Figure 117 shows the calculated *SSC* volume required when the stoppage period starts at different times in a year. It can be seen that if the stoppage occurs during the summer season in a year, larger storage volume would be required. Normalising the *SSC* against the largest possible size shows a potential of ~20% saving in the *SSC*, if the absorber stoppage time is initiated around

autumn–winter seasons. This is clearly evident if the absorber stoppage time is scheduled in the April–July timeframe as shown in Figure 117.
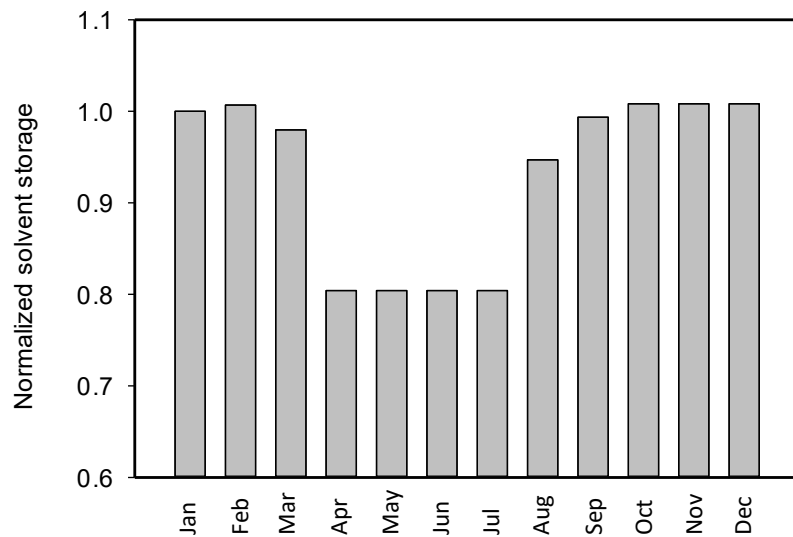


**Figure 117: Compared storage volume (normalised against the largest value) between scenarios with different stoppage starting hour. The stoppage duration is kept at 18 days in all scenarios. The stoppage period starts at the beginning of the calendar month in each scenario.**

To demonstrate this point in detail, the annual profiles of the $SL_R$ and $SL_L$ in two representative scenarios are illustrated in Figure 118. The absorber stoppage time of 18 days starting on 27 Feb is compared with an equal stoppage period starting on 6 April. In the first scenario, the absorber stoppage period coincides with the rich solvent-depleting period, which happens in summer more often, where intensive solar availability facilitates substantial solvent regeneration. This means the absorber stoppage period only aids to drain the rich solvent in the rich storage tanks faster, while accelerating the accumulation of lean solvent in the lean storage tanks. In contrast, for the second scenario, the profile of $SL_R$ shows a break in the ascending trend of the rich solvent. Hence, the profile curve of a single hump can be split into two lower humps as evident in Figure 118-B, which provides more potential for reducing the volume of the $SSC$. Consistently, the $SL_L$ profile, instead of heading down, climbs back to a second hump within the absorber stoppage period as shown in Figure 118-A. This climb back in the $SL_L$ profile is within the $SSC$ design (as evident by the second hump level almost equalising the first hump) and does not need extra volume. It is found that on the same scale of $SSC$ sizing, the optimisation of stoppage time can save up to 17% of the $SSC$ for the rich solvent and 18% for the lean solvent, respectively (Figure 118).
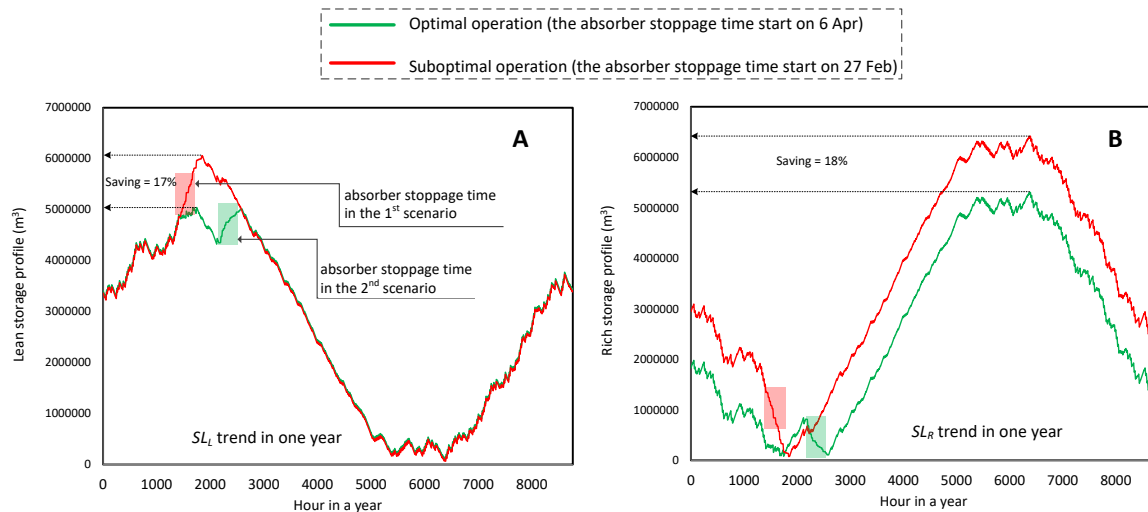
**Figure 118: (A) Lean and (B) rich storage profiles for two scenarios with different stoppage starting time, i.e. 27 February *vs* 6 April. The shaded area indicates the stoppage duration of 18 days in each scenario. The amount of physical storage saved is determined by comparing the maximum solvent volume as illustrated in the rich solvent profile (subfigure B). The saving is found to be 1,053,368 m³ (17%) and 1,158,457 m³ (18%) for the lean and rich storage, respectively.**

Consequently, we suggest that the optimum absorber stoppage period should start during the rich solvent accumulating period that often happens in autumn–winter seasons. The logic behind this rationale is because by shaving off any portion of the rich solvent during the accumulation period (i.e. in poor solar availability), that portion will not occupy more room in the rich storage facility, hence resulting in possible downsizing of the *SSC*. As evident from Figure 117, all scenarios that illustrate an absorber stoppage period within the April–July timeframe would form a break in the rich solvent accumulation trend, indicating that the optimum condition falls between these upper and lower bounds. From the process perspective, since there is no constraint on choosing a stoppage time period other than to minimise the *SSC* size, an arbitrary condition within this optimal range can be selected. In practical applications, we suggest that one should determine this period by assessing the cumulative rich solvent profile first without stoppage time. After that, the stoppage starting hour can then be optimised with a similar sensitivity analysis.

## 6.3.2  Synchronising *SM* and *SSC*

In this subsection, we discuss an exclusive method to reduce the solvent storage size. The logic behind this method is to establish a trade-off between the SCF size and the solvent storage volume. Hence, if the So-St field can regenerate more solvent per hour, the required *SSC* can be reduced. This could be achieved by simply over-sizing the SCF, which is often expressed using the term 'solar multiple' (*SM*) [86]. When *SM* =1, the entire SCF (represented by the nominal design of So-St network) is operating in diurnal times to the fullest capacity and regenerates an upper limit of the rich solvent capped by the SCF capacity. Nonetheless, if the number of So-St modules is increased (i.e. *SM* >1), those extra So-St modules will help

to exceed the cap and regenerate more solvent when solar energy is abundant. This means a portion of these extra So-St units will only operate in those good solar hours and proportionally to the solar intensity. Obviously, increasing *SM* >>1 will have a substantial economic footprint. However, this option will also reduce the demand for large solvent storage facilities (i.e. large *SSC*), as the trend of solvent regeneration in the SCF can be brought closer to the absorber demand, thus reducing the need for a massive solvent inventory. This approach will save on solvent cost (as less solvent is needed) and solvent storage infrastructure (fewer storage tanks, less storage land, and a smaller piping/pumping network is needed). Therefore, a trade-off between SCF size *vs.* the solvent inventory and storage must be reached and economically optimised. The above discussed design protocol is structured for *SM* = 1. While for *SM* >1 scenarios, the number of So-St modules will be multiplied by the updated *SM*. For example, the 21st design listed in Table 22 has 1,229 So-St modules as initially determined by the design protocol, but later the number is refined to 1,413 by the storage sizing algorithm. The 1,413 So-St modules number is for *SM* = 1, and if one wants to use *SM* = 2, the number of So-St modules theoretically be doubled to 2,826.
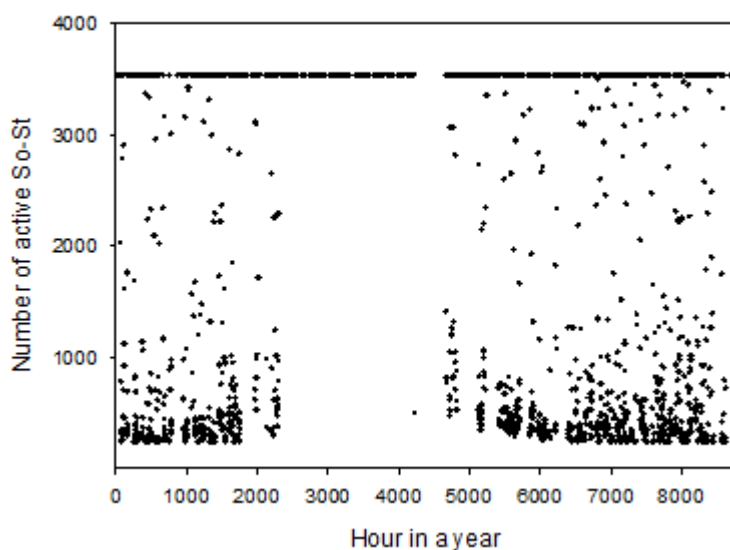


**Figure 119: The number of So-St in operation during a year when *SM* = 2.5. The number of modules is 1,413 x 2.5 = 3,533 and the prefill percentage is 70%. The storage volume is then reduced to 624,530 m$^3$ per tank.**

The developed algorithm shown in Figure 115 can be used in sensitising the effect of *SM* on the *SSC* sizing, but would require two major modifications. The first modification is making the number of So-St modules as a constant input. For example, when *SM* = 1, the number of So-St modules is 1,413 and when *SM* = 2, the number of So-St modules will be 1,413 x 2 = 2,826. However, since the nominal rich solvent flowrate is fixed based on the annual $CO_2$ capture budget of 1.5 M tonne, it is possible that at some timesteps there is not enough rich solvent available to meet the So-St flow demand as the number of So-St modules is increased. To overcome this challenge, a second modification incorporating an '*if*' statement in the design protocol can be introduced:

*'If there is not enough rich solvent in the inventory to operate all So − St modules*
*→ determine at least how many So − St modules can be operated'*

The '*if statement*' means that in those solvent deficit timesteps, some of the total number of the So-St modules need to be switched-off or defocused during the operation as demonstrated in Figure 119. It is evident that the SCF works at full load in many hours of the year, but at a substantial number of hours it works at a partial to minimal load. Accordingly, the effect of *SM* on the *SSC* volume is sensitised from 1 to 4 and the result is presented in Figure 120. It can be seen that increasing *SM* reduces the *SSC* size requirement; however, the relationship between *SM* and *SSC* is an exponential decay, which suggests the trade-off can be optimised. It is evident that after *SM* = 2.5, the extent of *SSC* size reduction seems to be smaller than the extent of *SM* increases. Thus, the *SM* might be at an optimum around *SM* ≈ 2.5. However, for robust judgement, the *y* axis needs to be converted into the overall normalised cost based on a rigorous economic assessment.



The chart shows data points with the fitted equation $y = 1.1384x^{-1.969}$ and $R^2 = 0.9791$. The y-axis is labeled "Normalized storage size" (0.00 to 1.20) and the x-axis is labeled "Solar multiple factor" (0.00 to 5.00).
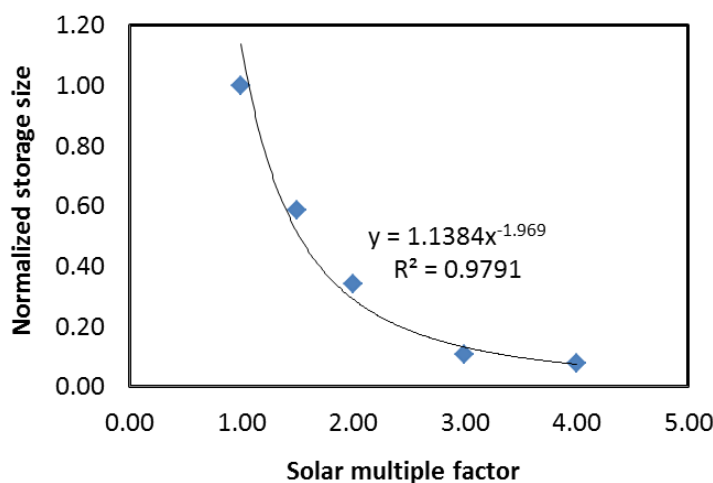
**Figure 120: The effect of different solar multiples on the *SSC* sizing. The y axis represents the storage size and has been normalised against the largest value.**

## 6.3.3  Examining multi-tank mix-match strategy

It is well known that rich and lean solvents differ in their physicochemical properties and it is impermissible for them to mix [87]. Figure 121-A shows the typical rich and lean solvent levels ($SL_R$ & $SL_L$) profiles in the storage tanks. Both storage tanks have a storage volume ($V$), hence, the total solvent storage volume will be doubled ($2 \times V$). In summer extreme conditions, the lean storage tank is full, and the rich storage tank is almost empty, while in winter extremes the situation is reversed (Figure 121-B). Carefully examining the filling pattern of these two tanks, it can be seen that they pose an opposite trend; i.e. when the lean tank is full, the rich tank will be relatively empty and vice versa. Another observation is that at any timestep, the combined $SL_R$ and $SL_L$ values will always complement each other to occupy 100% of the total volume. This means if the rich SST is at 30% capacity, the other tank will be intrinsically at 70% capacity. This theoretically means that only the volume of one tank (i.e. 1 x $V$) would be

sufficient to store the excess solvent. Practically, the rich and lean solvents cannot physically be mixed and, therefore, they must be kept separated. Although the volume of one tank is ultimately needed, it is impractical to mix both solvents in one tank. Therefore, a suboptimal solution is proposed in this study by using the sub-storage or 'mix-match' concept. Mix-match operation strategy is anticipated to bring great economic and/or environmental advantages and has been used in a number of other applications [88]. In this instance, one can substitute the (*1 x V*) tank into smaller storage portions for the purpose of switching empty tanks between the two solvents when appropriate.
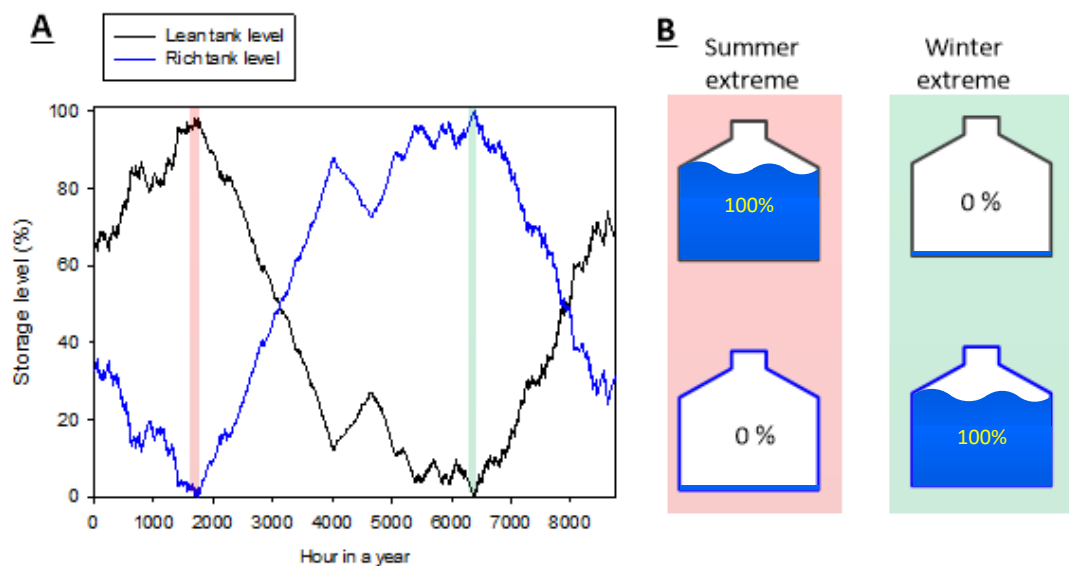


**Figure 121: A typical lean and rich tank level profile in one-year operation. Two extreme operations are marked on the plot with graphical illustration on the right.**

Figure 122 shows three different scenarios to compare the total volume of required tanks and the optimised number of sub-storage tanks. Scenario 1 is the base-case scenario as presented in Figure 121-B. Each sub-tank is designed with 100% capacity. In this case, only two large tanks are needed, each with the capacity of 1 x *V*. Compared with the theoretical storage demand for both solvents (1 x *V*), scenario 1 would require double the volume (2 x *V*), hence the storage facility is comparatively over-sized by 100%. In scenario 2, the sub-storage tank volume is 50% (i.e. 0.5 x V); this would result in reduced oversizing. In scenario 3, the sub-storage tank volume is further reduced to 25% (i.e. 0.25 x V); up to 5 small storage tanks each at 25%*V* capacity are required, but the extent of oversizing is further reduced. Overall, by designing a smaller sub-storage tank capacity, one can reduce the amount of storage oversizing but will need more sub-storage tanks. To calculate the number of sub-storage tanks needed, one still needs to use the storage sizing algorithm outlined in Figure 115 to determine the total volume. For example, assume one uses the algorithm and determines the total volume is 500,000 $m^3$. This means scenario 1 would need two tanks for the rich and lean solvent, each being 500,000 $m^3$. For scenario 2, one would need 3 tanks, each being 250,000 $m^3$ (i.e. 0.5 x 500,000). For scenario 3, one would need 5 tanks, each being at 125,000 $m^3$ (i.e. 0.25 x 500,000).

**Table 24: Different storage designs; the volume has been normalised to 1.**

|  | Scenario 1 | Scenario 2 | Scenario 3 |
|---|---|---|---|
| Normalised sub-storage tank capacity | 1 | 0.5 | 0.25 |
| Number of total sub-storage tanks for both lean and rich solvents | 2 | 3 | 5 |
| Total normalised volume | 2 | 1.5 | 1.25 |
| Theoretical storage volume demand | 1 | 1 | 1 |
| Combined storage oversizing (%) | 100% | 50% | 25% |
| *SSC* saving compared with the base-case scenario | - | 25% | 37.5% |

To elaborate further on the operational principles of these three scenarios, Figure 122 shows the combination at both summer and winter extremes of these three scenarios. For the base-case scenario (scenario 1), the lean and rich storage tanks are used only for the designated solvent without any changeover to the other solvent. Using the sub-storage tank approach as in scenario 2 and 3, some of the sub-storage tanks will need to switch between the lean and rich solvent depending on the time of year. For example, in extreme summer conditions, there will be mostly lean solvent stored, and the rich solvent is minimal. In this condition, most of the sub-storage tanks would be used for the lean solvent and only one sub-storage tank would be needed for the rich solvent. Transiting to the other extreme in winter, the original lean storage tanks would have been emptied and filled by rich solvent. Overall, there will be a time when either lean or rich storage is minimal, but if the storage volume is designed at smaller volumes, the empty tank(s) would be fewer in quantity and in volume.
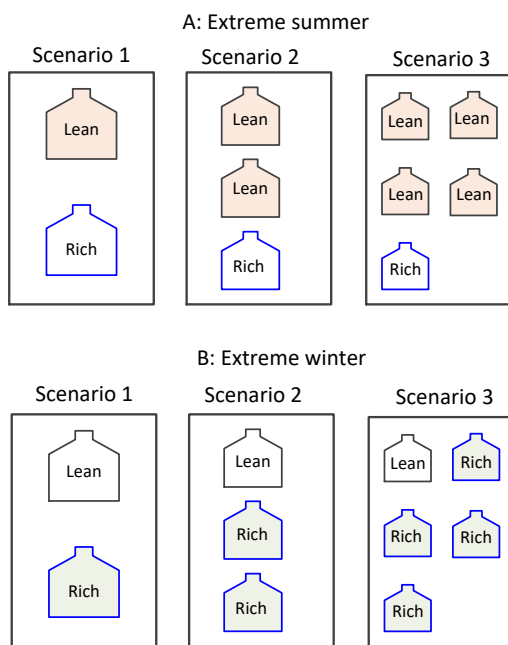


**Figure 122: Graphical illustration of the three scenarios outlined in Table 24.**

Figure 123 illustrates the filling pattern of this sub-storage mix-match concept for scenario 3 integrated with the absorber stoppage time. It can be seen that at any timestep, the total sub-storage tanks for the lean and rich solvent are equal to five. Anytime during a year, there is at least one sub-storage tank dedicated for either the lean or rich solvent, respectively, while ensuring sufficient empty tanks are ready for the inflow solvent. Three timeframes of action as indicated by three green arrows are captured and explained in Figure 123-B. At the beginning of the absorber stoppage time, there are three tanks are occupied by lean solvent but only two of them are full and the third is at 80% capacity at $t$ = 2,165 h. During the absorber stoppage time, the So-St field continues regenerating more rich solvent and filling up the third tank with lean solvent moving towards the fourth tank. By the end of the stoppage period at $t$ = 2,511 h, three tanks are full of lean solvent and the fourth is 21% of its capacity. Then, as a result of poor solvent regeneration in the winter season, the rich solvent resumes accumulation and at $t$ = 2,997 h, the fourth tank has been drained of the lean solvent and is ready to switch to rich solvent once the single rich solvent tank is filled up. In short, it is demonstrated that combining the idea of absorber stoppage time with the mix-match sub-storage tanks concept works favourably in saving a substantial volume of *SSC*.
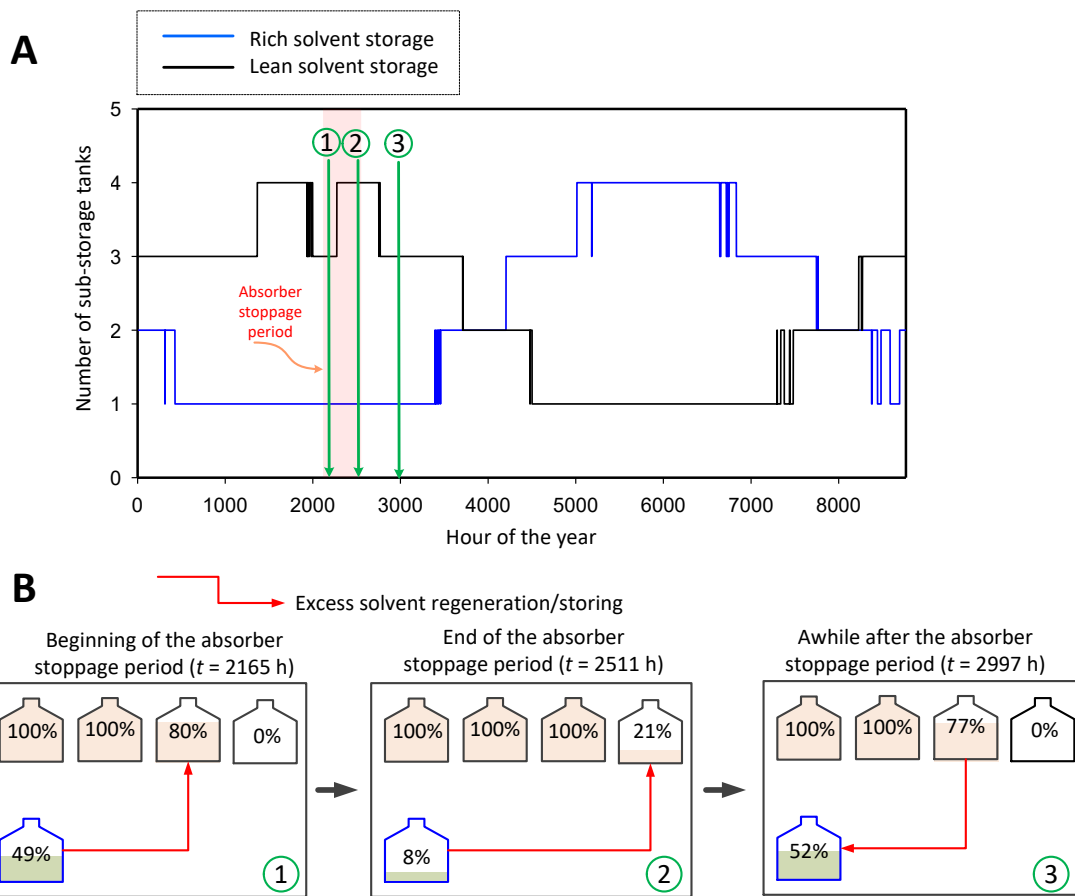


**Figure 123: The role of each sub tank in scenario 3. (A) The profile of which solvent is stored during a year; and (B) storage during and after the absorber stoppage time (blue is rich solvent storage and black is lean solvent storage). In this example, the stoppage time starts on 1 April and continues for 18 days as optimised in the previous section.**

This generic model is further developed and applied for large-scale commercially available liquid storage systems to tangibly calculate how many storage tanks are required for a particular design. For commercial tank sizes, the American Petroleum Institute (API) standard sizing is used to ensure more realistic results are being achieved [89]. The number of API tanks are calculated based on the reference largest tank capacity of 151,000 BBL (~24,007 m$^3$) available in the market [90]. Accordingly, by synchronising the trade-off between the *SM* with the *SSC*, a number of combined scenarios are created and compared. Thus, this synchronisation of API tank designs with the matching *SMs* are incrementally sensitised to determine an optimum condition. It is found that for a *SM* =1 scenario, a total storage volume of 4,465,674 m$^3$ would be required, corresponding to 186 large storage tanks. Figure 124 illustrates the filling pattern of the rich and lean solvents in those 186 SSTs, respectively. It is evident that during summer or winter extremes most of the SSTs will be filled by either lean or rich solvent, respectively. Tuning the *SL* for both lean and rich solvent at the end of the year to match the *SL* for start of the year is accurately performed by this algorithm (presented by the red dashed lines in Figure 124). In contrast, increasing the solar field size by 2.5-fold (*SM* =2.5) reduces the total storage volume to only 672,252 m$^3$ and would only require 28 storage tanks (Table 25).
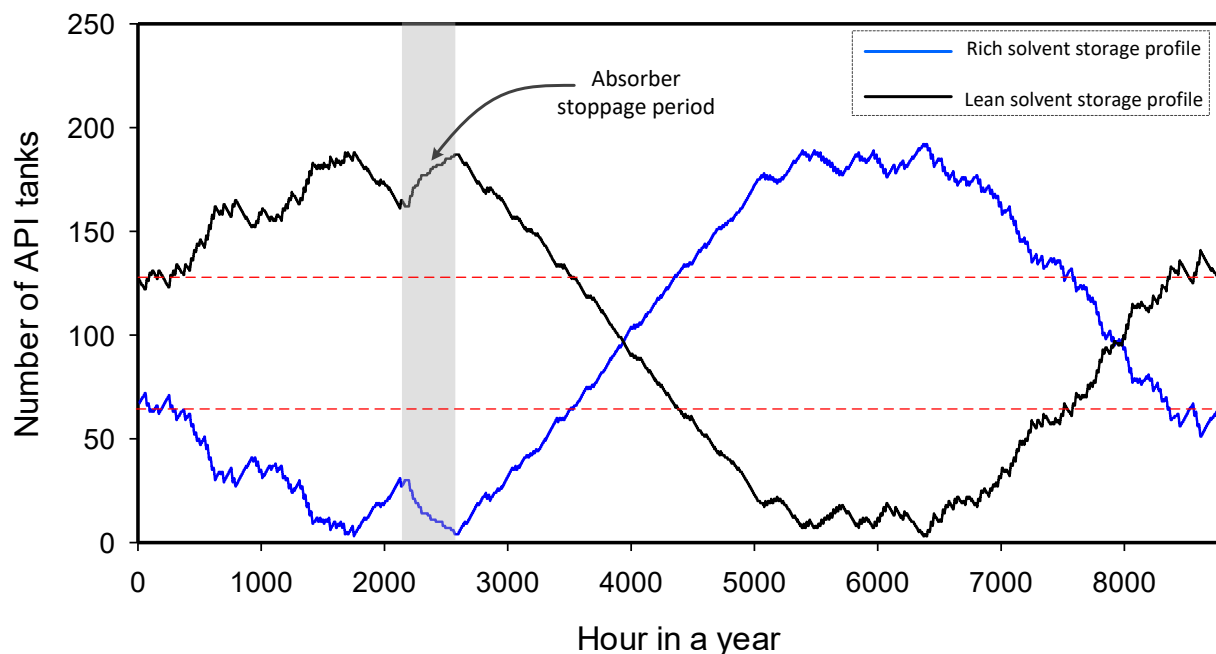


**Figure 124: The filling pattern of 186 large storage tanks (each has a 151,000 BBL capacity). The absorber ceases operation on 1 April for 18 days (shaded area). The horizontal red dashed lines indicate the *SL$_L$* and *SL$_R$* at the beginning and end of the year at the same level.**

Figure 125-A demonstrates that the relationship between the API tank design and the *SM* values result in non-linear trend. In sensitising the API tank size, using smaller tanks in volume would certainly require higher number of tanks, and vice versa. This is expected because for the same *SM*, the solvent cumulative profile is not affected by the subdivision arrangement of the storage facility. To sensitise this divergence in economic terms, the cost of a sub storage

tank is normalised against a real example. The closest real example is molten salt thermal storage, of which a practical storage size is 4,335 m³ (diameter = 22.4 m and height = 11 m) as reported in [91]. This storage size is in the range of commercial API sizes and used as a reference to normalise the storage facility cost. Interestingly, when the preliminary normalised cost is calculated, all API tank designs with the same *SM* values almost result in a similar cost (Figure 125-B). This could be because even when using smaller tank volumes, proportionally more tanks would still be required, provided that the cost trend is proportional to tank size. Thus, for any *SM* value, the total physical storage volume (tank volume *x* number of tanks) is almost identical. The preliminary result might imply that for the same *SM* value, one can choose any API tank setup without having an impact on the overall economics of the plant. However, there are other potential capital & operational expenditure (*CAPEX/OPEX*) costs (e.g. piping network and land value) that may influence the economics of the solvent storage infrastructure. Figure 125-B also fundamentally suggests the *SM* value strongly affects the storage cost, as evident by the large gaps in between different *SM* trends. Overall, a larger SCF results in a smaller storage facility cost and vice versa. From the above, the optimum storage sizing can conveniently be determined using the results in this framework together with the rigorous economic evaluation presented in the next chapter.
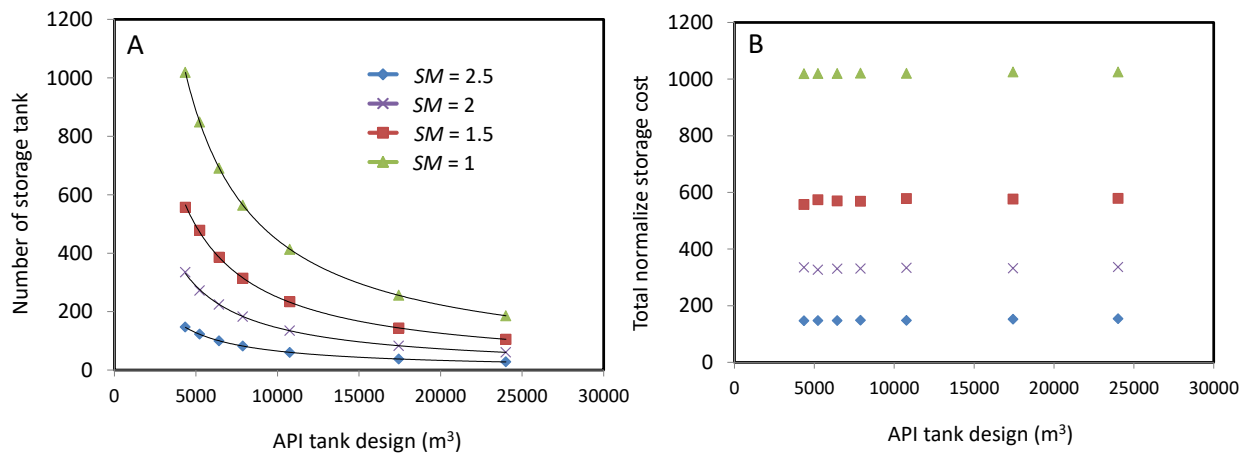


**Figure 125: The effect of storage size (API standard) and *SM* values on the number of the required API storage tanks and the normalised cost. In B, the total cost (include number of API tank and tank size) is normalised against the cost of one API tank 4,335 m³.**

Consequently, the solar field and solvent storage design for various *SM*s are summarised in Table 25. For each *SM* value, the SCF is calculated based on no land restriction and, therefore, the *W:L* ratio is equal to 1 (a square shape). Accordingly, the volume and the number of SSTs for each *SM* are calculated based on two categories: the basic (BAS) sizing, and the API multi storage tanks (MST) sizing. The former category is the standard two tanks (that only store either rich or lean solvent) and the latter is the proposed mix-match storage approach (can store both lean and rich solvents). For the MST approach (more than two tanks required), the tank volume is chosen to be 24,009 m³ based on the largest tank of the API design list. These designs are evolved from the original 21st design presented in Table 22, after a few rounds of design refinement and optimisation. The large SCF area is typically subdivided into a number

of subfields, where each subfield has its own header sets [29]. This option is used as a reference point to optimise the multi solar subfield layout, which allows manipulation of the overall width and length of the total SCF area.

For the *SM*=1 example, the total physical storage volume for the BAS category of 8,845,406 m$^3$ has been reduced to 4,465,674 m$^3$ in the MST category, which equates to ~49.5% reduction in physical solvent storage volume. As the SCF size and the pertinent *SM* increase, the *SSC* and the number of SSTs proportionally decrease. At *SM*=2.5 the number of required API tanks would be only 28 tanks with a total saving in solvent storage volume of ~46.2% related to the BAS category. Compared to *SM*=1 case, the total storage volume in *SM*=2.5 has been reduced to only 15% on the API scale, and down to 7.6% if compared with BAS storage of *SM*=1 scenario. However, the SCF land area has increased by 2.5-fold. This calculation shows the trade-off between the *SM vs. SSC*, which can only be enhanced via a rigorous economic optimisation.

Notably, these results are reported for this Sydney case-study, where the day/night and seasonal variations are substantial and imply a very large *SSC* to maintain consistent operation over the year. In locations closer to the equator where the day/night and seasonal variations are less, the solar radiation profile is more consistent and the gap between summer and winter productivity is slighter. In those locations, the potential of size reduction for both *SM* and *SSC* is relatively high. Overall, this project demonstrates the feasibility of SP-PCC away from direct reliance on the power plant's steam cycle. Moreover, we should emphasise the financial credits gained from steam preservation for power production and the resulting positive impact on the overall life cycle analysis. These aspects of possible revenue from steam preservation will be extensively discussed in Chapter 8.

**Table 25: Potential design for different solar multiples (*SMs*). Note that BAS is business as usual with two separate lean and rich storages; MST is mixed tank strategy in which each tank can periodically be used for storing either lean or rich solvent.**

| Solvent storage strategy | *SM* = 1 | | *SM* = 1.5 | | *SM* = 2 | | *SM* = 2.5 | |
|---|---|---|---|---|---|---|---|---|
| | BAS | MST | BAS | MST | BAS | MST | BAS | MST |
| Total So-St modules | 1,413 | 1,413 | 2,120 | 2,120 | 2,827 | 2,827 | 3,534 | 3,534 |
| Length per So-St module (m) | 705 | 705 | 705 | 705 | 705 | 705 | 705 | 705 |
| Length of the SCF (m) | 724 | 724 | 724 | 724 | 724 | 724 | 724 | 724 |
| Width of the SCF (m) | 21,195 | 21,195 | 31,802 | 31,802 | 42,402 | 42,402 | 53,003 | 53,003 |
| Aperture land area (km$^2$) | 15.345 | 15.345 | 23.024 | 23.024 | 30.699 | 30.699 | 38.374 | 38.374 |
| Number of subfields | 5 | 5 | 6 | 6 | 7 | 7 | 8 | 8 |
| So-St modules per subfield | 283 | 283 | 353 | 353 | 404 | 404 | 442 | 442 |
| Length including all subfields (m) | 3,670 | 3,670 | 4,404 | 4,404 | 5,138 | 5,138 | 5,872 | 5,872 |
| Width including all subfields (m) | 4,239 | 4,239 | 5,300 | 5,300 | 6,057 | 6,057 | 6,625 | 6,625 |
| Total SCF land area (km$^2$) | 15.557 | 15.557 | 23.342 | 23.342 | 31.123 | 31.123 | 38.904 | 38.904 |
| Number of *SSTs* | 2 | 186 | 2 | 105 | 2 | 61 | 2 | 28 |
| Volume per tank | 4,422,703 | 24,009 | 2,484,984 | 24,009 | 1,433,058 | 24,009 | 624,530 | 24,009 |
| Total storage volume (m$^3$) | 8,845,406 | 4,465,674 | 4,969,969 | 2,520,945 | 2,866,117 | 1,464,549 | 1,249,061 | 672,252 |
| *SSC* saving (%) | - | 49.5% | - | 49.3% | - | 48.9% | - | 46.2% |
| *SSC* demand compared with the BAS of *SM* = 1 (%) | 100% | 50.5% | 56.2% | 28.5% | 32.4% | 16.6% | 14.1% | 7.6% |

## 6.4 Concluding remarks

In this chapter, we have developed a comprehensive design protocol for sizing the entire So-St field. The protocol has been developed to facilitate rapid design generation and selection without the need for extensive simulation of individual designs. To synchronise the operation for the entire SP-PCC, the design protocol was structured based on three sub-models: the absorber, the So-St network and the solvent storage.

Based on a fully synchronised operation between these three components, a design protocol comprising two parts was established. The first part creates a general design database comprises all possible physical layout options. Then, several filters (criteria) might be applied to shortlist favourable designs distinguished by specific physical or performance indicators. For the solvent storage sizing, a direct relationship with the SCF sizing standards was realised.

Accordingly, three optimisation tools were facilitated to reduce the overall *SSC* and possibly enhance the economic model. The first tool assessed the impact of the absorber stoppage time on the *SSC* and optimised for the ideal stoppage time for periodic maintenances. The second tool evaluated the influence of *SM* on the *SSC* and established an exponential decay relationship between these two variables. The third tool examined the novel concept of multi-tank mix-match strategy using the API standard tank sizes to notably reduce the *SSC* requirement.

A full analysis was conducted for this SP-PCC at various *SMs* incrementing by 0.5 in value. It was found that at *SM*=2.5, the *SSC* requirement was reduced to only 15.1% on the API scale and 7.6% of the basic *SSC* requirement for *SM*=1. This calculation demonstrated the significant trade-off implications between the *SM* vs. *SSC* which can only be enhanced via a rigorous economic optimisation. Yet, for locations with abundant solar irradiance, clearer skies, longer daytimes (especially in winter), less seasonal variability in solar resources and less expensive land, the SP-PCC would be a more appealing technology option than conventional PCC.

# 7.    Techno-economic analysis

In this chapter, we set up a fair and transparent appraisal platform to compare four scenarios illustrated by a block diagram in Figure 126. Scenario (A) represents the reference case of a power-plant without $CO_2$ capture unit; scenario (B) represents a power-plant integrated with a typical PCC; scenario (C) for a power-plant integrated with a solar-assisted PCC (SA-PCC); and scenario (D) represents a power-plant integrated with the adopted configuration in this project, the solar-powered PCC (SP-PCC). For power systems, it is widely acknowledged that solar systems as standalone entities often have a less attractive economic footprint because of the overinvestment required for a massive SCF and TES, and therefore are usually optimised in hybrid modes. The performance for each SCF hybrid with the power-plant is often evaluated via the levelised cost of energy (*LCOE*) and the payback period (*PBP*) values. Thus, the solar multiple (*SM*) is optimised for the lowest *LCOE* and/or *PBP* values [92].
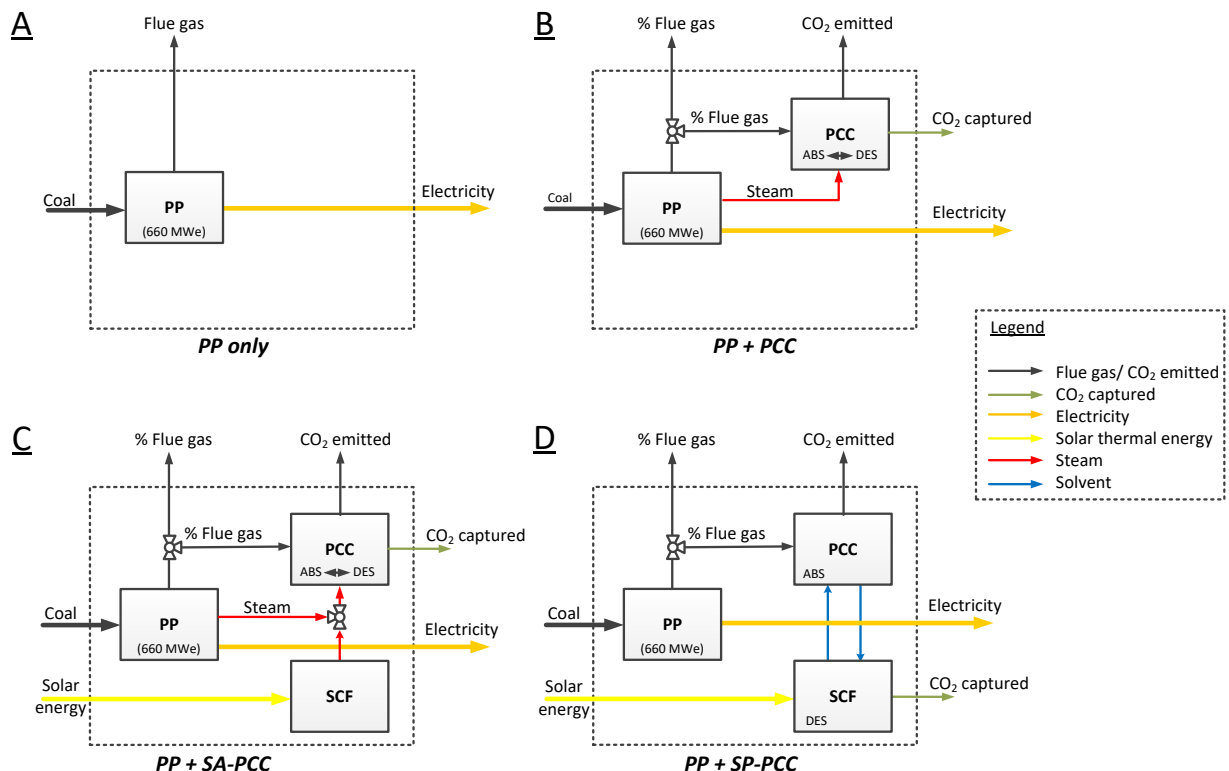


**Figure 126: Block diagram of four scenarios set for economic comparison. Scenario (A) a power-plant only; (B) for a power-plant integrated with a typical PCC; (C) for a power-plant integrated with a solar-assisted PCC; and (D) is for a power-plant integrated with a solar-powered PCC [93].**

In scenarios (B) and (C) in the figure, the absorption (ABS) and the desorption (DES) units are combined within the confinement of the PCC, while in scenario (D) the $CO_2$ desorption and removal directly occur in the SCF. All scenarios, excluding the base-case, are set for a capture target of 1.5M tonnes$_{CO2}$/year. Scenarios (C) and (D) are solar related and, therefore, the

typical meteorological year (TMY) data for our case-study (Sydney) is selected for this assessment. However, locations closer to the equator with clearer skies and fewer day/night and seasonal variations would require a smaller SCF size and reveal considerably better techno-economics [29].

Since these scenarios are constructed by combining different sub-plants (i.e. the power-plant, PCC, SCF, and thermal energy/solvent storage), individual components were distinctly modelled using Aspen® and/or Microsoft Excel (Microsoft Corporation, USA). The power-plant component is a standard 660 MW$_e$ coal-fired power-plant. Although the power production fluctuates hourly depends on the load and power demand, the flue gas that flows to the absorber for capturing $CO_2$ is assumed to be constant at 34% of the total flue gas at full power-plant capacity. This assumption alleviates the dynamics of power production from our analysis, which results in a consistent approach and valid comparison between scenarios. In addition, future work can safely adopt these results since they are not affected by the load variation or the volatility of the electricity market. The net electricity produced per year at 100% capacity is calculated by multiplying the net power-plant output by the hours of operation per year. The total $CO_2$ emissions per year are calculated in a similar way and then divided by the net electricity produced per year to determine the levelised capture rate in the units of tonnes$_{CO2}$/MWh. Figure 127 presents the economic model structure for the adopted scenarios. This model consists of the structured *CAPEX* & *OPEX* sub-models. The *OPEX* sub-model is subdivided into the fixed O&M (*FOM*) costs and the variable O&M (*VOM*) costs. The summary of the model assumptions and equations along with the validation method are presented next.
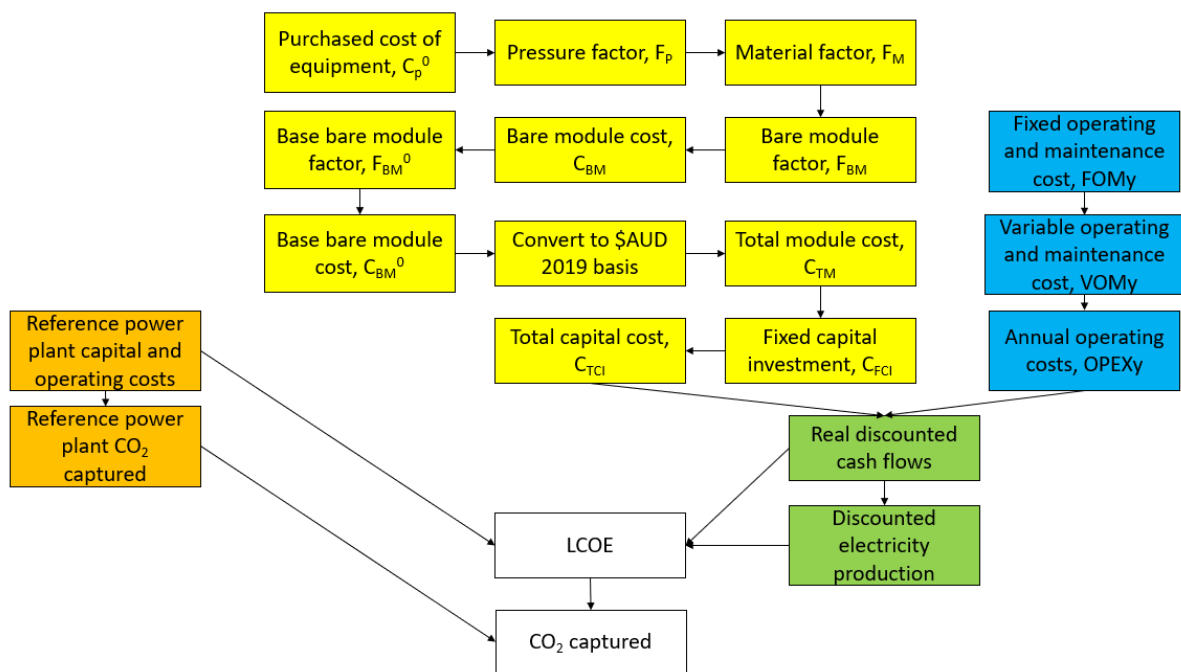


**Figure 127: Flowchart process of cost calculation procedure [93].**

## 7.1    Economic parameters and assumptions

A 660 MW$_e$ coal-fired power-plant is used as the reference plant. A comparative 650 MW$_e$ power-plant from Li *et. al.* [94] was also used, and the associated costs and the *LCOE* are scaled-up and adjusted based on given parameters to match the 660 MW$_e$ power-plant specifications. These parameters are listed in Table 26.

**Table 26: Power-plant specifications, PCC parameters and conversion rates. All dollar values are given in AUD 2019 basis.**

| Parameter | Value |
|---|---|
| **Key economic parameters** | |
| Economic basis | AU$ 2019 |
| CEPCI (Chemical Engineering Plant Cost Index) | 607.5 |
| **Reference power-plant specifications** | |
| Net power-plant output (MW$_e$) | 660 |
| $CO_2$ emission (tonnes/h) | 595 |
| Capacity factor | 0.85 |
| Capacity factor (first year operation) | 0.50 |
| Discount rate, $r$ (real) | 0.064 |
| Plant life (y) | 30 |
| Total hours of operational per year (h/y) | 8760 |
| Net electricity produced (MWh) | 5,780,000 |
| $CO_2$ emission (tonne/MWh) | 0.90 |
| *LCOE* (power-plant only) (AU$/MWh) | 123.67 |
| Discounted sum of electricity produced (MWh) | 57,700,000 |
| Capital costs (AU$/kW) | 6,447 |
| Fixed O&M (*FOM*) costs (AU$/kW/y) | 75.02 |
| Variable O&M (*VOM*) costs (AU$/MWh) | 8.84 |
| Coal costs (AU$ M/y) | 177 |
| Total costs (AU$ M) | 7,140 |
| **PCC parameters** | |
| PCC solvent | 30 *wt%* MEA |
| $CO_2$ capture target (million tonnes/y) | 1.5 |
| PCC construction time (y) | 3 |
| Budget fraction allocated (year 1) | 0.40 |
| Budget fraction allocated (year 2) | 0.30 |
| Budget fraction allocated (year 3) | 0.30 |
| Absorber shut down period for maintenance (day/y) | 18 |

## 7.1.1  Capital expenditure (*CAPEX*)

The third Edition of Capital Equipment-Costing Program (CAPCOST) is used to estimate the main components of the capital cost of the depicted scenarios with a $CO_2$ capture budget of 1.5 million tonnes per year [95, 96]. Cost calculations using this method are on a USD 2001 basis (Chemical Engineering Plant Cost Index (CEPCI) = 397) and are explicitly converted to AU\$ 2019 basis. Design specifications for equipment found in the conventional PCC, the SA-PCC, and the SP-PCC technologies are listed in Table 27. For SA-PCC, a new process model is developed in Excel to compute the design specifications. The base-case scenario for SA-PCC is designed for a reference solar fraction (*SF*) of 23%. In an earlier study [19], it was found that for Sydney case-study, a *SF*= 23% can give an optimal positive revenue when carbon price ≥AU\$ 44/tonne$_{CO2}$. This *SF* is adopted as a base-case scenario for SA-PCC and assigned a solar multiple *SM* = 1. Because of the desorption unit elimination in the SP-PCC counterpart, the *SF* is always maintained at 100% to fully power the solvent regeneration process. Changing the *SM* in SP-PCC scenario would severely impact the required solvent storage capacity (*SSC*). If the 23% *SF* is equivalent to *SM*=1 in SA-PCC scenario, it is found for SP-PCC counterpart that the equivalent *SM* would equal 5.3 for the *SF* to reach 100%.

**Table 27: Design specs and capacity for equipment used in conventional PCC, SA-PCC (*SF* = 23%, *SM*=1) and SP-PCC (*SF* = 100%, *SM* = 5.3).**

| Equipment | PCC | SA-PCC | SP-PCC |
|---|---|---|---|
| Flue gas blower: flow rate ($m^3$/s); capacity (MW) | 252; 6 | 252; 6 | 252; 6 |
| Absorber: diameter (m); height (m) | 18; 15 | 18; 15 | 18; 15 |
| Absorber packing: volume ($m^3$) | 3,817 | 3,817 | 3,817 |
| Desorber: diameter (m); height (m) | 12; 13 | 12; 13 | - |
| Desorber packing: volume ($m^3$) | 1,470 | 1,470 | - |
| Condenser: area ($m^2$) | 9,117 | 9,116.71 | 9,116.71 |
| Lean/rich HX: area ($m^2$) | 8,342 | 8,341.59 | 8,341.59 |
| Lean cooling HX: area ($m^2$) | 1,265 | 1,264.56 | 1,264.56 |
| Reboiler: area ($m^2$) | 9,538 | 9,537.55 | - |
| Rich pump: Capacity (kW); annual consumption (MWh) | 100; 800 | 100; 800 | 100; 800 |
| Drum: diameter (m); height (m) | 4.1; 21 | 4.1; 20.97 | 4.1; 20.97 |
| Cycle pump: number; nominal capacity (kW); annual consumption (MWh) | - | 1; 300; 1748 | 13050; 0.2; 3453 |
| Storage tank: number; diameter (m); height (m) | - | 2; 45.7; 14.6 | 197; 45.7; 14.6 |
| Solar collector field: PTC aperture area ($m^2$) | - | 1,340,924 | 7,155,750 |
| Solar multiple (*SM*) | - | 1 | 5.3 |
| Solar fraction (*SF*) (%) | - | 23 | 100 |
| Solvent mass (tonne) | 11,000 | 11,000 | 5,000,000 |
| Molten salt (tonne) | - | 41,000 | - |

The purchased cost of equipment ($C_p^0$) is determined by *Eq. 75* as follows:

$$C_p^0 = 10^{K_1 + K_2 \, log_{10}(X) + K_3 (log_{10}(X))^2}$$
*Eq. 75*

Where $K_1$, $K_2$ and $K_3$ are constants defined for each piece of equipment; and $X$ is the capacity of the equipment with units specified by the CAPCOST method (Table 28). The sizes of the equipment are determined through Aspen® models. For HXs, an overall heat transfer coefficient of 2000 W/m²K [94] is used to estimate the size of the required HXs. The pressure factor ($F_P$) for process materials is determined by *Eq. 76*, assuming base material conditions:

$$F_P = \frac{\frac{(P+1)D}{2(850 - 0.6(P+1))} + 0.00315}{0.0063}$$
*Eq. 76*

Where $P$ is the pressure (barg); and $D$ is the diameter (m) of the vessel, respectively. For other process equipment, *Eq. 77* is used to determine the pressure factor:

$$F_P = 10^{C_1 + C_2 \, log_{10}(P) + C_3 (log_{10}(P))^2}$$
*Eq. 77*

Where $C_1$, $C_2$ and $C_3$ are constants defined for each type of equipment in the CAPCOST method; and $P$ is the pressure (barg). The SCF cost elements are calculated separately. For the parabolic trough collectors (PTCs) used in the So-St network, assuming a cost factor of USD100/m² is quite achievable (equivalent to $186.80/m² AUD 2019) [97]. For the SA-PCC HTF and the molten salt storage system, the default values used in SAM [98] are USD60/m² and USD62/kWh$_t$ converted to $112.09/m² and $115.83/kWh$_t$ for AUD 2019, respectively. The bare module factor ($F_{BM}$) is calculated by *Eq. 78:*

$$F_{BM} = B_1 + B_2 F_M F_P$$
*Eq. 78*

Where $B_1$ and $B_2$ are constants defined for each type of equipment in the CAPCOST method; $F_M$ is the material factor; and $F_P$ is the pressure factor.

**Table 28: CAPCOST equipment constants for capital cost calculations. All pressures in barg.**

| Equipment | Capacity | Unit | $X_{low}$ | $X_{high}$ | $K_1$ | $K_2$ | $K_3$ | $P_{low}$ | $P_{high}$ | $C_1$ | $C_2$ | $C_3$ | $F_M$ | $B_1$ | $B_2$ |
|---|---|---|---|---|---|---|---|---|---|---|---|---|---|---|---|
| Flue gas blower | gas flow rate | m³/s | 1 | 100 | 3.5391 | -0.3533 | 0.4477 | 1 | 16 | 0 | 0.20899 | -0.0328 | 1 | 2.74 | - |
| ABS/DES vessel | volume | m³ | 0.3 | 520 | 3.4974 | 0.4485 | 0.1074 | - | - | Eq. 76 | | | 3.1 (SS) | 2.25 | 1.82 |
| Vessel packing (structured) | volume | m³ | 0.03 | 628 | 3.07 | 0.97 | 0.01 | - | - | 0 | 0 | 0 | 1 | 4.2 | - |
| Shell and tube HX | area | m² | 10 | 1,000 | 4.3247 | -0.303 | 0.1634 | - | <5 | 0 | 0 | 0 | 2.73 | 1.63 | 1.66 |
| | | | | | | | | 5 | 140 | 0.03881 | -0.11272 | 0.08183 | | | |
| Reboiler (kettle) | area | m² | 10 | 100 | 4.4646 | -0.5277 | 0.3955 | - | <5 | 0 | 0 | 0 | 2.73 | 1.63 | 1.66 |
| | | | | | | | | 5 | 140 | 0.03881 | -0.11272 | 0.08183 | | | |
| Centrifugal pump | Shaft power | kW | 1 | 300 | 3.3892 | 0.0536 | 0.1538 | 10 | 100 | -0.3935 | 0.3957 | -0.00226 | 2.3 (SS) | 1.89 | 1.35 |
| Horizontal drum | volume | m³ | 0.1 | 628 | 3.5565 | 0.3776 | 0.0905 | - | - | - | - | - | 2.3 (SS) | 1.49 | 1.52 |
| Storage tank (API) | volume | m³ | 90 | 30,000 | 4.8509 | -0.3973 | 0.1445 | - | - | - | - | - | 3.1 (SS) | 1.1 | - |

The bare module cost ($C_{BM}$), base bare module factor ($F_{BM}^0$) and base bare module cost ($C_{BM}^0$) are then calculated by *Eqs. 79–81*. These costs are then adjusted from a 2001 USD basis to AUD 2019 basis by *Eq. 82*:

$$C_{BM} = C_P^0 F_{BM}$$
<div align="right">*Eq. 79*</div>

$$F_{BM}^0 = B_1 + B_2$$
<div align="right">*Eq. 80*</div>

$$C_{BM}^0 = C_P^0 F_{BM}^0$$
<div align="right">*Eq. 81*</div>

$$C_{2019} = C_{2001} \left(\frac{I_{2019}}{I_{2001}}\right) \frac{F_L}{R_{2019}}$$
<div align="right">*Eq. 82*</div>

Where $C_{2001}$ is the cost of equipment in the base year 2001; $C_{2019}$ is the cost of equipment in the year 2019; $I_{2001}$ is the chemical engineering plant cost index in the base year 2001 (CEPCI = 397); $I_{2019}$ is the chemical engineering plant cost index in the year 2019 (CEPCI = 607.5); $F_L$ is the location factor; and $R_{2019}$ is the 2019 exchange rate ($1 AUD = $0.70 USD, averaged over 2019 from the Reserve Bank of Australia). Since the location factor is provided in a USD 2003 basis [99], it can be converted to an AUD 2019 basis by *Eq. 83*:

$$F_L = F_{L2003} \times \frac{R_{2019}}{R_{2003}} = 1.21 \times \frac{0.6952}{0.6524}$$
<div align="right">*Eq. 83*</div>

Where $F_{L2003}$ is the location factor on a 2003 basis ($F_{L2003} = 1.21$); and $R_{2003}$ is the 2003 exchange rate ($1 AUD = $0.65 USD, averaged over 2003 from the Reserve Bank of Australia). The bare module cost and base bare module cost are summed for all components. The total module cost ($C_{TM}$) is presented by *Eq. 84*:

$$C_{TM} = (1 + \alpha_1 + \alpha_2)\Sigma C_{BM}$$
<div align="right">*Eq. 84*</div>

Where $\alpha_1$ is the contingency fraction; and $\alpha_2$ represents the contractor fees fraction. The fixed capital investment ($C_{FCI}$) is presented by *Eq. 85*:

$$C_{FCI} = C_{TM} + \alpha_3 \Sigma C_{BM}^0$$
<div align="right">*Eq. 85*</div>

Where $\alpha_3$ is the cost fraction of auxiliary facilities. The total capital costs are presented by *Eq. 86*:

$$C_{TCI} = C_{FCI} + C_{wc} = C_{FCI} + \alpha_4 C_{TM}$$
<div align="right">*Eq. 86*</div>

Where $C_{wc}$ is the working capital; and $\alpha_4$ is the working capital fraction. These constants are summarised in Table 29.

**Table 29: Constants used in cost estimation. All dollar values are given on AUD 2019 basis.**

| Constant | Symbol | Value for | | References |
|---|---|---|---|---|
| | | PCC | SCF | |

| | | | | |
|---|---|---|---|---|
| Contingency fraction | $\alpha_1$ | 0.15 | 0.07 | [95, 98, 100] |
| Contractor fees fraction | $\alpha_2$ | 0.03 | 0.11 | [95, 98] |
| Auxiliary facilities fraction | $\alpha_3$ | 0.50 | - | [95] |
| Working capital fraction | $\alpha_4$ | 0.15 | - | [95] |
| Fixed O&M fraction | $\beta$ | 0.035 | 0.018 | [94, 98, 100] |
| Number of periods in a year | TPY | 1 | | [96] |
| Land cost ($/m$^2$) | $C_L$ | 0.53 | | [101] |
| Pool price electricity ($/MWh) | $EEP_y$ * | 55.36 | | [96] |
| Cooling energy price ($/GJ) | $CEPy$ # | 0.54 | | [96] |
| Solvent price ($/tonne) * | $SP_y$ ^ | 388.5 | | [102] |
| SCF variable cost by generation ($/MWh$_t$) | $VOM_{solar}$ | 7.47 | | [98] |

* Pool Price is the price established and reported by the Independent System Operator at year 'y'.
# the price for cooling energy in the PCC at year 'Y'.
^ The pure MEA cost for 2020 is averaged ≈USD 1000/tonne [102] and the diluted solvent (30 wt% MEA) is converted to AUD.

The storage system in the SA-PCC and SP-PCC technologies are calculated separately. The SA-PCC uses the costly TES that would require a special arrangement for thermal insulation, thus the cost is often based on the thermal capacity expressed in kWh$_t$. While for the SP-PCC scenario, the solvent storage does not require thermal insulation and typical liquid storage tanks can be used. The cost of the *SSC* is estimated based on the solvent cost [102] using the standard API tanks [89]. The total land area required for the SCF (including non-solar area) is assumed to be 1.4 times the solar aperture area [98].

## 7.1.2  Operating expenditure (*OPEX*)

The operating expenses are calculated as the sum of fixed and variable O&M costs, respectively. The fixed O&M costs (*FOM$_y$*) are simplified as a fraction ($\beta$) of the total *CAPEX* (*C$_{TCI}$*) [94]. Unlike power-plants fired by fossil fuels, the *LCOE* in a SCF is mostly attributed to the initial *CAPEX*, which accounts for ~80% of the total cost, and the rest is related to O&M costs and the plant insurance [100]. Therefore, the $\beta$ fraction is almost halved in the SCF (Table 29) because the SCF does not have moving parts and consequently would not require much O&M as in the case of PCC.

$$\boldsymbol{FOM_y = \beta \times C_{TCI}} \qquad\qquad Eq.\ 87$$

The annual variable operation and maintenance costs (*VOM$_y$*) is computed by *Eq. 88* [96] for the PCC.

$$\boldsymbol{VOM_y = TPY \times \Sigma VOM} \qquad\qquad Eq.\ 88$$

$$\boldsymbol{VOM_y = TPY\left(EEP_y(E^B + E^{T.P}) + CEP_y(Q^{LCHX} + Q^{Des.CHX}) + SP_y(F^{MU})\right)} \qquad Eq.\ 89$$

Where $TPY$ is the number of operation periods within a year; $EEP_y$ is the pool price electricity; $E^B$ is the total energy of blower/s; $E^{T.P}$ is the total energy of pump/s; $CEP_y$ is the cooling energy

price; $Q^{LCHX}$ is the duty of the lean cooling HX; $Q^{Des.CHX}$ is the duty of the desorption cooling HX; $SP_y$ is the solvent price; and $F^{MU}$ is the amount of solvent makeup required at a rate of 1.5 kg solvent per tonne of $CO_2$ captured. For the SA-PCC and SP-PCC scenarios, the variable O&M costs for the SCF components are determined in terms of a variable cost by generation ($VOM_{solar}$) (Table 29), where the generation refers to the fraction of thermal reboiler duty supplied by the SCF.

$$VOM(solar) = VOM_{solar} \times SF \times reboiler\ duty(MWh_t) \qquad \textit{Eq. 90}$$

This is then added to the $VOM_y$ equation for the SA-PCC and SP-PCC technologies.

$$VOM_y = TPY\big(EEP_y\big(E^B + E^{T.P}\big) + CEP_y\big(Q^{LCHX} + Q^{Des.CHX}\big) + SP_y\big(F^{MU}\big) + VOM(solar)\big) \ \textit{Eq. 91}$$

Finally, the annual operation expenses are defined by *Eq. 92*:

$$OX_y = FOM_y + VOM_y \qquad \textit{Eq. 92}$$

### 7.1.3  The levelised cost of energy (LCOE)

Accordingly, the *LCOE* can be calculated as shown in *Eq. 93*:

$$LCOE = \frac{initial\ costs + \Sigma(annual\ costs_n) \times (1+r)^{-n}}{\Sigma(electricity_n \times (1+r)^{-n})} \qquad \textit{Eq. 93}$$

Where $electricity_n$ is the electricity produced each year (MWh); *r* is the discount rate; and *n* is the plant lifetime (30 years). These are expressed as real costs. Therefore, the *LCOE* for each of the PCC technologies can be calculated by *Eq. 94*:

$$LCOE_{PCC} = \frac{(initial\ costs + \Sigma(annual\ costs_n) \times (1+r)^{-n})_{PP} + (initial\ costs + \Sigma(annual\ costs_n) \times (1+r)^{-n})_{PCC}}{\Sigma(electricity_n \times (1+r)^{-n})} \ \textit{Eq. 94}$$

For the PCC technologies, the electricity produced each year is determined by *Eq. 95*:

$$electricity_n(MWh) = capacity\ factor \times electricity_{net} - s \times Q_{reb} \qquad \textit{Eq. 95}$$

Where the $electricity_{net}$ is the net electricity produced by the power-plant in year *n*; *s* is the conversion of heating duty to electricity (0.35); and $Q_{reb}$ is the reboiler duty. Finally, the cost of $CO_2$ captured can be determined by *Eq. 96*:

$$cost\ CO_2\ captured\left(\frac{\$}{t_{CO2}}\right) = \frac{LCOE_{PCC} - LCOE_{ref}}{CO_{2\,captured}} \qquad \textit{Eq. 96}$$

Where $LCOE_{PCC}$ is the *LCOE* depending on the PCC technology ($/MWh); $LCOE_{ref}$ is the *LCOE* for the reference power-plant only ($/MWh); $CO_{2\,captured}$ is the $CO_2$ captured by the PCC technology (tonne$_{CO2}$/MWh).

### 7.1.4  Economic model validation

For the purposes of model validation, the economic model is adjusted to follow the same

assumptions as used for the reference power-plant and PCC [94]. The reference PCC costs are scaled so that the $CO_2$ capture capacity is identical in all scenarios (1.5 million tonnes$_{CO2}$/year). The absorber and the reboiler capital costs are found to be poorly estimated in the CAPCOST method in comparison with the literature. As such, the bare module costs of these components are estimated based on literature values according to the capture capacity as summarised in Table 30. These reference points are used to estimate the cost of the absorber (and packing) and the reboiler for the model. After cost adjustments, the *CAPEX* and *OPEX* costs of the PCC are given in Table 31. The *LCOE* of the PCC model differs from the calculated reference PCC by less than 5%, so our method of calculation is in good agreement with published values.

**Table 30: Normalised absorber and reboiler costs for PCCs of different $CO_2$ capture capacities. All dollar values are given on AUD 2019 basis.**

| Capture capacity (million tonne$_{CO2}$) | Bare module costs | | | | Reference |
|---|---|---|---|---|---|
| | Absorber ($/tonne$_{CO2}$) | Absorber Packing ($/tonne$_{CO2}$) | Absorber + Packing ($/tonne$_{CO2}$) | Reboiler ($/tonne$_{CO2}$) | |
| 1 | 20.29 | 15.26 | 35.55 | 5.27 | [94] |
| 1 | 19.96 | 14.58 | 34.54 | 7.59 | [94] |
| 2 | - | - | 22.12 | 0.46 | [103] |
| 3 | - | - | - | 7.45 | [104] |
| 3.5 | 5.04 | 9.94 | 14.98 | 2.94 | [23] |

**Table 31: *CAPEX* & *OPEX* of the PCC economic model with a $CO_2$ capture capacity of 1.5 M tonne$_{CO2}$/y. All dollar values are given on AUD 2019 basis. Reference PCC from Li et. al. [94].**

| Equipment | This model | | Reference PCC | |
|---|---|---|---|---|
| | Specs | Bare Module Cost ($/tonne$_{CO2}$) | Specs | Bare Module Cost ($/tonne$_{CO2}$) |
| Blower ($m^3$/s) | 252 | 0.51 | 200 | 0.19 |
| Absorber ($m^3$) | 3817 | 17.11 | 1074 | 19.96 |
| Absorber packing ($m^3$) | 3817 | 13.92 | 792 | 14.58 |
| Desorber ($m^3$) | 1470 | 19.60 | 420 | 5.42 |
| Desorber packing ($m^3$) | 1470 | 3.03 | 309 | 3.49 |
| Condenser ($m^2$) | 9117 | 8.43 | 800 | 0.73 |
| Reboiler ($m^2$) | 9538 | 5.13 | 4250 | 7.59 |
| Lean/rich HX ($m^2$) | 8342 | 7.67 | 9100 | 3.58 |
| Lean cooling HX ($m^2$) | 1265 | 1.34 | 1200 | 1.24 |
| Pumps | 98 (kW) | 0.12 | 461 (L/s) | 0.50 |
| Drum ($m^2$) | 277 | 1.17 | 1800 | 0.92 |
| Total capital investment ($M) | 181 | | 196 | |
| Fixed O&M costs ($M/y) | 6.35 | | 6.87 | |
| Variable O&M costs ($M/y) | 9.31 | | 12.96 | |
| *LCOE* ($/MWh) | 165.31 | | 172.88 | |

## 7.2    Base-case designs

Table 27 summarised the base design specifications for the three capture scenarios. In comparing the SA-PCC and SP-PCC scenarios, the SCF size and storage requirement in the former are much smaller than the latter. For example, SA-PCC only requires two API-equivalent TES tanks, whereas the SP-PCC counterpart requires 197 API solvent storage tanks (SSTs) (27). This is because the solar contribution in the SA-PCC is optimised at 23% solar fraction (*SF*) [19], whereas SP-PCC counterpart, the *SF* is at full capacity of 100%, which enlarges the total size of the SCF by approximately 5.3 fold (*SM* = 5.3).

The cost categories of these three scenarios are summarised in Table 32. The cost categories for the PCC are noticeably different from the CAPCOST model used for model validation in Table 31 because of changing some design specifications that resulted in lower *LCOE* value. As expected, the SA-PCC and SP-PCC technologies result in higher *LCOEs* compared with the conventional PCC. The *LCOE* for SA-PCC is \$141.6/MWh, which is 8.4% higher than the *LCOE* for conventional PCC, mostly driven by the upfront *CAPEX* investment of the SCF and thermal storage installation. Meanwhile, the *LCOE* for SP-PCC is \$206.6/MWh, which is 57.8% and 45.9% higher than the PCC and SA-PCC counterparts, respectively. Due to the removal of the desorption unit in the SP-PCC scenario, the solvent must be fully regenerated in the SCF. Therefore, the SCF is oversized to respond to a 100% *SF*. Furthermore, the *SSC* is also oversized to maintain process continuity and to prevent interruptions that could result from solvent deficit on both sides of the solvent cycle. These two factors have driven the *CAPEX* very high (~\$5,552 M as compared with \$995 M of the SA-PCC counterpart), mostly attributed to the physical installation of the solar collectors (24%) and solvent cost (35%).

The key benefit of this upfront high investment in the SP-PCC is in the steam preservation for power production, which would increase the revenue and the sustainability of the SP-PCC technology. Compared to the typical PCC, increasing the *CAPEX* & *OPEX* by many times in the SP-PCC scenario has increased the overall *LCOE* by only 58%. The reason for the multi-fold *CAPEX* being not fully reflected in the *LCOE* is attributed to two key factors: the captured revenue from steam preservation for power production, and the cost saving resulted from eliminating the stripper and the reboiler (estimated at 25-30% of the total PCC cost [24]).

**Table 32: Summary of the key economic results for conventional PCC, SA-PCC (*SF* = 23%, *SM* = 1) and SP-PCC (*SF* = 100%, *SM* = 5.3). The costs are reported in AUD.**

| Cost categories | PCC | SA-PCC | SP-PCC |
|---|---|---|---|
| *CAPEX* (\$M) | 201 | 995 | 5,552 |
| *FOM* (\$M/y) | 7 | 12.6 | 42.6 |
| *VOM* (\$M/y) | 6.5 | 9.3 | 18.4 |
| *LCOE* (\$/MWh) | 130.9 | 141.6 | 206.6 |
| $CO_2$ capture cost (\$/tonne$_{CO2}$) | 67.4 | 108.4 | 358.9 |

Despite the major benefits of the SP-PCC option, it is found that SP-PCC endures a substantial increase in *LCOE* due to the bulk solvent and large SCF requirements to operate at 100% *SF*. To reduce the overall cost and subsequently the *LCOE*, the *SSC* and SCF cost must be reduced. For this

purpose, different SCF and *SSC* sizes for SP-PCC are sensitised to determine the effect of *SM* variation on the *SSC* and SCF requirement. Figure 128 shows the effect of possible size reduction of SCF and *SSC* on the *LCOE* as compared with the SA-PCC scenario. The hypothetical results confirm that if the combined SCF and *SSC* sizes are reduced by up to 80% (i.e. *SM* ≈ 1), the *LCOE* will match the SA-PCC counterpart. To provide a full assessment for the SCF and storage size variation for both SA-PCC and SP-PCC scenarios, we must sensitise these two parameters for both scenarios. In SA-PCC, it is understood that increasing the SCF size will increase *SF* and proportionally reduce steam bleeding from the power-plant. At 100% *SF*, the SA-PCC will completely stop steam bleeding from the power-plant and would entirely rely on steam production within the SCF and/or TES.
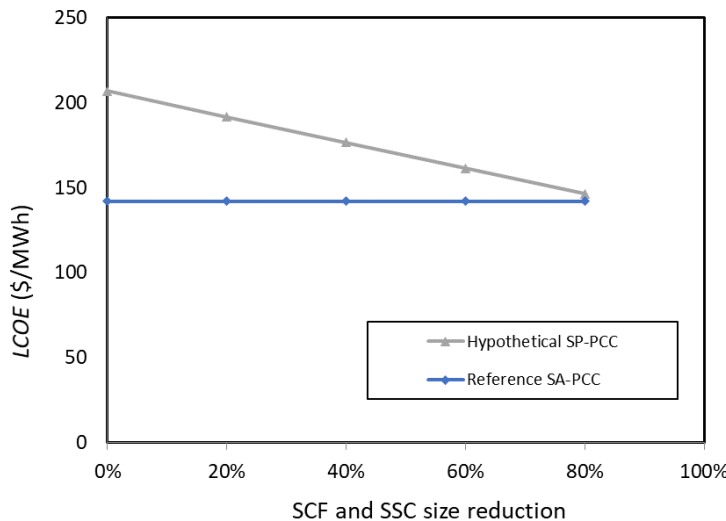


**Figure 128: the *LCOE* trend of SP-PCC when the SCF and *SSC* sizes are hypothetically reduced.**

## 7.3     Sensitise SCF and storage

Table 33 shows design specifications for SA-PCC and SP-PCC scenarios at different *SMs*. The same economic models outlined above are used to simulate different designs and calculate the resulting *LCOE*. The results of this sensitivity analysis are plotted in Figure 129. In general, larger SCFs resulted in higher *SF* and larger TES potential for the SA-PCC scenario. However, in the SP-PCC scenario, larger SCFs decrease the solvent storage requirement (i.e. fewer API tanks are needed). These observations confirm the benefit of tuning the SCF size for optimal process performance and economic footprint.

**Table 33: Design specifications for SA-PCC and SP-PCC at various SCF sizes (the unit of *SM* = 1, SCF area = 1,340,924 m$^2$ and *SF* = 23%).**

|  |  | SA-PCC |  |  |  |  |  |
|---|---|---|---|---|---|---|---|
| Solar multiple (*SM*) |  | 1 | 1.9 | 2.9 | 3.8 | 4.8 | 5.7 |
| Oil quantity (tonne) |  | 328 | 619 | 928 | 1237 | 1,547 | 1,856 |
| Molten salt quantity (x1000 tonne) |  | 41 | 183 | 717.5 | 3211 | 7,200 | 11,840 |
| No. cold storage tanks |  | 1 | 3 | 9 | 35 | 77 | 127 |

| | | | | | | |
|---|---|---|---|---|---|---|
| No. hot storage tanks | 1 | 3 | 9 | 35 | 77 | 127 |
| No. cycle pump | 7 | 13 | 19 | 24 | 29 | 34 |
| Cycle pump total nominal capacity (kW) | 1,976 | 3,713 | 5,504 | 6,926 | 8,470 | 10,011 |
| Cycle pump annual consumption (MWh) | 1,748 | 3,283 | 4,866 | 6,276 | 7,603 | 9,009 |
| Thermal storage (x100 kWh$_t$) | 1.80 | 7.16 | 28.10 | 127.45 | 287.23 | 466.51 |
| Solar fraction (%) | 23 | 44 | 64 | 81 | 93 | 100 |

| | SP-PCC | | | | |
|---|---|---|---|---|---|
| SM | 5.3 | 7.95 | 10.6 | 13.25 | 26.5 |
| Solvent quantity (x1000 tonne) | 4,960 | 3,239 | 1,849 | 754 | 342 |
| No. lean storage tanks | 97 | 64 | 37 | 16 | 3 |
| No. rich storage tanks | 97 | 64 | 37 | 16 | 3 |
| No. cycle pump | 13,050 | 19,575 | 26,100 | 32,625 | 65,250 |
| Cycle pump total nominal capacity (kW) | 2,610 | 3,915 | 5,220 | 6,525 | 13,050 |
| Cycle pump annual consumption (MWh) | 3,453 | 3,031 | 2,788 | 2,664 | 2,388 |
| Solar fraction (%) | 100 | 100 | 100 | 100 | 100 |
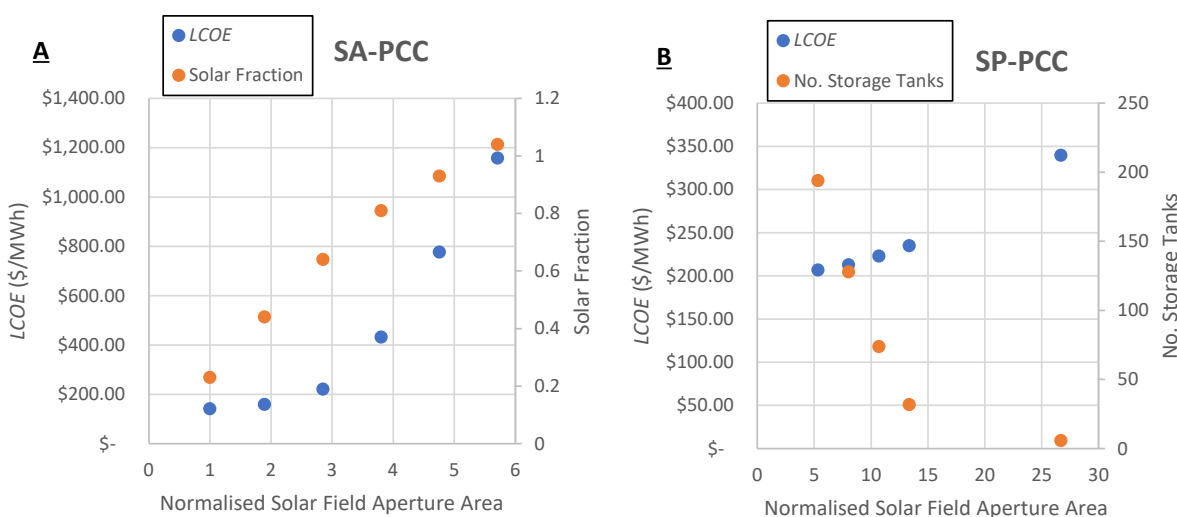


**Figure 129: The trend of *LCOE* for design specifications of SA-PCC and SP-PCC technologies at different SCF sizes.**

In the SP-PCC category, increasing the SCF size typically leads to a higher *LCOE*. However, to better understand this trend, the effect of changing *SM* on the *SSC* (number of API storage tanks) is plotted, as these two cost components make up a large portion of the *CAPEX*. The result is shown in Figure 130. It is found that increasing the SCF size does not result in a linear decrease in *SSC* requirement. For example, doubling the *SM* (100% increase) only results in ~62.7% size reduction in *SSC*. Nevertheless, at very large *SMs* (e.g. *SM* >10), the cost reduction in solvent storage might be insufficient to justify the cost increase in the SCF (Figure 130). This fact is clearly demonstrated in

Figure 129-B where the trend of *LCOE* is generally increasing despite the substantial decrease in the number of API storage tanks.
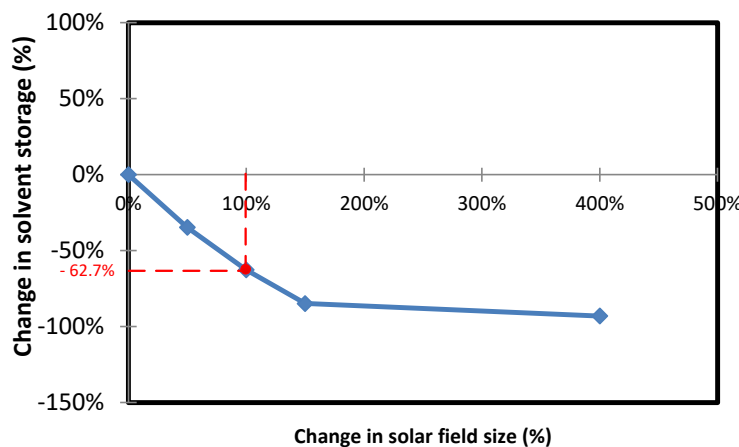


**Figure 130: Change in solvent storage capacity (*SSC*) per change in SCF size.**

In contrast, Figure 129-A reveals an interesting *LCOE* trend for the SA-PCC scenario. As SCF size increases, it is expected that the *LCOE* increases linearly and proportionally to the SCF size, because the cost unit ($/m$^2$) of the SCF is modular and constant. However, the *LCOE* trend shows an exponential growth, suggesting increasing SCF size may also interact with other factors. To understand this trend, all *CAPEX* components for both SA-PCC and SP-PCC scenarios are plotted in Figure 131. For SA-PCC (Figure 131-A), it can be seen that increasing the SCF size leads to a proportional increase in *CAPEX*, but the most driving component is related to the TES cost. The grey-coloured bars representing the TES cost show an exponential trend contribution to the *LCOE* trend.
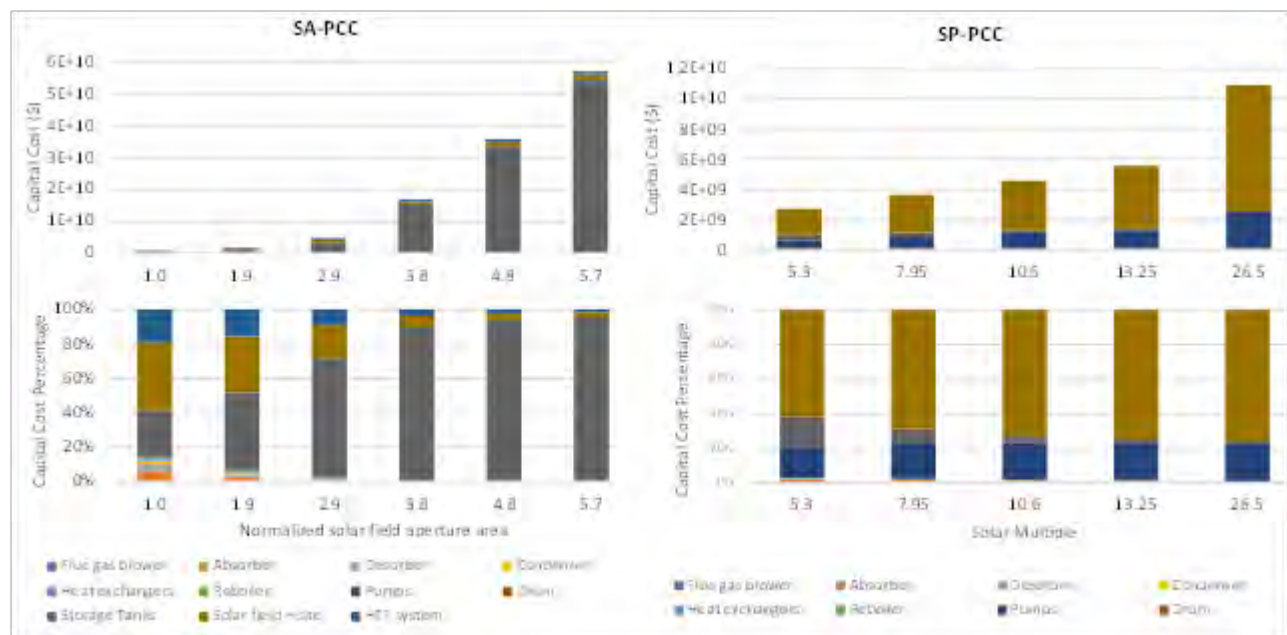


**Figure 131: Bare module cost and bare module cost percentage composition for: (left) SA-PCC, and (right) SP-PCC components for designs at various solar multiples.**

To better understand the exponential trend in TES cost at the operational level, the cumulative trends of molten salt mass at two *SM* values (*SM* = 2.9 and *SM* = 3.8) are compared. This comparison

is chosen because it displays a significant change in TES cost when changing the *SM* from 2.9 to 3.8. Figure 132 shows that when the *SM* = 3.8, the TES media (i.e. molten salt) is accumulating mostly in the summer season and almost drains in winter (Figure 132-B). Whereas in *SM* = 2.9 case, the extent of molten salt accumulation is far less in summer and would require a much smaller TES size (Figure 132-A). These profiles explain why the TES size in the *SM* = 3.8 design is significantly larger than that of the *SM* = 2.9 design. Overall, at larger SCFs, more hot molten salt can accumulate for later uses; hence the TES size must be large. In contrast, small SCFs produce insufficient hot molten salt for storage, but it is used up quickly and promptly. As in most renewable hybrid projects, the high upfront *CAPEX* of solar-storage facilities often limits the economic viability for very high *SFs*.
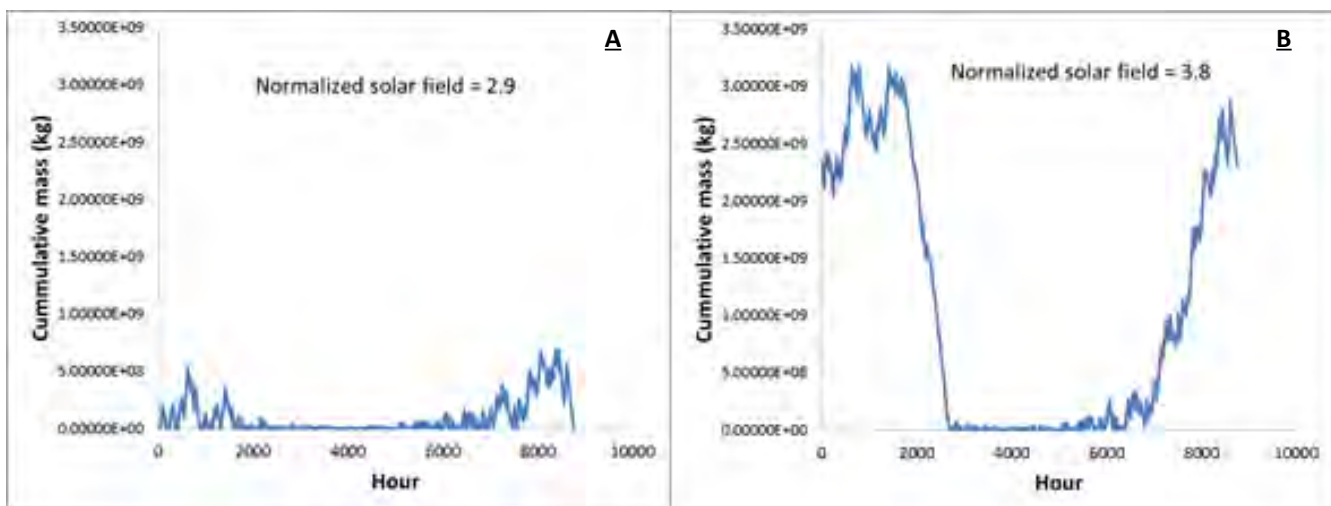


**Figure 132: Cumulative hot molten salt mass for two different designs of SA-PCC scenario.**

In hybrid power systems, the *SF* is often optimised and stimulated by various legislative support schemes, such as government subsidies, carbon price and renewable energy certificate programs. A carbon price is one of the potential incentives programs to encourage the deployment of low-emission technologies and/or renewable hybridisation. An SA-PCC plant helps to produce extra electricity via steam preservation for the purpose of power production, but at the same carbon footprint as the conventional PCC plant. Therefore, it could be eligible for carbon credits (CCs) on the zero-carbon incremental electricity produced. In this context, four carbon pricing scenarios have been explored where an average carbon tax over the 25 years life of the plant is used. The carbon prices are averaged over the 25 years lifetime in these four scenarios as \$11.53/tonne, \$23/tonne, \$44/tonne, and \$58/tonne of the captured $CO_2$, respectively [19].

Figure 133 presents an overview of the effect of *SF* variation on the 'power-plant + SA-PCC' scenario at different potential government incentive programs for the Sydney case-study. It can be seen that at low carbon prices (e.g. \$11.53/tonne$_{CO2}$), the power-plant operator is unable to capture any positive revenue from SA-PCC at any *SF*. When the carbon price is doubled to \$23/tonne$_{CO2}$, a 'subsidy + REC' combined program starts to show a little positive revenue around 23% *SF*. This positive revenue is quite tangible at carbon prices >\$44/tonne$_{CO2}$, where the 'subsidy + CC' combined program also started to show a positive tangible revenue at ~23% *SF* (Figure 133). Therefore, we selected this *SF* of 23% as an optimum solar contribution for SA-PCC scenario.
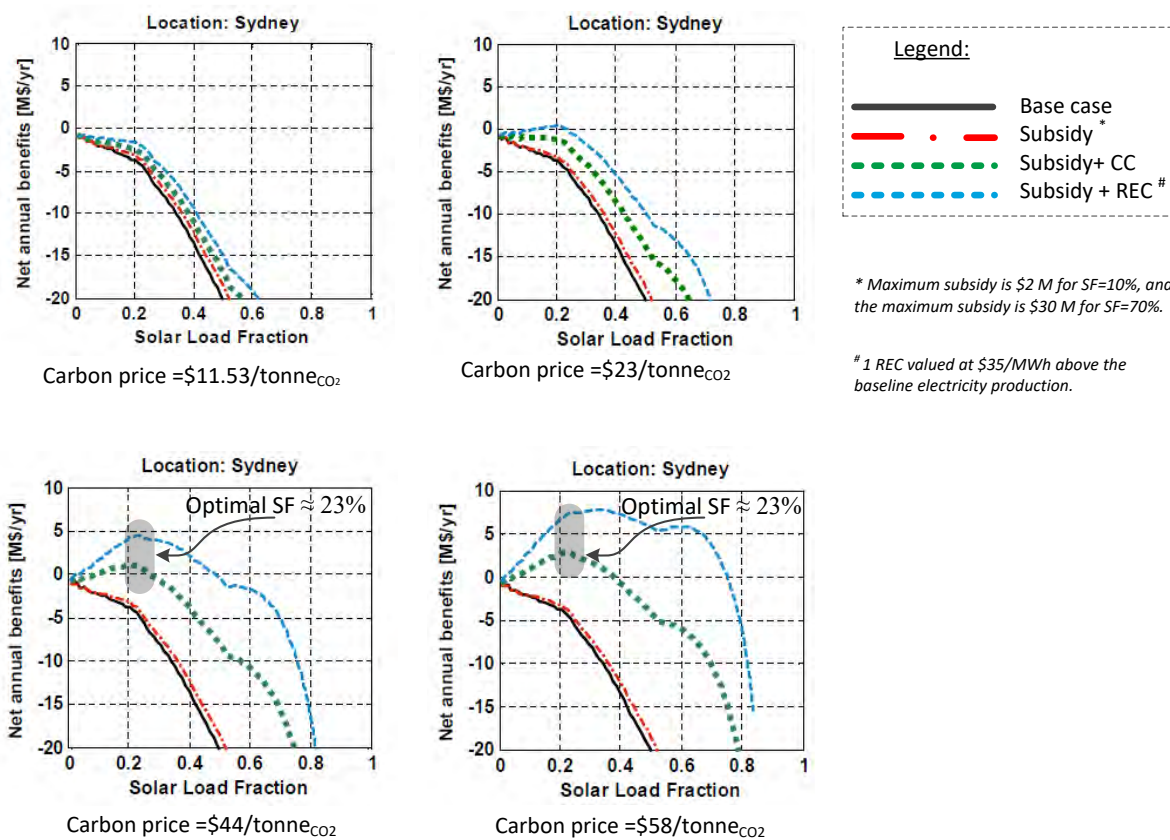
**Figure 133: The net annual profit trends for the power-plant owners/operators when combined with SA-PCC at different government incentive programs and for various carbon price schemes.**

For a fair assessment between the techno-economic viability of the SA-PCC and SP-PCC scenarios, the *SF* in the SA-PCC scenario must also match the 100% *SF*. Figure 134 shows the *FOM, VOM, CAPEX* components and *LCOE* comparison for SA-PCC and SP-PCC scenarios when both are sized at 100% *SF*. The main aim for this comparison is to find out under similar assumptions (e.g. 100% *SF*) which solvent regeneration method is the more economically viable option. It can be seen that the *CAPEX* of SA-PCC is substantially higher (Figure 134-C), mostly driven by the large TES requirement as discussed earlier. Similarly, under the *FOM* category, the SA-PCC would be much higher than the SP-PCC because it is calculated as a portion of the *CAPEX* (Figure 134-A). Meanwhile, the *VOM* expenses are almost matching due to the same operational categories serving both SCFs at similar *SM* (Figure 134-B). These factors have driven the *LCOE* for the SA-PCC to more than five times that of the SP-PCC counterpart (Figure 134-D). The results also suggest storing solar energy in a thermal application is less efficient compared with the solvent storage in the SP-PCC scenario. Ballpark calculations are conducted to determine the material mass required in storage to capture 1 kg of $CO_2$. For SA-PCC, each $CO_2$ capture requires approximately 4 MJ thermal energy, which can be supplied by cooling 27.8 kg of molten salt from 350 to 250ºC (Figure 135). Hence, the SA-PCC requires 27.8 kg of storage material per 1 kg $CO_2$ capture. For SP-PCC, to capture 1 kg of $CO_2$, the amount of solvent required is 3.3 kg. As a result, TES will be significantly less efficient than solvent storage for $CO_2$ capture applications.
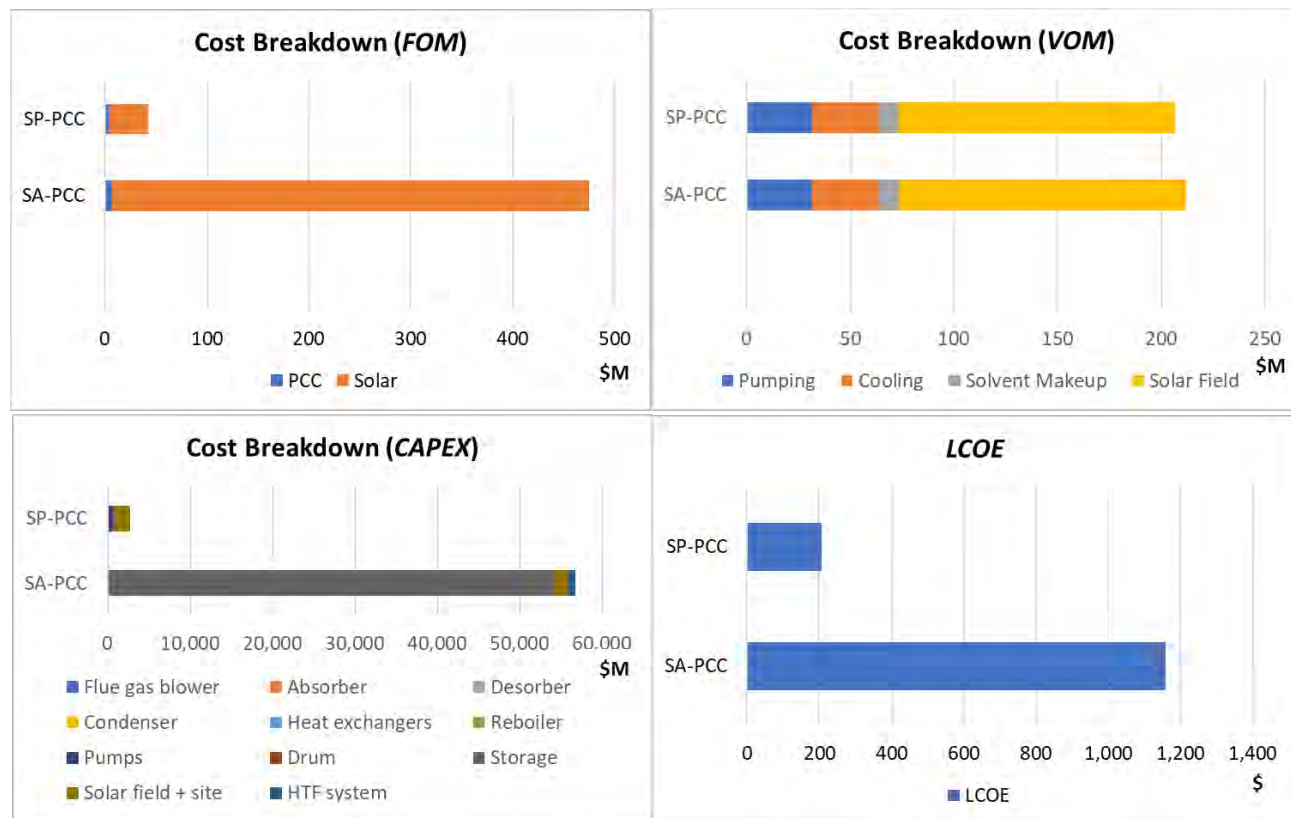
**Figure 134: *FOM*, *VOM*, *CAPEX* and *LCOE* comparison for both SA-PCC and SP-PCC scenarios under 100% *SF* scenarios.**
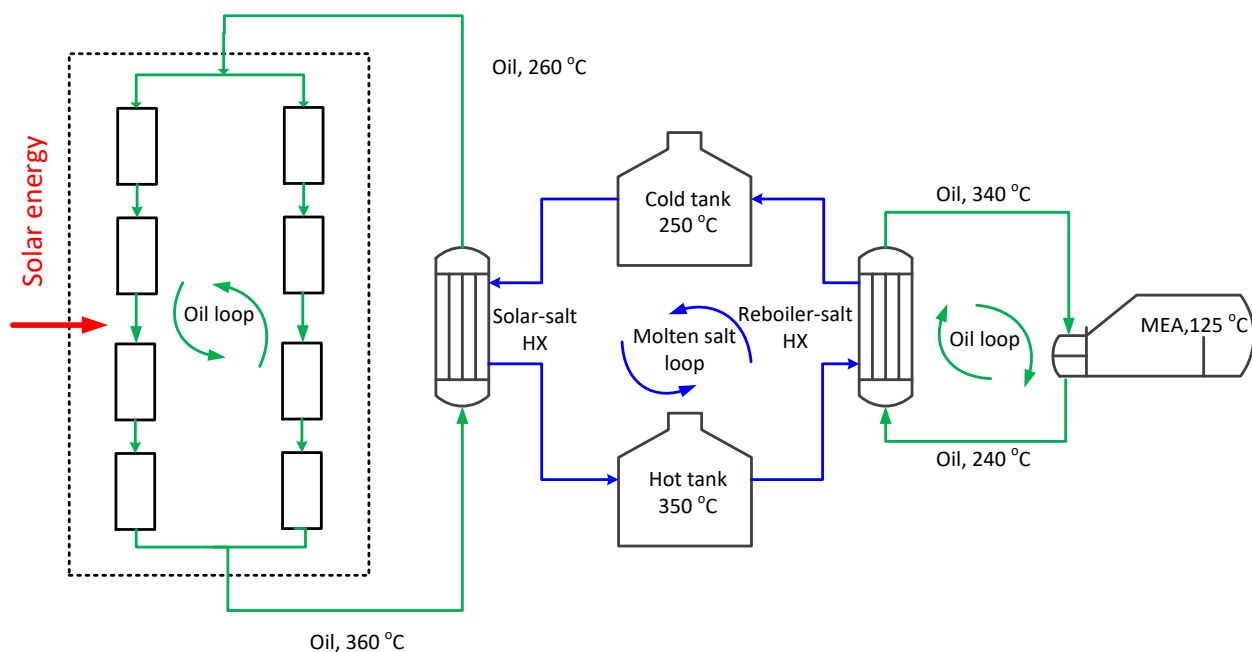


**Figure 135: Thermal transformation in an SA-PCC plant. The oil loop in the SCF uses commercial Therminol VP and the molten salt in the storage uses Hitect salt.**

## 7.4    Sensitising economic parameters

It is possible that our economic assumptions may slightly vary in future. The following sensitivity analysis is therefore necessary to evaluate how favourably each of the technologies would respond to these changes. Using the Tornado chart method [105], a sensitivity test is performed on the three main scenarios of: conventional PCC, optimised SA-PCC at *SM=1* (*SF* = 23%), and independent SP-PCC at *SM=5.3* (*SF*=100%) to determine the impact of key economic parameters on the *LCOE*. Parameters selected for this sensitivity analysis are: capacity factor, discount rate and unit cost of the SCF. The *CAPEX* & *OPEX* cost elements, the *LCOE*, and the cost of the captured $CO_2$ presented in Table 32 were all calculated based on a capacity factor of 85%, discount rate of 6.4% and the SCF unit cost of AUD 186.80/m². Figure 136 presents the sensitivity analysis for these three parameters at ±10% (solid bars) and ±5% (hatched bars) variation. It is found that the *LCOE* for all three technologies are most sensitive to changes in the capacity factor, followed by changes in the discount rate. Hence, it is always preferable for the power-plant to operate at a higher capacity factor, as this allows for more electricity generation and revenue. For the capacity factor, the changes are more significant for the SP-PCC, followed by the SA-PCC and the PCC counterpart.

Similarly, a lower discount rate is also preferable for *LCOE* reduction. The changes in the *LCOE* are also more significant for the SP-PCC, followed by the SA-PCC and the PCC counterpart. As expected, the SCF cost has no impact on the conventional PCC technology, as it has no SCF component. Changes in the price of the SCF cost unit are not very significant for the SA-PCC technology, but are more significant for the SP-PCC because this cost element significantly contributes to the *CAPEX* of this technology. As such, changes to the investigated parameters have a greater impact on the SP-PCC technology compared with the SA-PCC counterpart. We conclude that any future reduction in these elements would bring tremendous benefits specifically for the SP-PCC technology.
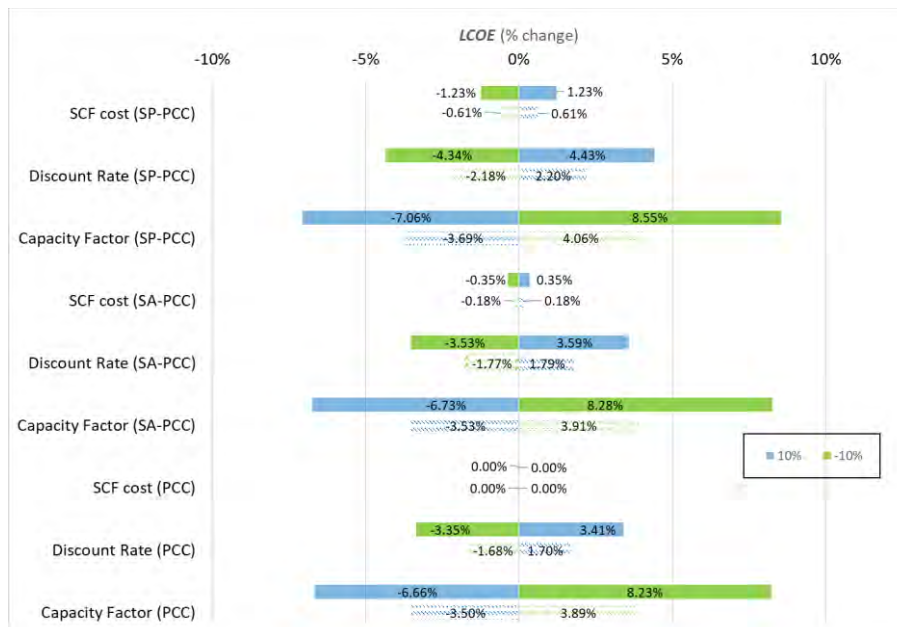


**Figure 136: Sensitivity of the *LCOE* to the variation of economic parameters within ± 5% (hatched bars) and 10% (solid bars), respectively.**

## 7.5     Carbon capture subsidy

In this analysis, a hypothetical scenario is proposed where subsidies (e.g. in the form of carbon tax/credit) are awarded per tonne of captured $CO_2$. Revenue generated from this potential award scheme for carbon capture subsidies is included in the cash flow model to calculate the *PBP*, which provides an insight to the hypothetical carbon price to make the SP-PCC technology profitable. Figure 137-A shows that without a carbon price award, the SP-PCC will never be profitable because the *PBP* trend increases exponentially with the decrease in carbon price and will never touch the y-axis. However, at approximately $150/tonne$_{CO2}$, the initial investment can be recuperated after 15 years of the project lifetime.

In a second hypothetical analysis, it is assumed the carbon capture subsidy is applicable only for the 100% solar utilisation (100% *SF*) processes to stimulate renewable energy applications. Under this assumption, the PCC and SA-PCC would not be eligible because they do not utilize 100% solar energy. Figure 137-B shows that for the SP-PCC technology, a break-even point occurs at approximately $300/tonne of captured $CO_2$. Although this is a comparatively very high carbon price for SP-PCC to be economically viable, this assessment could be used as a reference for government subsidy discussions and incentive programs in promoting solar energy use in power production sectors. Note that in all techno-economic assessments discussed above, two key advantages of SP-PCC have been neglected in the model cashflow of this technology: i) the convenience and added value of keeping the PCC operation away from the power cycle of the power-plant, and ii) the enhanced sustainability and lower carbon footprint of the SP-PCC in comparison to the alternatives. The potential of the latter advantage would require a comprehensive life cycle analysis (LCA) to unlock the full potential of the SP-PCC technology.
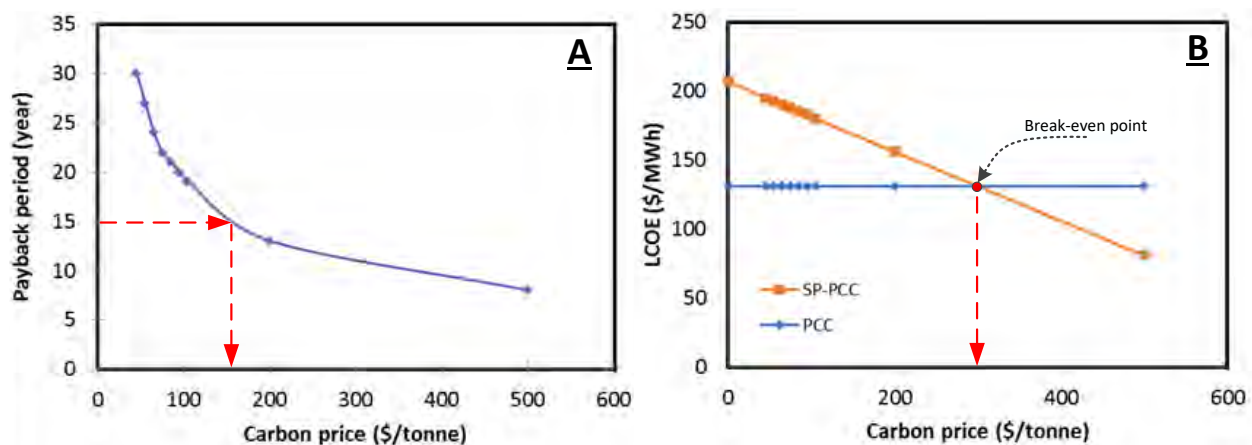


**Figure 137: (A) Payback period, and (B) the *LCOE* under difference carbon price scenarios for SP-PCC technology.**

## 7.6     Concluding remarks

In this chapter, we have evaluated the economic footprint of the novel concept of SP-PCC, which uses a So-St network to directly regenerate the rich solvent in the SCF. The economic model of the SP-PCC was compared with the typical PCC (steam completely bled from the power-plant steam cycle) and SA-PCC (steam produced in the SCF to partially contribute for the reboiler duty in the

PCC) counterparts. With a basic design, the *LCOE* for SP-PCC was AUD 206.6/MWh in reference to the AUD 141.6/MWh for the SA-PCC and AUD 130.9/MWh for the conventional PCC. This makes SP-PCC 57.8 and 45.9% higher than the PCC and SA-PCC counterparts, respectively. Similarly, the levelised cost of captured $CO_2$ was computed at AUD 358.9 /tonne$_{CO2}$ in reference to the AUD 108.4 /tonne$_{CO2}$ for the SA-PCC and AUD 67.4 /tonne$_{CO2}$ for the conventional PCC, respectively. It was found that the high cost of the SP-PCC was due to the 100% solar energy supply, with a large SCF and solvent storage required. Under the same 100% solar energy constraint, the *LCOE* of the SA-PCC scenario was prohibitively higher than that of SP-PCC. Therefore, if a process requires 100% solar energy usage where steam production is not part of the normal routine (i.e. steel and cement industries), SP-PCC would be the best technology option. Our comprehensive analysis of the economic parameters revealed potential areas for *LCOE* reductions. To realise the full potential of this new SP-PCC technology, future work should examine ways of leveraging solvent thermochemical properties and process innovations. Furthermore, the potential for enhancing sustainability via preserving steam production solely for power generation needs to be fully addressed in a comprehensive LCA.

# 8.    Life cycle analysis

In the previous chapters, the design and control aspects of the SP-PCC have been extensively investigated and have culminated in the final design specifications of the So-St network. A techno-economic analysis was undertaken to determine the commercial viability of the SP-PCC and to determine areas for reducing the levelised cost of electricity (*LCOE*). The economic viability of the SP-PCC was further compared with conventional PCC and also SA-PCC counterparts.

In this chapter, a life cycle analysis (LCA) is conducted to investigate the potential of SP-PCC in terms of its environmental impact: in particular its capacity to reduce greenhouse gas (GHG) emissions. Hence, an LCA boundary must be formulated based on cradle-to-gate, cradle-to-grave or cradle-to-cradle, which are distinguished by where the boundary ends. Cradle-to-gate takes the product from raw material extraction to the end of product manufacture; cradle-to-grave takes the product further through post-production and up to the end-of-life stage; and cradle-to-cradle creates an ecological loop where the end-of-life product is recycled and becomes an input to the initial cradle.

In this LCA, a cradle-to-grave method is applied to gain a thorough representation of the environmental burden for the SP-PCC, spanning from the initial extraction of coal to $CO_2$ sequestration, with a further consideration of waste disposal and decommissioning methods at the end of the project life (Figure 138). The choice of this boundary method is based on its greater breadth compared with the cradle-to-gate method, and its greater validity compared with the cradle-to-cradle method, since there is no clear path linking the sequestered $CO_2$ product to the initial coal extraction.
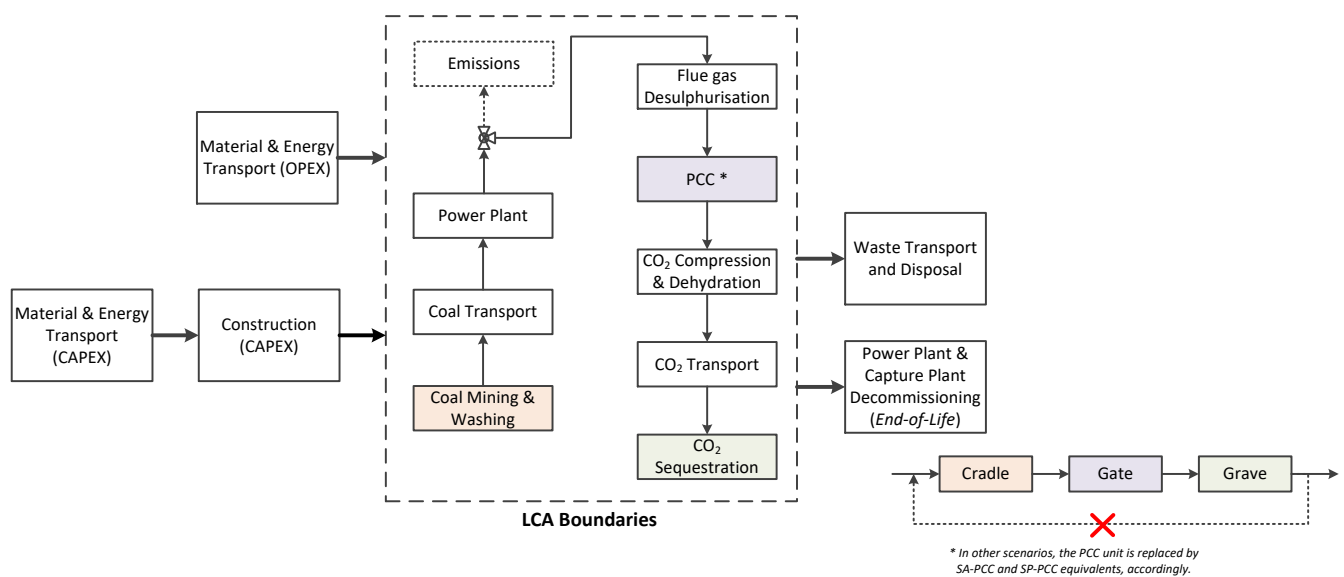


**Figure 138: The LCA appraisal block diagram. The cradle-to-grave framework is selected in this comparison to account for the environmental impact starting from the basic raw material extraction up to the end-of-life stage.**

Adopting a comparative structure similar to the techno-economic analysis, the SP-PCC is compared with four other scenarios: power-plant only, power-plant with conventional PCC, power-plant with SA-PCC at 23% solar fraction (*SF*), and power-plant with SA-PCC at 100% *SF*. The 23% SA-PCC scenario refers to the economically optimised specification that unvaryingly admits an energy penalty, despite the penalty being lower than that of conventional PCC. The 100% SA-PCC scenario refers to an idealised process that operates at the same *SF* as SP-PCC and is completely independent from the power-plant steam cycle. Having two scenarios for comparison, instead of the 23% commercial SA-PCC alone, enables a fairer assessment of the SP-PCC, since it has the advantage of liberation from the power-plant steam cycle. A sensitivity analysis is conducted to determine how the flue gas capture rate affects the levels of the global warming potential (GWP) abatement relative to the power-plant only scenario. Furthermore, the SP-PCC process is sensitised for different solar multiples (*SMs)* to gauge how the balance of SCF and solvent storage capacity (*SSC*) size can reduce GHG emissions. This chapter therefore provides an answer to the advantages and disadvantages of SP-PCC in terms of its environmental burden, and describes key methods of improvement that will incentivise the incorporation of SP-PCC into existing coal-fired power-plants.

## 8.1     LCA methodology

Life Cycle Analysis (LCA) is a tool for investigating the environmental burden of a process throughout its entire life span. The standardised method for conducting LCA (ISO14040) is used in this chapter [106]. This method consists of four key stages: goal and scope definition, inventory analysis, impact assessment and improvement analysis.

### 8.1.1  Goal and scope definition

The first goal of this LCA is to quantitatively determine the absolute environmental burden of SP-PCC. The second goal is to compare its impact with conventional PCC and SA-PCC to ascertain whether SP-PCC is environmentally advantageous. Five scenarios in total are investigated and are summarised with abbreviations as per the following:
1.   Power-plant without PCC (power-plant only)
2.   Power-plant with conventional PCC (PCC)
3.   Power-plant with solar-assisted PCC (SA-PCC) at 23% *SF*.
4.   Power-plant with solar-assisted PCC (SA-PCC) at 100% *SF*.
5.   Power-plant with solar-powered PCC (SP-PCC).

An additional sensitivity analysis is conducted to determine how the environmental burden can be improved by increasing the flue gas processing rate and the solar multiple (*SM*). As will be later discussed, the sensitivity for the flue gas processing rate is achieved by replicating the five scenarios for a power-plant with half the power output. The sensitivity analysis for the *SM* is conducted for the SP-PCC unit only by considering three other *SM* values, as will be later described. Similar to the Chapter 7, two SA-PCC scenarios are investigated, which enables a comparison of SP-PCC to the optimal SA-PCC process at its commercially viable capacity (23% *SF*) and an idealised SA-PCC process operating at an equivalent capacity to SP-PCC (100% *SF*).

In previous chapters, we have formulated the SP-PCC design with a capacity to capture 1.5 million tonnes per annum from a 660 MW$_e$ coal-fired power-plant. A 660 MW$_e$ power-plant is therefore used across all scenarios. However, the PCC capacity assumes only 34% of the power-plant flue gas is processed, and there is a scope to increase this percentage to have a greater emissions reduction. Thus, a sensitivity analysis will consider the effect of doubling this percentage by analysing a half-capacity power-plant at 330 MW$_e$, which ultimately produces half the flue gas volume.

A well-chosen functional unit is essential for ensuring a fair comparison between scenarios. For LCA of PCC processes, the functional unit is commonly levelised by either an energy unit (MWh) or a mass unit (tonnes of $CO_2$ captured). For ease of formulating the life cycle inventory, the functional unit is selected as a mass unit, in particular the capture and sequestration of 1 tonne of $CO_2$. This choice causes all scenarios to have consistent inventories upstream and downstream of the PCC unit, since the processing of 1 tonne $CO_2$ specifies the mass of coal input to the power-plant according to the mass balance principles. The only variable external to the PCC unit which changes between scenarios is the energy output (MWh) from the power-plant, due to the energy penalty when steam is bled from the power-plant steam cycle to be used in the reboiler duty for the desorber of the PCC. Inventories for the PCC unit itself will differ between all scenarios, based on the different material and energy components. An energy functional unit will also be used in the final analysis to determine emissions per MWh power production.

To conduct an effective and comprehensive LCA, the process system boundary must be defined. A cradle-to-grave assessment is conducted, which accounts for processes of resource extraction, transportation, combustion, carbon capture, sequestration and the disposal of waste products at the end of their life cycle, as depicted in Figure 138. It must be noted that the power-plant only scenario does not include the chain of process blocks downstream from the power-plant (desulfurisation, PCC, $CO_2$ compression and dehydration, $CO_2$ transport, $CO_2$ sequestration). Only the construction of the power-plant, PCC unit, $CO_2$ transport and $CO_2$ sequestration are considered since they contain the major vessels.

## 8.1.2  Life cycle inventory

The life cycle inventory (LCI) collects and quantifies the energy and material inputs, waste outputs and emissions data relevant to the defined process system boundary. All assumptions used in the model formulation are also defined in the LCI. The scenarios were modelled using openLCA (v.1.10), which is an open-source software developed by GreenDelta. The *EcoInvent 3.6* database was integrated into openLCA as a source for the emissions data of inputs and outputs within the life cycle boundary. Table 34 shows the overall process specifications based on our previous parameters. This LCI uses similar assumptions to the work of Weihs et al. 2020 [107].

**Table 34: Summary of overall process specifications based on previous assumptions for this case-study.**

| Parameter | Value | Units |
|-----------|-------|-------|
| Net power-plant output | 660 | MW$_e$ |
| $CO_2$ emission | 595 | t/h |

| | | |
|---|---:|---|
| Plant life | 30 | y |
| Hours operational per year | 8760 | h/y |
| Net electricity produced | 5,780,000 | $MW_h$ |
| Levelised $CO_2$ emission | 0.9 | $t/MW_h$ |
| $CO_2$ captured | 1.5 | Mt/y |

Given the choice of functional unit, all energy and material values spanning the entire project lifetime must be scaled down to reflect their contribution to the capture of 1 tonne $CO_2$. In particular, all capital material and energy flows have to be scaled down, since they are initial inputs with impacts that must be distributed over the project lifespan. A capital multiplier is calculated as below as a scaling factor for capital materials and energy flows [108]. This method assumes there is no social discount factor for future $CO_2$ emissions:

$$\textbf{\textit{Capital Multiplier}} = \frac{CO_2 \ functional \ unit}{CO_2 \ over \ lifespan} = \frac{1 \ t_{CO2}}{1.5 \times 10^6 \frac{t_{CO2}}{y} \cdot 30 \ y} = \textbf{2.22} \times \textbf{10}^{-8} \qquad \textit{Eq. 97}$$

### Coal production inventory

Coal production entails the mining and washing required to prepare the coal for use in the power-plant. Bituminous (black) coal is assumed as the base fuel for generating power. The inventory for coal is taken from the *EcoInvent 3.6* database, which accounts for emissions from inputs and outputs of the coal mining operation and preparation. In terms of coal transport, the power-plant location is assumed to be within 30 km of the mine site. This distance is segmented into transport distances of 20 km by rail and 10 km by conveyor, which is an arrangement commonly adopted at the NSW power-plants of Mt. Piper, Bayswater and Eraring [108]. The calorific value of black coal was assumed as the average value across Mt. Piper, Eraring and Bayswater power-plants [109]. The electrical energy is assumed to be supplied from the Australian power grid.

### Power-plant inventory

The power-plant inventory is summarised in Table 35. It is assumed that 34% of the flue gas from the power-plant is processed in the PCC unit, and that a 90% $CO_2$ capture efficiency is achieved for this processed flue gas [29]. The coal input flow is specified based on the 1 tonne $CO_2$ capture constraint, after assuming values for specific $CO_2$ emissions and coal calorific value [108]. The water consumption requirements are based on literature data [110]. Fly ash emissions from the power-plant are based on data from the NREL [111], and it is assumed that these emissions are treated and disposed of according to the *EcoInvent* database. The power-plant construction requirements are also based on data from the NREL [111]. The key construction materials considered are concrete, steel, aluminium and iron; all minor materials including plastics, copper, wood and glass are assumed negligible due to insufficient data. Here, the LCI for construction accounts for the emissions of the construction material production processes. It does not account for the emissions from the construction process itself, due to the lack of accurate data and being deemed negligible compared with other contributors since it is a capital input. For decommissioning of the power-plant, a 75% materials recovery is assumed for the construction materials to be used as scrap metal in secondary metal production operations while the remaining percentage is sent to landfill [111].

**Table 35: Summary of power-plant inventory assumptions.**

| Parameter | Value | Units | Reference |
|---|---|---|---|
| $CO_2$ captured | 1 | tonne | - |
| $CO_2$ capture efficiency | 90 | % | - |
| Power-plant flue gas processed | 34 | % | [29, 84] |
| Specific $CO_2$ emissions | 0.874 | tonne/MWh | [108] |
| Coal calorific value | 23.8 | MJ/kg coal | [108] |
| Higher heating value efficiency | 36 | % | [108] |
| Energy generated (electrical) | 3.74 | $MWh_e$ | Aspen® |
| Energy generated (thermal) | 10.386 | $MWh_t$ | Aspen® |
| Total coal input | 1.571 | tonne | - |
| Water (boiling and cooling) | 146.3 | $L/MWh_e$ | [110] |
| **Emissions/waste** | | | |
| $CO_2$ captured | 1 | tonne | - |
| $CO_2$ processed by PCC (34%) | 1.11 | tonne | - |
| $CO_2$ unprocessed (66%) | 2.16 | tonne | - |
| $CO_2$ total power-plant emissions | 3.27 | tonne | - |
| Fly ash specific emissions | 26,580 | $kg/GWh_e$ | [111] |
| Fly ash emissions | 99.4 | $kg/tonne_{CO2}$ | - |
| **Coal transport** | | | |
| Freight distance | 20 | Km | - |
| Conveyor distance | 10 | km | - |
| **Construction** | | | |
| Concrete | 158,758 | $kg/MW_e$ | [111] |
| Steel | 50,721 | $kg/MW_e$ | [111] |
| Aluminium | 419 | $kg/MW_e$ | [111] |
| Iron | 619 | $kg/MW_e$ | [111] |
| Construction materials recovery | 75 | % | [111] |

The power-plant energy output varies across all scenarios, particularly for SA-PCC, due to the differences in *SF* contributions, which are summarised in Table 36. The desorber unit is constant across the PCC and SA-PCC scenarios, and the thermal energy contributions of the power-plant steam therefore create an energy penalty to the overall electrical output of the power-plant. The desorption energy requirements for SP-PCC are greater than the other scenarios, since the redesign of the desorber to the So-St configuration using $CO_2$-rich MEA solvent causes a larger thermal energy requirement. Note that the calculated energy penalties are lower than the reported energy penalties, which are in the range of 19.5–40% [112]; however, this results from the specified 34% of flue gas from the reference 660 $MW_e$ power-plant being processed rather than the entire amount. If all the flue gas was processed at a $CO_2$ capture rate of 90%, then the energy penalty would be almost tripled and in the range of literature values.

**Table 36: Power-plant energy outputs across scenarios.**

| Parameter | PCC | SA-PCC 23 | SA-PCC 100 | SP-PCC | Units |
|---|---|---|---|---|---|
| Solar fraction | 0 | 23 | 100 | 100 | % |
| **Desorber energy requirements** | | | | | |

| | | | | | |
|---|---|---|---|---|---|
| Total | 1.04 | 1.04 | 1.04 | 2.44 | MWh$_t$/tonne$_{CO2}$ |
| | 3.74 | 3.74 | 3.74 | 8.78 | GJ$_t$/tonne$_{CO2}$ |
| Solar contribution | 0 | 0.24 | 1.04 | 2.44 | MWh$_t$/tonne$_{CO2}$ |
| | 0 | 0.86 | 3.74 | 8.78 | GJ$_t$/tonne$_{CO2}$ |
| Power-plant steam contribution | 1.04 | 0.80 | 0 | 0 | MWh$_t$/tonne$_{CO2}$ |
| | 3.74 | 2.88 | 0 | 0 | GJ$_t$/tonne$_{CO2}$ |
| **Power-plant energy outputs** | | | | | |
| Net thermal energy | 9.34 | 9.59 | 10.39 | 10.39 | MWh$_t$/tonne$_{CO2}$ |
| | 33.62 | 34.52 | 37.40 | 37.40 | GJ$_t$/tonne$_{CO2}$ |
| Net electrical energy | 3.36 | 3.45 | 3.74 | 3.74 | MWh$_e$/tonne$_{CO2}$ |
| | 12.10 | 12.42 | 13.46 | 13.46 | GJ$_e$/tonne$_{CO2}$ |
| Energy penalty | 10.0 | 7.7 | 0 | 0 | % |

The flue gas composition is summarised in Table 37. The mass flowrate and flue gas compositions were determined using our Aspen® model. However, the flue gas stream in the Aspen® model only contains the major components ($H_2O$, $CO_2$, $O_2$ and $N_2$) and does not include $SO_2$, $NO_x$ and trace elements due to ensuring computational simplicity in previous modellings. Therefore, emissions data for the excluded components were gathered based on Weihs et al. 2020 [107]. These emissions are accounted for in the unprocessed flue gas from the power-plant; however, it is assumed that the processed flue gas is cleaned of these components through an electrostatic precipitator (ESP), desulfurisation unit and the de-$NO_x$ units. The energy and material requirements for these processes are deemed negligible compared with the rest of the power-plant for this LCA study.

**Table 37: Summary of flue gas composition.**

| Parameter | Value | Units | Reference |
|---|---|---|---|
| **Main flue gas components (per tonne of $CO_2$ in the flue gas)** | | | |
| $H_2O$ | 0.187 | tonne/tonne$_{CO2}$ | Aspen® |
| $O_2$ | 0.336 | tonne /tonne$_{CO2}$ | Aspen® |
| $N_2$ | 3.878 | tonne /tonne$_{CO2}$ | Aspen® |
| $SO_2$ | 0.0019 | tonne /tonne$_{CO2}$ | [108] |
| $NO_x$ | 0.0022 | tonne /tonne$_{CO2}$ | [108] |
| **Trace flue gas components (per tonne of $CO_2$ in the flue gas)** | | | |
| Si | 0.018501 | kg/tonne$_{CO2}$ | [108] |
| Fe | 0.003307 | kg/tonne$_{CO2}$ | [108] |
| Mg | 0.000824 | kg/tonne$_{CO2}$ | [108] |
| Ti | 0.000389 | kg/tonne$_{CO2}$ | [108] |
| Ca | 0.000320 | kg/tonne$_{CO2}$ | [108] |
| K | 0.000183 | kg/tonne$_{CO2}$ | [108] |
| Ba | 0.000114 | kg/tonne$_{CO2}$ | [108] |
| Mn | 0.000057 | kg/tonne$_{CO2}$ | [108] |
| P | 0.000034 | kg/tonne$_{CO2}$ | [108] |
| V | 0.000023 | kg/tonne$_{CO2}$ | [108] |

### *PCC inventory*

The PCC inventory is where key variation between scenarios emerges. The chemical emissions for the PCC inventory are summarised in Table 38. The major emissions of $CO_2$, MEA and water were

based on our Aspen® Model. Minimal emissions in gaseous, aqueous and solid forms were accounted for based on literature values [113]. These minimal emissions were assumed constant across all scenarios, since they mostly emerge from the absorber unit which is unchanged parameter across all scenarios. Any variation of emissions due to the desorption process is unaccounted for due to lack of data for our novel So-St process.

**Table 38: Assumptions for PCC chemical emissions.**

| Parameter | Value | Units | Reference |
|-----------|-------|-------|-----------|
| **Emission to air** | | | |
| $CO_2$ | 111 | kg/tonne$_{CO2}$ | Aspen® |
| Monoethanolamine | 42.7 | g/tonne$_{CO2}$ | Aspen® |
| Ammonia | 1.8 | g/tonne$_{CO2}$ | [113] |
| Formaldehyde | 4.3 | g/tonne$_{CO2}$ | [113] |
| Acetaldehyde | 4.7 | g/tonne$_{CO2}$ | [113] |
| Acetone | 5.2 | g/tonne$_{CO2}$ | [113] |
| Methyl amine | 3.4 | g/tonne$_{CO2}$ | [113] |
| Acetamide | 0.0011 | g/tonne$_{CO2}$ | [113] |
| **Emission to water** | | | |
| Monoethanolamine | 2.14 | kg/tonne$_{CO2}$ | Aspen® |
| Water | 667.8 | kg/tonne$_{CO2}$ | Aspen® |
| Ammonia | 0.4 | g/tonne$_{CO2}$ | [113] |
| Diethanolamine | 0.0044 | g/tonne$_{CO2}$ | [113] |
| Formaldehyde | 0.0001 | g/tonne$_{CO2}$ | [113] |
| Acetone | 0.0023 | g/tonne$_{CO2}$ | [113] |
| Methyl amine | 0.0012 | g/tonne$_{CO2}$ | [113] |
| **Solid** | | | |
| Gypsum | 4.3 | kg/tonne$_{CO2}$ | [113] |

Various other parameters and assumptions are held constant across the different LCA scenarios, which are summarised in Table 39. The capacities of the lean cooling HX for the absorber and condenser for the desorber are constant, enabling a calculation of the equivalent cooling water mass based on the specific heat formula:

$$Q_c = m_w C_{p,w} \Delta T \qquad\qquad Eq.\ 98$$

Where $Q_c$ is the total cooling duty; $m_w$ is the cooling water mass flowrate; $C_{p,w}$ is the specific heat capacity of water; and $\Delta T$ is the water temperature gradient based on an assumed 10°C pinch. The construction requirements are based on the major cylindrical vessels, with dimensions specified in the previous techno-economics work.

**Table 39: Major vessel specifications from the techno-economics work.**

| Equipment | Parameter | PCC | SA-PCC-23% | SA-PCC-100% | SP-PCC |
|-----------|-----------|-----|------------|-------------|--------|
| Absorber | Diameter (m) | 18 | 18 | 18 | 18 |
| | Height (m) | 15 | 15 | 15 | 15 |
| Desorber | Diameter (m) | 12 | 12 | 12 | - |
| | Height (m) | 13 | 13 | 13 | - |

| | | | | | |
|---|---|---|---|---|---|
| Flash drum | Diameter (m) | 4.1 | 4.1 | 4.1 | 4.1 |
| | Height (m) | 20.97 | 20.97 | 20.97 | 20.97 |
| Storage tank | Number | - | 2 | 253 | 193 |
| | Diameter (m) | - | 45.7 | 45.7 | 45.7 |
| | Height (m) | - | 14.6 | 14.6 | 14.6 |

A vessel thickness and steel density were assumed, which enabled the vessels' masses to be calculated based on the following equation:

$$V = \frac{\pi H((D+2t)^2 - D^2)}{4} + 2\frac{\pi t(D+2t)^2}{4}$$

*Eq. 99*

Where $V$ is the cylindrical surface volume; $D$ is the vessel diameter; $H$ is the vessel height; and $t$ is the vessel thickness. The steel density is based on low-alloy carbon steel [108], and a standard vessel thickness is assumed [95]. The construction of pumps, blowers and heat exchangers is not considered due to being of lower masses and having less contribution to the overall emissions of the process. The construction of parabolic trough collectors (PTCs) requires various materials with mass contributions based on literature values [114]. Similar to the power-plant process, the construction emissions consider the materials productions only and exclude the energy requirements for construction activities due to insufficient data.

**Table 40: General PCC assumptions.**

| Parameter | Value | Units | Reference |
|---|---|---|---|
| **Heat exchangers (HX)** | | | |
| Condenser duty | 0.532 | MWh/tonne$_{CO2}$ | Aspen® |
| Lean cooling HX duty | 0.502 | MWh/tonne$_{CO2}$ | Aspen® |
| Total cooling duty | 1.035 | MWh/tonne$_{CO2}$ | Aspen® |
| Water specific heat capacity | 4.18 | kJ/kg K | - |
| Water temperature gradient $(70-25°C)$ | 45 | K | - |
| Cooling water mass | 19.8 | tonne/tonne$_{CO2}$ | - |
| **Solvent-PCC construction** | | | |
| Vessel thickness | 14.7 | mm | [95] |
| Steel density | 7850 | kg/m$^3$ | [108] |
| Construction materials recovery | 75 | % | [111] |
| **PTC construction** | | | |
| Galvanised steel | 0.98 | kg/MWh | [114] |
| Stainless steel | 0.029 | kg/MWh | [114] |
| Low iron float glass | 0.65 | kg/MWh | [114] |
| Ceramic | 0.0033 | kg/MWh | [114] |
| Silicone | 0.0033 | kg/MWh | [114] |
| Borosilicate glass | 0.043 | kg/MWh | [114] |
| Concrete | 0.00032 | m$^3$/MWh | [114] |

The variables that differ between the scenarios are summarised in Table 40. The MEA and water inputs are based on both the capital and operation flows according to the Aspen® model. The SP-PCC process requires more MEA and water due to the large amount of solvent storage. The electrical

power demand is constant across scenarios for the flue gas blower and rich solvent pump; however, the cycle pump has varying electrical output in order to pump the solvent across the SCF due to its large size. An auxiliary correction factor of 5% is assumed to account for extra auxiliaries not accounted for in the typical PCC process.

The breakdown of the vessel construction material requirements is also shown in Table 40, based on specifications from the techno-economics chapter, and the PTC construction materials are calculated based on the energy capacity demanded by the SCF. The land area of the SCF is accounted for, due to being significantly large. It must be noted that the land inventory is in units of $m^2y$, since the impact of land is distributed across the entire project lifespan. All other land requirements are excluded in this LCI due to being deemed negligible compared with that of the SCF. The SA-PCC process has an added requirement of thermal energy storage (TES), with inputs of oil, nitrate salts and insulation calculated based on the previous techno-economics chapter. The insulation for the TES tanks is chosen to be rockwool with 30 mm thickness.

**Table 41: Comparative PCC parameters.**

| Parameter | PCC | SA PCC 23 | SA PCC 100 | SP PCC | Units |
|---|---|---|---|---|---|
| MEA Input | 2.255 | 2.255 | 2.255 | 35.25 | kg/tonne$_{CO2}$ |
| Water Input | 466.5 | 466.5 | 466.5 | 543.5 | kg/tonne$_{CO2}$ |
| **Electrical Energy** | | | | | |
| Flue Gas Blower | 52,560 | 52,560 | 52,560 | 52,560 | MWh/y |
| Rich Solvent Pump | 800 | 800 | 800 | 800 | MWh/y |
| Cycle Pump | 0 | 1,748 | 9009 | 3,453 | MWh/y |
| Total Electricity | 53,360 | 55,108 | 62,369 | 56,813 | MWh/y |
| Specific Electricity | 35.57 | 36.74 | 41.58 | 37.88 | kWh/tonne$_{CO2}$ |
| Auxiliary Correction Factor | 5 | 5 | 5 | 5 | % |
| Adjusted Electricity | 37.35 | 38.58 | 43.66 | 39.77 | kWh/tonne$_{CO2}$ |
| **Solvent-PCC Construction** | | | | | |
| Absorber (mass) | 157 | 157 | 157 | 157 | tonne |
| Desorber (mass) | 83 | 83 | 83 | - | tonne |
| Drum (mass) | 34 | 34 | 34 | 34 | tonne |
| Cold/Lean Storage Tank (mass) | - | 621 | 78,558 | 59,928 | tonne |
| Hot/Rich Storage Tank (mass) | - | 621 | 78,558 | 59,928 | tonne |
| Total Construction Steel | 274 | 1,516 | 157,390 | 120,047 | tonne |
| **PTC Construction** | | | | | |
| Solar Energy | 0 | 0.2 | 1.04 | 2.44 | MWh$_t$/tonne$_{CO2}$ |
| Galvanised steel | - | 0.237 | 1.022 | 2.396 | kg/tonne$_{CO2}$ |
| Stainless steel | - | 0.007 | 0.030 | 0.071 | kg/tonne$_{CO2}$ |
| Low iron float glass | - | 0.158 | 0.678 | 1.589 | kg/tonne$_{CO2}$ |
| Ceramic | - | 0.0008 | 0.0034 | 0.0081 | kg/tonne$_{CO2}$ |
| Silicone | - | 0.0008 | 0.0034 | 0.0081 | kg/tonne$_{CO2}$ |
| Borosilicate glass | - | 0.0104 | 0.0448 | 0.1051 | kg/tonne$_{CO2}$ |
| Concrete | - | 0.00008 | 0.00033 | 0.00078 | m$^3$/tonne$_{CO2}$ |
| **Solar Field Area** | | | | | |
| Land Area | - | 1,877,294 | 10,725,920 | 10,018,050 | m$^2$ |

| | | | | | |
|---|---|---|---|---|---|
| Land Inventory | - | 56,318,819 | 321,777,591 | 300,541,500 | $m^2$ y |
| **Thermal Storage** | | | | | |
| Oil | - | 328 | 1856 | - | t |
| Nitrate salts | - | 41,000 | 11,840,000 | - | t |
| Insulation (Rockwool) | - | 3,288 | 415,932 | - | $m^2$ |

### *Compression, dehydration, transport and sequestration inventory*

The inventory for compression, dehydration, transport and sequestration are summarised in Table 41. The $CO_2$ compression stage is essential for enabling the ease of $CO_2$ transport within the pipeline. The work ($W$) required for compression was calculated according to the following equation:

$$W = \frac{ZRT}{M} \cdot \frac{N\gamma}{\gamma-1}\left[\left(\frac{P_2}{P_1}\right)^{\frac{\gamma-1}{N\gamma}} - 1\right]$$   *Eq. 100*

Where $Z$ is the compressibility; $R$ is the ideal gas constant (J/mol K); $T$ is the suction temperature (K); $M$ is the gas molar mass (g/mol); $N$ is the number of compressor stages; $\gamma$ is the heat capacity ratio; $P_1$ is the inlet pressure; and $P_2$ is the outlet pressure. The compression stream specifications are based on [84]. The electricity for compression is calculated according to *Eq. 101*, where $\eta_{is}$ is the isentropic efficiency and $\eta_m$ is the mechanical efficiency.

$$E = \frac{W}{\eta_{is} \cdot \eta_m}$$   *Eq. 101*

The construction materials and fugitive emissions of the compressor and dehydration processes are not accounted for, since they are deemed less significant than the power-plant and PCC unit vessels. The assumptions for the transportation stage are based on Weihs et al. [107], which gathered pipeline specifications based on an Integrated Carbon Capture and Storage Economic Model. The sequestration site is deemed to be the Darling Basin. The total transport distance is 850 km, taken as the average distance from Mt. Piper, Bayswater and Eraring power-plants to the Darling Basin sequestration site (Figure 139). The insulation for the pipeline is chosen to be rockwool with 30 mm thickness. The large distance of pipeline transport naturally creates a pressure-drop in the $CO_2$ stream. The specific pressure loss is taken to be 0.06 bar/km [115], and the recommended number of booster stations is one per 100 km [116]. Nine booster stations are therefore assumed and the electrical energy for recompression is calculated using *Eqs. 100* and *101*. The construction of these booster stations is deemed to have a trivial contribution to the overall emissions and is therefore neglected. The fugitive emissions that occur across the $CO_2$ pipeline are also considered [115]. Table 42 lists the main inventory items for compressor, pipeline transport and sequestration.
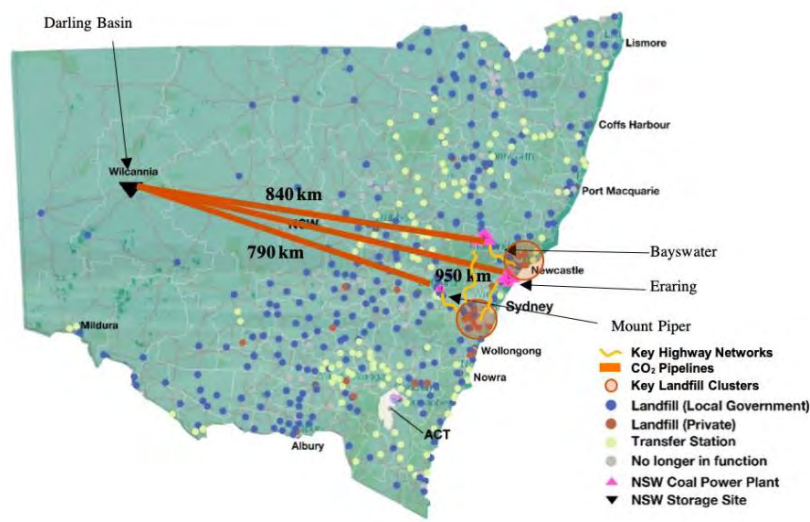
**Figure 139: Map of pipeline transport distances from three power-plants (Mt. Piper, Bayswater and Eraring) to the Darling Basin sequestration site. Figure recreated from Weihs et al., 2020 [107].**

The sequestration inventory is based on [117] which assumes six injection wells with depths of 1.5 km over a 30 year lifespan. Their work derived values for the indirect $CO_2$ emissions of construction and decommissioning, along with the specific electrical consumption of the sequestration site. The values are scaled linearly since sequestration sites in Australia, such as the Gippsland Basin, are reported to be 2.5 to 3 km [118]. Emissions due to maintenance are considered negligible in this LCI due to the lack of data, while also having a much lower order of magnitude than other components. Furthermore, various construction components such as the construction of buildings and offices are neglected for simplicity and due to data unavailability.

**42: Inventory for compressor, pipeline transport and sequestration.**

| Parameter | Value | Units | Reference |
|---|---|---|---|
| **Compressor** | | | |
| Compressibility (Z) | 0.9942 | - | [108] |
| Ideal Gas Constant € | 8.3145 | J/mol K | - |
| Suction Temperature (T) | 303.15 | K | [84] |
| Molar mass (M) | 44.01 | g/mol | - |
| Inlet Pressure | 2 | bar | Aspen® |
| Outlet Pressure | 110 | bar | [84] |
| Heat capacity ratio | 1.2938 | - | - |
| Compressor Stages | 4 | - | [84] |
| Isentropic efficiency | 0.8 | - | [108] |
| Mechanical Efficiency | 0.99 | - | [108] |
| Work (W) | 256.2 | MJ/tonne$_{CO2}$ | - |
| Electricity € | 89.9 | kWh/tonne$_{CO2}$ | - |
| **Pipeline Construction** | | | |
| Pipeline Distance | 850 | km | [108] |
| Pipeline Diameter | 0.3 | m | [108] |
| Pipeline Thickness | 8.53 | mm | [108] |
| Steel density | 7850 | kg/m³ | [108] |
| Pipeline Mass | 55,168,000 | kg | - |

| | | | | |
|---|---|---|---|---|
| Insulation (Rockwool) Area | 1,602,212 | m$^2$ | | - |
| **Pipeline Recompression** | | | | |
| Specific Pressure Loss | 0.06 | bar/km | | [115] |
| Specific Booster Stations | 1 | /100 km | | [116] |
| No. Booster Stations | 9 | | | - |
| Pressure Loss per Booster Station | 5.67 | bar | | - |
| Work (W) per Booster Station | 0.75 | MJ/tonne$_{CO2}$ | | - |
| Electricity € per Booster Station | 0.26 | kWh/tonne$_{CO2}$ | | - |
| Total Recompression Electricity | 2.38 | kWh/tonne$_{CO2}$ | | - |
| **Pipeline Emissions** | | | | |
| Fugitive $CO_2$ emissions | 2.32 | tonne$_{CO2}$/(km y) | | [115] |
| **Sequestration** | | | | |
| Construction & Decommissioning Emissions | 0.12 | kg$_{CO2}$/tonne$_{CO2}$ | | [117] |
| Electricity Consumption | 7 | kWh/tonne$_{CO2}$ | | [117] |
| Scaling Factor | 2 | | | Scale 1.5 to 3 km |
| Scaled Emissions | 0.24 | kg$_{CO2}$/tonne$_{CO2}$ | | [117] |
| Scaled Electricity Consumption | 14 | kWh/tonne$_{CO2}$ | | [117] |

## 8.1.3  Impact assessment

The ReCiPe Midpoint (H) method is used in this LCA to convert the LCI results into a list of impact indicator scores. The 'H' stands for 'hierarchical' which is the default impact assessment method under consensus. The ReCiPe method has a broad range of global impact categories, summarised in Table 43.

**Table 43: Summary of impact categories for ReCiPe Midpoint (H) method.**

| Name | Unit |
|---|---|
| Water depletion (WDP) | m$^3$ |
| Terrestrial acidification (TAP100) | kg$_{SO2-eq}$ |
| Ionising radiation (IRP_HE) | kg$_{U235-eq}$ |
| Climate change (GWP100) | kg$_{CO2-eq}$ |
| Photochemical oxidant formation (POFP) | kg$_{NMVOC}$ |
| Human toxicity (HTPinf) | kg$_{1,4-DCB-eq}$ |
| Metal depletion (MDP) | kg$_{Fe-eq}$ |
| Ozone depletion (ODPinf) | kg$_{CFC-11-eq}$ |
| Agricultural land occupation (ALOP) | m$^2$a |
| Marine ecotoxicity (METPinf) | kg$_{1,4-DCB-eq}$ |
| Terrestrial ecotoxicity (TETPinf) | kg$_{1,4-DCB-eq}$ |
| Marine eutrophication (MEP) | kg$_{N-eq}$ |
| Natural land transformation (NLTP) | m$^2$ |
| Freshwater ecotoxicity (FETPinf) | kg$_{1,4-DCB-eq}$ |
| Freshwater eutrophication (FEP) | kg$_{P-eq}$ |
| Particulate matter formation (PMFP) | kg$_{PM10-eq}$ |
| Urban land occupation (ULOP) | m$^2$a |

| Fossil depletion (FDP) | $kg_{oil-eq}$ |
|---|---|

## 8.2    Impact analysis results

The five main scenarios at the 660 $MW_e$ power-plant were successfully simulated using the *openLCA* software according to their respective LCIs. The environmental impacts were identified and compared between the scenarios. The main impact factor of interest is expressed as the climate change impact, which is quantified by the notion of the global warming potential (GWP). The GWP relates the heat absorbed by a GHG emission and quantifies it as the amount of $CO_2$ that will absorb an equivalent amount of heat as the GHG [119]. Figure 140 compares the GWP impact for each scenario for the same coal intake, and then calculates the levelised GWP per $MWh_e$ power-plant electrical output. Given the choice of functional unit, the impacts were calculated as 'emissions per tonne $CO_2$ captured', which enables a direct comparison between the PCC units since they capture a constant mass of $CO_2$. However, the results are also converted into 'emissions per $MWh_e$', which is a more relevant unit for comparing the overall process system, since it bases the emissions on the power-plant electrical power output. The LCA model can be shown to be validly formulated with satisfactory accuracy by comparing the GWP of the power-plant only study to the literature values. In this study, the GWP for the power-plant only scenario is calculated as 1055 $kg_{CO2-eq}$/MWh, which is of a similar magnitude to literature values of 938 $kg_{CO2-eq}$/MWh [108], 990 $kg_{CO2-eq}$ /MWh [120] and 888 $kg_{CO2-eq}$ /MWh [121]. The calculated value being slightly larger than the literature values shows that a conservative LCI has been employed, which may cause some overestimation of the GWP.
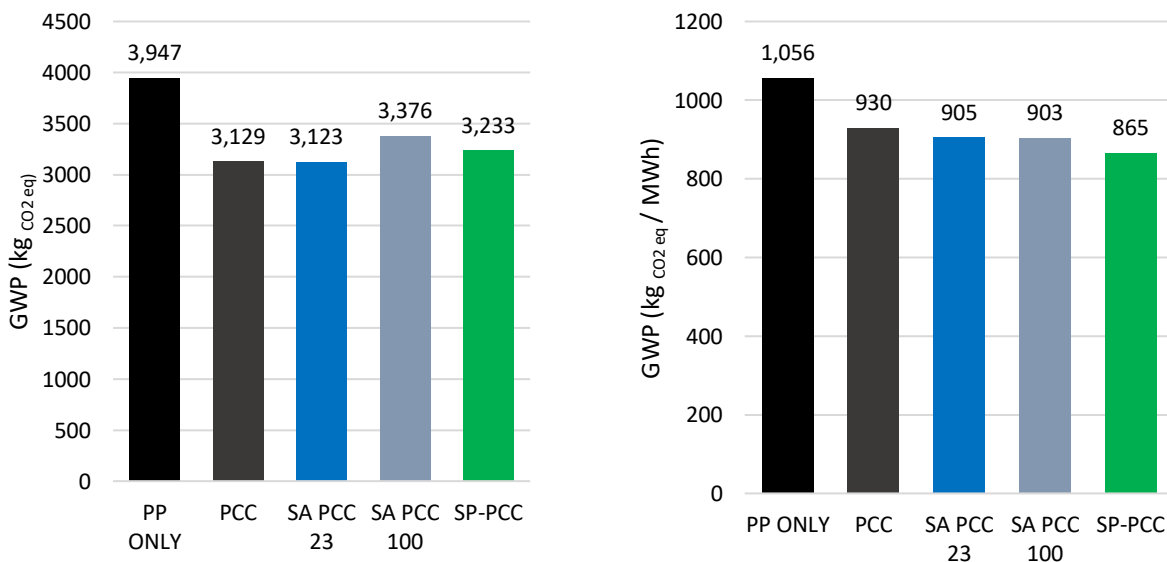


**Figure 140: Global warming potential (GWP) for each 660 $MW_e$ scenario: (left) the net GWP for each scenario where all PCC scenarios capture 1 tonne $CO_2$ and power-plant only scenario operates at the same coal intake to PCC scenarios; (right) GWP per $MWh_e$ power-plant electrical output.**

The power-plant only scenario has the greatest GWP as expected, since all of its $CO_2$ emissions are released to the atmosphere. The conventional PCC and SA-PCC-23% scenarios are the most efficient in reducing the GWP, depicted by the lowest emissions per mass unit. As the *SF* increases in the SA-

PCC-100% and SP-PCC scenarios, the emissions per mass unit is larger. This displays the decreased efficiency of having 100% solar contribution, which is largely a result of the environmental impact of the large TES system for SA-PCC-100%, and large solvent storage system for the SP-PCC counterpart. Despite this, the emissions per energy unit conveys the advantages of the SP-PCC process.

The SP-PCC scenario emits the lowest amount of $CO_2$ per $MWh_e$ output by the power-plant. This is because SP-PCC does not contribute an energy penalty to the power-plant, meaning that more electrical output is generated by the power-plant relative to the $CO_2$ emissions. Thus, even though the SP-PCC unit causes greater emissions than conventional PCC and SA-PCC at the same $CO_2$ capture rate, the SP-PCC makes up for this by removing the energy penalty and causing the overall power-plant to emit less $CO_2$ for a constant energy output. The overall aim for CCS technologies is to reduce the $GWP/MWh_e$ of the power-plants; hence, this finding shows that SP-PCC would be highly environmentally advantageous compared with the other comparable PCC technologies.

The SA-PCC-23% shows a natural trend of having less GHG emissions than the conventional PCC, due to the integration of the solar component lowering the energy penalty. Notably, the SA-PCC-100% performs poorly compared with the SA-PCC-23%, which is a result of the large TES system having significant construction and nitrate salt requirements, thus bringing a notable environmental burden. It is therefore not environmentally advantageous to manipulate the SA-PCC by making the reboiler in the desorption unit completely independent of the power-plant steam cycle through increasing the solar-penetration (*SF*) ratio. The introduction of SA-PCC must therefore necessarily impose an energy penalty for the power-plant, in order to be environmentally sustainable. SP-PCC does not have this disadvantage, since it can achieve lower GHG emissions while being completely independent from the power-plant steam cycle. The abatement of emissions relative to the power-plant only scenario is displayed in Figure 141. The SP-PCC has the greatest abatement of GHG emissions per energy unit (190.8 $kg_{CO2-eq}$/MWh) and its advantage compared with SA-PCC-23% is 40.1 $kg_{CO2-eq}$/MWh (21% improvement). The GWP abatement further supports the advantage of SP-PCC in reducing the environmental burden of coal-fired power-plant processes.
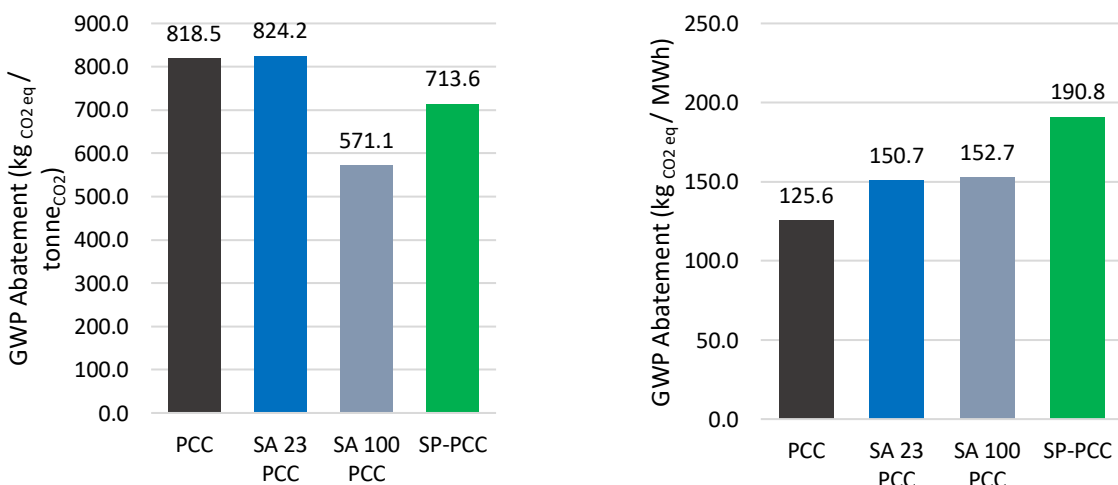


**Figure 141: Abatement of global warming potential (GWP) for each 660 MW$_e$ scenarios relative to the power-plant only scenario, in terms of kg$_{CO2-eq}$ emitted per tonne CO$_2$ captured (left) and kg$_{CO2-eq}$ emitted per MWh$_e$ produced from the power-plant (right).**

In order to understand the variation between the scenarios, a breakdown of the GWP contributors for each scenario is summarised in Table 44. Clearly, the power-plant only scenario is dominated by emissions from the power-plant itself, since the flue gas is not processed, but is directly emitted to the atmosphere. A comparison of SA-PCC-23% and SP-PCC displays that the increased emissions per mass unit for the latter are primarily a result of the large amount of MEA solvent required in the SP-PCC process, due to the large solvent storage system. Other factors such as the increased steel production and solar glass production also cause the SP-PCC to have greater emissions per mass unit than the SA-PCC-23%. The reason that the GWP performance of the SA-PCC-100% is inferior to the SA-PCC-23% is a result of the significant mass requirements for nitrate salts for TES. Nitrate salts are the third-largest GWP contributor in the SA-PCC-100% scenario. A key factor that may improve the viability of SA-PCC at 100% *SF* could be the implementation of TES systems that require less material input. The GWP breakdown further confirms that the predominant reason for SP-PCC to be advantageous over the other scenarios is its lack of energy penalty, which causes the relative contribution of each LCI component ($kg_{CO2-eq}$ / MWh) to be reduced due to the ultimately larger power output.

**Table 44: Breakdown of GWP for each scenario with top five GWP contributors.**

| Scenario | Process | $kg_{CO2-eq}$ / $tonne_{CO2}$ | $kg_{CO2-eq}$ / MWh |
|---|---|---|---|
| Power-plant only | GWP Total | 3,947.04 | 1,055.61 |
| | Power-plant | 3,547.50 | 948.76 |
| | Coal Mining and Preparation | 393.45 | 105.23 |
| | Transport (Conveyor) | 2.22 | 0.59 |
| | Steel Production | 1.80 | 0.48 |
| | Transport (Rail) | 1.64 | 0.44 |
| | Other | 0.43 | 0.12 |
| PCC | GWP Total | 3,128.57 | 930.06 |
| | Power-plant | 2,435.75 | 724.10 |
| | Coal Mining and Preparation | 393.45 | 116.96 |
| | Electricity | 171.07 | 50.85 |
| | PCC | 110.78 | 32.93 |
| | MEA Production | 6.60 | 1.96 |
| | Other | 10.93 | 3.25 |
| SA PCC (23%) | GWP Total | 3,122.80 | 904.88 |
| | Power-plant | 2,435.75 | 705.79 |
| | Coal Mining and Preparation | 393.45 | 114.01 |
| | Electricity | 163.59 | 47.40 |
| | PCC | 110.78 | 32.10 |
| | MEA Production | 6.60 | 1.91 |
| | Other | 12.63 | 3.66 |
| SA PCC (100%) | GWP Total | 3,375.99 | 978.24 |
| | Power-plant | 2,435.75 | 705.79 |
| | Coal Mining and Preparation | 393.45 | 114.01 |

| | | | |
|---|---|---|---|
| | Nitrate Salts | 237.16 | 68.72 |
| | Electricity | 169.21 | 49.03 |
| | PCC | 110.78 | 32.10 |
| | Other | 29.63 | 8.59 |
| SP PCC | GWP Total | 3,233.49 | 864.78 |
| | Power-plant | 2,435.75 | 651.43 |
| | Coal Mining and Preparation | 393.45 | 105.23 |
| | Electricity | 164.91 | 44.10 |
| | PCC | 110.78 | 29.63 |
| | MEA Production | 103.13 | 27.58 |
| | Other | 25.46 | 6.81 |

The values for the remaining impact assessment criteria are displayed in Table 45 and Table 46. Visual representations of the tabular data can be referred to in Appendix B. The following criteria are excluded, since they contributed zero impact across all scenarios: metal depletion (MDP), agricultural land occupation (ALOP), natural land transformation (NLTP), urban land occupation (ULOP), and fossil depletion (FDP).

**Table 45: Summary of impact results for ReCiPe Midpoint (H) impact assessment method (per tonne$_{CO2}$).**

| Name | Power-plant | PCC | SA PCC 23% | SA PCC 100% | SP-PCC | Unit |
|---|---|---|---|---|---|---|
| Water depletion | 0.00784 | 0.00784 | 0.00784 | 0.00784 | 0.00784 | m$^3$ |
| Terrestrial acidification | 14.44 | 12.37 | 11.80 | 12.99 | 12.99 | kg$_{SO2-eq}$ |
| Ionising radiation | 7.06 | 7.97 | 7.89 | 14.95 | 14.95 | kg$_{U235-eq}$ |
| Photochemical oxidant formation | 10.11 | 8.27 | 8.08 | 9.10 | 9.10 | kg$_{NMVOC}$ |
| Human toxicity | 1036.6 | 1096.7 | 1182.0 | 1251.5 | 1251.5 | kg$_{1,4-DCB-eq}$ |
| Ozone depletion | 9.99E-06 | 1.12E-05 | 1.11E-05 | 3.01E-05 | 3.01E-05 | kg$_{CFC-11-eq}$ |
| Marine ecotoxicity | 25.55 | 27.74 | 29.80 | 33.74 | 33.74 | kg$_{1,4-DCB-eq}$ |
| Terrestrial ecotoxicity | 0.0461 | 0.0520 | 0.0511 | 0.0737 | 0.0737 | kg$_{1,4-DCB-eq}$ |
| Marine eutrophication | 3.48 | 2.82 | 2.80 | 3.13 | 3.13 | kg$_{N-eq}$ |
| Freshwater ecotoxicity | 26.83 | 29.19 | 31.36 | 35.77 | 35.77 | kg$_{1,4-DCB-eq}$ |
| Freshwater eutrophication | 1.59 | 1.68 | 1.82 | 1.89 | 1.89 | kg$_{P-eq}$ |
| Particulate matter formation | 3.98 | 3.44 | 3.28 | 4.10 | 4.10 | kg$_{PM10-eq}$ |

**Table 46: Summary of impact results for ReCiPe Midpoint (H) impact assessment method (per MWh).**

| Name | PP | PCC | SA PCC 23% | SA PCC 100% | SP-PCC | Unit |
|---|---|---|---|---|---|---|
| Water depletion | 0.00210 | 0.00233 | 0.00227 | 0.00210 | 0.00210 | m$^3$ |
| Terrestrial acidification | 3.86 | 3.68 | 3.42 | 3.47 | 3.47 | kg$_{SO2-eq}$ |
| Ionising radiation | 1.89 | 2.37 | 2.29 | 4.00 | 4.00 | kg$_{U235-eq}$ |
| Photochemical oxidant formation | 2.70 | 2.46 | 2.34 | 2.43 | 2.43 | kg$_{NMVOC}$ |
| Human toxicity | 277.2 | 326.0 | 342.5 | 334.7 | 334.7 | kg$_{1,4-DCB-eq}$ |
| Ozone depletion | 2.67E-06 | 3.34E-06 | 3.22E-06 | 8.04E-06 | 8.04E-06 | kg$_{CFC-11-eq}$ |
| Marine ecotoxicity | 6.83 | 8.25 | 8.64 | 9.02 | 9.02 | kg$_{1,4-DCB-eq}$ |

| | | | | | |
|---|---|---|---|---|---|
| Terrestrial ecotoxicity | 0.0123 | 0.0155 | 0.0148 | 0.0197 | 0.0197 | $kg_{1,4-DCB-eq}$ |
| Marine eutrophication | 0.932 | 0.838 | 0.811 | 0.838 | 0.838 | $kg_{N-eq}$ |
| Freshwater ecotoxicity | 7.18 | 8.68 | 9.09 | 9.57 | 9.57 | $kg_{1,4-DCB-eq}$ |
| Freshwater eutrophication | 0.425 | 0.498 | 0.528 | 0.506 | 0.506 | $kg_{P-eq}$ |
| Particulate matter formation | 1.064 | 1.022 | 0.952 | 1.097 | 1.097 | $kg_{PM10-eq}$ |

According to these impact criteria, the disadvantages of the SP-PCC are as follows: i) ionising radiation, ozone depletion, terrestrial ecotoxicity, and marine eutrophication are relatively high due to the significant production of MEA solvent; and ii) marine and freshwater toxicities are high due to a combination of the increased MEA requirements and the steel requirements for construction. However, advantages for the SP-PCC are lower terrestrial acidification, photochemical oxidant formation, freshwater eutrophication and particulate matter formation emissions relative to the other scenarios. Despite GWP being the main impact factor for assessing the environmental viability of SP-PCC, the consideration of these other impact categories allows better decision making for methods of improving the SP-PCC process and reducing its emissions.

## 8.3    Sensitivity analysis of capture rate

Given that the SP-PCC design has been based on a constant $CO_2$ capture rate (1.5 Mt/y), there is scope to improve the relative GWP reductions by increasing the relative capture rate of the PCC processes. A sensitivity analysis is undertaken by investigating a scenario at half the power-plant capacity (330 $MW_e$). The annual $CO_2$ mass capture rate is kept constant (1.5 $Mtonne_{CO2}$), thus the percentage of the flue gas from the power-plant processed by the PCC unit is multiplied by a factor of two (~68%). This sensitivity analysis shows how GWP reductions can be enhanced by having a greater percentage of capture rate, instead of the specified 34%.

In these 330 $MW_e$ scenarios, the PCC unit and its downstream processes are constant in size compared with the 660 $MW_e$ scenarios, since the PCC units are processing the same capacity of $CO_2$. However, the variables that are no longer constant are the coal mass requirements, power-plant construction requirements, and power-plant waste disposal and emissions. All material and energy requirements are halved due to having half the energy production capacity. Because the percentage of the flue gas captured by the PCC unit for 330 $MW_e$ power-plant is now 68%, as opposed to the original 34% for 660 $MW_e$ power-plant, it is expected that the GWP abatement for the units will be larger in magnitude and more environmentally friendly compared with the power-plant only scenario.

The 330 $MW_e$ conditions were computed for each PCC scenario and the GWP levels are directly compared with the 660 $MW_e$ conditions in Figure 142. The increase in percentage capture rate, by a lower power-plant energy output, causes all the PCC scenarios to have much lower GWP values relative to the power-plant only scenario, when compared with the 660 $MW_e$ scenarios. The net GWP for the scenarios when capturing 1 tonne of $CO_2$ is less than half for the 330 $MW_e$ conditions compared with the 660 $MW_e$ conditions. This is because less flue gas emissions for the power-plant are emitted directly to the atmosphere, since the flue gas processing rate has increased. In terms of GWP per energy unit, the power-plant only scenario has a relatively constant value between power-plant energy outputs. This is because $CO_2$ emissions are proportional to the electrical energy

produced by the power-plant. For the PCC scenarios, the GWP per energy unit values are lower for the 330 $MW_e$ capacity, since a greater fraction of emissions are being processed.
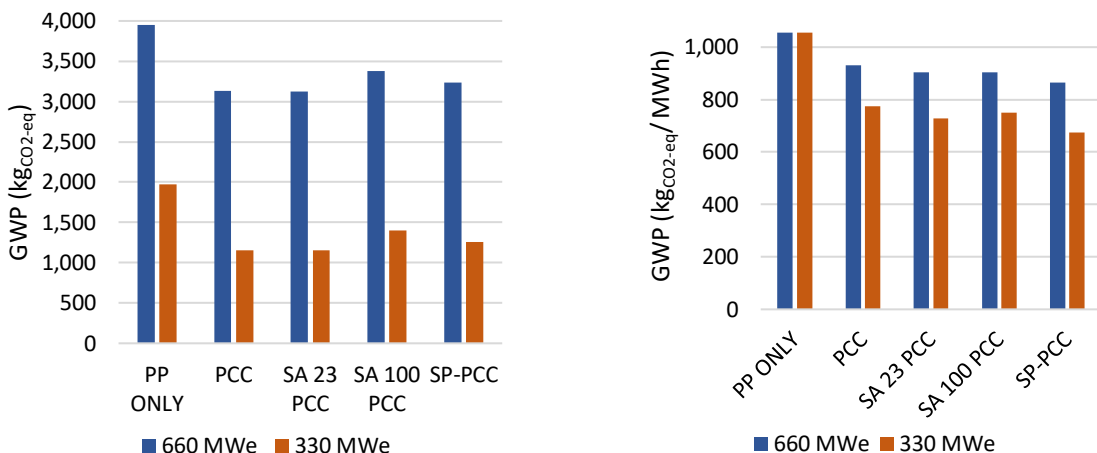


**Figure 142: Comparison of global warming potential (GWP) for each 660 $MW_e$ and 330 $MW_e$ scenario: (left) the net GWP for each scenario where all PCC scenarios capture 1 tonne $CO_2$ and the power-plant only scenario operates at the same coal intake to PCC scenarios; (right) the GWP per $MWh_e$ power-plant electrical output.**

The magnitudes of GWP abatement are shown in Figure 143. When comparing the abatement values between the 330 $MW_e$ and 660 $MW_e$ cases, it is seen that the GWP abatement per $tonne_{CO2}$ is approximately equal between the two plant capacities. This is because all scenarios process the same amount of $CO_2$ regardless of the power-plant energy production rate, meaning the net reduction in GWP is consistent. However, the GWP abatement per MWh is approximately doubled for the 330 $MW_e$ scenario compared with the 660 $MW_e$ scenario. This pattern is a result of the energy capacity being halved for the 330 $MW_e$ scenario, causing twice as much GWP reduction per energy output. Overall, increasing the flue gas processing rate causes a relatively greater reduction in GWP relative to the power-plant energy output.
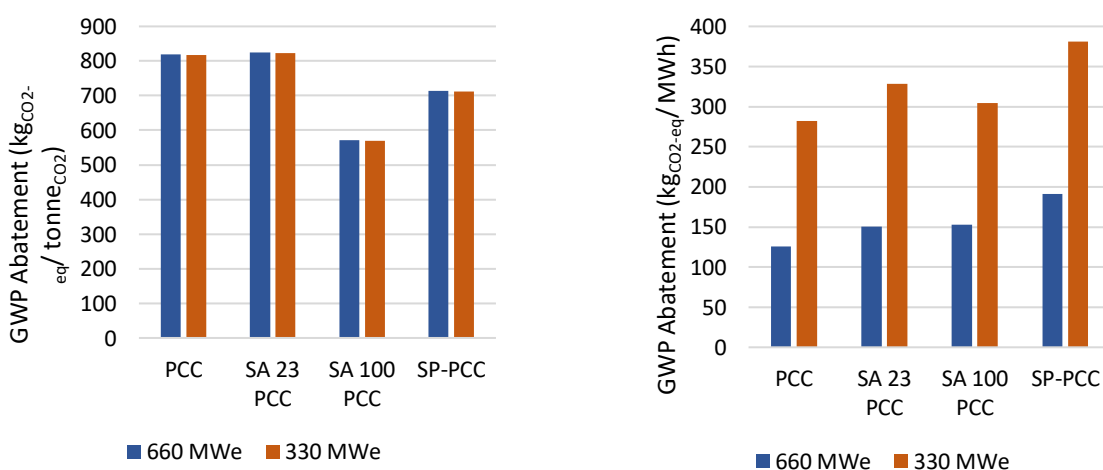


**Figure 143: Abatement of global warming potential (GWP) for both 330 $MW_e$ and 660 $MW_e$ cases relative to the power-plant only scenario, in terms of $kg_{CO2-eq}$ emitted per tonne $CO_2$ captured (left) and $kg_{CO2-eq}$ emitted per MWh produced from the power-plant (right).**

Another direct comparison of the 660 MW$_e$ and 330 MW$_e$ conditions is shown in Figure 144, which displays the percentage of GWP abatement relative to the power-plant only scenarios in both power-plant capacities (660 MW$_e$ *vs.* 330 MW$_e$). Clearly, the percentage abatement is approximately doubled for the 330 MW$_e$ scenarios. This displays how efforts to increase the SP-PCC capture capacity will significantly reduce the environmental burden of power-plants.
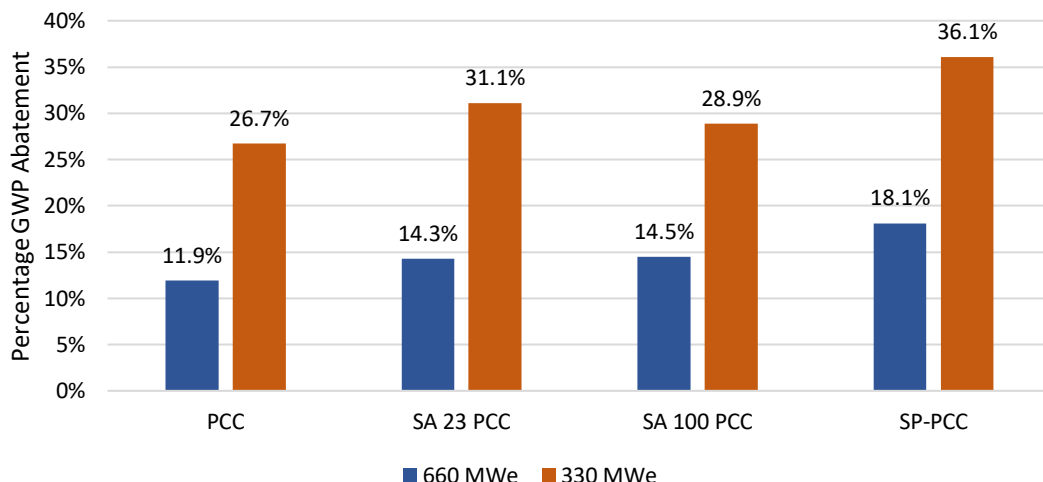


**Figure 144: The percentage abatement of global warming potential (GWP) for the 660 and 330 MW$_e$ scenarios relative to the power-plant only scenario.**

## 8.4     Sensitivity analysis of solar multiple (*SM*)

As defined, the *SM* refers to the ratio of the thermal power produced by the SCF at the design point, and the thermal power required by the power block at nominal conditions. Hence, increasing the *SM* of the SP-PCC process refers to oversizing the SCF so it can yield more thermal energy, and therefore require a smaller solvent storage system, since the So-St network will work more efficiently to desorb the $CO_2$ from the rich solvent. Naturally, the benefits of increasing the *SM* incur a proportional penalty in *CAPEX* & *OPEX*.

The *SM* of the SP-PCC process is sensitised to determine how changing the balance between the SCF size and the CCS affects the overall GWP of the SP-PCC process. As seen from the previous sections, the solvent storage system has a significant impact on the overall GWP, and thus *SSC* size reductions may favour GWP abatement if it is not outweighed by the effect of increasing the SCF size. A similar set of scenarios to the techno-economic analysis are analysed (*SM* = 1.5, *SM* = 2.0, *SM* = 2.5) and compared with the base case SP-PCC scenario (*SM* = 1). These scenarios are for a 660 MW$_e$ power output of the power-plant. Table 47 summarises the design specifications, which vary between different *SM* scenarios. In summary, as *SM* increases the SCF area, the pumping requirements would increase, while the number of SSTs and the inventory solvent mass would decrease.

**Table 47: Summary of varying design specifications between *SM* scenarios.**

| Solar multiple (*SM*) | 1 | 1.5 | 2 | 2.5 |
|---|---|---|---|---|
| SCF area (m$^2$) | 7,155,750 | 10,733,625 | 14,311,500 | 17,889,375 |
| Number of API tanks | 193 | 128 | 73 | 31 |
| Solvent mass (tonne) | 4,959,734 | 3,238,774 | 1,849,155 | 753,894 |

| SCF pumping energy (MJ/y) | 12,429,688 | 10,910,690 | 10,034,897 | 9,589,732 |
| Number of pumps | 13,050 | 19,575 | 26,100 | 32,625 |

The LCA was conducted for all the *SM* scenarios to determine their GWPs. Figure 145 shows a comparison between the net GWP of each *SM* scenario, while Figure 146 compares the GWP abatement of the scenarios relative to the power-plant only scenario at 660 MW$_e$.
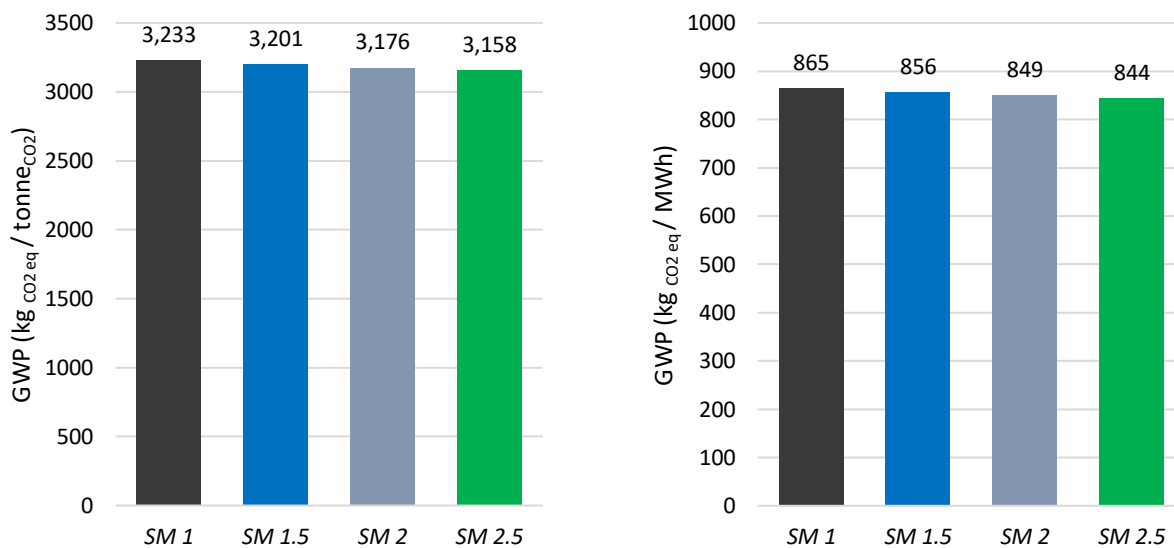


**Figure 145: Global warming potential (GWP) for each *SM* scenario at 660 MW$_e$: (left) net GWP per capture of 1 tonne $CO_2$ (right) GWP per MWh power-plant electrical output produced.**
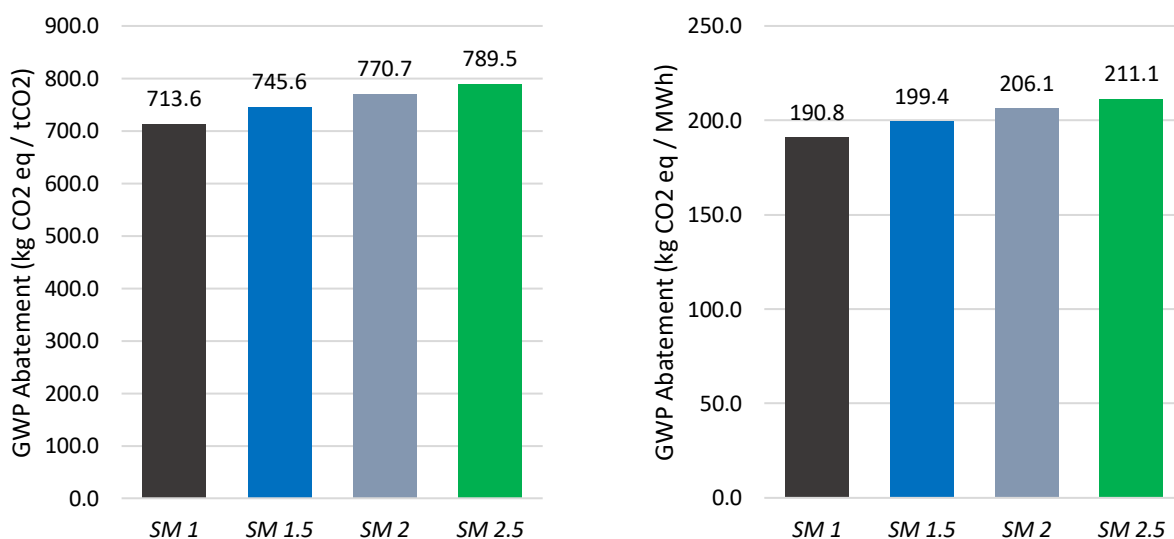


**Figure 146: GWP abatements for each *SM* scenario at 660 MW$_e$ relative to the power-plant only scenario: (left) GWP abatement per capture of 1 tonne $CO_2$ (right) GWP abatement per MWh$_e$ power-plant electrical output produced.**

The observations from Figures 145 & 146 are that increasing the *SM* causes a decrease in GWP for the SP-PCC process, or equivalently a greater GWP abatement. For example, increasing the *SM* by a factor of two causes the GWP abatement to increase by 57.1 kg$_{CO2-eq}$ / tonne$_{CO2}$ captured or by 15.3 kg$_{CO2-eq}$ / MWh output of the power-plant; these are equivalent to 8% increases in the GWP

abatement. To account for this effect, a breakdown for the contributions of the solvent storage and the SCF towards the overall GWP is displayed in Figure 147.
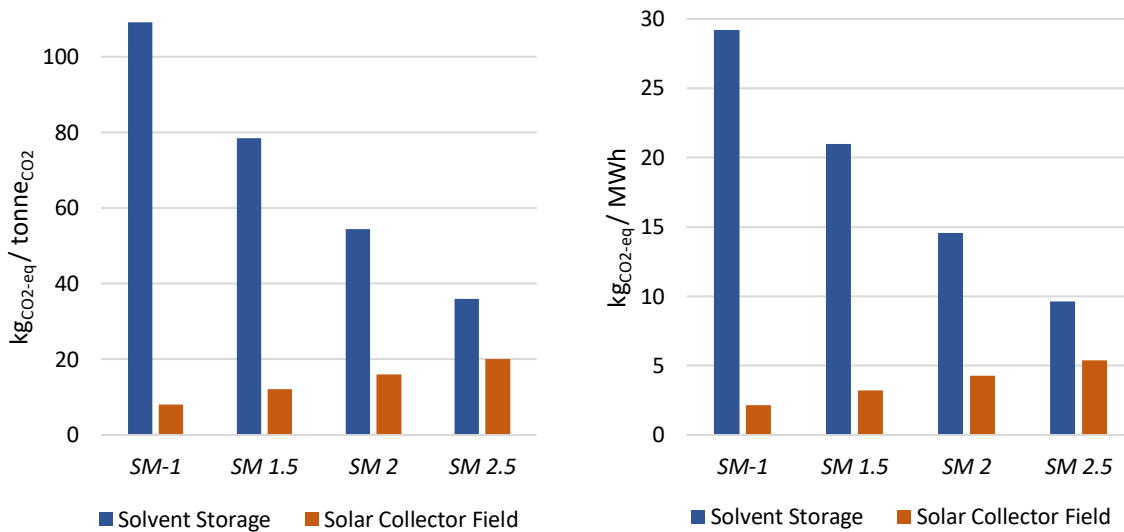


**Figure 147: Net GWP for solvent storage and the SCF for each *SM* scenario at 660 MW$_e$: (left) net GWP abatement per capture of 1 tonne CO$_2$, (right) GWP abatement per MWh power-plant electrical output produced.**

As expected, an increase in *SM* causes the GWP of the solvent storage system to decrease since there is less solvent mass and fewer storage tanks required. In contrast, an increase in *SM* causes the SCF to contribute greater GWP due to requiring greater amounts of construction materials. Despite these factors having opposite impacts on the system, the decrease in solvent storage GWP is at a much steeper gradient compared with the increase in the SCF GWP. This is because MEA solvent production has a significant contribution to the overall GWP, compared with the relevant construction materials. Overall, this imbalance causes the greater *SM* value to have lower GWP impact.

## 8.5    CO$_2$ abatement costs

The cost of CO$_2$ abatement can be determined by integrating the LCA results with the techno-economic results from the previous chapter. A summary of the economics results and the calculated CO$_2$ abatement cost is shown in Table 48. The total life cost refers to the amount of money spent throughout the entire project lifespan. The specific life cost is the scaled amount of money used to capture 1 tonne of CO$_2$ and is calculated as per *Eq. 102,* while the CO$_2$ abatement cost is the money required to remove the emission of 1 tonne CO$_2$ equivalent, and is calculated according to *Eq. 103*.

$$\boldsymbol{Specific\ Life\ Cost} = \frac{\$ \boldsymbol{Total\ Life\ Cost}}{1.5 \frac{\boldsymbol{Mt\ CO_2}}{\boldsymbol{y}} \cdot 30\ \boldsymbol{y}} \qquad \text{Eq. 102}$$

$$\boldsymbol{\$CO_2 Abatement} = \frac{\boldsymbol{Specific\ Life\ Cost} \left[ \frac{\$}{\boldsymbol{tonCO_2}} \right]}{\boldsymbol{CO_2\ Emissions\ Abatement} \left[ \frac{\boldsymbol{kgCO_2,eq}}{\boldsymbol{tonCO_2}} \right]} \qquad \text{Eq. 103}$$

**Table 48: Summary of economics and consequent CO₂ abatement costs for the main capture scenarios from the 660 MW_e power-plant.**

| Parameter | PCC | SA-PCC (23%) | SP-PCC | Units |
|---|---|---|---|---|
| Capital cost | 201 | 995 | 5552 | $M |
| Fixed *O&M* | 7 | 12.6 | 42.6 | $M/y |
| Variable *O&M* | 6.5 | 9.3 | 18.4 | $M/y |
| Total *O&M* | 13.5 | 21.9 | 61 | $M/y |
| Total life cost | 606 | 1652 | 7382 | $M |
| Specific life cost | 13.5 | 36.7 | 164.0 | $/tonne_{CO2} |
| CO₂ abatement | 818.5 | 824.2 | 713.6 | kg_{CO2-eq}/ tonne_{CO2} |
| **CO₂ abatement cost** | **16.5** | **44.5** | **229.9** | **$/tonne_{CO2} avoided** |

The $CO_2$ abatement cost for the SP-PCC is more than five times as expensive as the optimised SA-PCC. Therefore, for SP-PCC, the increase in power production efficiency of reducing GWP comes at a significant economic cost. This is predominantly due to the large amount of solvent storage, which involves significant capital costs. As seen in the techno-economic study, the economic benefit of SP-PCC that lacks an energy penalty will allow the power-plant to work at full capacity and have more electricity available to be sold to retailers. Although there is a potential to partially offset the large $CO_2$ abatement cost in the SP-PCC due to the greater profits from higher electrical output, the techno-economic study found the electricity profits are not significant enough to offset the overall process costs. The SP-PCC is a highly efficient method of mitigating GHG emissions, but it is hindered by its economic viability.

The $CO_2$ abatement costs are compared in Table 49 for the various *SM* scenarios for SP-PCC. Increasing the *SM* has been shown to increase the GWP abatement; however, this comes at larger *CAPEX* & *OPEX*. An analysis of this interplay between environmental and economic burdens shows that the $CO_2$ abatement cost increases for larger *SM* values. This means that the increase in *SM* does not make the process more economically viable. Currently, an investor must therefore judge whether the enhancement in GWP abatement is worth the extra investment.

**Table 49: Summary of economics and consequent CO₂ abatement costs for various *SM* scenarios of the SP-PCC.**

| Parameter | *SM=1.0* | *SM=1.5* | *SM=2.0* | *SM=2.5* | Units |
|---|---|---|---|---|---|
| Capital cost | 5552 | 5985 | 6585 | 7352 | $M |
| Fixed *O&M* | 42.6 | 45.6 | 49.8 | 55.2 | $M/y |
| Variable *O&M* | 18.4 | 18.4 | 18.4 | 18.4 | $M/y |
| Total *O&M* | 61 | 64 | 68.2 | 73.6 | $M/y |
| Total life cost | 7,382 | 7,905 | 8,631 | 9,560 | $M |
| Specific life cost | 164.0 | 175.6 | 191.8 | 212.4 | $/tonne_{CO2} |
| CO₂ abatement | 713.6 | 745.6 | 770.7 | 789.5 | kg_{CO2-eq}/tonne_{CO2} |
| **CO₂ abatement cost** | **229.9** | **235.6** | **248.8** | **269.1** | **$/tonne_{CO2} avoided** |

## 8.6     Improvement analysis

SP-PCC is currently advantageous in its effect of preserving steam for power production and its process independency from the power-plant operation and control. This has enabled it to have an overall increase in GWP abatement per power-plant energy output. However, there is a significant scope for process improvement to make the SP-PCC have an even lower GWP contribution. The main method for decreasing the environmental burden of the SP-PCC will be in the solvent storage system. Currently, SP-PCC requires large volumes of solvent and a large number of storage vessels. Any design improvements that can decrease the load required by the solvent storage system will be greatly beneficial for making SP-PCC more environmentally sustainable.

As seen earlier, one method of achieving this goal would be increasing the *SM*, which involves increasing the SCF size and consequently lowers the solvent requirements. However, the disadvantage of this is the increased burden for *CAPEX* & *OPEX* at larger *SMs*. As per $CO_2$ abatement costs, a decision maker must also therefore judge whether the enhancement in GWP abatement is worth the extra investment. Another method of GWP reduction would be the introduction of an alternative solvent to the benchmark MEA with a lower GWP burden.

In terms of the economic viability of SP-PCC, it will be essential to develop ways of mitigating the current capital and operating costs to make the cost of $CO_2$ abatement more economically viable. As discussed in the techno-economics analysis (Chapter 7), the large cost is predominantly due to the large volume of solvent storage required for SP-PCC to run at a 100% *SF*, as well as the larger SCF area. Therefore, any efforts to reduce these economic burdens will enable the GWP reduction potential for the SP-PCC technology to be better realised. In this context, process innovation or design improvement can have a substantial impact on the SP-PCC viability and sustainability. For example, improving the heat transfer within the So-St tube via using the correct inserts can result in major SCF size reductions, as demonstrated by our CFD study (Chapter 4).

## 8.7     Concluding remarks

We conducted an LCA study to investigate the environmental burden of the novel SP-PCC process. Its environmental impact was compared with four other scenarios: power-plant only, power-plant with conventional PCC, and power-plant with SA-PCC at 23% (optimised) and 100% (ideal) solar fractions. The key result is that the GWP per MWh for SP-PCC is the lowest out of all scenarios (864.8 $kg_{CO2-eq}$/MWh). The abatement of $CO_2$ relative to the power-plant only scenario is therefore highest for SP-PCC (190.8 $kg_{CO2-eq}$/MWh) and results in a 18% GWP abatement for a 660 $MW_e$ plant and 38.1% GWP abatement for a 330 $MW_e$ plant.

We showed that increasing the $CO_2$ capture rate percentage will cause a greater percentage decrease in GWP, since more $CO_2$ is processed. Furthermore, the GWP abatement is also proportionally increased with the *SM* value, since increasing *SM* value would substantially lower the solvent storage requirements. However, an increase in *SM* does not make the process more economically viable. Despite the efficiency of GWP reductions for SP-PCC, it has the greatest $CO_2$ abatement cost ($269.1/$tonne_{CO2}$). This $CO_2$ abatement cost for the SP-PCC is over more than five times expensive as the optimised SA-PCC counterpart, which currently makes it economically

unviable compared with the current commercial technologies. Although SP-PCC creates no energy penalty for the power-plant, this advantage is not yet sufficient to offset the economic burden of the PCC unit. Overall, efforts to reduce the cost of $CO_2$ capture by SP-PCC will be greatly advantageous for incorporating SP-PCC into existing coal-fired power-plants to mitigate global warming.

# 9.    Project conclusions

This final chapter is structured to combine the concluding remarks from all chapters, summarise the key results from this project, and provide suggestions for possible future work to continue developing the novel concept of 'solar-powered' post-combustion capture (SP-PCC) technology and advance its ranking on the technology readiness ladder (TRL) towards commercialisation.

## 9.1   Conclusions

This project is part of CSIRO's ongoing efforts in developing and demonstrating novel ideas for GHG emissions reduction to lower economic and environmental footprints. It is well-aligned with the Coal Innovation New South Wales (CINSW) goal to advance low-emissions coal technologies R&D across the state.

In this project, we proposed an innovative concept in solarising carbon capture technology to become almost independent from the power plant. Clearly, this notion would have tremendous advantages in terms of keeping the power cycle intact via liberating the carbon capture process to be completely powered by solar energy. Accordingly, it will not only provide convenience to power plant owners and operators from operational stability and process control perspective, but will also maximise environmental benefits via preserving the steam energy for power production only. Therefore, this project is unique in transforming the traditional concept of solar-assisted PCC (SA-PCC) to the new frontier of 'solar-powered' PCC (SP-PCC).

At this inaugural stage, this project has developed the first steps in the SP-PCC commercialisation pathway. It comprised deep theoretical and modelling studies in seven interconnected milestones to evaluate this novel technology and optimise different processes, designs and sizing variables. These seven milestones were represented in seven interconnected chapters in this report, summarised below.

- In Chapter 2, we started from the initial perception of a stripper tube heated by solar energy named a 'solar-stripper' (So-St). We listed the main kinetic and thermodynamic drivers and assessed the effect of temperature, pressure and other design variables on the $CO_2$ stripping process. We found that a hybrid design principle of the So-St can combine both the counter-current stripping mode (used in conventional strippers) and the co-current stripping mode (used in a typical heated tube) to lower the energy demand. The principle of the hybrid design comprises of short So-St segments connected in series with vapour/gas removal ports placed in between segments. This design helps reduce the residence time of the released $CO_2$ molecules, which continuously provide the necessary driving force for $CO_2$ separation from the aqueous phase. We directed our attention to better understand the evolving flow regimes while being subjected to constant heat. The results suggested the flow regime could be controlled by choosing an appropriate tube diameter and in-range superficial liquid/gas velocity. The concept

of intercooling could further improve the performance of hybrid design, but in-depth heat transfer analysis would be required to identify the main process variables and constrains.

- In Chapter 3, we presented an advanced thermodynamic analysis for the So-St design. We first evaluated the role of excessive water vaporisation on the energy demand of the stripping process and found this matter is very important. We tested methyl diethanolamine (MDEA), an alternative solvent to monoethanolamine (MEA), to understand where and how solvent choice may affect the stripping process. This revealed the need to find or develop an alternative solvent specific for So-St process to replace the reference MEA. Further elaboration on this research route will be presented next in the 'Future directions' section. We also fundamentally analysed the evolving flow regimes in two extreme tube setups (horizontal *vs.* vertical). Although the vertical setup is almost impractical for the So-St process, this comparison was conducted to induce possible topographical gradients to enhance the $CO_2$ stripping process. It was found that vapour molar fraction (*VMF*) is the foremost variable that can command the flow regime and heat transfer coefficient. As the *VMF* and pressure-drop are interrelated, the nominal value for the *VMF* was systematically optimised for the design of a So-St network. Accordingly, the length, diameter and number of So-St segments and parallel So-St modules can be configured, and the whole So-St network can be sized. We compared different tube diameters and found that smaller diameter tubes require a longer So-St tube length. We adopted 76 cm tube diameter for the So-St design because it allowed a smaller So-St tube length and used higher heat flux. Accordingly, we have developed a design protocol to size the whole So-St field for a constant/nominal solar heat flux. Different operational aspects including process control, vapour–liquid separation and $CO_2$ purification were discussed to derive a robust So-St design protocol.

- In Chapter 4, we shifted away from our typical modelling expertise through the lens of 'black-box' to dynamically study physio-chemical and thermo-chemical phenomena inside the So-St tube. For this purpose, we used a robust CFD platform (COMSOL Multiphysics®) aiming at improving internal design inside the So-St tube. Two alternative inserts were considered for this study and compared with a conventional bare tube. Acknowledging the substantial limitations of the CFD packages in terms of extensive time and computational power demand, this study was tremendously beneficial in evaluating alternative designs and assessing the weighing factor for design improvement. A hierarchical modelling structure was applied starting from 2-D geometry frames to inform the more accurate 3-D geometries that have a high computational load. Enhanced heat transfer via porous and solid baffles were assessed compared with the reference bare tube. We analysed bubble nucleation at the early stages of heat transfer and categorised how bubble development can impact the overall $CO_2$ stripping process and possible solvent degradation. This study, the first of its kind, provided a clearer picture on how inserts can serve to transform large bubbles into more effective film evaporation and promote healthier $CO_2$ stripping. We also extended our analysis to weigh up such design improvement on the overall SCF size and pumping power. We estimated that using porous and solid baffles instead of bare tubes may reduce the SCF size by 56% and 65% respectively, but that would be at a cost of 2.5 and 6 times more pumping power required for porous and solid baffles, respectively.

These findings open a new window for design improvement to enhance the economic footprint of SP-PCC.

- In Chapter 5, we capitalised on our expertise in process control to innovate a new process control expert system specifically tailored for SP-PCC technology. In this system we did not look only into controlling process variables inside the So-St tube or even the entire SCF, but aimed at the whole superstructure to synchronise the process across the absorption-desorption terminals while tuning the operation with solvent storage to maintain healthy process continuity over time. Three different control strategies were investigated for the same control objectives but with different manipulated variables. We developed an operational procedure to determine a suitable control strategy based on dynamic solar irradiation. Based on the defined control strategies, we constructed five control scenarios and compared the average $CO_2$ capture rates per annum. We found that the control scenario with a lean loading component can provide the highest capture rate. This is because the lean loading control can digest a relatively high *SHF* range (up to 3.6 kW/m) and helps to maintain the solvent regeneration process within the desirable thermodynamic regime on both sides of the solvent cycle. Practical application of lean loading control should also incorporate temperature control to monitor the solvent temperature and provide appropriate remedy control actions in case the lean loading control pushes the solvent into thermally unstable territory.

- In Chapter 6, we completed our design protocol to size the entire So-St field. This design protocol was structured by synchronising three sub-models: the absorber, the So-St modules network and the solvent storage. We first created a general design database comprising all possible physical layout options. Then, several filters (criteria) were applied to shortlist favourable designs distinguished by specific physical or performance indicators. In sizing the solvent storage, a direct relationship with the SCF sizing standards was realised. Accordingly, three optimisation methods were investigated to reduce the overall *SSC* and possibly enhance the economic model. The first method assessed the impact of absorber stoppage time on the *SSC* and optimised for the ideal stoppage time necessary for periodic maintenance. The second method evaluated the influence of *SM* on *SSC* sizing and established a relationship between these two variables. The third method examined a novel concept of multi-tank mix-match strategy, the first of its kind, using American Petroleum Institute (API) standard tank sizes to notably reduce the *SSC* requirement. A full analysis was conducted for the SP-PCC at various *SMs* incrementing in value by 0.5. We found that at *SM*=2.5, the *SSC* requirement was reduced to only 15.1% on the API scale and 7.6% of the basic *SSC* requirement at *SM*=1. This calculation demonstrated the significant trade-off implications between the *SM* vs. *SSC,* which can only be enhanced via a rigorous economic optimisation. This design protocol can be used in sizing the appropriate SCF and solvent storage for SP-PCC at any scale and any location. We are confident that our design protocol would reveal promising results in a very compact timeframe, particularly for locations with abundant solar irradiance, clearer sky, longer daytimes, less seasonal variability in solar resources, and less expensive land.

- In Chapter 7, we assessed the economic footprint of our novel SP-PCC in comparison with the typical PCC (where steam is totally bled from the power-plant steam cycle) and SA-PCC (where

steam is produced in the SCF to partially contribute for the reboiler duty in the PCC). A full economic model was structured and validated, estimating all *CAPEX* and *OPEX* components to calculate the levelised cost of energy (*LCOE*) in those scenarios. Similar to all entirely 'solar-powered' projects, the *LCOE* for SP-PCC was found to be relatively high. With the basic design, the *LCOE* for SP-PCC was AUD 206.6/MWh compared with the AUD 141.6/MWh for SA-PCC and AUD 130.9/MWh for conventional PCC. This makes SP-PCC 57.8 and 45.9% higher than its PCC and SA-PCC counterparts, respectively. Similarly, the levelised cost of captured $CO_2$ was computed at AUD $358.9/tonne_{CO2}$ compared with AUD $108.4/tonne_{CO2}$ for SA-PCC and AUD $67.4/tonne_{CO2}$ for conventional PCC. The high cost of SP-PCC was mainly attributed to a 100% solar energy supply, which would necessitate a substantially large SCF and solvent storage to fully drive solvent regeneration in all seasons. Distributing the bulk amount of rich solvent in a complex network of So-St modules would require an extended number of solar collectors that would occupy a massive amount of land. However, this cost estimate was conducted for nominal bare tubes and the reference MEA solvent. We believe that enhanced process optimisation and design improvements could substantially cut the cost and reduce it to competitive levels. As outlined in Chapter 6, we believe these cost estimates are location-specific and would strongly argue that locations with better solar resources and less seasonal variability can have tremendous advantages for our SP-PCC proposal. For a fair comparison between the performance of SA-PCC and SP-PCC under the same 100% *SF* scenario, we found the *LCOE* of the SA-PCC was prohibitively higher than that of SP-PCC. Therefore, if a process requires 100% solar energy utilisation where the steam cycle would remain intact or it is not part of the normal industrial routine (such as steel and cement industries), SP-PCC would be the best technology option.

- In Chapter 8, we undertook a comprehensive life cycle assessment to investigate the environmental burden of the novel SP-PCC process. Similar to Chapter 7, we continued the comparative way of assessing SP-PCC with the equivalent conventional PCC and SA-PCC at two different *SFs*: the optimised 23% and the idealistic 100% solar fraction. In this assessment, the global warming potential (GWP) was categorised by the $CO_2$-equivalent unit for impact assessment. The cradle-to-grave framework was selected to account for the environmental impact starting from the basic raw material extraction up to the end-of-life stage. Consequently, the life cycle inventory for each stage of this chain of processes was defined and assessed. The results were levelised in two categories: per mass unit (tonne of captured $CO_2$) and per energy unit (MWh of power production). Compared with SA-PCC, the results showed that SP-PCC acted less favourably per mass unit, but was more attractive per energy unit. The reason for this originates from its steam preservation for power production, while other types of capture utilise a portion of the steam for capture purpose which would proportionally impact the power plant capacity. The GWP per MWh for SP-PCC was the lowest of all scenarios (864.8 $kg_{CO2-eq}$/MWh). The $CO_2$ abatement relative to a power-plant only scenario was therefore the highest for SP-PCC and resulted in a 18% GWP abatement for a 660 $MW_e$ plant and 36.1% GWP abatement for a 330 $MW_e$ plant. We demonstrated that increasing the $CO_2$ capture rate percentage will cause a greater percentage decrease in GWP, since more $CO_2$ is being processed. Furthermore, the GWP abatement was also affected by the *SM* value, since increasing *SM* value would substantially

lower the solvent storage requirements, but at increased demand for steel and glass production for the extended SCF. This trade-off in the GWP impact between the *SSC vs.* the SCF acts favourably towards solvent storage, which means the decrease in solvent storage GWP was at a much steeper gradient than the increase in the SCF GWP. This is because MEA solvent production has a significant contribution to the overall GWP compared with the relevant construction materials of the SCF. Overall, this imbalance causes a greater *SM* value to have lower GWP impact. However, an increase in *SM* does not make the SP-PCC system more economically viable. Currently, due to the cheaper PCC technology as described in Chapter 7, the cost of avoided $CO_2$ to the atmosphere via SP-PCC technology would still be higher.

Overall, our project has contributed extensively to increase fundamental knowledge about the novel technology of SP-PCC and transparently outlined its advantages, limitations, and possible methods for process improvement. We have also proposed some innovative design optimisation approaches (e.g. solvent storage multi-tank mix-match strategy) to increase the attractiveness and comparativeness of this technology. In addition to the aim and objectives of this research project, several other benefits were achieved, including increasing collaboration between various Australian institutes, and training several talented Australian students. A number of valuable research outcomes resulted from this project and have been successfully published or are on their way for publication. Moreover, our project has been introduced to the carbon capture and storage community at several conferences and has been widely acknowledged. The list of publications and their current status are listed in Appendix C.

## 9.2    Future directions

During this project, we have identified two major pathways to improve the process efficiency and, therefore, the techno-economics of the SP-PCC technology.

**Solvent screening:** MEA is often considered as a reference solvent in most PCC applications, although, we knew from the outset that MEA might not be the ideal solvent for So-St application. Our comparative modelling work (MEA vs. MDEA) in Chapter 3 has confirmed the superiority of MDEA, because the equilibrium partial pressure for $CO_2$ is higher than $H_2O$ in most of the loading range. The key attributes for an ideal solvent in So-St application are:

- have the lowest water vaporisation in the $CO_2$ desorption process
- be able to tolerate sudden temperature/heat spikes
- be thermally stable and shows less degradation rate over time
- be able to break bonds and release $CO_2$ at the lowest energy demand
- work at higher pressure to suppress water vaporisation.

Work is ongoing to improve solvent thermo-physical properties in many institutes around the world, including CSIRO. This type of research would require advanced chemistry expertise and a well-developed solvent screening database. In our interactions with peers at conferences when this project was displayed, experts suggested ionic liquids might be good candidates for this type of application. Future work should screen in-depth solvent properties for this application. There might

be no single solvent that can perfectly address all these challenges, but a combination/blend of solvents may have a better outcome. This type of work may also require extensive experimental work to find and validate candidate solvents.

**Internal geometry:** In our CFD work, we modelled two types of inserts (porous and solid baffles) and compared their performance with the reference bare tube. We found these types of inserts may provide a promising avenue to capitalise on process intensification and more compact designs. However, CFD alone would not be sufficient to investigate the properties of these inserts in details. CFD platforms often suffered from excessive computational power and time demands and other limitations in respect to physics integration. Furthermore, as this kind of research is relatively new in the CFD world, few resources are available in open literature to validate CFD work, and other types of 3-D inserts, such as twisted tapes or foam packings are almost impossible to model in a CFD platform. This research direction is therefore an interesting avenue for experimental work starting at benchtop level. Setting up a small apparatus rig to physically test different inserts at a laboratory scale is quite achievable, and would help to validate and innovate new methods for process intensification.

Once the most applicable solvent is confirmed and the best internal geometry for the So-St tube is assured, this project may jump to the next phase of prototyping. We are very keen to continue and are seeking funding opportunities to pursue the next challenges of this high-calibre project to raise its ranking on the TRL towards commercialisation.

# References

1.      World Coal Association. *Coal & Electricity*. 2021  [cited 19/04/2021]; Available from: https://www.worldcoal.org/coal-facts/coal-electricity/.

2.      Department of Industry, S., Energy, and Resources. *Electricity Generation in Australia*. 2019 [cited 28/04/2021]; Available from: https://www.energy.gov.au/data/electricity-generation.

3.      Rubin, E.S., J.E. Davison, and H.J. Herzog, *The cost of CO2 capture and storage.* International Journal of Greenhouse Gas Control, 2015. **40**: p. 378-400.

4.      Metz, B., O. Davidson, and H. De Coninck, *Carbon dioxide capture and storage: special report of the intergovernmental panel on climate change*. 2005: Cambridge University Press.

5.      Page, S., A. Williamson, and I. Mason, *Carbon capture and storage: Fundamental thermodynamics and current technology.* Energy Policy, 2009. **37**(9): p. 3314-3324.

6.      Harkin, T., A. Hoadley, and B. Hooper, *Reducing the energy penalty of CO2 capture and compression using pinch analysis.* Journal of Cleaner Production, 2010. **18**(9): p. 857-866.

7.      Harkin, T., A. Hoadley, and B. Hooper, *Optimisation of power stations with carbon capture plants–the trade-off between costs and net power.* Journal of Cleaner Production, 2012. **34**: p. 98-109.

8.      Khalilpour, R. and A. Abbas, *HEN optimization for efficient retrofitting of coal-fired power plants with post-combustion carbon capture.* International journal of greenhouse gas control, 2011. **5**(2): p. 189-199.

9.      Milani, D., et al., *Process enhancement in aqueous ammonia PCC using a direct contact condenser.* Greenhouse Gases: Science and Technology, 2019. **9**(2): p. 245-260.

10.     Zhao, B., et al., *Enhancing the energetic efficiency of MDEA/PZ-based CO2 capture technology for a 650 MW power plant: process improvement.* Applied energy, 2017. **185**: p. 362-375.

11.     Adibhatla, S. and S. Kaushik, *Energy, exergy and economic (3E) analysis of integrated solar direct steam generation combined cycle power plant.* Sustainable Energy Technologies and Assessments, 2017. **20**: p. 88-97.

12.     Ugolini, D., J. Zachary, and J. Park, *Options for hybrid solar and conventional fossil plants.* Bechtel Technol. J., 2009. **2**(1): p. 133-143.

13.     Behar, O., et al., *A review of integrated solar combined cycle system (ISCCS) with a parabolic trough technology.* Renewable and Sustainable Energy Reviews, 2014. **39**: p. 223-250.

14.     Parvareh, F., et al., *Integration of solar energy in coal-fired power plants retrofitted with carbon capture: a review.* Renewable and Sustainable Energy Reviews, 2014. **38**: p. 1029-1044.

15.     Mokhtar, M., et al., *Solar-assisted post-combustion carbon capture feasibility study.* Applied Energy, 2012. **92**: p. 668-676.

16.     Qadir, A., et al., *Potential for solar-assisted post-combustion carbon capture in Australia.* Applied energy, 2013. **111**: p. 175-185.

17.     Li, H., J. Yan, and P.E. Campana, *Feasibility of integrating solar energy into a power plant with amine-based chemical absorption for CO2 capture.* International Journal of Greenhouse Gas Control, 2012. **9**: p. 272-280.

18.     Sharma, M., F. Parvareh, and A. Abbas, *Highly integrated post‐combustion carbon capture process in a coal‐fired power plant with solar repowering.* International Journal of Energy Research, 2015. **39**(12): p. 1623-1635.

19.     Abdul Manaf, N., et al., *Model-based optimisation of highly-integrated renewables with post-combustion carbon capture processes*. 2016, ANLEC R&D.

20.     Parvareh, F., et al., *Solar repowering of PCC-retrofitted power plants; solar thermal plant dynamic modelling and control strategies.* Solar Energy, 2015. **119**: p. 507-530.

21.     Wibberley, L., *Co2 capture using solar thermal energy*. 2010, Google Patents: USA.

22.     Khalilpour, R., et al., *A novel process for direct solvent regeneration via solar thermal energy for carbon capture.* Renewable Energy, 2017. **104**: p. 60-75.

23.     Manzolini, G., et al., *Economic assessment of novel amine based CO2 capture technologies integrated in power plants based on European Benchmarking Task Force methodology.* Applied Energy, 2015. **138**: p. 546-558.

24.     Abu-Zahra, M.R., et al., *CO2 capture from power plants: Part II. A parametric study of the economical performance based on mono-ethanolamine.* International journal of greenhouse gas control, 2007. **1**(2): p. 135-142.

25.     Monteiro, J.G.-S. and H.F. Svendsen, *The N2O analogy in the CO2 capture context: Literature review and thermodynamic modelling considerations.* Chemical Engineering Science, 2015. **126**: p. 455-470.

26.     Aronu, U.E., et al., *Solubility of CO2 in 15, 30, 45 and 60 mass% MEA from 40 to 120°C and model representation using the extended UNIQUAC framework.* Chemical Engineering Science, 2011. **66**(24): p. 6393-6406.

27.     Greer, T., *Modeling and simulation of post combustion CO2 capturing*. 2008, Høgskolen i Telemark.

28.     Li, Z., et al., *Verification of a solvent optimization approach for postcombustion CO2 capture using commercial alkanolamines.* International Journal of Greenhouse Gas Control, 2016. **44**: p. 59-65.

29.     Milani, D., et al., *Tailored solar field and solvent storage for direct solvent regeneration: A novel approach to solarise carbon capture technology.* Applied Thermal Engineering, 2020. **171**: p. 115119.

30.     Hibiki, T., S. Hogsett, and M. Ishii, *Local measurement of interfacial area, interfacial velocity and liquid turbulence in two-phase flow.* Nuclear engineering and design, 1998. **184**(2-3): p. 287-304.

31.     Al-Naser, M., M. Elshafei, and A. Al-Sarkhi. *Two-Phase Flow Regimes Identification using Artificial Neural Network with Nonlinear Normalization*. 2015.

32.     Anglart, H. and D. Caraghiaur, *CFD modeling of boiling annular-mist flow for dryout investigations.* Multiphase Science and Technology, 2011. **23**(2-4).

33.     Frisk, D.P. and E.J. Davis, *The enhancement of heat transfer by waves in stratified gas-liquid flow.* International Journal of Heat and Mass Transfer, 1972. **15**(8): p. 1537-1552.

34.     Dirker, J., et al., *Thermal Energy Processes in Direct Steam Generation Solar Systems: Boiling, Condensation and Energy Storage.* Frontiers in Energy Research, 2019. **6**.

35.     Bellos, E. and C. Tzivanidis, *Assessment of the thermal enhancement methods in parabolic trough collectors.* International Journal of Energy and Environmental Engineering, 2018. **9**(1): p. 59-70.

36.     Wang, S., et al., *Numerical Study on Heat Transfer Performance in Packed Bed.* Energies, 2019. **12**(3): p. 414.

37.     Arachchige, U.S.P. and M.C. Melaaen, *Selection of packing materials for gas absorption.* 2012.

38.     Milani, D. and A. Abbas, *Multiscale modeling and performance analysis of evacuated tube collectors for solar water heaters using diffuse flat reflector.* Renewable energy, 2016. **86**: p. 360-374.

39.     Abdulhamed, A.J., et al., *Review of solar parabolic-trough collector geometrical and thermal analyses, performance, and applications.* Renewable and Sustainable Energy Reviews, 2018. **91**: p. 822-831.

40.     Bellos, E., C. Tzivanidis, and K.A. Antonopoulos, *Exergetic and energetic comparison of LiCl-H2O and LiBr-H2O working pairs in a solar absorption cooling system.* Energy conversion and management, 2016. **123**: p. 453-461.

41.     Fouda, A., S. Nada, and H. Elattar, *An integrated A/C and HDH water desalination system assisted by solar energy: Transient analysis and economical study.* Applied Thermal Engineering, 2016. **108**: p. 1320-1335.

42.     Chafie, M., et al., *Experimental investigation of parabolic trough collector system under Tunisian climate: design, manufacturing and performance assessment.* Applied Thermal Engineering, 2016. **101**: p. 273-283.

43.     Gladis, A., et al., *Comparison of the Kinetic Promoter Piperazine and Carbonic Anhdrase for CO2 Absorption.* Energy Procedia, 2017. **114**: p. 719-725.

44.     Aghaie, M., N. Rezaei, and S. Zendehboudi, *A systematic review on CO2 capture with ionic liquids: Current status and future prospects.* Renewable and Sustainable Energy Reviews, 2018. **96**: p. 502-525.

45.     Chen, J.C., *Correlation for Boiling Heat Transfer to Saturated Fluids in Convective Flow.* Industrial & Engineering Chemistry Process Design and Development, 1966. **5**(3): p. 322-329.

46.     Thome, J., *Boiling in Microchannels: A Review of Experiment and Theory.* International Journal of Heat and Fluid Flow, 2004. **25**(ARTICLE): p. 128-139.

47.     Collier, J.G. and J.R. Thome, *Convective boiling and condensation*. 1994: Clarendon Press.

48.     Zeigarnik, Y.A., *Annular flow*, in *Thermopedia*. 2010.

49.     Choi, K.-I., et al., *Pressure drop and heat transfer during two-phase flow vaporization of propane in horizontal smooth minichannels.* 2009.

50.     Milani, D., et al., *Analysis for a solar stripper design for carbon capture under transient conditions.* International Journal of Heat and Mass Transfer, 2021. **166**: p. 120799.

51.     Huh, C. and M.H. Kim, *Pressure drop, boiling heat transfer and flow patterns during flow boiling in a single microchannel.* Heat Transfer Engineering, 2007. **28**(8-9): p. 730-737.

52.     Maddi, M. and D. Rao, *Experimental studies on flow boiling in inclined tubes: in the regions encountered in solar collectors.* The Canadian Journal of Chemical Engineering, 1995. **73**(1): p. 73-84.

53.     Şahin, U., *A new non-iterative friction factor correlation for heat transfer fluids in absorber tube of parabolic trough collector.* Engineering Science and Technology, an International Journal, 2018. **21**(1): p. 89-98.

54.     Copetti, J.B., et al., *Flow boiling heat transfer and pressure drop of R-134a in a mini tube: an experimental investigation.* Experimental Thermal and Fluid Science, 2011. **35**(4): p. 636-644.

55.     Yüncü, H., O.T. Yildirim, and S. Kakaç, *Two-phase flow instabilities in a horizontal single boiling channel.* Applied Scientific Research, 1991. **48**(1): p. 83-104.

56.     May, E.K. and A. Chialva, *Advanced Energy Delivery for Food Processing: Direct Steam Generation in Parabolic Trough Solar Collectors: Final Project Report. Appendices*. 2013: California Energy Commission, Energy Research and Development Division.

57.     Tuo, H. and P. Hrnjak, *Vapor–liquid separation in a vertical impact T-junction for vapor compression systems with flash gas bypass.* International Journal of Refrigeration, 2014. **40**: p. 189-200.

58.     Mikheev, N., et al., *Cyclone separator for gas-liquid mixture with high flux density.* Powder Technology, 2018. **339**: p. 326-333.

59.     Sinnott, R.K., *Coulson and Richardson's Chemical Engineering Volume 6 - Chemical Engineering Design (4th Edition)*. Elsevier.

60.     Milani, D., et al., *Optimizing an advanced hybrid of solar-assisted supercritical CO2 Brayton cycle: A vital transition for low-carbon power generation industry.* Energy Conversion and Management, 2017. **148**: p. 1317-1331.

61.     Dai, Z., et al., *Combination of ionic liquids with membrane technology: A new approach for CO2 separation.* Journal of Membrane Science, 2016. **497**: p. 1-20.

62.     Bellos, E. and C. Tzivanidis, *Alternative designs of parabolic trough solar collectors.* Progress in Energy and Combustion Science, 2019. **71**: p. 81-117.

63.     Cheng, Z., et al., *Numerical simulation of a parabolic trough solar collector with nonuniform solar flux conditions by coupling FVM and MCRT method.* Solar Energy, 2012. **86**(6): p. 1770-1784.

64.     Davis, J. and G. Rochelle, *Thermal degradation of monoethanolamine at stripper conditions.* Energy Procedia, 2009. **1**(1): p. 327-333.

65.     Sandeep, H. and U. Arunachala, *Solar parabolic trough collectors: A review on heat transfer augmentation techniques.* Renewable and sustainable energy reviews, 2017. **69**: p. 1218-1231.

66.     Kharangate, C.R. and I. Mudawar, *Review of computational studies on boiling and condensation.* International Journal of Heat and Mass Transfer, 2017. **108**: p. 1164-1196.

67.     Lobón, D.H., et al., *Modeling direct steam generation in solar collectors with multiphase CFD.* Applied Energy, 2014. **113**: p. 1338-1348.

68.     Lobón, D.H., L. Valenzuela, and E. Baglietto, *Modeling the dynamics of the multiphase fluid in the parabolic-trough solar steam generating systems.* Energy Conversion and Management, 2014. **78**: p. 393-404.

69.     Yerdesh, Y., et al., *Modeling two-phase flow in pipe of the solar collector.* International Journal of Mathematics and Physics, 2018. **9**(1): p. 12-19.

70.     Yılmaz, İ.H. and A. Mwesigye, *Modeling, simulation and performance analysis of parabolic trough solar collectors: A comprehensive review.* Applied energy, 2018. **225**: p. 135-174.

71.     Mwesigye, A., T. Bello-Ochende, and J.P. Meyer, *Heat transfer and entropy generation in a parabolic trough receiver with wall-detached twisted tape inserts.* International Journal of Thermal Sciences, 2016. **99**: p. 238-257.

72.     Diwan, K. and M. Soni, *Heat transfer enhancement in absorber tube of parabolic trough concentrators using wire-coils inserts.* Universal Journal of Mechanical Engineering, 2015. **3**(3): p. 107-112.

73.     Kumar, K.R. and K. Reddy, *Thermal analysis of solar parabolic trough with porous disc receiver.* Applied Energy, 2009. **86**(9): p. 1804-1812.

74.     Kumar, K.R. and K. Reddy, *Effect of porous disc receiver configurations on performance of solar parabolic trough concentrator.* Heat and Mass Transfer, 2012. **48**(3): p. 555-571.

75.     Reddy, K., K.R. Kumar, and C. Ajay, *Experimental investigation of porous disc enhanced receiver for solar parabolic trough collector.* Renewable Energy, 2015. **77**: p. 308-319.

76.     Zheng, Z.-J., M.-J. Li, and Y.-L. He, *Thermal analysis of solar central receiver tube with porous inserts and non-uniform heat flux.* Applied Energy, 2017. **185**: p. 1152-1161.

77.     Nelson, S., et al., *Transforming the desorption unit in carbon capture technology through a novel solar-driven process.* Chemeca 2020: Renew, Sustain, Disrupt, Advance, 2020: p. 61.

78. Wilcox, D.C., *Formulation of the kw turbulence model revisited.* AIAA journal, 2008. **46**(11): p. 2823-2838.

79. Liu, S. and M. Sakr, *A comprehensive review on passive heat transfer enhancements in pipe exchangers.* Renewable and sustainable energy reviews, 2013. **19**: p. 64-81.

80. Bergman, T.L., et al., *Fundamentals of heat and mass transfer*. 2011: John Wiley & Sons.

81. Nelson, S., et al., *A CFD Study of a Direct Solar-Driven Desorption Process for Carbon Capture under Transient conditions.* Sustainable Energy Technologies and Assessments, 2021. 47: p. 101516.

82. Xue, B., et al., *A comparative study of MEA and DEA for post-combustion CO 2 capture with different process configurations.* International Journal of Coal Science & Technology, 2017. **4**(1): p. 15-24.

83. May, E.K. and A. Chialva, *ADVANCED ENERGY DELIVERY FOR FOOD PROCESSING: DIRECT STEAM GENERATION IN PARABOLIC TROUGH SOLAR COLLECTORS*. 2013, Energy Research and Development Division.

84. Milani, D., et al., *A model-based analysis of CO2 utilization in methanol synthesis plant.* Journal of CO2 Utilization, 2015. **10**: p. 12-22.

85. Milani, D., et al., *Process control expert system for solar-powered carbon capture under transient solar conditions.* Energy, 2021. **Under Review**.

86. Montes, M., et al., *Solar multiple optimization for a solar-only thermal power plant, using oil as heat transfer fluid in the parabolic trough collectors.* Solar energy, 2009. **83**(12): p. 2165-2176.

87. Damartzis, T., A.I. Papadopoulos, and P. Seferlis, *Process flowsheet design optimization for various amine-based solvents in post-combustion CO2 capture plants.* Journal of Cleaner Production, 2016. **111**: p. 204-216.

88. Basrawi, F., et al., *Effect of operation strategies on the economic and environmental performance of a micro gas turbine trigeneration system in a tropical region.* Energy, 2016. **97**: p. 262-272.

89. Okpala, A.N. and P. Jombo, *Design of diesel storage tank in consonance with requirements of American Petroleum Institute (API) standard 650.* Industrial Engineering Letters, 2012. **2**(4): p. 7-20.

90. American Petrolium Insttiute. *API tank size*. 2016 [accessed on 13/01/2021]; Available from: https://www.piping-designer.com/index.php/disciplines/mechanical/stationary-equipment/88-tank/1527-api-tank-size.

91. Gabbrielli, R. and C. Zamparelli, *Optimal design of a molten salt thermal storage tank for parabolic trough solar power plants.* Journal of solar energy engineering, 2009. **131**(4).

92. Zhao, Y., H. Hong, and H. Jin, *Optimization of the solar field size for the solar–coal hybrid system.* Applied Energy, 2017. **185**: p. 1162-1172.

93. Milani, D., et al., *Techno-Economic Analysis of 'Solar-Powered' Post-Combustion Carbon Capture.* Available at SSRN 3812039, 2021.

94. Li, K., et al., *Systematic study of aqueous monoethanolamine (MEA)-based CO2 capture process: Techno-economic assessment of the MEA process and its improvements.* Applied Energy, 2016. **165**: p. 648-659.

95. Turton, R., et al., *Analysis, synthesis and design of chemical processes*. 2008: Pearson Education.

96. Khalilpour, K.R. and A. Zafaranloo, *Generic techno-economic optimization methodology for concurrent design and operation of solvent-based PCC processes.* International Journal of Greenhouse Gas Control, 2020. **99**: p. 103079.

97. Schuknecht, N., J. McDaniel, and H. Filas. *Achievement of the $100/m2 parabolic trough*. in *AIP Conference Proceedings*. 2018. AIP Publishing LLC.

98.     NREL, *System Advisor Model.* Avaiable from: https://sam.nrel.gov/, 2018(Version 2018.11.11).

99.     Towler, G. and R. Sinnott, *Chemical engineering design: principles, practice and economics of plant and process design*. 2012: Elsevier.

100.    Gielen, D., *Renewable energy technologies: Cost analysis series.* International Renewable Energy Agency, 2012. **1** (2/5).

101.    Rural Bank. *Australian Farmland Values*. 2020  [cited 27/11/2020]; Available from: https://www.ruralbank.com.au/knowledge-and-insights/publications/farmland-values/.

102.    Intratec. *Production cost reports*. 2021  [cited 20/01/2021]; Available from: https://www.intratec.us/.

103.    Oh, H.-T., et al., *Techno-economic analysis of advanced stripper configurations for post-combustion CO2 capture amine processes.* Energy, 2020. **206**: p. 118164.

104.    Versteeg, P. and E.S. Rubin, *A technical and economic assessment of ammonia-based post-combustion CO2 capture at coal-fired power plants.* International Journal of Greenhouse Gas Control, 2011. **5**(6): p. 1596-1605.

105.    Pour, R.A., D. Kennedy, and S. Davydycheva. *On the Efficacy of Tornado Charts*. in *SPWLA 52nd Annual Logging Symposium*. 2011. Society of Petrophysicists and Well-Log Analysts.

106.    Standardization, I.O.f., *Environmental Management: Life Cycle Assessment; Principles and Framework*. Vol. 14044. 2006: ISO.

107.    Fimbres Weihs, G.A., et al., *Feasibility assessment of Bioenergy with Carbon Capture and Storage (BECCS) deployment with Municipal Solid Waste (MSW) co-combustion at New South Wales (NSW) coal power plants.* Coal Innovation NSW Fund Round 3 seed grants, 2020.

108.    Weihs, G.F.H., Minh; Wiley, Dianne; Malik, Rameen Hayat; Jones, Joseph; Abbas, Ali; Zhai, Jake; Meka, Wahyu; Fennell, Paul *Feasibility assessment of Bioenergy with Carbon Capture and Storage (BECCS) deployment with Municipal Solid Waste (MSW) co-combustion at New South Wales (NSW) coal power plants.* Coal Innovation NSW Grant, 2020.

109.    Brown, P., et al., *A Life Cycle Assessment of the New South Wales Electricity Grid.* 2006.

110.    Ou, Y., H. Zhai, and E.S. Rubin, *Life cycle water use of coal-and natural-gas-fired power plants with and without carbon capture and storage.* International Journal of Greenhouse Gas Control, 2016. **44**: p. 249-261.

111.    Spath, P.L., M.K. Mann, and D.R. Kerr, *Life cycle assessment of coal-fired power production*. 1999, National Renewable Energy Lab., Golden, CO (US).

112.    Parvareh, F., et al., *Integration of solar energy in coal-fired power plants retrofitted with carbon capture: A review.* Renewable & Sustainable Energy Reviews, 2014. **38**: p. 1029-1044.

113.    Grant, T., C. Anderson, and B. Hooper, *Comparative life cycle assessment of potassium carbonate and monoethanolamine solvents for CO2 capture from post combustion flue gases.* International Journal of Greenhouse Gas Control, 2014. **28**: p. 35-44.

114.    Klein, S.J. and E.S. Rubin, *Life cycle assessment of greenhouse gas emissions, water and land use for concentrated solar power plants with different energy backup systems.* Energy Policy, 2013. **63**: p. 935-950.

115.    Koornneef, J., et al., *Life cycle assessment of a pulverized coal power plant with post-combustion capture, transport and storage of CO2.* International journal of greenhouse gas control, 2008. **2**(4): p. 448-467.

116.    Knoope, M., A. Ramírez, and A. Faaij, *Economic optimization of CO2 pipeline configurations.* Energy procedia, 2013. **37**: p. 3105-3112.

117.    Yujia, W., X. Zhaofeng, and L. Zheng, *Lifecycle analysis of coal-fired power plants with CCS in China.* Energy Procedia, 2014. **63**: p. 7444-7451.

118.   O'Brien, G., et al., *Victorian carbon dioxide geological storage options; an engineering evaluation of storage potential in southeastern Australia.* Energy Procedia, 2011. **4**: p. 4739-4746.

119.   Khan, F.I., K. Hawboldt, and M. Iqbal, *Life cycle analysis of wind–fuel cell integrated system.* Renewable energy, 2005. **30**(2): p. 157-177.

120.   Odeh, N.A. and T.T. Cockerill, *Life cycle GHG assessment of fossil fuel power plants with carbon capture and storage.* Energy Policy, 2008. **36**(1): p. 367-380.

121.   WNA, *Comparison of Lifecycle Greenhouse Gas Emissions of Various Electricity Generation Sources.* 2011.

122.   Park, S.S., H.J. Jeong, and J. Hwang, *3-D CFD modeling for parametric study in a 300-MWe one-stage oxygen-blown entrained-bed coal gasifier.* Energies, 2015. **8**(5): p. 4216-4236.

123.   Ranade, V.V., S.M. Mahajani, and G.A. Samdani, *Computational Modeling of Underground Coal Gasification*. 2019: CRC Press.

124.   Monteiro, J. and H. Svendsen, *The N2O analogy in the CO2 capture context: Literature review and thermodynamic modelling considerations.* Chemical Engineering Science, 2015. **126**: p. 455-470.

125.   Kvamsdal, H.M., J.P. Jakobsen, and K.A. Hoff, *Dynamic modeling and simulation of a CO2 absorber column for post-combustion CO2 capture.* Chemical Engineering and Processing: Process Intensification, 2009. **48**(1): p. 135-144.

126.   Maradiya, C., J. Vadher, and R. Agarwal, *The heat transfer enhancement techniques and their Thermal Performance Factor.* Beni-Suef University Journal of Basic and Applied Sciences, 2018. **7**(1): p. 1-21.

# 10.  Appendices

## 10.1    Appendix A – Fundamentals of the CFD study

In this appendix, we outline the fundamental structure of our computational fluid dynamics (CFD) modelling framework to build a rigorous So-St model for studying micro-scale phenomena, e.g. bubble nucleation, chemical reaction. We discretised a So-St segment into smaller control volumes and describe physical-chemical phenomena per volume using sets of equations. COMSOL Multiphysics® was used as a modelling tool to execute the equations. The So-St model comprises different modules, e.g. thermodynamic, tracking of vapour–liquid interface. The model was also validated with literature data and the Aspen model's results. Using the COMSOL model, we have shown the use of physical insert (e.g. packing) in the So-St tube can induce significant liquid mixing, thus can result in higher heat transfer. The outcomes from this preliminary study helped us to setup the correct method for our CFD model.

CFD only models the flow of solvent irrespective of other phenomena (e.g. mass transfer, chemical reaction). To include other phenomena, we have utilised the Multiphysics modelling paradigm, which considers different physics coupled via an appropriate interface. We have developed a modelling framework that depicts the thermo-physical operation in So-St interpreted into meaningful physics and suggests appropriate integration between these physics. Each of these physics is individually analysed to ensure the simulation results are meaningful. Finally, the result of the developed COMSOL model is validated with our Aspen model to safeguard reasonable accuracy. By achieving that, we can capitalise on the validated Aspen model with confidence to size the entire SCF including all So-St modules and segments. This approach is often utilised in literature when there is a need to perform multiscale simulations [122, 123].

### 10.1.1  Multiscale modelling framework

This subsection formulates the strategy to model the Multiphysics problem in COMSOL (v5.5). COMSOL uses a finite control volume (FCV) method which discretises the entire model domain into small control volumes. We are mostly interested in the species concentration. Based on the proposed framework, the adjacent control volumes interact with each other via the transport of species ($H_2O$, $CO_2$, MEA and the relative ionic species), governed by diffusive (from concentration gradient) and convective (pressure gradient) forces (Figure 148-A). In each control volume, important physics are hierarchically assembled to compute the flux of $CO_2$ and other species between vapour and liquid phase. Five physical phenomena determine the mass transfer rate, e.g. the chemical reaction physics affects the $CO_2$ partial pressure term in the mass transfer calculation. We have grouped the physical phenomena so that they can be modelled as sub-model components, allowing us to validate the simulation results of each individual physical phenomenon to confirm they are reasonable (Figure 148-B). The equation in green box in Figure 148-B  is known as the two-film theory mass transfer rate ($N$ in mol/m$^3$s); each term is as follows: $k$ (mol/m$^2$ Pa) is mass transfer

coefficient, $a$ (m$^2$/m$^3$) is gas–liquid interface area; $P_{CO2}$ (Pa) is the actual $CO_2$ partial pressure in gas; $P_{CO2*}$ (Pa) is equilibrium $CO_2$ partial pressure in gas.   Note that all the above physical phenomena are needed to compute $CO_2$ transfer between vapour–liquid; however, the fundamental properties of individual physical phenomena are not affected by the others. Thermodynamic-chemical reactions are grouped together because they can be modelled separately, and the validation can be performed with a predefined gas–liquid interface by selecting a boundary for liquid and gas separately in COMSOL. In other words, we do not need to compute the evolution of the gas–liquid interface. The interface evolution and hydrodynamic are grouped together as per COMSOL's suggestion. We could validate and/or solve this model by assuming a water-only scenario, thus the vaporisation is the function of water saturation temperature. The heat transfer physical phenomenon is implicitly coupled to all other phenomena because the thermodynamic-chemical reaction generates/consumes heat. Both the interface evolution and hydrodynamic are affected by the vapour pressure, which is a function of the temperature due to the ideal gas law. The proposed modelling framework will allow us to validate each model component separately. This ensures that once all components are fully coupled, we will obtain reasonable results. Next, we describe each model component and our modelling approach. For all tests and model validations, the model inputs are shown in Table 50, unless stated otherwise.
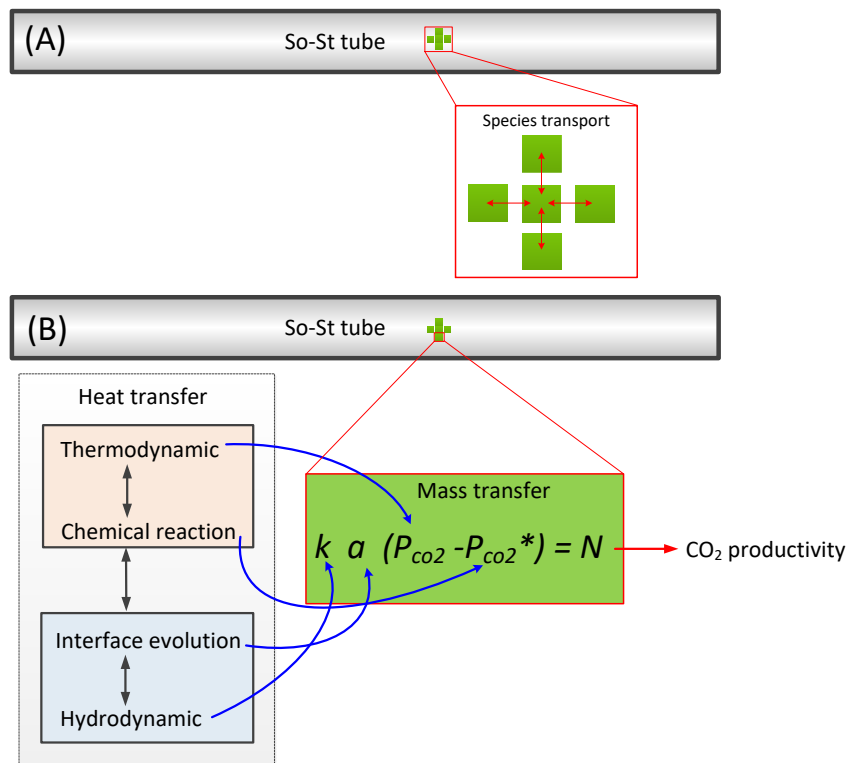


**Figure 148: The multi-scale modelling framework to model So-St operation comprised of coupled multi-physic phenomena. (A) Describing the interaction between control volumes via transport of species (e.g. MEA, $CO_2$, $H_2O$ etc.); (B) the physical phenomena occurring in one control volume.**

**Table 50: Design specification for So-St model testing and validation.**

| Design specification | Value | Unit |
|---|---|---|
| Rich loading | 0.4 | – |

| | | |
|---|---|---|
| Inlet velocity | 1.2 | m/s |
| Inlet temperature | 80 | °C |
| So-St length | 1 | m |
| So-St inner/outer diameter | 7.6/8.1 | cm |
| Saturation temperature | 100 | °C |

Thermodynamic principle and reaction kinetics were discussed in section 2.1 in details. The key chemical reactions and their equilibrium constants were disclosed in that section. Based on those discussions, we propose the coupling of thermodynamic and chemical reaction physics in next section.

## 10.1.2  Coupling thermodynamic and chemical reaction

The next modelling aspect is mass transfer between liquid and vapour. Since this aspect is strongly coupled to the liquid–gas interface, i.e. in a complete model, one would need to track this interface simultaneously while solving for the mass transfer equation. In this model development stage, we want to first validate our implementation of mass transfer in COMSOL. Recall the mass transfer between liquid–gas is governed by Henry's law. We incorporated the mass transfer by calculating the molar flux of each species after each time step and use the results to calculate the next integration. Here the film theory is used to estimate the rate of mass transfer between the gas phase and liquid phase. By using the generalised Frick's law, the molar fluxes of MEA and $H_2O$ can be written as [125]:

$$N_{MEA} = k_{MEA}(p_{MEA} - p_{MEA}^*)$$
<div align="right">*Eq. 104*</div>

$$N_{H_2O} = k_{H_2O}(p_{H_2O} - p_{H_2O}^*)$$
<div align="right">*Eq. 105*</div>

where $N_{MEA}$ (mol/m²/s) and $N_{H_2O}$ (mol/m²/s) are the molar fluxes of MEA and $H_2O$ from gas to liquid, respectively; $p_{MEA}$ (Pa) and $p_{MEA}^*$ (Pa) are the partial pressures of MEA in the gas phase and at the gas–liquid interface, respectively (e.g. if $p_{MEA}^* > p_{MEA}$, MEA is transferred from liquid to gas); $p_{H_2O}$ (Pa) and $p_{H_2O}^*$ (Pa) are the partial pressures of $H_2O$ in the gas phase and at the gas–liquid interface, respectively; $k_{MEA}$ (mol/m²/Pa.s) and $k_{H_2O}$ (mol/m²/Pa.s) are the gas film mass transfer coefficients for MEA and $H_2O$, respectively. The mass transfer of $CO_2$ is similar to how $CO_2$ would escape when a beverage bottle is opened. After the $CO_2$ bubbles nucleate and form, they will grow by the diffusion of excess $CO_2$ into the bubbles. In this physical phenomenon, the bubble–liquid interface can be assumed to be in equilibrium with the bubble. Molar flux for $CO_2$ can be estimated as:

$$N_{CO_2} = k_{CO_2}(p_{CO_2} - p_{CO_2}^*)$$
<div align="right">*Eq. 106*</div>

where $k_{CO_2}$ (mol/m²/Pa/s) is the overall mass transfer coefficient for $CO_2$ ; $p_{CO_2}$ (Pa) and $p_{CO_2}^*$ (Pa) are the partial pressures of $CO_2$ in the gas phase and at the gas–liquid interface, respectively. The

mass transfer coefficient for spherical bubble can be estimated using the Sherwood relation, defined as follows:

$$Sh = 2 + 0.6415(ReSc_j)^{0.5}$$

*Eq. 107*

Where *Re* and *Sc* are two dimensionless numbers and *j* is the component of interest (MEA, $CO_2$ or $H_2O$). To compute these numbers, the velocity and vapour phase field from the hydrodynamic and interface evolution physics are required as demonstrated in Figure 148. The transport of species is modelled with diffusive and convection phenomenon as follows:

$$\nabla . (-D_j \nabla c_j) + u . \nabla c_i = R_i$$

*Eq. 108*

Where *D* ($m^2$/s) is diffusivity, *c* (mol/$m^3$) is concentration; subscript '*j*' is the species and *R* (mol/$m^2$s) is the rate of generation. The rate is a lump term to describe reaction rate and mass transfer rate. Figure 149 shows simulation set-up in COMSOL which allows us to study the mass transfer aspect of the CFD model. The aim is to validate whether the model can reproduce a typical mass transfer scenario (e.g. given a supersaturated $CO_2$ solvent, $CO_2$ should be transferred from liquid to gas, etc.). We assume this is a small-enclosed control volume with no mass transfer to the outside and mass transfer is governed purely by diffusion, thus allowing us to observe whether a concentration gradient can form or not. This aspect is very important in the $CO_2$ bubble formation and growth. Mass transfer coefficient for all species are assumed to be constant (0.001 mol/$m^2$/Pa/s) in these simulations, allowing us to isolate the effect of driving force on mass transfer.
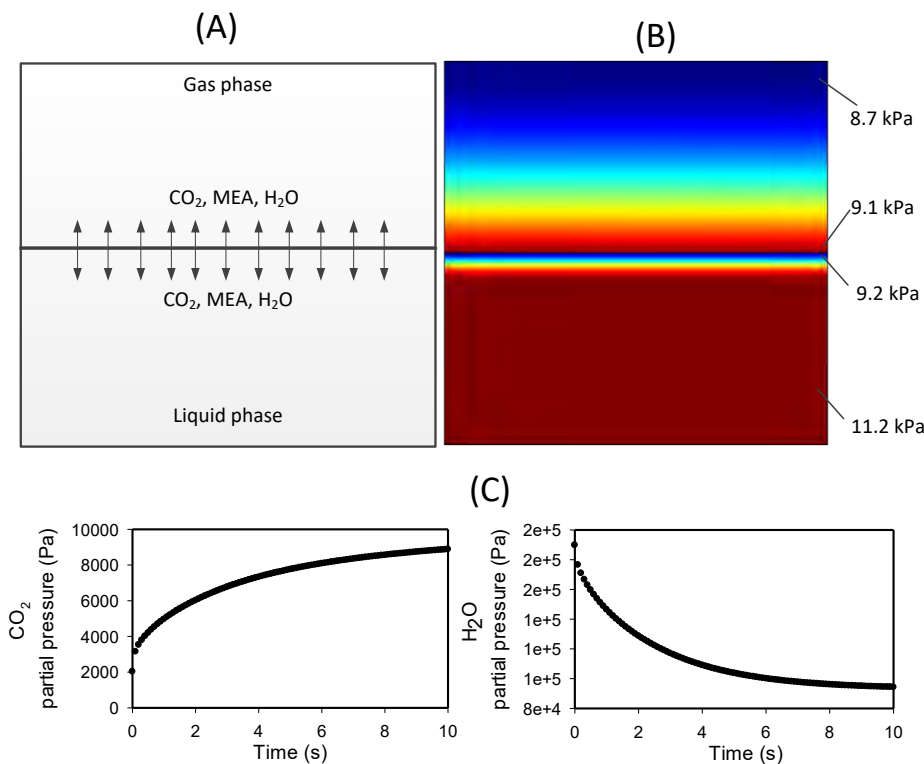


**Figure 149: COMSOL simulation set-up to validate the mass transfer aspect of the CFD model; (B) simulation snapshot showing $CO_2$ partial pressure at different points on the grid. $CO_2$ mass transfer will happen in the direction of high partial pressure towards the low partial pressure region. Note that the colour scale is adjusted for each**

**phase separately to highlight the interface pressure gradient. (C) Evolution of CO₂ partial pressure in the gas phase, increasing over time due to CO₂ being transfer from liquid to gas. Initial total pressure is set to 2 bar.**

As can be seen in Figure 149-B, there is a developed gradient of $CO_2$ partial pressure at the gas–liquid interface, indicating $CO_2$ is transferred from the liquid phase to the gas phase. This mass transfer will only end when the $CO_2$ partial pressure in both phases is equal. Figure 149-C shows the evolution of $CO_2$ partial pressure in the gas phase, showing more $CO_2$ accumulation over time. The water in vapour phase reduces over time, indicating water transfer from the vapour phase back to liquid, i.e. condensation. The temperature in the gas and liquid phases is fixed at 100°C; hence the water vapour pressure plateaus around 100 kPa. From the above, it can be concluded that the model can realistically reproduce the mass transfer phenomenon.

The role of CFD in this project is to aid in the design and optimisation of the So-St. Although different parts of a completed model are not yet assembled because they first need to be fully validated, here we perform a possible design-guide analysis using CFD to highlight a potential avenue for design optimisation. It is noted that the pressure gradient is different between gas and liquid phases. This is because in the gas phase, species diffuse at significantly higher rates as compared with the liquid phase (Figure 150). From this observation, we conclude that mixing enhancement will be necessary in some So-St sections to improve species transfer. This could be at the entrance when the vapour fraction is small. The effectiveness of mixing could be studied by altering the diffusion coefficient in this model set-up.
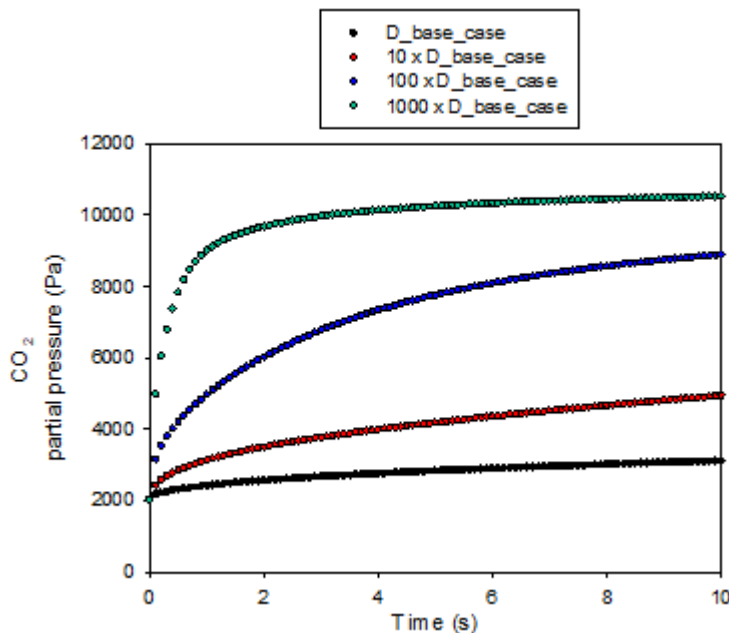


**Figure 150: Evolution of CO₂ partial pressure under increasing mixing conditions, stimulated by increasing the input values of the diffusion coefficient of species (D, SI unit is m/s) against the D_base_case (typically takes a value in the order of 10⁻⁹ m/s).**

## 10.1.3  Interface evolution

In the previous section, we discussed the mass transfer formulation and arrived at a formula for mass flux, $N$ (mol/m²/s). If $N$ is equated to '1', that means for every 1 m² liquid-vapour contact area, the mass transfer rate is 1 mol/s. This means to complete the mass transfer formulation we will

need to compute liquid–vapour contacting area. Unlike the conventional desorber, So-St does not readily have a gas phase to carry away the excess $CO_2$. In this case, $CO_2$ might escape via a similar route as the excess $CO_2$ in beverages. The bubbles can nucleate via two main different mechanisms: homogeneous and heterogeneous. In the first case, the $CO_2$ bubbles nucleate throughout the solution, whereas in the latter nucleation happens on solid surface and can be accelerated by packing materials. The criterion to determine the predominant factor is a function of supersaturation ratio, as follows:

$$S = \frac{C_{CO2}}{C_{sat,CO2}} \quad (typically\ S > 1\ for\ supersaturation) \quad\quad Eq.\ 109$$

In which $C_{CO2}$ is the concentration of $CO_2$ in liquid phase and $C_{sat,CO2}$ is the saturation concentration. The higher the $S$ ratio, the higher chance of homogenous nucleation can occur. For $S$ value less than 100, nucleation most likely happens on the solid surface. The So-St has a relatively low $S$ (around 2) (from Aspen equilibrium calculation) ratio as compared with commercial beverages (around 5). This is because the $CO_2$ vapour in So-St accumulates along each segment, thus quickly increasing the $C_{sat,CO2}$ term and reducing the $S$ ratio. Once a bubble forms and detaches it can grow further by absorbing the excess (but still dissolved) $CO_2$ in the bulk solution. This mass transfer can be formulated using the flux equation developed in the previous section. The mass transfer mechanism is shown in Figure 151.
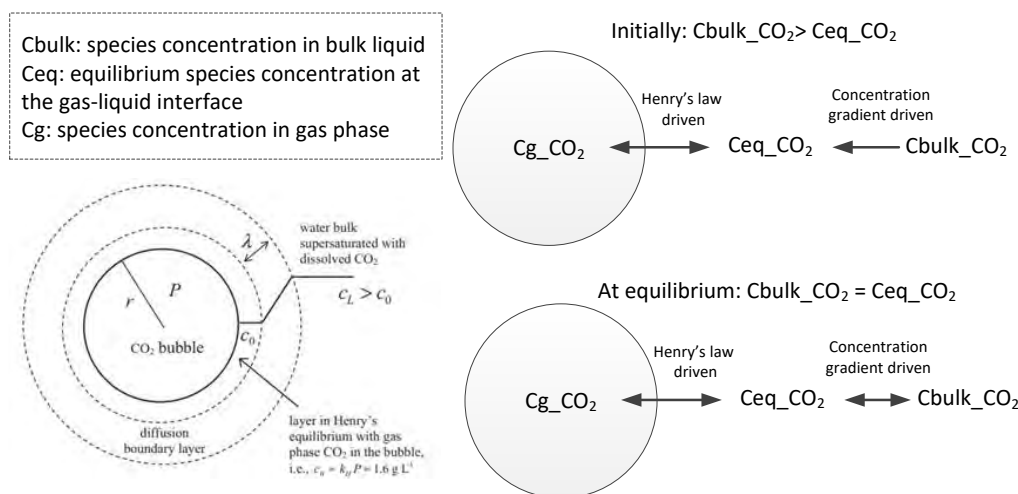


**Figure 151: $CO_2$ mass transfer with a formed bubble.**

Another way for $CO_2$ bubbles to escape is via water bubble formation during water boiling. This would happen for low loading desorption because more water can be vaporised as shown in Figure 152. Compared to the $CO_2$ bubble-driven diffusion, the water bubble case will have higher rate because the presence of water vapour helps reduce the $CO_2$ partial pressure, thus providing a driving force for $CO_2$ to diffuse into the bubble. Base on the above fundamental bubble dynamics, we propose two mechanism of mass transfer:

1. $CO_2$ bubbles nucleate either from surface or from solution. These bubbles can further desorb the $CO_2$ from the solvent. This mechanism is likely to happen in the loading range from 0.45 to 0.32 in which Aspen simulation suggests the $CO_2$ is released without water boiling.
2. Water boils rapidly, creating bubbles which can absorb the excess $CO_2$. This requires water to boil, thus is most likely to happen when the $CO_2$ loading drops below 0.32.
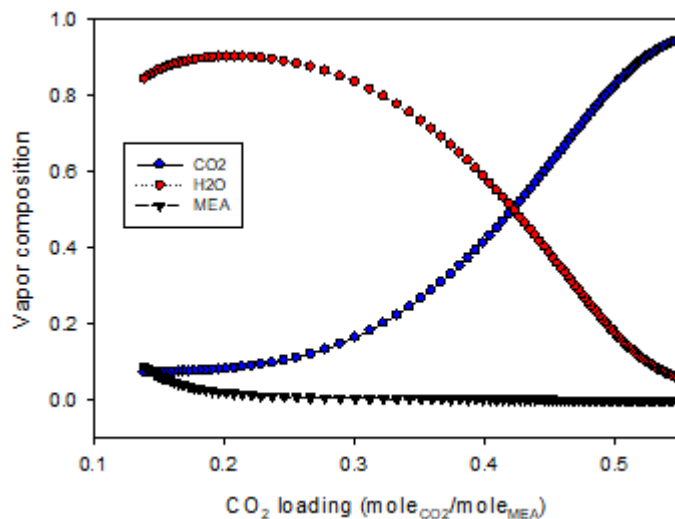
**Figure 152: Vapour mole fraction during So-St desorption.**

In COMSOL, there are two modelling approaches to track the gas–liquid interface: separated and dispersed models (Figure 153). The separate method (or phase field) is more accurate to determine the gas–liquid interface; however, it requires high computational power and is only suitable for tracking a small number of bubbles. In contrast, the dispersed model does not track individual bubble evolution but considers many bubbles forming a second phase (dispersed phase) in the liquid. Each of these methods is discussed below.
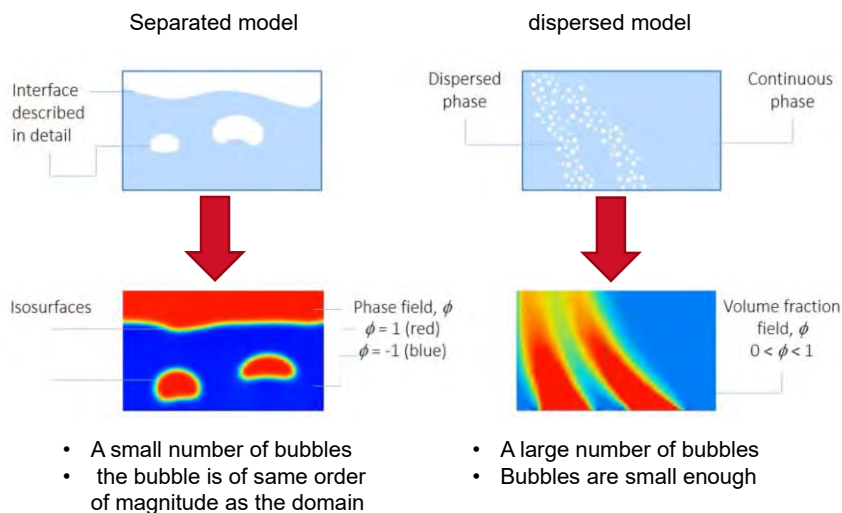


**Figure 153: Separated and dispersed modelling methods for interface tracking.**

## Type I: dispersed model

Since the bubbles are small, we have assumed the bubbles form a dispersed phase within the liquid phase. The vapour fraction is used to calculate average properties required in the Navier-Stoke equation. The gas phase is then tracked by a gas transport model. This is called the bubbly model and is available from the Physics tree in the COMSOL library. There is no existing equation to define the bubble nucleation rate. We have started to formulate a separate module to define the rate of $CO_2$ bubbles detaching from the wall of the So-St. We assume the rate of bubble flux is a function

of bubble detachment frequency and the supersaturation ratio; higher S means higher rate of bubble formation:

$$f_b = f_{ref} \log(S)$$
<div align="right">*Eq. 110*</div>

Where $f_b$ is the bubble frequency for using in the simulation and $f_{ref}$ is the reference frequency obtained from similar systems in literature (typically between 1 and 10). The bubble flux (in term of mass, $J$ in kg/m$^2$/s) can be calculated as follows:

$$J = \left(\frac{f_b}{A_w}\right) V_b \rho_{CO2}$$
<div align="right">*Eq. 111*</div>

Where $A_w$ is the bubble cover area on the surface and $V_b$ is the bubble volume. These two terms would depend on the bubble size, which can be determined either assuming a fixed size or an additional model to describe bubble growth. In the current model, we have assumed the bubble diameter is fixed at 1 mm; however, future works might need a more rigorous bubble dynamic model to determine the bubble size and bubble detachment frequency. The current model framework is formulised such that it can flexibly adapt to a new plug-in model to describe more detailed physics. To demonstrate the capability of the bubbly flow model in COMSOL, we carried out a simple simulation of a small section along So-St. To reduce computational need, we have assumed the liquid phase has a saturation ratio about 3 (i.e. $C_{CO2}$ = 10 mol/m$^3$ and $C_{s,CO2}$ = 3 mol/m$^3$). In this simulation, we aim to find out:

1. Does the bubbly model track the gas phase evolution appropriately? This is because the mass transfer equation calculation needs the 'a' (interfacial area) input and this term change its values depending on the gas volume fraction.
2. Can the model account for mass transfer between liquid and vapour? This is because the bubble upon attachment will grow due to mass exchange with the excess (but still dissolved) $CO_2$.

The simulation results are shown in Figure 154. Overall, the bubbly model is capable of tracking the gas phase, as evidenced by reasonable changes when the So-St adapt different tilt angle. The model can also track the quantitative changes in the gas fraction (i.e. the amount of bubble presence). However, we discover one major limitation, which is that the bubbly model does not account for bubble accumulation underneath the upper wall. This means when the gas phase approaches the upper wall (blue arrow in Figure 154) it will flow out and not accumulate. In reality, this outcome reassembles a gas membrane removal operation. Hence, the model fails to track the interface evolution underneath the wall. While this is ideal for So-St as the $CO_2$ release driving force is maintained, its feasibility will need to be assessed thoroughly because of the small So-St size. Since the bubbly model was provided by COMSOL, we will consult their engineering team to discuss this issue. In the meantime, the current bubbly model can be used to study the system at micro-scale to explore the bubble dynamics and how they influence the $CO_2$ transfer phenomenon. Understanding these questions will aid us to make decision at macro-scale level, e.g. whether it is adequate to assume vapour–liquid equilibrium is always achieved along the So-St. The mass transfer aspect of the bubbly model is examined and important variables are shown in Figure 154-C. It can be seen that the vapour fraction increases the mass transfer rate and the $CO_2$ concentration in the liquid phase drops accordingly. This shows the bubbly model reproduces realistic mass transfer physics.

Once we fix the bug in the interface tracking equation in COMSOL, this would complete the model for type I $CO_2$ desorption.
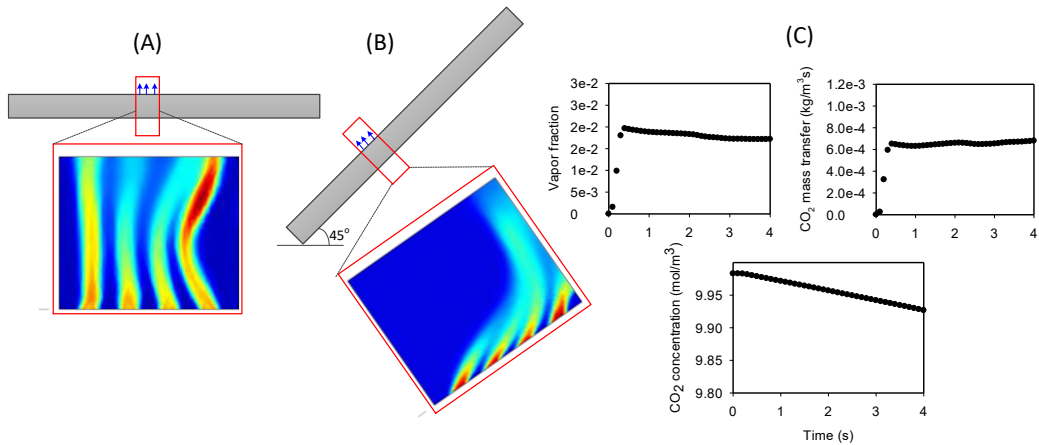


**Figure 154: (A, B) Simulating the gas phase field of a small section. The colour code is relative (blue mean no bubble presence and red means highest bubble presence). (C) Evolution of different terms in the mass transfer equation.**

**Type II: separate model (phase field method)**

This approach uses the phase field method to track the interface. It is accurate to track individual bubbles and the evolution of the gas–liquid interface, but at the expense of intensive computer power. Since the bubbly model fails to capture the vapour accumulation (fate) phenomena, until this issue is resolved with the COMSOL engineering team, we continue using this phase field model to determine the gas–liquid interface. The phase field method combines Navier-Stokes equation with Cahn-Hilliard diffusion equation:

$$\nabla \cdot \mathbf{u} = 0$$

*Eq. 112*

$$\frac{\partial(\rho\mathbf{u})}{\partial t} + \nabla \cdot (\rho\mathbf{u}\mathbf{u}) - \nabla \cdot (\mu\nabla\mathbf{u}) - \nabla\mathbf{u} \cdot \nabla\mu = -\nabla p + \mathbf{F}_{st} + \mathbf{F}_{ext}$$

*Eq. 113*

$$\frac{\partial\phi}{\partial t} + \mathbf{u} \cdot \nabla\phi = \nabla \cdot \frac{\gamma\lambda}{\varepsilon^2}\nabla\psi$$

*Eq. 114*

$$\psi = -\nabla \cdot \varepsilon^2\nabla\phi + (\phi^2 - 1)\phi + \left(\frac{\varepsilon^2}{\lambda}\right)\frac{\partial f}{\partial\phi}$$

*Eq. 115*

Where $p$ is the pressure; $\mathbf{u}$ is the fluid velocity field; $\mu$ is the fluid viscosity of liquid; $\mathbf{F}_{ext}$ is the external body force, e.g., the gravity; $\phi$ is the phase variable, which varies in [-1, 1], i.e., $\phi = 1$ in the pure gas phase and $\phi = -1$ in the pure liquid phase; $\gamma$ is the mobility parameter; $\psi$ is a modified

chemical potential that decomposes a fourth-order equation into two second-order equations; $\lambda$ is the mixing energy density; and $\varepsilon$ is a control parameter for the interface thickness that scales with thickness of the interface. The parameters λ and ε are related to surface tension σ through the equation, and the surface tension effect can be considered as a body force.

$$\sigma = \frac{2\sqrt{2}\lambda}{3\varepsilon^2}$$

*Eq. 116*

$$\mathbf{F}_{st} = \left( \frac{\lambda}{\varepsilon^2}\psi - \frac{\partial f}{\partial \phi} \right)\nabla\phi$$

*Eq. 117*

Where $f$ is an external free energy defined by users. In the phase field model, the interfacial thickness $\varepsilon$ and mobility $\gamma$ are two particularly important parameters. A smaller interfacial thickness ε requires a much finer mesh and thus leads to a great increase in computing cost/time and causes difficulties in convergence with the phase field method, though it would be close to the solution with a sharp-interface assumption. So, the value of $\varepsilon$ should be related to the current mesh size. Then, according to the expression of surface tension $\sigma$, the mixing energy density $\lambda$ can be obtained. The mobility parameter $\gamma$ determines the time scale of the Cahn-Hilliard diffusion, and thereby governs the diffusion-related time scale for the interface. A suitable value for $\gamma$ is the maximum velocity magnitude occurring in the model, and a higher mobility is much helpful to obtain the correct pressure variation crossing the interface.

To validate the phase field model, we performed a simulation for water flow only. The result is shown in Figure 155 revealing different flow boiling regimes, which agrees well with experimental observations. The flow starts with a single liquid phase and approaches an annular regime. COMSOL is therefore able to plausibly reproduce the occurrence of small liquid entrainment.
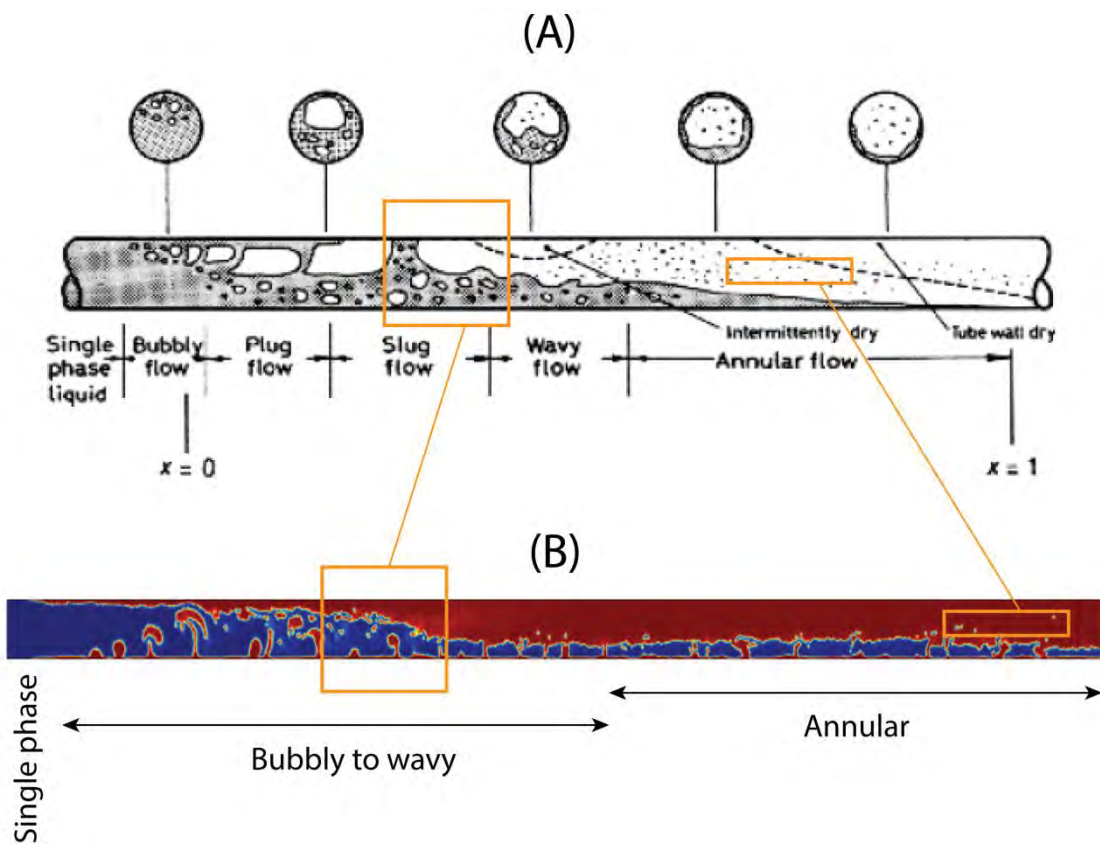
**Figure 155: Comparing the phase evolution from the experiment observation (A), and our COMSOL model (B).**

## 10.1.4  Hydrodynamic – modelling turbulence

The Reynolds number in the So-St (at 1.2 m/s liquid velocity) is around 133,000 (calculated from Aspen model for the base design) which falls under a turbulent regime. This physical phenomenon will solve for the velocity field, which is required for calculating the heat transfer coefficient as well as the convective term in the species transport equation. Figure 156 shows fluctuation in velocity under turbulence, and suggests the velocity always fluctuates around an average value; thus, no steady-state solution could be obtained. This is computationally intensive and not suitable for some applications. COMSOL developed an alternative method called RANS (Reynolds-averaged Navier-Stokes) which solves for the average velocity (dashed line in Figure 156) instead of the actual value. The details of this model are explained in the COMSOL manual. To validate the turbulence model, we perform a 3-D simulation as shown in Figure 157. The So-St geometry has a symmetrical line through the middle; thus, it is appropriate to simulate half of the tube as shown. It can be seen that the baffles induce zonal recirculation. This agrees with literature studies on turbulent flow.
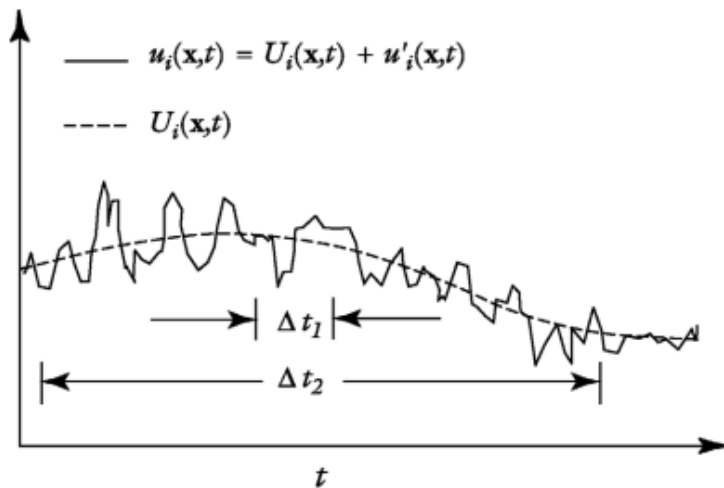
**Figure 156: Velocity as a function of time under turbulent flow conditions.**

**Model development summary**

- We almost accomplished the proposed modelling framework (Figure 158)

- We broke down the model into different interactive physical phenomena which can be coupled in COMSOL

- Individual physical phenomena were implemented and validated successfully

- We successfully coupled the main physical phenomena together
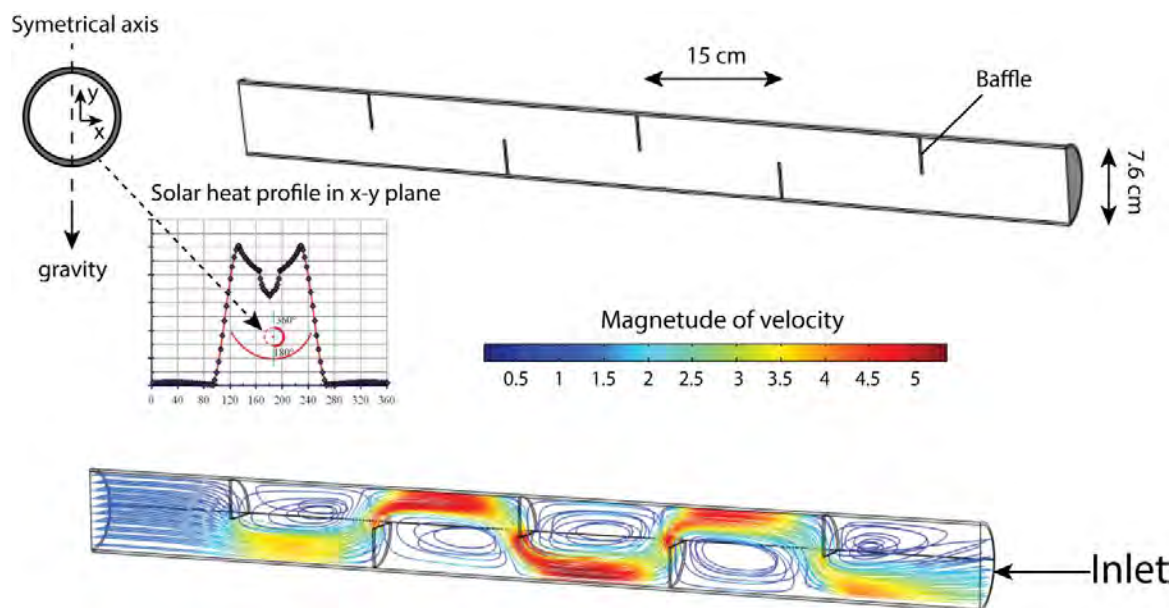


**Figure 157: Setup turbulent flow simulation. The So-St has baffles 15 cm apart. The streamlines track the flow of some 'particles' of water.**
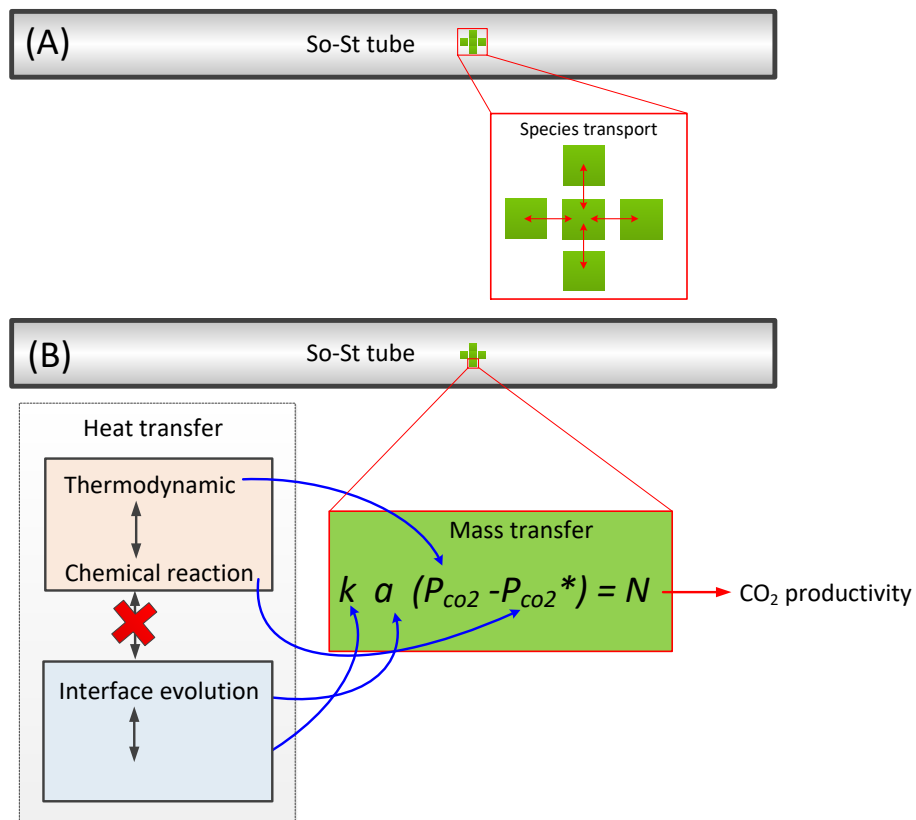
**Figure 158: Completed physics within the modelling framework comprised of major physical phenomena.**

## 10.1.5  COMSOL sub-model analysis

This section analyses different sub-models that have been developed to answer more fundamental questions on guiding design to address potential operation issues related to solar concentration variations. One of the most important operational aspects is effective heating of the solvent. This section analyses some key variables. The base case simulation is shown in Figure 159 with the heat flux on the tube surface assumed to only approach the bottom half of the tube. This assumption is made to reduce computation speed and allow us to preliminarily evaluate heat transfer performance under a variety of So-St designs. We have analysed the temperature distribution of a few Cross-sections along the So-St. The results reveal a very different temperature between the liquid and the tube surface. In close proximity to the surface (slide 4, Figure 159), the liquid temperature becomes very high. This could cause local solvent degradation if the temperature becomes excessive. From the above result, we observed very poor heat transfer performance, indicating a slow heat transfer rate. The heat transfer rate is proportional to temperature driving force and heat transfer coefficient. We first analyse the temperature driving force. We computed simulations for three different levels of solar concentration: 100, 200 and a very extreme 300 kW/m², respectively. The results are shown in Figure 160.
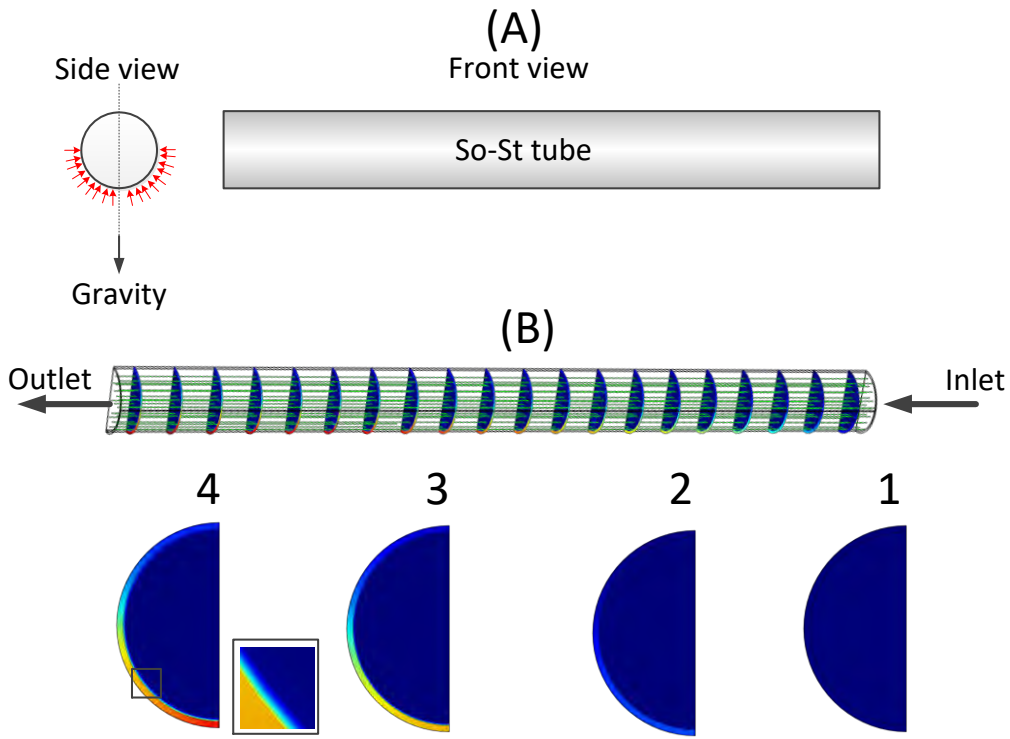
**Figure 159: Temperature profile (colour) and velocity line (green line) for base-case simulation (1 m length, 100 kW/m², 1.2 m/s). Note that the So-St tube solid surface has a high temperature because it is in direct contact with solar heat and its thermal conductivity is very high. The So-St tube is vertically symmetrical in the direction of gravity; hence we only simulated the left half of the tube to reduce computational power.**

It can be seen that increasing the solar concentration does not effectively enhance the overall heat transfer, but instead only the local heat transfer. This fact can be arrived by probing the liquid temperature in proximity to the tube surface (Figure 160). This is highly undesirable due to solvent degradation issues under high temperature. As a result, increasing the temperature driving force is not an effective strategy to enhance the overall heat transfer rate.
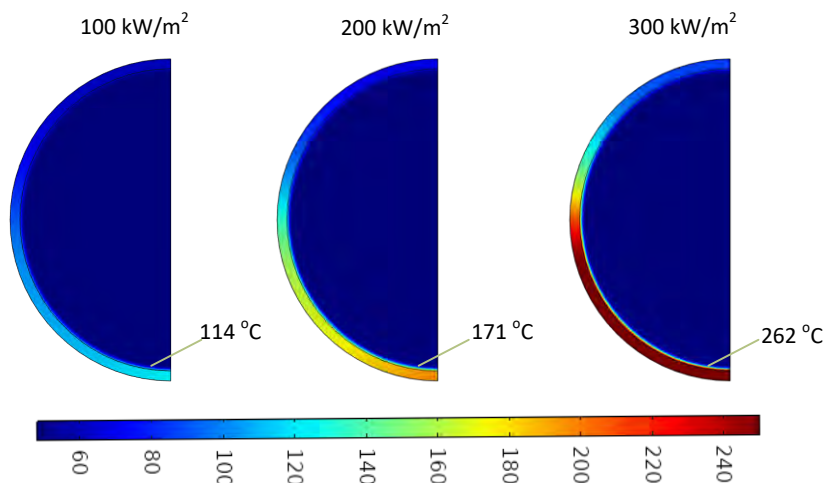


**Figure 160: The effect of increasing heat flux on the solvent temperature. The temperature of the solvent in proximity to the tube surface is shown.**

## 10.1.6  Internal design modifications

It has been shown that insertion of baffles increases the flow turbulence, resulting in boosting the heat transfer rate [126]. This practice has been proposed and studied for a parabolic trough. In this analysis, we focus on one type of baffle (semi-spherical) and sensitise the effect of baffle inter-distance. The outcome of this analysis can guide us towards a better internal So-St design. We also include the reaction sub model to study how the baffle influences the distribution of species, particularly $CO_2$. This is because the $CO_2$ concentration affects the saturation ratio, thus bubble nucleation and growth. Due to the excessive computational demand, we have simplified the So-St geometry to 2-D instead of 3-D. We have simulated a cut-plane in the centre of the horizontal So-St tube. The simulations are shown in Figure 161, showing the velocity magnitude and streamline for two inter-baffle distances (5 cm and 15 cm; baffle height is 3 cm and baffle-to-diameter ratio is 2.53). Overall, the baffle design increases the velocity magnitude and varies the flow direction. These two effects would increase the heat transfer as compared with no baffle. Interestingly, the zonal recirculation only appears in the 10 cm design but not the 5 cm. This means the zonal recirculation is design dependent. The unique characteristic of this zone is that the velocity is much lower than the main flow zone (main flow zone is where the streamline is straight). It seems like the zonal recirculation zone is completely isolated from the main flow. Comparing the 5 cm and 15 cm designs, the 15 cm has lower main flow area because the recirculation zone is large. Therefore, it could be the case that the 15 cm design has a lower average heat transfer rate as compared with the 5 cm, due to smaller heat exchange area. We tested other spacing distance and as shown in Figure 162, the zonal recirculation appears when the distance is more than 10 cm. The recirculation occurs at the bottom corners of each baffle. In addition, the zonal circulation last longer when the baffle distance is 15 cm and 20 cm. In the 10 cm design, the circulation disappears after the sixth baffle. From the above, we conclude the baffle spacing should be more than 15 cm if one wants to obtain a high number of recirculation zones. As discussed above, the recirculation zone is isolated. From the heat transfer perspective, it accumulates more heat as compared with the main flow zone. This can be seen from Figure 162, revealing the distinct temperature values of the recirculation when compared with those of the main flow zone.
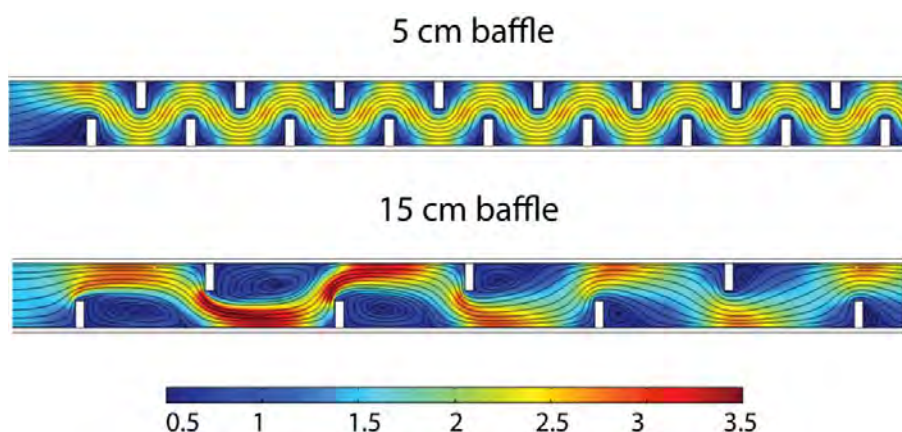


**Figure 161: Velocity magnitude and streamline for two inter-baffle spacing. Flow direction is from left to right.**
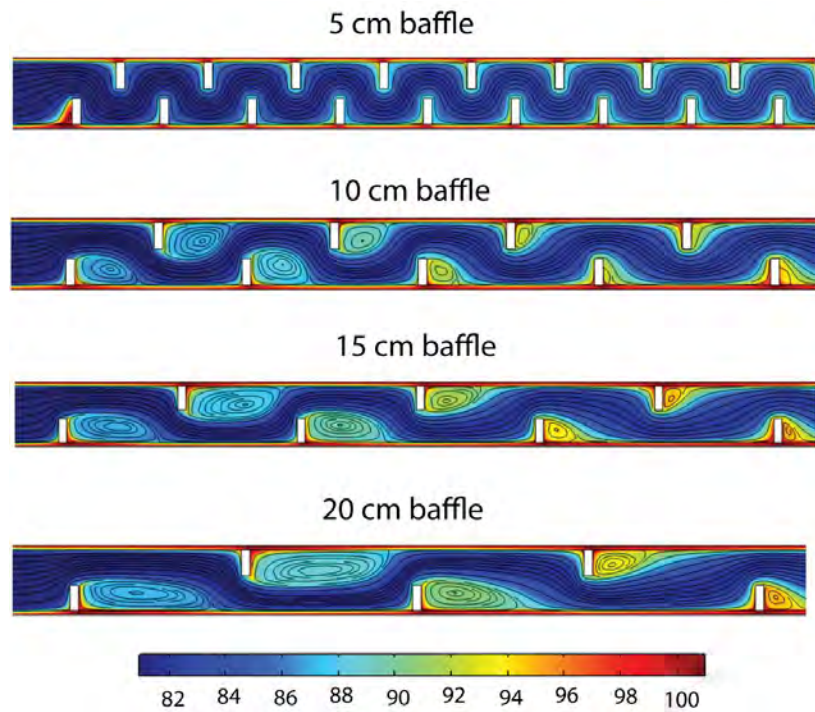
**Figure 162: Temperature profile and velocity streamlines for different inter-baffle distance. Flow direction is from left to right.**

Since the main purpose of baffle installation is to enhance heat transfer, we have evaluated the temperature increases in each design and the results are shown in Figure 163-A. Note that the base case (no baffle) is not plotted; the temperature increase in this case is minimal, about 0.1°C. All baffle designs give significant increases in temperature. The 5 cm design yields the highest performance. This confirms the recirculation zone reduces heat transfer area of the main flow, thus lowering heat transfer. Even so, the design with significant recirculation (20 cm) still yields higher temperature increases above the base case. This confirms the heat transfer enhancement effect of having baffles. While the 5 cm design gives the highest temperature increases, the pressure-drop is impossible to be handled in practice (Figure 163-A). The lowest pressure-drop among the designs is about 15 kPa in the 20 cm design. This is only 1 m So-St length, so if the length is 20 m, the total pressure-drop would be 300 kPa, i.e. 3 bars. This is still impractical because So-St inlet pressure is only 2 bar. Hence, practical application needs to consider baffle spacing larger than 20 cm; around 30 cm would be appropriate.
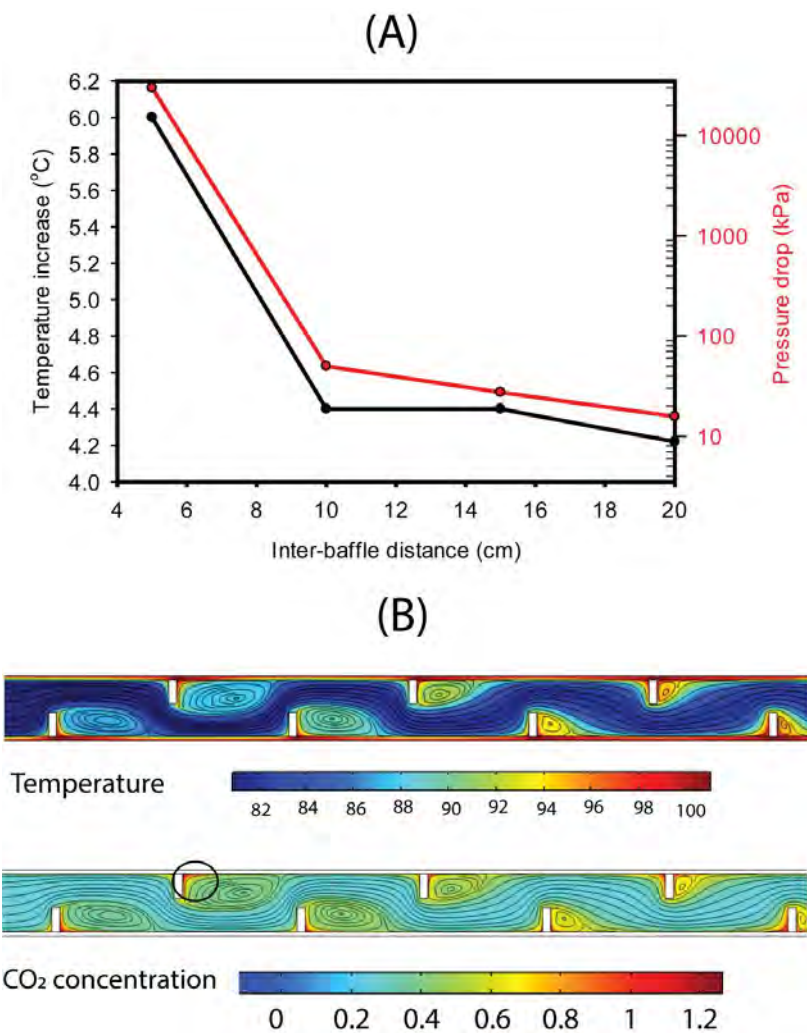
**Figure 163: (A) Evaluating the performance of different inter-baffle spacing. (B) Average temperature at the exit and CO₂ concentration profile. When there is no baffle at all, the temperature increase is small, around 0.2°C.**

The recirculation zone not only accumulates heat but also increases the $CO_2$ concentration. This is shown in Figure 163-B. In the recirculation zone, the temperature increases. This enhances the $CO_2$ reaction and breaks the MEA–$CO_2$ reaction bonds. In circulation areas, the $CO_2$ concentration is distinctively higher than the main flow zone. In real application, this would mean more $CO_2$ bubbles will form around the recirculation zone(s). One desirable effect of this outcome is that more $CO_2$ bubbles could be formed as higher $CO_2$ concentration boosts the saturation ratio, enhancing $CO_2$ bubble nucleation and growth. However, the recirculation zone might be isolated from the main flow zone, i.e. the '$CO_2$' within that zone cannot escape. Any $CO_2$ bubbles will follow the flow of solvent and also be trapped in the recirculation zone. This can be seen in Figure 164, showing the accumulation of $CO_2$ bubbles. It can be seen that more $CO_2$ bubbles were trapped in the recirculation zone, hence in those areas there are more bubbles and higher mass transfer of $CO_2$ from liquid phase to vapour phase (i.e. bubbles) can occur. This might have a positive effect as it enhances mass transfer (as more bubbles mean higher gas–liquid interface area); however, the drawback in this geometry is less driving force for mass transfer. Once we complete the last coupling interface in the next report, this aspect can be studied further to clarify the full picture.
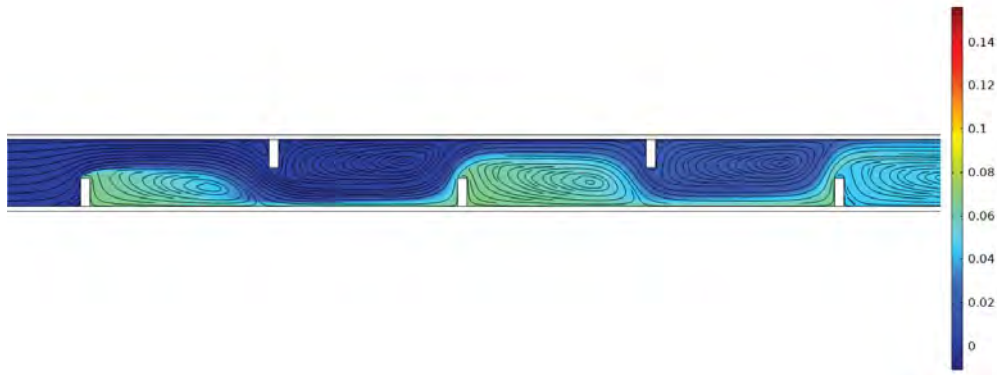
**Figure 164: Cumulative bubble volume fraction along 1 m So-St when the CO₂ bubble concentration at the bottom is 0.1 kg/m³. The streamlines represent flow direction.**

## 10.1.7  Aspen model validation

It is important at this stage to validate the Aspen model we have developed in this report. This is because the detailed COMSOL model requires intensive computer power, and thus is not always suitable for process optimisation and sensitivity analysis. In the current report, we can only validate the Aspen flow boiling result which gives vapour fraction accumulation along So-St, but not the chemical and thermodynamic results. Figure 165 shows the vapour fraction accumulation along a So-St for water flow only. This is because as shown in Figure 158, the coupling interface between the two major groups of physical phenomena has not yet been completed. The Aspen model agrees very well with the COMSOL model. Since boiling is a macroscale phenomenon (e.g. we can observe the boiling effect), we may conclude the Aspen model is sufficient to present a realistic So-St system.
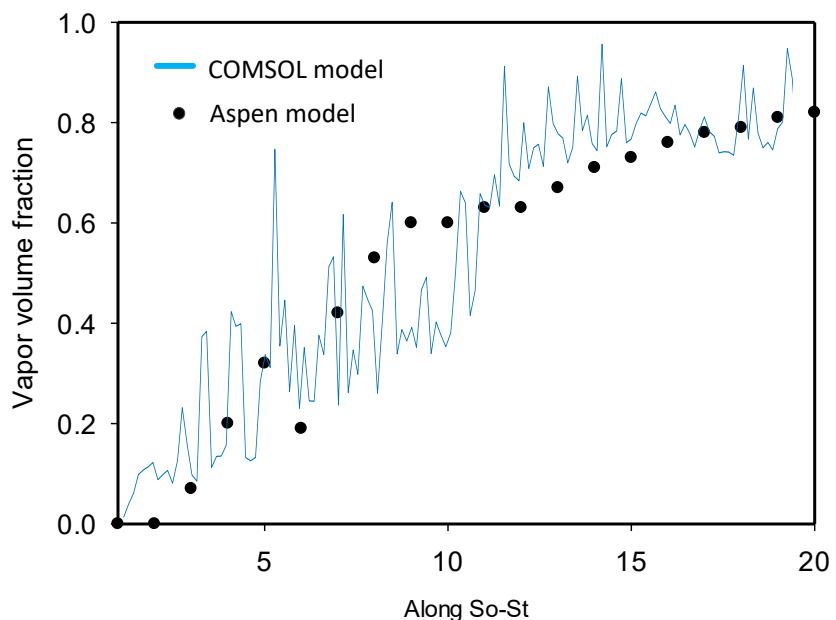


**Figure 165: Flow boiling simulation for water only. The So-St was normalised and divided into 20 equal sections. The So-St length in COMSOL is 1 m while in Aspen model it is 15 m; the shorter length in COMSOL is because we increased the heat flux by about 13 times so we can observe the evolution of vapour fraction and the flow regime in a reasonable computation time.**
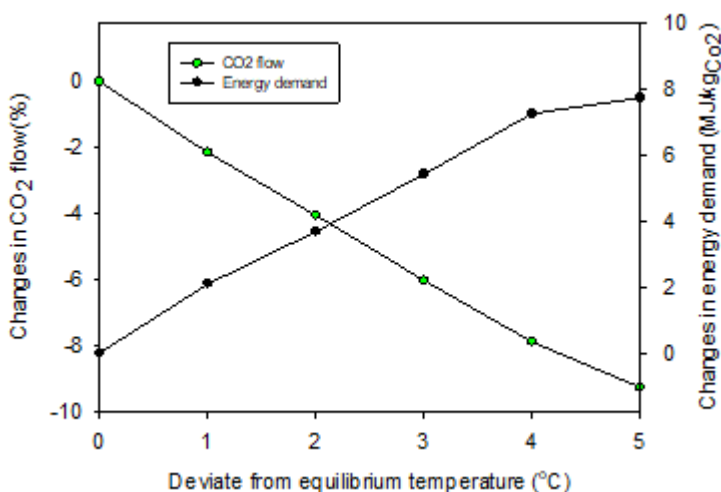
**Figure 166: Changes in CO₂ flow rate in vapour at the exit of the final So-St segment and energy demand when in practical application and the system is not at equilibrium at the solvent temperature. The equilibrium temperature is set to deviate from 120°C. For example, when temperature is 120°C but the equilibrium deviation is 1°C, then the solvent conditions are established as if it is only at 119°C. If the equilibrium deviation is 0°C, the solvent conditions are established as if it is only at 120°C.**

The uncertainty in the Aspen model when predicting thermodynamic and chemical equilibria deserves further analysis. The Aspen model assumes that at any point along a So-St, all species in vapour and liquid phases are in equilibrium, but in fact they might not be in equilibrium. To sensitise the effect of deviation from equilibrium, we have performed Aspen model simulations with different extents of deviation from the equilibrium temperature. For example, when the system is at 100°C, Aspen assumes the system is in equilibrium at 100°C, but in reality, the system established equilibrium at 90°C. The result is shown in Figure 166. It can be seen that when the system is not at equilibrium of the solvent temperature, $CO_2$ productivity drops and energy demand increases almost linearly. The drops in $CO_2$ productivity are not significant. These results suggest that in real application, even when the system is not at equilibrium as predicted by Aspen, the outcomes are not severe and still curable (e.g. changing the flow rate etc.). If the next phase of this project would involve experimental work, we can work out a correction factor to account for temperature deviation. This practice is widely used for many industrial processes, e.g. in distillation column design, a common practice when calculating the number of trays is to double the number of equilibrium trays. From the above discussion, we may conclude that the Aspen model is appropriate to use for analysing the effect of variation in solar supply.

In summary, we developed a modelling framework to build a rigorous So-St model for studying micro-scale phenomena, e.g. bubble nucleation and chemical reaction. We discretised a So-St segment into smaller control volumes and describe physical-chemical phenomena per volume using sets of equations. The software COMSOL Multiphysics was used as a modelling tool to execute the equations. The So-St model comprises different modules, e.g. thermodynamic and tracking of vapour–liquid interface. The model was also validated with some literature data and Aspen model's results. Using the COMSOL model, we have shown the use of physical inserts (e.g. packing) in the So-St tube can induce significant liquid mixing, and thus can result in higher heat transfer. The outcomes from this study encouraged us to pursue a new direction in CFD to ultimately be able to reduce SCF size.

## 10.2    Appendix B – Summary figures for impact categories in the LCA



water depletion (WDP)



terrestrial acidification (TAP100)



ionising radiation (IRP_HE)



photochemical oxidant formation (POFP)



human toxicity (HTPinf)



ozone depletion (ODPinf)



marine ecotoxicity (METPinf)



terrestrial ecotoxicity (TETPinf)



marine eutrophication (MEP)
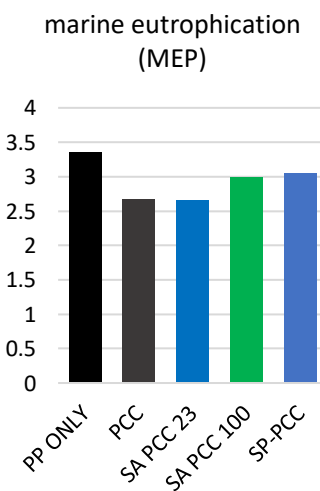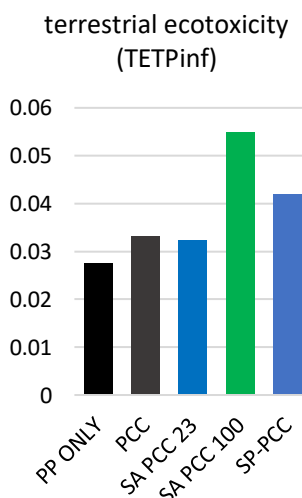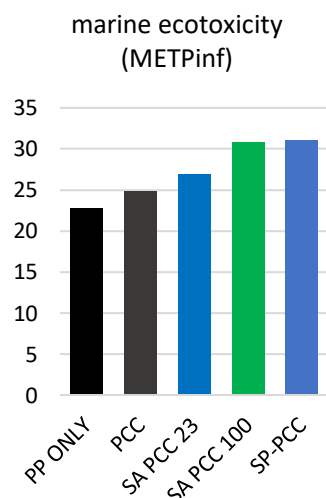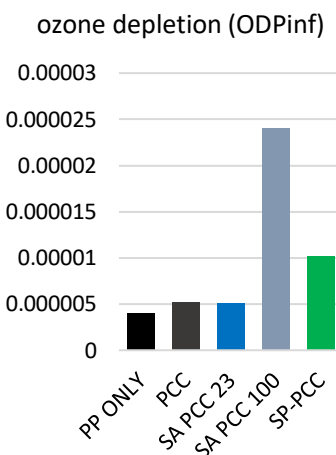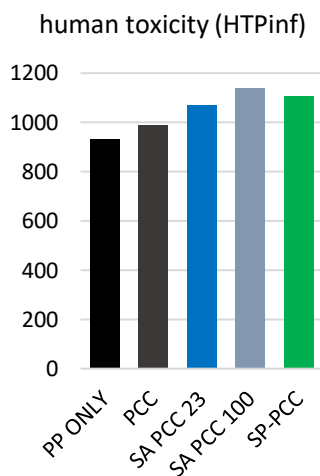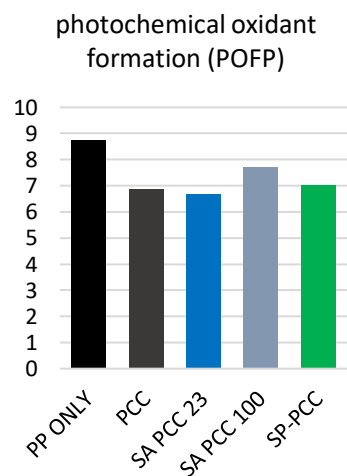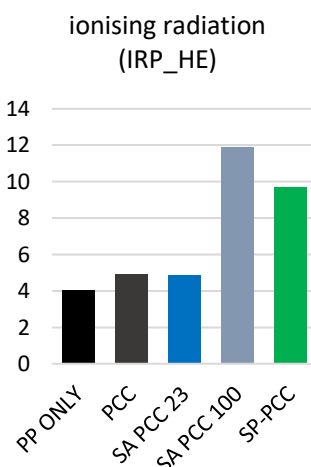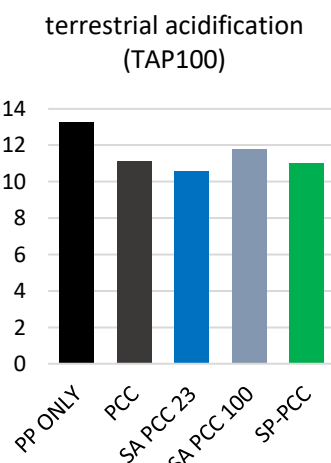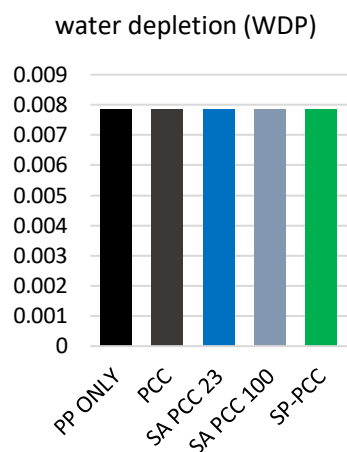
## freshwater ecotoxicity (FETPinf)
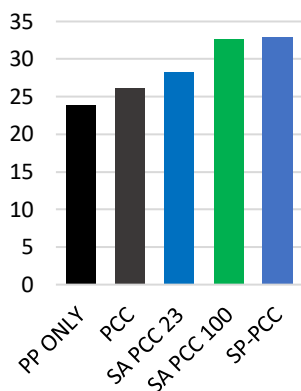
## freshwater eutrophication (FEP)
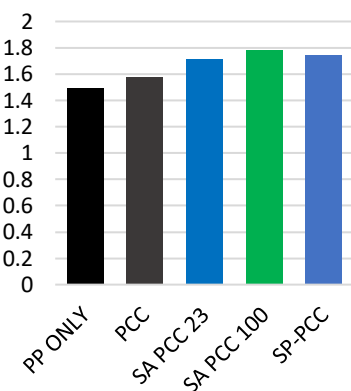
## particulate matter formation (PMFP)
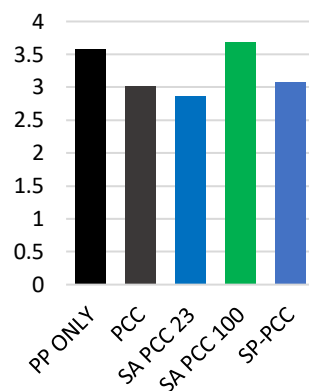
## 10.3    Appendix C – Research outputs from this project

**Journal articles & conference proceedings**

|   | Title | Journal/publisher | status |
|---|-------|-------------------|--------|
| 1 | Tailored solar field and solvent storage for direct solvent regeneration: A novel approach to solarise carbon capture technology | Applied Thermal Engineering/ Elsevier | Published |
| 2 | Analysis for a solar stripper design for carbon capture under transient conditions | International Journal of Heat and Mass Transfer/ Elsevier | Published |
| 3 | Techno-economic analysis of 'solar-powered' post-combustion carbon capture | GHGt-15/ SSRN | Published |
| 4 | Transforming the desorption unit in carbon capture technology through a novel solar driven process | Chemeca 2020 | Published |
| 5 | A CFD study of a direct solar-driven desorption process for carbon capture under transient conditions | Sustainable Energy Technologies and Assessments/ Elsevier | Published |
| 6 | A novel design protocol for solar-powered carbon capture | Thermal Science and Engineering Progress/ Elsevier | Published |
| 7 | Process control expert system for solar-powered carbon capture under transient solar conditions | Energy the International Journal/ Elsevier | Under-review |
| 8 | Solar-Powered PCC: An Upfront Levy for Sustainable Carbon Capture | International Journal of Greenhouse Gas Control/ Elsevier | Under-review |

**Conferences**

|   | Title | Journal/publisher | status |
|---|-------|-------------------|--------|
| 1 | A novel process automation and control to solarize carbon capture technology | IEAGHG 5th Post Combustion Capture Conference (PCCC-5) | presented |
| 2 | Transforming the desorption unit in carbon capture technology through a novel solar driven process | Chemeca 2020: Renew, Sustain, Disrupt, Advance | presented |
| 3 | Techno-economic analysis of 'solar-powered' post-combustion carbon capture | 15th International Conference on Greenhouse Gas Control Technologies (GHGT-15) | presented |
| 4 | Solar-powered carbon capture: the way forward | The 2nd Asia Pacific International Conference on Industrial Engineering and Operations Management | Future dated 15/9/2021 |
| 5 | A comparative LCA for solar-powered PCC to unlock the potential of steam preservation for power production only | IEAGHG 6th Post Combustion Capture Conference (PCCC-6) | Future dated 19/10/2021 |

## 10.4    Appendix D – Special Acknowledgment

The authors would like to thank the listed people from different organisations for providing support, advice, and administration services throughout this project.

| Name | Position | Organisation |
|---|---|---|
| Dr. Paul Feron | Science leader/ Group Leader | CSIRO |
| Dr. Graeme Puxty | Principal research scientist / Team leader | CSIRO |
| Dr. Hai Yu | Principal research scientist / Team leader | CSIRO |
| Dr. Merched Azzi | Former Group Leader | CSIRO |
| Dr. Robbie McNaughton | Former Team Leader | CSIRO |
| Dr. Mehdi Aghaei Meybodia | Research Scientist | CSIRO |
| Ann-Maree Doughty | Finance & Projects Advisor | CSIRO |
| Astrid Soiland | Contract Manager | CSIRO |
| Dr. Alejandro Montoya | Associate Professor | The University of Sydney |
| Hanan Mohsin | Engineering Graduate | The University of Sydney |
| Yiqing Liu | Student | The University of Sydney |
| Dr. James Knight | Senior Project Officer | Coal Innovation NSW |
| Tully Matthews | Acting Manager Coal Innovation | Coal Innovation NSW |
| Alice Van Tilburg | Assistant Project Officer | Coal Innovation NSW |
| Lewis Brent | Project Officer | Coal Innovation NSW |

# 11.  Sign-off

I, the undersigned, being a person duly authorised by the Grantee, certify that:

(a) the above information is true and complete;

(b) the expenditure of the Funding received to date has been solely on the Project; and

(c) there is no matter or circumstances of which I am aware, that would constitute a breach by NSW Department of Planning, Industry and Environment or, if applicable the End Recipient, of any term of the Funding Agreement between NSW Department of Planning, Industry and Environment and the Grantee dated [insert date] that has not been notified by the Grantee.

Signature:

Name: Dia Milani

Position: Research Scientist - CSIRO

Date: 10/09/2021